

On the Role of Doubly-Diffusive Mixing in Low-Mass Red Giant Branch Stars

George Christopher Angelou

BSc (Hons)

A thesis submitted for the degree of Doctor of Philosophy.

Monash Centre for Astrophysics,
School of Mathematical Sciences,
Monash University, Australia.

May 2014

Per aspera ad astra

De Omnibus Dubitandum

Contents

Declaration	ix
Abstract	xiii
Acknowledgements	xiv
Publications	xvii
Preface	xix
My Motivation	xix
Why Study Stars?	xix
The Importance of Stars in Astrophysics	xxiii
The Importance of This Study	xxvi
Outline	xxviii
I Introduction	1
1 Background	3
1.1 Low-Mass Stellar Evolution	3
1.1.1 Evolution Prior to the Core Flash	4
1.1.2 Post-RGB Evolution	10
1.2 The Globular Cluster C-N Anticorrelation	13
1.2.1 The Evidence for Extra Mixing	13
1.2.2 The Evidence for Multiple Populations	19
1.2.3 The Chemical History of Globular Clusters	24
2 Extra Mixing Mechanisms	25
2.1 Overview	25
2.2 The Goldreich-Schubert-Fricke Instability	28
2.2.1 The Development of ‘Blob Theory’	30
2.3 Doubly-Diffusive Mixing	35
2.3.1 Stability	35
2.3.2 Oceanographic History	36
2.3.3 Fluid Stability Analysis	38
2.4 Doubly-Diffusive Mixing in Stars	50
2.4.1 Semi-Convection	51
2.4.2 Thermohaline Mixing (Ulrich 1972)	54
2.4.3 Thermohaline Mixing (Kippenhahn et al. 1980)	58
2.4.4 Stellar Stability Criteria	60

2.4.5	The Red Giant Branch Instability	62
2.5	Summary	71
2.5.1	Linear Theory	72
2.5.2	Stellar Theory	73
II	Numerical Modelling	75
3	The Evolution Code	77
3.1	Overview of the Monash Codes	77
3.2	Overview of the Stellar Evolution Code	78
3.2.1	The Equations of Stellar Structure	78
3.2.2	The Numerical Scheme	80
3.2.3	The Input Physics	80
3.2.4	The Mixing Algorithm	82
3.2.5	The Meshing Routine	87
3.3	Changes to the Stellar Evolution Code	87
3.3.1	Thermohaline Mixing	89
3.3.2	The Diffusion Equation Solver	91
3.3.3	The Meshing Routine	95
3.3.4	New Species	96
3.3.5	The Equation of State	99
3.3.6	MONSTAR_GRID	99
3.4	Summary	101
4	The Nucleosynthesis Code	103
4.1	Overview of the Nucleosynthesis Code	103
4.1.1	The Nuclear Network	104
4.1.2	The Meshing Routine	104
4.1.3	The Mixing Algorithm	106
4.1.4	The Numerical Scheme	111
4.2	Changes to the Code	115
4.2.1	Thermohaline Mixing	115
4.2.2	Meshing Routine	115
4.2.3	Initial Abundances	116
4.3	Summary	117
III	Application to Globular Clusters	119
5	Calibrating Thermohaline Mixing in the Archetypal Globular Cluster, NGC 5272 (M3)	123
5.1	Introduction	123
5.2	The Formula for the Diffusion Coefficient	125
5.3	Models and Results	127
5.4	Modeling the Globular Cluster M3	132
5.5	Mass Loss	138

5.6	The Onset of Mixing	139
5.7	Conclusions	139
6	The Role of Thermohaline Mixing in Intermediate- and Low-Metallicity Globular Clusters	145
6.1	Intermediate metallicity: M3 and M13	145
6.2	Low Metallicity	149
6.2.1	NGC 5466	149
6.2.2	M92	150
6.2.3	M15	154
6.3	Discussion	155
6.3.1	Comparison Across Metallicity	155
6.3.2	The Inconsistency at Low Metallicity	158
6.3.3	The Role of Thermohaline Mixing	158
6.4	Conclusions	161
7	The Globular Cluster Na-O Anticorrelation	163
7.1	Introduction	163
7.2	The Oxygen-Sodium Anticorrelation	165
7.2.1	M15, M92 and NGC 5466	165
7.2.2	M3 and M13	166
7.3	Resurrecting the Deep Mixing Scenario	166
7.4	Calculations and Results	169
7.4.1	Structure and Evolution	169
7.4.2	Nucleosynthesis	175
7.4.3	Discussion	178
7.5	Conclusions	180
IV	Lithium in Globular Cluster Stars	181
8	Lithium abundances in globular cluster giants: NGC 6218 (M12) and NGC 5904 (M5)	185
8.1	Introduction	185
8.2	Observations, data reduction and analysis	188
8.2.1	Error budget	191
8.3	Results and Discussion	194
8.3.1	NGC 6218 (M12)	194
8.3.2	NGC 5904 (M5)	200
8.3.3	The Li spreads in GCs	208
8.4	Summary and concluding remarks	211
9	Diagnostics of Mixing in Globular Cluster Red Giant Branch Stars	215
9.1	Introduction	215
9.2	Overview of the Stellar Models	217
9.3	Observations of Lithium in Globular Clusters	219

Declaration

I hereby declare that this thesis entitled *On the Role of Doubly-Diffusive Mixing in Low-Mass Red Giant Branch Stars* contains no material which has been accepted for the award of any other degree or diploma in any university or other institution. To the best of my knowledge, this thesis contains no other material previously published or written by any other person except where due reference is made in the text. Those parts of this thesis which have been published or accepted for publication and to which the author made a significant contribution are as follows:

- Material from Chapters 1, 5 and 6 was published as: Angelou, G. C., Church, R. P., Stancliffe, R. J., Lattanzio, J. C., and Smith, G. H. (2011). Thermohaline Mixing and its Role in the Evolution of Carbon and Nitrogen Abundances in Globular Cluster Red Giants: The Test Case of Messier 3. *The Astrophysical Journal*, **728**:79 and was completed in collaboration with these authors.
- Material from Chapters 1 and 6 was published as: Angelou, G. C., Stancliffe, R. J., Church, R. P., Lattanzio, J. C., and Smith, G. H. (2012). The Role of Thermohaline Mixing in Intermediate- and Low-metallicity Globular Clusters. *The Astrophysical Journal*, **749**:128 and was completed in collaboration with these authors.
- Material from Chapters 1 and 7 was published as: D’Orazi, V., Lucatello, S., Lugaro, M., Gratton, R. G., Angelou, G., Bragaglia, A., Carretta, E., Alves-Brito, A., Ivans, I. I., Masseron, T., and Mucciarelli, A. (2013). Fluorine Variations in the Globular Cluster NGC 6656 (M22): Implications for Internal Enrichment Timescales. *The Astrophysical Journal*, **763**:22 and was completed in collaboration with these authors.
- Material from Chapter 8 has been submitted as: D’Orazi, V., Angelou, G. C., Gratton, R. G., Lattanzio, J. C., Bragaglia, A., Carretta, E., Lucatello, S., and Momany, Y. (2014). Lithium Abundances in Globular Cluster Giants: NGC 6218 (M12) and NGC 5904 (M5) and was completed in collaboration with these authors.
- Material from Chapter 9 is to be submitted as: Angelou, G. C., D’Orazi, V., Constantino, T., Church, R. P., Stancliffe, R. J., and Lattanzio, J. C., (2014). Diagnostics of Mixing in Globular Cluster Red Giant Branch Stars and was completed in collaboration with these authors.


George Christopher Angelou
Monash University, August, 2014.

PART A: General Declaration

Monash University

Declaration for thesis based or partially based on conjointly published or unpublished work

General Declaration

In accordance with Monash University Doctorate Regulation 17.2 Doctor of Philosophy and Research Masters regulations the following declarations are made:

I hereby declare that this thesis contains no material which has been accepted for the award of any other degree or diploma at any university or equivalent institution and that, to the best of my knowledge and belief, this thesis contains no material previously published or written by another person, except where due reference is made in the text of the thesis.

This thesis includes two original papers published in peer reviewed journals and two unpublished publications. The core theme of the thesis is mixing in red giant branch stars. The ideas, development and writing up of all the papers in the thesis were the principal responsibility of myself, the candidate, working within the School of Mathematical Sciences under the supervision of Professor John Latanzio.

The inclusion of co-authors reflects the fact that the work came from active collaboration between researchers and acknowledges input into team-based research.

Thesis Chapter	Publication Title	Publication Status	Nature of Candidate's Contribution
5	Thermohaline Mixing and its Role in the Evolution of Carbon and Nitrogen Abundances in Globular Cluster Red Giants: The Test Case of Messier 3.	Published	Primary research and paper writing (80%)
6	The Role of Thermohaline Mixing in Intermediate- and Low-metallicity Globular Clusters.	Published	Primary research and paper writing (70%)
8	Lithium Abundances in Globular Cluster Giants: NGC 6218 (M12) and NGC 5904 (M5).	Submitted	Secondary research and significant paper writing (30%)
9	Diagnostics of Mixing in Globular Cluster Red Giant Branch Stars.	Submitted	Primary research and paper writing (80%)

In the case of chapters five, six, eight and nine my contribution to the work is stated in the above table.

I have renumbered sections of submitted or published papers in order to generate a consistent presentation within the thesis.

Candidate's
Signature _____



Date 28-Aug-2014 _____

Copyright Notice

Under the Copyright Act 1968, this thesis must be used only under the normal conditions of scholarly fair dealing. In particular no results or conclusions should be extracted from it, nor should it be copied or closely paraphrased in whole or in part without the written consent of the author. Proper written acknowledgement should be made for any assistance obtained from this thesis.

I certify that I have made all reasonable efforts to secure copyright permissions for third-party content included in this thesis and have not knowingly added copyright content to my work without the owner's permission.

Abstract

The purpose of this thesis is to investigate mixing in red-giant stars. Thanks particularly to the observations of globular clusters, it is clear that that standard stellar evolution fails to reproduce measured stellar abundances as a function of (red giant branch) luminosity. The empirical data has demonstrated that theorists are missing vital physics in their codes during this phase of evolution. Solutions to this problem have been postulated for many decades now, with mechanisms attributed (but not limited) to rotation, magnetic fields or internal gravity waves. A recently suggested instability, namely thermohaline mixing, serves as the focus of this investigation. It is caused by the competition between heat and chemical diffusion and is only possible due to the unique conditions following dredge-up events. Using observations of lithium and carbon we determine whether this mechanism and/or its current parameterisation can influence the surface composition of red giant branch stars. The quality of the data collected from the Very Large Telescope in Chile, some of which is gathered from our own observing programs, allows us to further constrain the mixing process(es) involved and improve the stellar models.

Acknowledgements

No matter what direction the rest of my life takes me in, I will always have the honour of having completed a Ph.D. under Professor John Charles Lattanzio. I wish to thank him for his guidance, patience, generosity and friendship over the years. I have no idea why he agreed to take me on as a student. When I began as a research assistant it wasn't clear that his investment would be rewarded. I am not sure if he spent much time thinking about his decision but the result has meant the world to me. Because of him, I have been able to complete a life-long dream for which I owe him a debt of gratitude.

It is not just his role during my formal education that I am thankful for. I have become accustomed to a professor's lifestyle even though I survive on a student's wage. It's amazing how humble a wardrobe I am willing to endure if it means there is money to spend on good food and alcohol. I have learnt to appreciate many new wine varietals under his tutelage, and his most damaging act of his kindness was no doubt introducing me to cognac.

My time at Monash has been filled with many experiences that can be traced back to the generosity of John. For a kid who comes from along line of fishermen, farmers and priests, visiting the U.S. national labs, flying business class around the world, going to The Royal Enclosure at Ascot to see Black Caviar, giving a presentation in the very library where Einstein and Eddington discussed relativity and attending the Founder's Feast at Churchill College were beyond my wildest dreams. John's reach and generosity making all this and more possible. Having said that, wine dinners as well as port and cheese with JL, Joy and the many guests that came to visit will remain my fondest memories.

I am truly sad to be leaving Monash and such a great mentor. His academic credentials speak for themselves. His students always leave equipped to succeed in their next endeavour, whether it be astronomy related or not. He is much loved by members of the community and its not hard to see why. He has had an immeasurable impact on the person I am and he will remain someone whose opinion I respect greatly. Thanks for everything professor.

Richard Stancliffe and Ross Church, Ross Church and Richard Stancliffe. It seems unfair to talk about one before the other as both have played an equally vital role in my development as an astronomer. My two associate supervisors were often on the front lines dealing with misconceptions, false positives, rookie mistakes and debugging. They are kind, brilliant, quintessentially British (which is novel for Australians!) and have served as great role models. They may not know this, but they made me realise how far I had to go and how much harder I would need to work to just to get to par in this field. Thanks for your help, patience and belief along the way.

I want to thank my family, the Angelou clan. I love my family dearly. My sisters, parents and I are very close and it will be difficult to leave. I am lucky to have had such a supportive environment in which I could pursue my studies. Always having a bed or a home-cooked meal close to Monash made things so much easier. The opportunities for higher education were only possible through the life my parents set up here and for that I thank them. They have always been

supportive of me and encouraged me to study whatever makes me happy. Thank you for putting up with me for much longer than you really needed to. Thank you to my sisters who have always been very loving and brave no matter what we have been faced with. I am very proud of you both.

I want to thank the students and staff at MoCA and the Mathematics Department. Thanks to Maria for always having wise advice when I needed it. Afternoon tea with Carolyn was a compulsory affair that broke up the day. If I was ever worried about something, she had the calming words that I needed to hear. Simon always made time to answer any questions I had - no matter how busy he was. His thesis is the subject of legend at Monash and set a standard for us later students to strive towards. I have learnt a tremendous amount from Valentina. I am a better scientist having collaborated with you and finding out about your weekend adventures was always a highlight! Thank you to Hamed who encouraged me to apply for work in Göttingen, and for his warm demeanour, friendship and helpful advice throughout my time at Monash. To Stuart, Tom, Joelene, Kate and Athira I hope your candidature is enjoyable as mine was. I wish to also thank Alex, Gertrude, Gareth, Trent Duncan, Dave Halliwell, Andrew Prentice, and the admin staff for always being there for a chat and to lend a helping hand.

There are many great scientists that I have been lucky enough to meet and become good friends with. Many thanks to Amanda Karakas, Jarrod Hurley, Rob Izzard, Marco Pignatari, Shравan Hanasoge, Brad Gibson, Christian Iliadis, Hans Van Winkel, Sergio Cristallo, Pillar Gil Pons, Graeme Smith, Gayandhi De Silva and Sarah Martell who have been extremely kind to me and helpful in their discussions. Lionel Siess, Sandro Chieffi and Christopher Tout I have turned to more than most and wish to acknowledge their influence. Thanks especially to Chris for hosting me at Cambridge, you live the dream!

I have many friends and family who I wish to thank and the list would be too long if I named you all. Thank you to those people in my life who have always been there for me. I wish to acknowledge the gentlemen at Vandelay Industries who remain like brothers to me. There have been times that I keeled over laughing because of our escapades and I have very much enjoyed the company of those from Dunder Mifflin who have come into the fold.

Finally, I want to thank the most kind hearted person I have ever met. Bianca Festa, I love you and want to thank you for helping me to remain (relatively) sane through my Ph.D. Weekends with you, striking a balance between work and life, have been essential to me staying motivated and having a refreshed mind when returning to the thesis. I know timescales have been uncertain over the last few years and for that I apologise. Thank you for being so supportive and understanding. You have made a lot of sacrifices so that I can continue with astronomy and I can't wait for the adventures that now await us.

Publications

Accepted

1. Campbell, S. W., D’Orazi, V., Yong, D., Constantino, T. N., Lattanzio, J. C., Stancliffe, R. J., Angelou, G. C., Wylie-de Boer, E. C., and Grundahl, F. (2013). Sodium content as a predictor of the advanced evolution of globular cluster stars. *Nature*, 498:198–200
2. D’Orazi, V., Lucatello, S., Lugaro, M., Gratton, R. G., Angelou, G., Bragaglia, A., Carretta, E., Alves-Brito, A., Ivans, I. I., Masseron, T., and Mucciarelli, A. (2013b). Fluorine Variations in the Globular Cluster NGC 6656 (M22): Implications for Internal Enrichment Timescales. *ApJ*, 763:22
3. Angelou, G. C., Stancliffe, R. J., Church, R. P., Lattanzio, J. C., and Smith, G. H. (2012). The Role of Thermohaline Mixing in Intermediate- and Low-metallicity Globular Clusters. *ApJ*, 749:128
4. Campbell, S. W., Yong, D., Wylie-de Boer, E. C., Stancliffe, R. J., Lattanzio, J. C., Angelou, G. C., D’Orazi, V., Martell, S. L., Grundahl, F., and Sneden, C. (2012). Cyanogen in NGC 1851 Red Giant Branch and Asymptotic Giant Branch Stars: Quadrимodal Distributions. *ApJ*, 761:L2
5. Angelou, G. C., Church, R. P., Stancliffe, R. J., Lattanzio, J. C., and Smith, G. H. (2011). Thermohaline Mixing and its Role in the Evolution of Carbon and Nitrogen Abundances in Globular Cluster Red Giants: The Test Case of Messier 3. *ApJ*, 728:79–+
6. Stancliffe, R. J., Church, R. P., Angelou, G. C., and Lattanzio, J. C. (2009). The depletion of carbon by extra mixing in metal-poor giants. *MNRAS*, 396:2313–2318
7. Angelou, G. and Lattanzio, J. (2008). A Small Step on the Long Road to Understanding the R Stars: CNO Cycling in Candidate R Star Progenitors. *Publications of the Astronomical Society of Australia*, 25:155–160¹

¹Published prior to candidature

Submitted and In Preparation

1. Angelou, G. C., D'Orazi, V., Constantino, T., Church, R. P., Stancliffe, R. J., and Lattanzio, J. C., (2014). Diagnostics of Mixing in Globular Cluster Red Giant Branch Stars.
2. D'Orazi, V., Angelou, G. C., Gratton, R. G., Lattanzio, J. C, Bragaglia, A., Carretta, E., Lucatello, S., and Momany, Y. (2014). Lithium Abundances in Globular Cluster Giants: NGC 6218 (M12) and NGC 5904 (M5).
3. Church, R. P., Lattanzio, J. C., Angelou, G. C., Tout, C.A., Stancliffe, R. J., (2014). Which Physics Determines the Location of the Mean Molecular Weight Minimum in Red Giants?
4. Lattanzio, J. C., Siess, L., Church, R. P., Angelou, G. C., Doherty, C. L., Stephen, T., Stancliffe, R. J., Campbell, S. W., (2014) . On the Numerical Treatment and Dependence of Thermohaline Mixing in Red Giants.

Preface

My Motivation

Nothing is so conducive to greatness of mind as the ability to subject each element of our experience in life to methodical and truthful examination, always at the same time using this scrutiny as a means to reflect on the nature of the universe.

- Marcus Aurelius

“It is impossible for someone to dispel his fears about the most important matters if he doesn’t know the nature of the universe but still gives some credence to myths. So without the study of nature there is no enjoyment of pure pleasure.”

- Epicurus

Why Study Stars?

“Why waste your time studying stars? They have no effect on our everyday lives. What is the point?” Many a time I have been expected to defend my profession and its usefulness to society. I usually fumble around the topic or try to change the subject because it is obvious from the tone in which the question is asked, that the provocateur has no intention of considering a balanced argument. I wish I could answer this question in a manner that is satisfying to those who subscribe to the tenets of economic rationalism. But there lies the crux of the issue. Not everyone believes in the same value system. Everybody has a measure of self worth; the scale by which a person judges themselves. As we do not judge by the same criteria, it sometimes renders the actions of others curious or inexplicable. For some of my friends, it is difficult to comprehend that I do not measure my wealth in material gain. So why study stars? Simply put, some of us are compelled to, not just study the stars, but nature, the Universe and the human condition. If you have to ask the question then you will neither understand nor appreciate the answer.

When I think about the Universe, a spectrum of emotions are evoked within. I

am certain that for those who question why we bother studying the stars, pondering the nature of the Universe does not elicit the same response; it is perhaps an uninspiring and underwhelming affair. Scientists are incorrectly stereotyped as being unsentimental, cold and stoic. That their egos thrive on removing all the sense of mystery about the world. Nothing can be further from the truth. The emotions we are accused of lacking are amplified in our musings, reducing the most cynical researchers to childlike wonderment. I remember distinctly when my father told me that our Sun is one of 200 billion in the Milky Way. As I continue to learn new things about the Universe, I am still consumed by the same feeling of awe. These emotions are not fleeting, nor fickle, they do not come back any weaker on subsequent occasions. Some 20 years later, when I first gazed upon the Hubble Ultra-Deep Field, I was that five-year-old boy again. I wish I could share these visceral experiences with others to make them understand why I choose to study the stars but the exercise is futile. It would be like someone proclaiming to me that these emotions can only truly exist by opening my heart to the divine.

With new-age luxuries and social pressures it is easy to become distracted and for society's priorities to change. To this end, money has become the be all and end all in the modern world. If you cannot make someone a lot of money from a profession or see an immediate return on investment then what is the point? Before answering that, let us not forget that every great civilization studied the heavens in one way or another. Based on their immediate experiences, they crafted an understanding of how the world around them worked. They tried to determine how the Universe came into being and how it might end. The societies of the Middle East, having to endure the harshness of the desert, predicted our end in an Apocalypse by fire. In the face of long dark winters, the great Nordic nations foresaw our demise in the form of a frozen wasteland. Through some great fluke of nature we acquired the ability to communicate with each other and to partake in abstract thought. The gift of consciousness inspired these existential questions in our earliest ancestors; nearly all recorded societies have such myths and thus, these questions are inherent to human nature. Thankfully, despite the distractions, some vestige of this original curiosity remains and many people today still seem genuinely interested in astronomy.

Although too abstract and idealist for some, there are important anthropological reasons for studying the stars. It is often overlooked that astronomy, and in fact all research, adds value to our culture. A dynamic and evolving culture is one of the cornerstones of any society. One might as well ask what use are books, music or any form of art if: a) You don't like them b) You don't understand them c) They are not popular enough to make a lot of money. Yet the same could be asked of jobs that serve no other purpose than to keep people employed. Not all forms of endeavour appeal to every individual equally, but through this diversity we are able to learn about ourselves and our humanity. I am reassured that there is someone, somewhere adding to a particular aspect of knowledge that I may not think about or be able to contribute to. I am just as glad that there is someone, somewhere playing music in a style that I do not appreciate. This helps society and its many sub-cultures form an identity. It exists to make us question ourselves, reflect, and rise above our primitive instincts. Our culture allows us to frame fun-

damental issues such as morality and ethics. It is a measure of how far we have come as a species. For many of us this is why deriving knowledge for knowledge's sake is such a powerful argument. Sadly, it is often not compelling enough for a Government trying to get re-elected and appeal to the self interests of a voting populace. The perception of study taking place in the ivory tower just seems too far removed from 'the real world' and easily portrayed as a common enemy to be pillaged.

At the risk of touting a clichéd response, there are also several concrete arguments for our continual study of the stars, physics and astrophysics alike. With many fields of scientific research, the technological benefits are not always immediate, although over time will become apparent. One only needs to search the internet for NASA spin-off technologies to realise the modern innovations derived from astronomy and space-exploration research. High profile examples include Teflon, GPS satellites and advanced optics, but many contributions are still taken for granted by society at large. Objects such as stars and active galactic nuclei allow scientists to study physics in the most extreme of environments and may, in future, lead to technologies that shape our everyday lives (e.g., harnessing of nuclear fusion). Faraday and Maxwell did not justify their research by promising to provide electricity to every home. Today's most popular forms of entertainment-TV, radio and mobile phones (the very mediums idolised by the masses), were not invented without prior knowledge of physics. They were only possible once physicists understood the electromagnetic spectrum. Medical instruments that are standard in today's hospitals (e.g., MRI scanners) only exist because of pioneers like Zeeman who were interested in the behaviour of subatomic particles in the presence of a magnetic field.

Another method to measure the sophistication of a civilisation is through its ability to colonise. When looking through human history, the speed of transport and frontiers of exploration are a good indication of the relative technological capabilities at the time. Hunter-gathers were able to move as fast as their legs could carry them, agrarian societies invented the wheel and used horses for transport, the industrial revolution was characterised by the steam engine and the modern age by rockets and jet engines. Few cynics oppose technological advancement and innovation. In order to progress, we must explore new frontiers whilst reducing the time taken to travel the growing distances. A new age will begin once we set foot on another planet and, further into the future, again when we probe other solar systems. If we wish to follow our innate desire to explore, we will need to develop technology that goes beyond regular chemical propulsion. The vast distances between stars renders interstellar travel too lengthy with current technology. For those that deem astronomy related research a waste of money, the need to travel further and faster clearly has applications to defence and commercial transport. The technologies that will fly us from Melbourne to London in three hours will be based on those used to launch exploratory satellites and probes.

With all the injustice and uncertainty that exists in the world it may seem like folly to look too far into the future. But without long term planning and the ability to consider large threats we have learnt nothing from history. We must always have one eye on the ultimate survival of the human race. This seems like a

fantasy given that most people are too selfish to even tackle climate change. The Earth will not remain habitable forever. For many people this problem is so far into the future that it is barely worth considering and definitely not worth any change to their lifestyle. Even though our closest neighbour, Venus, is a stark reminder of a runaway greenhouse, the dangers seem too remote. Governments are re-elected on a three or four year cycle and most people have scant regard for the Earth's fate beyond their lifetime. Through astronomy and its related disciplines we have learnt what dangers humanity will inevitably have to face. We know what awaits if pollution remains unregulated. The Earth's surface is scarred with evidence of massive asteroid impacts, with the fossil record indicating that extinction level events (where over 90% of life is wiped out) are as cyclical as our orbit around the Galaxy. By studying the Sun and the stars, we have realised that the Earth is ultimately doomed on a nuclear timescale. The Sun will scorch the Earth, evaporating all the water long before it reaches the red giant phase. With the exponential rate at which technology has developed over the last century, and the canny resourcefulness of the human race, these problems are worth considering.

There are currently many exoplanet searches under way, with Kepler and CoRoT revolutionising the field in the duration of my Ph.D. candidature. Their scientific purpose is related to perhaps the biggest question of them all; the creation of life itself. DNA from all living organisms suggests that life has arisen (independently) only once on this planet, that all living things possess a common ancestor some 3.6 billion years ago. These missions aim to find suitable candidate planets that may harbour life. When the technology allows, observations of these targets may reveal life's biosignature. Abiogenesis and the development of consciousness remain two of the most important but least understood questions in science. Is life an inevitable outcome of organised matter? Does it develop wherever it can? Is intelligence and consciousness an evolutionary advantage and frequent in our Galaxy? If evidence of life is found elsewhere, I would hope that it changes our outlook and perspective. I have these grand delusions that such a discovery will make us forget our differences and usher in a new era of co-operation. I am not too naive to know that this is probably unlikely but hopefully it would at least be enough to justify why we study the stars.

Finally, on a personal note I have used the term 'studying the stars' as a metaphor for astronomy and astrophysics in general. While I have outlined above the value of such research, I also wish to convey what I love about stellar evolution in particular, given the diverse field of astronomy. Stellar evolution is one of the most successful fields of astronomy, and we have learnt much in the last century. It is the combination of empirical, theoretical and numerical sciences. It requires an understanding of physics on many different scales. From the quantum tunnelling that allows the Coulomb barrier to be penetrated, to the fluid dynamics of convective cells, to the force of gravity which the gas pressure (mostly) balances. One needs to have at least a basic idea of reaction rates, opacities, equations of state, mixing and turbulence, wave propagation and pulsation, absorption and emission spectra to name but a few. This is in addition to the details of numerical modelling and photometry/spectroscopy/asteroseismology. It provides a motivation and a path to improve as a scientist because it touches upon the many differ-

ent fields of chemistry and physics. How well-rounded one becomes is up to the individual but the impetus is there.

We humans like to think that we are pretty smart, but nature has found ways to generate more power in one second than we have created since the dawn of our existence. Stars, objects hotter than I can imagine, are powered by protons, particles smaller than I can see. They are separated by distances that have no meaning to a hominid crossing the plains of Africa. The temperature of the empty(ish) space between the stars is only 2.7 degrees above the theoretical limit from which you can extract energy from a particle. The lowest-mass stars live as long as the universe, essentially forever as far as human lifetimes are concerned, whilst the most massive stars end their lives as black holes; regions of space where the laws of physics seem to (but may not) break down. When the degenerate remnants of the low-mass stars accrete enough mass to challenge one of the last bastions of pressure support, the quantum mechanical electron degeneracy pressure, they produce explosions that outshine all the stars in their galaxy. These explosions were used to show that the acceleration at which the Universe is expanding is unexpectedly increasing. It has been shown that the total light emitted from stars, and hence the total mass, is not enough to account for the way galaxies rotate. In simple terms, stars have indirectly helped with the inference of dark energy and dark matter. Stars take the most light atoms in the Universe and convert them to the most heavy. Even when the Coloumb barrier gets too large to overcome, they sneakily use charge-less neutrons to create even heavier nuclei. The very atoms that I and everything around me are made from were fused in the interiors of at least two different stars (in reality, probably thousands). As I finish typing this paragraph, billions of almost massless neutrinos, permeating from the core of the Sun, are flying through my body paying no attention to the fact that I am breathing, thinking or even here! Nature has provided me with only modest ability to understand her inner workings. I know that I am but a bug in the ecosystem of science, a minnow in comparison to the giants before me, but I am compelled to press on and learn as much as I can.

The Importance of Stars in Astrophysics

Were it not for the twinkling of the stars, our solar system would appear isolated; an island in an eternal universe. Had we been born in a dense stellar system, say a globular cluster, the light from our millions of nearby neighbours would outshine the distant galaxies. It seems the Earth was formed in a region of space where the light from the stars can truly reveal our cosmic origins. Not only are we in a position to understand the stars around us, but also the large scale structure of the Universe. Humanity only began to untangle this story once we understood the wealth of information contained in starlight.

The true nature of light has been debated throughout human history from Aristotle and Euclid, to Newton, Maxwell and Einstein. Thanks to Einstein's explanation of the photoelectric effect (which won him the 1921 Nobel Prize), it is accepted that light exists as a wave-particle duality. In some instances its behaviour is mathematically described by a wave equation (Maxwell's Equations)

and sometimes as a quantised packet of energy (photon), but thus far it has never been observed to act as both at the same time. The ancient Greeks were well aware of the wave-like properties of light, that it could be reflected and refracted (the former mathematically described by Euclid) but they also knew that it travelled in a straight line; behaviour others later attributed as particle like. The path to modern astrophysics was paved by a gradual understanding of the electromagnetic spectrum. The contribution from Sir Isaac Newton was the first in a string of key discoveries.

When Cambridge closed down as a precaution against the Bubonic Plague, Newton locked himself away in isolation and emerged with theories on calculus, gravitation and optics. His two years in isolation are arguably the most productive period by an individual in scientific history. Newton's most famous body of work, *Philosophiae Naturalis Principia Mathematica*, outlines the foundations of classical mechanics and gravity, but he also made seminal contributions to the study of light and optics. He was quite fond of passing sunlight through prisms; an exercise we now identify as breaking light up into its frequency spectrum. He noted that the component colours did not change even when subsequently reflected, refracted or scattered. He reasoned that that the colours must therefore be intrinsic to the light itself and not generated by the prisms or instruments. Prior to this revelation sunlight was thought to be colourless.

During the 19th century our understanding of electromagnetic radiation was revolutionised. In 1800, William Herschel determined that each component colour of the frequency spectrum corresponded to a different temperature. Herschel used a prism to create a stellar spectrum for which he measured the temperature of each colour. By setting a thermometer beyond the red end of the spectrum, he had intended to measure the ambient temperature of the room. To his shock, the temperature was in fact hotter than measured by the thermometers placed inside the colour spectrum. He had in fact discovered infrared light and correctly concluded that there must exist invisible radiation in the spectrum beyond red light. Over the course of the next century, the full spectrum of electromagnetic radiation was pieced together. By 1815 Wollaston and Fraunhofer had realised that the colours in sunlight did not blend continuously, that discrete bands unexpectedly populated the spectrum. Sixty years later Kirchhoff and Bunsen were able to explain the origin of these dark strips; they are in essence fingerprints from the chemical elements. Each element absorbs light at specific frequencies resulting in discrete strips at predictable locations. The bands could therefore be used to identify the composition of the emitting source. Of course a true understanding of this phenomenon was not possible until the particle like behaviour of light was formulated in the 20th century.

A single stellar spectrum will contain many lines. In order to determine to which element a specific line belongs, a database of chemical fingerprints must be built up. This is done in laboratories on Earth that provide us with a rest wavelength/frequency. Although it is the particle-like behaviour of light that gives rise to the formation of spectral lines, ironically these discrete bands undergo a wavelike frequency shift in the spectra of distant stars/galaxies. This effect was first predicted by Christian Doppler who determined that all waves should

undergo a shift in wavelength depending on the relative motion of the emitting and observing bodies. The classic example, relatable to our every day experience, is that of the siren on an emergency vehicle. The pitch of their siren (sound wave) is perceived to increase as the vehicle approaches then perceived to decrease as it speeds away. The same principle can be applied to light to determine if the target is moving away from us or hurtling towards us. Using the light from distant galaxies Edwin Hubble demonstrated that the recessional velocities of the galaxies increase with their distance from Earth. He determined that the universe was in fact expanding. His work was able to estimate the rate at which the Universe was expanding and for how long it has been doing so (i.e., an estimate of its age). If applied to the stars in the Milky Way, such spectroscopic studies can reveal the presence of extrasolar planets. When I started my undergraduate degree only a handful of extrasolar planets were known. When I started my Ph.D, some 120 systems had been confirmed. Since then, advances in technology and a combination of techniques have led to the discovery of over 1500 extrasolar planet candidates.

It is through a complete understanding of the electromagnetic spectrum (not to mention the development of the microprocessor) that modern astrophysics has flourished. Telescopes now examine the universe in all frequencies of the spectrum, providing clues to its inner workings. Stars are the predominant source of this radiation with details of their birth, death, physical properties and interaction the motivation for many fields of astrophysics. As far as the universe is concerned stars have two distinct roles:

1. They function as massive chemical reactors, converting the primordial hydrogen and helium into heavier nuclei, and
2. They locally increase the entropy of the Universe, whilst the stars themselves become more ordered as they evolve.

To understand these two points we must incorporate knowledge from thermodynamics, electromagnetism, classical mechanics, statistical mechanics, quantum mechanics, relativity, nuclear physics, particle physics, atomic physics and molecular physics.

Analysing the light from distant objects has obviously driven the field of stellar evolution. By placing stars on a diagram of surface temperature and brightness we were able to determine an evolutionary sequence and identify the important internal processes. Stellar evolution theory, in turn, relies on advances in multiple areas of physics. Nuclear reactions, opacities and equations of state are constantly under revision and result in improved models. Knowledge of optics, nuclear transitions and turbulence have a role in the observations that constrain said models. Stellar physics provides the motivation for many areas of nuclear physics, fluid dynamics and numerical modelling research. In some cases, comparing the models to observations is the only real test of the physics we have; the extreme conditions in astrophysical sites are unable to be replicated in Earth-based laboratories.

Not all stars are the same mass, radius, temperature, luminosity, composition and age. The distributions of stellar populations throughout time are key probes of the evolution of galaxies. As galaxies get older, they change morphology due

to the rate at which they form stars. The star formation rate provides insight into the chemical history of the Milky Way and determines how galaxies are built. Stars like to form in associations, with most stars in binary systems. They clump together in galaxies, and galaxies like to clump together in clusters. By studying the way galaxies rotate as well as the large scale structure of the Universe, we have inferred the existence of dark matter. When we apply spectroscopy to the diffuse star light from distant galaxies, the shifting of the spectral lines can reveal the rate of expansion of the Universe and a means to constrain its age. Supernova explosions from degenerate stellar objects in distant galaxies have helped constrain cosmology and divulged the acceleration of the Universe.

Spectroscopy, as well as photometry (brightness) studies in our own Galaxy provide us with the abundances of numerous stars. In addition their temperature, brightness, surface gravity, magnetic field strength, rotation rates and recessional velocities can all be determined. If the stars are close enough, and our instruments sensitive enough, we can detect the existence of extrasolar planets and infer information about these solar systems, many of which clearly do not have the same history as our own. Oscillations in the stellar brightness can also be used to probe the internal structure, revealing the hidden layers.

Since the dawn of civilisation the stars have captured the imagination of those who have looked up. Heroic legends and grand villains are immortalised in the constellations. Man has always looked to draw meaning from the stars, and now we understand that their light does indeed tell a story; the history of our universe. By collecting and analysing the electromagnetic radiation from distant stars we know what exotic objects are out there. We are able to simultaneously look into our past and into our future. The door to the Universe has been opened, allowing us to answer some of the most fundamental questions about our origins.

The Importance of This Study

It is claimed that much of stellar evolution is well understood. The advent of computers made it straightforward to solve the equations of stellar structure. Even though this claim is only partly true, many people believe that the field is known well enough to move onto larger scale problems and never look back. There have indeed been many successes in stellar theory. The seminal work of Burbidge et al. (1957) and Cameron (1957) for example, outlined those processes responsible for the production of all nuclei in the cosmos. Two of these in particular, the s-process and r-process, are the focus of current research with their formation in astrophysical sites not yet fully understood. Hoyle (1954) predicted a resonant state of carbon that was necessary for ^{12}C production via the triple-alpha process. Although experimentally verified (Cook et al., 1957), even today physicists struggle with the first principle calculations (Epelbaum et al., 2011). Comparing the predicted neutrino flux of the Sun with that measured from specialised detectors, Bahcall (1964) and Davis (1964) revealed an inconsistency that remained unsolved for 40 years, the solution to which changed our understanding of fundamental physics and led to a Nobel Prize. The problems that do remain are inevitably difficult yet interesting.

The purpose of nuclear astrophysics is to understand when, where and how each isotope on the table of the nuclides was made and in what quantity. This aim is slightly less tongue in cheek than that of Erwin Sedlmayer who claimed “The purpose of nuclear astrophysics is to make dust”. He was of course referring to the fact that the expelled envelope of stars cool enough for molecules to form; the eventual end of many complex nuclear burning phases. In order to understand the production of the nuclei, it is essential that we understand how the stars mix matter in their interiors.

Currently, mixing in stellar evolution codes is determined by gradients in the local temperature and composition. If unstable, it is assumed that a parcel travels a characteristic mixing length before losing its identity. The theory in effect averages the behaviour of material in the convection zone. The use of local information to gauge stability means that the behaviour of material with inertia is incorrectly treated at these stable boundaries. Recent 3D hydrodynamical models suggest that a convective zone can drive mixing in a radiative region, a process known as turbulent entrainment. Observations also indicate that convection is not the only means by which stars mix material. Current theories of mixing do not unequivocally predict the growth of instabilities owing to influences such as rotation or magnetic fields. How exactly these instabilities grow, how much mixing they generate, and how to formalise the processes in 1D stellar evolution codes is a key focus of stellar theory.

There is a wealth of evidence to suggest that stellar evolution codes do not contain all the necessary stellar physics to match observations. Clues exist at all phases of stellar evolution and in all stellar environments. This study focusses on one such non-convective mixing mechanism, namely thermohaline mixing. The conditions for the instability to form are thought to exist in all low-mass stars following dredge-up events. Whether this translates to efficient mixing, and whether the abundance patterns match observations are two key questions of this thesis.

In comparison to the giants before me the aims of this study are quite modest; a small step on the long road to understanding the stars. But the results do have implications for our understanding of stellar evolution and mixing, Big Bang Nucleosynthesis (whether the Big Bang and stellar evolution are consistent), and galactic chemical evolution. Since the seminal paper by Eggleton, Dearborn and Lattanzio in 2006 (Eggleton et al., 2006), thermohaline mixing has spawned 60-odd publications. We have employed a multidisciplinary approach to understanding the instability. We have drawn upon low-resolution and high resolution-spectroscopy, studies of globular cluster stars, linear stability analysis, stellar modelling, improvements in stellar microphysics, improvements in numerical methods, comparisons to multidimensional models and as yet unsuccessful (but still hopeful!) attempts at our own direct 3D hydrodynamical modelling of the process. The best laid schemes o’ mice an’ men do not always come into fruition, it is indeed the nature of research. There are still other approaches one could have taken, questions that remain unanswered, methods that could be improved, other mechanisms and their interaction included. This they now do.

Outline

“The worthwhile problems are the ones you can really solve or help solve, the ones you can really contribute something to. ... No problem is too small or too trivial if we can really do something about it.”

- Richard Feynman

Science is a way of trying not to fool yourself. The first principle is that you must not fool yourself, and you are the easiest person to fool.

- Richard Feynman

I wish to apologise (especially to the examiners) for the length of this dissertation. Although well within the acceptable word limit, it still feels long. I was fortunate enough to be involved in a variety of projects during my time at Monash. My four supervisors afforded me the latitude to explore the literature and participate in collaborations that piqued my interest. As is the nature of research, the results were not always noteworthy. I wanted to document the more successful avenues of pursuit primarily for my own benefit. Academia is extremely competitive and takes advantage of the passion of those who decide to enter its ranks. Whilst there is usually a first post-doc position for every graduate, beyond that, the pools get smaller and the sharks swim faster. The odds are stacked against any new starry-eyed scientist. If I do not climb to the top rungs of the academic ladder, then I will have something to look back on fondly from this period of my life

Although a thesis documents impartial research, there is still room for the author to add a personal touch. I have included an epigraph at the beginning of each chapter, drawing on famous words from a collection of scientists, thinkers, leaders and writers that I admire. Often the epigraph gives a glimpse into my mindset as I was writing each chapter, however a common theme throughout is the esteem in which I hold the endeavour of scientific research. Some of the quotations have inspired me. Others are from history’s greatest thinkers who have dared to challenge the status quo. I do not necessarily agree with the positions of all the people quoted, but including them here is my way of acknowledging their unconventional way of thinking and the eloquence in which their point of view was presented.

The thesis topic itself, extra mixing, has a long history in stellar evolution theory. For decades we have known that the surface abundances predicted by standard stellar models do not match observations of red giant branch stars. Some physical process, not modelled in the stellar codes, drives mixing in stars during the upper part of the red giant branch. Most solutions to this problem have focussed

on including the effects of rotation or magnetic fields in the calculations. The work presented here was motivated by a different type of mechanism. Thermohaline mixing is a secular instability that arises in regions that are stable according to the Ledoux criterion but where the mean molecular weight increases outward. The competition between the stabilising temperature and destabilising composition sees the mechanism referred to as a doubly-diffusive process. Thermohaline convection occurs when the the destabilising agent is the slower of the diffusing quantities. Through observations of globular cluster stars, we determine whether this mechanism can account for the surface composition of red giant branch stars.

The dissertation is divided into six parts. It is presented in a way that tells a story but the reader may not find this chronological account the most useful way to follow the material. For example, the background provided by the linear stability analysis in Part I flows naturally into the review of 3D hydrodynamical simulations of thermohaline mixing in Part V, the work in between draws on other aspects of astronomy for analysis.

Part I

Part I covers the necessary background material for this project. The first chapter describes the evolution of a low-mass star, modelled *ad nauseam* throughout this work and typical of those that populate the red giant branches of globular clusters. We compare the numerical models with decades of observational data to convince the reader that stars undergo a mixing episode not predicted by standard stellar evolution theory. Observations of stars in globular clusters form a central part of this investigation and we take the time to describe their complex chemical history. We outline the convergent lines of evidence that indicate that globular clusters are comprised of multiple stellar populations. The internal abundance variations that arise from the presence of multiple populations must be taken into account when interpreting the effects of extra mixing.

Chapter two offers an in-depth historical account of the development of thermohaline theory. It does, however, begin with an analysis of the Goldreich-Schubert-Fricke instability. This secular rotational instability is doubly-diffusive in nature and served as the inspiration for the first applications of thermohaline mixing in a stellar context. It is an oft overlooked fact that the true stellar origins of thermohaline mixing can be partly attributed to a rotational instability. In addition, Kippenhahn's analysis of the Goldreich-Schubert-Fricke instability introduces the formalism used for his study of thermohaline mixing decades later.

Prior to its application in stars, doubly-diffusive phenomena had been identified in the ocean. We perform the classical linear stability analysis to highlight the complex behaviour that stems from doubly-diffusive systems. The calculations provide a means to differentiate semi-convection from thermohaline mixing, both of which we summarise in a stellar context. The inclusion of thermohaline mixing in stellar evolution codes has been via a diffusion equation. In regions unstable to thermohaline mixing, the diffusion coefficient is calculated from a formula designed to mimic the process. We analyse the derivation of four such parameterisations.

Part II

Part II is dedicated to the numerical method. We describe the codes used throughout this work and the necessary changes that allowed additional physics to be considered. The stellar models are calculated via a dedicated evolution code whilst detailed nucleosynthesis is determined from a post-processing code. The significant modifications to both codes required hours of testing and benchmarking. For the reader's sake, only the essential results are included. The reader will notice that the mixing algorithms of each code are described in detail. The question of how to best model this process is a reoccurring theme throughout this dissertation.

Part III

In Part III we present stellar models with the predictions from the diffusive-thermohaline formalism. Reproducing the behaviour of $[\text{C}/\text{Fe}]$ as a function of magnitude in globular clusters serves as the key test of the models. Initially the archetypal globular cluster, M3, is used to constrain the formula for the diffusion coefficient. Observations of this system also allow us to determine the best value of the free parameter in the theory. The ubiquity of the calibration is scrutinised across globular clusters of various luminosity (mass) and metallicity. These tests are the first indication that thermohaline mixing may not be the panacea that theory is searching for.

Part IV

The $[\text{C}/\text{Fe}]$ data used in Part III had many associated uncertainties, especially in the low-metallicity clusters. To better understand the mixing history of these systems, and remove any ambiguity in our results, we required a highly sensitive tracer of mixing. In collaboration with experienced observers, we surveyed the lithium abundances of stars in three globular clusters. The results for two of these are presented in Chapter 8. The data collected had applications beyond extra mixing. It could be used to constrain the polluting progenitors of each cluster, those stars responsible for the imprinted abundance patterns observed today. The results indicated that the polluters are required to produce lithium (to different levels) favouring a significant contribution from asymptotic giant branch stars. We also combined our Li data with that from previous studies and demonstrated a statistically significant correlation between the spread in Li within a globular cluster and the cluster's luminosity.

Data from our surveys in Chapter 8, combined with previous studies from the literature, equipped us with a powerful diagnostic of mixing in red giant branch stars. The observations offered insight into the first dredge-up event as well as the extra mixing episode. Medium-to-high resolution spectroscopic surveys of lithium in globular clusters, as well as complimentary photometric analysis, provided a means to determine the predictive power of stellar theory during the red giant branch phase of evolution. We determined that stellar models overestimate the magnitude of the bump in the globular cluster luminosity function (it seemingly coincides with the onset of extra mixing) which could be impacting upon our tests

of thermohaline mixing. A direct comparison of theoretical and observed bump magnitudes yielded significant inconsistencies at low metallicities. We also compared the magnitude difference between the main-sequence turn off and the bump, ΔM_V^{MSTO} , which is independent of distance. This method suggested a systematic offset at all metallicities and that the depth of first dredge-up is not correctly predicted in the models. We investigated the role of the stellar microphysics, including the equation of state, and concluded that any reasonable variations are unable to reconcile the discrepancy. The inclusion of overshoot at the base of the convective envelope, however, enabled the models to reproduce the empirically determined ΔM_V^{MSTO} parameter but disagreement with direct comparison remained. Having refined our models through observations of Li, we conducted one final test of thermohaline mixing. We found that our chosen formalism could not simultaneously account for the depletion of [C/Fe] and A(Li) in the globular cluster sample.

Parts V and VI

Part V summarises the work conducted during this dissertation and offers some final thoughts on the mechanism. We dedicate a chapter of the discussion to 3D hydrodynamical studies of thermohaline mixing and the (further) doubt they cast on the 1D diffusive formalism. The author was fortunate enough to have visited Lawrence Livermore Laboratories during his candidature. It was hoped that collaboration would produce 3D hydrodynamical models of thermohaline mixing that would compliment the linear studies. Although this did not eventuate, many accomplished groups were able to offer insight. The common theme coming from the 3D simulations is that secondary instabilities play a significant role in this mixing mechanism. It is far more complex than the description provided by the linear theory with the interaction with gravity waves a seemingly ubiquitous outcome. Part VI is a collection of appendices and hosts the bibliography.

A consistent colour scheme has been used throughout this dissertation. The colours black, (sky) blue, vermilion and lavender/purple in particular feature prominently. The exact hex codes of these colours are important as it has been shown that they are distinguishable to people with all forms of colour blindness². In addition, these four colours are either ‘cool’ or ‘warm’ shades making them identifiable even if printed in black and white.

²see <http://jfly.iam.u-tokyo.ac.jp/color/> for more information.

Part I

Introduction

Chapter 1

Background

1.1 Low-Mass Stellar Evolution

“The flame that burns twice as bright burns half as long.”

- Lao Tzu (Attributed)

The above proverb was made famous by the character Eldon Tyrel in the movie Blade Runner but its origins date back to the 6th century BCE. Contention still exists over the authorship, although, it is often attributed to the Chinese philosopher Lao Tzu; a contemporary of Confucius. The proverb is a comment on human mortality but if we take the liberty of applying it to a stellar evolution context, it is a manifestation of the laws of physics. One of the first relationships taught in introductory astronomy is that between mass, M , and luminosity, L , and their link to the lifetime of a star, τ :

$$\frac{L}{L_{\odot}} = \left(\frac{M}{M_{\odot}} \right)^a \quad (1.1)$$

where $1 < a < 6$ and usually given as $a \approx 4$ to describe a main-sequence star¹

$$\Rightarrow L \propto M^4.$$

Since the main sequence more or less approximates the lifetime of the star then:

$$\tau_* \propto \frac{M}{L} \approx \frac{M}{M^4} \approx \frac{1}{M^3} \quad (1.2)$$

Mass is clearly the principal determinant in the evolution of stars. The more massive the star, the larger the inward gravitational force and the brighter it must burn in order to supply the balancing gas pressure. Massive stars are cursed to

¹Fitting to observational data suggests $a = 4$ for stars $0.43 M_{\odot} < M < 2 M_{\odot}$, $a = 3.5$ for stars $2 M_{\odot} < M < 20 M_{\odot}$, whilst it can be proven that $a = 3$ for a completely radiative star.

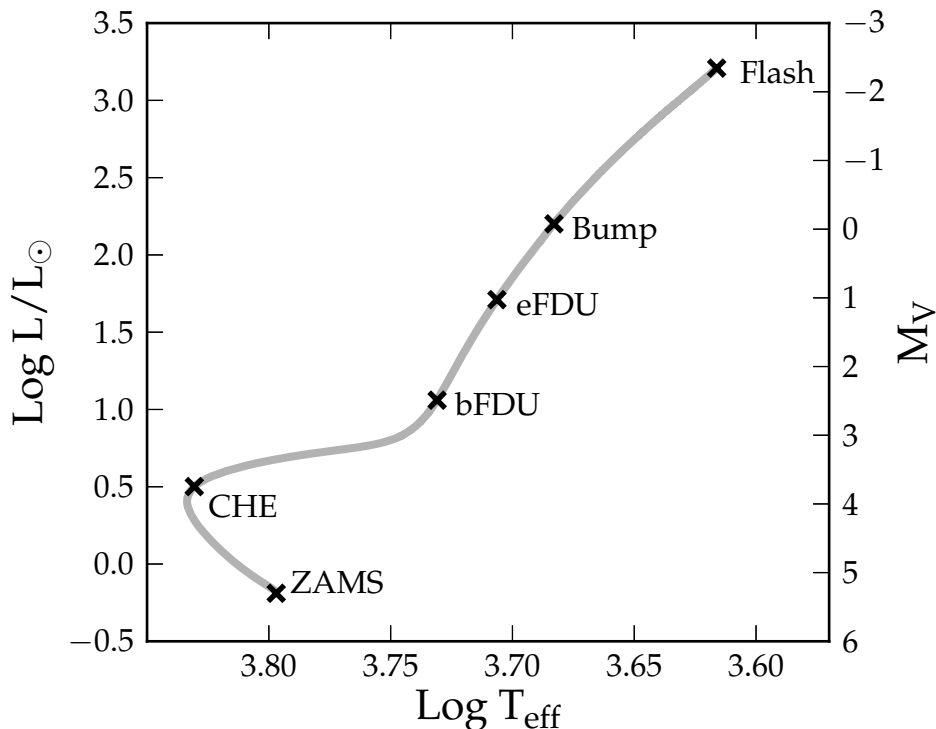


Figure 1.1: HR diagram for a $M=0.8 M_{\odot}$ $Z=0.0005$ star. Marked are several evolutionary features: Zero-age main sequence (ZAMS), core hydrogen exhaustion (CHE), the beginning of first dredge-up (bFDU), the end of first dredge-up (eFDU), the advance of the hydrogen shell on the composition discontinuity left behind by FDU (Bump) and the core flash (Flash).

burn brightly at the expense of being short-lived. By contrast, low mass stars, such as those found in globular clusters and which we consider in this study, are long-lived. We are in fact concerned with the abundances of low-mass red giant branch (RGB) stars and thus summarise the relevant evolutionary events until the end of this stage.

1.1.1 Evolution Prior to the Core Flash

Figure 1.1 is an example of a Hertzsprung-Russell (HR) diagram; one of the most important tools in stellar astronomy. Plotted is the evolutionary track of a typical star found on the giant branch of the globular cluster M3. The relevance of this cluster shall be revealed in Part III. The left axis is the luminosity scale, calculated theoretically from the nuclear energy generation and equations of stellar structure. A more practical scale is that of the right axis, the corresponding absolute visual magnitude. Converting luminosity into an observable quantity, i.e., how bright the star would appear in the sky, allows for the comparison of stellar models to observational data in the later sections.

The star we consider, like all stars, begins its evolutionary path in the lower left hand corner of the diagram. It joins the zero-age main sequence (ZAMS) once it has ignited hydrogen in its core. Prior to ignition, the proto-stellar gas cloud, from which the star forms, is gravitationally unstable. Proto-stars above a critical mass ($0.075 M_{\odot}$) slow collapse by processing deuterium and ${}^3\text{He}$ leading to the conditions necessary for central hydrogen burning. The main sequence is a quiescent stage of evolution, marked by a gradual increase in surface temperature and luminosity. For stars in the mass range we consider, hydrogen in the central regions is processed radiatively via the pp chains facilitating the growth of a degenerate ${}^4\text{He}$ -rich core. Towards the surface, a shallow convective envelope is present. For such stars, the main-sequence burning lifetime is in excess of 10 Gyr. The end of this phase is marked in Figure 1.1 as CHE, core hydrogen exhaustion, the location at which all the central hydrogen has been converted into helium. Beyond this point the star begins its transition to the RGB.

Following CHE, the inert core no longer provides the supporting pressure through nuclear burning. In order to maintain hydrostatic equilibrium, the star turns to its only available source of energy in the release of gravitational potential. In the core, contraction releases a fraction of the energy previously liberated through nuclear processes. The steep temperature gradient that was required to transport energy from hydrogen burning dissipates, and the core becomes isothermal (note that the release of gravitational potential will result in a small temperature gradient). The bottom panel in Figure 1.2 demonstrates the evolution of the temperature profile during the transition from central hydrogen burning to to an inert isothermal core. Time evolution is demonstrated by the transition of darker curves (earlier epochs) to lighter curves (later epochs). The figure illustrates several points of interest. First, it highlights the development of an isothermal core. The core boundary is clearly defined by the steep temperature gradient that develops just outside. Also demonstrated is the increase in temperature as the core contracts in radius. Note also, the corresponding core growth in mass which is due to the development of shell-hydrogen burning during the RGB.

The top panel of Figure 1.2 shows the corresponding contraction of the core and development of the density contrast at the core boundary. As a result of contraction, the pressure supplied by degeneracy increases. Meanwhile, the compressible material at the base of the envelope is eventually subjected to nuclear burning conditions allowing hydrogen to ignite in a thick spherical shell. This sudden generation of energy forces a brief period of rapid envelope expansion, as such, the outer layers start to cool and become convective signalling the onset of the red giant structure.

Thus far, we have only stressed the importance of mass in the stellar life cycle. However, evolution is also dictated by composition. Stars with higher metallicity will process more of their hydrogen through the catalytic CNO cycle rather than the pp chains, affecting their temperature profile and structure. In metal-rich stars slightly more massive than the Sun, the burning conditions and the availability of more CNO nuclei result in a core hydrogen burning phase dominated by CNO cycling. The higher temperature dependence of the CNO cycle and energy production rate leads to the development of convective cores and differences in

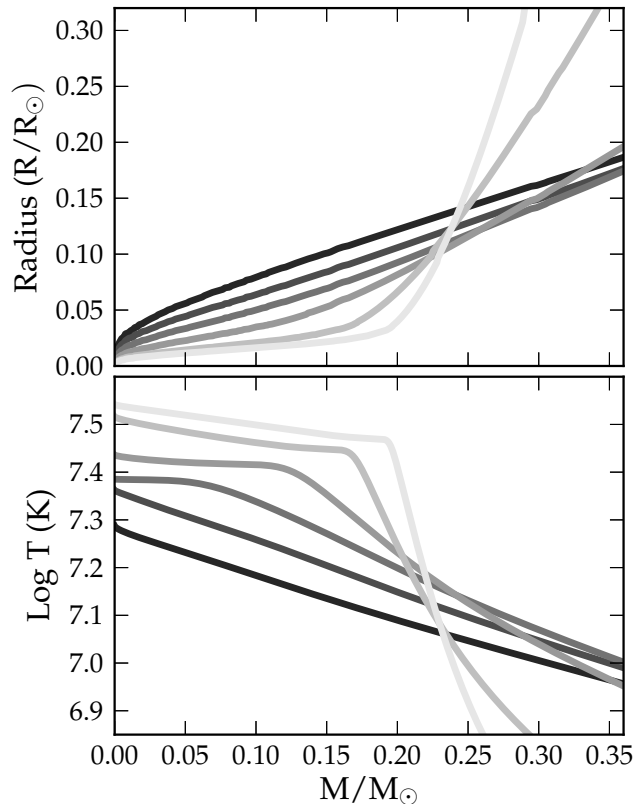


Figure 1.2: Top panel: Time evolution of radius as a function of mass. Curves denote various evolutionary periods from core hydrogen exhaustion to shell burning. Time evolution is non-linear and illustrated by a transition from dark to light curves. In later periods (lighter curves) the density contrast at the core boundary becomes apparent. Bottom panel: Time evolution of the temperature as function of mass. Curves correspond to the same epochs in the above panel. The flattening of the temperature gradients indicates the development of an isothermal core.

envelope composition. At the other end of the spectrum, Campbell and Lattanzio (2008) describe the interesting evolution of zero metallicity stars; stars we will not consider here.

During the giant phase, the composition starts to play a significant role in the evolution of the star. The envelope expansion leads to cool outer layers which allow for the formation of H^- ions. This ion dictates how opaque the outer regions are to radiation. In the low-mass regime we consider here, where surface temperatures are in the range $4000K \leq T \leq 8000K$, the Rosseland mean opacity of the H^- ion, $\bar{\kappa}_{H^-}$ ², is approximated by

$$\bar{\kappa}_{H^-} \approx 2.5 \times 10^{-31} \frac{Z}{Z_\odot} \rho^{\frac{1}{2}} T^9 \quad \text{cm}^2 \text{ g}^{-1} \quad (1.3)$$

²Integrated over all frequencies.

where Z is the metallicity, Z_{\odot} is the metallicity of the Sun, ρ is the density and T is the temperature. The importance of composition arises as the H^{-} opacity is proportional to the electron density (a fact hidden by the simplified approximation in Equation 1.3). The prevalence of the H^{-} ion allows the surface to cool further and for convection to develop as the primary mode of energy transport. In metal-rich stars the greater abundance of low ionisation metals (i.e., Ca, Na, K, and Al) provide a source of free electrons and contributes to the stronger opacity. In metal-poor stars the only free electrons are those from ionised hydrogen thus the metal-rich stars are able to develop deeper convective envelopes.

Convection is an extremely efficient method of energy transport. The ascent up the giant branch (i.e., the increase in luminosity) is a result of the increasing depth of the convection zone. The shell becomes less blanketed and the energy transported to the surface increases. The inward migration of the convective envelope marks the beginning of first dredge-up, bFDU in Figure 1.1. The chemical profile within the convective zone very quickly homogenises, and material within the star is ‘dredged up’ to the surface. At its deepest extent, the convective envelope approaches the hydrogen burning shell. This is labelled as the end of first dredge-up in the figure (eFDU) as the convection zone has stopped penetrating into unmixed regions and therefore no new material is brought to the surface.

We can see from Figure 1.3 that first dredge-up (FDU) is associated with significant changes to the surface composition of the star. The products of partial hydrogen burning, namely ${}^4\text{He}$, ${}^{14}\text{N}$ and ${}^{13}\text{C}$ are observed to increase as they enter and are mixed through the convection zone. Conversely, ${}^7\text{Li}$ and ${}^{12}\text{C}$ abundances decrease as they are diluted through the extending envelope.

Following FDU, the convective zone recedes, leaving behind a region that is homogeneous in composition. Meanwhile, the hydrogen burning shell continues to advance towards regions once occupied by the envelope, adding helium ashes to the core as it does so. As material is drawn into yet higher temperature and densities the shell reacts by compressing the burning region and increasing the energy generation. Eventually the shell encounters the composition discontinuity left behind by FDU, noted as ‘Bump’ in Figure 1.1. Detecting a change in the composition, the star readjusts its structure accordingly; it now has more hydrogen to burn. The new opacity in the burning region initially leads to a decrease in luminosity; this is highlighted in Figure 1.4. Once thermal equilibrium is re-established, the increase in available hydrogen sees the star continue to evolve along a ‘younger’ track (Iben, 1968b).

We have adopted the term ‘Bump’ as this event coincides with the so called luminosity function bump (LF bump or bump hereinafter) in globular clusters which is crucial to our later discussions. Along the RGB, the luminosity function is defined by counting the number of stars in a binned magnitude range. We can see in Figure 1.4 that we expect more stars at the magnitude of the bump as they readjust their structure and ‘double take’ along their evolutionary path. The number of stars observed at a given magnitude then decreases as evolution speeds up towards the tip of the RGB.

In Figure 1.4 we highlight the surface effects of the shell encountering the homogenised region left behind by FDU. Note that the effect on the surface lumi-

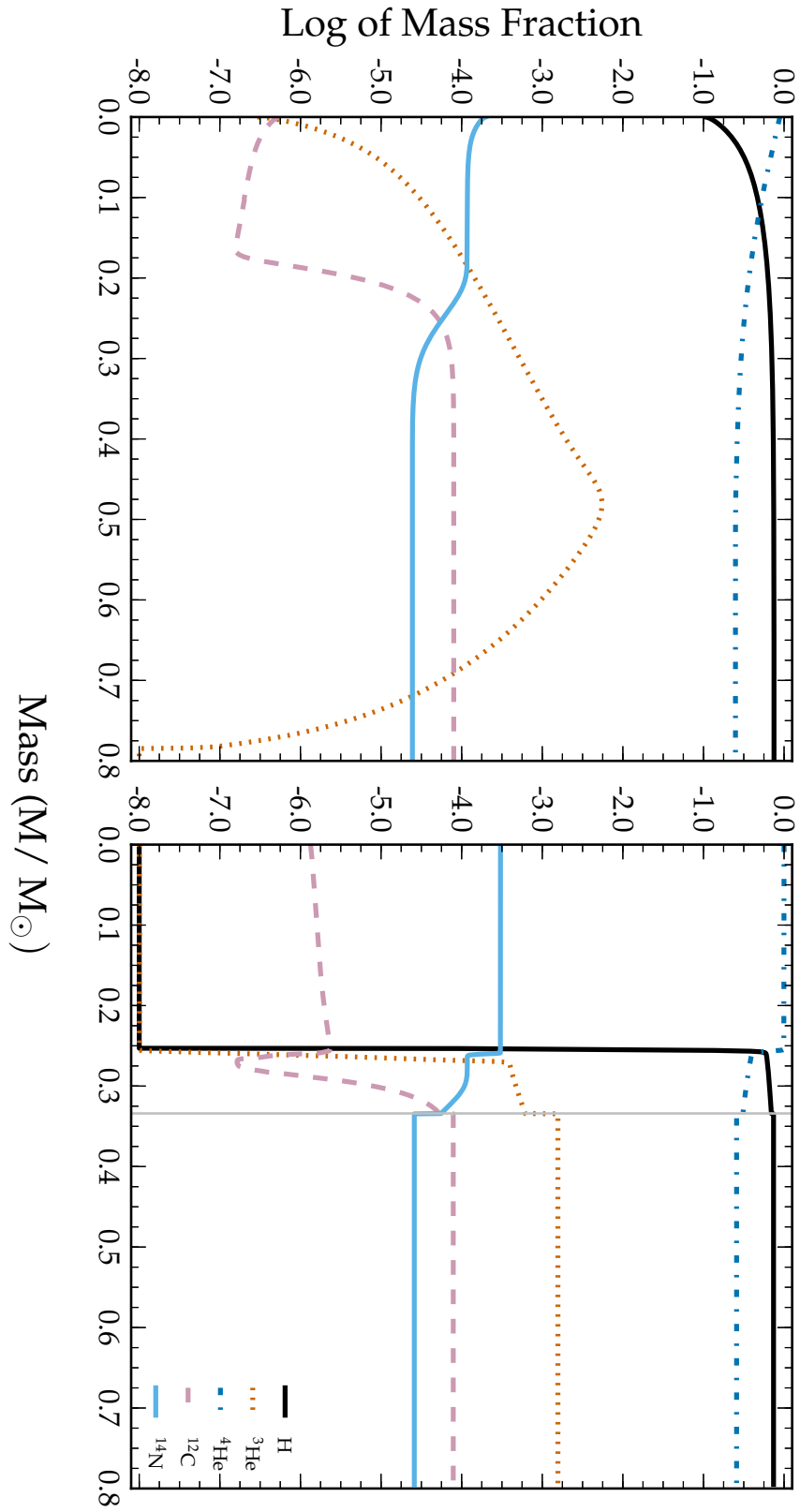


Figure 1.3: Composition profiles before and after first dredge-up for a star of mass $M = 0.8M_{\odot}$ and metallicity $Z = 0.0005$. The grey vertical line marks the deepest extent of the convective envelope.

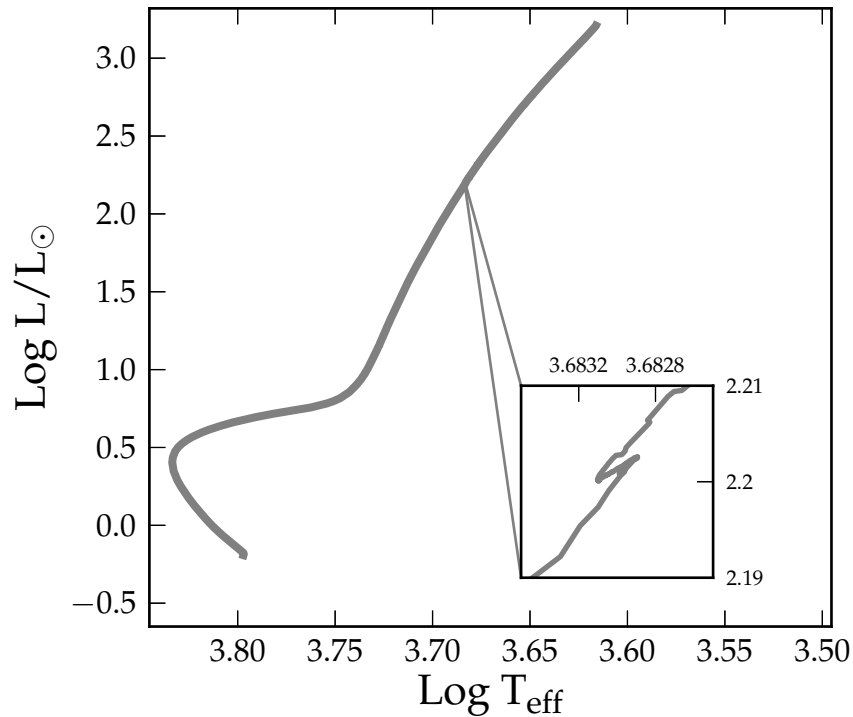


Figure 1.4: The HR diagram from Figure 1.1 with an inset highlighting the structural readjustment of the star when the hydrogen-burning shell encounters the composition discontinuity left behind by first dredge-up.

nosity is dependent on the hydrogen contrast encountered by the shell. Metal-rich stars like the Sun have deeper FDU than metal-poor stars and therefore a greater discontinuity in the hydrogen profile that develops after first dredge-up. This will in turn change the luminosity at which the shell encounters the composition discontinuity. Once again the effects of chemical composition on stellar evolution are highlighted.

Following the bump, the shell approaches the base of the (receding) convective envelope. The end of the RGB evolution is characterised by large neutrino losses at the very centre of the degenerate core. As temperatures reach 100 MK the conditions allow for the ignition of the triple alpha process. Since the core is supported by degeneracy pressure the equation of state is only weakly dependent on temperature. Ignition under these conditions occurs via a violent flash, and with no thermostatic control to expand and cool the core, runaway burning ensues. Once enough energy is produced to lift the degeneracy, the core can expand and cool leading to stable core helium burning.

1.1.2 Post-RGB Evolution

Although, in this study we are concerned with RGB structure and nucleosynthesis, for completeness we will briefly describe the later stages of stellar evolution. Evolution beyond the RGB has been the subject of investigations by Lugaro (2001), Karakas (2003), Stancliffe (2005) and Campbell (2007) with reviews by Herwig (2005), Busso et al. (1999) and Iben and Renzini (1983) containing further details. During core-helium burning, another quiescent phase of evolution, there is little change to the surface luminosity. Nuclear energy generation is provided primarily by the conversion of ^4He into ^{12}C via the triple-alpha reaction and to a lesser extent by the subsequent alpha captures on ^{12}C to give ^{16}O . A thin burning shell surrounding the core continues to process the hydrogen-rich envelope leaving behind ashes that are rich in ^4He . This phase of evolution lasts about one tenth that of the main-sequence lifetime, during which time low-mass stars display only a small increase in their surface temperature before the central supply of helium is exhausted.

As was the case with the main sequence analogue, the exhaustion of fuel in the core facilitates the development of shell burning. The new structure sees a secondary shell, burning ^4He and fuelled by the ashes of the hydrogen burning shell, surrounding a degenerate C/O core. Once again, with the shell(s) providing the energy generation, the star is forced to expand and cool. The effects on the stellar structure are this time more pronounced; our $M = 0.8 M_{\odot}$, $Z = 0.0005$ star will grow to a radius four times its peak RGB size. As before, the convective envelope will deepen and with this new configuration the star ascends the asymptotic giant branch (AGB). The AGB is called so because the early colour-magnitude diagrams revealed that these stars asymptoted to the location of first ascent giant branch stars (i.e., RGB) and occupy the same colour-magnitude space. The core flash has illustrated the thermal instability associated with helium burning, the AGB too is plagued by this condition. The AGB phase of evolution is characterised by periods of stable burning followed by thermal instability (Schwarzschild and Härm, 1965; Weigert, 1966; Iben and Renzini, 1983; Busso et al., 1999; Herwig, 2005).

During stable periods, the helium-burning shell remains essentially dormant while hydrogen burning adds ^4He -rich material to the intershell region. As the temperature and pressure increases at the bottom of the intershell region, the conditions give rise to helium ignition in the form of a thermonuclear runaway. The relatively thin intershell region, geometrically-thin shell structure, slight degeneracy and high temperature dependence of the helium burning reactions all contribute to the thermal runaway (also referred to as a thermal pulse or shell flash). Sackmann (1977) and Stancliffe (2005) amongst others have described why this occurs. In the words of the latter:

First, if energy from nuclear burning is dumped into the shell, then the temperature must rise. Secondly, the increased radiative loss due to the raising of the shell temperature must not carry energy away from the shell faster than it is being generated. If both these conditions are satisfied then the temperature in the shell continues to build up and a thermonuclear runaway results.

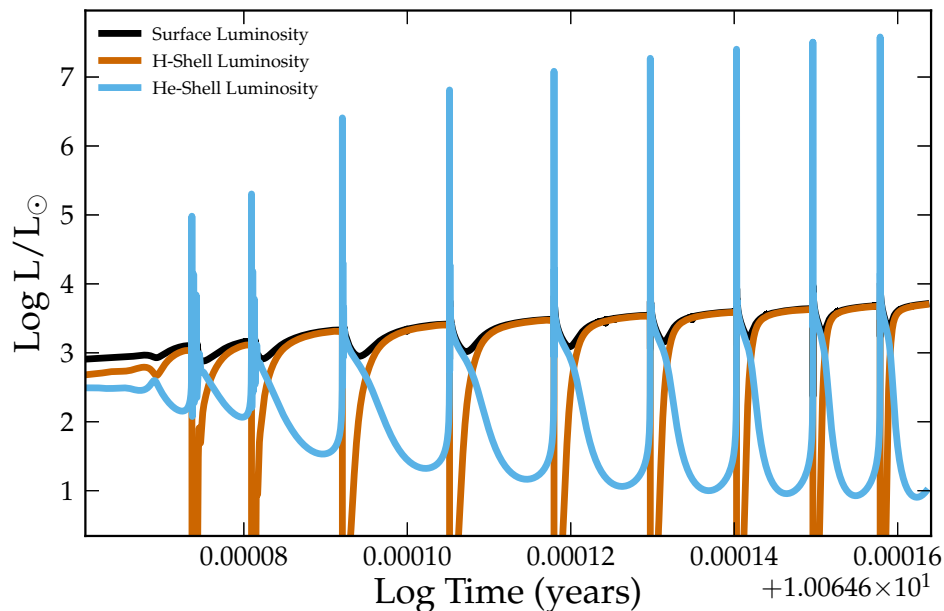


Figure 1.5: Luminosity as a function of time for an M3 type star during the thermally pulsing AGB. The black curve corresponds to the luminosity observed at the surface, the vermilion line corresponds to the luminosity generated by the hydrogen-burning shell and the blue curve the luminosity generated by the helium-burning shell.

The sudden deposition of energy does not manifest itself as a luminosity spike at the star's surface. Rather, the energy generated by the pulse drives an intershell convection zone which mixes the products of partial ${}^4\text{He}$ burning (${}^{12}\text{C}$ and ${}^{16}\text{O}$) into the intershell region. In Figure 1.5 we once again turn to our M3 type star as an example. Plotted is the surface luminosity (black curve), the luminosity generated by the hydrogen-burning shell (vermilion curve) and the luminosity generated by the helium-burning shell (blue curve) all as a function of time during the AGB.

As the helium burning begins to subside so does the pulse driven convection zone. The energy generated is absorbed in driving the expansion of the star (Iben, 1975). This can be seen in Figure 1.5 by the slight decrease in surface luminosity following the flash. With an extended structure, the outer regions begin to cool and the hydrogen burning shell is extinguished. This is accompanied by the inward migration of the convective envelope which may extend into regions where the intershell convection zone has mixed the products of helium burning. This event, the so called third dredge-up, is linked to each thermal pulse. The single shell configuration lasts a matter of decades before helium burning once again loses its potency. The outer layers are able to contract and the hydrogen burning shell is reignited. The cycle is repeated many times (occurring every few centuries, see Figure 1.5) leaving us with strange situation in stellar evolution where most stars undergo FDU, only some stars undergo second dredge-up ($M \gtrsim 4M_{\odot}$) and stars

that undergo third dredge-up, do so multiple times.

The AGB accounts for only a fraction of the stellar lifetime yet it is the most studied phase of evolution. The reason being that these stars undergo complex nucleosynthesis and are a key source of enrichment for the Galaxy and interstellar medium. Third dredge-up is responsible for bringing the products of helium-burning to the surface of the star. Its operation can be inferred observationally through the high C/O ratios found in AGB envelopes (Straniero et al., 2006) or the presence of short lived nuclei such as technetium (Lebzelter and Hron, 2003). The nucleosynthesis of the lighter elements also provide a diagnostic of the AGB interior. Changes in ${}^7\text{Li}$, ${}^{19}\text{F}$, ${}^{23}\text{Na}$ as well as the Al and Mg isotopes are all possible with the final yield depending on the mass and composition of the star (Karakas, 2010; Lugaro et al., 2012; Doherty et al., 2014). Their abundances indicate the internal burning conditions with ${}^{19}\text{F}$, ${}^{23}\text{Na}$ in particular, probes of hot bottom burning (Renzini and Voli, 1981; D’Orazi et al., 2013b). In the next section we will see that these stars may also be responsible for the signatures of hot hydrogen burning found in globular cluster stars, stars we will use to constrain the current study of doubly-diffusive mixing (Part III). Finally, it would be remiss not mention AGB stars most striking contribution to the enrichment of the interstellar medium. These stars are responsible for the production of (many) nuclei beyond iron. The AGB has been identified as a site of the *s*-process (slow neutron capture, see the review by Gallino et al. 1997) with the exact abundance pattern depending on the neutron source (${}^{13}\text{C}$ or ${}^{22}\text{Ne}$) in the intershell region.

AGB stars enrich the interstellar medium through their intense mass loss. As a comparison, the Sun will lose approximately $10^{-14}M_{\odot}$ each year, AGB stars on the other hand lose around $10^{-7} - 10^{-4} M_{\odot}$ in the same period (Winters et al., 2000; Lugaro, 2001). As discussed in Lagadec et al. (2012), the mass-loss mechanism is not fully understood but it is often attributed to a two-step process (Winters et al., 2000). It is thought that long period pulsation (distinct from the thermal pulses) extends the tenuous envelope where the cool dense conditions in the outer atmosphere allow for the formation of dust grains. Radiation pressure on the dust drives mass loss, the large grains are accelerated away whilst the gas is carried along by friction. Eventually mass loss will strip the entire envelope, returning to the interstellar medium the products of AGB nucleosynthesis and leaving behind a naked degenerate white dwarf core.

1.2 Observational Constraints – The Globular Cluster C-N Anticorrelation

“Get your facts first, and then you can distort them as much as you please.”

- Mark Twain

“The truth is rarely plain and never simple.”

- Mark Twain

As discussed in the preface, one of the triumphs of 20th century astrophysics has been the development of stellar theory. What is now known about the internal constitution of stars is due to the complimentary disciplines of observation, experiment and theory. Progress is garnered through the scientific method and this demands that theories be falsifiable. In the case of stellar evolution we must rely on observational validation. This study utilises globular clusters (GCs) and the stars within to help constrain theoretical models. Stellar clusters are the classic examples of simple stellar populations whereby it is assumed the stars have the same age and composition. Although we will see that this assumption must be relaxed for GCs, many of their properties make them the ideal systems to test theoretical models. Their size provides a populated colour-magnitude diagram, with inferred distances and ages. Although these systems traverse the Galaxy, the stars within are gravitationally bound and unless perturbed, remain in the environment where they were born. Thus they are preferable to collections of field stars that may contain targets that vary in age, composition, distance and origin. Moreover, distance and age determinations are more uncertain for field stars. GCs are almost certainly fossil remnants of the early star-forming subsystems from which the galaxy was built (Larson, 1996). Thus their distribution in metallicity can also serve as a probe of galaxy formation.

1.2.1 The Evidence for Extra Mixing

As we have seen in §1.1, standard stellar evolution theory predicts that only one mixing event will change the surface composition of a low-mass star as it ascends the red giant branch. That event is the so-called first dredge-up (see Iben 1967) associated with the inwards migration of the base of the convective envelope into regions where hydrogen burning via the CNO-bicycle has occurred. Relatively modest changes in surface C and N abundance are predicted, and once the convective envelope recedes outwards these changes are brought to a halt. However, observations of low-mass red giants ($M < 2.5 M_{\odot}$, see for example Charbonnel and Do Nascimento 1998) for a range of metallicities show trends among light element

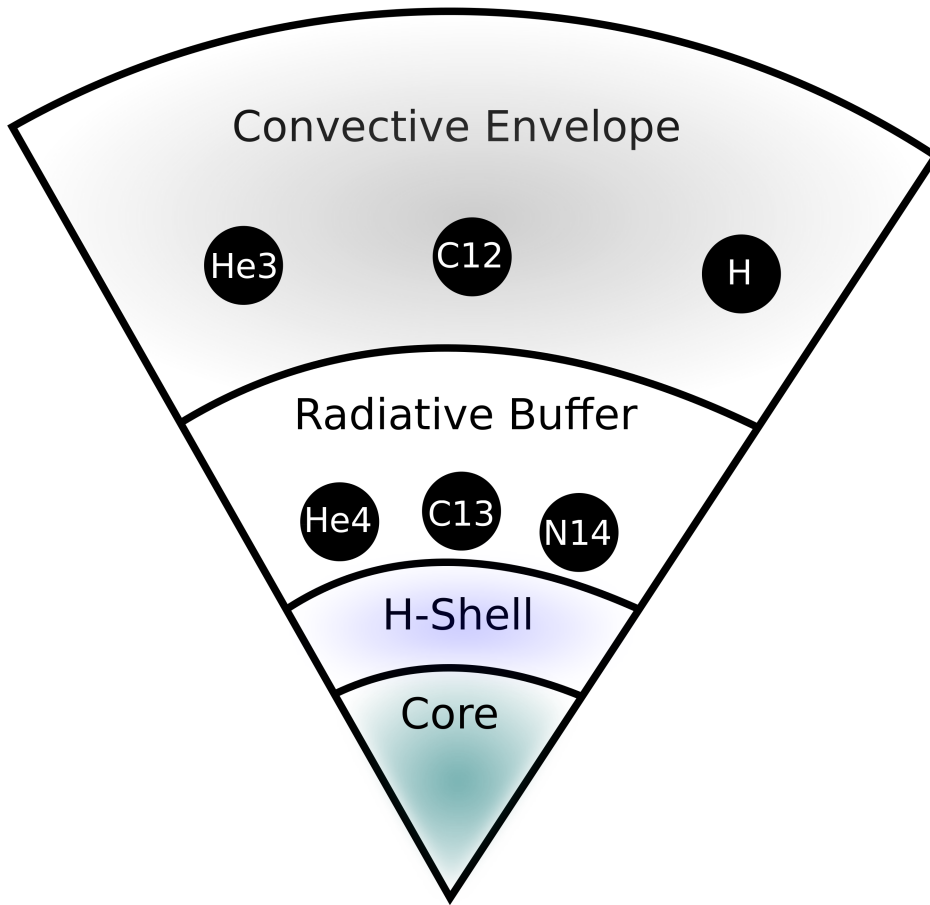


Figure 1.6: Schematic of the internal structure of an RGB star. Observations suggest CN-cycled material near the top of the H-shell is transported through the radiative region into the convection zone.

abundances that cannot be accounted for by the FDU. A form of mixing, not predicted by standard stellar models, seems to occur whereby greater amounts of the products of partial hydrogen burning are cycled into the convective envelope over a much longer timescale, and during more advanced phases of RGB evolution, than can be explained by the FDU. The stellar structure of an RGB star is illustrated in Figure 1.6. This so called “extra mixing” requires some mechanism to transport material across the radiative buffer, to the top of the hydrogen shell, where it encounters the relevant burning temperatures. Processed material is cycled back to the convective envelope accounting for the observed compositions. Identifying the exact physics that induces this mixing has proven to be a challenging task for stellar astrophysics.

Regardless of what the physical mechanism is, extra mixing is required to conform to the following observational criteria:

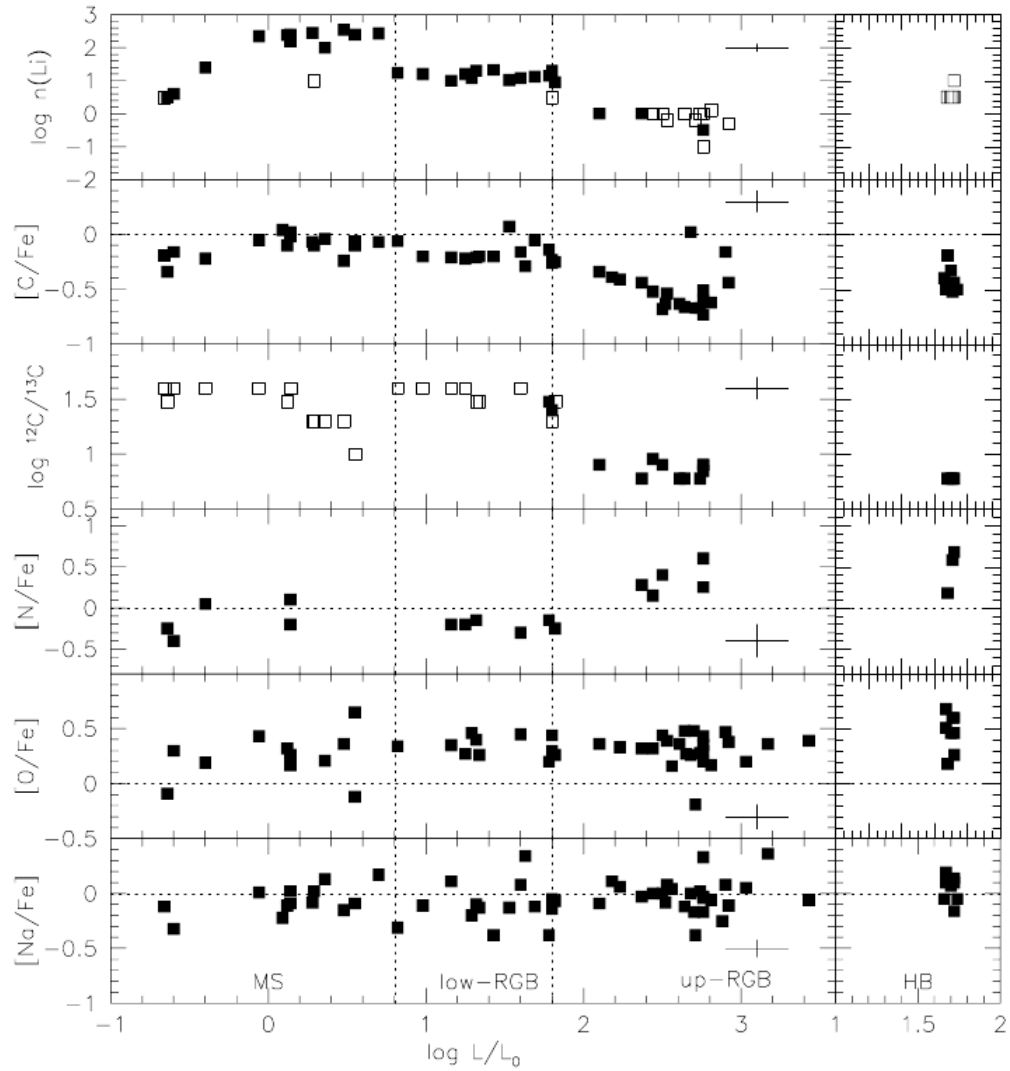


Figure 1.7: The abundances of metal-poor field stars as a function of luminosity. The figure is taken from Gratton et al. (2000, their figure 10) and their survey of field stars with metallicity ranging from $-2 < [\text{Fe}/\text{H}] < -1$. Several properties of the extra mixing process can be inferred from the figure. Reproduced with permission © ESO.

1. It commences after the hydrogen burning shell has erased the composition discontinuity in the radiative zone that marked the innermost limit of the convective envelope during the FDU event, and may continue to at least the tip of the RGB (Gilroy and Brown, 1991; Charbonnel et al., 1998; Gratton et al., 2000; Smith and Martell, 2003; Shetrone, 2003; Weiss and Charbonnel, 2004; Martell et al., 2008b). The onset of the extra mixing is thus thought to coincide with a local maximum (the so-called “bump”) observed in the RGB luminosity function of globular clusters. A property that is evident from Figure 1.8d where lithium depletion in NGC 6397 coincides with the magnitude of that cluster’s LF bump.
2. It must occur over a range of masses and metallicities (Smiljanic et al., 2009, and references therein), being active in giants of all metallicities from solar to at least as low as $[\text{Fe}/\text{H}] \approx -2.5$ (Gratton et al., 2000) and masses less than $\approx 2.5 M_{\odot}$ (Lambert and Ries, 1977), although not necessarily with equal efficiency throughout this mass and metallicity ranges. In fact data from Brown (1987) and Gilroy and Brown (1991) amongst others demonstrate that the mixing is more efficient at low metallicity. Figure 1.7 is taken from (Gratton et al., 2000) and their survey of metal-poor field stars. It demonstrates the large metallicity range that the mixing operates over ($-2 < [\text{Fe}/\text{H}] < -1$ in this figure).
3. It must deplete ${}^7\text{Li}$ (Charbonnel et al., 1998; Smiljanic et al., 2009; Lind et al., 2009) as seen in Figure 1.7 (field stars, first panel) and Figure 1.8d (GC stars).
4. It must decrease the ${}^{12}\text{C}/{}^{13}\text{C}$ ratio (Charbonnel, 1994, 1996), since values lower than predicted by the FDU are found among Population I field giants (Tomkin et al., 1976; Lambert and Ries, 1981; Charbonnel et al., 1998), open cluster giants (Gilroy, 1989; Gilroy and Brown, 1991; Smiljanic et al., 2009; Mikolaitis et al., 2010), globular cluster giants (Shetrone, 2003; Recio-Blanco and de Laverny, 2007) and halo field giants (Snedden et al., 1986; Gratton et al., 2000; Spite et al., 2006). This aspect of the mixing is highlighted in field stars (Figure 1.7, third panel) and GC stars (Figure 1.8c).
5. It must decrease the total carbon abundance since systematic decreases with advancing luminosity on the upper half of the red giant branch are seen both among globular clusters and halo field giants (Suntzeff, 1981, 1989; Carbon et al., 1982; Trefzger et al., 1983; Langer et al., 1986; Gratton et al., 2000; Bellman et al., 2001; Smith and Martell, 2003; Spite et al., 2005; Martell et al., 2008b; Shetrone et al., 2010). In Population II giants the behaviour of the carbon abundance can serve as an even more potent probe of the extent of extra mixing than the ${}^{12}\text{C}/{}^{13}\text{C}$ isotope ratio, because the latter can attain near-equilibrium values for only moderate amounts of mixing that would otherwise cause only small (≈ 0.1 dex) changes in $[\text{C}/\text{H}]$ (Snedden et al., 1986). Depletion of $[\text{C}/\text{Fe}]$ is evident in Figure 1.7 (field stars, second panel) and Figure 1.8a (GC stars).

6. As a consequence of the previous point it must increase the nitrogen abundance. The results of CN cycling are observed on the upper half of the red giant branch. Halo field stars on the upper RGB were found by Gratton et al. (2000) to show an excess of nitrogen compared to those on the lower RGB. Their results can be found in the fourth panel of Figure 1.7. In GC stars, enhanced nitrogen has been observed by Smith and Martell (2003) in the GC M3 (see Figure 1.8b).

Where $[A/B]$ is the usual relative logarithmic abundance:

$$[A/B] = \log(N_A/N_B)_* - \log(N_A/N_B)_\odot. \quad (1.4)$$

Note that for lithium in particular, we will also express abundances in the form $A(X)$ throughout. Where

$$A(X) = \log(N_X/N_H) + 12 \quad (1.5)$$

and N_X is the number density of species X. It is expected that the mechanism(s) will also destroy ^3He inside the star (Dearborn et al., 1986; Hata et al., 1995; Dearborn et al., 1996; Sackmann and Boothroyd, 1999; Charbonnel and Zahn, 2007a,b). As we cannot measure ^3He in stellar atmospheres, this is not a direct observational constraint (abundances are based on ^3He observed in the interstellar medium) but it is a significant requirement from the study of chemical yields and galactic evolution. The importance of ^3He is discussed in §2.4.5.

The key piece of evidence that suggests the mixing occurs *in situ* is that variations in abundance manifest themselves as a function of luminosity as stars ascend the giant branch. This is clearly seen in Figure 1.8 which highlights the luminosity dependence of C, N, $^{12}\text{C}/^{13}\text{C}$ and Li in various GCs. Panels 1.8(a) and (b) display the evolution of $[C/Fe]$ and $[N/Fe]$ respectively. Data are taken from Smith and Martell (2003) and their study of M3. The (anti)correlation between carbon depletion and nitrogen production is a clear indication of CN cycling. Panel 1.8(c) shows the reduction of the $^{12}\text{C}/^{13}\text{C}$ ratio in the cluster M71 (Smith et al., 2007), whilst data from Lind et al. (2009) demonstrates the evolution of lithium in NGC 6397 in panel 1.8(d). It is only these ‘lighter’ species that appear to evolve with magnitude and they therefore place a constraint on the mixing mechanism; material is not transported beyond CN cycling temperatures. We note that in the GC M13, there is evidence of oxygen depletion at the tip of the RGB (Johnson and Pilachowski, 2012; Sneden et al., 2004). We discuss the significance of this finding in Chapter 7.

We can also determine another property of the mixing process from Figure 1.8. Marked with a solid black line is the magnitude of the LF bump for the respective clusters (Nataf et al., 2013). Recall that one of the observational criteria for extra mixing is that its onset seemingly coincides with the LF bump of GCs. The mixing is therefore thought to begin once the hydrogen shell has encountered the composition discontinuity left behind by first dredge-up. This property is particularly evident in panel in 1.8(d) where stars brighter than the bump have depleted lithium. The internal process(es) responsible for the surface changes do

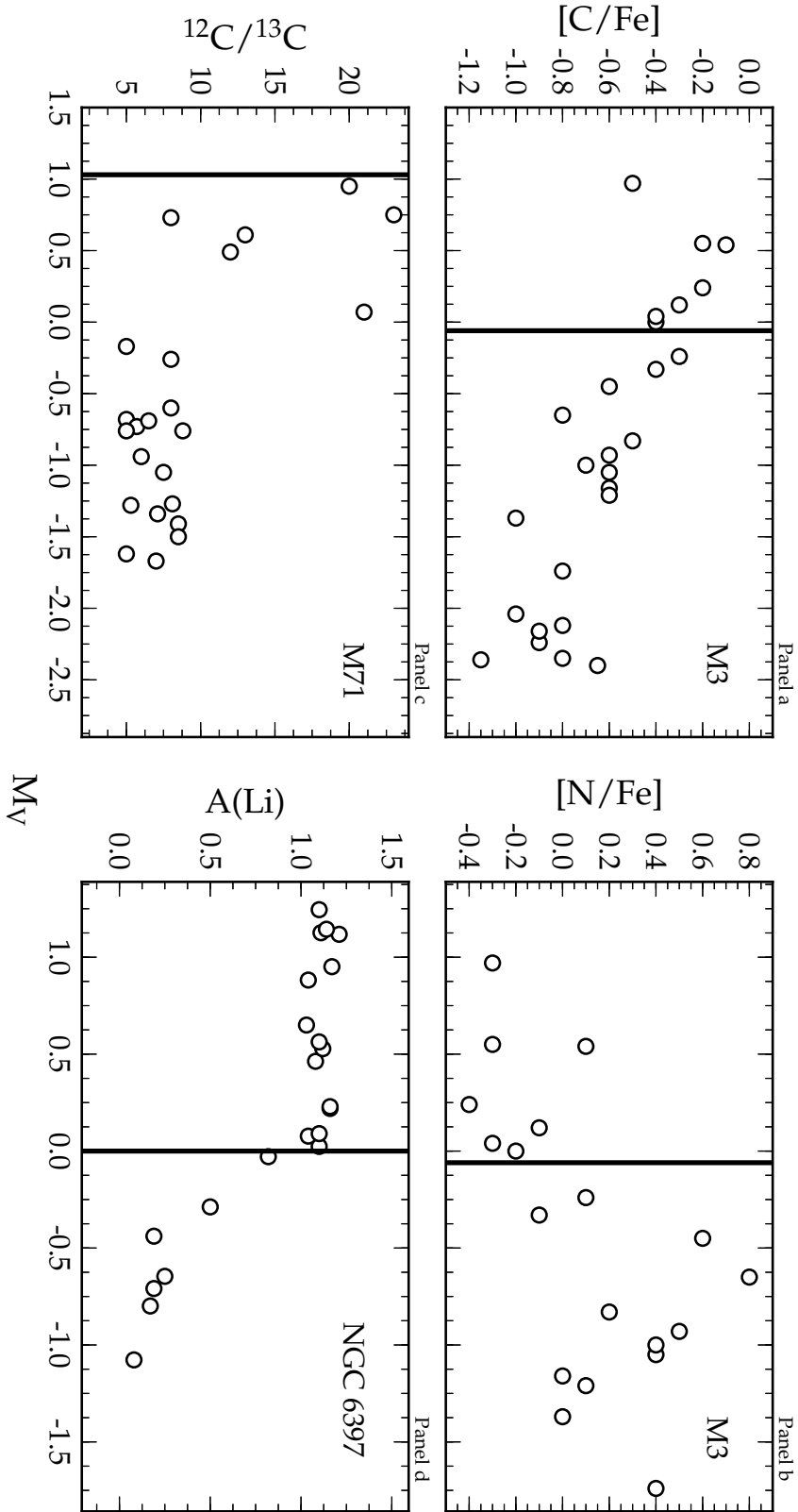


Figure 1.8: Abundances for individual stars in various globular clusters as a function of absolute magnitude. The vertical line marks the LF bump for the respective clusters. See text for details.

not manifest themselves until after the bump because the composition discontinuity left behind by first dredge-up prevents material in the radiative zone reaching the convective envelope. The composition discontinuity, and hence discontinuity in the molecular weight (μ) gradient, acts as a barrier to any extra mixing process. The gradient provides a strong stabilising effect against any fluid motions (Sweigart and Mengel, 1979; Charbonnel et al., 1998). Such arguments were made with meridional circulation in mind but in §2.4.5 we discuss the inhibiting effects of the LF bump in the context of doubly-diffusive mixing.

Finally, Figure 1.8 highlights the diagnostic capabilities of each species/isotopic ratio during the RGB mixing events. $[C/Fe]$ and $[N/Fe]$ show negligible change at the stellar surface during FDU, but they gradually adjust along the upper RGB. Matching the $[C/Fe]$ evolution as a function of luminosity, and likewise $[N/Fe]$, serves as a robust test of any non-canonical process. Observations of these two species from various GCs are used in Part III to scrutinise a theory of extra mixing, namely the doubly-diffusive thermohaline mechanism. The exercise is somewhat complicated by the fact that GCs possess multiple stellar populations. The $^{12}C/^{13}C$ ratio has often been used to probe the results of FDU (Dearborn et al., 1975a; Tomkin et al., 1976; Charbonnel, 1994) however it saturates rather rapidly once extra mixing has begun. Although $^{12}C/^{13}C$ is ideal for tracing the envelope behaviour during FDU, during extra mixing it simply provides a final abundance rather than an evolutionary profile for the models to match. Lithium is perhaps the most versatile probe of RGB evolution as it clearly identifies the onset of each mixing event. Much like the $^{12}C/^{13}C$ ratio, it is sensitive to the penetration of the convective envelope, depleting significantly during FDU. It depletes further during extra mixing, and much like the $[C/Fe]$ abundance, does so over several magnitudes.

1.2.2 The Evidence for Multiple Populations

Historically GCs have been utilised as test-beds for stellar theory and we adopt this approach throughout the current investigation. Some of the earliest published studies of GCs (Arp et al., 1952; Arp, 1955; Sandage, 1953) coincided with the first modern detailed computer calculations of stellar evolution (Oke and Schwarzschild, 1952; Iben and Ehrman, 1962). The initial mass spread of the stars and their presumed coeval nature contributed to the colour-magnitude diagram's usefulness as a diagnostic tool for the developing theory (Sandage, 1954; Johnson and Sandage, 1955; Iben and Faulkner, 1968). During this time, GCs were considered as simple stellar populations; that is, the stars in any given cluster were assumed to be of the same age and composition. Hence the structure found in the colour-magnitude diagram was an outcome of variations in stellar mass and described by a single isochrone. Presented in Figure 1.9 is an example of an early colour-magnitude diagram for the cluster M3. The original figure found in Sandage (1953) has been annotated to indicate the various evolutionary stages.

The first study to challenge the simple stellar population hypothesis was that of Popper (1947). He measured CN band strength in the stars of M3 and M13 and found a CN-strong star amongst many CN-weak. The importance of Pop-

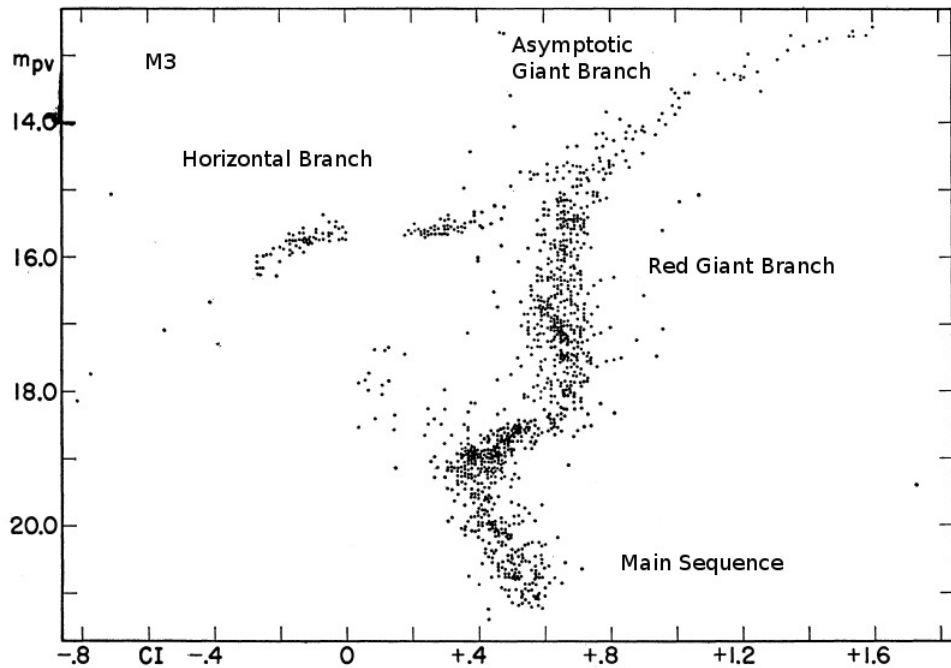


Figure 1.9: An early colour-magnitude diagram of the cluster M3. The original figure appeared in Sandage (1953, his figure 1). Labelled are the locations of stars at various evolutionary stages.

per’s find was highlighted by Osborn (1971) who found CN-strong stars in M5 and M10. These were the first clues that GCs possess heterogeneous C and N abundances. We illustrate the heterogeneity of M5 in Figure 1.10 with data taken by your author during a five night run at the Anglo-Australian Telescope (AAT). Plotted in left panel of Figure 1.10 is the strength of the S(3839) cyanogen band, a proxy for nitrogen, as a function of B magnitude. Note that the stars separate into a dichotomy and that the bimodality is present at all magnitudes. This CN dichotomy is further elucidated in the form of a double peaked histogram in the adjacent panel. We include a kernel density estimate (black curve) to further highlight the bimodality of this system. The purpose of this study was to investigate the CN-band strengths of RGB and AGB stars in multiple globular clusters. Our preliminary results (Campbell et al., 2010, 2011) indicated that a majority of CN-strong stars fail to make it to the AGB phase of evolution. Our survey also revealed that the GC NGC 1851 has a quadrimodal CN band distribution rather than bimodal (Campbell et al., 2012). The interpretation being that this system is the outcome of two merged clusters (each with their own CN dichotomy).

The heterogeneity of stars within GCs extends beyond carbon and nitrogen. It is clear that GC stars exhibit large changes in the C, N, O, Na, (with some systems also demonstrating variations in Mg, and Al) abundances, whereas (in archetypical systems at least) internal spreads in iron-peak, heavy α - (Ca, Ti) and *slow* neutron-capture (*s*-process) elements all remain constant within observational uncertainties

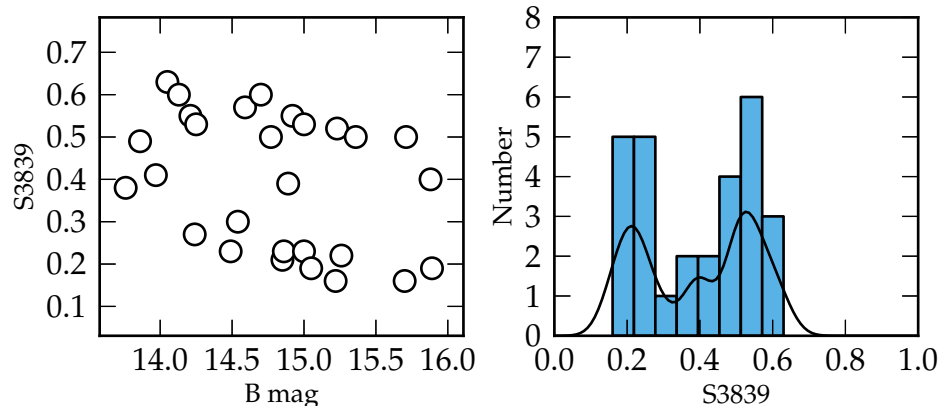


Figure 1.10: Left Panel: Strength of the $S(3839)$ CN band as a function of B magnitude luminosity for stars in the globular cluster NGC 5904 (M5). The stars separate into a strong and weak group at all magnitudes along the RGB. Right Panel: Histogram of the $S(3839)$ band strength with bin sizes of 0.125. The overlotted black curve is a kernel density estimate (Gaussian kernel, bandwidth = 0.01) of the $S(3839)$ bandwidth strength to further highlight the bimodality of this system.

(James et al., 2004; Smith, 2008; Carretta et al., 2009a,b; D’Orazi et al., 2010a). The changes in the proton-capture elements give rise to a clear chemical pattern: depletion in C, O, and Mg abundances always correspond to enhancements in N, Na, and Al (the so-called light-element anticorrelations). This behaviour is evidence of H burning at high temperature and points to the presence of multiple stellar generations. It is argued that the ejecta from a fraction of first generation of stars (initially C-O-Mg rich, sharing the same chemical composition of field stars at the same metallicity) mix with primordial gas, providing a medium from which the second generation stars (C-O-Mg poor and N-Na-Al rich) formed. (see Gratton et al. 2004, 2012a and Kraft 1994 and references therein). In this scenario the H-burning abundance patterns from the first generation stars are imprinted in the second generation and are present from birth. The nature of the stars that enriched the intra-cluster gas remains uncertain but possible candidates include intermediate-mass AGB stars undergoing hot bottom burning (Fenner et al., 2004; Ventura and D’Antona, 2011), massive rotating stars (Brown and Wallerstein, 1993; Smith, 2006; Decressin et al., 2007; Charbonnel, 2010), super AGB stars (Doherty et al., 2014; Ventura and D’Antona, 2011), massive binaries (de Mink et al., 2009) and novae (Maccarone and Zurek, 2012; Smith and Kraft, 1996). This pollution scenario is consistent with the presence of C-N-O-Na-Mg-Al abundance dispersions on the main sequences of GCs.

The formation of a second generation of stars from gas that is rich in CNO-processed material provides a paradigm that explains the observations of bimodal CN band strengths in GC stars. The CN band strength is a useful indicator of

nitrogen content of globular cluster RGB star atmospheres. New stars that form from the polluted gas are inherently enriched in nitrogen as well as (presumably) ^4He compared to the primordial generation (Norris et al., 1981). The fact that the dichotomy in the CN band strength has been detected below the bump in the luminosity function (LF bump), albeit for clusters that are of intermediate to high metallicity, provides strong evidence for the pollution scenario (Hesser and Bell, 1980; Briley et al., 1991; Suntzeff and Smith, 1991; Buonanno et al., 1994; Cannon et al., 1998; Cohen, 1999; Briley and Cohen, 2001; Pancino et al., 2010). Figure 1.11 highlights that the dichotomy has even been detected below the sub-giant branch arguing that the origin of this abundance pattern is primordial rather than *in situ*.

As we have alluded to, evidence for the multiple population scenario can be inferred through the other proton-capture nuclei. The burning patterns give rise to the well well known globular cluster anticorrelations (C-N, Na-O, Mg-Al) with the Na-O anticorrelation considered by many to be the globular cluster’s defining feature. The fact that these abundance patterns are detected above and below the sub giant branch implies that a previous generation of stars have activated CNO, NeNa ($T > 45$ million K), and MgAl ($T > 65$ million K) cycles in their interiors in order to deplete O and Mg and enhance Na and Al, respectively. These temperatures are generally thought inaccessible during the early phases of evolution. At all magnitudes along the RGB, large $[\text{Na}/\text{Fe}]$ variations in GCs (often in excess of 1 dex) have been measured (Snedden et al., 1997, 2000; Carretta et al., 2006, 2007; Carretta et al., 2009b,a). Carretta et al. (2009b) have used these large sodium variations within GCs to determine a definition for the constituent populations. In our study of NGC 6752 (Campbell et al., 2013), we also used the sodium abundances to confirm (our preliminary finding) that a majority of second generation stars do not reach the AGB in the GC environment. Stars that are Na-rich are correspondingly CN-strong but using Na (rather than CN) to distinguish the populations is considered more robust. Cyanogen bands are affected by many uncertainties (including extra mixing) whereas hot bottom burning and hence more massive stars ($M > 4 M_{\odot}$) are required for any *in situ* processing of sodium. It is therefore a more reliable tracer of stellar population.

Further evidence for the multiple population scenario is provided by high resolution photometric studies of GCs (see Catelan et al. 2002; Anderson et al. 2009; Piotto 2009 and references therein). Isochrone fitting of GC systems requires distinct ^4He abundances in these populations to explain main-sequence splitting in the colour magnitude diagrams. Examples of such clusters include: Omega Centauri (Piotto et al., 2005; Lee et al., 2005; Sollima et al., 2007), NGC 2808 (D’Antona et al., 2005; Lee et al., 2005; Piotto et al., 2007) and 47 Tucanae (Anderson et al., 2009). In addition to multiple main sequences, splitting of the sub giant branch (e.g., NGC 1851, Cassisi et al. 2008; Piotto et al. 2012), splitting of the red giant branch (e.g., NGC 362, Carretta et al. 2013a) or combinations thereof have also been identified. The simplest interpretation being that there are multiple populations present, separated in age and/or composition. Furthermore these populations reproduce the horizontal branch in many clusters; their morphology cannot be explained by a single population (Sandage and Wildey, 1967;

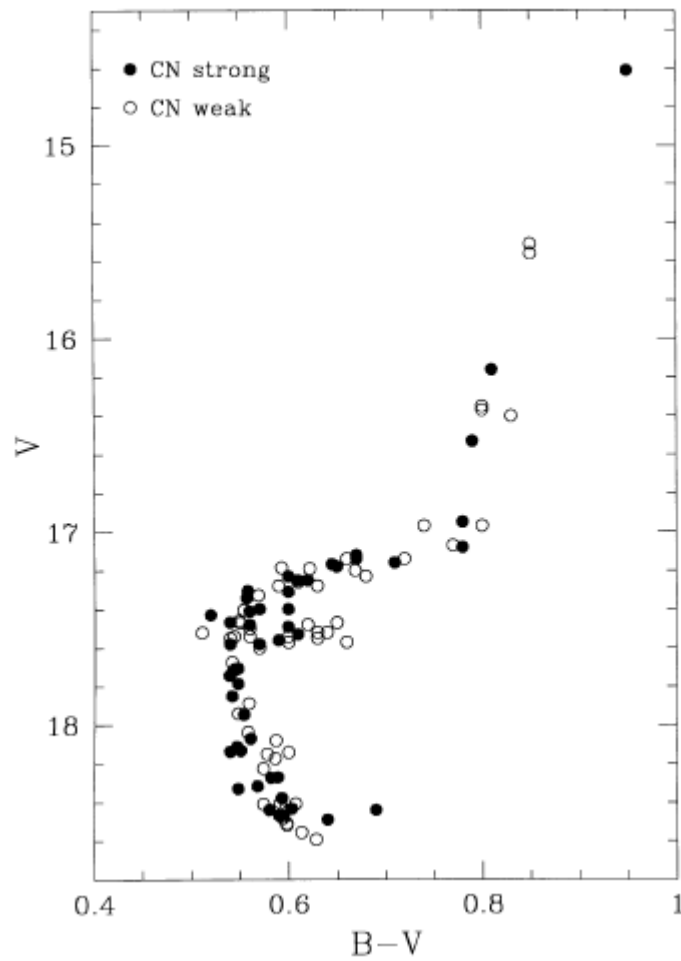


Figure 1.11: Colour-magnitude diagram from Cannon et al. (1998, their figure 6) showing the upper main sequence and sub-giant branch of 47 Tuc. Closed circles denote CN-strong stars, open circles denote CN-weak stars. The dichotomy extends down to the main sequence arguing for a primordial rather than *in situ* origin.

Norris et al., 1981; D'Antona et al., 2002; D'Antona and Caloi, 2008).

1.2.3 The Chemical History of Globular Clusters

GC stars possess distinct abundance patterns imprinted from birth. The most straightforward explanation is that the ejecta from a fraction of first generation of stars (initially C-O-Mg rich, sharing the same chemical composition of field stars at the same metallicity) mix with primordial gas, providing a medium from which the second generation stars (C-O-Mg poor and N-Na-Al rich) formed. In addition, these stars, along with their counterparts in the Galactic field, undergo *in situ* processing as they ascend the RGB. This extra mixing must operate in each generation (Suntzeff and Smith, 1991; Denissenkov et al., 1998; Briley et al., 1999; Smith, 2002) further altering the inherent abundance patterns. The presence of multiple populations and their chemical heterogeneity must be considered when using GCs as a testbed for extra mixing processes. This paradigm serves as the basis for our investigation of thermohaline mixing. In the next chapter we describe the physics of the mechanism in detail.

Chapter 2

Extra Mixing Mechanisms

An original idea. That can't be too hard. The library must be full of them.

- Stephen Fry

Every beginning is difficult, (this) holds in all sciences.

- Karl Marx

2.1 Overview

It is through studying the stellar atmosphere that we have gained knowledge of the stellar interior. The previous chapter outlined those surface abundance changes, during the RGB, that are not predicted by standard theory. Such a discrepancy arises because canonical evolution does not lead to mixing beyond the FDU event, at least not until later evolutionary phases. The simplifying assumptions imposed on the stellar structure, that is that the models are 1D hydrostatic, non-magnetic and spherically symmetric inhibit the development of instabilities that may otherwise lead to further mixing. Whatever the cause of an instability, if it is not included in the stellar evolution code then no further mixing can occur; mixing in canonical stellar evolution codes is determined by gradients in the local temperature and composition.

Observations have placed constraints on the process(es) responsible. Through studies of GCs, it has been identified that surface abundance changes seem to coincide the magnitude of the LF bump, that is the process is linked to the hydrogen shell encountering the composition discontinuity left behind by FDU. Observations of the stellar surface have determined those species affected by extra mixing, and thus, indirectly inferred the (temperature) depth to which material is transported.

This has led to the development of phenomenological models of extra mixing that can match the general abundance trends associated with the *in situ* processing (Palmerini et al., 2011a,b; Denissenkov and Vandenberg, 2003; Wasserburg et al., 1995). These models aim to reproduce the abundance changes by specifying a mixing depth and mixing speed without attributing a physical mechanism to the process.

Whilst phenomenological models serve their purpose, they do not identify the missing physics that leads to extra mixing. In such models the depth to which material is transported is usually a constant temperature (T) from the top of the advancing hydrogen burning shell,

$$\Delta \log T = \log T(r_c) - \log T(r_{mix}) \quad (2.1)$$

or a constant mass (M) from the growing hydrogen exhausted core

$$\delta M_{mix} = (M_{mix} - M_c)/(M_{bce} - M_c) . \quad (2.2)$$

In the above equations r is the radius coordinate, subscript c signifies the location of the hydrogen exhausted core, subscript bce the location of the base of the convective envelope and subscript mix the coordinate down to which mixing occurs.

One of the earliest attempts to understand the processes involved stemmed from the work of von Zeipel (1924a,b) who showed that strict radiative equilibrium is impossible for cylindrically rotating stars. Eddington (1925) and Vogt (1925) both showed that in order to compensate for the radiative flux variations, meridional circulation should develop in radiative regions. Such circulation should see material cycled into the interior at the poles and back to the surface near the equator. Sweigart and Mengel (1979) used this fact to investigate whether meridional circulation could be the cause of abundance changes in red giant branch stars above the LF bump. The seminal work has spurred much research in the area (Chanamé et al., 2005; Palacios et al., 2006).

Considerations of the magnetic fields have led Palmerini et al. (2009), Nordhaus et al. (2008), Busso et al. (2007) and Hubbard and Dearborn (1980) to suggest that magnetic buoyancy may be responsible for the red giant branch abundances. These studies are based on the premise that magnetic fields are organised in toroidal flux tubes. The tubes are stressed by the stellar rotation and develop magneto-hydrodynamical instabilities. Material in the flux tubes receive a magnetic pressure and become buoyant.

The interaction of material at radiative-convective boundaries may generate internal gravity waves (Denissenkov and Tout, 2000) which could drive mixing in radiative regions. In this picture convective plumes beating at stable boundaries will set up oscillations that can drive mixing. Although they considered higher mass stars, 3D hydrodynamical simulations from Meakin and Arnett (2007a, 2006) have shown that these waves are in fact generated and can traverse radiative regions.

Thermohaline mixing is the most recent extra-mixing paradigm and serves as

the focus of this study. Although we present the historical development of the process in the coming sections, we begin with a brief outline here. The instability had originally been identified in the oceans (Stern, 1960) and previously applied to other astrophysical contexts (Ulrich, 1972; Kippenhahn et al., 1980). It arises when material of higher mean molecular weight (μ) sits upon that of lower μ . Whether such a situation is stable depends on the ratio of heat and composition diffusivities. The competition of diffusion between these two properties has seen the process labelled doubly-diffusive (DD). Using a 3D hydrodynamics code, Eggleton et al. (2006) fortuitously identified that the μ inversion can develop in all low-mass RGB stars; the circumstances following FDU may allow a positive gradient to develop. The effect of this gradient has been investigated through the first 1D parameterisations (Charbonnel and Zahn, 2007a; Eggleton et al., 2008) and they indicate that the mechanism could lead to efficient mixing along the RGB. Once FDU has ended, the convective envelope recedes and leaves behind a homogenised region. When the hydrogen burning shell first encounters the homogenised region, the low temperature pp reactions will be the first to occur. The ${}^3\text{He}({}^3\text{He}, 2\text{p}){}^4\text{He}$ reaction in particular is efficiently processed. Note the number of reactants and products. Although a fusion reaction, more particles are produced than are consumed thereby lowering the local mean molecular weight. The point at which the reaction causes an inversion in the star's μ profile ultimately sets the mixing depth of the mechanism. Normally the effect of this reaction is swamped by those that raise the value of molecular weight. That FDU has removed the previous μ gradient is necessary for the mixing to develop. We will see that with the same (single) parameter the mechanism can fit the results of laboratory experiments (Charbonnel and Zahn, 2007a), observations of field stars (Charbonnel and Lagarde, 2010), observations of globular cluster stars (Angelou et al., 2011, 2012) and explains the behaviour of enhanced metal poor giants and carbon enhanced metal poor giants (Stancliffe et al., 2009). Although all three environments require the same empirically derived value for the free parameter, we will explore why they disagree with the current 3D numerical simulations (Denissenkov and Merryfield, 2011; Traxler et al., 2011a).

In addition to understanding the individual mechanisms, the combined effect of these processes is also an area of active research. One-dimensional spherically-symmetric models with multiple extra-mixing mechanisms include those of Cantiello and Langer (2010), Charbonnel and Lagarde (2010) and Lagarde et al. (2012), all of whom demonstrate that the thermohaline mixing diffusion coefficient is larger than the radial component of rotational mixing. Cantiello and Langer (2010) also show the thermohaline coefficient to be larger than that of magnetic buoyancy. These codes do not explicitly treat the interaction of the mixing mechanisms or how any given instability may react due to the presence of other processes. Rather, they simply add the diffusion co-efficients. Charbonnel and Zahn (2007b) have investigated an instance of multi-process interaction through linear analysis and argue that magnetic fields could serve to inhibit the effects of thermohaline mixing. Denissenkov and Pinsonneault (2008a) have also argued that the mixing may be inhibited by horizontally induced turbulence, a point we return to in Chapter 10.

2.2 The Goldreich-Schubert-Fricke Instability

There is a wealth of literature dedicated to understanding extra mixing processes throughout the evolution of a star; the above summary cites only a sample of references dedicated to the RGB. By far, the most studied mechanism has been rotational mixing. Rotation can lead to various instabilities such as shearing (Mathis et al., 2004; Maeder, 1997), meridional circulation (Chaboyer and Zahn, 1992; Mestel, 1953) and Goldreich-Schubert-Fricke (GSF) (Goldreich and Schubert, 1967; Fricke, 1968; Kippenhahn, 1969; Knobloch and Spruit, 1982). Although the focus of this study is thermohaline mixing on the RGB, investigations into a similarly secular, but rotational, instability provided the impetus for the pioneering work of Ulrich (1972) and Kippenhahn et al. (1980) into our area of interest.

Through linear stability analysis (which we apply to DD mixing in §2.3.3) Goldreich and Schubert (1967) and Fricke (1968) found independently that a chemically homogeneous star, with a given angular velocity distribution $\omega(s, z)$, is secularly unstable if either one of the following conditions is violated:

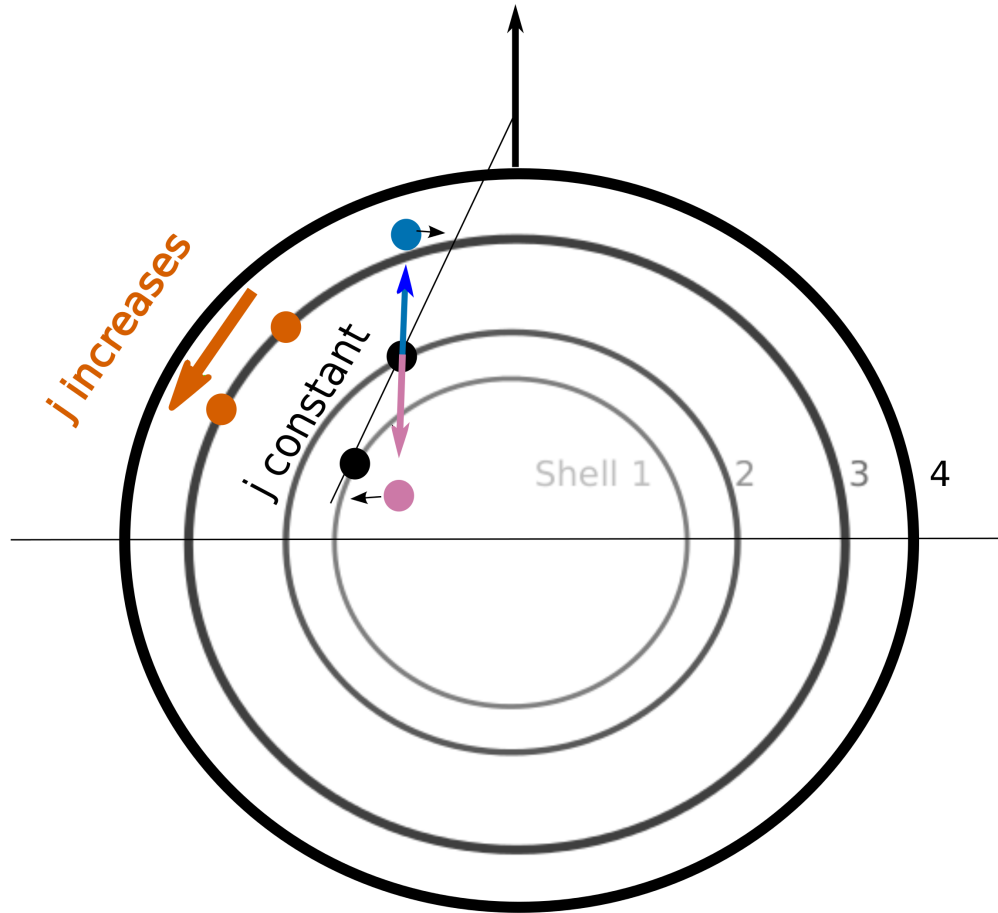
$$\frac{\partial(\omega s^2)}{\partial s} \geq 0, \quad (2.3)$$

$$\frac{\partial\omega}{\partial z} = 0, \quad (2.4)$$

where s is the distance from axis of rotation and z is the distance from the equatorial plane. The first criterion states that the specific angular momentum must increase outwards along the axis of rotation, a restating of Rayleigh's theory for rotational stability but under compressibility. The second criterion is a form of the Taylor-Proudman theorem; that the flow is a function of the horizontal plane due to the stabilising action of the Coriolis force.

They found that because stars operate in the inviscid limit (low Prandtl number $Pr \ll 1$, i.e., ratio of kinematic viscosity to thermal diffusivity), any stable angular momentum stratification which exists in a radiative zone cannot prevent an instability and the development of meridional circulation.

Figure 2.1 demonstrates the premise behind GSF instability. Illustrated is the cross section of a star with the equator in the horizontal direction and axis of rotation in the vertical direction. Each shell represents isobars due to shellular rotation (dependent on radius only) such that pressure decreases concentrically outward. In order to remain dynamically stable, Equation 2.3 must be enforced so that the specific angular momentum increases outward. In the shellular approximation, the angular velocity is constant on isobars so that the specific angular momentum, j , increases on an isobar moving towards the equator as it increases its distance from the rotational axis (see vermilion fluid element on the Shell 3 isobar). Any line of constant j must therefore cross different isobars (line connecting black circles in Figure 2.1). Any point right of the line of constant j will have lower specific angular momentum, and any point to the left will have a higher specific angular momentum. If our black parcel is displaced in the direction of the lavender arrow, its angular momentum will be larger than that of its environment and, in par-



$P(\text{Shell 1}) > P(\text{Shell 2}) > P(\text{Shell 3}) > P(\text{Shell 4})$
 -Where shells are iso-pressure surfaces

Figure 2.1: The GSF instability. Surfaces of constant specific angular momentum make an angle relative to the rotation axis. See text for more details.

particular, its angular velocity will be greater than other bubbles located the same distance from the rotational axis. Without a restoring force the bubble is pushed outward. If the particle is displaced in the direction of the blue arrow, it will find itself in a region that possesses higher angular momentum and the bubble would be pushed towards the rotational axis in the absence of a density gradient. In a stably stratified star the buoyancy force is restoring and usually able to suppress the growth of the instability, as is the presence of a molecular weight/compositional gradient or any other instability in operation.

Goldreich and Schubert (1967) and Fricke (1968) showed that it is possible, even with a stable angular momentum stratification, that energy leakage will lead to the development of meridional circulation. As we discuss in the next section, viscosity serves to smooth out any disturbances in a fluid. Given the low Prandtl number

in the stellar interior, thermal energy can diffuse much faster than the ability of viscosity to dissipate the excess evenly. Heat exchange between a displaced fluid parcel and its surroundings counteracts the restoring force of buoyancy. For the instability to grow, disturbances must occur on the smallest scales such that the effects of viscous diffusion are too weak to reduce the effectiveness of the destabilizing angular momentum gradient that ensues.

2.2.1 The Development of ‘Blob Theory’

The GSF instability is a form of a doubly-diffusive instability that stems from rotation. Many authors (Acheson, 1978; Goldreich and Schubert, 1967; Fricke, 1968; Kippenhahn, 1969; Ulrich, 1972) realised the similarities to thermohaline mixing in the oceans (Stern, 1960). Whereas the oceanic instability has heat and composition in diffusive competition, the GSF instability has heat and the diffusion of angular momentum in competition. In order to determine a mixing speed and timescale for the GSF instability, Kippenhahn (1969) considered how a displaced blob interacts with its surroundings. The development of the ‘blob theory’ is the basis for later work in Kippenhahn and Weigert (1990). We will use the terms ‘blob’, (mass) ‘element’ and ‘parcel’ interchangeably throughout. The basic tenets of the theory are discussed below. They provide the ground work for a comparison between Kippenhahn et al. (1980) and Ulrich (1972) on thermohaline mixing in stellar interiors (§2.4).

Kippenhahn’s study of the GSF instability is carried out using the thermodynamic quantities common to stellar astrophysics. It is assumed that the region of interest is chemically homogeneous, dynamically stable, with a non-vanishing temperature gradient:

$$\left(\frac{\partial \ln T}{\partial \ln P}\right) < \left(\frac{\partial \ln T}{\partial \ln P}\right)_{ad}, \quad (2.5)$$

where subscript ad represents the adiabatic value. We express Equation 2.5 in standard stellar physics notation, $\nabla < \nabla_{ad}$, hereinafter. The blob itself is restricted to the topology of a sphere, although it may be slightly deformed. Furthermore, it is assumed that any motion is sufficiently slow that the inertia of the blob can be neglected and rising blobs do not interfere with each other. As a consequence, the force imparted on the blob can be estimated via Stoke’s law: the description of flow past a spherical object. In Kippenhahn’s formulation the force exerted on the blob is given by

$$K = 3\pi f\eta vd \quad (2.6)$$

where K is the force on the blob, η is the coefficient of viscosity, v is the Stoke’s velocity of the blob, d is the mean diameter of the parcel and f is a dimensionless factor which takes into account its geometric deformation. As alluded to, Stoke’s law makes certain assumptions about the behaviour of the blob:

1. the flow is laminar,
2. the blob is spherical,
3. the fluid is homogeneous in composition,

4. the surface of the blob is smooth,

Kippenhahn eased the fourth condition by including the parameter f in Equation 2.6.

In order to get an estimate for v , the velocity in Equation 2.6, he considered the displacement of the blob as illustrated in Figure 2.2. Within a given time Δt the blob will move a distance Δx , during which time it may change its temperature by an amount dT and its surroundings may change by ΔT . He adopted the convention that subscript i denotes the interior of the blob, e denotes the surroundings, 0 for the initial quantities and no subscript for quantities at the end of the displacement. The system is described schematically in Figure 2.2. Thus the

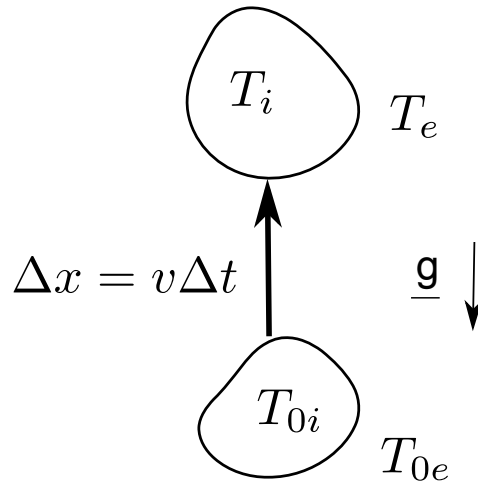


Figure 2.2: Quantities in the system describing a displaced element as described by Kippenhahn (1969).

change in temperature of the blob is given by

$$dT = T_i - T_{0i} \quad (2.7)$$

and the change in temperature of the surrounding material by

$$\Delta T = T_e - T_{0e}. \quad (2.8)$$

Initially, any difference in temperature between the blob and its surroundings is given by

$$DT_0 = T_{0i} - T_{0e}. \quad (2.9)$$

The final difference in temperature is given by

$$DT = T_i - T_e = DT_0 + dT - \Delta T. \quad (2.10)$$

Furthermore, it is assumed that the element is always in pressure equilibrium. Through some simple algebra, and various substitutions (see Kippenhahn 1969 for more detail) it can be shown that the velocity of the blob is related to the rate at

which the temperature difference between the blob and its surroundings changes such that

$$\frac{\partial(DT/T)}{\partial t} + \frac{1}{\tau} \frac{DT}{T} = (\nabla - \nabla_{ad}) \frac{v}{H_P}. \quad (2.11)$$

Here H_P is the pressure scale height, the distance over which the pressure changes by a factor of e , and τ is the timescale for thermal adjustment. τ , is in effect, the equivalent of a Kelvin-Helmholtz timescale for radiative losses and does in fact approach the Kelvin-Helmholtz value as the diameter of the displaced blob approaches the diameter of the star. τ is given by

$$\tau = \frac{3C_P \kappa \rho^2 \zeta d^2}{8acT^3}, \quad (2.12)$$

where C_P is the specific heat capacity, κ is the opacity, ρ is the density, ζ is a dimensionless factor, d is the diameter of the perturbed blob, a the radiation density constant, c the speed of light and T the temperature.

Equation 2.11 can be further simplified if

$$\left| \frac{dv}{dt} \right| \ll \left| \frac{v}{\tau} \right| \quad (2.13)$$

so that the time derivative can be ignored. In other words, if the velocity does not change very much a quasi-steady state is achieved.

Having used his formalism to describe the motion of a blob through a region that is chemically homogeneous, dynamically stable, and with a non-vanishing temperature gradient, Kippenhahn considered the behaviour of a blob when the condition given by Equation 2.3 was violated then separately when the condition given by Equation 2.4 was violated. If $\partial\omega s^2/\partial s < 0$ then a force will push an element (or ring of material) outwards into a region where it will have higher angular velocity than that its surroundings. This will lead to shearing and ultimately a loss of identity. For such an instability the maximum possible distance displaced will be a function of the Richardson number

$$Ri = \frac{N^2}{\left(\frac{du}{dx}\right)^2} > Ri_{cr} = \frac{1}{4} \quad (2.14)$$

where du/dx is the velocity gradient in the region the blob transitions (see below), N^2 is the Brunt-Väisälä frequency and Ri_{cr} is the critical condition for stability. The physical meaning of this number is discussed in Kippenhahn and Thomas (1978). It is the ratio of the work done against the buoyancy force to the kinetic energy (or turbulence). Under the influence of a gravitational field turbulence will be hindered by a density distribution increasing towards the centre of gravity. If this turbulence is caused by shear motion, then to maintain the turbulence, the work against gravity has to be smaller than the kinetic energy of the turbulent elements. Simply put the blob will retain its identity whilst $Ri > 1/4$. Kippenhahn erred on the side of caution and assumed a critical value of $Ri_{cr} = 1$.

If we relate the Richardson number to the picture painted in Figure 2.1 then

du/dx is the velocity gradient across the transition region from one concentric shell to another thus

$$\frac{du}{dx} \equiv \frac{2sD\omega}{d}, \quad (2.15)$$

as $sD\omega$ is the difference in velocity (recall s is the distance from the rotational axis) and $d/2$ is the thickness of the transition zone. If a parcel has moved outwards along a path l , then through conservation of momentum,

$$\frac{D\omega}{\omega} = -l \frac{\partial \ln \omega s^2}{\partial s}. \quad (2.16)$$

If we also express

$$N^2 = \frac{g}{H_P}(\nabla_{ad} - \nabla) \quad (2.17)$$

then through substitution Equation 2.14 becomes

$$Ri = \frac{\nabla_{ad} - \nabla}{4} \frac{g}{\omega s} \frac{d^2}{sH_P l^2} \left(\frac{\partial \ln \omega s^2}{\partial s} \right)^{-2}. \quad (2.18)$$

Applying Kippenhahn's criterion of stability as $Ri = 1$ the maximum value for l is given by

$$l = \frac{d}{2} \left(\frac{g}{\omega s} \frac{\nabla_{ad} - \nabla}{sH_P} \right)^{1/2} \left(\frac{\partial \ln \omega s^2}{\partial s} \right)^{-1}. \quad (2.19)$$

From Equation 2.16 and 2.19 one can derive the expression for the velocity

$$v = \frac{d}{\delta\tau} \left[\frac{H_P}{s(\nabla_{ad} - \nabla)} \frac{\omega^2 s}{g} \right]^{1/2} \quad (2.20)$$

where the thermodynamic quantity $\delta = 1$ for a perfect gas. The resulting (simplified) diffusion equation for a given unstable angular momentum distribution is cast in terms of v_{ev} , the Eddington-Vogt velocity for meridional circulation (Baker and Kippenhahn, 1959)

$$D = vl = \frac{1}{2\zeta\delta} \frac{\nabla_{ad} - \nabla}{\nabla} \frac{v_{ev} g}{\omega^2 s} |\nabla \ln \omega s^2|^{-1}. \quad (2.21)$$

In his analysis of the GSF instability, Kippenhahn utilises the simplified version of Equation 2.11, in that he ignores the time derivative. He demonstrates that this assumption is valid as long as

$$\frac{\tau v}{l} = \frac{(\omega^2 s/g)}{\delta(\nabla_{ad} - \nabla)} H_P |\nabla \ln \omega s^2| \ll 1. \quad (2.22)$$

This suggests that the simplification is valid as long as the angular momentum does not change considerably over the pressure scale height. Whether such an assumption can be extended to thermohaline mixing during the RGB, where instead the composition gradient is considered, is a source of contention. The issue is examined in §2.4 where blob theory is used to derive an expression for an el-

ement moving through an inhomogeneous medium. We will determine both the full solution and solution to the steady state approximation in the thermohaline regime.

Finally, we briefly outline Kippenhahn's argument as to why instability is inevitable if the condition given by Equation 2.4 is violated. If a ring of material at a distance, s , from the rotational axis, z , possesses angular velocity ($\partial\omega/\partial z \neq 0$), then a torque will drive circulation. Circulation will be in the meridional plane as demonstrated in figure 3 of Kippenhahn (1969). Because the region is thermally stable ($\nabla < \nabla_{ad}$), there will be a restoring force due to buoyancy that serves to prevent the circulation. However given the low Prandtl number of the stellar interiors, heat exchange with the environment will counteract the restoring buoyancy force. As in the example above, the parcel will find itself in a region where its angular momentum is different to its surroundings and a similar stability criterion will apply.

2.3 Doubly-Diffusive Mixing

The seminal paper by Eggleton et al. (2006) has created somewhat of a Renaissance for DD mixing in astrophysical literature. Recently, the focus has been on its role as an extra mixing mechanism during the RGB but prior to 2006, there have been many other stellar applications considered. In the following sections, DD mixing is systematically analysed, not just in the stellar context but also in the oceans where our understanding of the instability developed. The oceanic history not only clarifies some key conceptual ideas required in understanding the stellar process but is also responsible for the etymology of the term thermohaline. The tools of analysis derived here in §2.3, provide the necessary background to investigate the 3D simulations of double diffusion (Denissenkov and Merryfield, 2011; Traxler et al., 2011a) in §10. It is essential to distinguish between ‘simulations’ of the process as opposed to the prescriptions used in stellar models. Simulations solve the Navier-Stokes equations whereas models try to reproduce the results of these simulations in an approximate and computationally viable manner. We begin by summarising some of the key ideas of stability in a fluid then proceed by carrying out a stability analysis in the context of the oceans. In section 2.4 the same concepts are extended to stellar modelling. There we look at specific conditions in which DD mixing may occur in stars before finally focusing on DD mixing during the RGB and rigorously analysing its applicability as an extra-mixing mechanism.

2.3.1 Stability

In nature it is highly unlikely that a steady system remains in isolation and unperturbed indefinitely. Stability is in essence the study of how a fluid reacts to any disturbances. If a perturbation decays with time, the original state of the system is recovered and the configuration is stable. If on the other hand, a perturbation grows with time (usually exponentially) it may lead to turbulence or mixing and alter the future evolution of the fluid. Disturbances can come in a variety of forms. Many of these disturbances and the resulting instabilities, have been well studied in the fluids literature and form the focus of many elementary texts (see Riahi 2000; Drazin and Reid 2004 for example). As these texts discuss, disturbances may be due to external agents:

- buoyancy,
- surface tension,
- surface tension gradient,
- forces due to the presence of a magnetic field,
- boundary forces such as boundary imperfections,
- roughness and walls,
- centrifugal and Coriolis forces,

or internal forces:

- inertia,
- pressure gradient forces,
- stabilising or destabilising effects of molecular diffusion for momentum (viscosity), heat (thermal diffusivity), mass concentration (solute diffusivity),
- boundary conditions,
- environmental effects.

A fluid remains in a steady state because an equilibrium exists between the forces present. When an instability develops, the configuration has been energetically perturbed. Disturbances such as those listed above, extract a sufficient amount of kinetic energy from the steady flow to upset the force balance. If the viscosity of the fluid is high enough, the energy extracted by a disturbance can be dissipated back throughout the fluid and thus avoid destabilisation. The same is true for any diffusing quantity which smooth out differences in momentum (viscosity), heat (thermal diffusivity), or mass concentration (solute diffusivity).

The transfer from steady to unsteady flow can be investigated through the use of a stability parameter. When considering fluid flow problems it is convenient to analyse the governing system of equations in terms of non-dimensionalised variables. The type of system will dictate what kind of forcing is required to instigate mixing. In shear flow systems the appropriate stability parameter is given by the Reynolds number, Re , which is a measure of the ratio of inertia to viscous forces. For thermal flow systems, such as those we consider, the stability parameter is given by the Rayleigh number, Ra , which is the measure of the ratio of (destabilising) buoyancy to (stabilising) viscous forces.

Viscous forces are not always stabilising. Diffusing processes may allow the disturbance to draw upon the energy available in the basic flow. Such behaviour is characteristic of DD systems and one of the reasons why they are so interesting. In DD systems with opposing temperature and composition gradients, e.g., warm salty water upon cool freshwater, having a density gradient that increases in the direction of gravity is not a guarantee of stability. Diffusion, which is usually stabilising in fluids containing a solute that is uniform in either temperature or composition, can now act to release potential energy in the component which is heavy on top. We will see in the proceeding sections that the energy is most efficiently utilised when the fluid takes on the geometry of long salt fingers. We will also investigate DD systems with the opposite configuration with cool freshwater overlying warm salty water. Such a system leads to ‘overstable’ motions as they possess a net buoyancy force in the direction of the restoring force. Such behaviour allows oscillations to grow even when the energy is dissipated.

2.3.2 Oceanographic History

Our understanding of DD mixing owes its origins to the study of stratified fluids in oceanography. The theory emerged from a simple experiment devised by Stommel

et al. (1956) which is schematically reproduced in Figure 2.3. Stommel et al. (1956) inserted a long narrow conducting pipe in a tank where warm salty water overlaid cool fresh water. If the lower-lying cooler (and hence denser) water is initially pumped upwards, the conducting walls will heat the fresh water to the same temperature as the surrounding salt water. The fresh water near the surface, which is in temperature equilibrium with the salt water would be less dense (owing to absence of the salt) at the same level. They found that after an initial period of pumping the configuration would be perpetually flowing (and in fact true no matter which direction the pumping occurred) as long as there is a vertical gradient of salinity to supply potential energy. They imagined that such a configuration could be used to clean tanks.

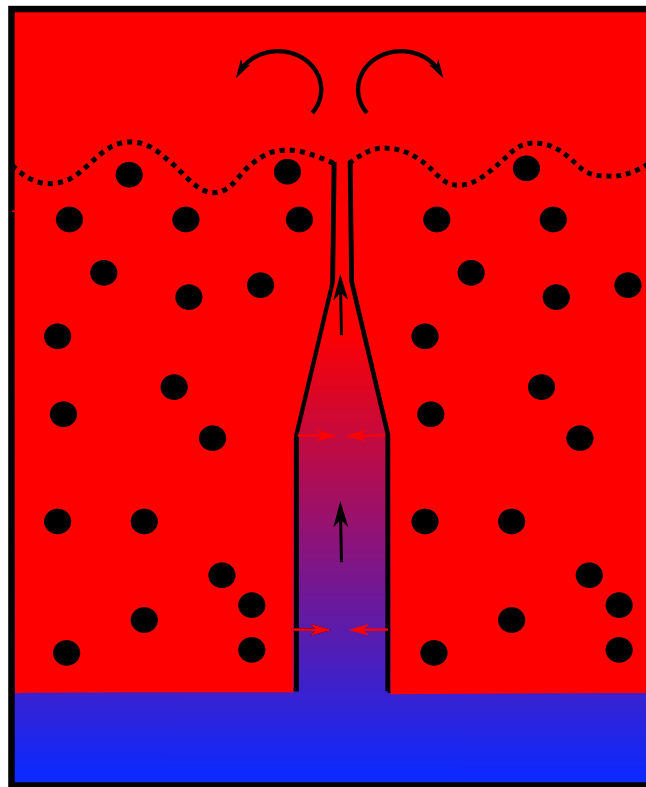


Figure 2.3: The original ‘perpetual salt fountain’ concept of Stommel et al. (1956). The red background denotes warm fluid whilst blue denotes fluid that is cool. The presence of salt is illustrated with black circles and the interface of salty and fresh water by the broken lines. The flow of the fluid through the conducting pipe (after pumping) is marked by black arrows and the diffusion of heat through the conducting pipe is illustrated by red arrows.

Stern (1960) realised that owing to the large molecular diffusivities between salt (composition) and heat, ‘perpetual salt fountains’ could develop in the oceans without the need for solid boundaries or conducting walls. He argued that if a small parcel of material is displaced downwards in the direction of gravity (al-

though) into a region where the mean density increases, it may continue to sink because the heat of the parcel will diffuse on a faster time scale than the salt composition. The decrease of mean salinity in the direction of gravity provides the energy source for the motions through the buoyancy force. He recognised that this could be an important mechanism for the vertical transportation of composition and heat in the oceans. Published in the original Stern (1960) paper, laboratory experiments from Stommel and Fowler showed that fluid is transported by means of ‘salt fingers’; the process is illustrated in Figure 2.4. The formation of finger-like convection is possible for any two stratified fluids with competing diffusivities (e.g., salt water and sugar water). The competing diffusivities ensured that the study of the instability is referred to as doubly diffusive, however in this oceanic context the transport of material via heat (thermo) and salt (haline) has seen it referred to as thermohaline mixing. Even though the salt water is of higher molecular weight, the arrangement remains stratified owing to the higher temperature of the top layer. If a parcel of warm salty water is displaced downward, buoyancy will return the parcel to its equilibrium position as long as a heat difference remains. If the parcel loses heat on the time scale of its excursion into the cooler layer, it will start to sink in the form of long fingers.

There are a wide range of possible behaviours arising from doubly-diffusive systems, such examples include the effects of sidewall heating (Thorpe et al., 1969; Sabbah et al., 2001) and development of thermohaline staircases (Tait and Howe, 1971; Radko, 2003; Schmitt et al., 2005). The configuration described by Stern (1960) has warm salty water upon cool fresh water where both temperature and salinity increase in the opposite direction to gravity. The temperature acts to stabilise the stratification whilst the composition serves to destabilise hydrostatic equilibrium. If the temperature gradient is sufficient to maintain stratification, then we can also consider an element from the cooler less saline region displaced upwards into the warmer saltier fluid. The element will absorb heat from its new surroundings and, owing to the speed of thermal diffusivity, temperature equilibrium will be established rapidly. The discrepancy in salinity remains, and therefore so does a density difference, and the displaced element would continue to rise. Such a configuration can lead to an instability highlighting the fact that, for DD systems, convection can occur even under hydrostatically stable situations. We explore this idea further in §2.3.3

We previously alluded to a slightly different arrangement in which DD mixing can develop. Veronis (1965) analysed the case where warmer salty water underlays cool fresh water. He considered a warm parcel of fluid that is displaced upwards. Because heat will diffuse much faster than the salt, when the element cools buoyancy forces will drive the parcel back towards its initial position. We will see that such a configuration eventually leads to oscillatory motion.

2.3.3 Fluid Stability Analysis

Deriving criteria for instability will help determine which DD mixing regime (Veronis or Stern) is in operation in stellar material (Stern, 1960; Veronis, 1965; Kozitskii, 2000). We adopt the choice of non-dimensionalisation and the notation

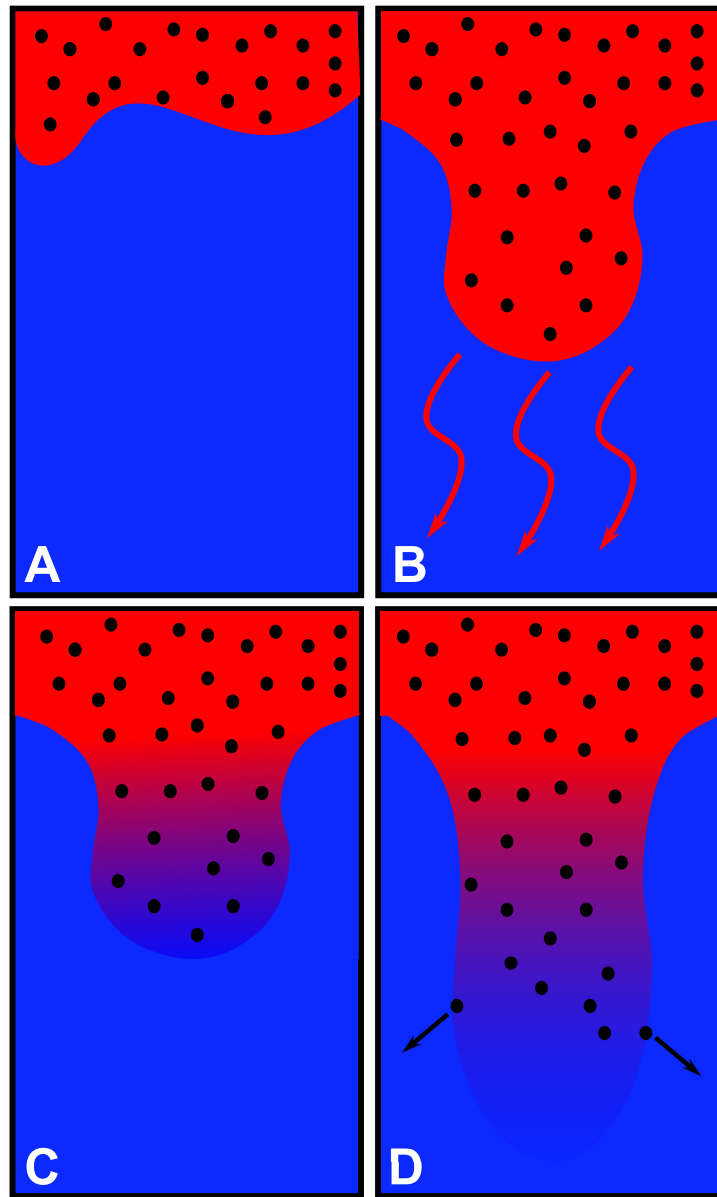


Figure 2.4: In all panels warm fluid is denoted by red shading, and cool fluid by blue shading. Salt molecules are represented by black circles. **Panel A:** Temperature can act to stratify two fluids despite the presence of salt in the top layer. The wave like interface denotes a disturbance from the equilibrium configuration. **Panel B:** As a result of the disturbance a parcel of fluid is displaced into the cooler regions and loses energy to its surroundings (denoted by red arrows). **Panel C:** The displaced blob, having reached temperature equilibrium during its excursion into the cooler region has a higher density than its surroundings due to the presence of salt. **Panel D:** The parcel extends down in search of neutral buoyancy in the form of a long finger. Eventually the diffusion of salt into the surroundings (denoted by black arrows) causes the parcel to mix with its surroundings and lose its identity.

of Turner (1973). The analysis is a precursor to the work of Ulrich (1972) and Kippenhahn et al. (1980) who developed an expression for turbulent diffusivity and applied the mixing to stellar environments. We consider the stability to infinitesimal disturbances of a system described by Veronis (1965). This case is gravitationally opposite to Stern (1960); the proceeding analysis considers warm salty water underlying cool fresh water. As Veronis (1965) argues one can treat the two problems by considering the same configuration but changing the direction of gravity. We can therefore derive stability conditions for both types of DD mixing by following his method.

In Figure 2.5 the initial set up of the fluid is described. The layer is of depth d and the boundaries are taken as dynamically free as well as perfect conductors of both heat, T , and salt, S . We assume motions are limited to the x-z plane with linear gradients of of salt and temperature decreasing in the the opposite direction to gravity. The analysis was carried out with the ocean in mind but T and S could be any competing quantities where S is the slower diffusing of the two.

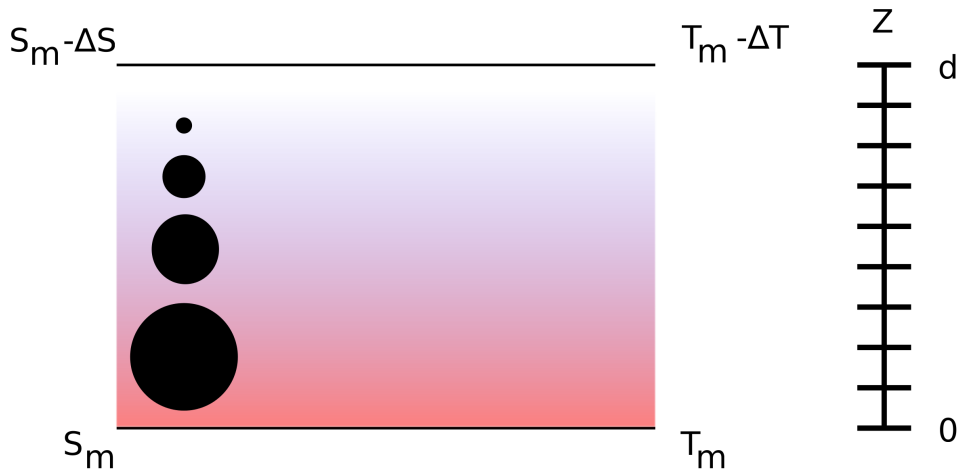


Figure 2.5: The initial set up of the fluid is illustrated. The background colour gradient denotes the decreasing temperature whilst the behaviour of the salinity gradient is represented by circle size. T_m and S_m are the temperature and salinity at the base of the system. The temperature at any point is given by $T = T_m - \Delta T(z/d)$ and similarly for salinity, $S = S_m - \Delta S(z/d)$.

The fluid under consideration has velocities much less than the sound speed so that shocks are not an issue. Furthermore, we assume that the temperature difference, ΔT , is small throughout the layer of the fluid. It therefore follows that any variation in density is also small. In such cases one can employ the Boussinesq approximation to the Navier-Stokes equations. This approximation allows for the variation in density to be ignored in all terms except for the buoyancy which may still drive motions. The equations for momentum and continuity take the form;

$$\frac{\partial}{\partial t} \mathbf{v} + \mathbf{v} \cdot \nabla \mathbf{v} = -\frac{1}{\rho_m} \nabla P + g(\alpha T - \beta S) \mathbf{k} + \nu \nabla^2 \mathbf{v} \quad (2.23)$$

$$\frac{\partial u}{\partial x} + \frac{\partial w}{\partial z} = 0. \quad (2.24)$$

The equations for conservation of heat and salt are

$$\frac{\partial T}{\partial t} + \mathbf{v} \cdot \nabla T - w \Delta T = K_T \nabla^2 T \quad (2.25)$$

$$\frac{\partial S}{\partial t} + \mathbf{v} \cdot \nabla S - w \Delta S = K_S \nabla^2 S \quad (2.26)$$

where v is the velocity of the fluid, P the pressure, g the gravitational acceleration and ν the kinematic molecular viscosity. Equation 2.24 is the two-dimensional continuity equation such that u and w are the Cartesian components of the velocity along our axes of interest (x and z respectively). Within the Boussinesq approximation the linearised equation of state

$$\rho = \rho_m(1 - \alpha T + \beta S), \quad (2.27)$$

appears only in the buoyancy (the body force term \mathbf{k} in Equation 2.22 is a unit vector positive upward) and utilises ρ_m , the mean density of the system. K_T and K_s are kinematic coefficients of diffusion of heat and salt. α and β are the respective coefficients of expansion and are defined in such a way that they are both positive for temperature and salinity changes at constant pressure,

$$\alpha = -\frac{1}{\rho} \left(\frac{\partial \rho}{\partial T} \right)_{S,P}, \quad \beta = \frac{1}{\rho} \left(\frac{\partial \rho}{\partial S} \right)_{T,P}. \quad (2.28)$$

In fluid analysis, generality can be extended through non-dimensionalising the quantities that describe the problem. This allows the system to be scaled and applied to regimes beyond that initially studied. It is also more useful to measure quantities relative to some unit that describes an intrinsic property of the fluid. Following the procedure of Veronis (1965), the variables are non-dimensionalised in the following way:

$$\begin{aligned} \mathbf{v} &= (K_T/d)\hat{\mathbf{v}} \\ t &= (d^2/K_T)\hat{t} \\ (x, z) &= d(\hat{x}, \hat{z}) \\ T &= (\Delta T)\hat{T} \\ S &= (\Delta S)\hat{S} \\ \zeta &= Pd^2/\rho_m\nu K_T. \end{aligned} \quad (2.29)$$

Dropping the \wedge , Equations 2.23 - 2.26 now take the form:

$$\frac{1}{Pr} \left(\frac{\partial \mathbf{v}}{\partial t} + \mathbf{v} \cdot \nabla \mathbf{v} \right) = -\nabla \zeta + (Ra T - Rs S)\mathbf{k} + \nabla^2 \mathbf{v} \quad (2.30)$$

$$\frac{\partial u}{\partial x} + \frac{\partial w}{\partial z} = 0 \quad (2.31)$$

$$\frac{\partial T}{\partial t} + \mathbf{v} \cdot \nabla T - w = \nabla^2 T \quad (2.32)$$

Notation	Parameter
d	Layer depth
T	Temperature
S	Salinity
T_m	Temperature at the base of the layer
S_m	Salinity at the base of the layer
\mathbf{v}	Velocity vector of the fluid
P	Pressure
g	Gravitational acceleration
ν	Kinematic molecular viscosity
u	Cartesian component of the velocity along the x axis
w	Cartesian components of the velocity along the z axis
ρ	Density
ρ_m	Mean density of the fluid.
\mathbf{k}	Unit vector that is positive in the opposite direction of gravity
K_T	Kinematic coefficient of diffusion for heat
K_s	Kinematic coefficient of diffusion for salt
α	Coefficient of thermal expansion
β	Coefficient of haline expansion
ζ	Non dimensionalised expression for pressure
τ	Inverse Lewis number (K_S/K_T)
Pr	Prandtl number (ν/K_T)
Ra	Temperature Rayleigh number $(g\alpha\Delta T d^3)/(\nu K_T)$
Rs	Salt Rayleigh number $(g\beta\Delta s d^3)/(\nu K_T)$
R_ρ	Density ratio of competing quantities
ψ	Stream function
\mathfrak{S}	Determinant of Jacobian matrix
a	Horizontal wavenumber
n	Vertical wavenumber
p	Complex number that describes the growth and behaviour of a wave
k^2	Composite waveumber $\pi^2(a^2 + n^2)$
Ra_c	Effective Rayleigh number beyond which unstable direct modes develop
Ra_c^o	Effective Rayleigh number beyond which oscillatory modes develop
a_*	Maximum horizontal wavenumber in the thermohaline-finger regime

Table 2.1: Reference of the variables and their meanings used throughout the stability analysis.

$$\frac{\partial S}{\partial t} + \mathbf{v} \cdot \nabla S - w = \tau \nabla^2 S. \quad (2.33)$$

The instability can now be characterised by four dimensionless variables:

- The ratio of diffusivities sometimes referred to as the inverse Lewis number, $\tau = K_S/K_T$.
- The Prandtl number, the ratio of viscosity to thermal diffusivity, $Pr = \nu/K_T$.
- The density ratio, $R_\rho = \beta \Delta S / \alpha \Delta T$.
- The Rayleigh number, the ratio of buoyancy to the diffusive processes of conduction and viscosity $Ra = g \alpha \Delta T d^3 / \nu K_T$ and for salt $R_s = g \beta \Delta S d^3 / \nu K_T$.

Note how they describe the ratio of various stabilising and destabilising quantities. Most of the information in the density ratio can be derived from the Rayleigh numbers. We will therefore utilise only the latter for the current analysis. The importance of the density ratio is explored further in §2.4.4 as it is essential for determining stability in stellar models. Table 1 of Denissenkov (2010) outlines typical values of these numbers in the oceanic context, this is partially reproduced in Table 2.2:

Parameter	Notation	Value
Viscosity	ν	$10^{-2} \text{ g}/(\text{s} \cdot \text{cm})$
Thermal Diffusivity	K_T	$1.4 \times 10^{-3} \text{ cm}^2/\text{s}$
Haline Diffusivity	K_S	$1.1 \times 10^{-5} \text{ cm}^2/\text{s}$
Gravitational Acceleration	g	$9.8 \times 10^2 \text{ cm}/\text{s}^2$
Thermal Expansion	α	$2 \times 10^{-4} \text{ K}^{-1}$
Haline Expansion	β	$7.5 \times 10^{-4} \text{ }^0/\text{ }_{00}^{-1}$
Temperature Gradient	$\frac{\partial T_0}{\partial z}$	$3 \times 10^{-3} \text{ K}/\text{cm}$
Density Ratio	R_ρ	1.6
Prandtl Number (ν/K_T)	Pr	7
Inverse Lewis Number (K_S/K_T)	τ	8×10^{-3}

Table 2.2: Typical oceanic values for those parameters that describe a doubly diffusive system.

It is a well known result that the two dimensional continuity equation can be satisfied by introducing a stream function, ψ in the form

$$u = \frac{\partial \psi}{\partial z}, \quad w = -\frac{\partial \psi}{\partial x}. \quad (2.34)$$

The stream functions are constant along streamlines which represent the trajectories of particles along the steady flow. Streamlines are perpendicular to equipotential lines and tangent to the velocity vector of the flow. By utilising Equation 2.34 we can eliminate 2.31 and recast Equation 2.32 as follows

$$\frac{\partial T}{\partial t} + \mathbf{v} \cdot \nabla T - w = \nabla^2 T \quad (2.35)$$

$$\Rightarrow \frac{\partial T}{\partial t} - \nabla^2 T - w = -\mathbf{v} \cdot \nabla T \quad (2.36)$$

$$\Rightarrow \left(\frac{\partial}{\partial t} - \nabla^2 \right) T - w = -\mathbf{v} \cdot \nabla T. \quad (2.37)$$

Remembering

$$\mathbf{v} = u_x + w_z \quad (2.38)$$

and introducing a 2D stream function such that

$$u = \frac{\partial \psi}{\partial z}, \quad w = -\frac{\partial \psi}{\partial x}, \quad (2.39)$$

and expressing ∇T in the form of its components, a substitution for \mathbf{v} and w can be made in Equation 2.37

$$\left(\frac{\partial}{\partial t} - \nabla^2 \right) T + \frac{\partial \psi}{\partial x} = - \left(\frac{\partial \psi}{\partial z}, -\frac{\partial \psi}{\partial x} \right) \cdot \left(\frac{\partial T}{\partial x}, \frac{\partial T}{\partial z} \right) \quad (2.40)$$

$$= - \left(\frac{\partial \psi}{\partial z} \frac{\partial T}{\partial x} - \frac{\partial \psi}{\partial x} \frac{\partial T}{\partial z} \right) \quad (2.41)$$

$$= \frac{\partial \psi}{\partial x} \frac{\partial T}{\partial z} - \frac{\partial \psi}{\partial z} \frac{\partial T}{\partial x} \quad (2.42)$$

$$= \mathfrak{S}(\psi, T). \quad (2.43)$$

The right hand side of Equation 2.42 is the definition of the Jacobian which we express as $\mathfrak{S}(\psi, T)$ hereafter. A similar substitution can be made for Equation 2.33. A further step is required to simplify Equation 2.30 in that the pressure term, ζ , can be removed via cross differentiation. The resultant equations are:

$$\left(\frac{1}{Pr} \frac{\partial}{\partial t} - \nabla^2 \right) \nabla^2 \psi = -Ra \frac{\partial T}{\partial x} + Rs \frac{\partial s}{\partial x} + \frac{1}{Pr} \mathfrak{S}(\psi, \nabla^2 \psi) \quad (2.44)$$

$$\left(\frac{\partial}{\partial t} - \nabla^2 \right) T + \frac{\partial \psi}{\partial x} = \mathfrak{S}(\psi, T) \quad (2.45)$$

$$\left(\frac{\partial}{\partial t} - \tau \nabla^2 \right) S + \frac{\partial \psi}{\partial x} = \mathfrak{S}(\psi, S). \quad (2.46)$$

Boundary conditions need to be specified for our system. The simplest case is to employ free slip conditions which is the approach taken in most analyses of this problem. These boundary conditions assume that the free surface acts as

a rigid surface with tangential slip but no tangential stresses. That is, the only restriction on the flow field is that the component of the fluid velocity normal to the (stationary) surface is zero. The dependent variables are chosen to be zero, which implies that the temperature and salinity at the boundaries of the region are constant. Thus

$$\psi = \frac{\partial^2 \psi}{\partial z^2} = T = S = 0 \quad \text{at } z = 0, 1. \quad (2.47)$$

Stability is gauged through investigating the effect of infinitesimal perturbations in the case where temperature and salinity have constant gradients. The configuration of the fluid has cool fresh water overlying salty water that is heated. In such a system the salinity gradient is stabilising and temperature destabilising. Our aim is to investigate whether small perturbations to the fluid interface will grow into large amplitudes, furthermore we wish to do so whilst the fluid is in its equilibrium configuration. Therefore the linearised perturbation equations need to be solved where:

$$\left(\frac{1}{Pr} \frac{\partial}{\partial t} - \nabla^2 \right) \nabla^2 \psi = -Ra \frac{\partial T}{\partial x} + Rs \frac{\partial s}{\partial x} \quad (2.48)$$

$$\left(\frac{\partial}{\partial t} - \nabla^2 \right) T + \frac{\partial \psi}{\partial x} = 0 \quad (2.49)$$

$$\left(\frac{\partial}{\partial t} - \tau \nabla^2 \right) S + \frac{\partial \psi}{\partial x} = 0. \quad (2.50)$$

The usual method for solving such systems of equations is via normal mode analysis whereby the modes take on an assumed form containing an exponential and sine component. As Veronis (1965) highlights the equations have constant coefficients so that a Fourier representation of the variables can be introduced. A set of functions can be written down that satisfy the above equations and the boundary conditions (Baines and Gill, 1969):

$$\psi \sim e^{pt} \sin \pi a x \sin n \pi z \quad (2.51)$$

$$T, s \sim e^{pt} \cos \pi a x \sin n \pi z,$$

where πa is a horizontal wavenumber and πn is a vertical wavenumber. Here a is unrestricted but n must be an integer and p is a complex number where the real part represents the growth rate and imaginary part describes the time-oscillatory character of the solution. Note that authors such as Kozitskii (2000) and Nield (1967) assume a different set of functions; the free boundary conditions allow for functions in the simple form of the product of an exponential and sine. As Riahi (2000) discusses, the flow disturbances evolve in time from some initial spatial distribution, so that the wavenumbers are real while the frequency is in general, a complex function of the wavenumbers. Given the family of exponential solutions, the solution to the growth rate p is a cubic in the form

$$p^3 + \Lambda_2 p^2 + \Lambda_1 p + \Lambda_0 = 0 \quad (2.52)$$

which relies on the non-dimensional parameters and the wave vectors. Here

$$\Lambda_2 = (Pr + 1 + \tau)k^2 \quad (2.53)$$

$$\Lambda_1 = (Pr + \tau Pr + \tau)k^4 - (Ra - Rs)Pr \pi^2 a^2 / k^2 \quad (2.54)$$

$$\Lambda_0 = \tau Pr k^6 + (Rs - \tau Ra)Pr \pi^2 a^2 \quad (2.55)$$

which yields the third order dispersion relationship

$$p^3 + (Pr + 1 + \tau)k^2 p^2 + [(Pr + \tau Pr + \tau)k^4 - (Ra - Rs)Pr \pi^2 a^2 / k^2]p + \tau Pr k^6 + (Rs - \tau Ra)Pr \pi^2 a^2 = 0, \quad (2.56)$$

where k is the wavenumber ($k^2 = a^2 + n^2 \pi^2$ and a is the horizontal wavenumber and n the vertical wavenumber). As Equation 2.56 is cubic in p and p is complex, the equation can be separated into its real and imaginary parts (odd and even powers of p) and solved for the respective roots. Following the procedures of Baines and Gill (1969) and Veronis (1965) the behaviour of the roots for any any given values of Pr , τ , Ra , Rs can be examined. Figure 2.6 which is based on figure 8.2 in Turner (1973) demonstrates the nature of these roots with variation of Ra and Rs (but fixed Pr and τ). The Figure is not drawn to scale but is a diagram indicating the nature of the roots for typical oceanic values of $Pr = 10$ and $\tau = 0.01$.

The figure highlights that the complexity of doubly-diffusive systems goes beyond either finger or oscillatory mixing. The regime in which a parcel finds itself will dictate how energy is drawn from the system and in turn affect the geometry and behaviour of the dominant modes. We will establish the criteria that determine the respective regimes and interpret the physical mechanism by which mixing develops.

In a doubly-diffusive system, neutral buoyancy is attained when the Rayleigh number of the two competing fields are equal. In Figure 2.6 the line AB marks the locus where $Ra = Rs$. We are interested in testing the stability of the system to infinitesimal disturbances of various wavenumbers k . As such, we wish to find the minimum value of Ra for which there is no growth of our disturbing waves ($p = ip_i$, i.e., the real part of p , $p_r = 0$). Substituting this into our dispersion relation and noting that Ra is at its minimum when $n = 1$ and $a^2 = \frac{1}{2}$ the stability criteria are given by the resulting roots:

$$CD : \quad Ra = \frac{Rs}{\tau} + \frac{27\pi^4}{4} \quad (2.57)$$

$$DE : \quad Ra = \frac{Pr + \tau}{Pr + 1} Rs + (1 + \tau) \left(1 + \frac{\tau}{Pr}\right) \frac{27\pi^4}{4} \quad (2.58)$$

We have expressed Ra (which is proportional to the destabilising temperature gradient) as a function of Rs (which is proportional to the stabilising salt gradient). In the quadrant where Rs is positive and Ra negative both gradients are stabilising and no disturbances can grow. In the opposite quadrant where Ra is positive and Rs negative all points above CD are unstable; both gradients are destabilising. Given that our configuration has warm salty water underlying cool fresh water, the unstable direct modes that develop are in the form of regular Rayleigh-Bénard

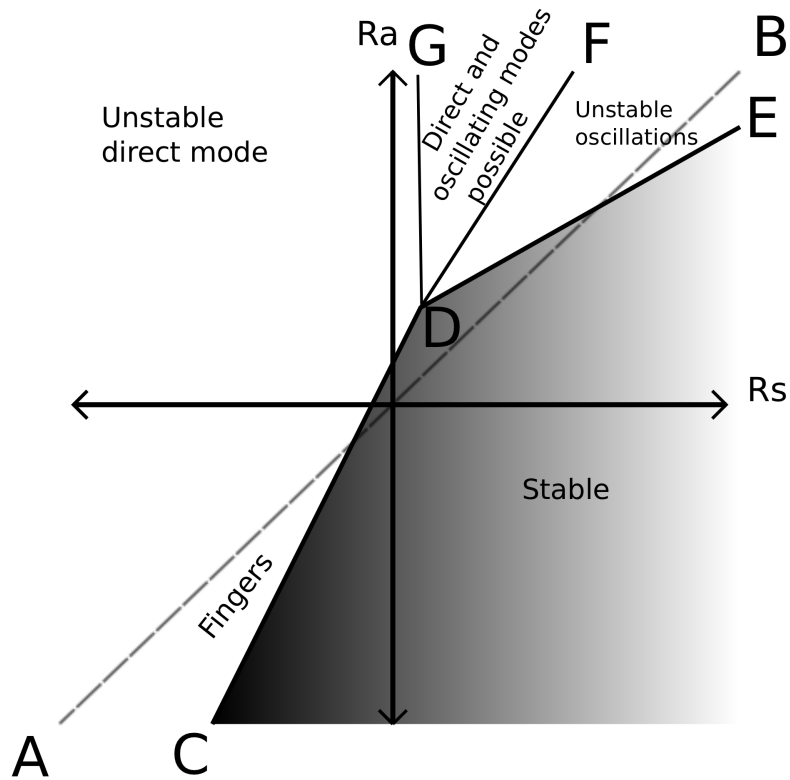


Figure 2.6: Possible convection regimes stemming from doubly-diffusive systems. In the region CDE the dispersion relation has no root with a positive real part. EDF: two complex roots with positive real part, FDG: two positive real roots, GDC: one positive real root.

(RB) convection. From Equation 2.57 we can express an effective Rayleigh number above which RB convection develops

$$Ra_c \equiv Ra - \frac{Rs}{\tau} = \frac{27\pi^4}{4}, \quad (2.59)$$

where $Ra_c = \frac{27}{4}\pi^4$ is the critical Rayleigh number for RB convection to occur in a single solute fluid. Veronis (1965) points out an interesting fact for the oceanic case. Given a very stable salt gradient i.e.,

$$R_S > \frac{27}{4}\pi^4 \quad (2.60)$$

in order for RB convection to occur, the temperature gradient must exceed the stabilising salt gradient by a factor of 100. If this is the case then as salinity increases in the direction of gravity ($\Delta S > 0$), the vertical density profile must be highly unstable gravitationally before convection can develop. In general, this of course is dependent on the ratio of diffusivity (τ) of the two components involved.

In the quadrant where Ra and Rs are both negative any points beyond the

line CD are unstable to perturbations, although all points below the line of neutral buoyancy are statically stable. Just to the left of the line CD the finger regime is marked. It can be seen that this type of instability requires a stabilising temperature but destabilising salt gradient. The motions in this region are exponentially growing direct modes that draw their potential energy from the component of lower diffusivity and are thus reliant on the value of τ . The mixing occurs in the regime where the net gradient is still statically stable but it can be seen that it is possible for the fluid to remain stable to perturbation in this quadrant when the temperature is strongly stabilising $|Ra| \gg |Rs|$. For large negative values of Ra and Rs , convection can only occur while $|Ra| < |Rs|/\tau$ or

$$\frac{\alpha\Delta T}{\beta\Delta S} < \frac{K_T}{K_S} \quad (2.61)$$

which becomes an important consideration when the diffusivities are comparable. Therefore the criteria for finger-like thermohaline mixing is:

$$\frac{Rs}{\tau} < Ra - \frac{27\pi^4}{4} < Rs < 0. \quad (2.62)$$

Above the line DE (Ra and Rs both positive) the instability that develops in the form of overstable or oscillatory modes for reasons discussed in the previous section ($K_T \gg K_S$) leads to reversal of the buoyancy gradient every half cycle). Such modes are possible in the region GDE, where the line DE is given by Equation 2.58 and line DG by

$$Ra = \frac{Pr + \tau}{(Pr + 1)\tau^2} Rs. \quad (2.63)$$

These modes induce mixing through gravity waves (Stellmach et al., 2011; Maeder, 2009). The line DF marks the boundary at which direct modes can also develop. Baines and Gill (1969) demonstrate that the locus for the most rapidly growing direct mode (convective) is so close to the line DF, that in this regime almost always motions will occur through the direct mode. Note that if $Ra > Rs$ the density continues to increase upwards and the direct modes should develop as a modified Rayleigh-Taylor instability. This instability also leads to finger-like mixing however the growth rate of the most unstable modes are faster than those in the thermohaline regime.

In oceanic conditions $\tau \ll 1$, and if we again substitute the wave numbers such that Ra is a minimum, the minimum value of R required for over stable motions can be simplified to

$$Ra_c^o = \frac{Pr}{1 + Pr} Rs + \frac{27\pi^4}{4}. \quad (2.64)$$

This implies that given a stable salt gradient, Ra must exceed the minimum value for direct-mode convection by $\frac{Pr}{1+Pr} Rs$. In the case of a very stable salt gradient i.e., $Rs \gg (27/4)\pi^4$ then only a small effect from the destabilising temperature gradient is required to initiate the unstable oscillatory modes. Hence, mixing can

occur when the net density field is stable.

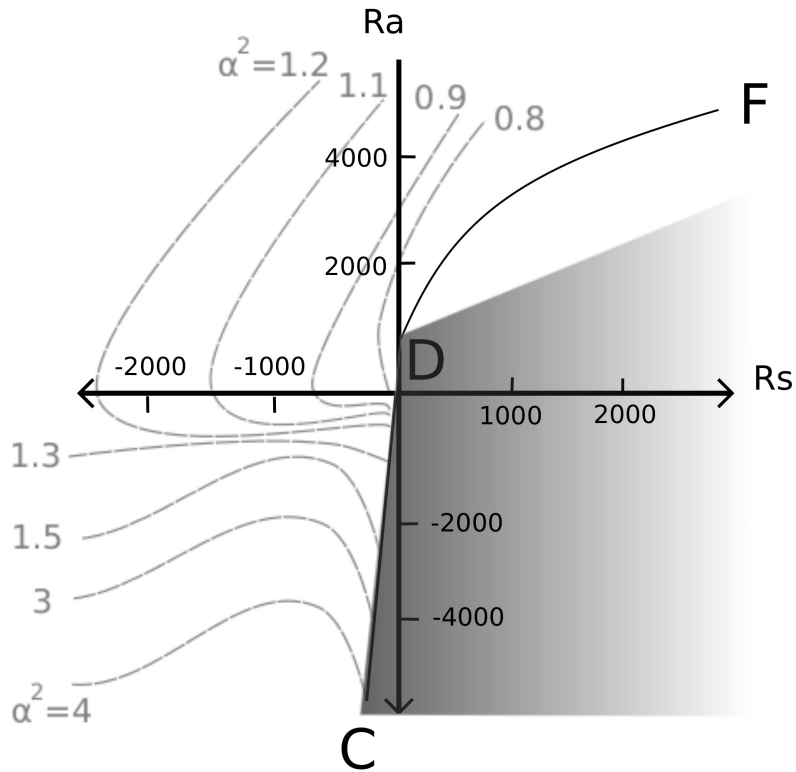


Figure 2.7: Curves showing the nature of the most unstable mode for combinations of Ra and Rs . It is assumed that the vertical wavenumber $n=1$, whilst our curves follow constant horizontal wavenumber α .

Baines and Gill (1969) also used stability analysis to investigate the geometry of the most rapidly growing cells; Figure 2.7 illustrates their findings. The diagram demonstrates the nature of the most unstable modes for various ranges in Ra and Rs . The most unstable modes in the $Ra - Rs$ plane always correspond to a vertical wave number $n=1$, this is not necessarily the case for the horizontal wave number a . In the regions where $Ra > 0$, where the component with the higher rate of diffusivity is responsible for driving the motions, they found that the most unstable modes corresponded to both n and a of order unity. The curves for the oscillating modes have not been plotted for clarity but their respective gradients asymptote to unity. Irrespective of direct or oscillating motions the cells are as high as they are wide. In the lower left quadrant however whilst $n=1$, a always exceed unity suggesting cells are tall and thin. For high $|Ra|$, the cells release the potential energy from the salt more efficiently under this elongated geometry. Such aspect ratios of the cells agree with observations (see work by Stommel and Faller published in Stern (1960) as well as more recently Krishnamurti (2003) and the references therein) and justify the use of the name ‘salt fingers’. There is a limit to the possible range of aspect ratios. Stern (1960) demonstrated that asymptotically

as $|Ra| \rightarrow \infty$ the wavenumber of maximum growth, a_* is given by

$$\pi a_* \approx \left(\frac{g\alpha\Delta T/d}{\nu K_T} \right)^{\frac{1}{4}}. \quad (2.65)$$

Through linear stability analysis we have been able to gain insight into the complex behaviour that stems from doubly-diffusive systems. We summarise some of the key points below:

1. Configurations that are convectively stable in singly-diffusive systems can be unstable in doubly-diffusive systems.
2. Density gradients that are highly unstable in singly-diffusive systems can remain stable in a doubly-diffusive configuration.
3. Thermohaline convection occurs when the the destabilising agent is the slower of the diffusing quantities.
4. Oscillatory or ‘diffusive’ convection occurs when the destabilising agent is the most rapidly diffusing of the two quantities.
5. Thermohaline mixing can only occur in the regime of marginal stability.
6. In the thermohaline regime, the fastest growing modes dominate the mixing. For the fastest growing modes, energy exchange in this regime is most effective when the geometry is finger like.
7. In the regime governed by GDF in Figure 2.6, where direct and oscillating modes are possible, i.e., $Ra > Rs$, unstable direct modes will dominate the fluid transport. The direct modes will occur predominately in the form of a modified Rayleigh-Taylor instability.
8. For large values of Ra where Rs is also destabilising unstable direct modes occur in the form of regular Rayleigh-Barnard convection.

2.4 Doubly-Diffusive Mixing in Stars

So far, the focus of this chapter has been on DD mixing in the context of the oceans. Much insight was gained through analysing the internal properties of the fluid by means of the various dimensionless numbers. We were able to determine the regimes in which mixing occurs as well as the behaviour of the dominating modes. We have developed clear conditions for stability in the oceanic environment and the aim hereafter is to extend the analysis using a formalism appropriate to stellar quantities. We will draw upon the linear theory to derive models of DD mixing that can be applied to stellar codes; the most straightforward means is to determine a diffusion equation. This work serves as the basis for later investigations into globular clusters.

DD mixing has been studied comprehensively in the astrophysical literature. The oscillatory and finger instabilities have stellar analogues in ‘semi-convection’

and ‘thermohaline mixing’ respectively. The former is thought to be a significant source of uncertainty in the evolution of massive stars; it also plays a role in low-mass stars during the core-helium burning phase. Semi-convection was first reported by Schwarzschild and Härm (1958) and analysed more recently by Castellani et al. (1971), Langer et al. (1985) and Spruit (1992) to name but a few.

Almost a decade after Stern (1960), Stothers and Simon (1969) were the first to consider how thermohaline mixing may impact upon the structure and subsequent evolution of a star. They contended that binary accretion could result in a system similar to that described by Stern. They give the example of an evolved star donating hot astrated material (of higher molecular weight) onto the surface of a hydrogen-rich, main-sequence companion. They realised that this configuration is unstable to thermohaline convection and questioned whether it could be responsible for the pulsations of β Cepheids. Of course the term thermohaline is inappropriate here and simply borrowed from oceanography. There are no ‘haline’ fingers in stars but rather the composition (molecular weight) assumes the role of the salt gradient and acts as the competing quantity. Soon after Abraham and Iben (1970) and Ulrich (1971) recognised an unusual property of the reaction



which is that despite being a *fusion* reaction, it actually reduces the mean molecular weight because it produces three particles from two. These particles also have more kinetic energy than the initial two particles, because the reaction is exothermic. More specifically they thought that the reaction may have an important role during pre-main-sequence contraction once convection had homogenised the star. This would create an inversion in the local mean molecular weight due to ${}^3\text{He}$ burning and allow a thermohaline instability to develop. This was later found to have little effect due to the short time scale of the pre-main-sequence.

In the following sections these well studied examples of DD mixing will be analysed. Although our ultimate focus is the contribution of DD processes to (RGB) extra mixing, there is much to learn from configurations that are considered well understood. We will look at semi-convection and thermohaline mixing independently, but as Rosenblum et al. (2011) and Knobloch and Spruit (1983) discuss, they can occur simultaneously when considering multiple dimensions. The 1D spherically-symmetric geometry of stellar evolution codes precludes this from our framework.

2.4.1 Semi-Convection

We will first give a qualitative explanation of semi-convection before discussing the mathematical prescriptions. Whilst it is known to play a role during the main-sequence phase of massive stars, we will examine the development of the mixing following the core He-flash in low-mass stars; stars relevant to our investigation of globular clusters. Semi-convection occurs in regions that are Schwarzschild unstable

$$\nabla - \nabla_{ad} = \left(\frac{\partial \ln T}{\partial \ln P} \right) - \left(\frac{\partial \ln T}{\partial \ln P} \right)_{ad} > 0 \quad (2.67)$$

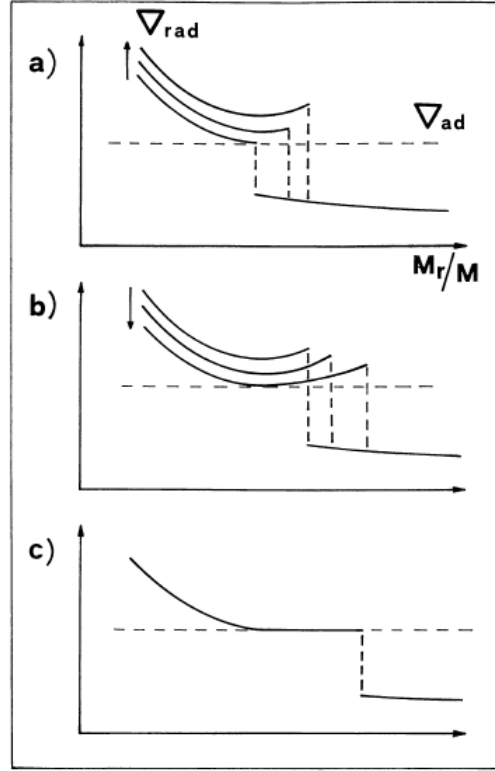


Figure 2.8: Evolution of the radiative gradient during semi-convection. The boundary of stability, $\nabla_{ad} = \nabla_{rad}$ is given by the broken horizontal line. Figure as seen in Castellani et al. (1971).

but are stable according to the Ledoux (1947) criterion

$$\nabla < \nabla_{ad} + \frac{\varphi}{\delta} \nabla_{\mu} \Leftrightarrow \left(\frac{\partial \ln T}{\partial \ln P} \right) < \left(\frac{\partial \ln T}{\partial \ln P} \right)_{ad} + \frac{\varphi}{\delta} \left(\frac{\partial \ln \mu}{\partial \ln P} \right) \quad (2.68)$$

where the Ledoux criterion reduces to the Schwarzschild criterion in the absence of a molecular weight gradient. No subscript denotes the temperature gradient in the star, *ad* the adiabatic temperature gradient, and μ the molecular weight gradient. Here $\delta = -(\partial \ln \rho / \partial \ln T)_{P, \mu}$ and $\varphi = (\partial \ln \rho / \partial \ln \mu)_{P, T}$. The variables δ and φ allow for a non-perfect gas which includes radiation pressure and degeneracy. For the regimes we consider i.e., a perfect gas,

$$\varphi = \delta = 1. \quad (2.69)$$

As is the case in the Veronis configuration, we are concerned with the doubly-diffusive instability in the presence of a strongly stabilising composition gradient. One can deduce that stabilising requires $\nabla_{\mu} > 0$ as heavier material displaced upwards into lighter material will be drawn back by gravity.

During core helium burning, the conversion of ${}^4\text{He}$ into ${}^{12}\text{C}$ and ${}^{16}\text{O}$ steadily

increases the opacity of the core. Within this region, the increase in ^{12}C raises ∇_{rad} creating a clear discontinuity at the (Schwarzschild) convective boundary. A discontinuity develops in both the ratio of the temperature gradients and the composition. The former is highlighted in Figure 2.8(a) where the radiative temperature gradient is plotted as a function of mass. The broken horizontal line indicates the value of ∇_{ad} .

In such a region the Brunt-Väisälä frequency, that is the buoyancy frequency, is given by

$$N^2 = \frac{g}{H_P} [\nabla_\mu - (\nabla - \nabla_{ad})]. \quad (2.70)$$

Here g is the gravitational acceleration, H_P the pressure scale height and the other quantities are as defined above. The Schwarzschild criterion should indicate the location of neutral buoyancy and result in a stable boundary, however, the molecular weight gradient each side of the boundary will ensure that stability is not the case. Inside the core $N^2 > 0$ and there is a positive acceleration outward, outside the core $N^2 < 0$ and there is a restoring force back inward. Such a configuration is conducive to overshooting and hence core growth.

In Figure 2.8(b) we find that within the convective core, the minimum in the radiative gradient does not coincide with the Schwarzschild boundary as one might expect. This is on account of the growing core and overshooting; material that is rich in ^4He is mixed in beyond the boundary. Once the opacity is lowered enough, radiation transport is sufficient to move energy, quenching the convection. Whilst convection continues to operate in the inner most regions (driven by nuclear burning via the triple alpha process), the ^4He rich material beyond the minimum is isolated. We can see by the ratio of the gradients that this region is not homogeneous. The presence of a stable chemical gradient, in a region that is destabilised by the temperature gradient leads to oscillatory doubly-diffusive mixing. Figure 2.8(c) shows that this slower (than convection) mixing returns the configuration to stability however the growing core (on account of core helium burning) will periodically encounter this instability.

The correct treatment of semi-convection is highly uncertain in stellar codes. Stothers (1970) carried out a systematic study of 11 different prescriptions and found all but two inappropriate. More recently Langer et al. (1985) have modelled semi-convection as a diffusive process with

$$D = \frac{\alpha K}{6} \frac{\nabla - \nabla_{ad}}{\nabla_{ad} - \nabla - \frac{\varphi}{\delta} \nabla_\mu}, \quad (2.71)$$

where α is a parameter that relates the vibrational instability to a semiconvective mixing length and K is the thermal diffusivity. Kippenhahn and Weigert (1990) describe semi-convection as a vibrational instability. In terms of ‘blob theory’ a displaced element will oscillate with increasing amplitude. Heat loss during the blob’s motions will allow the restoring force to increase despite the stabilising effect of the molecular weight gradient in Equation 2.68.

2.4.2 Thermohaline Mixing (Ulrich 1972)

Ulrich (1972) was the first to derive an expression for the turbulent diffusivity of thermohaline mixing in a perfect gas. The analysis was carried out in such a manner that the oceanic and stellar environments could be investigated concurrently. In analogy with Equations 2.23-2.26, he started with the equations of conservation of momentum, thermal energy and chemical composition:

$$C \frac{dw}{dt} = -\frac{GM_r}{r^2} \frac{\rho_1}{\rho} + \nu \nabla^2 w \quad (2.72)$$

$$\frac{dT_1}{dt} = -w \frac{dT}{dr} + K_T \nabla^2 T_1 \quad (2.73)$$

$$\frac{d\mu_1}{dt} = -w \frac{d\mu}{dr} + D \nabla^2 \mu_1. \quad (2.74)$$

where subscript 1 denotes a perturbed fluctuation in the respective quantities, w the vertical velocity, C the inertial mass per volume (set to $C = 2$ by Ulrich) which is designed to take into account the effect of the pressure of the surrounding matter on the momentum of the flow, and all other symbols are as defined earlier. Note that K_S the kinematic coefficient of diffusion for salt is replaced by a diffusion coefficient, D . Due to the way numerical codes calculate stellar models (e.g., mass as the independent variable, treatment of mixing, see Chapter 3), comparing the two regimes is not as simple as non-dimensionalising the above equations. As discussed by Rosenblum et al. (2011), stellar codes consider entropy and temperature separately whereas in oceanic modelling the two properties are treated concurrently. A more general form of Equation 2.73 is required to analyse both environments:

$$\frac{dT_1}{dt} = w \left[\left(\frac{dT}{dr} \right)_{\text{ad}} - \frac{dT}{dr} \right] + K_T \nabla^2 T_1 \quad (2.75)$$

where

$$\left(\frac{dT}{dr} \right)_{\text{ad}} = - \left(\frac{\partial T}{\partial P} \right)_{\text{ad}} \frac{GM_r}{r^2} \rho. \quad (2.76)$$

The $\left[\left(\frac{dT}{dr} \right)_{\text{ad}} - \frac{dT}{dr} \right]$ term is the advection of the background entropy gradient. In the oceanic regime Equation 2.76 is zero which recovers the original Equation 2.73 from 2.75. Furthermore, μ takes on distinct meanings. In the oceanic case it represents the salinity whereas in stellar material it is the average mass per particle.

In order to simplify the analysis, the above equations were slightly modified based on the following assumptions:

1. Motions will occur primarily in the vertical direction.
2. Motions will occur primarily in the form of long fingers.
3. The effect on momentum of the finger can be approximated by a virtual mass. (This is Ulrich's justification for using a constant, C , in Equation 2.72 to model the interaction between the rising material and its environment)

4. The relative narrowness of the moving region means that the ∇^2 can be approximated by the horizontal Laplacian ∇_h^2 .

Ulrich used the same normal mode analysis as Stern (1960) and Baines and Gill (1969) and which we reproduced in §2.3.3. It is clear that some of these simplifying assumptions were a result of previous work from the above authors. Of course Ulrich's starting equations meant that the analyses were not identical. For instance, one should understand that the stellar case required the inclusion of a more complicated equation of state. Ulrich acknowledged that his assumptions meant the approach was less rigorous, however this did not undermine its validity; he still recovered a dispersion relation equivalent to Equation 2.56 and the formula for the fastest growing modes (Equation 2.65).

Given the vastly different conditions, Ulrich (1972) was concerned with the scaling of stable oceanic flows to stellar environments. He extended the work of Stern (1960) by systematically considering the stability of a growing cell in both regimes. He argued that the displacement of a cell will grow at a rate that is limited by either:

- (a) the diffusion rate of the thermal energy,
- (b) the viscous drag of the surroundings,
- (c) the maximum gravitational potential energy available from the chemical gradient.

Thus far our analysis has only considered regimes described by (b) and (c). The stability analysis in §2.3.3 pertains to (b) with its dependence on the Prandtl number and is the situation described by Stern (1960) whereas case (c) appears to be a reference to the situation described by Veronis (1965). Case (a), the thermally limited modes, are those whose horizontal scale is so large that the growth of velocity is limited by the rate at which energy can diffuse out. Under these conditions the effects of the composition diffusion become negligible. One of the core assumptions of our analysis, and first asserted by Stern (1960), has been that the fastest growing modes tend to dominate the motions. If thermally limited modes are to dominate mixing, then those viscous modes previously explored must somehow be inhibited.

In fact, Ulrich argues this is exactly what must be occurring in stellar interiors if mixing is operating via the DD mechanism. He contends that the excessively long and narrow geometry characteristic of the aquatic experiments can not be attained in these environments and that thermally limited modes are more effective at transporting material. Kippenhahn (1969), in his analysis of the GSF instability, assumed that the motions can be described by Stoke's law. It is therefore inherent that the flow is initially laminar. We have seen that the onset of turbulence in the presence of rotational shearing is governed by the Richardson criteria. But in the case of a free flow, such as thermohaline convection, the critical Reynolds number is the appropriate stability criterion to employ. The Reynolds number is defined by:

$$Re = \frac{v\lambda}{4\nu} \quad (2.77)$$

where v is the velocity, $\lambda/4$ the radius of the ‘finger’ (flow) and ν the viscosity of the fluid. The critical value (Re_c) upon which a thermohaline like flow is expected to transition from laminar to turbulent conditions occurs at $Re_c \approx 30$. The laboratory experiments by Stommel and Fowler, in which the fingers are driven by the smallest and fastest growing modes, are disrupted on a length scale an order of magnitude less than predicted by the laminar theory. Given the conditions found inside stars, this suggests that an element would start to break up before it is displaced, rendering mixing governed by (b) and (c) inefficient. If this is the case, and if we accept that the flow is initially turbulent, then those modes that grow the fastest need not be responsible for mixing. It is possible that the turbulence can affect the smaller modes whilst the larger ones have time to grow an appreciable multiple of their width. Ulrich contends that the inevitable growth of shear instabilities in the thermally limited modes may only enhance the molecular diffusion rather than disrupt the flow. This would allow the fingers time to grow.

The key assumption of Kippenhahn (1969) in deriving a diffusion coefficient for the GSF instability was that one could neglect the time derivative in Equation 2.11. With the thermally-limited modes one cannot assume that the change of velocity is slow which limits this approach to thermohaline mixing in the stellar context. In order to determine the growth rate, velocity and expression for the turbulent diffusivity, Ulrich non-dimensionalised Equations 2.72 - 2.74 and arrived at a dispersion relation like our Equation 2.56. The assumptions that thermally limited modes dominate the mixing means that D and $\nu \nabla_h w$ can be set to zero in his governing equations. The growth rate, p , can then be determined by equating Λ_1 and Λ_0 terms in equation 2.56. With Ulrich’s choice of non dimensionalisation and substituting in the stellar quantities, the growth rate in thermally limited regime is given by

$$p = k^2 K \frac{\nabla_\mu}{\nabla - \nabla_{ad} - \nabla_\mu}, \quad (2.78)$$

where K is the thermal conductivity and k is the total horizontal wavenumber as before.

Ulrich assumed that no one length scale should dominate the mixing, and like the mixing length theory (MLT), one can average the possible element geometries. This was parameterised such that the parcels could grow some length l that is a multiple of the dimensional wavenumber, λ ,

$$l = \alpha \lambda \quad (2.79)$$

where α is a free parameter that is akin to a mixing length and describes the aspect ratio of the fingers. The total horizontal wavenumber, k , is related to λ simply through $\lambda = 2\pi/k$. Ulrich assumes that for a cylindrical disturbance, the wavenumber in any direction, say k_x , can be given by $k_x^2 \approx 0.5k^2$. We can therefore express Equation 2.79 as

$$l = \alpha \lambda = 2^{\frac{3}{2}} \frac{\pi}{k_x} \alpha \quad (2.80)$$

Note that the assumptions about the cylindrical disturbance contributes to Ulrich’s dimensionless free parameter in the linear theory (the factor of 8 in Equation

2.84, the factor of 3 incidentally comes from assumptions about the minimum requirements for motions of the thermally limited modes).

Ulrich gave an estimation for the velocity of the fingers in terms of their growth rate

$$v \approx p \cdot l \quad (2.81)$$

although other authors in the literature prefer $v \approx p \cdot l/2$, (e.g., Kunze 2003, Denissenkov 2010). From this, he was able to determine a diffusion coefficient through

$$D_{thm} = pl \cdot l = v \cdot l \quad (2.82)$$

If we substitute the stellar parameters and our recent identities in Ulrich's equation 24, his expression for the diffusion coefficient, we arrive at

$$D = vl = \frac{8\pi^2\alpha^2}{3} \frac{4acT^3}{3\rho\kappa} \frac{1}{\rho C_P} \frac{-\nabla\mu}{\nabla_{ad} - \nabla + \nabla\mu}. \quad (2.83)$$

Although Ulrich simplifies this to

$$D = vl = \frac{8\pi^2\alpha^2}{3} \frac{4acT^3}{3\rho\kappa} \frac{1}{\rho C_P} \frac{-\nabla\mu}{\nabla_{ad} - \nabla}. \quad (2.84)$$

in his paper for reasons that are not quite clear. Note that the dimensional wavenumber λ has been eliminated through our identities which results in an expression for D_{thm} in terms of the dimensionless aspect ratio α . Here C_P is the specific heat capacity, κ is the opacity, ρ is the density, a the radiation density constant, c the speed of light and T the temperature as defined earlier.

There are two further caveats with the use of this formula. One must ensure that the Reynold's number of the fluid of interest is above $Re = 30$. if it is below this value then the laminar theory should hold and the viscous modes dominate once more. Secondly, in the case of the GSF instability, Kippenhahn assumes the flow dissolves once it is unstable against shear flow. In all stellar conditions such thermohaline fingers should be unstable to shear flow, but Ulrich gives the example of solar granules which are predicted to also be highly unstable yet are able to maintain their identity initially. He also argues that any lateral velocities in conjunction with internal turbulence may disrupt the efficiency of mixing. This point serves as a major criticism of thermohaline mixing (Denissenkov and Pinsonneault, 2008a) and will be discussed in Chapter 10.

There were three stellar environments in which Ulrich considered the operation of thermohaline mixing:

- During the pre-main sequence, the convective envelope homogenises most of the the proto-star. Without core hydrogen burning deuterium and ${}^3\text{He}$ burning provide radiative support. He argued that the reaction ${}^3\text{He}({}^3\text{He}, 2p){}^4\text{He}$ could create a molecular weight inversion and transport material from the burning region. Ulrich realised that the timescales involved would see the process have negligible effect. See also Siess (2009) for the super AGB case.
- The accretion of ${}^4\text{He}$ -rich material from an evolved star onto a hydrogen-rich

companion would see material of higher molecular weight sitting upon that of lower molecular weight. Chen and Han (2004) and Stancliffe and Glebbeek (2008) amongst others have investigated instances of this configuration.

- A similar configuration arises during the core flash when off centre helium burning leads to ^{12}C sitting upon ^4He . Once again thermohaline mixing is unlikely to have an appreciable effect during the core flash due to the timescales involved. Furthermore, Dearborn et al. (2006) showed that a small amount of overshooting inwards could remove the molecular weight inversion on a dynamical timescale, thus removing the possibility of any mixing.

2.4.3 Thermohaline Mixing (Kippenhahn et al. 1980)

Kippenhahn et al. (1980) envisaged thermohaline mixing having a significant effect when helium rich material overlies material that is hydrogen rich. They give the classic example of accretion from an evolved star onto a main-sequence companion as well as carbon overlying helium during the non-central core flash. Like Ulrich (1972), they determined a diffusion coefficient appropriate for stellar mixing.

Following on from Kippenhahn (1969) and the analysis of the GSF instability, Kippenhahn et al. (1980) utilised the ‘blob theory’ formalism to determine how a displaced blob of helium would move through a region rich in hydrogen. It is implicit in their configuration (hotter helium overlying cooler hydrogen) that there is a difference in μ between the two layers ($D\mu \neq 0$) but each medium is homogeneous ($\nabla\mu = 0$). Kippenhahn et al. (1980) demonstrated that two stably stratified fluids with this configuration are secularly unstable. Their stability analysis indicates a positive growth rate for any disturbance. They argue that the time of growth is determined by the thermal adjustment of regions characterised by the wavelength of the perturbation. As long as the perturbation results in a spherical blob then the τ , the timescale of thermal adjustment is given by

$$\tau = \frac{C_P \kappa \rho^2 d^2}{16acT^3} = \frac{C_P \rho d^2}{12k}, \quad (2.85)$$

where C_P is the specific heat capacity, ρ is the density, T the temperature, a the radiation density constant, c the speed of light and d is the diameter of the perturbed blob. k is the thermal conductivity given by

$$k = \frac{4acT^3}{3\rho\kappa}. \quad (2.86)$$

In this equation κ is the opacity.

Recall that the motion of displaced blob is governed by Equation 2.11,

$$\frac{\partial(DT/T)}{\partial t} + \frac{1}{\tau} \frac{DT}{T} = (\nabla - \nabla_{ad}) \frac{v}{H_P}, \quad (2.87)$$

where the variables have the same meanings as above. As was the case in the GSF instability, it is assumed that the velocity does not change much during the time τ so that the time derivative of Equation 2.87 can be ignored. Furthermore,

from the equation of state it can be shown that a displaced blob can remain in equilibrium with its chemically distinct surroundings, provided there exists a temperature difference between the material:

$$\delta \frac{DT}{T} = \varphi \frac{D\mu}{\mu} \quad (2.88)$$

$$\Rightarrow \frac{DT}{T} = \frac{\varphi}{\delta} \frac{D\mu}{\mu}, \quad (2.89)$$

where $\delta = -(\partial \ln \rho / \partial \ln T)_{P,\mu}$ and $\varphi = (\partial \ln \rho / \partial \ln \mu)_{P,T}$ as above. Substituting Equation 2.89 into 2.87 yields the following expression for velocity

$$v_\mu = |v| = \frac{\varphi H_P}{\delta(\nabla_{ad} - \nabla)\tau} \frac{|D\mu|}{\mu}. \quad (2.90)$$

The mean free path an element can travel before losing its identity is the fundamental difference between the derivations of Kippenhahn et al. (1980) and Ulrich (1972). Ulrich (1972) suggests that a blob can maintain its identity for at least a displacement of length equal to its diameter. Kippenhahn et al. (1980) were worried that the linear theory does not capture all aspects of the fully developed instability. The conditions under which they suggested that this process could develop required two stratified layers with hotter higher molecular weight material on top and with an initial displacement in the direction of gravity. Due to hydrostatic equilibrium, a displaced helium blob in the surrounding hydrogen material is always hotter than its neighbourhood, energy will flow into the neighbouring regions and heat the material just outside the blob. The circulation system that develops as a result of the blob itself will ultimately lead to its destruction.

An outcome of this picture is the formation of fully mixed transition layers. A perturbation with wavelength L begins to form fingers but at the same time the circulation from its temperature excess immediately leads to mixing with its surroundings. The process is repeated between these layers (themselves typically of length L) but on a longer timescale as the molecular weight difference has been reduced. The interpretation of which is that turbulence or the circulation inhibits the formation of fingers by smearing the μ profile. Having derived expressions for the velocity and mixing length, the resultant formula for the diffusion coefficient is given by

$$D = v_\mu L = \frac{H_P L^2}{(\nabla_{ad} - \nabla)\tau} \left| \frac{d\mu}{dr} \right| \frac{1}{\bar{\mu}}. \quad (2.91)$$

Of course inside stars it is not always the case that two layers are stratified such that $D\mu \neq 0$ but $\nabla_\mu = 0$. Maeder (2009) amongst others, considered the case of a parcel moving through a region in the presence of a molecular weight gradient such that $\nabla_\mu \neq 0$. Like Ulrich (1972), Maeder does not assume that the time derivative in Equation 2.87 can be ignored. We can estimate an expression for the

time derivative:

$$\begin{aligned}
\frac{\partial}{\partial t} \left(\frac{DT}{T} \right) &\approx \frac{\partial}{\partial t} \left(\frac{\varphi}{\delta} \frac{D\mu}{\mu} \right) \\
&\approx \frac{\partial}{\partial t} \left(\frac{\varphi}{\delta} \frac{\nabla_\mu}{H_P} D r \right) \\
&\approx \frac{\varphi}{\delta} \frac{\nabla_\mu}{H_P} v_\mu.
\end{aligned} \tag{2.92}$$

This leads to the following expression for the velocity in an inhomogeneous medium

$$D = v_\mu L = \frac{H_P L^2}{(\nabla_{ad} - \nabla + \frac{\varphi}{\delta} \nabla_\mu) \tau} \frac{\varphi}{\delta} \left| \frac{d\mu}{dr} \right| \frac{1}{\bar{\mu}} \tag{2.93}$$

$$= \frac{H_P L^2}{(\nabla_{ad} - \nabla + \nabla_\mu) \tau} \left| \frac{d\mu}{dr} \right| \frac{1}{\bar{\mu}}. \tag{2.94}$$

We have assumed that $\frac{\varphi}{\delta} = 1$ in a perfect gas and have omitted these terms in the above equation. This generalisation gives the diffusion coefficient for the formation of ‘salt fingers’ in an ambient medium with a molecular weight gradient; the environment pertaining to stellar interiors.

2.4.4 Stellar Stability Criteria

Before investigating DD mixing on the RGB it is worth summarising under what conditions semi-convection and thermohaline mixing develop in stellar interiors. A proper understanding of each process will help us investigate the RGB mechanism. In §2.3.3 the stability parameter for doubly-diffusive oceanic flow is given by the density ratio

$$R_\rho = \frac{\beta \Delta S}{\alpha \Delta T} \tag{2.95}$$

where

$$\alpha = -\frac{1}{\rho} \left(\frac{\partial \rho}{\partial T} \right)_{S,P}, \quad \beta = \frac{1}{\rho} \left(\frac{\partial \rho}{\partial S} \right)_{T,P}. \tag{2.96}$$

For application to stellar context we can express the two coefficients of expansion in a more convenient form

$$\alpha = - \left(\frac{\partial \ln \rho}{\partial T} \right)_{S,P}, \quad \beta = \left(\frac{\partial \ln \rho}{\partial S} \right)_{T,P}. \tag{2.97}$$

We can also define the superadiabatic gradient γ

$$\gamma = \left[-\frac{\partial T}{\partial z} + \left(\frac{\partial T}{\partial z} \right)_{\text{ad}} \right]. \tag{2.98}$$

These expressions can be used to determine the relative contribution of the composition, N_S , and temperature, N_T , to the Brunt-Väisälä frequency N^2 (Kelley, 1984; Canuto, 1999),

$$N_T^2 = -g\alpha\gamma = \frac{-g}{H_P}(\nabla - \nabla_{ad}) \quad (2.99)$$

$$N_\mu^2 = g\beta \frac{\partial S}{\partial z} = \frac{-g}{H_P} \nabla_\mu \quad (2.100)$$

$$\Rightarrow \beta \frac{\partial S}{\partial z} = \frac{-\nabla_\mu}{H_P} \quad (2.101)$$

such that

$$N^2 = \frac{-g}{\rho} \frac{\partial \rho}{\partial z} = N_T^2 - N_\mu^2 = \frac{g}{H_P} [\nabla_\mu - (\nabla - \nabla_{ad})]. \quad (2.102)$$

Rather than replacing the oceanic values with stellar variables so that

$$R_\rho = \frac{\beta \Delta S}{\alpha \Delta T} \equiv \frac{g\beta \partial S / \partial z}{g\alpha \partial T / \partial z}, \quad (2.103)$$

in the stellar regime the superadiabaticity will indicate convective motions. Underlying warm fluid is necessary but not sufficient to ensure convection. Here we have made the same substitution as Ulrich (1972) for the temperature gradient in Equation 2.75. Note also that the components of the Brunt-Väisälä frequency provide a comparative importance of the gradients in question. Thus a more appropriate measure for stellar purposes, with considerations of the background entropy gradient is

$$R_\mu = -\frac{g\beta \partial S / \partial z}{g\alpha \beta} = \frac{N_\mu^2}{N_T^2} = \frac{\nabla_\mu}{\nabla - \nabla_{ad}}. \quad (2.104)$$

The density ratio, which we denote by R_μ to distinguish the stellar environment (as per Canuto), is in essence a stability parameter similar to the Richardson number in §2.2.1. In analogy to Equation 2.14, the critical value for transition from stability to instability according to Ledoux occurs when

$$R_\mu < R_\mu^{cr} = 1, \quad (2.105)$$

although many studies such as Canuto (1999) suggest that this is an over restrictive criterion. For both semiconvection and salt fingers we require

$$R_\mu = \frac{\nabla_\mu}{\nabla - \nabla_{ad}} > 0 \quad (2.106)$$

In §2.2.1 and §2.4.1 we touched upon the role of the Brunt-Väisälä frequency in determining stability; it is the natural ‘buoyancy frequency’ of an element and describes how it reacts to displacement. A system is stable if $N^2 > 0$, so that a displaced element receives a restoring force and it is unstable if $N^2 < 0$ and it is driven away. From the bracketed term in Equation 2.102 it is trivial to show that

if

$$\nabla_{\mu} > \nabla - \nabla_{ad} \Rightarrow N^2 > 0 \Rightarrow \text{Ledoux stable} \quad (2.107)$$

$$\nabla - \nabla_{ad} > \nabla_{\mu} \Rightarrow N^2 < 0 \Rightarrow \text{Ledoux unstable} \quad (2.108)$$

Similar to the respective Rayleigh numbers, the components of the Brunt-Väisälä frequency tell us a great deal about stabilising and destabilising quantities.

As per Canuto (1999, 2009), we can use the thermodynamic quantities and the Brunt-Väisälä frequency to characterise DD mixing in stellar interiors:

$$\begin{aligned} \text{Semiconvection, } \quad & \nabla - \nabla_{ad} > 0, \quad \nabla_{\mu} > 0, \quad \nabla_{rad} > \nabla \Rightarrow \nabla_{rad} > \nabla > \nabla_{ad} \\ & N_T^2 < 0, \quad N_{\mu}^2 < 0, \quad R_{\mu} > 0 \\ \text{Thermohaline, } \quad & \nabla_{ad} - \nabla > 0, \quad \nabla_{\mu} < 0, \quad \nabla > \nabla_{rad} \Rightarrow \nabla_{ad} > \nabla > \nabla_{rad} \\ & N_T^2 > 0, \quad N_{\mu}^2 > 0, \quad R_{\mu} > 0. \end{aligned} \quad (2.109)$$

Semi-convective regions are characterised by instability according to Schwarzschild. However, as is the case with the GSF instability, the molecular weight gradient can act to stabilise any motions. With both the temperature and molecular weight increasing in the direction of gravity, one finds a configuration akin to warm salty water underlying cool fresh water. If the molecular gradient is steep we find instability according to Schwarzschild but not Ledoux. In this regime the density ratio, R_{μ} will indicate just how strongly stabilising the composition gradient is. This point is highlighted by the terms that describe the the contributions to the Brunt-Väisälä frequency. The temperature gradient serves to destabilise ($N_T^2 < 0$) while the contribution from the composition will ensure a restoring force ($N_{\mu}^2 < 0$, recall that $N^2 = N_T^2 - N_{\mu}^2$).

Thermohaline mixing requires both Ledoux and Schwarzschild stability. One can see that the condition of an adverse molecular weight gradient is not sufficient for instability, the superadiabatic term may be stabilising enough to prevent any motions. As heat loss occurs $\nabla_{ad} - \nabla > 0$ or ($\nabla - \nabla_{ad} < 0$) results in $R_{\mu} > 0$ ($\nabla_{\mu} < 0$). As ∇_{μ} is so small one can see from the Brunt-Väisälä contributions that thermohaline mixing occurs in the regime of marginal stability, consistent with our findings in §2.3.3.

2.4.5 The Red Giant Branch Instability

2.4.5.1 Eggleton, Dearborn and Lattanzio (2006)

Thus far, we have discussed DD mixing in the form of semi-convection in the context of the main sequence of massive stars, and during core-helium burning of their lower mass counterparts. The thermohaline regime has been thought to act on the surface of accreting stars, during the off centre core flash of low mass stars and on the pre-main sequence. A further application, and the one of interest to

us here, was proposed by Eggleton et al. (2006) (EDL06). During main-sequence evolution a low mass star produces a substantial amount of ${}^3\text{He}$. Close to the centre, all of the ${}^3\text{He}$ has been destroyed in completing the pp chains. But at lower temperatures the ${}^3\text{He}$ remains (e.g. see Figure 1.3). When the FDU occurs it mixes the envelope abundances over a large region, producing a homogeneous envelope with a ${}^3\text{He}$ content that is far above the equilibrium value. Following FDU, the convective envelope recedes, leaving behind a region that is homogeneous in composition.

When the hydrogen burning shell advances, the fragile ${}^3\text{He}$ begins to burn. It reduces the mean molecular weight leading to an inversion. Note that ${}^3\text{He}$ burning alone is not sufficient to drive the mixing. Whenever there is hydrogen burning via the pp chains the ${}^3\text{He}({}^3\text{He}, 2p){}^4\text{He}$ reaction (Equation 2.66) will decrease μ . However the combined effect of the other reactions and the low abundance of ${}^3\text{He}$ usually makes the effect of the ${}^3\text{He}({}^3\text{He}, 2p){}^4\text{He}$ reaction on μ negligible. If one can homogenise the region beforehand, then the effect of ${}^3\text{He}({}^3\text{He}, 2p){}^4\text{He}$ dominates. This way the mixing is initiated at essentially the same point as the bump in the luminosity function, since both are caused by the H-shell reaching the abundance discontinuity left behind from FDU. Eggleton et al. (2008, EDL08 hereinafter) have shown that the change in μ must be

$$\delta\mu = \mu^2 \frac{\delta X({}^3\text{He})}{6}, \quad (2.110)$$

where $X({}^3\text{He})$ is the mass fraction of ${}^3\text{He}$. They found the magnitude of such inversions to be of the order

$$\frac{\delta\mu}{\mu} \sim 10^{-4}. \quad (2.111)$$

Although this seems small, convection is in fact driven by a similarly small superadiabaticity. EDL06 first detected evidence of the instability through the use of the 3D radiation-hydrodynamics code ‘Djehuty’ (Dearborn et al., 2001; Bazan et al., 2001; Turcotte et al., 2002; Eggleton et al., 2002; Bazán et al., 2003). Djehuty was developed at Lawrence Livermore Laboratories and has been applied to many astrophysical problems such as type 1a supernova (Dolan et al., 2007) and proton ingestion episodes (Stancliffe et al., 2011). Whilst the primary focus of their investigation was to study the core flash hydrodynamically, EDL06 noticed the development of motions in radiative regions. Upon closer inspection they found the motions coincided with regions that possessed a molecular weight inversion, and that the inversion was of order suggested by Equation 2.111. Such an inversion is present in 1D codes, but without hydrodynamics, they require prescriptions to tell them when and how to mix.

Initially, EDL06 thought they had found a Rayleigh-Taylor like instability, however, in a follow up paper (EDL08) they recognised that the process was in fact DD. Although EDL06 laboured over the nature by which the mixing occurs, they were the first to recognise the key role that ${}^3\text{He}$ burning provides in the onset of the mixing. The paper demonstrated that mechanism is an elegant means to ensure that stellar nucleosynthesis and Big Bang Nucleosynthesis remain consistent

(Dearborn et al., 1986; Hata et al., 1995; Dearborn et al., 1996; Sackmann and Boothroyd, 1999; Charbonnel and Zahn, 2007a,b). Measurements of ^3He in HII regions and planetary nebula (Rood et al., 1984; Hogan, 1995; Charbonnel, 1995; Charbonnel and Do Nascimento, 1998; Tosi, 1998; Palla et al., 2000; Romano et al., 2003) match the predicted yields from Big Bang Nucleosynthesis. Canonical models predict that low-mass, main-sequence stars are net producers of ^3He which is returned to the ISM through mass loss. Hata et al. (1995) have shown that about 90% of the ^3He produced on the main sequence by low-mass stars must be destroyed in order to reconcile the two fields. We saw above how these stars produced ^3He , and the newly discovered mechanism now also destroys it, removing the inconsistency with Big Bang Nucleosynthesis. This will still allow for the existence of the minority of planetary nebula that show large ^3He abundances (Balsler et al., 1997, 1999, 2006; Charbonnel and Zahn, 2007b). The DD mixing mechanism described will operate until the ^3He is destroyed, which may be beyond the tip of the RGB (Stancliffe, 2010; Cantiello and Langer, 2010; Charbonnel and Lagarde, 2010).

It was suggested in EDL08 that the instability should be referred to as ‘ $\delta\mu$ mixing’ to distinguish the mechanism from the other occurrences of DD mixing; we have discussed the many applications in the stellar context. Furthermore, they were concerned that the subtleties of the mixing may be overlooked given how well DD processes have been studied in the past.

2.4.5.2 Application of the Stellar Stability Criteria

The molecular weight inversion develops in a region that is stable according to both Schwarzschild and Ledoux criteria and thus cannot be semi-convection. Mixing develops on account of the composition profile, that is the molecular weight profile is the destabilising agent whilst the temperature is the stabilising quantity. In §2.3.3, it was identified that overstable modes should develop when the destabilising agent is the most rapidly diffusing of the two quantities. Conversely, finger-like convection should develop if the destabilising agent is the slower of the diffusing quantities. From these arguments and the conditions outlined in Equation 2.109 one would argue the process is in the thermohaline regime similar to the situation described by Ulrich (1972) on the pre-main sequence. We can further test this with the stellar stability criteria outlined in Chapter 2.4.4.

The panels in Figure 2.9 contain plots that describe the internal structure of a $1.0 M_{\odot}$ star with metallicity $Z=0.02$. The model is calculated from the stellar code described in Chapter 3. The evolutionary status corresponds to a star on the RGB after the LF bump but before the RGB tip. Left panels display the entire mass range of the star whilst right panels show the quantities over the region pertaining to the EDL06 instability. The blue curves in the top panels show the molecular weight profile with the right panel clearly showing the inversion that develops on account of ^3He burning. The second row has the temperature of the star plotted in logarithmic form and it is clear that, although the temperature gradient is steep in the region of interest, the temperature is smooth and monotonic. The behaviour of ∇_{μ} , the molecular weight gradient, is depicted by the vermilion curve in the third

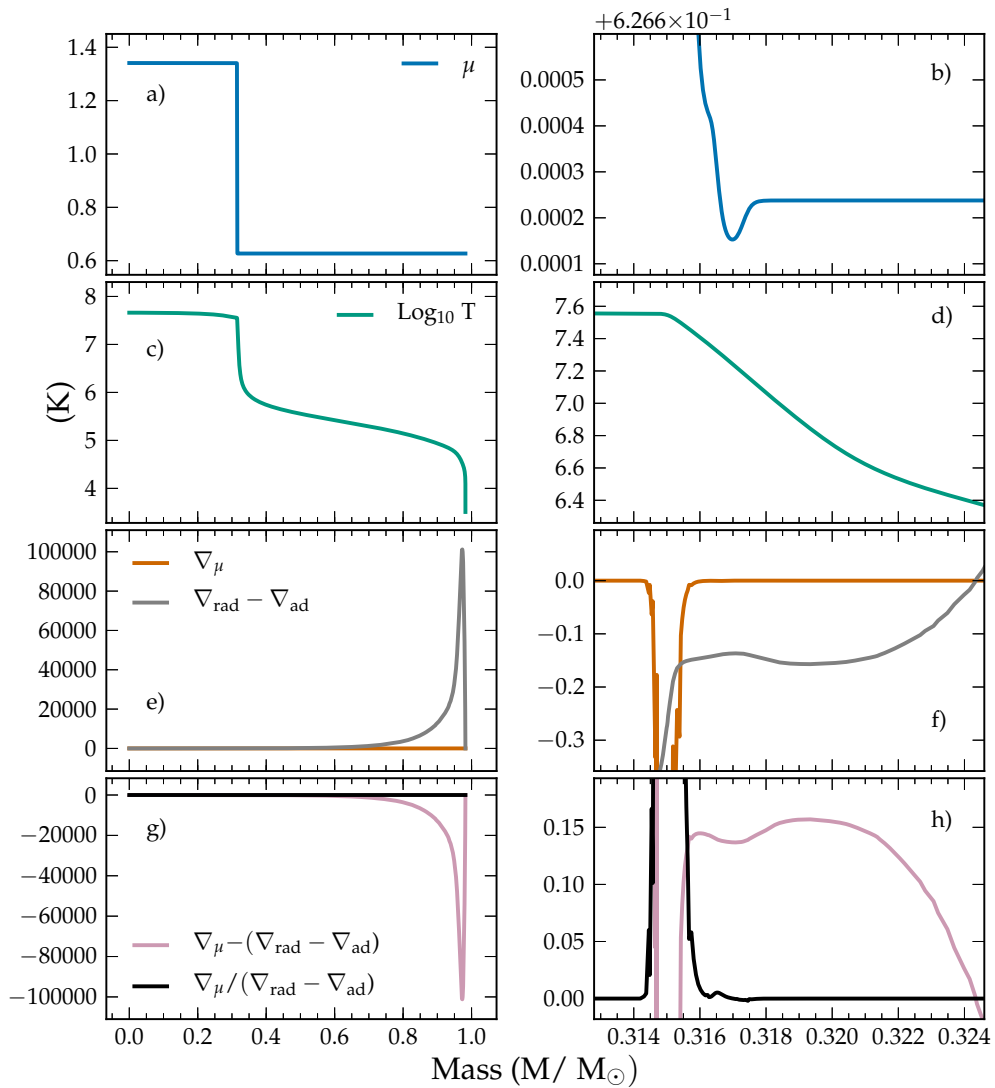


Figure 2.9: Left hand panels show the behaviour of the respective quantities over the entire mass range of the star, right hand panels focus on the region where DD mixing operates. **Panels (a) and (b)**: The blue curve corresponds to the molecular weight μ . **Panels (c) and (d)**: The green curve represents the temperature profile of the star. μ . **Panels (e) and (f)**: The vermilion curve demonstrates the behaviour of the molecular weight gradient and the grey curve indicates stability according to the Schwarzschild criterion. **Panels (g) and (h)**: The black curve corresponds to the bracketed term in the Brunt-Väisälä frequency and the lavender curve to the density ratio, R_μ .

row of panels. We also plot the term $\nabla_{\text{rad}} - \nabla_{\text{ad}}$ in grey, i.e., the Schwarzschild criterion for convective stability. Regions in which $\nabla_{\text{rad}} > \nabla_{\text{ad}}$ correspond to convection, conversely those regions where $\nabla_{\text{rad}} - \nabla_{\text{ad}} < 0$ are radiative. Finally in the last row of panels we plot two useful quantities for analysis. The lavender curve corresponds to the bracketed term in the Brunt-Väisälä frequency (Equation 2.102). Recall that this will indicate whether displaced material receives a restoring force in its new environment. The black curve is the calculated density ratio (R_μ) for the region, i.e., the stability parameter Equation 2.104.

The strong composition discontinuity in Figure 2.9(a) marks the location of the advancing hydrogen-burning shell. The region below is the growing core whilst ahead of the shell is the envelope and homogeneous region left behind by FDU. In Figure 2.9(b), the scale of the molecular weight inversion and its proximity to the shell is apparent. Due to the proximity to the burning shell, it is unsurprising the inversion falls in a region with a steep temperature gradient (Figures 2.9(c) and 2.9(d)). On account of the composition discontinuity, $|\nabla_\mu| \rightarrow \infty$. The scale used in Figures 2.9(e) and 2.9(f) are not sufficient to detect changes in the gradient at the mass coordinate of the μ inversion. From the curve denoting the Schwarzschild criterion, one can expect that there can be very little overshooting beyond the location of the μ inversion. The grey curve suggests that as one approaches the source of the nuclear energy generation, the temperature gradients become very strongly stabilising. Recall that

$$\nabla_\mu > \nabla - \nabla_{\text{ad}} \Rightarrow N^2 > 0 \Rightarrow \text{Ledoux stable}$$

$$\nabla - \nabla_{\text{ad}} > \nabla_\mu \Rightarrow N^2 < 0 \Rightarrow \text{Ledoux unstable}$$

which means that in Figure 2.9(h) the grey curve confirms that the region of interest is in fact both Ledoux and Schwarzschild stable. Figure 2.9(g) demonstrates that the star is Ledoux unstable in the convective envelope. Finally, notice how the spike in the density ratio at the location of the μ inversion ensures that the criteria set out in Equations 2.105 and 2.106 are met. It can therefore be inferred that the region meets the conditions for a thermohaline instability to develop.

2.4.5.3 Application of Blob Theory

In the previous section the stability criteria, derived from other examples of DD mixing, was applied to the RGB environment. We were able to determine that the region is susceptible to thermohaline mixing but we were provided with no information on how mixing occurs. In order to gauge stability of the EDL06 configuration, we must analyse how a parcel reacts when displaced from its initial position. One must consider the direction in which an element is displaced as the pressure gradient will effect the volume and hence buoyancy of the element. The two thermohaline examples described by Kippenhahn et al. (1980), accretion and the core flash, are unstable if a blob is displaced in the direction of gravity; the configurations are similar to the salt fingers described by Stern (1960) in §2.3.2. Hot salty (heavier) water sitting on cool freshwater. Similarly, Canuto (1999) gives

the following description:

When both the T and S fields increase from the bottom to the top of the ocean, the result is warm salty water over cold fresh water. Since the T field is stable while the S field is unstable (heavy at the top), the latter causes an instability called salt fingers.

We have seen that for this configuration the temperature excess of the salty material will ensure that it remains buoyant and return to its initial position. If however, the parcel loses heat on the time scale of its excursion into the cooler layer, it will start to move away. This example clearly highlights the importance of the competition between heat diffusion and composition diffusion. Let us now consider displacement in the opposite direction of gravity. In the case of accretion the solution is trivial, the accreted matter forms the outer layer of the star and can not be displaced outwards. In the example of the core flash, the star has strongly stabilising temperature and composition gradients radially outward. The equivalent Rayleigh numbers would fall in the shaded region of Figure 2.6 thus any disturbances are damped out.

Naively, it appears that this does not describe the configuration of the EDL process. The molecular weight inversion develops ahead of a strongly stabilising composition gradient, from Figure 2.9(a) it can be seen that this is almost discontinuous. Any displacement in the direction of gravity will therefore be subject to a strong restoring force. Furthermore, we do not have distinct well mixed layers as in the Kippenhahn examples; there is a gradient in composition rather than a dichotomy. Ulrich (1972) describes the process his formalism models:

Under normal conditions with $\frac{d\mu}{dr} < 0$ no instability exists when the density gradient and temperature gradient are both stable. However, in the presence of an inverted distribution of mean molecular weight, the adverse heat fluctuation associated with a displaced cell of material in thermally stable surroundings may diffuse out of the cell and leave a residual favourable density fluctuation resulting from the chemical composition.

This ‘favourable density fluctuation’ is clarified in Ulrich (1971)

As long as the velocity is sufficiently small, the temperature and pressure inside a cell of moving matter will be the same as that outside and the fluctuation in μ leads to a fluctuation in density which drives the motion.

We can draw a clear link to the GSF instability here. Although dynamically stable, on a secular timescale instability can occur due to the rapid diffusion of heat. If we do not include some prescription in stellar evolution codes to allow for this secular instability then the dynamical stability derived from the temperature gradients does not result in mixing.

The picture painted from the EDL06 model is as follows. In the region homogenised by FDU, ^3He burning on a nuclear timescale, creates an inversion in

the mean molecular weight profile. If we compare to the oceanic regime, then the situation arises where hot lighter material underlies cool heavier material. One would expect this to be dynamically unstable, however we must remember that in the stellar environment that it is not the temperature that is the competing quantity but $\nabla - \nabla_{ad}$. On scales such that background entropy cannot act to stabilise motions and such that perturbed material is of constant μ , a blob displaced in the opposite direction of gravity will enter a cooler region of slightly lower pressure. This means that the blob has a higher pressure than it requires for its position. Hence it quickly expands (and begins to cool) in order to establish pressure equilibrium. The expansion reduces the density and therefore the element becomes buoyant. The parcel rises until it finds an equilibrium point where the external pressure and density are equal to that inside the bubble. This is expected to be a small displacement which occurs on a dynamical timescale. Note that this is the ‘favourable density fluctuation’ described by Ulrich.

As the molecular weight inside the bubble is lower than its surroundings, the equilibrium point must correspond to a place where the external temperature is higher than that of the bubble. The temperature inside the bubble will be lower than its surroundings (we may assume a perfect gas equation of state):

$$\frac{T_i}{T_o} = \frac{\mu_i}{\mu_o}, \quad (2.112)$$

where subscript i denotes the inside of the bubble and subscript o denotes the surroundings. As heat begins to diffuse into the parcel, layers will start to strip off in the form of long fingers. It is this secondary mixing that governs the overall mixing timescale. The mixing cycles in fresh ${}^3\text{He}$ from the envelope reservoir, to replace the ${}^3\text{He}$ -depleted material that is rising toward the star’s convective envelope.

It is worth highlighting the similarities between the EDL06 picture and that of Ulrich (1972). EDL06 do not consider the effect of energy losses from the blob on its surroundings. According to Kippenhahn et al. (1980) the heat leakage that creates the initial instability will create a circulation system that destroys the blob before it has a chance to move an appreciable fraction of its size. EDL assume that the fluid rises and does not break up through energy exchange with its environment; a blob is able to lose heat and settle in a location in which the surroundings are cooler. The mixing cycles in fresh ${}^3\text{He}$ from the envelope reservoir, to replace the ${}^3\text{He}$ -depleted material that is rising toward the star’s convective envelope. This upward-flowing material will also have experienced other burning, such as CN cycling, while in the hotter region. It will also experience further burning in the future as the material is cycled through this region on subsequent occasions. The fact that this model predicts that heat diffusion into the blob will strip off layers means that, like Ulrich, the authors assume that the thermally limited modes dominate the mixing. The length scale must be such that heat can diffuse and increase the buoyancy of material before the whole parcel is thermalised with its surroundings.

2.4.5.4 Eggleton, Dearborn and Lattanzio (2008)

Having determined theoretical upper and lower limits for the mixing speed, Eggleton et al. (2008) elected to model the motions with a formalism similar to the one already used for convective mixing in their 1D stellar evolution code.

$$D = \begin{cases} \frac{F_{\text{inv}} r^2}{t_{\text{nuclear}}} (\mu - \mu_{\text{min}}) & \text{if } (k \geq k_{\text{min}}) \\ 0 & \text{if } (k \leq k_{\text{min}}), \end{cases} \quad (2.113)$$

where k is the mesh point number, counted outwards from the centre of the model, k_{min} is the value of k for which μ takes its minimum value of μ_{min} , r is the radial coordinate, F_{inv} is a constant which is selected to obtain the desired mixing efficiency and t_{nuclear} is an estimate of the nuclear evolution timescale. The nuclear timescale along the RGB can be estimated as follows

$$t_{\text{nuclear}} = \frac{EX_0M}{L}, \quad (2.114)$$

where E is the energy available from hydrogen burning, X is the hydrogen abundance in the outer layers (≈ 0.7), and L is the luminosity. This form was chosen so that it is consistent with the convective prescription inside the Eggleton code (Eggleton, 1971, 1972). In a standard convective region the diffusion coefficient D scales quadratically with the temperature gradient excess over the adiabatic value, and inversely with the nuclear timescale,

$$D = \frac{F_{\text{conv}} r^2}{t_{\text{nuc}}} [\max(0, \nabla_{\text{rad}} - \nabla_{\text{ad}})]^2 \quad (2.115)$$

2.4.5.5 Charbonnel and Zahn (2007)

With EDL06 outlining the role of ${}^3\text{He}$ and the μ inversion, Charbonnel and Zahn (2007a, CZ07a hereinafter) also realised the DD nature of the mixing and adopted the following prescription:

$$D_t = C_t K \left(\frac{\varphi}{\delta} \right) \frac{-\nabla_{\mu}}{(\nabla_{\text{ad}} - \nabla)} \quad \text{for } \nabla_{\mu} < 0, \quad (2.116)$$

where K is the thermal diffusivity and C_t is a dimensionless free parameter. In fact C_t is related to the aspect ratio, α , of the fingers in the following manner:

$$C_t = \frac{8}{3} \pi^2 \alpha^2. \quad (2.117)$$

It can be shown that this is equivalent to Equation 2.84 in the formulation of Ulrich. The thermal diffusivity, K , is given by

$$K = \frac{k}{\rho C_P} \quad (2.118)$$

where k is the thermal conductivity, ρ the density and C_P the specific heat capacity at constant pressure. k , the thermal conductivity is defined as

$$k = \frac{4acT^3}{3\rho\kappa} \quad (2.119)$$

where the variables have the same meaning as Equation 2.86. Substituting Equations 2.118 and 2.119 into Equation 2.116 as well as the fact $\varphi/\delta = 1$ in non-degenerate conditions then we arrive at Ulrich's expression Equation 2.84 for the diffusion coefficient. Furthermore, it can be shown that this is equivalent to the expression of Kippenhahn et al. (1980) with $\alpha \approx 1$. Starting with Equation 2.91

$$D = v_\mu L = \frac{H_p L}{(\nabla_{ad} - \nabla)\tau_{kh}^*} \eta \approx \frac{H_p L^2}{(\nabla_{ad} - \nabla)\tau_{kh}^*} \left| \frac{d\mu}{dr} \right| \frac{1}{\bar{\mu}} \quad (2.120)$$

As Kippenhahn et al. (1980) have shown that the fastest growing modes are disrupted by the circulation system they create, the appropriately L to use in this context is of the order of the bubble themselves, i.e., $d \approx L$. Making this substitution along with expression for thermal adjustment (Equation 2.85)

$$\tau_{kh}^* = \frac{c_p \kappa_0 \rho_0^2 d^2}{16acT_0^3} = \frac{c_p \rho_0 d^2}{12K_0} \quad (2.121)$$

into Equation 2.120, we can express the Kippenhahn et al. (1980) diffusion equation as

$$D = \frac{12K_0 H_p}{\rho c_p} \frac{dP}{dr} \frac{d\mu}{dp} \frac{1}{\mu} \frac{1}{\nabla_{ad} - \nabla}. \quad (2.122)$$

By definition

$$\nabla_\mu = \frac{\partial \ln \mu}{\partial \ln P} = \frac{d\mu}{dP} \frac{P}{\mu} \quad (2.123)$$

$$\Rightarrow D = \frac{12k H_p}{\rho c_p} \frac{1}{P} \frac{dP}{dr} \frac{\nabla_\mu}{\nabla_{ad} - \nabla}. \quad (2.124)$$

The pressure scale height, H_P , can be expressed as

$$H_P = \frac{-dr}{d \ln P} = -P \frac{dr}{dP} \quad (2.125)$$

$$\Rightarrow D = \frac{12k}{\rho c_p} \frac{-\nabla_\mu}{\nabla_{ad} - \nabla} \quad (2.126)$$

From Equation 2.118

$$D = 12 \cdot K \frac{-\nabla_\mu}{\nabla_{ad} - \nabla} \quad (2.127)$$

which is now in the same form as Equation 2.116

$$\begin{aligned} \Rightarrow C_t &= 12 \\ \Leftrightarrow \frac{8}{3}\pi^2\alpha^2 &= 12 \\ \Rightarrow \alpha &= 0.67 \approx 1 \end{aligned} \tag{2.128}$$

EDL06, EDL08 and Charbonnel and Zahn (2007a) demonstrated that as an RGB extra-mixing mechanism, the thermohaline instability reproduced many of the requirements outlined in §1.2.1, namely:

1. The mixing begins once the hydrogen burning shell has advanced through the composition discontinuity left behind by first dredge-up. This coincides with the bump in the luminosity function in globular clusters and the magnitude at which observations show changes to stellar surface abundances.
2. It displays the required mass and metallicity dependence.
3. The mixing is a means to reconcile RGB ^3He yields with predictions of the Big Bang and measurements of the interstellar medium.
4. The mixing impacts upon the abundances of ^{12}C , ^{13}C , ^{14}N , and ^7Li .

In the following sections we undertake a quantitative analysis of thermohaline mixing and compare the results to observations and 3D simulations. The ability to match observations is the first step in determining whether the process does govern the surface abundances of low-mass RGB stars.

2.5 Summary

Here marks the end of Part I, the introductory background material. The aim thus far has been to develop the required tools to analyse the role of thermohaline mixing during the RGB. Knowing for the sake of knowing is motivation in itself, but for those who required further justification we began by highlighting the significance of this study in an astrophysical context. Summarising low-mass evolution allowed us to identify the shortfall in the current theory and highlighted the need for extra mixing during the RGB. One of stellar evolution's usefulness to the broader community lies in its ability to predict abundances for Galactic chemical evolution models. For this reason RGB evolution is often overlooked. It was therefore essential to demonstrate the contribution of RGB stars to the chemical evolution of the galaxy; the role of the ^3He abundance served as the primary concern. Those further species expected to be affected by extra mixing were identified and related back to globular clusters and the associated chemical anomalies. The well studied GCs will serve as a testbed for the thermohaline mechanism in this work and the multiple population scenario paradigm in which we must operate was reviewed.

Although the focus of this study is thermohaline mixing, it is one of many postulated extra mixing mechanisms. Understanding the process responsible has been the source of much contention and has resulted in a wealth of literature. Of those we summarised, rotational mixing has been the most studied process. Thus, time was taken to understand one of rotation instabilities in the GSF mechanism. The GSF instability, itself a doubly-diffusive process, provided the impetus for the development of ‘blob theory’; a framework later utilised to understand thermohaline mixing.

2.5.1 Linear Theory

Thermohaline mixing first entered the astrophysics literature in the late 1960’s and the theory was well developed in stars by the time EDL06 suggested their new application. Rather than simply applying the derived formulations, the oceanic origins of the mixing were explored. The exercise not only revealed the rich behaviour stemming from DD systems but has also provided us with a strong background for analysing the numerical simulations reviewed in §10. The situation in the ocean is somewhat simpler than in the stellar environment, thus allowing for a more gentle introduction of concepts such as the competing gradients and stabilising and destabilising quantities. The main findings from the oceanic analysis are summarised below.

Much insight into the behaviour of a flow can be gained through dimensionless numbers that describe the internal properties of the fluid. Through non-dimensionalising the Navier-Stokes equations and applying the Boussinesq approximation the dimensionless numbers of interest to DD mixing are:

- The ratio of diffusivities sometimes referred to as the inverse Lewis number $\tau = K_s/K_T$.
- The Prandtl number, the ratio viscosity to thermal diffusivity. $Pr = \nu/K_T$.
- The Rayleigh number, the ratio of buoyancy to the diffusive processes of conduction and viscosity $Ra = g\alpha\Delta T d^3/\nu K_T$ and for salt $Rs = g\beta\Delta S d^3/\nu K_T$.
- The density ratio, $R_\rho = \beta\Delta S/\alpha\Delta T$.

By introducing boundary conditions and solving the dispersion relation, the mixing regimes possible in DD systems were revealed. The analysis focussed on oceanic conditions where $Pr = 10$ and $\tau = 0.01$. In DD systems:

- Finger-like convection occurs when the the destabilising agent is the slower of the diffusing quantities.
- Oscillatory or ‘diffusive’ convection occurs when the destabilising agent is the most rapidly diffusing of the two quantities.
- Density gradients that are highly unstable in singly-diffusive systems can remain stable in a doubly-diffusive configuration

- Configurations that are convectively stable in singly-diffusive systems can be unstable in doubly-diffusive systems.

Under the oceanic conditions, further analysis (Figure 2.7) shed light on the nature of the mixing. In the thermohaline regime it was found that the fastest growing modes dominate the mixing. For the fastest growing modes, energy exchange in this regime is most effective when the geometry is finger like.

2.5.2 Stellar Theory

The previous applications of DD mixing in the stellar regime were investigated. Semi-convection and thermohaline mixing have both been thought to significantly affect the evolution of stars. By comparing and contrasting the processes, clear stability criteria were derived and applied to the RGB mechanism. It was demonstrated that the point inside the star where EDL06 predict that mixing should develop meets the conditions for thermohaline instability to develop. The basis of the Ulrich (1972) and Kippenhahn et al. (1980) and EDL08 diffusion coefficients was outlined in detail. The assumptions each make about the mixing process is essential for comparisons to the 3D simulations. The key point of difference between the formalisms pertains to the mixing length and which modes can dominate the mixing.

Ulrich (1972)

- The background entropy gradient must be taken into account in the stellar environment so that $\nabla - \nabla_{ad}$ is the competing temperature term and μ is the competing composition quantity.
- In stellar conditions the fastest growing modes do not necessarily dominate the mixing. Self induced turbulence is expected to render these modes highly inefficient.
- The modes that dominate mixing are the thermally limited modes, those who's horizontal scale is so large that the growth of velocity is limited by the rate at which heat diffuses out.
- The resultant cells are not as long and thin as those in the oceans, but a cell can still grow by a factor of a few times its diameter before mixing with the surroundings. This is irrespective of the fact the fingers are unstable to shear flow.
- Horizontal turbulence on the other hand, say through circulation systems formed from its own heat loss, may inhibit the mixing efficiency.

Kippenhahn et al. (1980)

- Perturbations form blobs that are more or less spherical.

- The formulation for the diffusion coefficient can be shown to be equivalent to that of Ulrich with spherical blobs rather than long fingers the assumed geometry.
- Heat losses from the disturbed blob will create a circulation system that stops the blob travelling much further than its diameter.
- By inhibiting vertical mixing, turbulence leads to well mixed horizontal layers.

EDL06

- A favourable density fluctuation sees an element rise and cool. Heat loss to the environment does not disrupt the motions.
- The element will continue to cool and rise until it finds its equilibrium position. Due to the lower internal molecular weight it will settle in a region warmer than the internal temperature.
- Heat will diffuse in and strip layers off the element. This therefore means that the modes responsible are the thermally limited modes. Smaller modes will thermalise and mix with the surroundings before material can strip off.

Thermohaline mixing qualitatively reproduces the behaviour required to match observations. It is essential to test quantitatively whether it does in fact match observations. Such an exercise will also help constrain the above assumptions. In order to investigate the mixing on an evolutionary time scale it is necessary to implement a mixing prescription into 1D stellar codes. This is the focus of Part II.

Part II

Numerical Modelling

Chapter 3

The Evolution Code

To improve is to change; to be perfect is to change often.

- Sir Winston Churchill

I am an old man now, and when I die and go to heaven there are two matters on which I hope for enlightenment. One is quantum electrodynamics and the other is the turbulent motion of fluids. About the former I am rather optimistic.

- Sir Horace Lamb

3.1 Overview of the Monash Codes

Our investigations into the evolutionary effects of thermohaline mixing were carried out with two stellar physics codes:

1. MONSTAR (The Monash version of the Mt.Stromlo evolution code; see Campbell and Lattanzio 2008), which calculates the stellar structure.
2. MONSOON, the Monash post-processing nucleosynthesis code (Church et al., 2009).

In general, the abundances of elements in stellar models are calculated via one of two means. Either a post-processing scheme is employed (Pignatari et al., 2008) or the nucleosynthesis is coupled to the evolution (Eggleton, 1972). A small nucleosynthetic network is included in MONSTAR which follows those reactions that feed back on the structure of the star (pp chains, CNO cycles, ^4He burning). For more advanced nucleosynthesis, MONSOON takes the structural information and calculates the abundances of the nuclei specified in a user-defined network. In

theory, having a separate code to calculate the trace nuclei provides great flexibility in modelling. Investigations relating to hydrogen or helium burning can employ a truncated network which will reduce the computational cost. If, on the other hand, AGB evolution is of primary interest then the code can be adapted to efficiently calculate full s-process yields (e.g., MONTAGE see Church et al. 2009). Further advantages of the post-processing method include:

- When updating the rates of reactions involving trace elements it is not necessary to recalculate the structure.
- MONSOON can choose its own timestep which is determined by changes in composition rather than in structure, e.g., during the inter-pulse phase MONSTAR needs to take small timesteps to resolve the structure, but during the thermal pulse MONSOON requires smaller timesteps to trace the mixing. Allowing the codes to use the timestep most appropriate to their calculations can increase efficiency and numerical stability.
- MONSOON can choose its own mesh. With no need to resolve steep gradients such as the pressure, this may lead to fewer points and a decrease in computational cost (it does of course have to resolve steep gradients in composition). It also employs a shell shifting technique which allows for efficient following of the burning shells.

Most of the reactions possible in a star do not contribute enough energy to significantly feed back on the structure. Even so, a detailed consideration of all nuclei can still provide a probe of stellar interiors. In nearby systems observations of the $^{12}\text{C}/^{13}\text{C}$ (Dearborn et al., 1975b; Keller et al., 2001; Pavlenko et al., 2003) and $^{25}\text{Mg}/^{26}\text{Mg}$ (Shetrone, 1996b; Yong et al., 2003, 2006) isotopic ratios constrain the burning conditions inside stars. Detailed measurements of pre-solar grains can determine abundance ratios with levels of precision far beyond that of spectroscopy and provide insight into the properties of the stars in which they formed (Hoppe et al., 1994; Lugaro, 2005; Zinner, 2008; Ávila et al., 2012).

In this chapter we outline the details of MONSTAR as well as the necessary changes to implement thermohaline mixing in the stellar evolution code. In the subsequent chapter we extend the same analysis to the post-processing code.

3.2 Overview of the Stellar Evolution Code

3.2.1 The Equations of Stellar Structure

MONSTAR is a single-star evolution code based on the simplifying assumption of spherical symmetry (so that calculations can be carried out in one dimension). The code includes the forces of pressure and gravity but does not consider rotation or magnetic fields. MONSTAR determines a mathematical model that describes the structure of the star at a given time. This is done by solving the equations of stellar structure:

conservation of mass;

$$\frac{\partial r}{\partial m} = \frac{1}{4\pi r^2 \rho}, \quad (3.1)$$

hydrostatic equilibrium (conservation of momentum);

$$\frac{\partial P}{\partial m} = -\frac{Gm}{4\pi r^4}, \quad (3.2)$$

conservation of energy;

$$\frac{\partial L_r}{\partial m} = \varepsilon_{\text{nuc}} + \varepsilon_{\text{grav}} - \varepsilon_{\nu}, \quad (3.3)$$

energy transport;

$$\frac{\partial T}{\partial m} = -\frac{GmT}{4\pi r^4 P} \nabla, \quad (3.4)$$

as well as the governing equation of composition;

$$\frac{\partial X_i}{\partial t} = \frac{m_i}{\rho} \left(\sum_j r_{ji} - \sum_k r_{ik} \right), \quad i = 1, \dots, k \quad (3.5)$$

where the variables take on their usual meanings. Introductory texts such as Kippenhahn and Weigert (1990), Clayton (1983) and Hansen and Kawaler (1994) are recommended resources for the derivation of these equations. Note that in the energy transport equation, ∇ takes on distinct meanings depending on which region of the star is in consideration. In radiative regions

$$\nabla \equiv \nabla_{\text{rad}} = \frac{3}{16\pi acG} \frac{\kappa L_r P}{mT^4} \quad (3.6)$$

which results from assuming a photon diffusion model. In convective regions, which are determined by the Schwarzschild criterion (Equation 2.67), ∇ is calculated from the mixing length theory (Böhm-Vitense, 1958) and is often close to the adiabatic temperature gradient

$$\nabla_{\text{ad}} = \frac{P\delta}{T\rho C_P}. \quad (3.7)$$

In Equation 3.5 r_{ij} indicates the rates of reactions in which the species i is created from species j . r_{ik} denotes the rates of reactions in which species i is destroyed to create species k .

In §2.1 we alluded to the fact that the limitations of our modelling do not allow for the formation of instabilities that may develop in nature. Worthy of special mention is the condition of hydrostatic equilibrium, which is not always valid. For modelling purposes, a Lagrangian description is preferred as this simplifies the time derivatives in the structure equations. Without a mass-loss prescription the coordinate range remains constant whereas the radius varies greatly with time. A secondary advantage is the elimination of a density (coordinate) singularity at the centre of the star.

3.2.2 The Numerical Scheme

As is standard in modern stellar astrophysics, MONSTAR utilises the Henyey method (Henyey et al., 1964) to solve the structure equations numerically. This is a generalized Newton-Raphson method which relies on relaxation to converge sequential models. The general principle involves dividing the star into concentric mass shells; MONSTAR typically uses between 600-1200 shells. Each of the equations 3.1 - 3.5, is written as an implicit, finite difference equation across two consecutive mass shells. The use of a relaxation method implies that this is an iterative process whereby a new model is considered converged if a correction to the guessed solution is within a given set of tolerances. The Henyey procedure is reviewed in Kippenhahn and Weigert (1990) and Hansen and Kawaler (1994) and further details can be found therein.

The placing of mesh points is selected so to adequately resolve gradients of the dependent variables (L, T, r, P) as well as the composition. We will see that thermohaline mixing is sensitive to placing of these points and therefore we dedicate §3.2.5 and §3.3.3 to discussions of the spatial resolution (mesh). Time stepping control in MONSTAR is set by any one of seven criteria that ensure that the gradients of the dependent variables or composition do not change significantly between converged models (see Table 3.2.5).

The details of mixing in MONSTAR are described below but numerically it is treated in a semi-coupled manner with the structure. As described in Frost (1997) the code uses the rate of change of composition to extrapolate from the last converged model. The extrapolation serves as an initial estimate for the new model and a converged model is generated by iterating upon the state variables until the equations of stellar structure are satisfied. During each iteration the convective boundaries are determined from the current conditions but the abundances recalculated from the previous converged model so that any feedback on the point of neutrality is considered. As Frost (1997) stresses *“the code does not retain memory of the abundances from the previous iteration—nor should it, as iterations are not time-steps.”*

Alternative methods for calculating the mixing include converging the structure *then* using this configuration to compute the mixing and burning (Straniero et al., 2000). This method can be employed by MONSTAR but is only used when convergence difficulties arise. The third method available involves solving all the equations in a single timestep. Although some may suggest a moral inferiority by electing not to solve the abundances with the structure in the Henyey matrix, given adequate timestepping control, the iterative method should converge on the fully-coupled solution (Pols and Tout, 2001). Stancliffe (2006), however, has suggested that this is not necessarily the case during the thermally pulsing AGB phase.

3.2.3 The Input Physics

3.2.3.1 Equation of State

The equation of state (EOS) relates the thermodynamic state variables of a system. In the equations of stellar structure two of these quantities are the dependent

variables; in MONSTAR these are $\ln T$ and $\ln P$. They are calculated through the EOS, along with the constituent variables density (ρ), internal energy (U), specific heat capacity at constant temperature (C_P), degeneracy (ψ) as well as their respective derivatives at every mesh point. Under relativistic or electron-degenerate conditions, the fitting formula of Beaudet and Tassoul (1971) is employed. In case of failing convergence, a computationally more expensive analytic solution can be calculated. Note that this method still requires the numerical evaluation of the Fermi-Dirac integrals. Typically, degenerate conditions are associated with the core whereas most of the star can be described by a fully-ionised plasma. In these regions the state is governed by the ideal gas equation with allowances for radiation pressure. Towards the surface, where temperatures are considerably cooler, the gas is characterised by partial ionization. These regions are treated with the Saha equation as described by Bærentzen (1965).

3.2.3.2 Nuclear Energy Generation

As MONSTAR is concerned with the stellar structure, it only follows those species that are significant energetically, that impact upon μ or are important to the opacity. A six species network (^1H , ^3He , ^4He , ^{12}C , ^{14}N , ^{16}O), as well as a seventh pseudo-element that ensures baryon conservation, is sufficient to calculate feedback on the structure from the nuclear energy generation. The current network allows core hydrogen (pp-chains and CNO cycle) and helium burning phases of evolution (hence low-mass stars) but has recently been expanded to model super-AGB stars with a simplified treatment of core-carbon burning (Doherty et al., 2010). Whilst not traced explicitly, the less abundant isotopes are accounted for by assuming equilibrium is reached instantaneously. The set of reaction rates for hydrogen burning come primarily from Fowler et al. (1975) and Harris et al. (1983).

Besides those reactions that liberate energy, MONSTAR also considers reactions that cool the star. The effect of neutrino energy losses are significant primarily under degenerate conditions. They are treated according to Beaudet et al. (1967), Festa and Ruderman (1969), Ramadurai (1976) and Dicus et al. (1976).

3.2.3.3 Opacity

“You can not solve the equations of stellar structure in your head”. This sage advice from the author’s supervisor, is particularly relevant when trying to understand the interdependency between the microphysics included in stellar codes. In §1.1 we have seen an example of the role that the chemistry of the star plays in the opacity. The opacity, which contributes to the distribution of heat and energy throughout the star, will in turn affect the nucleosynthesis and further change the composition. Considerations of opacity are paramount on the AGB, where it can greatly affect the mass loss rate and lifetime of the star (Marigo and Aringer, 2009; Constantino et al., 2014). Apart from the negative H^- ion discussed previously, sources of opacity include electron scattering, free-free absorption, bound-free and bound-bound absorption, molecules, dust and conductive opacity.

Opacity calculations, pertaining to the mass and metallicity of RGB globular

cluster stars, are covered at the high temperature end by the OPAL Rosseland mean opacity tables (Iglesias and Rogers, 1996). MONSTAR interpolates between and across opacity tables for given temperatures and composition. The OPAL tables cover temperatures in the range $7000\text{K} < T < 5 \times 10^8\text{K}$ however below 10,000 K, C and N variable opacity tables from Lederer and Aringer (2009) are used (see Campbell 2007 and Campbell and Lattanzio 2008 for further details). Low-temperature molecular opacities for stellar envelopes were initially based on a fitting formula (Bessell et al., 1989; Chiosi et al., 1993) but changed to the Alexander (1975) and Alexander et al. (1983) tables. Prior to the current Lederer and Aringer (2009) tables, the Ferguson et al. (2005) low-temperature tables had been implemented. Although not required in this study, Campbell and Lattanzio (2008) also extended the tables to cover zero metallicity stars which necessitated the addition of high temperature opacities (Chieffi 2005, private communication). Variable C and N molecular opacities (Marigo and Aringer, 2009) and a more efficient interpolation routine have recently been added to a forked version of the code and are expected to be merged into the trunk shortly.

Conductive opacities are also included in MONSTAR. In the non-relativistic regime, electron conductivity is from the analytical fit of Iben (1975) to the Hubbard and Lampe (1969) and Itoh et al. (1983) tables. Relativistic electron conductivity is through the formulae of Itoh et al. (1983) and Mitake et al. (1984). Opacities for solid material (such as the occurrence of crystal formation) are from Raikh and Iakovlev (1982).

3.2.3.4 Mass Loss

In low-mass stars, the stellar wind is the only means by which material is returned to the interstellar medium. The rate at which mass is lost is critical in determining the chemical evolution of the Galaxy; we have already encountered the ^3He problem. MONSTAR has various mass-loss prescriptions available but for this study we apply the well tried Reimers (1975) rate

$$\dot{M} = 4 \times 10^{-13} \eta \frac{MR}{L} \quad (\text{M}_{\odot} \text{ yr}^{-1}). \quad (3.8)$$

Here M is the stellar mass, R the stellar radius, L the luminosity and the free parameter η is usually taken as 0.4. Although beyond the scope of this study, recently an updated version of Vassiliadis and Wood (1993) has been implemented for AGB evolution (Wood, 2007).

3.2.4 The Mixing Algorithm

MONSTAR utilises the MLT theory of convection. The treatment of convection is a major criticism of stellar evolution and further discussion is provided in Appendix A for the interested reader. The formalism is a single-eddy approach that approximates the different scales at which turbulence operates into a characteristic blob. The blob is assumed to travel a mixing length, ℓ , before losing its identity and mixing with its surroundings. It is usually assumed that the mixing length is

some factor (α) of the local pressure scale height (H_P) such that

$$\ell = \alpha H_P. \quad (3.9)$$

The mixing length is calibrated by evolving a $1 M_\odot$ stellar model to the current age of the sun (4.57 ± 0.02 Gyr, Bonanno et al. 2002; Bahcall et al. 1995), and adjusting α to match the observed solar radius and luminosity. How efficient convection needs to be will vary in each code and depends on the choice of geometric factors in the MLT. MONSTAR requires a value of $\alpha \approx 1.75$ for its solar model.

There are two points of interest we need to consider for our study. The mixing length parameter is chosen to match the Sun, a star nearly half way through its main sequence lifetime. The parameter is not changed for the later phases of stellar evolution nor is it altered for stars of different mass and metallicity. Given the stochastic nature of convection, this is almost certainly the wrong thing to do but is the standard practice. Our thermohaline diffusion coefficients (Equations 2.113 and 2.116) are highly dependent on the local temperature gradients and resultant velocity profiles. Any uncertainties therein are propagated in our thermohaline prescription e.g., the required free parameter (aspect ratio) required to match observations. Secondly it should be noted that MLT is not really a single parameter theory. Through the derivations of (Kippenhahn and Weigert, 1990) and Weiss et al. (2004) it can be seen that many assumptions go into the theory, much like those we made for the GSF instability in Equation 2.6. Although not relevant for RGB evolution, it should be noted for future comparisons that MONSTAR has a formalism for the treatment of internal-gravitational energy production due to heavy nuclei (see Wood 1981 for details). The associated change in entropy tends to result in a deeper third dredge-up than is otherwise predicted.

3.2.4.1 Mixing of the Chemical Composition

Instantaneous Mixing

During most phases of stellar evolution, the nuclear burning timescale exceeds the timescale for mixing by many orders of magnitude (the convective turnover timescale is of order hours to weeks). Thus it is convenient to assume that mixing occurs instantaneously compared structural changes. This is the approach originally employed by MONSTAR, where the chemical composition is homogenised inside each convection zone every timestep. However, in extreme cases, there are events where changes to the structure must be resolved on a comparable timescale to the mixing (e.g., proton ingestion episodes or the core flash). During such events the instantaneous mixing approximation is no longer valid and a time-dependent mixing algorithm is required.

Time-Dependent Diffusive Mixing

An alternative to the instantaneous approximation is to model the mixing as a diffusive process. Such an assumption is valid as long as the mean free path of

a blob is much less than the mixing zone (which is at least true for a convective envelope). The composition equation 3.5 is replaced by a diffusive term

$$\frac{dX_i}{dt} = \left(\frac{\partial X_i}{\partial t} \right)_{nuc} + \frac{\partial}{\partial m_r} \left((4\pi r^2 \rho)^2 D \frac{\partial X_i}{\partial m_r} \right), \quad (3.10)$$

where $\left(\frac{\partial X_i}{\partial t} \right)_{nuc}$ is a term that describes the change in abundance due to nuclear burning. The value of the diffusion coefficient, D , is determined by a formula that is designed to mimic the mixing process of interest (e.g., thermohaline).

Diffusive mixing was implemented into MONSTAR by Campbell (2007) and Campbell and Lattanzio (2008) for the purpose of investigating zero-metallicity stellar evolution. The time dependence of the mixing is an essential property when the mixing and evolutionary timescales become comparable, such as during the dual core flashes and dual shell flashes of primordial stars. Time-dependent mixing is also significant during events where mixing is slow or in cases where mixing does not result in homogeneity. The doubly-diffusive processes described in §2.4 are slow compared to convection. They rely on the smoothing out of a gradient rather than mixing to homogeneity in a single timestep. As such their mathematical prescriptions are given in terms of an equation for the diffusion coefficient, D which can then be applied to Equation 3.10.

3.2.4.2 Overshoot and Semi Convection

Although the models relevant to this study are run without semi convection, the focus is on a similar doubly-diffusive process. The implementation of semi convection and the closely related overshoot provides some insight into the limitations of the mixing algorithm in MONSTAR. It reiterates the fact that any mixing we expect beyond convection must be explicitly parametrised into the 1D codes and is plagued by uncertainty.

As we have discussed, the local formalism of MLT is unable to determine whether a convective parcel approaching a convective boundary possesses enough momentum to overshoot into a stably stratified region. Assuming overshooting does occur, we require a theory that predicts the depth of penetration. Overshooting in stellar interiors is supported by observations of binaries (Andersen et al., 1990; Ribas et al., 2000; Claret, 2007; Zhang, 2012a) and stellar clusters (Lattanzio et al., 1991; Demarque et al., 1994; Colucci and Bernstein, 2012). These systems have been modelled in order to constrain the extent of mixing. Zhang (2012b) explored whether overshooting during the main sequence is required to match the solar lithium abundance and Pumo et al. (2010) demonstrate how the process can lead to the production of s-process nuclei in massive stars. It is expected that over time the budding field of asteroseismology will shed light on the issue and provide further constraints (Noels et al., 2010). Hydrodynamical models of overshoot include those of Freytag et al. (1996), Singh et al. (1995) and Herwig et al. (2006) all of whom suggest that there is non-zero overshoot, and that the extent of penetration depends on the conditions at the edge of the convection zone. They also agree that the velocity of any overshooting material decays exponentially with

distance.

The treatment of semi convection and overshoot in MONSTAR is dependent on which mixing regime is employed. In the case of instantaneous mixing there is no formalism for true overshoot, rather the code utilises ‘a search for convective neutrality’ (Lattanzio, 1986). The algorithm uses the last two convective points to linearly extrapolate $\nabla_{\text{rad}}/\nabla_{\text{ad}}$ to the first radiative point. If according to the extrapolation $\nabla_{\text{rad}}/\nabla_{\text{ad}} > 1$, then the convective boundary is extended to the new point. Note that this algorithm only allows the location of the convective boundary to change by at most one mesh point every iteration. Similarly, the semi convection algorithm (Robertson and Faulkner, 1972) searches for neutrality between a convective core and small convective region outside the core. Recall that during semi convection, material just outside the core is unstable according to Schwarzschild but stable according to Ledoux. In this region, a slow mixing is applied to mimic the fact thermal stability can be attained without complete mixing. As we already alluded to, thermohaline mixing is sensitive to the mesh spacing in the region of interest. So too is the doubly-diffusive semi convection. Lattanzio (1984) found the need to introduce a parameter that controls the mesh spacing around the convective core.

With the introduction of diffusive mixing, Campbell (2007) was able to modify the formalisms of overshoot and semi-convection in MONSTAR. He followed Herwig et al. (1997) who parameterised the results of Freytag et al. (1996) in which numerical simulations of convection indicated an exponential decay in velocity of the overshooting material with radius (distance). In analogy to the pressure scale height, H_P , Herwig defines a ‘velocity scale height’, H_v , such that

$$H_v = f_{os} H_P \quad (3.11)$$

where f_{os} is a scaling factor. The resultant equation for the diffusion coefficient is then

$$D_{os} = D_0 e^{\frac{-2z}{H_v}} \quad (3.12)$$

where D_0 is the diffusion coefficient of the last convective point and z is distance from the convective boundary. The treatment for semi convection has been modified to search for regions that are stable according to the Schwarzschild criterion but unstable according to Ledoux. In regions where

$$0 < \nabla - \nabla_{ad} < \frac{\beta}{4 - 3\beta} \nabla_{\mu} \quad (3.13)$$

and where β is the ratio of gas to total pressure, the region is diffusively mixed. Slow mixing velocities are applied to mimic the nature of semi convection however there is no justification for the speed selected. The diffusion coefficient is simply set to 1000 in the semi-convective regions. In the future, this proof of concept (for diffusive semi convection) will be updated to include the formalisms of Langer et al. (1985) (i.e., Equation 2.71) or that of Grossman and Taam (1996).

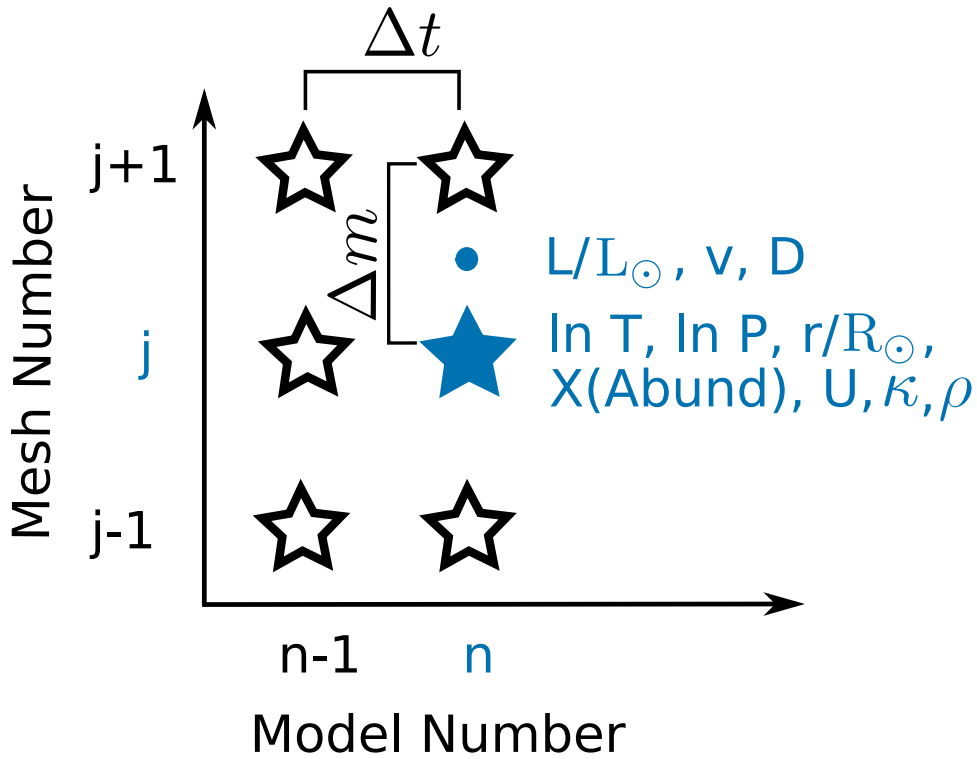


Figure 3.1: A 2D schematic of MONSTAR’s mesh as a function of time (model number). The dependent variables temperature ($\ln T$), pressure ($\ln P$), radius (r/R_{\odot}) as well as the mass fraction (X) of the seven abundances, the internal energy (U), opacity (κ) and density (ρ) are all calculated at mesh points (cell boundaries, denoted by stars in the figure). Luminosity (L/L_{\odot}), convective velocity (v) and the diffusion coefficient (D) are calculated at the midpoint of the cell (denoted by a circle for the current mesh point). A primary array calculates the mass location of each mesh point and a secondary array stores the mass locations of each midpoint.

3.2.5 The Meshing Routine

As discussed by Campbell (2007), the independent mass variable in MONSTAR is given in the form:

$$x = \left(\frac{m_r}{M} \right)^{\frac{1}{3}}. \quad (3.14)$$

This variable, introduced by Faulkner (1968), allows the central point to be included as a normal meshpoint and ensures that all the dependent derivatives are defined at this location. Figure 3.1 shows which variables the code calculates on mesh points and which are defined at the midpoint of the cell. The convention used in MONSTAR sets the core as meshpoint one and increases concentrically towards the surface. From this central mesh point, the simplest of the meshing criteria sets points at equidistant mass intervals. For the models in this study, the mass spacing does not exceed $\Delta M = 0.02 M_{\odot}$. There are further restrictions that ensure the four radial gradients of interest (L , T , r , P) are adequately resolved. The timestepping and meshing criteria are outlined in Table 3.2.5 along with typical values to ensure an adequately resolved evolutionary calculation. The limits for the respective variables are set as input parameters. MONSTAR has two criteria to follow the change in abundance across mesh points. There is a maximum arithmetic change in *any* of the chemical species. However this alone is not sufficient to resolve the composition. At the bottom of a burning shell, the change in abundance can easily be less than that specified by the arithmetic criterion. In order to resolve the nuclear burning, a geometric condition is added which limits the maximum value of the ratio of two adjacent abundance values. The combination of these criteria result in a spatial grid that is generally not uniformly distributed. MONSTAR’s adaptive mesh adds and removes points each model in an attempt to optimise the calculations.

3.3 Changes to the Stellar Evolution Code

The most straightforward means to include thermohaline mixing in the stellar models appeared to be as part of the post processing code. Adding the EDL08 formalism to MONSOON appeared simple enough and would have the advantage of not needing to recalculate the structure when exploring the effects of the mixing efficiency. The inclusion of the Ulrich (1972) and Kippenhahn et al. (1980) formalism (UKRT hereinafter, as we have shown the two prescriptions are equivalent save for the mixing efficiency) however, necessitated a change. Recall from Equation 2.116 that the UKRT formalism requires the calculation of various thermodynamic quantities. These quantities are not available to the post-processing code, whereas the EDL08 mixing coefficients (Equation 2.113) were. If we were required to recalculate the structure and write out these thermodynamic quantities when the mixing efficiency was varied, then it defeated the purpose of calculating the process in MONSOON. In the next Chapter we analyse the advective mixing algorithm in the post-processing code. We will see that the algorithm requires a mixing velocity and a mixing length in regions where mixing occurs. The UKRT formalism provides a diffusion coefficient but it is not clear what mixing length to

Criterion	Typical Value	Definition
SM	0.005	The maximum allowed mass spacing between consecutive mesh points.
SML	0.10	The maximum allowed change in L/L_{\odot} between consecutive mesh points.
SMT	0.15	The maximum allowed change in $\ln(T)$ between consecutive mesh points.
SMR	0.15	The maximum allowed change in r/R_{\odot} between consecutive mesh points.
SMP	0.15	The maximum allowed change in $\ln(P)$ between consecutive mesh points.
SMW	0.07	The maximum allowed change in any abundance between consecutive mesh points.
WRATIO	7.50	The maximum allowed ratio of any abundance at consecutive mesh points.
STT	0.2	The maximum allowed change in $\ln(T)$ between consecutive models at a given mesh point.
STP	0.2	The maximum allowed change in $\ln(P)$ between consecutive models at a given mesh point.
STW	0.2	The maximum allowed change in any abundance between consecutive models at a given mesh point.
STW1	0.2	The maximum allowed change in the abundance ratios between consecutive models at a given mesh point.
STL(H)	0.15	The maximum allowed change in the total hydrogen burning luminosity (L/L_{\odot}) between consecutive models.
STL(He)	0.15	The maximum allowed change in the total helium burning luminosity (L/L_{\odot}) between consecutive models.
STL(rad)	0.15	The maximum allowed change in the total radiated luminosity (L/L_{\odot}) between consecutive models.

Table 3.1: The set of meshing and timestepping criteria used in MONSTAR. The code picks the smallest timestep/mesh spacing to satisfy all of these conditions.

adopt in a region that is classically radiative. The appropriate mixing length is of course the distance the fingers travel before mixing with the background material. But it is not so straight forward to determine this. The premise of the linear analysis, from which the formula for the diffusion coefficient was derived (Equation 2.84), is that solutions to equation 2.56 indicate the growth rate of the fingers, p . It is then assumed that

$$D_{\text{thm}} \approx vl \approx \frac{1}{2}pl^2 \quad (3.15)$$

which eliminates the physical mixing length in favour of a dimensionless free parameter α . A parameter that is supposedly related to the aspect ratio of the rising material. The obvious mixing length to use in this case is simply $\alpha_{\text{MLT}} \times H_P$ which we do. Due to the combination of these issues, the decision was made to calculate the UKRT formalism in the evolution code. The addition of thermohaline mixing to MONSTAR's mixing algorithm was a collaboration between Prof. John Lattanzio, Dr. Ross Church, and the author. The required changes to the code are described below.

3.3.1 Thermohaline Mixing

The introduction of diffusive mixing (Campbell, 2007; Campbell and Lattanzio, 2008) provided a framework to implement thermohaline mixing in the evolution code. The flow chart in Figure 3.2 provides a basic overview of the thermohaline mixing algorithm in MONSTAR and the associated subroutines.

Once the code has a converged solution for the stellar structure, the subroutine *phys.f* calculates the energy transport and convective boundaries for the model. Of course in a real star convection mixes the composition and energy simultaneously, but computationally these are carried out in separate steps. *Abund-diffn.f*, which manages the nucleosynthesis in MONSTAR, then determines the change in abundance due to nuclear burning. Prior to diffusing the composition, the newly added *thermohaline.f* evaluates the value of μ and locates the position of the minimum (i.e., the depth of mixing in the radiative zone). It also determines the diffusion coefficients in the region undergoing thermohaline mixing. The code returns to *abund-diffn.f* and calculates the diffusion coefficients for the mixed regions before the subroutine *diffsolve.f* is called and the composition is mixed (the diffusion equation is solved).

The primary role of *phys.f* is to calculate the energy transport in MONSTAR. With knowledge of the nuclear energy generation and opacity, the subroutine determines the appropriate temperature gradient to use at each mesh point. *Phys.f* carries out a series of tests and applies the MLT only when necessary. Recalling that convective stability is governed by the Schwarzschild criterion (Equation 2.67):

1. The code first tests for efficient convection. In the case of efficient convection, the temperature gradient can be calculated straightforwardly and independent of time.
2. The code then checks for inefficient convection and applies the radiative

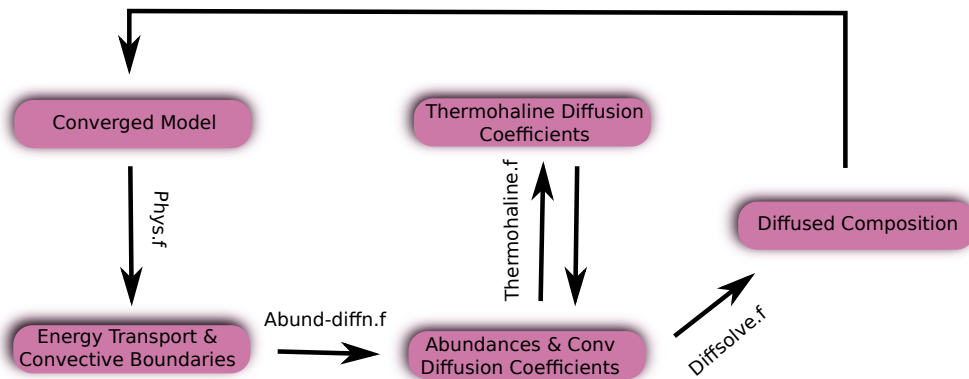


Figure 3.2: A flow chart showing the thermohaline mixing algorithm and relevant subroutines in MONSTAR.

temperature gradient, ∇_{rad} , if deemed necessary.

3. If neither of the first two conditions are met, MLT is applied to calculate ∇ .

As part of his thesis, Campbell (2007) also implemented a test according to the Ledoux criterion (Equation 2.68) in order to locate semi-convective regions. This test necessitated the calculation of the mean molecular weight gradient, ∇_{μ} . We have seen in §2.4.5 that for thermohaline mixing we are in search of changes to ∇_{μ} of order

$$\frac{\delta\mu}{\mu} \sim 10^{-4}. \quad (3.16)$$

This requires the use of double-precision floating point arithmetic. We determine μ via

$$\begin{aligned} \frac{1}{\mu} &= \sum_i \frac{N_e + 1}{A_i} X_i \\ \Rightarrow \mu &= \left[(1.98447151 \times {}^1\text{H}) + (0.994685297 \times {}^3\text{He}) + (0.749512217 \times {}^4\text{He}) \right. \\ &\quad + (0.583333 \times {}^{12}\text{C}) + (0.5714286 \times {}^{14}\text{N}) + (0.5625 \times {}^{18}\text{O}) \\ &\quad \left. + (0.54166667 \times \text{all other nuclei}) \right]^{-1}. \end{aligned} \quad (3.18)$$

Recall from Equation 2.120 that the UKRT thermohaline diffusion coefficient, which we shall temporarily denote by D_{Kipp} , is derived from the ratio of the temperature gradients ($\nabla_{\text{ad}} - \nabla$) and ∇_{μ} . Although we have stated that the thermohaline diffusion coefficients are calculated in *thermohaline.f* it would appear that *phys.f* is the logical subroutine in which to determine D_{Kipp} and we do in fact calculate it here. For reasons that will soon become apparent, we define D_{Kipp} , the UKRT thermohaline diffusion coefficient and D_{thm} , the thermohaline diffusion coefficient used by the code. The expression for D_{Kipp} in MONSTAR is based on the derivation of Kippenhahn et al. (1980) and Equations 2.120 - 2.127. In the

code

$$D_{Kipp} = \frac{16acT^3}{\kappa\rho^2C_P} \frac{-\nabla_\mu}{\nabla_{ad} - \nabla}. \quad (3.19)$$

Where we have used

$$\nabla_\mu = \frac{\partial \ln \mu}{\partial \ln P} = \frac{d\mu}{dp} \frac{P}{\mu} \quad (3.20)$$

and

$$H_P = \frac{-dr}{d \ln P} = -P \frac{dr}{dP} \quad (3.21)$$

to simplify Equation 2.122. We have previously shown that

$$D_{Kipp} = 12 \cdot K \frac{-\nabla_\mu}{\nabla_{ad} - \nabla} \equiv \frac{16acT^3}{\kappa\rho^2C_P} \frac{-\nabla_\mu}{\nabla_{ad} - \nabla} \quad (3.22)$$

which is equivalent to the formalism of Ulrich (1972) and Charbonnel and Zahn (2007a)

$$D_{thm} = C_t K \left(\frac{\varphi}{\delta} \right) \frac{-\nabla_\mu}{(\nabla_{ad} - \nabla)}, \quad (3.23)$$

with $C_t = 12$. Hereinafter we use the notation $F_{inv} = C_t/12$. The free parameter, F_{inv} , allows for different mixing speeds which mimic different geometries of the rising material (see Equation 2.117). It is the inclusion of this free parameter that distinguishes D_{thm} and D_{Kipp} in the code. The nucleosynthetic calculations in MONSTAR are managed by the subroutine *Abund.f* or its diffusive mixing analogue, *Abund-diffn.f*. Both routines determine the change in abundance due to nuclear burning however they (obviously) solve different mixing equations. Once the nuclear burning has been calculated, *thermohaline.f* is called and several diagnostics are performed. The subroutine first determines the location of the μ inversion and of the base of the convective envelope. It is in this routine that the D_{Kipp} values, calculated in *phys.f*, are multiplied by the input parameter F_{inv} to give D_{thm} . Once these values are stored, the code returns to *Abund-diffn.f* and determines all other diffusion coefficients (e.g., overshoot or convection).

3.3.2 The Diffusion Equation Solver

The addition of the thermohaline mechanism to MONSTAR's mixing algorithm was expected to be a trivial exercise. With a diffusive mixing regime already implemented for convective mixing, we simply needed to include the thermohaline diffusion coefficients in the tridiagonal matrix and use the Thomas Algorithm to solve the slightly larger system. It may not surprise the reader that the implementation of new physics initially led to convergence difficulties.

In theory, direct (elimination) methods for solving triagonal matrices should yield the exact solution for a given system of equations. In practice however, these schemes can result in large round off errors. The discretisation error tends to be larger than the accuracy of the machine arithmetic meaning errors are propagated throughout the calculation. In systems (like ours) that are large, sparse or have diagonals with values close to zero, the error propagation is significant. An ex-

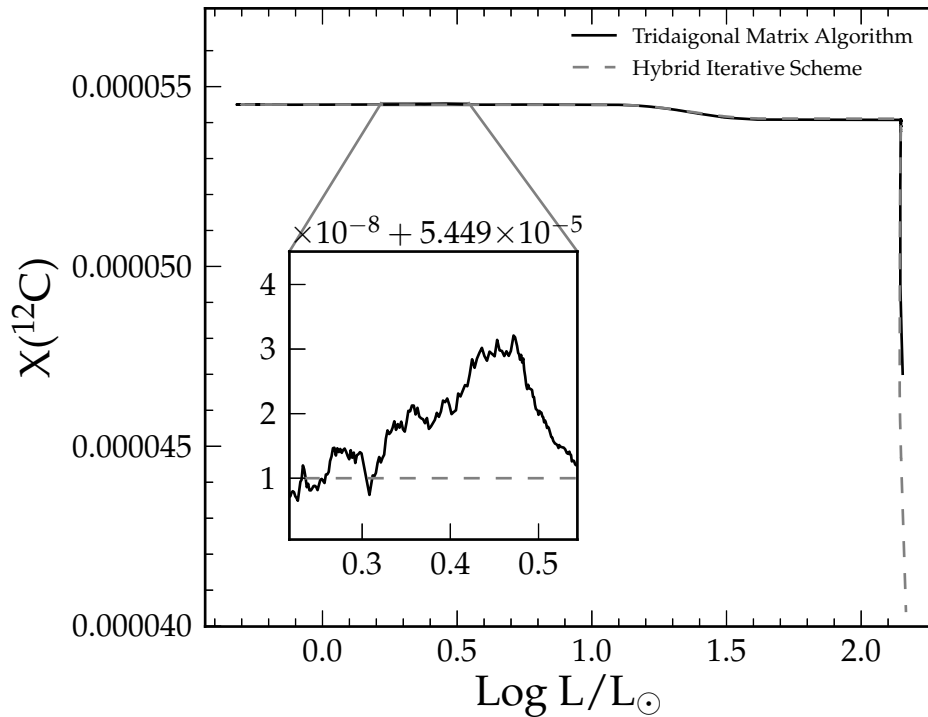


Figure 3.3: Surface ^{12}C abundance as a function of luminosity for a $M = 0.8 M_{\odot}$ $Z = 0.0005$ star using the tridiagonal matrix algorithm to solve the diffusion equation (black solid line) and also using the hybrid iterative scheme (dashed grey line). The inset shows the numerical error introduced during the main sequence when using the tridiagonal algorithm.

ample of this introduced error can be seen in Figure 3.3. The black curve shows the evolution of the surface ^{12}C abundance for a $M = 0.8 M_{\odot}$ $Z = 0.0005$ star as calculated with the tridiagonal matrix algorithm. The inset clearly shows that some numerical error is introduced from the scheme as we find minute fluctuations to the surface abundance in regions where we expect no change. In some cases it *may* be possible to offset the error by increasing the precision of the calculations but this is not always the case and it is useful to know whether such a system is ill conditioned. The condition number of a matrix (cond) can be used to quantify the system's amenability to direct methods

$$\text{Cond}(\mathbf{A}) = \|\mathbf{A}\| \|\mathbf{A}^{-1}\| \quad (3.24)$$

where $\|\mathbf{A}\|$ is the matrix norm. There are several ways to calculate the norm with the the Euclidean or Frobenius method the most widespread means

$$\|\mathbf{A}\| = \left(\sum_{i=1}^m \sum_{j=1}^n |a_{ij}|^2 \right)^{1/2} . \quad (3.25)$$

If $Cond(A) \gg 1$ then the introduced numerical error will be significant. If MONSTAR was to perform this test, the increase in the number of operations would undermine the computational advantage of using the tridiagonal matrix algorithm. Furthermore, if found to be ill conditioned, it was not clear that we could successfully suppress the introduced error and ensure convergence. Thus the decision was made to replace the current direct method with a hybrid iterative scheme. An iterative corrector step as per Press et al. (1992) was introduced but did not improve the stability so the method of Siess et al. (2000) and Siess (2006) was employed.

In general, direct (elimination) schemes are superior to iteration methods due to their wider applicability. However, there exists special cases of ill conditioned systems where iterative methods are preferable. When a matrix is sparse and diagonally dominant, iteration can be shown to be unconditionally stable, and if each iteration is cheap and the number of iterations small, they provide a competitive alternative to elimination. Iterative schemes have been applied to many linear problems and they are also efficient at solving partial differential equations, in particular when finite difference or finite element methods have been used. As their name suggests iterative solutions assume an initial (trial) solution which is systematically improved upon. They are analogous to the iterative methods used for root finding, e.g., Secant or a Newton-Raphson like algorithm. All iterative methods are based on the following premise: For a system

$$\mathbf{A} \cdot \mathbf{x} = \mathbf{b} \quad (3.26)$$

the procedure requires an initial guess of the unknown vector \mathbf{x} . The accuracy of this guess can be checked through the residual vector, \mathbf{r} ,

$$\mathbf{r} = \mathbf{A} \cdot \mathbf{x}_{\text{guess}} - \mathbf{b}. \quad (3.27)$$

If the residual is large, then there must be a large error, \mathbf{e} , in our guess,

$$\mathbf{e} = \mathbf{x} - \mathbf{x}_{\text{guess}}. \quad (3.28)$$

If we can determine this error then a correction can be applied to the initial guess

$$\mathbf{A} \cdot \mathbf{x}_{\text{guess}} = \mathbf{A}(\mathbf{x} - \mathbf{e}) = \mathbf{b} - \mathbf{r} \quad (3.29)$$

$$\Rightarrow \mathbf{A} \cdot \mathbf{x} - \mathbf{A} \cdot \mathbf{e} = \mathbf{b} - \mathbf{r} \quad (3.30)$$

$$\Rightarrow \mathbf{A} \cdot \mathbf{e} = \mathbf{r}. \quad (3.31)$$

Any scheme will improve each iteration by trying to modify components of the new $\mathbf{x}_{\text{guess}}$, e.g., most methods attempt to eliminate components in the residual vector. Convergence is obtained once the residual or correction meets a given tolerance. Procedures such as the successive over relaxation scheme and damped Newton-Raphson scheme employ a relaxation parameter to accelerate (usually decelerate) this convergence. Siess et al. (2000) and Siess (2006) have combined iterative relaxation with the Thomas Algorithm to minimise the error introduced by solving the diffusion equation and improve (code) stability.

We note first the differencing employed by Siess et al. (2000) and Siess (2006).

In analogy to Equation B.1 we wish to solve the second order equation,

$$\begin{aligned}
X_j^t &= \frac{\sigma_{j-\frac{1}{2}}^2 D_{j-\frac{1}{2}} \Delta t}{(m_{j+1} - m_{j-1})(m_j - m_{j-1})} X_{j-1}^{t+1} + \\
&\quad \left(1 - \frac{\sigma_{j-\frac{1}{2}}^2 D_{j-\frac{1}{2}} \Delta t}{(m_{j+1} - m_{j-1})(m_j - m_{j-1})} - \frac{\sigma_{j+\frac{1}{2}}^2 D_{j+\frac{1}{2}} \Delta t}{(m_{j+1} - m_{j-1})(m_{j+1} - m_j)} \right) X_j^{t+1} \\
&\quad + \frac{\sigma_{j+\frac{1}{2}}^2 D_{j+\frac{1}{2}} \Delta t}{(m_{j+1} - m_{j-1})(m_{j+1} - m_j)} X_{j+1}^{t+1}
\end{aligned} \tag{3.32}$$

where $\sigma = (4\pi r^2 \rho)^2$ and other variables have the same meanings as above. It is possible that reverting to the second order difference equation alone may reduce error. In order to simplify the calculations, Meynet et al. (2004) used the (moderately) variable radius coordinate in their differencing. Without proper timestep control this can provide a source of uncertainty, however, in the case of MONSTAR this was not found to be the underlying issue. Campbell (2007, see his figure 4.1) investigated the effects of different schemes by simulating hydrogen shell burning. His results are shown in our Figure 3.4 (see caption for more detail). The tests demonstrated that a second order differencing (solid green curve) and first order scheme described by Meynet et al. (2004) (the overlaying broken cyan curve) produce very similar abundance profiles with the same diffusion equation solver and for timestepping relevant to thermohaline mixing calculations.

In Appendix B we demonstrate that the Thomas Algorithm requires modification of the coefficients in a given tridiagonal system (Equation B.7). The method used to determine the new primed values (Equations B.8 and B.9) eliminates the lower diagonal values, a_i , in the matrix, \mathbf{A} . Back substitution is then performed to derive the abundances x at each mesh point i :

$$\begin{aligned}
x_n &= d'_n \\
x_i &= d'_i - c'_i x_{i+1} \quad i = n-1, n-2, \dots, 1.
\end{aligned} \tag{3.33}$$

The Siess procedure differs from the standard Thomas Algorithm during this phase. A relaxation parameter $\alpha = 0.75$ and a new abundance estimate, y_i , are introduced such that

$$y_i = y_i + \alpha x_i. \tag{3.34}$$

where y_i is initially set to d_i and then iterated upon. If y_i/x_i is not within a given tolerance the algorithm is repeated with the vector \mathbf{y} serving as the new current abundances (\mathbf{d}). The process is repeated until the tolerance is met at every meshpoint. We include two contingencies in the event of convergence issues. First, the the acceleration parameter is decreased in the hope of more gently approaching x_i . Failing this, we slightly decreasing the tolerance.

In Figure 3.3 we compare the results of the new diffusion equation solver with that of the Thomas Algorithm. Recall that the black curve represents the surface

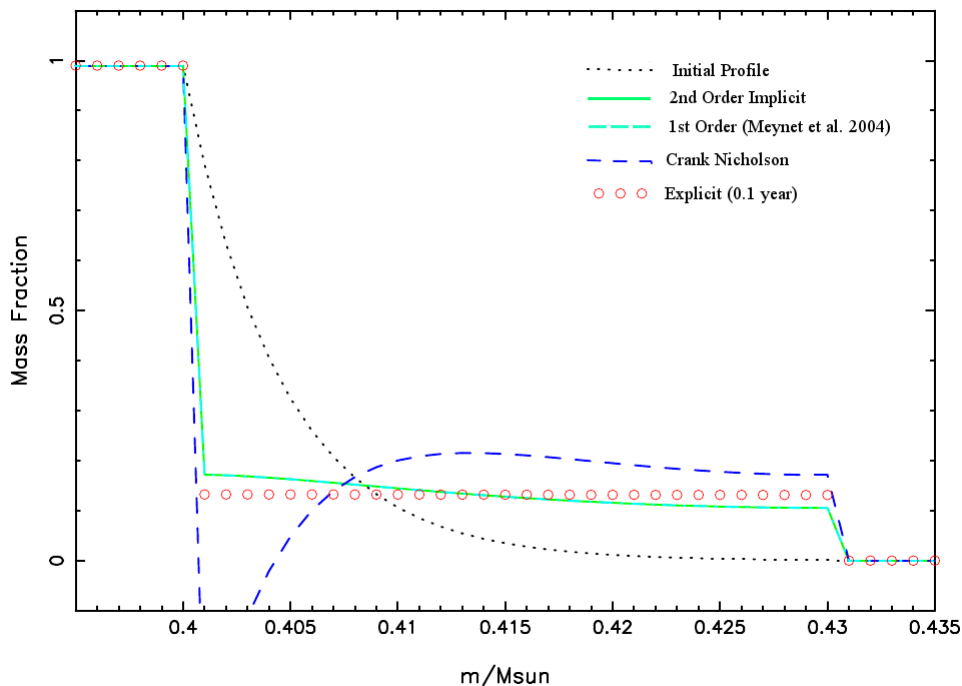


Figure 3.4: Helium abundance as a function of mass as taken from figure 4.1 in Campbell (2007). Here various differencing of the diffusion equation is tested in an environment similar to that found during hydrogen shell burning. The solid green line represents a second order differencing using an implicit scheme. The dashed cyan curve which overlies the green curve is the Meynet et al. 2004 scheme. The dashed blue line is an implicit Crank-Nicolson procedure and the red circles use an explicit method. The timestepping used for the implicit schemes is 3000 years whereas the explicit scheme required 0.10 year timesteps. Note here that there is no difference between the second order and first order approximation to the diffusion equation.

evolution of ^{12}C for a star of mass $M = 0.8M_{\odot}$ and $Z = 0.0005$ using the direct method. The broken grey curve shows the same calculation using the hybrid iterative scheme to solve the diffusion equation. The tighter control over numerical errors forces smaller timesteps along the RGB than previously required but results in greater stability for the thermohaline calculations. We found the increase in computational time an acceptable cost for improvements in stability. We note that smaller timesteps with the direct method did not provide the necessary level of stability.

3.3.3 The Meshing Routine

The standard meshing routine in MONSTAR did an adequate job of resolving the thermohaline mixing regions, however two new meshing criteria were added as a precaution:

1. If the current mesh point is within 100 mesh points of the minimum in μ , then $\Delta X(^3\text{He}) < 10^{-6}$ between adjacent mesh points.
2. If the current mesh point is above the minimum in μ , we enforce that $\Delta X(^3\text{He}) < 5.0 \times 10^{-6}$ and $\Delta M \leq 10^{-5} M_{\odot}$ between consecutive mesh points.

These extra conditions, whilst having a minor effect on the surface abundances, ensured that the location of the μ minimum was highly resolved.

3.3.4 New Species

The seven species network in MONSTAR provided a limited means by which to constrain therohaline mixing. Whilst carbon and nitrogen serve as robust tests against observations (see Part III), in Part IV we turn to lithium as a check of the stellar models because of its temperature sensitivity. Thus the decision was made to include a supplementary nucleosynthetic network in MONSTAR. Three new species, ^7Be , ^7Li and ^{13}C were included in our calculations.

3.3.4.1 Energy Generation and Reaction Rates

To ensure consistency across MONSTAR and MONSOON, some reaction rates in MONSTAR were updated. Typically, reaction rates are in the form given by Caughlan and Fowler (1988). In Table 3.2 we specify those rates which have changed from Campbell (2007). The Reaclib format allows reaction rates from MONSOON to be applied trivially to the evolution code.

Reaction Rate	Source
$^1\text{H}(p, e^+\nu)^2\text{H}$	Harris et al. (1983)
$^3\text{He}(^3\text{He}, 2p)^4\text{He}$	Caughlan and Fowler (1988)
$^3\text{He}(^4\text{He}, \gamma)^7\text{Be}$	Caughlan and Fowler (1988)
$^{12}\text{C}(p, \gamma)^{13}\text{N}$	Caughlan and Fowler (1988)
$^{14}\text{N}(p, \gamma)^{15}\text{N}$	Champagne 2004 (private comm.)

Table 3.2: Those reaction rates converted to Reaclib form.

For the structure, the $^{14}\text{N}(p, \gamma)^{15}\text{N}$ rate is the most significant of those changed. This is the location of the bottleneck in the CNO cycle. The rate provided by Champagne is 50% less than that suggested by NACRE. It is in effect the same rate given by Adelberger et al. (2011) and the LUNA collaboration. As it is the slowest reaction in the CNO cycle it will dictate how much energy is produced through this channel. Palmerini et al. (2011b) discuss the consequences of the new rate for low-mass stellar evolution including extra mixing. Our study of globular

clusters will focus on the C and N abundances and this updated rate is pivotal in our attempt to match observations.

In Table 3.3 we specify those new rates added to MONSTAR’s network in order to follow the ${}^7\text{Be}$, ${}^7\text{Li}$ and ${}^{13}\text{C}$ abundances.

Reaction Rate	Source
${}^7\text{Be}(e^-, \nu_e){}^7\text{Li}$	ReacliB electron capture database
${}^7\text{Be}(p, \gamma){}^8\text{B}$	Angulo et al. (1999)
${}^7\text{Li}(p, {}^4\text{He}){}^4\text{He}$	Descouvemont et al. (2004)
${}^{13}\text{C}(p, \gamma){}^{14}\text{N}$	Angulo et al. (1999)

Table 3.3: New reaction rates added to MONSTAR’s supplementary nucleosynthetic network.

3.3.4.2 Equilibrium Conditions

During the RGB, timestepping control in MONSTAR is most sensitive to changes in the abundances. Recall that one of our timestepping conditions limits the abundance change between consecutive models. The fierce hydrogen shell during this phase forces the code to reduce the timestep in order to resolve the nuclear burning. These changes to the composition dominate over changes to the structural gradients (L , T , r , P). Rather than follow all the reactions explicitly, the efficiency and stability of MONSTAR is improved by first testing whether a nucleus will reach equilibrium in a given timestep. When the production rate of a nucleus is equal to the rate at which it is destroyed, the abundance distribution of some elements can be described by straightforward algebraic expressions (Clayton, 1983; Iliadis, 2007). We can determine the profile a priori and it is not necessary to calculate the burning via all the nuclear reactions; note that we have already made assumptions about the distribution of many pp and CNO nuclei by not including them in our network. Deuterium, for example, is extremely fragile and it is assumed that its equilibrium abundance is instantly reached (many evolution codes also make this assumption because it reaches equilibrium in less than a year in most cases).

For our new species we can derive equilibrium conditions based on our treatment of ${}^3\text{He}$ in the code. Two of the new nuclei in the network, ${}^7\text{Be}$ and ${}^7\text{Li}$, are dependent on ${}^3\text{He}$ burning (see Clayton 1983, Equation 5-33). When the latter is in equilibrium so are our fragile new species as they have lifetimes of ≤ 1 year in hydrogen burning regions. To determine whether ${}^3\text{He}$ will reach equilibrium during the current timestep we test whether the amount of ${}^3\text{He}$ destroyed is less than the amount present. The destruction rate of ${}^3\text{He}$ is given by

$$\frac{d{}^3\text{He}}{dt} = -\frac{2\lambda_{33}X^2({}^3\text{He})}{2} - \lambda_{34}X({}^3\text{He})X({}^4\text{He}) \quad (3.35)$$

where we use the λ notation throughout, e.g., λ_{33} denotes $\langle \sigma v \rangle$ for ${}^3\text{He}+{}^3\text{He}$ reaction. The mass of ${}^3\text{He}$ destroyed during a single timestep is given by

$$\left(\frac{2\lambda_{33}X({}^3\text{He})^2}{2} + \lambda_{34}X({}^3\text{He})X({}^4\text{He}) \right) \times 3M_H \times \Delta t \quad (3.36)$$

where $M_H = 1.67377 \times 10^{-24}$ grams, the mass of the hydrogen atom (1 AMU) and Δt is the timestep in seconds. We therefore define our condition for when ${}^3\text{He}$ is not in equilibrium by

$$\left(\frac{2\lambda_{33}X({}^3\text{He})^2}{2} + \lambda_{34}X({}^3\text{He})X({}^4\text{He}) \right) \times 3M_H \times \Delta t < X({}^3\text{He}) \quad (3.37)$$

$$\Leftrightarrow (\lambda_{33}X({}^3\text{He}) + \lambda_{34}X({}^3\text{He})) \times M_H \times \Delta t < \frac{1}{3} \quad (3.38)$$

We also check whether either of ${}^7\text{Be}$ or ${}^7\text{Li}$ are in equilibrium. Following on from the same arguments as above the destruction rate of ${}^7\text{Be}$ is given by

$$\frac{d{}^7\text{Be}}{dt} = -\lambda_{e7}n_e X({}^7\text{Be}) - \lambda_{p7}X(H)X({}^7\text{Be}) \quad (3.39)$$

and therefore our (non)equilibrium condition is given by

$$(\lambda_{e7}n_e + \lambda_{p7}X(H)) \times M_H \times \Delta t < \frac{1}{7}. \quad (3.40)$$

Similarly, the destruction rate of ${}^7\text{Li}$ is given by

$$\frac{d({}^7\text{Li})}{dt} = -\lambda_{p7}X(H)X({}^7\text{Li}). \quad (3.41)$$

Thus our lithium non-equilibrium condition is

$$\lambda_{p7}X(H) \times M_H \times \Delta t < \frac{1}{7}. \quad (3.42)$$

Finally ${}^{13}\text{C}$ destruction is given by

$$\frac{d{}^{13}\text{C}}{dt} = -\lambda_{p13}X(H)X({}^{13}\text{C}). \quad (3.43)$$

Note that the inclusion of ${}^{13}\text{C}$ is not integral to the current study. In future work we will update the rate to take into account the ${}^{13}\text{C}(\alpha, n){}^{16}\text{O}$ reaction which should be significant during the thermally pulsing AGB phase. As a result of the reaction we consider, the current non-equilibrium condition is given by

$$\lambda_{p13}X(H) \times M_H \times \Delta t < \frac{1}{13}. \quad (3.44)$$

3.3.5 The Equation of State

In trying to match high resolution observations of GC stars (see Chapter 9), MONSTAR indicated several modelling issues with respect to the onset of the RGB mixing events. The inability to predict these fundamental evolutionary events (to the author’s satisfaction) points to a shortfall in the stellar physics and motivated a systematic investigation of possible causes. Such shortcomings will be a common theme in the coming years as we only now start to explore the large data sets available from asteroseismology and new medium-to-high resolution spectroscopic studies (APOGEE, GALAH).

Of all the physics in the code, the EOS remains pristine, untouched by the steady stream of Ph.D. students through Monash and Mt. Stromlo. The equation of state subroutine in MONSTAR calculates the relevant thermodynamic variables, (mesh)point wise, starting from the stellar surface. In partially ionised regions the dissociation and ionisation of hydrogen and helium are calculated using the Saha Equation. In fully-ionised regions the perfect gas equation with radiation pressure is utilised. Corrections due to electron degeneracy and electron positron pairs are calculated in further subroutines and applied to the EOS. There is also the option to use the fitting formula by Beaudet and Tassoul (1971) under relativistic or degenerate conditions. There have been many improvements to the approximations to the stellar EOS since these publications¹. For example, the Opal EOS tables (Rogers and Nayfonov, 2002) cover the temperature and density range of RGB evolution. These tables were considered the most straightforward method to implement and added to MONSTAR for later comparisons. The OPAL EOS suite determines a set of thermodynamic variables (see Rogers and Nayfonov 2002) interpolated in temperature and density (or pressure). The tables and interpolation routines were grafted into MONSTAR and the code’s necessary thermodynamic terms recast from the supplied variables.

We note that Constantino et al. (2014) have rewritten the equation of state routine to include the OPAL (Rogers and Nayfonov, 2002), Helmholtz (Timmes and Swesty, 2000) and Timmes equations of the state (Timmes and Arnett, 1999), all of which can be blended. Their investigations into asteroseismology and core-helium burning stars requiring a more versatile approach. The inclusion of these equations of state will allow starting models from MONSTAR to be mapped into 3D hydrodynamical codes such as Djehuty (Bazan et al., 2001) or Prompi (Meakin and Arnett, 2006). These changes will eventually be merged into the MONSTAR trunk.

3.3.6 MONSTAR_GRID

The inherited MONSTAR code has been changed significantly throughout the duration of this dissertation. New physics have been added and many subroutines updated. Diligence required hours of testing, debugging and benchmarking. Furthermore, the project itself, using GC stars to constrain a theory of extra mixing, involved a large exploration of the parameter space with many models run. MON-

¹The true EOS of the stars is, and has long been well known.

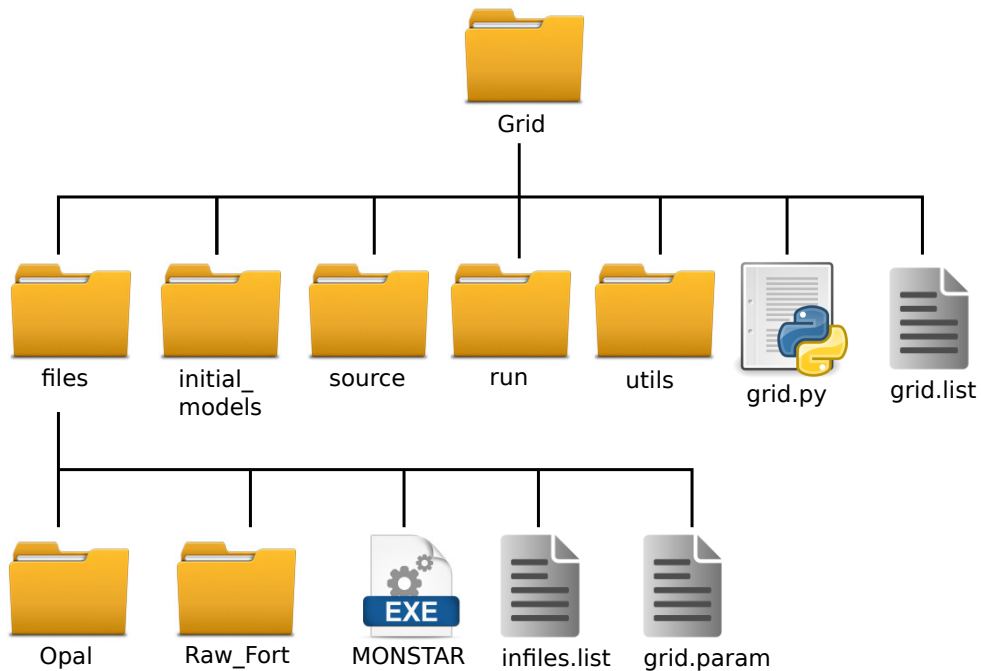


Figure 3.5: Hierarchy of the MONSTAR_GRID code.

STAR was born in an era when computational resources were scarce and the advent of multi-core desktop machines 40 years away. For each star, the executable code, opacity tables as well as the starting model and parameter files were copied into the run directory. Depending on the machine, a starting script may have also been required. If a starting model did not exist, it was created slowly, by hand. The mass and composition of a previous model changed, re-run, checked for realistic convergence², stopped after a few models, gradually altered again to a mass and metallicity closer to the desired values and the process repeated. If the code crashed during the evolution, all the output files needed to be changed or moved by hand before restarting the executable. This eventually became too much for the author to bare, especially when colleagues were asking for many combinations of masses and composition. Thus was born MONSTAR_GRID- an automated process for running a grid of stellar models.

The power of a compiled language, such as Fortran, lies with its ability to efficiently carry out arithmetic operations. Scripting languages, whilst not suited to such calculations, can perform many other complex tasks in just a few lines of coding. MONSTAR_GRID employs a Python wrapper to the *MONSTAR* executable and organises filenames, directories, starting models, and submission scripts for computer clusters automatically. It can restart runs that crash, automatically altering the input parameters as well apply homology transforms to reverse the pre-main-sequence evolution (although these were not implemented/required for the current study). It enforces a directory structure (see Figure 3.5) and naming

²to a model that was plausibly physical.

convention for models to ensure proper bookkeeping. We defer details of the grid code to Appendix C for the interested reader.

3.4 Summary

It is currently impossible to hydrodynamically model thermohaline mixing and determine what effects, if any, the process has on stellar surface abundances over a nuclear timescale. Our aim to quantitatively compare the predictions of thermohaline mixing to observations has required the implementation of a prescription that mimics the mechanism in a 1D stellar evolution code. For this purpose we have employed the thermohaline mixing prescriptions of Ulrich (1972) and Kippenhahn et al. (1980) in MONSTAR.

MONSTAR calculates the stellar structure under the assumptions of 1D spherical symmetry and hydrostatic equilibrium. The equations of stellar structure are solved using the Henyey method with adaptive timestepping and meshing control. Energy transport is determined from the mixing length theory and the mixing of the composition occurs via a diffusion equation. Through the diffusive mixing paradigm, the code already possessed prescriptions for the non-canonical mixing processes in semi convection and overshoot. A thermohaline mixing formalism was included and the coefficients added to the diffusion matrix. This seemingly trivial addition has necessitated several changes to the original code.

It was found that with the inclusion of thermohaline mixing the tridiagonal matrix algorithm used to solve the diffusion equation led to convergence difficulties. The Thomas Algorithm was amended to include an iterative step which reduced the numerical error. Extra meshing criteria were also added to ensure the location of the μ inversion was resolved accurately. In addition, a new supplementary nuclear network was introduced which followed some of the more fragile species present during hydrogen burning. Predictions of ${}^7\text{Be}$, ${}^7\text{Li}$ and to a lesser extent ${}^{13}\text{C}$ will provide stellar codes with a sensitive test by which to compare results. This will complement the robust observational based tests of trying to match ${}^{12}\text{C}$ and ${}^{14}\text{N}$ as a function of magnitude.

The purpose of MONSTAR is to calculate the stellar structure. The treatment of mixing in our 1D stellar evolution code has forced us to model thermohaline mixing as a diffusive process. In this paradigm the aspect ratio of the rising fingers, which are assumed to be cylindrically symmetric, are related back to a diffusion equation and a mixing velocity. Figure 3.6, which is a Kippenhahn plot for a star typical of those in the GC M3 (see caption for more detail), shows that mixing and burning occurs simultaneously in thermohaline regions. It may be the transport of material is better described as an advective process. We have at our disposal MONSOON, the post processing code to determine the nucleosynthesis of trace elements. Rather than a diffusive scheme, this code employs an advective mixing algorithm. In the next chapter we describe the code and its changes to include thermohaline mixing.

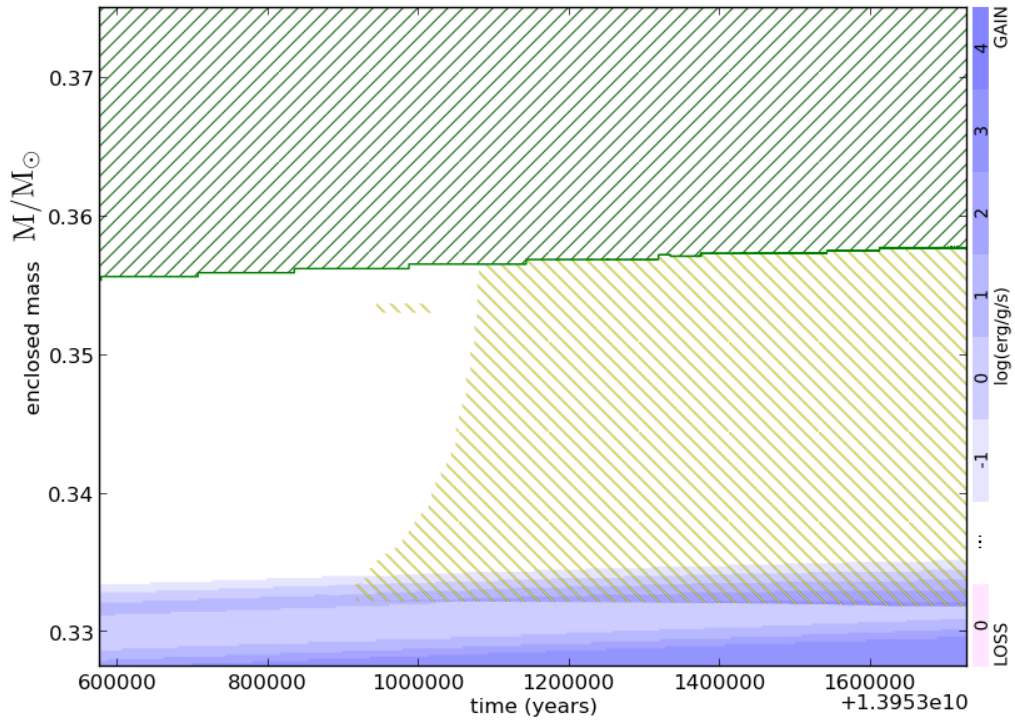


Figure 3.6: Kippenhahn plot for a star of mass $M = 0.08 M_{\odot}$ and $Z=0.0005$ near the onset of thermohaline mixing. The plot shows the structure of the star during a brief epoch of RGB evolution. Green shaded regions denote convective regions and orange shading denote regions undergoing thermohaline mixing. Blue shaded regions show energy generation with the scale provided above. The blue shading primarily traces the hydrogen burning shell. This plot highlights the fact that burning and mixing occur simultaneously in the thermohaline region.

Chapter 4

The Nucleosynthesis Code

Once upon a time, in some out of the way corner of that universe which is dispersed into numberless twinkling solar systems, there was a star upon which clever beasts invented knowing.

- Friedrich Nietzsche

4.1 Overview of the Nucleosynthesis Code

MONSOON, the Monash nucleosynthesis code, owes its origins to Cannon (1993) and the study of massive Thorne-Żytkow objects (Thorne and Żytkow, 1975, 1977; Cannon et al., 1992). Structurally, it is thought that Thorne-Żytkow stars possess degenerate neutron cores and most of the luminosity is generated from burning at the base of the envelope. The problem in consideration required a time-dependent mixing scheme as well as a nuclear network specific to the *rp*-process (rapid-proton process). The focus on a single stage of stellar evolution allowed for the implementation of a static Eulerian mesh.

The code has since been adapted to calculate the nucleosynthesis of low-mass stars at every evolutionary stage. The various shell configurations have required the introduction of a combination of Lagrangian and non-Lagrangian mesh points. The many reaction pathways have led to the addition of a variable, user-defined network. Although used almost exclusively with MONSTAR, MONSOON will take as its input the radius, pressure, temperature, density, mixing length and velocity as a function of mass and time from *any* stellar structure code. In most cases this information is not required at every evolutionary timestep; criteria based on changes in the structure are set in MONSTAR to ensure the optimisation of both codes. The nucleosynthesis code will calculate an abundance profile across consecutive (input) models using its own timestepping. A problem-specific nuclear network can be designated which has lead to a forking of the code. We distinguish between the version of the code that considers all types of reactions (MONSOON)

and the version that has an additional network dedicated to efficiently calculating neutron capture reactions on heavy elements (MONTAGE).

In order to produce *s*-process yields, MONTAGE calculates all types of reactions up to the iron peak (lower network hereinafter). The example provided in Figure 4.1 is a simplified network tailored to low-mass AGB nucleosynthesis. A secondary network, based on that of Straniero et al. (2006), is coupled to the lower network and is responsible for neutron capture calculations (the upper network). When activated, the upper network needs to consider only neutron capture, beta decay and electron capture reactions (Church et al., 2009). We note in both networks, the presence of the fictitious nucleus *g*. Fondly referred to as ‘the Gallino particle’ it is named in honour of Roberto Gallino and his contribution to *s*-process nucleosynthesis. Its purpose is to simulate the neutron cross section of the upper network and determine the neutron exposure. This method of calculating neutron capture nucleosynthesis has been utilised by other groups including Busso et al. (1988). If we wish to consider the nucleosynthesis of more massive stars, the example network in Figure 4.1 would need to be changed to include the charged particle pathways for heavier nuclei. A larger network that considers all neutron capture reactions could also be created for MONSOON, but this method of calculating *s*-process yields is significantly slower than the optimised MONTAGE.

4.1.1 The Nuclear Network

The nucleosynthesis code reads reaction rates in reaclib format (Rauscher and Thielemann, 2000) although this has been modified on occasion (to read in tables). The Reaclib format is comprised of a seven-component analytic fit to each reaction rate such that:

$$\lambda = \exp[a_0 + a_1/T_9 + a_2/T_9^{1/3} + a_3T_9^{1/3} + a_4T_9 + a_5T_9^{5/3} + a_6 \ln(T_9)], \quad (4.1)$$

where λ is the rate of reaction, a_x is the fit coefficient and T_9 is the temperature in units of 10^9K . In case of complex reaction rates, multiple sets of Equation 4.1 with differing parameters a_0 through a_6 can be summed to properly fit rates with numerous resonant and non-resonant contributions (Cyburt et al., 2010). As discussed in the previous chapter, many reaction rates in MONSTAR have been updated so that there is consistency between the two codes.

As MONSTAR is concerned with calculations of the stellar structure, its network only considers those species that are energetically significant. Other pp and CNO nuclei are included implicitly by assuming they are always at their equilibrium abundance. As well as simplifying the network, as discussed in the previous chapter, this assumption allows the evolution code to take larger timesteps than it otherwise could. Calculations with MONSOON in this work are carried out with network described in Figure 4.1.

4.1.2 The Meshing Routine

The code utilises a combination of Lagrangian and non-Lagrangian points with different meshing algorithms for each phase of evolution. During the main sequence

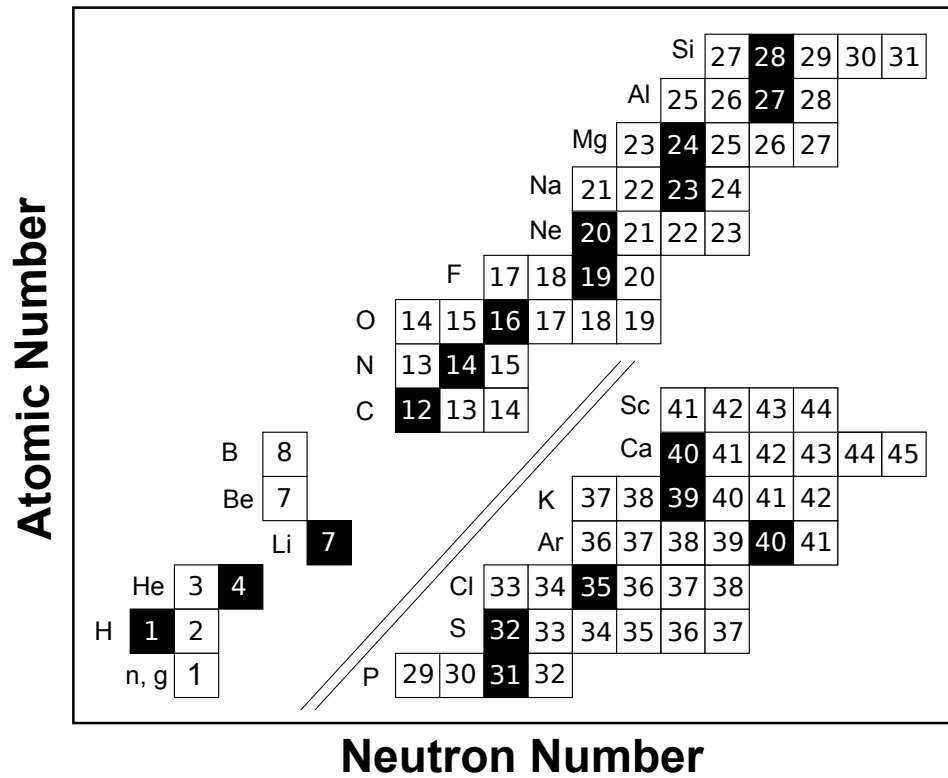


Figure 4.1: The standard 86 species (lower) network used in MONSOON/MONTAGE. Nuclei beyond Sc are considered in the s-process network. Dark shaded boxes indicate the location of elements in the network.

for example, points are geometrically spaced in mass, with separation increasing from the core to the surface. During the RGB and the AGB shell burning must be followed. For these phases of evolution, the core and intershell regions have constant mass spacing (i.e., Lagrangian). Between them lie the burning shells which are comprised of tightly spaced geometric profiles. The advance of each shell is tracked through the use of three fixed points. These points, which are defined by H and He abundances, identify the top, middle and bottom of the respective burning shells. They, along with all the non-Lagrangian points that constitute the shell, are interpolated between models and shifted to ensure sufficient resolution exists around areas of significant nucleosynthesis. Figure 4.2 demonstrates the basic principle of the shell-shifting technique. As the shell advances, burning becomes more fierce and confined to a smaller mass range. As such, non-Lagrangian points can be released if they are no longer required. They are adopted into the Lagrangian mesh of the region below. Similarly the shell consumes points and converts them into non-Lagrangian points as it burns outwards. For the most part the rest of the mesh is kept in place to reduce numerical diffusion, although points are added and removed as required. Special treatment exists for events such as dredge-up and composition discontinuities.

4.1.3 The Mixing Algorithm

We have seen that MONSTAR employs a diffusive algorithm to treat convective mixing. MONSOON, on the other hand, models convection as an advective process. In order to somewhat mimic the behaviour of convection, material is split into upward and downward moving streams. Figure 4.3 illustrates the principle behind the scheme. The model is divided into a number of levels each of which consists of two mesh points (except for the central point). Odd numbered mesh points describe the downward moving material and even numbered mesh points upward moving material. At each timestep, an advection equation is solved and odd numbered cells receive, from above, downward flowing material. Similarly even numbered cells receive upward moving material from the cell below. A gradient in the vertical flow requires that material moves laterally to conserve mass flux. There is also an allowance for diffusion between adjacent cells.

4.1.3.1 Derivation of the Mixing Coefficients

In Figure 4.3 the streams are illustrated with equal cross sections, however, the flows need not carry the same mass flux. Simulations (Herwig, 2001; Stancliffe et al., 2011) have shown that convection is characterised by narrow, fast moving downstreams and large slower upwellings. We can therefore define the fractional areas of the upstream, f_u , and the downstream, f_d , where $f_u + f_d = 1$. In order to conserve mass, the velocity of the rising material, v_u , and falling material, v_d , is such that $f_u v_u = f_d v_d$ at each level. The schematic in Figure 4.3 represents the case when $f_u = f_d = 0.5$ but Figure 4.4 demonstrates a more general example where the the up flows are arbitrarily larger than the downflows. Taking the velocity, density and mass from the structure code, the vertical mass flux, and hence the

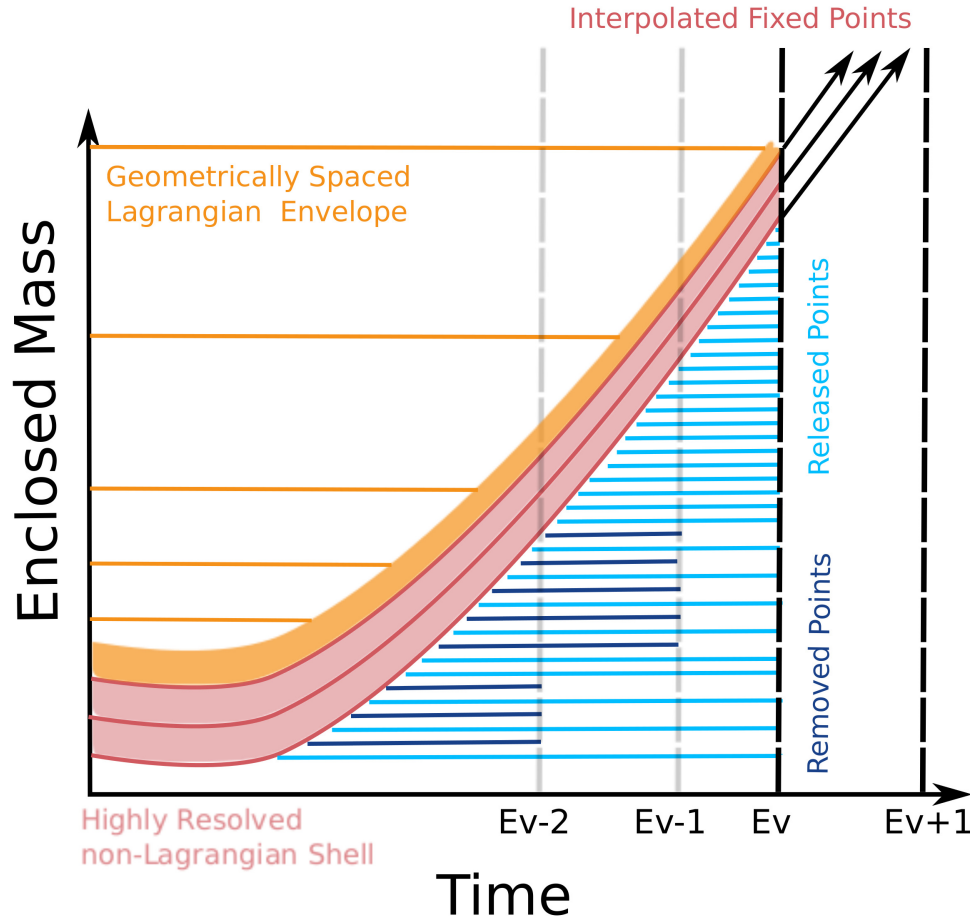


Figure 4.2: General overview of MONSOON’s meshing routine during the RGB. Two evolution models (Ev and $Ev+1$, not necessary consecutive evolution models) are read in and abundances calculated using the MONSOON’s own timestepping. Points in the convective envelope (yellow) are geometrically spaced and remain Lagrangian unless consumed by the advancing shell. Just above the shell they are very tightly packed so appear as block in this figure. The shell is traced by following three fixed points (dark red curves) which are identified by their hydrogen abundance. The rest of the non-Lagrangian shell (light red, but so densely packed they appear as a block rather than points) are shifted also. As burning becomes more fierce and the shell thins, some non-Lagrangian points are released (light blue) and remain Lagrangian until they are deemed unnecessary and removed (e.g., navy points).

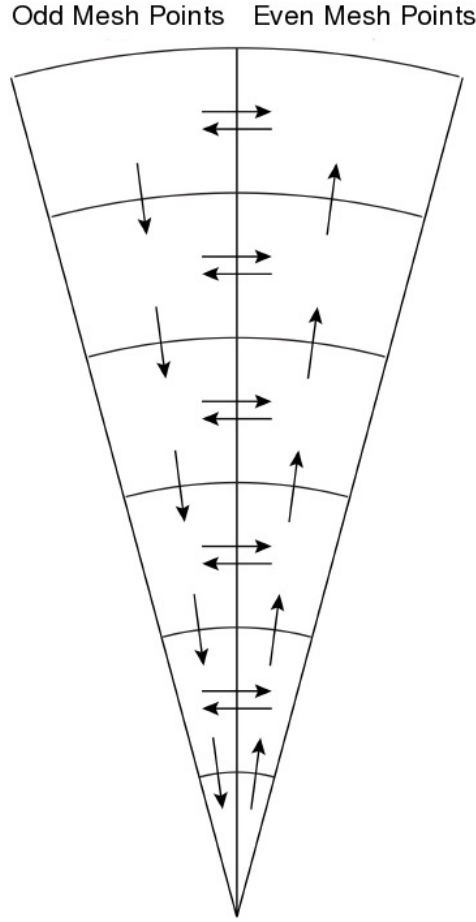


Figure 4.3: Schematic representation of MONSOON's advective mixing algorithm. The two-stream method only allows the composition in each cell to be linked to three other cells.

advective flow rate, α_k , through each cell at level, k , can be determined.

Consider Figure 4.4 which illustrates our general two stream case. Subscript d denotes material in the down flow and subscript u material in the up flow. The quantities radius (r), density (ρ) and velocity (v) are evaluated at cell boundaries whilst we evaluate the abundance, h , of species, i at the cell midpoint. We define the top boundary of the cell by superscript T and the bottom edge by superscript B . Let us, for the moment, only consider material in the downstream. Then the change in abundance is given by

$$\frac{dh_i^k}{dt}_{mix} = \alpha^k (h_i^{k+2} - h_i^k) + \beta^k (h_i^{k+1} - h_i^k). \quad (4.2)$$

The fraction of material replaced in the cell from the vertical flow, α_k , is given by

$$\alpha_k = \frac{4\pi(r^T)^2 \rho^T v_d^T}{m^k}. \quad (4.3)$$

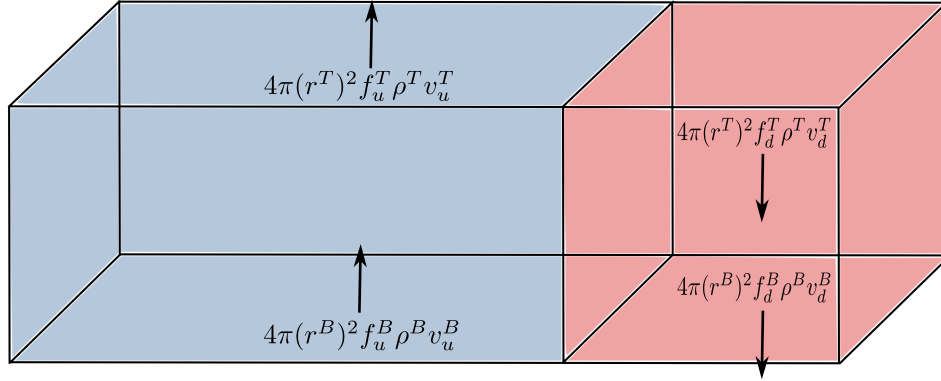


Figure 4.4: The upward (u) and downward (d) streams need not have the same cross sections. Here two we define the top edge (T) and bottom edge (B) of two cells at the same level.

The horizontal mass flow, β_k , is the sum of contributions from a difference in the vertical flow, ϕ , and from sideways diffusion, η . Once again from Figure 4.4 it can be seen that the gradient in the vertical flow is given by

$$\phi_d = 4\pi(r^T)^2 \rho^T v_d^T - 4\pi(r^B)^2 \rho^B v_d^B. \quad (4.4)$$

If more material is flowing into the top of the cell than is flowing out the bottom of the cell ($\phi_d > 0$), then in order to conserve mass, material is mixed horizontally into the upstream. The rate at which material is mixed into the upstream (due to the gradient in the downstream) is therefore given by

$$\beta^k = \frac{\phi_d}{f_d m^k}. \quad (4.5)$$

There is also a term that imposes horizontal diffusion between the two cells at level k . The argument is that the whole cell should have mixed after flowing over the course of a mixing length, ℓ and each box will have exchanged a (small) mass with its neighbour through diffusion

$$\Rightarrow \eta = \frac{v_c}{\ell_c}, \quad (4.6)$$

where subscript c denotes the logarithmic mean between the top and bottom values, and hence

$$\beta^k = \frac{v_c}{\ell_c} + \frac{\phi_u}{f_u m^k}. \quad (4.7)$$

Similarly, analogous terms can be derived for the upstream flow.

4.1.3.2 Advection vs Diffusion

The diffusive treatment of convection assumes that the composition difference between convective elements at the same level is negligible. This is not the case

for Thorne-Żytkow objects where many reactions occur with a timescale on the order of seconds (Biehle, 1991; Cannon, 1993). In such environments the upstream and downstream elements will have significantly different abundances and hence robust modelling necessitated the development of a two stream model. In low(ish) mass stellar evolution the reaction time-scale is much longer than the convective turnover time so that the diffusive approximation is appropriate. There are of course examples to the contrary, for example hot bottom burning in AGB stars. The algorithm in MONSOON uses a finite representation which, in the limit of rapid sideways diffusion, reduces to the diffusion equation (Biehle, 1991). Efficient horizontal mixing will result in up and down streams with an average homogeneous composition. In the limit of no sideways diffusion the scheme approaches a ‘conveyor belt model’ (Eich et al., 1989; Sackmann and Boothroyd, 1999; Charbonnel and Balachandran, 2000).

In the case of thermohaline convection, the turnover timescale is much longer than for standard convection. Eggleton et al. (2008) estimate the mixing speed to be between $0.2 < v < 2.0$ cm/s whereas convection yields velocities of order 10^4 cm/s. We investigate the mixing velocity required to match observations of globular cluster stars in Part III, and compare to 3D hydrodynamical simulations in Part IV. If the mixing speed is much slower than convection, then the turnover time is closer to the reaction timescale and we may expect different compositions for the up and downstreams. This of course means we should also expect differences in the abundance predictions between MONSTAR and MONSOON. How different these abundances are will give insight into whether a diffusive approximation is appropriate for the mechanism. This is subject of the next chapter.

4.1.3.3 The Treatment of Segments

Before describing how the code solves the advection equation, it is necessary to outline the algorithm for determining the abundance changes. In Figure 4.5 we provide a simplified summary of the steps involved. The first three steps are described here. In order to optimise calculations, the code has separate treatments for radiative and convective regions. The star is divided into *segments* which are groups of consecutive radiative or convective points. The compositions of radiative segments are calculated using a box model as there is no mixing. Without contribution from the α and β terms (Equations 4.3 and 4.5), the resultant matrix describes how the composition will change due to nuclear burning only. The system can be solved using the Henyey procedure with standard Gaussian elimination.

Convective segments are treated using the two stream model. As well as considering the effects of nuclear burning, the regions must also take into account the flow of material. For each meshpoint, our system requires a matrix that describes the nuclear burning, a matrix that describes the vertical flow of material (α) and a matrix that describes the horizontal flow of material (β). The resultant system is a tridiagonal matrix such as Equation B.7 but with matrices rather than scalar coefficients at every index, namely a block-tridiagonal matrix. An example can be seen in Figure 4.6. Note that the flow of a given species i , from the coupled cells can only affect the abundance of species i , hence the α and β matrices are all

diagonal.

MONSOON first reads in consecutive structure models. With knowledge of the convective velocities and convective boundaries it then determines the α and β values at every point. This is necessary because during convergence difficulties, a two stream solution is forced everywhere and the star treated as one large block-tridiagonal matrix. Solving the system in this way tends to increase stability but comes at a computational cost. In most cases, the star is broken up into radiative and convective segments and the order in which the segments treated is determined. If the star possesses too many convective pockets, the code will employ a two stream solution everywhere.

4.1.4 The Numerical Scheme

From the mixing scheme described above, it can be seen that each cell is coupled to three other cells. Each cell is linked to a cell from which it receives material, a cell to which it donates material and a neighbour cell on the same level which allows for horizontal diffusion. The scheme has been described as a $1 + \epsilon$ dimensional model but in general the geometry of a two dimensional flow gives rise to a block-tridiagonal matrix (Figure 4.6). Similar to the tridiagonal matrix resulting from the diffusion equation (in the evolution code, Equation B.3), this matrix tends to be sparse and can be solved with efficient algorithms. The system is solved using a multi-dimensional Newton-Raphson relaxation scheme which, in the case of radiative segments, is the same Henyey method used to solve the stellar structure equations in MONSTAR.

The principle behind using an iterative method to solve a system of coupled equations was outlined by Equations 3.26-3.31. Recall that we seek to improve upon our previous guess each iteration. Once the corrections are deemed small enough the system is then considered converged. From Equation 4.2 it can be seen that we seek to find corrections to \mathbf{dh} each iteration. The error \mathbf{e} , in our guess is given by

$$-\mathbf{e}_i = dt \times \left[\alpha^k (h_i^{k+2} - h_i^k) + \beta^k (h_i^{k+1} - h_i^k) \right] - dh_i^k - dt \sum R_i^k, \quad (4.8)$$

where $dt \sum R_i^k$ is the change in composition due to nuclear burning. Through clever bookkeeping we can determine a set of analytical derivatives in our Henyey matrix, \mathbf{H} . The rate at which each nuclear reaction will proceed depends on the abundances of the reactants, and the matrix describes how each reaction rate will change due to the presence of every species in the network i.e., $d(\text{reaction})/d(\text{species})$. This matrix, of course, is mostly empty. In radiative segments we need not consider the effect of mixing on the composition so we have adequately described our system. In matrix notation this is expressed as

$$\mathbf{H} \cdot \mathbf{dx} = -\mathbf{e} \quad (4.9)$$

where \mathbf{dx} is the correction applied to our iteration to determine our next guess at \mathbf{dh} . As in the evolution code, the system is solved using Gaussian elimination with

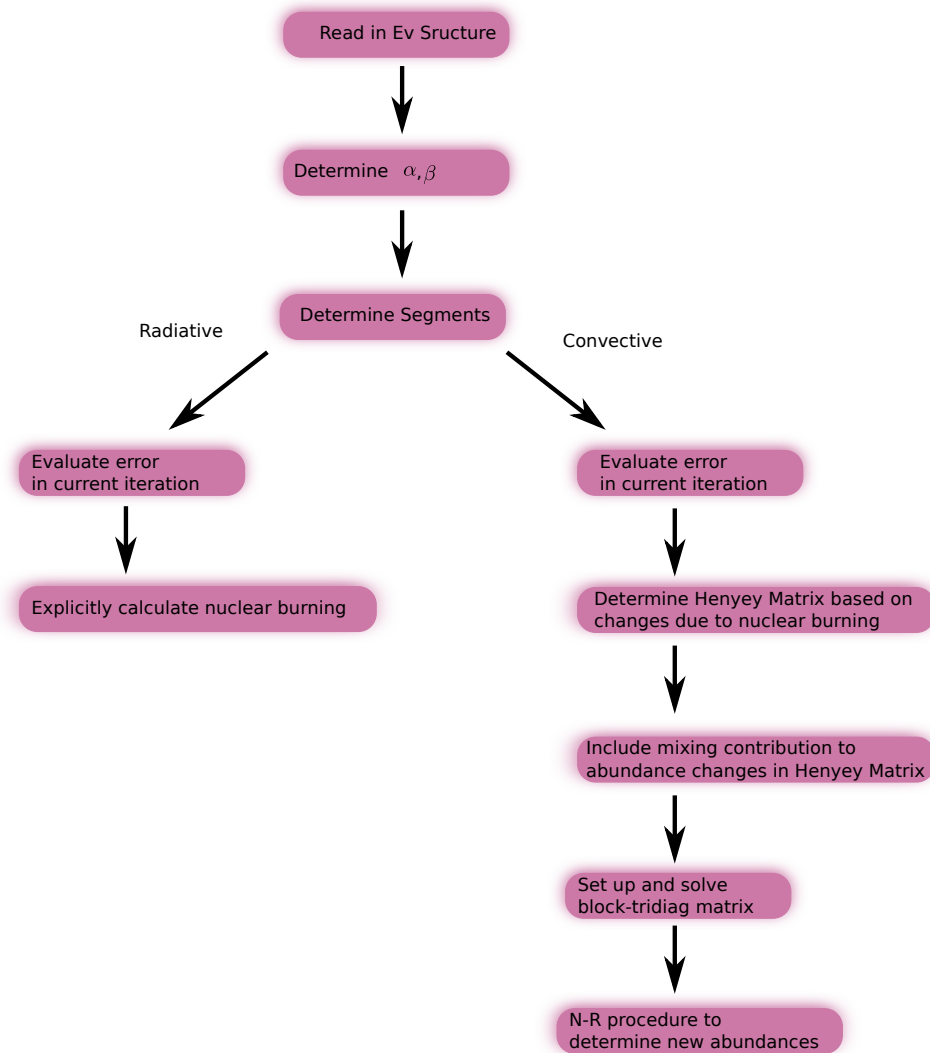


Figure 4.5: Simplified flow chart of the nucleosynthesis code. In radiative zones we assume a method which allows the abundances to be solved with standard Gaussian elimination. The geometry of a two stream flow used in convective regions yields a block-tridiagonal matrix and requires a dedicated algorithm to determine the composition. During convergence difficulties the whole star is solved using the two stream scheme.

% Time	Seconds	Calls	Name
36.96	9.59	489501	gausse
21.89	5.68	491521	drivs
17.57	4.56	2020	trbld

Table 4.1: Profile of the three most resource-expensive subroutines in MONSOON.

pivoting. Our analysis in Appendix B discusses how this scheme requires $O(N^3)$ operations where N is the number of unknowns in the system (i.e., mesh points). The procedure is repeated until our corrections are below a given tolerance and we have converged.

When considering convective regions the contribution of mixing must be included in the Henyey matrix. For each mesh point we consider the horizontal and vertical flow of material through the cell. This gives rise to coupled matrices that describe the vertical flow of material (α) and a matrix that describes the horizontal flow of material (β). The flow of a given species, i , from the coupled cells can only affect the abundance of species i , so these matrices are all diagonal. An example of the resultant system is given in Figure 4.6. The overall matrix is size $n_m \times n_m$ with each index a matrix of size $n_s \times n_s$, where n_m is the number of mesh points and n_s the number of species in the network. Through LU factorization the system can be efficiently solved, including by a variation of the Thomas algorithm described earlier. The extra steps involved by having matrices rather than scalars as the coefficients require $O(n_m \times n_s^3)$ operations.

By iterating upon our solution we are able to reduce the numerical error (see §3.3.2). The derivatives in the Henyey matrix are determined analytically and the equations are well behaved; both properties also improve convergence. The Newton-Raphson method also allows us to employ a convergence acceleration to help with stability. An underrelaxation scheme is used to ensure we approach the final solution, as in MONSTAR’s convergence routine. Finally, we note that in the case of MONTAGE, the upper s -process network uses its own efficient sparse matrix solver.

We finish our analysis of the post-processing code by analysing its efficiency. Table 4.1 demonstrates the results of profiling the nucleosynthesis code. MONSOON spends 75% of its time in three subroutines and although not shown here the next two subroutines account for a further 10% of the run time. The results in Table 4.1 are based on post-processing a star of mass $M = 0.8 M_\odot$ and metallicity $Z = 0.0005$ (representative of stars found in the globular cluster M3) from the main-sequence phase until part way up the RGB. We note that these three routines, *gausse* which performs Gaussian elimination for radiative segments, *drivs* which calculates the Henyey matrix and *trbld* which is the block-tridiagonal matrix solver, can all be parallelised. Such an improvement will be implemented in the near future.

4.2 Changes to the Code

4.2.1 Thermohaline Mixing

The introduction of thermohaline mixing in MOSOON proved far simpler than in the evolution code. The iterative matrix solver used to calculate the mixing and burning is believed to assist with stability. We included three different methods by which to calculate the process:

1. A simple EDL08-like formalism based on the location of the μ minimum and a free parameter.
2. The EDL08 formalism as given by Equation 2.113.
3. The UKRT formalism as calculated by MONSTAR (Equation 3.19).

It was previously mentioned that the nucleosynthesis code does not possess the necessary thermodynamic information to evaluate Equation 3.19. If we wish to investigate the effects of the UKRT with the mixing formalism in MONSOON then we must rely on output from the evolution code. The first two methods listed require the code to calculate the μ gradient throughout the star and readjust the mixing boundaries appropriately. The two formalisms differ only by the parameter in front of the $(\mu - \mu_{min})$ term. Recall the EDL formalism is expressed as

$$D = \frac{F_{inv} r^2}{t_{nuclear}} (\mu - \mu_{min}). \quad (4.10)$$

Here the r^2 and $t_{nuclear}$ terms have some physical basis. In our simple EDL-like scheme these factors are replaced with a constant.

4.2.2 Meshing Routine

The standard meshing routine employed by MONSOON did not provide enough spatial resolution to calculate thermohaline mixing accurately. The code places many points around the burning shell as in the absence of mixing this is where all the nucleosynthesis occurs along the RGB. Figure 3.6 shows that the thermohaline zone is above the shell, in the region where the nucleosynthesis code spaces cells geometrically in mass (recall that from the top of the hydrogen burning shell to the surface points are placed at geometric intervals, see Figure 4.2). With large mass spacings the small changes in the μ gradient are not resolved correctly and quite often the code finds the μ minimum in the envelope with its exact location due to numerical noise. As the original meshing routine proved to be inadequate, two alternatives were introduced.

4.2.2.1 Adaptive Mesh

The first meshing routine added recycled non-Lagrangian points to the top of the thermohaline region as they were released below the burning shell. In Figure 4.2 we see that as the hydrogen shell advances, some mesh points are released then

eventually removed by the code. This method had two advantages. It ensures that the regions of interest are always resolved, and it does so optimally by keeping the number of meshpoints to a minimum. This method of meshing proved to be unsuitable during the core flash and further development is needed to make this routine useful.

4.2.2.2 Brute Force Mesh

The brute force mesh ensured that all regions of interest were highly resolved during all periods of evolution. In order to limit numerical diffusion, a static mesh, evenly spaced in mass, was introduced prior to shell burning. From the core to a mass location $0.02 M_{\odot}$ below the deepest extent of FDU (determined from the evolution code) we evenly space points at $0.01 M_{\odot}$ intervals. A tightly packed, evenly spaced mesh was introduced for the burning shell and thermohaline region which also extended well into the convection zone. In these regions mass spacing is reduced to $0.0001 M_{\odot}$. The rest of the envelope was resolved using geometric spacing. Typically $\gtrsim 1500$ points are used to follow thermohaline mixing. The star is obviously over resolved, and as the mesh is kept as static as possible, the routine is quite stable. It is this meshing routine that has been adopted in our calculations.

4.2.3 Initial Abundances

As well as the structure at every timestep, MONSOON takes from the evolution code the initial ^1H , ^3He and ^4He abundances. These are used in the starting model as a first approximation with all other abundances read in from an initial composition file. MONSOON's natural unit of abundance is molar fraction but initially the code ensures that the mass fraction of those nuclei taken from MONSTAR and the initial abundance file sum to unity. If required, a scaling is applied to nuclei to conserve mass. The scaling usually results in a small difference in starting abundance between the two codes. For AGB nucleosynthesis this effect is minor, if not negligible. To help with future comparisons, an option was introduced so that MONSOON could read in all six species from the evolution code and the scaling algorithm edited to ensure that their abundances were not changed.

4.3 Summary

The original incarnation of MONSOON was designed to investigate Thorne-Żytkow objects. Nucleosynthesis in these stars occurs via the rp-process at the base of the convective envelope. Material circulates through the burning region on timescales of order ≈ 0.01 seconds (Cannon, 1993). The conventional method of treating mixing as a diffusive process is inappropriate in such conditions. An underlying assumption of diffusive mixing in a 1D stellar model is that within a given radial shell, the composition is uniform. In Thorne-Żytkow objects the composition of material approaching the burning region may differ significantly from that at the same radius returning from the base of the convective envelope. Mixing is therefore treated via an advection scheme.

MONSOON’s mixing scheme comprises upward and downward moving streams. Material also flows laterally to ensure mass conservation and include horizontal diffusion. The advection equation that governs mixing mimics the diffusion equation in the limit of rapid sideways diffusion as meshpoints at the same levels then have the same abundance. In the limit of no sideways mixing the scheme approaches a conveyor belt model. Numerical hydrodynamical simulations of convection suggest that the mixing is characterised by rapid narrow downflows and slower broader upwellings (Herwig, 2001; Stancliffe et al., 2011). MONSOON can also model this facet of mixing in parameterised form.

Numerically, the system is solved using a multi-dimensional Newton-Raphson procedure, in much the same way as the evolution code solves the stellar structure equations. As we are concerned with the abundances of trace elements, a user-defined nuclear network can include all the relevant species. The iterative method of solving the system of equations led to greater stability than was initially present in the evolution code. Thus the introduction of thermohaline mixing was rather straightforward.

The changes to MONSOON have ensured that there are three different means by which we can investigate the effects of thermohaline mixing:

- The process can be calculated *in situ* by a simple formalism based on the location of the inversion in μ gradient.
- The process can be calculated *in situ* with the formalism suggested by EDL08 (Equation 2.113).
- MONSTAR can calculate the mixing boundaries and a diffusion coefficient based on the UKRT formalism. A mixing velocity and mixing length is then fed to MONSOON which calculates its own mixing and burning.

The third method, requires a form of calibration. Recall that in MONSTAR, the v and l in convective regions can be determined from MLT. These are written out to MONSOON but combined to form a diffusion coefficient for MONSTAR’s diffusive mixing algorithm. In regions unstable to thermohaline mixing, MONSTAR determines a diffusion coefficient independent of a mixing length. We have seen how the mixing efficiency is parametrised in terms of a dimensionless aspect ratio.

Therefore have an infinite number of combinations of v and l for any diffusion coefficient. When writing out a v and l for MONSOON in thermohaline regions we assume $l \approx \alpha_{MLT} \times H_P$. With the addition of Li to MONSTAR's network we have two fragile species to which we can calibrate the mixing to (the other being ^3He). Multiplying the mixing velocities by ≈ 1.5 reproduces their abundances in the diffusive approximation. Whether the diffusive approximation to the mixing is the correct paradigm is another matter. If we consider extra mixing independent of any mechanism, but rather in terms of a mixing speed and mixing depth, a diffusive formalism may not be adequate to explain the observed abundances. Nuclei such as Li, which is dependent on efficient transport of material, may hold the key to such questions. A detailed comparison of each code's mixing algorithm is currently underway and will serve as a focus of future work.

Part III

Application to Globular
Clusters

Monash University

Declaration for Thesis Chapter 5

Declaration by Candidate

In the case of Chapter 5, a significant part of this work was published as:

Angelou, G. C., Church, R. P., Stancliffe, R. J., Lattanzio, J. C., and Smith, G. H. (2011). Thermohaline Mixing and its Role in the Evolution of Carbon and Nitrogen Abundances in Globular Cluster Red Giants: The Test Case of Messier 3. *The Astrophysical Journal*, 728:79.

The nature and extent of my contribution to the work was the following:

Nature of contribution	Extent of contribution (%)
Primary research and paper writing	80%

The following co-authors contributed to the work, none of whom are students at Monash University.

Name	Nature of contribution
Prof. John Lattanzio	Consultation and revision
Dr. Ross Church	Consultation and revision
Dr. Richard Stancliffe	Consultation and revision
Prof. Graeme Smith	Consultation and revision

The undersigned hereby certify that the above declaration correctly reflects the nature and extent of the candidates and co-authors contributions to this work

Candidate's  **Signature** _____ **Date** 28-Aug-2014

Supervisor's  **Signature** _____ **Date** 28-Aug-2014

Chapter 5

Calibrating Thermohaline Mixing in the Archetypal Globular Cluster, NGC 5272 (M3)

Nothing in life is to be feared, it is only to be understood. Now is the time to understand more so we fear less.

- Marie Currie

Scientific work must not be considered from the point of view of the direct usefulness of it. It must be done for itself, for the beauty of science, and then there is always the chance that a scientific discovery may become like the radium, a benefit.

- Marie Currie

5.1 Introduction

In Chapter 1 it was established that standard stellar theory fails to reproduce the surface composition of low-mass RGB stars. The discrepancy between theory and observation can be resolved if mixing in stellar interiors extends beyond the stable boundary as defined by the Schwarzschild or Ledoux criterion. Surface abundances suggest that the envelope must undergo CN cycling along the upper RGB. As the conditions at the base of the convective envelope are not sufficient to process the nuclei to the levels required, material must traverse across the radiative zone into

regions that approach the hydrogen burning shell. This extra mixing is expected to occur in all low-mass giants irrespective of stellar environment, however it is through observations of GCs that the corresponding mixing event has been tied to the hydrogen burning shell erasing the composition discontinuity left behind by FDU.

In this study we utilise GCs (for the reasons discussed previously) to test whether thermohaline mixing can explain the extra mixing required in models of low-mass stars. We outlined the care that must be taken when comparing stellar models to observations of stars in GCs. Although the CMD of a GC looks like an isochrone, these systems are not simple stellar populations; they are in fact comprised of multiple generations. The presence of multiple populations give rise to distinct abundance patterns which are not observed in the field. In GCs, the so called light-element anticorrelations (C with N, Na with O and Mg with Al) are not only found in the well-studied bright giants but also below the subgiant branch. The fact that these abundance patterns are detected above and below the sub giant branch implies that a previous generation of stars have activated CNO, NeNa, and MgAl cycles in their interiors in order to deplete O and Mg and enhance Na and Al, respectively. Furthermore, some dilution between the pristine material from which the first generation formed, and their ejecta is required to match the observed abundance patterns in the second generation stars. Primordial and *in situ* patterns must be separated when modelling these systems.

It was also during Chapter 1 that we outlined the evolution of low-mass stars. Rather than rely on the solar model as the preferred benchmark, we elected to describe the structure and evolution of star with mass $M = 0.8 M_{\odot}$ and metallicity, $Z = 0.0005$. The mass and composition of the star in our example is representative of those stars found in the GC M3. It is this GC that we have chosen to calibrate the 1D diffusive formalism of thermohaline mixing. The historical and theoretical developments of the instability (and its relation to similar DD instabilities) were described in Chapter 2. In Part II of this dissertation we detailed the changes required to our stellar physics codes to accurately include thermohaline mixing in the calculations. In the following sections we quantitatively test its application as an RGB extra-mixing mechanism. Thermohaline mixing is calibrated by matching [C/Fe] abundances as a function of luminosity in M3. Once a formalism and efficiency determined, the parameterisation will be applied to model multiple systems including low-metallicity GCs. In Part IV we turn our attention to observations of lithium rather than [C/Fe]. In Chapter 8 we present new lithium observations in the GCs NGC 5904 (M5) and NGC 6218 (M12). In Chapter 9 our high resolution lithium data is used to effectively probe both FDU and extra mixing, providing a robust test of stellar models.

Messier 3 was chosen as a test case for thermohaline mixing in Population II stars because in many respects it can be considered a typical globular cluster. A metallicity of $[\text{Fe}/\text{H}] = -1.4$ (Snedden et al., 2004; Cohen and Meléndez, 2005) means that it falls near the mode¹ in the metallicity distribution of halo globular

¹the metallicity distribution is of course continuous, however there are many clusters with $[\text{Fe}/\text{H}] \approx -1.5$

clusters. Among clusters of similar metallicity, the horizontal branch morphology of M3 has stars on both the red and blue sides of the RR Lyrae gap (Sandage, 1970; Buonanno et al., 1994), and the colour distribution is intermediate between extremes such as those of M13 and NGC 6752 (whose HBs have more extended blue tails; Newell 1970; Lee and Cannon 1980) and NGC 7006 (whose HB stars are more concentrated to the red side of the RR Lyrae gap; Sandage and Wildey 1967). Red giants with enhanced $\lambda 3883$ CN bands in their spectra were discovered in M3 by Suntzeff (1981), and further studied by Norris and Smith (1984). The CN distribution contains both CN-strong and CN-weak giants (i.e., high and low nitrogen abundance giants) as is typical of other clusters of similar metallicity (Norris and Smith, 1984). The behaviour of the CN bands at a given luminosity on the RGB appears to anticorrelate with carbon and oxygen abundance (Suntzeff, 1981; Smith et al., 1996). When giants of different luminosity are compared a significant trend becomes apparent in the carbon abundance. Among red giants with absolute magnitudes brighter than the horizontal branch $[C/Fe]$ declines with increasing luminosity (Suntzeff, 1981, 1989; Smith, 2002) in a manner that is typical of other globular clusters and halo field giants (Smith and Martell, 2003). It is this behaviour of carbon in particular that is of great use in constraining models of thermohaline mixing. The carbon isotope ratio $^{12}C/^{13}C$ has a low value of $\approx 4-6$ among the bright giants (Pilachowski et al., 2003; Pavlenko et al., 2003), although the number of stars for which this has been measured is small. In addition, M3 displays O, Na, and Al abundance inhomogeneities of the type that are commonplace within globular clusters of similar metallicity (Carretta et al., 2005). The cluster has a population of stars that are enhanced in Na and Al but depleted in oxygen (Kraft et al., 1992; Cavallo and Nagar, 2000; Sneden et al., 2004; Cohen and Meléndez, 2005; Johnson et al., 2005), but without the extremes in O abundance depletion and Na enhancement that are found in the oft-compared cluster M13 (Sneden et al., 2004). A substantial component of the O-Na-Al variations in M3 are arguably the products of early cluster self-enrichment, and thermohaline mixing on the first ascent giant branch is not expected to have played a role in their production. Work by CZ07a and Charbonnel and Lagarde (2010) also show that these elements are not affected by thermohaline mixing.

By matching our models to the carbon depletion (as a function of absolute magnitude) observed in this cluster we can attempt to constrain both the formula for the thermohaline diffusion coefficient and the values of any parameters contained therein. As carbon and nitrogen are intrinsically linked in the CN burning cycle we include observations of nitrogen as an additional tracer. Furthermore, we identify when extra mixing begins in the models and compare this to the observed luminosity function bump (LF bump) in the cluster.

5.2 The Formula for the Diffusion Coefficient

It is common in stellar interior calculations to use a diffusion equation to simulate mixing. It is important to remember that many mixing processes, such as convective mixing, are *advective* in nature, not *diffusive*. In the former, a property

is distributed as a result of bulk flows within the fluid. The latter follows from Fick's first law, which postulates that a flux exists between regions of high and low concentration of the quantity of interest. The equation governing this is

$$\vec{j} = -D\vec{\nabla}n \quad (5.1)$$

where n is the density of the quantity and \vec{j} is its flux. The parameter D is the "diffusion coefficient" of the "diffusivity". For particles with a mean-free-path l and typical speed v then

$$D = \frac{1}{3}vl. \quad (5.2)$$

As no theory for time dependent mixing exists, it is common to use a diffusion equation to simulate mixing in stellar interiors. Historically, this is also how thermohaline mixing has been calculated. A diffusion equation is solved for each species in the star, and thus determines the radial composition variation.

EDL08 used the following formula, based on estimates of the mixing velocity and the convective formalism in their evolution code:

$$D = \begin{cases} \frac{F_{\text{inv}}r^2}{t_{\text{nuclear}}}(\mu - \mu_{\text{min}}) & \text{if } (k \geq k_{\text{min}}) \\ 0 & \text{if } (k \leq k_{\text{min}}), \end{cases} \quad (5.3)$$

where k is the mesh point number, counted outwards from the centre of the model, k_{min} is the value of k for which μ takes its minimum value of μ_{min} , r is the radial coordinate, F_{inv} is a constant which is selected to obtain the desired mixing efficiency and t_{nuclear} is an estimate of the nuclear evolution timescale (see EDL08). This is an extension of the convective formula used in the EDL08 calculations, with the addition of a $\mu - \mu_{\text{min}}$ term to reflect the driving by the μ inversion. Thus this formula is not a local one as the value of D at a point in the star depends on the value of μ_{min} at some other location in the star. Nevertheless, it is a phenomenological form that recognises the role of the μ inversion in driving the mixing.

This formulation ensured the correct region was mixed but note that the mixing speed is formally zero at the position where μ has its minimum even though the mixing should presumably be the most efficient at this point. EDL08 give upper and lower estimates for the mixing velocity and find that they can change their free parameter F_{inv} , and consequently alter the speed by three orders of magnitude whilst still producing the observed levels of $^{12}\text{C}/^{13}\text{C}$ and leading to ^3He depletion.

CZ07a adopt the UKRT formulation for thermohaline mixing, which results from a linear analysis of the problem. They cast it in the following way,

$$D_t = C_t K \left(\frac{\varphi}{\delta} \right) \frac{-\nabla\mu}{(\nabla_{\text{ad}} - \nabla)} \quad \text{for } \nabla\mu < 0, \quad (5.4)$$

where K is the thermal diffusivity and C_t is a dimensionless free parameter. In fact C_t is related to the aspect ratio, α , of the fingers in the following manner:

$$C_t = \frac{8}{3}\pi^2\alpha^2 \quad (5.5)$$

The appropriate value to use for this parameter remains uncertain. To understand thermohaline mixing fully clearly requires a hydrodynamic theory that will determine the diffusion coefficient and any associated parameters. In lieu of such a theory, we can compare with observations and see what form of D and values of constants are needed to match the real world. This is the approach we have adopted.

Alternatively, one could try to determine C_t or α by comparison to laboratory experiments and the oceanic case, which has been well studied. Stommel and Faller carried out experiments of fluids in laboratory conditions. This work, published in Stern (1960), saw the development of long salt fingers with lengths that were larger than their diameters ($\alpha \approx 5$). This led Ulrich (1972) to determine that $C_t \approx 658$ which was the basis of the choice by CZ07a to use $C_t = 1000$. The huge differences between incompressible salty water and the self-gravitating plasma we are considering make direct comparisons very difficult, however (see Denissenkov 2010; Denissenkov and Merryfield 2011). In contrast to the oceanic case, Kippenhahn envisaged the classical picture where mixing is due to blobs. If Kippenhahn's expression is cast into the same form as Equation 5.4 then $C_t \approx 12$. This value seems to agree with the 2D- and 3D-hydrodynamical models of Denissenkov (2010) and Denissenkov and Merryfield (2011) as well as 1D models of Cantiello and Langer (2010), but is inconsistent with the value preferred by CZ07a and the present work (see below).

5.3 Models and Results

We use MONSTAR (The Monash version of the Mt.Stromlo evolution code; see Campbell and Lattanzio 2008 and Chapter 3) to produce stellar models for M3. The stars are evolved from the zero-age main-sequence until the core flash. They are of mass $M = 0.8M_\odot$, metallicity $Z = 0.0005$ and have a solar-scaled CNO abundance, as a first approximation. Population II subdwarfs in the globular cluster metallicity range tend to have $[C/Fe] \sim 0$ (e.g. Laird 1985). In M13 the work of Briley et al. (2004) shows an upper envelope to the data that approaches $[C/Fe] \sim 0$ to -0.2 near the main sequence.

Our mixing length parameter, α , is set to 1.75 and we run without any overshoot. Mixing is calculated using a diffusion equation, and we investigate different formulae for the diffusion co-efficient used for thermohaline mixing. These parameters approximate the stars in M3 quite well: M3 has an age estimated by various authors to be between 11.3 to 14.2 Gyr (Chaboyer et al., 1992; Jimenez et al., 1996; VandenBerg, 2000; Salaris and Weiss, 2002; Alves et al., 2004) and $[Fe/H] = -1.5$. In Figure 5.1, using the UKRT formulation for thermohaline mixing and $C_t = 1000$, we plot the variation of the surface $[C/Fe]$ as well as the $^{12}C/^{13}C$ ratio against M_V . A distance modulus of $V - M_V = 15.05$ was adopted as per Lee (1999) and Smith (2002) whilst theoretical model atmospheres from Castelli et al. (1997, ATLAS9) provide tables of bolometric corrections for the stellar models.

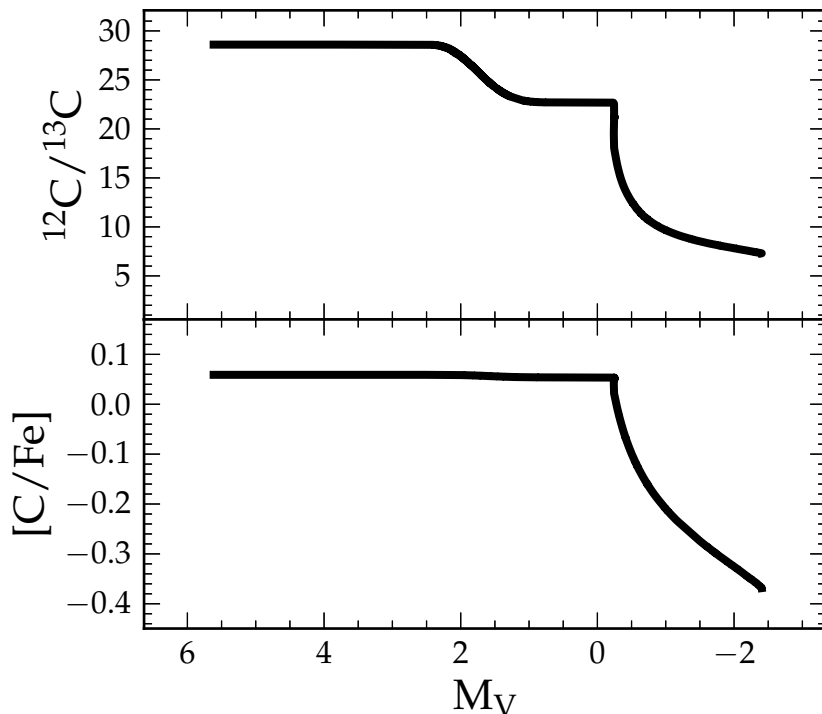


Figure 5.1: Top panel: $^{12}\text{C}/^{13}\text{C}$ as a function of magnitude. Bottom panel: $[\text{C}/\text{Fe}]$ as a function of magnitude. In this figure we compare the evolution of $[\text{C}/\text{Fe}]$ to that of $^{12}\text{C}/^{13}\text{C}$. The UKRT thermohaline mixing formula with $C_t=1000$ has been used in this model. It can be seen that the isotopic ratio reaches equilibrium soon after the onset of extra mixing, whereas $[\text{C}/\text{Fe}]$ depletes along the entire RGB.

In Figure 5.1 it can clearly be seen that the $^{12}\text{C}/^{13}\text{C}$ ratio drops below 10 very quickly, finally reaching as low as 6.5. This is in good agreement with the observations of 4-6 by Pilachowski et al. (2003) and Pavlenko et al. (2003). The gradual depletion of carbon throughout the entire RGB on the other hand provides a more sensitive constraint on the mixing.

Figure 5.2 compares the results with the EDL08 and UKRT formulae for the diffusion coefficient. In this figure open circles denote CN-weak stars, filled circles denote CN-strong stars and crosses represent CN-intermediate stars all from M3². In this figure, as well as the preceding figures, the errors in magnitude are smaller than the symbols used. The random errors in the abundance measurements can

²We note that there appears to be a lack of CN-strong stars on the lower RGB. This is an artifact of the original Suntzeff (1981) study in which the lower luminosity stars that were observed happened to be CN-weak. Norris and Smith (1984) showed that CN-strong giants do exist in M3 at luminosities corresponding to the faint limit of the Suntzeff (1981) survey. However, their later study concentrated on the $\lambda 3883$ CN band strength and did not measure the $[\text{C}/\text{Fe}]$ or $[\text{N}/\text{Fe}]$ abundances. Consequently, absence of CN-strong stars at the faintest limits of the abundance plots herein is a consequence of observational effects.

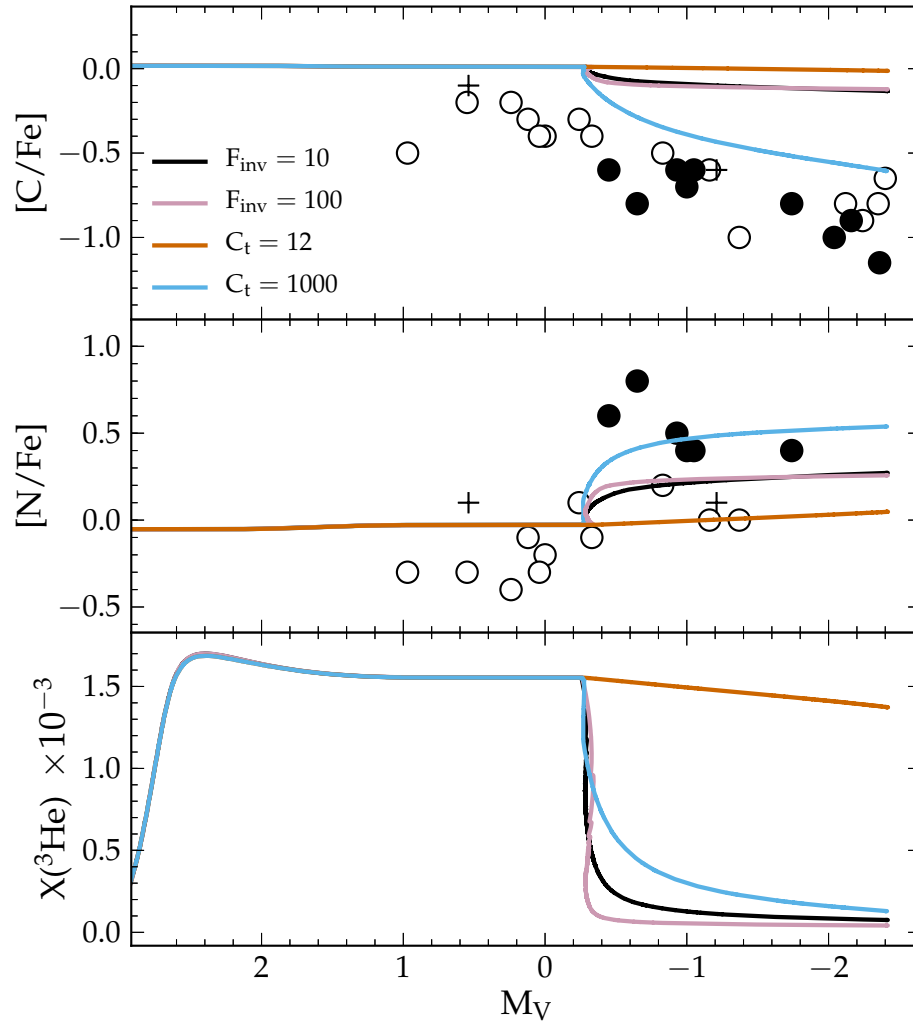


Figure 5.2: Abundances as a function of visual magnitude for giants in the GC M3. In this figure we compare the UKRT prescription for the diffusion coefficient to that of EDL. Open circles denote CN-weak stars in M3, filled circles denote CN-strong stars and crosses represent stars of intermediate CN strength, with all data taken from Smith (2002). The two UKRT models correspond to the vermilion line for $C_t = 12$ and the blue line for $C_t = 1000$. The two EDL models are denoted by the lavender curve for $F_{\text{inv}} = 100$ and the black curve for $F_{\text{inv}} = 10$, these sit nearly on top of each other on this scale. The models are all of mass $M = 0.8 M_{\odot}$ and $Z = 5 \times 10^{-4}$ with solar scaled CNO abundances. The errors in magnitude are smaller than the symbols used. The maximum error in $[C/Fe]$ and $[N/Fe]$ is ± 0.3 dex.

be up to ± 0.3 dex according to Suntzeff (1981), although this does not take into account potential systematic errors due to limitations in the stellar atmospheres code used in the abundance derivations. We have run four models to compare to the observations, two with thermohaline mixing that use the UKRT formula for the diffusion coefficient and two models that use the EDL08 formula. The vermilion line and the blue line are variations of the UKRT prescription, the vermilion curve uses $C_t = 12$ ($\alpha \approx 1$) as suggested by Kippenhahn et al. (1980) while the model represented by the blue curve uses $C_t = 1000$ ($\alpha \approx 6$), a geometry more akin to CZ07a. The lavender and black lines (which nearly sit on top of each other) are EDL08 models where $F_{inv} = 100$ corresponds to the lavender curve and $F_{inv} = 10$ corresponds to the black curve line. The two choices of F_{inv} lie within the three orders of magnitude that lead to the required level of $^{12}\text{C}/^{13}\text{C}$ depletion as discussed in EDL08.

The two EDL08 models destroy the available ^3He very quickly and are unable to cycle much CN processed material to the envelope. As previously mentioned, in the EDL08 formulation of the diffusion coefficient the mixing is dependent on the difference in μ , i.e. $(\mu - \mu_{min})$. Material near the envelope is cycled down faster and the mixing becomes less efficient closer to the location where μ has its minimum. Material is not replenished at the same rate it would be with a local condition on the μ gradient as seen with the UKRT prescription. In other words, ^3He is rapidly transported to high temperatures where it traverses slowly through the burning region. Its abundance is therefore quickly depleted.

The manner in which the material is mixed has consequences for the depth at which the minimum value of μ occurs. We can see in Figure 5.3 that the location at which μ has its minimum occurs further out in the EDL08 scheme. The steep temperature gradient ensures the fragile ^3He is easily destroyed while the carbon-rich material is not exposed to temperatures where it can burn significantly. CN cycling is therefore reduced whilst the driving fuel, ^3He , is easily processed irrespective of one’s choice of F_{inv} . The bottom panel in Figure 5.3 clearly demonstrates the dependence of the location of the minimum value of μ on the mixing scheme. The four models in Figure 5.2 are plotted with the same colours in Figure 5.3. We have plotted the velocities, carbon, nitrogen and molecular weight profiles at a hydrogen-exhausted core mass of $M_c = 0.32970 M_\odot$ corresponding to $M_V = -0.34$. The bottom panel demonstrates the depth to which the models mix. This highlights the fact that the two UKRT models have their μ minimum occurring closer to the hydrogen shell and mix deeper than the EDL08 models at the same core mass. As expected the two EDL08 abundance profiles show little CN processing. As shown by EDL08 this is sufficient to produce the observed $^{12}\text{C}/^{13}\text{C}$ values but as Figure 5.3 shows it is not enough to reproduce the $[\text{C}/\text{Fe}]$ or $[\text{N}/\text{Fe}]$ variations. Note that to calculate a velocity from Equation 5.2 we require a value for l . We have used $l = 1.75 \times H_p$ where H_p is the pressure scale height. This may not be an accurate estimate but it is expected to give us an indicative velocity.

The surface abundances are determined by both the depth to which the material is mixed as well as the speed of mixing. The depth of mixing in a “steady state” is determined by the location of the μ minimum which is in turn dependent on the mixing speed, so that the two are not independent. Consider the case

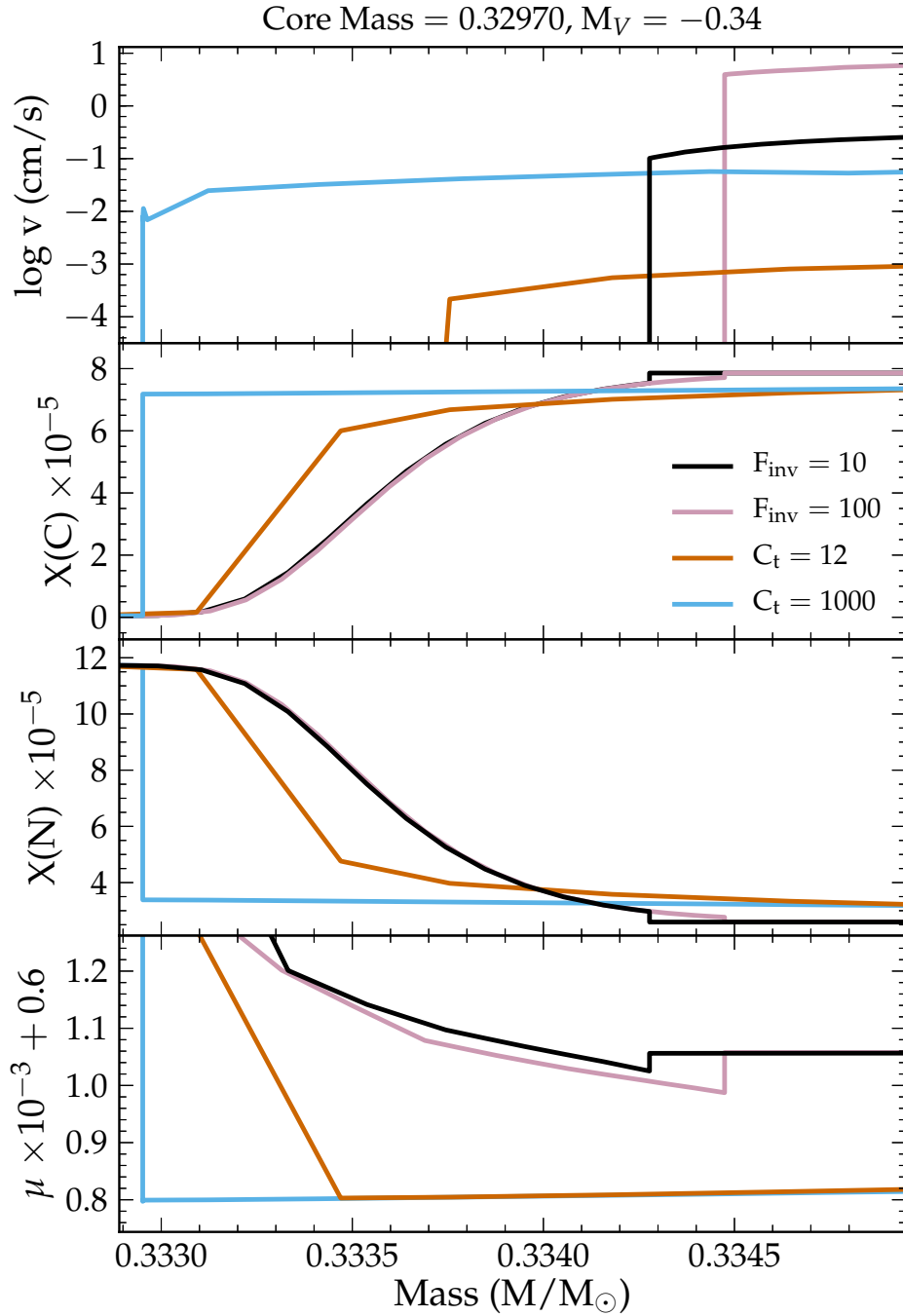


Figure 5.3: Various profiles for the same models as Figure 5.2. The same symbols are used. The profiles are all taken at the same stage in evolution, that is when the hydrogen-exhausted core mass $M_c = 0.32970 M_\odot$ and at $M_V = -0.34$. Top Panel: the mixing velocity in the region above the shell. Second Panel: the carbon abundance in the region above the shell. Third Panel: the nitrogen abundance in the region above the shell. Bottom Panel: variations at μ . Note that at this resolution the μ inversion is not clearly identifiable in the $C_t = 12$ model.

of very fast mixing, such as convection. The abundance would be homogeneous from the deepest point of mixing to the surface. Clearly the surface abundance is controlled by the burning conditions at the bottom of the mixed region - a case we call “burning limited.” Now consider the case of very slow mixing. The abundance profile is marginally altered from the radiative case. Although the material is mixed to the surface it proceeds so slowly that the advance of the burning region is almost independent of the (slow) mixing - just as it would be in the limiting case of no mixing (i.e. a radiative zone). Hence in the slow mixing case the surface abundances are “transport limited.” In Figure 5.2 the bottom panel suggests that the UKRT $C_t = 12$ model is transport limited and this, not the depth to which material is mixed, is responsible for the lack of processing. The bottom panel in Figure 5.3 shows that the EDL08 models do not mix as deep as the UKRT models. Yet the EDL08 models destroy essentially all of the ${}^3\text{He}$ (see Figure 5.2) while this is not true for the UKRT formulation. ${}^3\text{He}$ and consequently carbon in the $C_t = 12$ model are not destroyed because not enough material is physically transported through the radiative region and processed before the end of the RGB. In Figure 5.4 we see that there is almost a difference of two orders of magnitude between the mixing speeds in the two UKRT models. In addition at this stage of the evolution the $C_t = 12$ model does not connect the region of the μ -inversion (where the burning occurs) with the envelope to cycle in fresh fuel (it does so further up the RGB): this further hinders any processing.

It appears that the requirement for significant carbon depletion is two fold: the position of the minimum in μ must occur at a reasonably high temperature and we need a sufficiently fast mixing velocity. As a result of our comparison with M3 we prefer the UKRT formalism over that used by EDL08.

5.4 Modeling the Globular Cluster M3

As previously mentioned Kippenhahn et al. (1980), Ulrich (1972) and CZ07a differ in their choice of α , the aspect ratio of the fingers, by a factor of five and this translates to a difference of two orders of magnitude in C_t .

Having selected our preferred formalism we can now use observations to constrain the diffusion coefficient. In Figure 5.5a we illustrate the effect of standard evolution on the carbon and nitrogen abundances. In all the Figure 5.5 panels, open circles denote CN-weak stars, filled circles denote CN-strong stars and crosses represent CN-intermediate stars as before. The uncertainty in the data is as specified in Section 5. Figures 5.5b, 5.5c and 5.5d include thermohaline mixing with the UKRT prescription. In each panel we provide four models, these represent different values of C_t . We include: $C_t = 12$ as per Kippenhahn et al. (1980) (lavender lines, $\alpha \approx 1$), $C_t = 1000$ as per CZ07a (black lines, $\alpha \approx 6$) and two intermediate values, $C_t = 120$ (vermillion lines, $\alpha \approx 2$) and $C_t = 600$ (blue lines, comparable to Ulrich 1972 $C_t = 658$, $\alpha \approx 5$).

The canonical evolution (grey line, i.e., $C_t = 0$) in Figure 5.5a shows very little carbon depletion following FDU. This is contrary to the observations for the upper part of the RGB. We include this panel to highlight to the reader

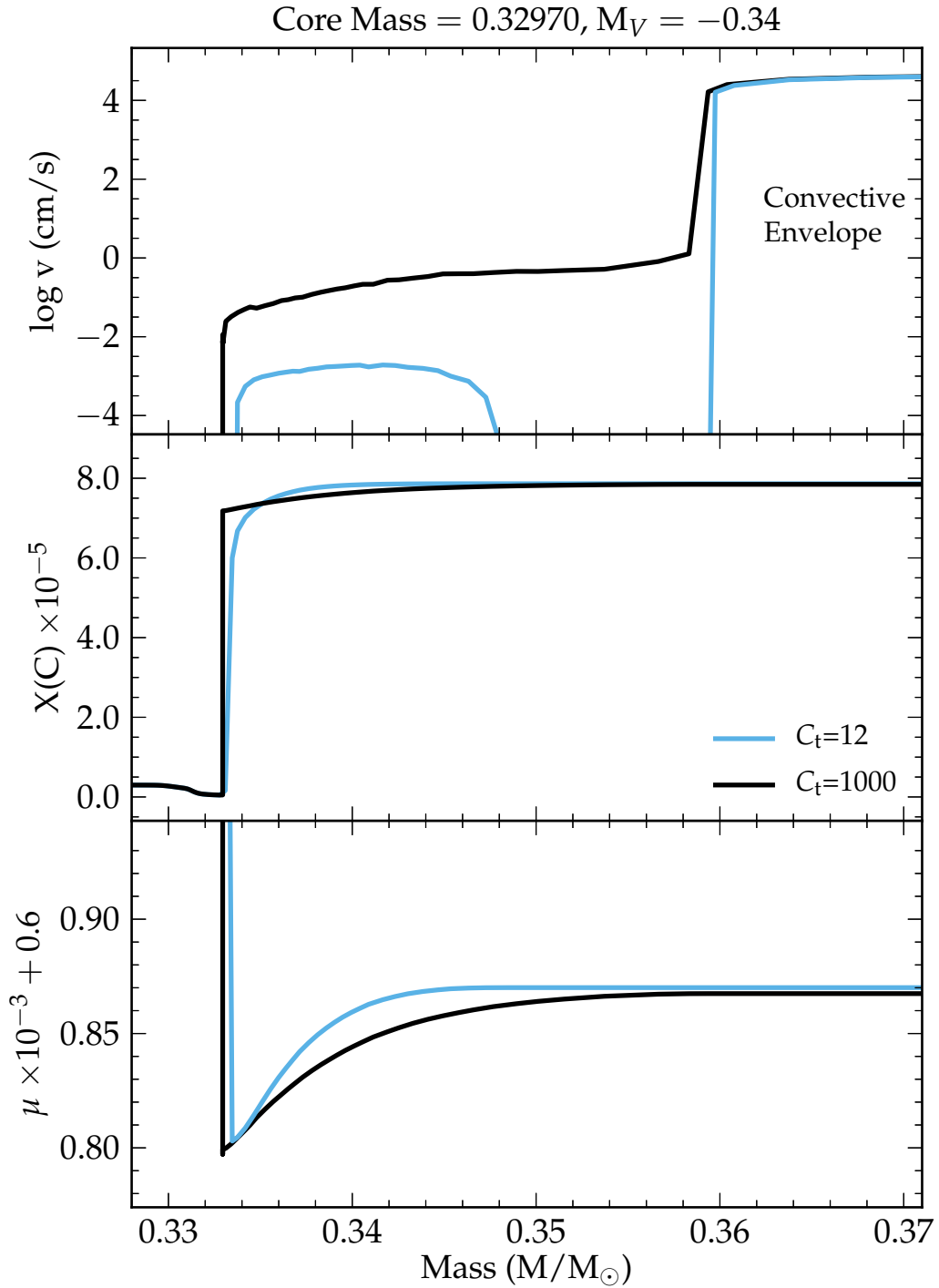


Figure 5.4: Velocity, $X(C)$ and μ profiles for the two UKRT models. This is an expanded plot of the first panel in Figure 5.3 so is once again taken at a hydrogen-exhausted core mass of $M_c = 0.32970 M_{\odot}$ and $M_V = -0.34$. The $C_t = 12$ model (blue line) mixes two orders of magnitude more slowly than the $C_t = 1000$ model (black line). It also fails to transport material to and from the envelope at this stage. It does connect with the envelope before the end of the RGB.

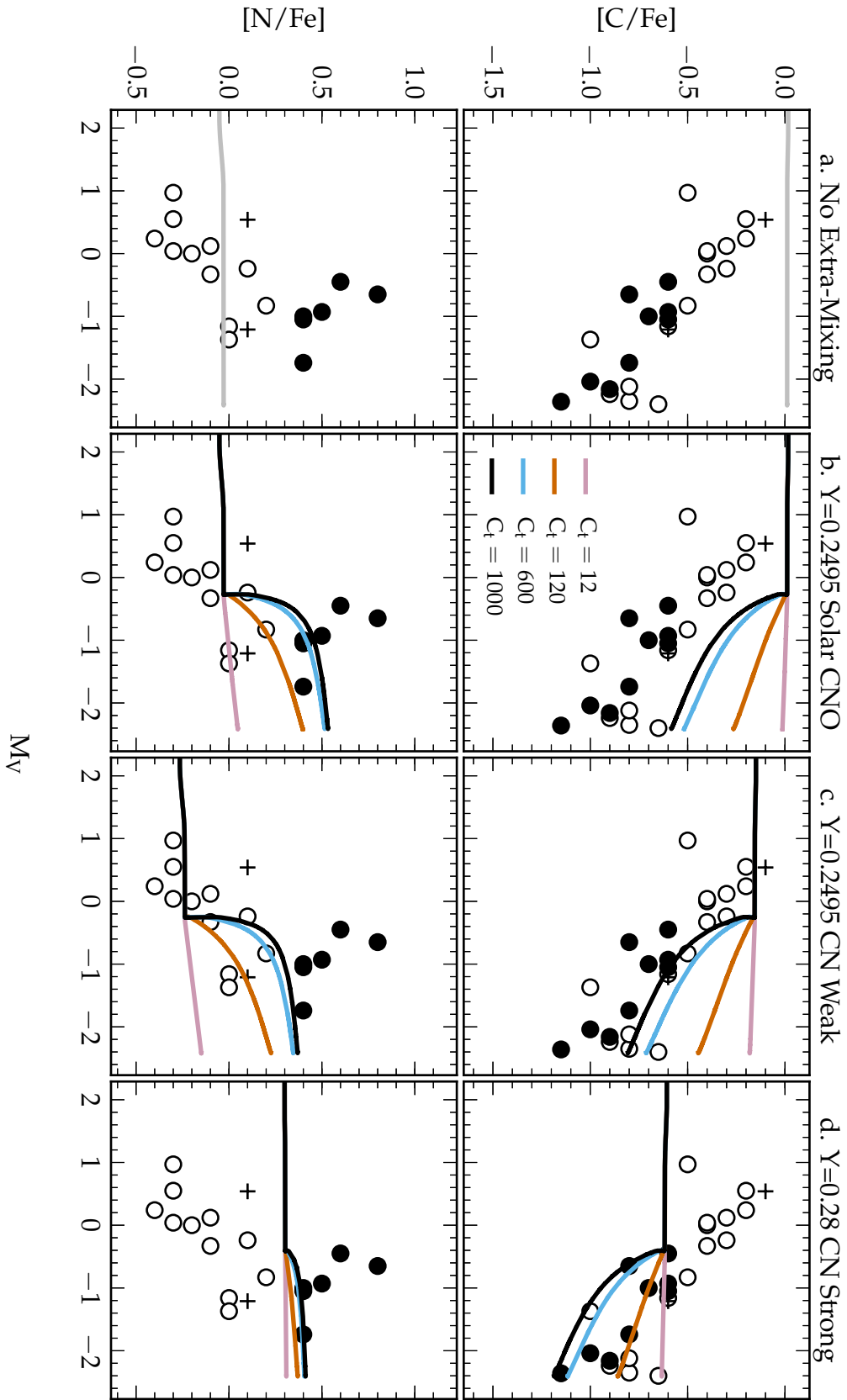


Figure 5.5: From previous page. Carbon and nitrogen abundances as a function of absolute magnitude in M3. Here we compare our models to the Smith (2002) compilation of M3 observations. Open circles denote CN-weak stars, filled circles CN-strong stars, whilst the crosses represent stars of intermediate CN strength. The errors in magnitude are smaller than the symbols used. The maximum error in $[C/Fe]$ and $[N/Fe]$ is ± 0.3 dex. Where extra mixing is included in our models lavender lines correspond to $C_t = 12$ ($\alpha \approx 1$), vermilion lines to $C_t = 120$ ($\alpha \approx 2$), blue lines to $C_t = 600$ ($\alpha \approx 5$) and black lines to $C_t = 1000$ ($\alpha \approx 2$). Figure 5.5c includes models with the following initial CNO abundances $X(C) = 5.45 \times 10^{-5}$, $X(N) = 1.5 \times 10^{-5}$ and $X(O) = 2.86 \times 10^{-4}$. In Figure 5.5d the initial CNO abundances are $X(C) = 1.9 \times 10^{-5}$, $X(N) = 5.5 \times 10^{-5}$ and $X(O) = 2.6 \times 10^{-4}$.

the need for extra mixing. In Figure 5.5b we have assumed a scaled solar CNO abundance and varied the free parameter as described above. It is unlikely that M3 possesses a scaled solar abundance. Russell and Dopita (1992) have already shown that Large Magellanic Cloud abundances are not scaled Solar and we would not expect the environment during globular cluster formation to resemble the solar neighbourhood.

In Figure 5.5c we have altered the initial C/N/O ratios whilst keeping the metallicity and total CNO content constant. As the carbon abundance does not change a great deal before the onset of extra mixing we have assumed the most carbon-rich stars are representative of the pre-FDU abundance, similarly for the most nitrogen-poor stars. To match the constraints, the following initial CNO abundances were assumed $X(C) = 5.45 \times 10^{-5}$, $X(N) = 1.5 \times 10^{-5}$ and $X(O) = 2.86 \times 10^{-4}$. We altered the carbon and nitrogen so that we arrived at our desired post-FDU value and adjusted the oxygen abundance in order to keep the total CNO constant³. We have decreased the carbon by a factor of 1.47 and the nitrogen by a factor of 1.63 (in relation to solar). These values could easily be fine-tuned to better fit the data but it is the proof of concept we are concerned with. The two slow mixing cases are unable to account for the depletion in carbon. Both $C_t = 600$ and $C_t = 1000$ are a good fit to the carbon and the nitrogen. It does appear that the mixing should begin at a slightly lower luminosity, however Sweigart (1978) demonstrated that lowering the ${}^4\text{He}$ abundance will cause the extra mixing to begin earlier because the shell reaches the discontinuity sooner. We find that our models provide a fit to the upper envelope of the run of $[C/Fe]$ vs M_V in Figure 5.5c but can only fit the nitrogen for the CN-weak stars. This argues that much of the spread in $[N/Fe]$ in the lower panels of Figure 4 is dominated by a variation that was present among the cluster stars before they commenced red giant branch evolution. The fact that none of the models in the lower panels of Figure 4 can reproduce the observed spread in $[N/Fe]$ is suggestive of the CN inhomogeneity in M3 having a predominantly primordial origin. This inference is consistent with the discovery in a number of clusters, including M3 (Norris and Smith, 1984), that

³Note that the effect of FDU is very small so the pre-FDU and post-FDU values are nearly the same.

N abundance variations (or equivalently CN band strength variations) are found both at and below the magnitude of the bump in the RGB luminosity function (e.g., see Suntzeff and Smith 1991; Briley et al. 2004; Carretta et al. 2005; for the clusters NGC 6752 and M13 which have similar $[\text{Fe}/\text{H}]$ to M3). This argues strongly for the spread being present in the stars at their birth.

In Figure 5.5d we have assumed the CN-strong stars are a separate population with their own CNO abundance. Moreover we have assumed there is a CN-[C/Fe] anticorrelation in which the CN-strong stars are initially 0.4 dex depleted in carbon relative to the CN-weak stars (Smith, 2002, and references therein). The CN-strong stars show the results of hot hydrogen burning in the gas from which they formed, including CN and ON cycling. We have therefore changed the initial helium abundance from $Y=0.2495$ to $Y=0.28$ as well as the CNO values⁴. Here we set $X(\text{C})=1.9 \times 10^{-5}$, $X(\text{N})=5.5 \times 10^{-5}$ and $X(\text{O})=2.6 \times 10^{-4}$. We find in this case the slower mixing is a good fit for the carbon abundance whilst the faster mixing is able to account for the more extreme observations of carbon depletion. These models are unable to match the more extreme nitrogen enhancements in the CN strong stars. The $[\text{N}/\text{Fe}]$ is initially so high even on the main sequence that any enhancement due to extra mixing only slightly raises the $[\text{N}/\text{Fe}]$. We conclude that much of the nitrogen spread in the CN strong stars is due to primordial variations as a result of hot hydrogen burning (in an early generation of stars that instigated cluster enrichment) rather than thermohaline mixing in the present-day giants.

Our findings are consistent with those of CZ07a in that $C_t = 1000$ is our preferred value of the free parameter in the UKRT thermohaline mixing prescription. Their choice based on the value advocated by Ulrich (1972) and experiments of oceanic conditions by Krishnamurti (2003). In Figure 5.6 we investigate the effect of increasing C_t beyond 1000. The blue line corresponds to the EDL08 prescription with $F_{inv} = 100$, the black line corresponds to $C_t = 1000$, the vermilion line to $C_t = 3000$ ($\alpha \approx 10$) and the lavender line $C_t = 12000$ ($\alpha \approx 20$). Once again we use the same symbols for the M3 data as in previous plots. The initial abundances are solar scaled CNO, however it is the shape of the profiles we are interested in here. We include the EDL08 model to compare the similarities in the ${}^3\text{He}$ depletion as a function of magnitude. The fact that the UKRT ${}^3\text{He}$ profiles begin to approach that of the faster mixing EDL08 model once again suggests that depth to which the UKRT models mix is responsible for the carbon depletion. Initially the faster mixing cases are able to deplete the carbon more efficiently than our preferred value of $C_t = 1000$. Although all three values of C_t begin to deplete at different rates they eventually lead to similar levels of CN processing. The similar levels of carbon depletion suggest that a steady state has been reached and for $C_t \geq 1000$ the process is burning limited (for $[\text{C}/\text{Fe}]$ at least).

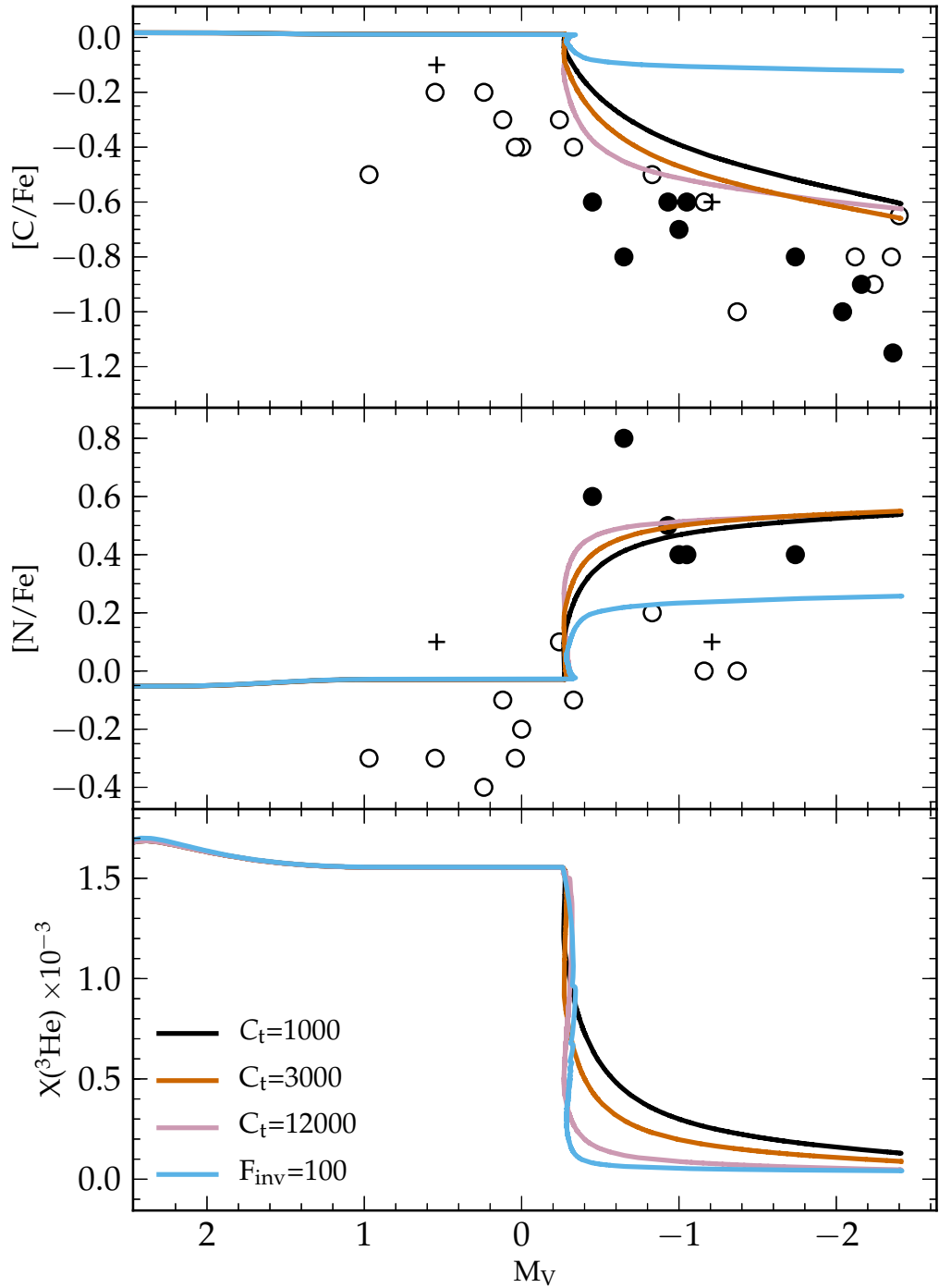


Figure 5.6: Abundances as function of magnitude. We consider values of C_t beyond 1000. M3 data is represented with the same symbols as in the previous figures. The dotted line corresponds to the EDL prescription with $F_{inv} = 100$, the solid line corresponds to $C_t = 1000$, the dashed line to $C_t = 3000$ ($\alpha \approx 10$) and the dash-dotted line to $C_t = 12000$ ($\alpha \approx 20$). There is little difference in the level of carbon depletion once $C_t > 1000$, because the depletion is limited by the burning rate rather than the transport rate.

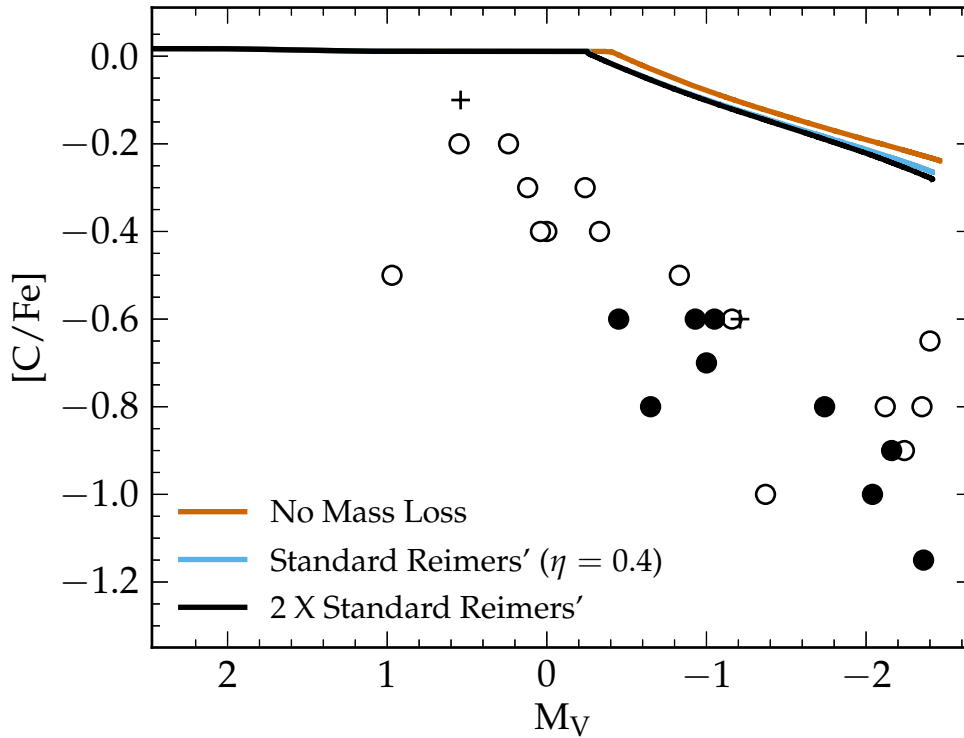


Figure 5.7: Carbon abundance relative to solar as a function of magnitude. Here we plot UKRT $C_t = 120$ models with varying levels of mass loss. Symbols are described in previous figures. The vermilion line corresponds to a model with no mass loss, the blue line to standard Reimers’ mass-loss rate and the black curve twice the mass-loss rate. There is little effect on the carbon depletion.

5.5 Mass Loss

Mass loss could have a significant effect on the level of carbon depletion in the models. If there is less envelope, the amount of carbon that needs to be processed to reduce the $[C/Fe]$ is also less. In Figure 5.7 we investigate the role of mass loss in the UKRT formula for mixing. We provide three models for the $C_t = 120$ case, standard Reimers’ mass loss (blue curve), no mass loss (vermilion curve) and a factor of two increase on the standard mass-loss rate (black curve). The effect of mass loss on the surface composition is greatest towards the tip of the giant branch where the mass-loss rate is highest, but even there the alteration in $[C/Fe]$ is slight compared to a zero mass-loss model. These findings are consistent with EDL08, who also find the effect of mass loss negligible after the onset of thermohaline mixing.

⁴We note that this is consistent with the growing literature on multiple stellar populations in GC and their presumed ^4He content (Piotto, 2009, and references there in).

5.6 The Onset of Mixing and the Location of the LF Bump

Our final observational test concerns the onset of mixing and the observed location of the abundance changes. The hydrogen-burning shell will reach the composition discontinuity independent of any thermohaline mixing, which only begins after this event. Once the mixing starts, the rate is dependent on the parameter C_t and so the surface abundance begins changing at a visual magnitude that depends slightly on C_t . The models for the four different values of C_t in Figure 5.5 commence thermohaline mixing within $\Delta M_V = 0.02$ mag of each other. In Figure 5.8 we have taken Figures 5.5c and 5.5d and marked the position of M3’s LF bump according to (Fusi Pecci et al., 1990, grey dashed line) and the position according to Smith and Martell (2003, dot-dashed grey line). In all four panels we indicate the magnitude of the LF bump according to the CN weak models⁵(the solid vertical line). Fusi Pecci et al. (1990) determine the LF bump of M3 to occur at $M_V = -0.06$, Smith and Martell (2003) at $M_V = 0.45$ whereas our models reach the composition discontinuity at $M_V = -0.26$. In the UKRT formula for the diffusion coefficient, the change in the surface abundances begins almost immediately after the bump. These results differ somewhat from the non-rotating case of Charbonnel and Lagarde (2010) who find there is a delay of ≈ 0.5 magnitudes before the onset of any changes to the surface abundance, albeit for different masses and metallicities to those considered here. The differences between the two quoted values for the LF bump are due to the respective choices of the distance modulus. We find our models are closer to the older results but we refrain from drawing any conclusions. A study that includes lower luminosity giants is required in order for us to make further comparisons to the observations.

In Figure 5.8b we find that increasing the amount of ^4He in the model has delayed the onset of the bump. These results are consistent with Sweigart (1978) who, in addition to this, showed that the size of the discontinuity is also reduced with increasing ^4He abundance. This is owing to the fact that an increase in ^4He translates to less hydrogen and less of a discontinuity. The fact that the hydrogen shell encounters the discontinuity later for models with higher initial ^4He is due to the effect the composition has on the penetration of the convective envelope. A higher hydrogen abundance allows for deeper penetration of the envelope and hence the shell reaches this depth sooner.

5.7 Conclusions

M3 is a well studied system that demonstrates the abundance patterns we commonly associate with globular clusters. Along with many other clusters it displays significant [C/Fe] depletion along the RGB, the implication being that some form of internal, non-canonical mixing must be occurring. Our models with thermohaline mixing show that the carbon and nitrogen observations can be explained if we

⁵Technically, we plot the local luminosity maximum that occurs during this phase; this is $L_{b,\max}$ in the notation of Charbonnel and Lagarde (2010).

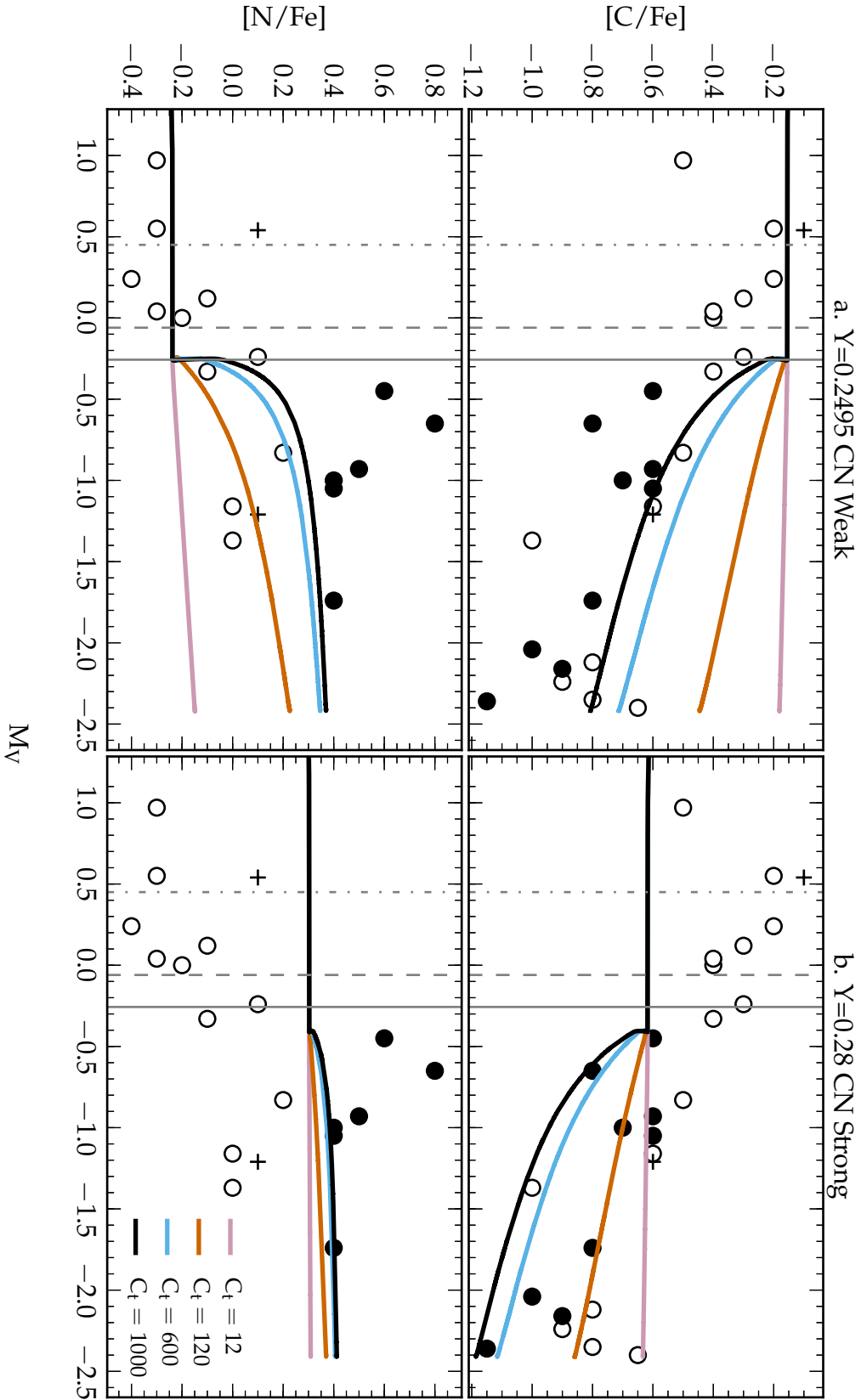


Figure 5.8: Carbon and nitrogen abundances as a function of absolute magnitude in M3. These are the same panels as Figures 5.5c and 5.5d with the location where the local luminosity maximum occurs when the hydrogen shell meets the composition discontinuity (solid vertical line), the location of the LF bump for M3 from Fusi Pecci et al. (1990) (dashed vertical line) and location of the LF bump for M3 from Smith and Martell (2003) (dot-dashed vertical line).

adopt the hybrid theory outlined in Smith (2002), where stars in the cluster are undergoing extra mixing as they ascend the RGB and the presence of primordial abundance inhomogeneities due to ON cycling are needed to explain the initial carbon and nitrogen abundances. We have used observations of M3 to investigate our theoretical understanding of thermohaline mixing. Our findings are summarised below:

1. The variation of $[\text{C}/\text{Fe}]$ with magnitude provides a much more stringent test of any proposed extra-mixing mechanism than simply matching the final $^{12}\text{C}/^{13}\text{C}$ ratio. When data of sufficient quality is available this can constrain the details of any proposed extra-mixing formulation. In the present case the UKRT formulation of thermohaline mixing is a far better fit than the phenomenological prescription given by EDL08, although both fit the constraint provided by the carbon isotope ratio.
2. The UKRT prescription of thermohaline mixing with $C_t = 1000$ seems to best fit the data for M3. This is consistent with the results of Charbonnel and Lagarde (2010) for higher metallicities ($M = 1.25 - 2.2 M_\odot$, $Z = Z_\odot$) and CZ07a for a range of metallicities ($M = 0.9 M_\odot$, $[\text{Fe}/\text{H}] = -1.8, -1.3, -0.5$).
3. We infer that there is a spread of ≈ 0.3 to 0.4 dex in $[\text{C}/\text{Fe}]$ in the stars in M3 from their birth. Without this initial difference in $[\text{C}/\text{Fe}]$ between the two populations, thermohaline mixing cannot reproduce the change in $[\text{C}/\text{Fe}]$ seen on the giant branch. That there are two populations is absolutely required, because once C_t is sufficiently large, an increase of this coefficient doesn't produce a bigger $\Delta[\text{C}/\text{Fe}]$. Primordial C and N inhomogeneities have been directly observed as abundance differences among main sequence stars in globular clusters such as M13 and NGC 6752 (Briley et al., 2004; Carretta et al., 2005), which have similar metallicity to M3.
4. To reproduce the entire spread of $[\text{C}/\text{Fe}]$ values seen in the giants of M3 it is essential that thermohaline mixing operate in both the CN-strong and CN-weak populations identified in (3). In this case we can explain the full spread in $[\text{C}/\text{Fe}]$ seen near the tip of the giant branch in M3. A similar exercise was carried out by Denissenkov and Vandenberg (2003) for the case of M92, modelled with a simple parameterized extra-mixing formulation. The data for M92 are from many different sources and make it difficult to estimate precisely where the extra mixing begins. Applications to clusters of lower metallicity are discussed in the next chapter.

5. Thermohaline mixing can produce a significant change in $[N/Fe]$ as a function of M_V on the RGB for initially CN-weak stars but not for initially CN-strong stars, which have so much N to begin with that any extra mixing does not significantly affect the surface composition.
6. The level of depletion of carbon is dependent on the depth to which the material is mixed and how fast it is mixed.
7. Mass loss has little effect on the surface abundances.
8. Both the predicted and observed composition changes take place at a luminosity that is higher than the LF bump as given by Fusi Pecci et al. (1990). The observed abundances begin to decrease at a luminosity lower than the LF bump preferred by Smith and Martell (2003). Uncertainties in the distance modulus make it difficult to draw further conclusions.

We have seen that the linear theory of Ulrich (1972) and Kippenhahn et al. (1980) provides a fit to the carbon and nitrogen abundances in the giants in M3 (assuming there are two different populations initially). CZ07a have shown that the same theory (and indeed the same parameter $C_t = 1000$) seems to fit field stars of a range of metallicities (see also Charbonnel and Lagarde 2010). It is important to note that thermohaline mixing is more than a theory with an adjustable parameter. For example, its beginning is determined clearly by the fusion of ^3He which produces a molecular weight inversion. Also, the hydrodynamics provides the physical formulation for the diffusion co-efficient used, and hence its variation throughout the star, to within a constant which depends on the geometry of the fingers expected in the mixing process. Nevertheless, until we have a complete theory that also determines this geometric factor, or at the least some numerical simulations, there is a gap between understanding the fundamental physics and the sort of work presented here, to match the observations. To this end we note the work of Denissenkov (2010) and Denissenkov and Merryfield (2011) which addresses this issue and dedicate Chapter 10 to such discussions.

This work further supports the ability of thermohaline mixing to explain extra mixing on the RGB. But although our models can explain M3 very well, the question remains whether this work can be extended to all clusters. The UKRT prescription for thermohaline mixing appears to model the internal mixing of a young metal rich cluster. Old metal-poor clusters such as M92 will have undergone a different mixing history. Furthermore Sweigart (1978) suggests changing the metallicity and helium content will drastically alter the location and size of the LF bump. These questions are the subject of the next chapter.

Monash University

Declaration for Thesis Chapter 6

Declaration by Candidate

In the case of Chapter 6, a significant part of this work was published as:

Angelou, G. C., Stancliffe, R. J., Church, R. P., Lattanzio, J. C., and Smith, G. H. (2012). The Role of Thermohaline Mixing in Intermediate- and Low-metallicity Globular Clusters. *The Astrophysical Journal*, 749:128.

The nature and extent of my contribution to the work was the following:

Nature of contribution	Extent of contribution (%)
Primary research and paper writing	70%

The following co-authors contributed to the work, none of whom are students at Monash University.

Name	Nature of contribution
Prof. John Lattanzio	Consultation and revision
Dr. Ross Church	Consultation and revision
Dr. Richard Stancliffe	Consultation and revision
Prof. Graeme Smith	Consultation and revision

The undersigned hereby certify that the above declaration correctly reflects the nature and extent of the candidates and co-authors contributions to this work

Candidate's  **Signature** _____ **Date** 28-Aug-2014

Supervisor's  **Signature** _____ **Date** 28-Aug-2014

Chapter 6

The Role of Thermohaline Mixing in Intermediate- and Low-Metallicity Globular Clusters

Astronomy compels the soul to look upward, and leads us from this world to another.

- Plato

6.1 Intermediate metallicity: M3 and M13

In Chapter 5 and Angelou et al. (2011), we showed that the chemical evolution of the stars in M3 is consistent with contribution from primordial and *in situ* components. In intermediate metallicity clusters, the contribution of primordial enrichment can be traced through measurements of the CN bands and these were used in M3 to infer the distinct populations. Furthermore, in each population the evolution of $[C/Fe]$ along the RGB was well modelled by thermohaline mixing. It is important to test whether this result pertains to other clusters of similar metallicity. As such, we turn our attention to M13. M3 and M13 are a second parameter pair of metallicity $[Fe/H] \approx -1.4$ and ages between 11.3 and 14.2 Gyr (Chaboyer et al., 1992; Jimenez et al., 1996; VandenBerg, 2000; Salaris and Weiss, 2002; Alves et al., 2004). Similarities between the two clusters exist in age, metallicity, Na-O anticorrelation (Snedden et al., 1992; Kraft et al., 1992), Na spread (Cohen, 1978; Peterson, 1980; Kraft et al., 1992) and r-process variation (Roederer, 2011); it is only horizontal branch morphology that differs significantly. We therefore expect thermohaline mixing operating in multiple populations to also model the variation of $[C/Fe]$ (and $[N/Fe]$) in M13.

We use data for M3 and M13 from a variety of sources. The M3 data are taken from Smith (2002) which is compiled from previous studies in the literature, namely Suntzeff (1981), Smith et al. (1996) and Lee (1999) with a zero point offset applied in order to reduce systematic uncertainties in the data. In addition to determining carbon and nitrogen abundances as a function of absolute magnitude, Suntzeff (1981) and Norris and Smith (1984) measured the CN strength for M3 giants. We do not possess measurements of CN strength for the stars in the M13 sample but (unlike M3) observations of $[C/Fe]$ and $[N/Fe]$ exist on the main sequence. For M13 we incorporate the studies of Suntzeff (1981), Smith et al. (1996), Briley et al. (2002), Briley et al. (2004) and Smith et al. (2005). Offsets to allow for systematic differences have been applied by Briley et al. (2004) for all but the most recent study. We assumed a distance modulus of $m - M = 14.43$ which is an average of various measurements ($m - M = 14.44$ from Buckley and Longmore 1992, $m - M = 14.33$ from Harris 1996, $m - M = 14.47$ from Gratton et al. 1997, $m - M = 14.48$ from Reid 1997). The uncertainty introduced here is no larger than the measurement error of the observations.

In Figure 6.1 we plot the determined $[C/Fe]$ and $[N/Fe]$ values against absolute visual magnitude for M13 and M3. Each symbol corresponds to a particular study; the legend can be found in the figure. We include two calculations (the black and grey curves) used to model M3 (see Angelou et al. 2011 and the previous chapter). The models are of mass $M = 0.8M_{\odot}$ and metallicity $Z = 0.0005$. In these calculations we run without convective overshoot, our mixing length parameter α is set to 1.75 and thermohaline mixing parameter $C_t = 1000$. In both clusters the solid black curve represents our CN-weak model with initial abundances $Y = 0.2495$, $X(C) = 5.45 \times 10^{-5}$, $X(N) = 1.5 \times 10^{-5}$ and $X(O) = 2.86 \times 10^{-4}$. The initial carbon and nitrogen values were selected to match the measurements of these species in the CN-weak stars in M3. The solid grey curve corresponds to our CN-strong model with $X(C) = 1.9 \times 10^{-5}$, $X(N) = 5.5 \times 10^{-5}$ and $X(O) = 2.6 \times 10^{-4}$ to match the CN-strong population in M3. As the stars are likely to have undergone CN cycling we increased our ${}^4\text{He}$ to $Y = 0.28$ which only has a marginal effect on the location of the LF bump.

Thermohaline mixing operating in two populations models the behavior of $[C/Fe]$ along the RGB in both M3 and M13. In the case of M13 we have the added constraint of observations along the main-sequence. In this cluster the CN strong model acts as a lower envelope to the RGB observations and simultaneously accounts for most of the main-sequence data. However, there are a number of subgiant and main-sequence stars at lower $[C/Fe]$ than seen in the M3 data. In order to match the entire main-sequence spread we have taken our CN strong model and reduced the initial carbon by a further 0.4 dex. This is the blue curve where we set initial abundances to $X(C) = 7.7 \times 10^{-6}$, $X(N) = 8.8 \times 10^{-5}$ and $X(O) = 2.4 \times 10^{-4}$. By design this model matches the most carbon depleted subgiants (except for the three extreme cases with $[C/Fe] < -1$) but the predicted abundances along the RGB are systematically lower than the current observations. It appears as if these most-carbon-depleted subgiants lack counterparts on the RGB. This could be the role of small statistics in that we do not have a large enough sample of the cluster, or the effect of systematic offsets from different data sources; recall we do not apply

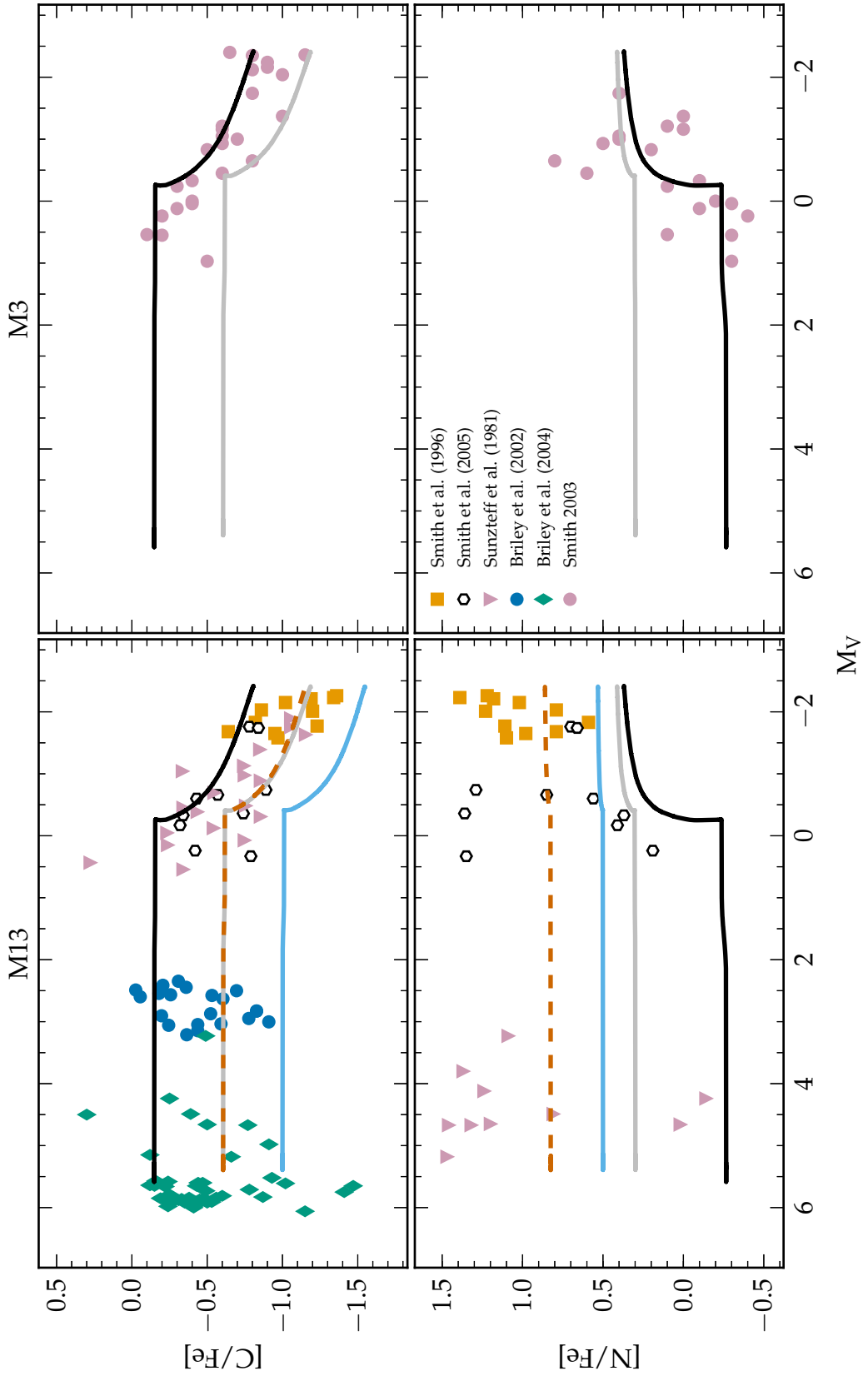


Figure 6.1: $[C/Fe]$ and $[N/Fe]$ vs M_V for M13 (left panels) and M3 (right panels). The various studies from which the data are taken are listed in the Figure. In all panels the solid black curve represents our CN-weak model and the solid grey curve corresponds to our CN-strong model. For M13 we also provide a nitrogen enhanced model (vermilion dashed line) and a model designed to match the main-sequence carbon spread of the cluster (blue line). In all models the metallicity is set to $Z = 0.0005$ and the thermohaline mixing parameter $C_t = 1000$.

an offset for the Smith et al. (2005) study. We are unable to account for the two most carbon-poor stars in M13 ($[C/Fe] \approx -1.5$). These stars are at the faint end of the Briley et al. (2004) catalogue and hence have large associated errors (Cohen 2011, private communication).

Compared to M3, there appears to be a larger star-to-star variation in nitrogen in M13; a significantly N-enhanced model is required to reproduce the upper envelope of the data. In the context of the current paradigm the enrichment is proposed to be due to ON cycling in the polluting generation of stars. To investigate this we constructed an ON-cycled model (dashed vermilion line) with half the oxygen converted to N, giving $X(C) = 1.9 \times 10^{-5}$, $X(N) = 1.85 \times 10^{-4}$ and $X(O) = 1.3 \times 10^{-4}$. The figure shows that the change in $[N/Fe]$ produced by thermohaline mixing is negligible. The initial nitrogen in these stars is sufficiently high that any nitrogen brought to the surface via thermohaline mixing makes little difference to the envelope composition.

We note from Figure 6.1 that even the ON cycled model (vermilion dashed line) fails to account for the N-rich stars which show nearly 1 dex more N than this model. Even processing all the O into N would not produce a sufficiently high N abundance. We must consider the possibility, therefore that C+N+O is higher in M13 than in M3. This is a testable prediction.

As we have stated there are a larger number of stars in M13 that are enriched in nitrogen; Smolinski et al. (2011) find the cluster contains four times as many CN-strong stars than CN-weak ones. In terms of the multiple population scenario this is interpreted as the cluster containing a majority of second generation stars. In Smith (2002) and Smolinski et al. (2011) the observations suggest that the M3 stars are evenly split amongst the CN-weak and CN-strong populations. The inferred ratios of the stellar populations within the clusters, determined from measurements of the CN bands agree with the horizontal branch analysis of D’Antona and Caloi (2008). They have independently determined that more than 70% of stars in M13 and 50% in M3 are required to be enriched in ^4He (a product of CN cycling along with N enrichment) to reproduce the respective horizontal branch morphologies.

In M3 there is a distinct lack of CN-strong stars at low luminosity. As discussed in Angelou et al. (2011) this is an artifact of the original Suntzeff (1981) study in which the lower luminosity stars that were observed happened to be CN-weak. Norris and Smith (1984) showed that CN-strong giants do exist in M3 at luminosities corresponding to the faint limit of the Suntzeff (1981) survey, as did Smolinski et al. (2011). The latter show the CN band strength remains clearly dichotomous in M3 even at low luminosity. We assume this will be reflected in

the $[\text{N}/\text{Fe}]$ abundances and therefore $[\text{C}/\text{Fe}]$. So whilst we possess measurements of the CN bands for our M3 sample and a few observations of $[\text{C}/\text{Fe}]$ at low luminosity, conversely in M13 we possess many low-luminosity observations of $[\text{C}/\text{Fe}]$ but no measurements of the CN bands. Once again the work of Smolinski et al. (2011) provides some insight. They demonstrate an obvious dichotomy in the CN bands along the RGB of M13. The dichotomy is not as clear below the sub giant branch as the temperatures are too high to allow molecule formation. Smolinski et al. (2011) also show a greater spread in the CN band values especially in the CN strong stars; this is reflected in the large spread in $[\text{N}/\text{Fe}]$ observed in the cluster.

6.2 Low Metallicity

6.2.1 NGC 5466

Carbon depletion along the RGB of NGC 5466 has been observed by Buonanno et al. (1985), Fekadu et al. (2007) and Shetrone et al. (2010). In this study we use the data from Shetrone et al. (2010) as the observations are from a single instrument, they cover a large luminosity range and for each star $[\text{C}/\text{Fe}]$ and the CN band strength were determined. As was the case for the intermediate-metallicity clusters, we plot $[\text{C}/\text{Fe}]$ as a function of absolute visual magnitude. In Figures 6.2a and 6.2b the NGC 5466 data are plotted according to CN band strength; lavender circles denote CN-weak stars, vermilion circles denote CN-strong stars¹. The black solid curve in Figure 6.2a is our thermohaline mixing model with initial abundances of $Y = 0.25$, $X(\text{C}) = 1.6 \times 10^{-5}$, $X(\text{N}) = 5.03 \times 10^{-6}$ and $X(\text{O}) = 4.57 \times 10^{-5}$. The model is of mass $M = 0.8M_{\odot}$ and metallicity $Z = 0.0001$ corresponding to the observed $[\text{Fe}/\text{H}] = -2.2$ and age between 11 and 16 Gyr (di Cecco et al., 2010; Grundahl et al., 2000). We run without convective overshoot, set the mixing length parameter to $\alpha = 1.75$ and set the thermohaline mixing parameter to $C_t = 1000$. Highlighted also are the locations of the important mixing events along the RGB. Common to all panels are the solid vertical line and dotted line. The solid vertical line represents the end of first dredge-up as calculated in the models; this occurs at $M_V \approx 0.56$. The dotted line corresponds to the LF bump at $[\text{Fe}/\text{H}] = -2.2$ according to Martell et al. (2008b) based on a metallicity-LF bump relation; this occurs at $M_V \approx -0.55$. For each individual cluster we also include the dashed line which represents a photometrically derived value of the LF bump magnitude. In NGC 5466 this was determined by Fekadu et al. (2007) and occurs at $M_V \approx -0.2$ ($V_{\text{bump}} = 16.2$, $(m - M)V = 16.0$). The end of first dredge-up marks the end of any surface composition changes expected by canonical theory. For stars of this mass and metallicity there is no visible change to the envelope composition from first dredge-up: the change in surface mass-fraction of carbon is 6×10^{-8} in our models. The position of the LF bump represents the earliest point at which thermohaline mixing can begin to operate. It corresponds to the point when the hydrogen burning shell meets the composition discontinuity left behind by first dredge-up.

¹The solid star is CN strong but it is most likely a CH star and hence a binary.

Figure 6.2a suggests that our solar scaled model (black curve) is a good fit to observations of $[C/Fe]$ in NGC 5466. Surface depletion in the cluster appears to begin after the LF bumps determined by Fusi Pecci et al. (1990) and Martell et al. (2008b). We find that the bump determined by Martell et al. (2008b) is a more convincing fit to the models than that of Fekadu et al. (2007). Fekadu et al. (2007) also inferred the LF bump magnitude by isochrone fitting and obtained a value 0.3 magnitudes brighter agreeing with the Martell et al. (2008b) prediction. The determination of the LF bump at low metallicity is difficult. We return to this point in Section 6.3.1

Although a single CN population undergoing thermohaline mixing is a satisfactory fit to the data, in Figure 6.2b we provide an equally plausible fit drawn by eye. The black solid line (which applies to Figures 6.2b, 6.2d & 6.2f) tries to take into account our belief that carbon depletion should not occur until after first dredge-up but does not take into consideration any preconceptions of the mixing profile. If we assume the bump luminosity calculated by Fekadu et al. (2007) is correct then depletion begins after the LF bump, as expected. If, however, we use the bump luminosity calculated by Martell et al. (2008b) then the mixing may be argued to begin before the bump is reached. The fit by eye here is by no means a statistical or quantitative test, we have included these fits simply to highlight the apparent depletion profile in these clusters.

NGC 5466 requires almost no spread in the initial composition to account for the spread of carbon. Our model provides a particularly strong locus to the CN-strong stars. In addition to measurements of $[C/Fe]$, Shetrone et al. (2010) analyzed the CN bands of the stars in their sample. The results hinted that a CN dichotomy, which is typical in globular cluster red giants, may be present but as we can see from Figure 6.2a the stars do not separate as clearly as those in the more metal rich clusters. Shetrone et al. (2010) used a linear least-squares fit in the plane of the $S(3839)$ CN index (Norris et al., 1981) versus absolute V magnitude to divide relatively CN-strong stars (those above the line) from CN-weak stars (those below the line). As in other studies of low-metallicity globular clusters (e.g., Martell et al. 2008a), the mean separation in CN band strength between the two groups is not large relative to the scatter within each group. Whilst the data suggest that there is a CN bimodality in NGC 5466, its low metallicity reduces the effectiveness of CN band strength as a marker of multiple populations in this cluster.

6.2.2 M92

The M92 data in Figures 6.2c and 6.2d are those adopted by Smith and Martell (2003) and comprise data from various sources to which offsets have been applied in order to remove systematic differences in abundance scales. These original sources are studies by Carbon et al. (1982), Langer et al. (1986) and Bellman et al. (2001) and we highlight the target stars in each catalogue (see the legend in the figure). Even with typical errors of ± 0.2 dex there is a much larger spread in $[C/Fe]$ at any given magnitude than was seen in NGC 5466. In these M92 panels the dotted line is the photometrically derived LF bump identified by Nataf et al. (2013). These

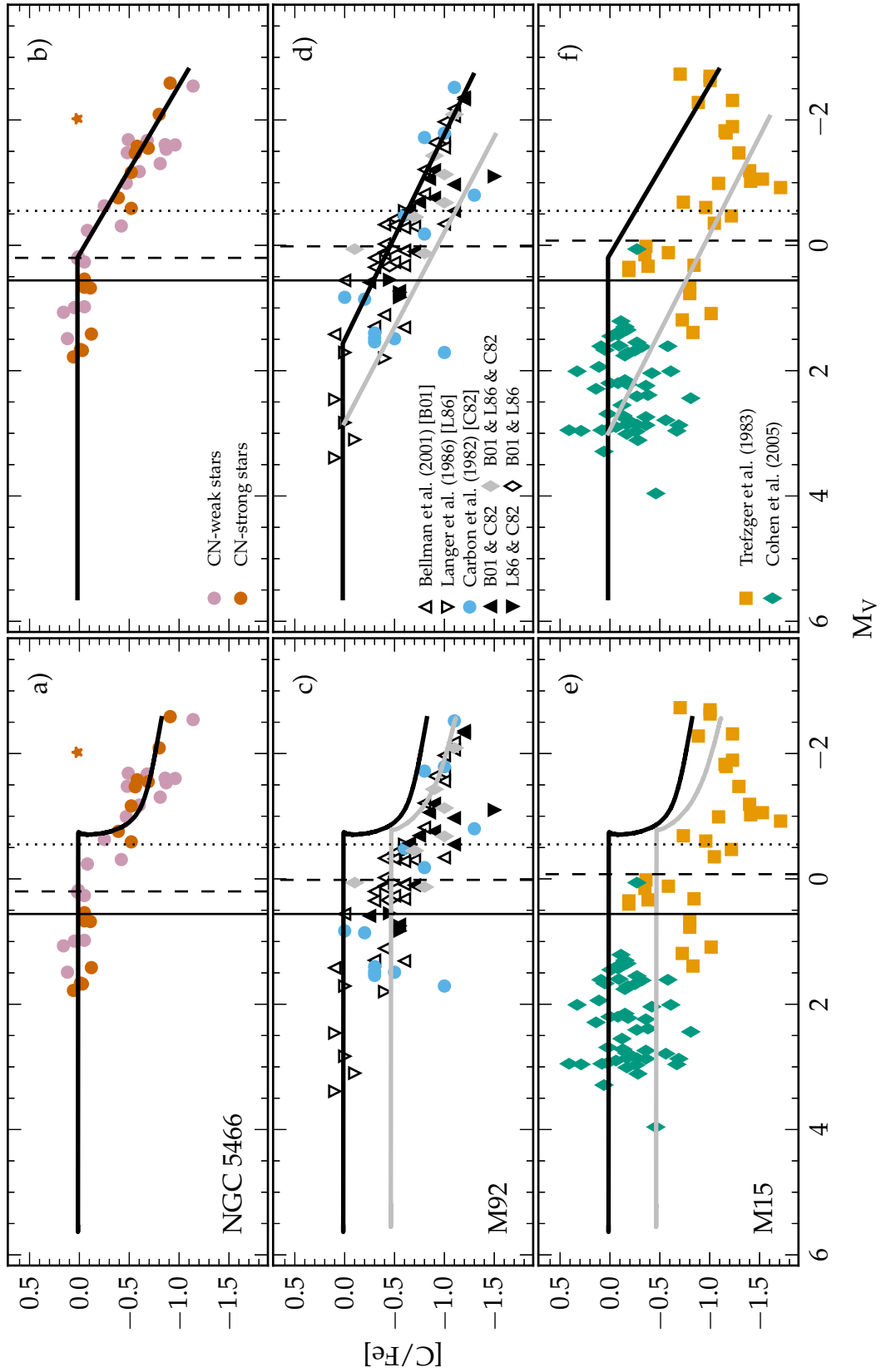


Figure 6.2: From previous page. $[C/Fe]$ vs M_V for NGC 5466 (top panels), M92 (middle panels) and M15 (bottom panels). In the left panels the black curve represents our solar scaled model (CN-weak) and the grey curve is our CN-strong model for these clusters. The solid vertical line represents the end of first dredge-up according to the models. The dotted line corresponds to the LF bump according to Martell et al. (2008b). The dashed lines are photometric derivations of the LF bump for each cluster: for M92 and M15 the magnitude is taken from Nataf et al. (2013), and for NGC 5466 from Fekadu et al. (2007). In the right panels we provide lines of best fit by eye which helps highlight the strange behavior of the clusters.

authors have utilised previous high resolution HST observations to determine the LF bump in many globular clusters. Their measured value of the magnitude of the bump $M_V \approx 0.016$. ($V_{bump} = 14.666 \pm 0.013$, $(m - M)V = 14.65$) differs from the older Fusi Pecci et al. (1990) value of $M_V \approx -0.39$. We do not possess measurements of CN band strength for the M92 stars plotted in Figures 6.2c and 6.2d but Norris and Pilachowski (1985) and Smolinski et al. (2011) have provided evidence that a bimodality may exist. As is the case for NGC 5466 the separation in the populations is marginal, a property that appears common at low metallicity. Even without the CN bands the spread in $[Na/Fe]$ (Snedden et al., 2000, 1997), and the spread in $[C/Fe]$ at low luminosities is evidence for mixing between the two populations.

The depletion of $[C/Fe]$ in M92 has previously been investigated by Denissenkov and Vandenberg (2003) but over a smaller luminosity range. Their (canonical) extra mixing formulation requires two models, one depleted by 0.1 dex and the other by 0.5 dex in $[C/Fe]$ to match the abundance spread. Angelou et al. (2010) considered the depletion of $[C/Fe]$ with a different implementation of thermohaline mixing to that used here. They highlighted that M92 appeared to show surface depletion of carbon before FDU, a property in disagreement with not just thermohaline mixing but also canonical stellar theory. This strange behavior has been discussed by (at least) Martell et al. (2008b), Gratton et al. (2004) Bellman et al. (2001), and Langer et al. (1986).

This apparent pre-FDU depletion is highlighted in Figure 6.2d. Here the black solid line is an eye fit based on the assumption that carbon depletion should not occur until after FDU while the grey curve is a best fit by eye to the data without any preconceived luminosity for the onset of carbon depletion. If we follow the latter fit, then by the time the end of FDU is reached the stars have depleted almost 0.5 dex in $[C/Fe]$. This is unusual because, as we have stated, at this mass and metallicity we expect changes due to FDU to be of the order $\Delta X(C) = 6 \times 10^{-8}$ at the surface. Between the end of first dredge-up ($M_V \approx +0.5$) and the determined location of the LF bump according to Martell et al. (2008b) ($M_V \approx -0.5$; the earliest point at which thermohaline mixing is expected to begin) the stars in M92 are depleted by roughly a further 0.3 dex in $[C/Fe]$. Depletion is present but not as pronounced if the Nataf et al. (2013) bump magnitude is used. It is possible that these are the observable effects of other extra-mixing mechanisms and this may also

explain the carbon depletion prior to the end of first dredge-up. If true, this would have significant implications for stellar theory. First of all such depletion was not seen in other clusters (Smith and Martell, 2003; Shetrone et al., 2010). In most scenarios, extra mixing is inhibited until the star reaches the LF bump and the advancing H-shell removes the molecular weight discontinuity left behind by the receding convective envelope. In the case of M92 some stars on the giant branch have already depleted their $[C/Fe]$ by about 0.8 dex when the models reach this stage. If we have to postulate that some form of mixing begins sufficiently early to produce this depletion, then the mixing must necessarily remove the abundance discontinuity that is itself responsible for the LF bump. If the apparent behavior is real, we believe this is a significant problem for stellar astrophysics.

If we assume that M92 displays an initial spread of $[C/Fe] = 0.5$ dex then can we remove the issue of mixing before the end of FDU? The black curve in Figure 6.2c is the same solar scaled model applied to match the stars in NGC 5466. As we now require a greater spread in carbon to match this cluster we include a second model (grey solid curve) run with the same physical parameters but a composition that is reduced in C and enhanced in N. For this model we set $Y = 0.25$, $X(C) = 5.46 \times 10^{-6}$, $X(N) = 1.60 \times 10^{-5}$ and $X(O) = 4.57 \times 10^{-5}$ giving $[C/Fe] = -0.5$. We have not changed Y in the model. The main effect of changing Y is to alter the the location of the LF bump and as we have seen in M3 and M13 this is negligible. These two thermohaline models with large initial carbon spread remove the apparent pre FDU depletion. Assuming such a spread in $[C/Fe]$ raises the issue that there are no stars observed with $[C/Fe] = -0.5$ below a magnitude of $M_V \approx 2$. Only four stars have been observed at such magnitudes and all have $[C/Fe] \approx 0$. A large spread in $[C/Fe]$ is observed in M15 and M13 below the sub giant branch. We expect this is the case in M92 but require a targeted study to confirm this assumption.

A large spread in $[C/Fe]$ does not solve all the problems associated with M92. Mixing still appears to be occurring before the LF bump, even for the model with an initial $[C/Fe] = -0.5$. There is approximately 1 magnitude between the location where the carbon abundances turn down and where the models suggest depletion should begin. Of greater concern is the inability of the models to match the upper RGB abundances of stars in M92. The initial abundances were selected to cover the spread in $[C/Fe]$ before the onset of extra mixing. No stars that have depleted $[C/Fe]$ (magnitude brighter than $M_V = 0$) fall along the evolutionary path predicted by the solar scaled model (black curve). If such stars do exist and are governed by thermohaline mixing, we expect them to be bright members in the cluster (ascending the RGB). It would be perverse if by chance they were not selected for any of the three spectrographic studies (unless of course, they are all in the centre of the cluster). The initially depleted model (grey curve) provides an upper envelope to the mixed RGB data, however the composition was selected to form a lower limit of the initial M92 abundance spread. It is sobering to see how many data points fall below this curve. Although the two models with an initial spread of 0.5 dex in $[C/Fe]$ can encompass fainter stars ($M_V > 0.5$ there are very few stars between the curves once carbon depletion has begun. Thermohaline does not deplete carbon to the levels seen in M92: the models are unable to

simultaneously account for both the sub-giant branch and RGB data.

The M92 sample is a combination of three different studies and although attempts have been made to homogenize the data, systematic differences in the studies still may lead to offsets of ≈ 0.3 dex in the $[\text{C}/\text{Fe}]$ abundances. At such low metallicity one has to wonder if inhomogeneity in the data may be affecting our interpretation of the mixing history. Extensive measurements of $[\text{C}/\text{Fe}]$ at various magnitudes in this cluster would provide a robust test for stellar evolution models.

6.2.3 M15

$[\text{C}/\text{Fe}]$ as a function of magnitude is plotted for M15 in Figures 6.2e and 6.2f. The data are a combination of those from Trefzger et al. (1983, squares) and Cohen et al. (2005, diamonds) and plotted as given in these sources. No offsets have been applied to correct for systematic errors so the data are marked according to their source. As is the case with M92 we do not possess CN band strength measurements for our sample but Smolinski et al. (2011) show there would be little separation between the mean values of the CN-strong and CN-weak stars, a common aspect of the three metal poor clusters studied here. The same is also true for (at least) NGC 5053 a cluster with metallicity $[\text{Fe}/\text{H}] = -2.3$ (Smolinski et al., 2011). In Figures 6.2e and 6.2f the dotted vertical line represents the magnitude of the M15 LF bump determined by Nataf et al. (2013) which occurs at $M_V \approx -0.075$ ($V_{\text{bump}} = 15.315 \pm 0.021$, $(m - M)V = 15.39$). This is similar to Zoccali et al. (1999) who also used HST data to determine a bump magnitude of $M_V \approx -0.02$ ($V_{\text{bump}} = 15.41$, $(m - M)V = 15.39$).

In Figure 6.2e we plot the two thermohaline mixing models applied in M92. In both clusters thermohaline mixing does not deplete carbon to the degree seen in the observations. Like M92 there is evidence that M15 is mixing between the end of FDU and the LF bump. This is highlighted by Figure 6.2f where we plot our lines drawn by eye rather than the stellar models. This effect would be exacerbated had we adopted the location of the LF bump according to Zoccali et al. (1999). It is possible this is an artefact of combining inhomogeneous data. There is some luminosity overlap between the two studies and it is only when they are combined that it appears as if pre-bump depletion is occurring. This same argument can be used to explain any pre-FDU mixing alluded to by the grey line of best fit in Figure 6.2c. A homogeneous set of observations over this luminosity range (as exists for NGC 5466) is required.

While similarities exist there are also slight differences between M15 and M92. A large spread of $[\text{C}/\text{Fe}]$ is present in M15, which extends below the sub-giant branch. This is justification for the inclusion of our initial $[\text{C}/\text{Fe}] = -0.5$ model (grey curve in Figures 6.2c and 6.2e). In M92 it is the dearth of observations at low luminosity that raises many questions about the behavior of the cluster and its initial abundance spread. We note there seems to be a lack of stars with high $[\text{C}/\text{Fe}]$ just before FDU in M15. We assume these stars exist and the current void is a result of combining two studies that focus on stars at different stages of evolution. Perhaps the most curious aspect of M15 is the behavior of the stars

at $M_V \approx -1$. The stars appear to suddenly increase their carbon abundance. We await confirmation of this behavior before speculating on its cause as it is inconsistent with our current understanding of stellar nucleosynthesis.

Lind et al. (2009) and Mucciarelli et al. (2011) use lithium to trace extra mixing along the giant branches of NGC 6397 and M4 respectively. Such studies provide a complimentary diagnostic to the variation of C and N with luminosity. Lithium is very sensitive to nuclear burning: it is destroyed at low temperatures. Any transport of material into warmer regions will be reflected through a depletion in the surface lithium abundance. In the case of M15 and M92 this would hopefully help identify the magnitude at which extra mixing begins in these clusters. Given the behavior of M15 and M92, the point at which surface depletion begins (after first dredge-up) must be considered distinct from the LF bump (even though there are good theoretical reasons why the two should coincide as they seem to at higher metallicity). For our purposes we can only rely on high level photometry (and statistical analysis) of the clusters to distinguish the location of the bump and, as we discuss in section 6.3.1, this can be difficult.

6.3 Discussion

6.3.1 Comparison Across Metallicity

In our two intermediate-metallicity clusters the spread in $[C/Fe]$ is explained by distinct populations which clearly separate according to CN band strength. This is not the case in low-metallicity clusters (Shetrone et al., 2010; Smolinski et al., 2011). Any CN bimodality is marginal at best. The difference between the mean value of a CN index such as $S(3839)$ between CN-strong and CN-weak stars is so small that their distribution can be interpreted as a single CN population with scatter. There is still clear evidence for multiple populations in the metal poor clusters from the large spreads in O, Na, Al abundance within them. We therefore expect that a polluting generation will enrich the cluster with CN processed material and 4He . This should be reflected in the carbon and nitrogen abundances. In M15 there is a large spread in both $[C/Fe]$ (≈ 1.5 dex) and $[N/Fe]$ (≈ 3 dex, Cohen et al., 2005) but only a marginal change in the CN bands (Smolinski et al., 2011). In these low metallicity clusters the CN band strength is not necessarily representative of the nitrogen abundance in the stars.

According to our stellar models with thermohaline mixing, the clusters studied here are close enough in metallicity that we should expect a similar degree of carbon depletion. In the intermediate metallicity clusters (M3 and M13), we are able to match the depletion of $[C/Fe]$ along the RGB using two models of different initial abundances. In the metal poor systems thermohaline mixing can account only for the evolution of $[C/Fe]$ in NGC 5466. In M15 and M92 not only do the clusters appear to have depleted far more carbon than we predict but this depletion has begun before the LF bump. Such behavior is not only inconsistent with thermohaline mixing but also standard stellar evolution.

It is worth noting that the LF bump in extremely metal-poor clusters (e.g., M92, M15 and NGC 5466) is not as clearly visible as it is in more metal-rich

clusters. There are two theoretical reasons why this is so. Firstly the depth of first dredge-up is a function of metallicity. Metal-rich stars have deeper convective envelopes than metal poor stars and therefore a greater discontinuity in the hydrogen profile that develops after first dredge-up. The burning shell in metal-poor stars will encounter a smaller hydrogen difference and spend less time readjusting the stellar structure. Because less time is spent at the magnitude of the bump the likelihood of observing stars at this location is reduced. Secondly, evolution on the RGB speeds up as stars move towards brighter luminosities, so the expected number of stars scales inversely with the luminosity in a volume limited sample (but not in a magnitude limited sample). Hence the higher the luminosity at which the bump occurs (i.e., the lower the metallicity), the lower the overall number of stars one should expect to observe and the harder it is to identify the bump.

Fusi Pecci et al. (1990) identified an LF bump in M92 by co-adding data for three very similar clusters. Their determined value of $M_V \approx -0.39$ differs slightly from that of Martell et al. (2008b) who find $M_V \approx -0.55$ based on the use of multiple clusters to determine a LF bump-metallicity relation. Work by Paust et al. (2007) provides little evidence for a bump in the observed LF of M92 however recent work by Nataf et al. (2013) using HST data suggests that it is present at a magnitude of $M_V \approx 0.016$. For NGC 5466 Fekadu et al. (2007) identified a bump using statistical arguments. The bump in M15 was more easily identifiable through the use of HST data as was done by Nataf et al. (2013) and Zoccali et al. (1999).

One possible cause for altering the location of the bump (and hence the onset of thermohaline mixing) in our models is to decrease the ^4He abundance (Sweigart, 1978). However, extrapolating from the Sweigart (1978) results to match the observations would require an initial ^4He well below the Big Bang Nucleosynthesis value. Alternatively, if first dredge-up penetrates deeper than the models predict, then the hydrogen burning shell will encounter the homogenized region at lower luminosities. In Figure 6.3 we plot our metal-poor model with solar scaled abundances, in which the convective envelope extended down to a mass of $M = 0.368 M_\odot$. We have included a model (grey line) with the same initial abundance but artificially homogenized (mixed from the surface) down to a mass of $M = 0.320 M_\odot$ at the time of FDU. The results show that extending the depth of first dredge-up by about 15% in mass translates to the mixing beginning about one magnitude fainter. Note that the artificial model undergoes a period of adjustment as it returns to the structure of the standard metal-poor model. During this brief phase the burning shell is closer to the homogenized region than the structure would dictate if deeper dredge-up occurred normally. As a consequence the temperatures are such that ^3He is easily destroyed but carbon depletion is still inefficient; this can be seen in Figure 6.3. Angelou et al. (2011) call this situation a “burning limited” regime. The material is efficiently transported to the desired regions but the processing is inefficient due to the burning conditions. The artificial model therefore has less ^3He to drive the mixing near the tip of the RGB when the conditions are more conducive to carbon depletion, a regime Angelou et al. (2011) call “transport limited”. In this scenario the inefficient transport of material to the burning regions is the limiting factor in the processing. This however is a side

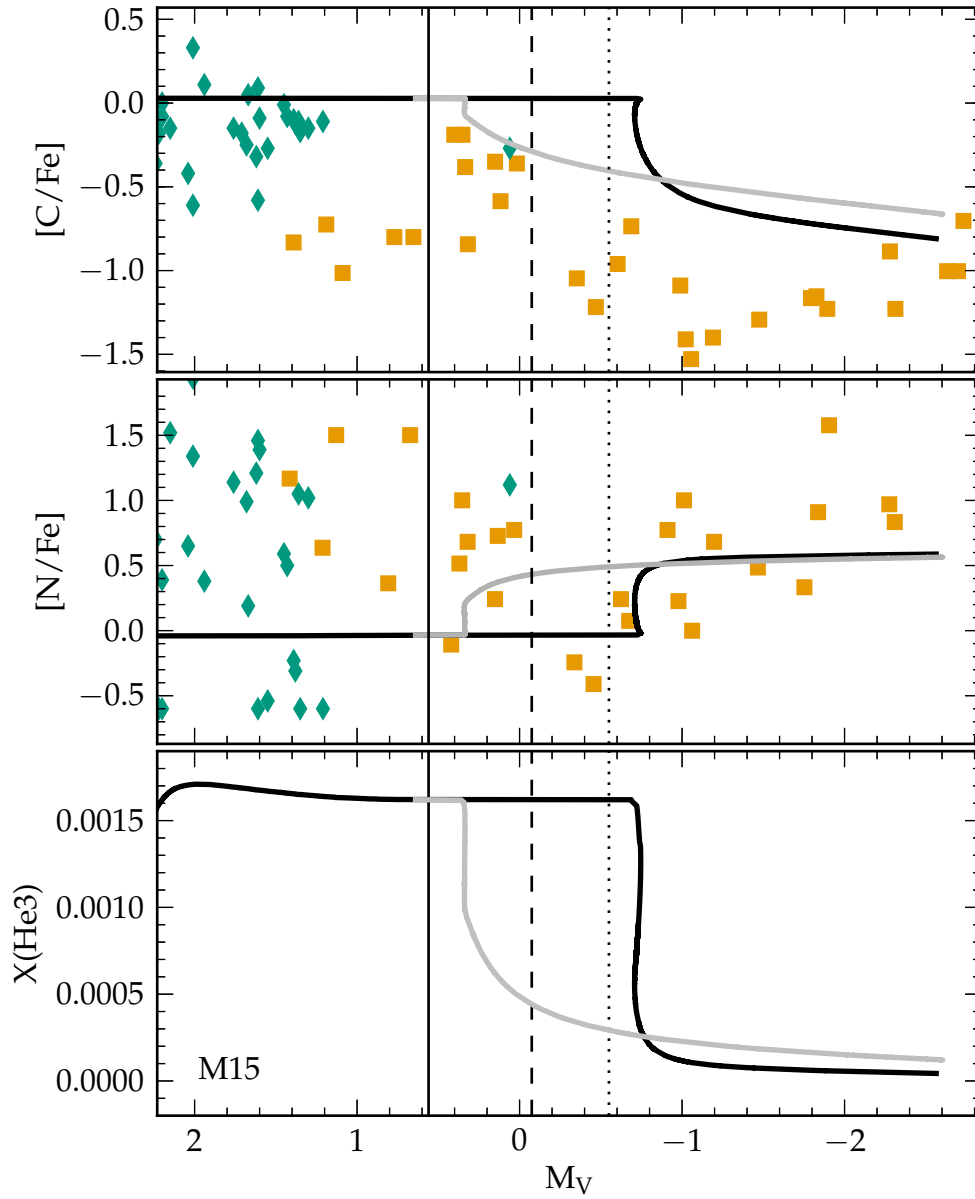


Figure 6.3: $[C/Fe]$ $[N/Fe]$ and $X(^3\text{He})$ vs M_V for M15. As above the observational data is taken from Trefzger et al. (1983) (orange squares) and Cohen et al. (2005) (green diamonds). The solid black curve corresponds to the thermohaline mixing model with standard dredge-up depth (see Figure 6.2) where the envelope extends down to a depth of $M = 0.368 M_\odot$. The grey curve represents our model where we have artificially homogenized beyond the depth of first dredge-up to a mass of $M = 0.320 M_\odot$. The solid vertical line represents the end of first dredge-up according to the normal models. The dotted line corresponds to the LF bump of Martell et al. (2008b) based on a metallicity-LF bump relation. This occurs at $M_V \approx -0.55$. The dashed line is a photometric derivation of the LF bump taken from Nataf et al. (2013) and occurs at $M_V \approx -0.075$.

issue stemming from the artificial model; the important point is that one way for the models to match the observations is to make first dredge-up occur deeper in the low-metallicity stars but not those in NGC 5466.

6.3.2 The Inconsistency at Low Metallicity

We are left wondering why there is such an inconsistent picture of globular clusters at low metallicity. M92 and M15 possess large spreads in $[C/Fe]$ whilst NGC 5466 shows a much narrower distribution. We find that in the cluster where we have uniform observations thermohaline mixing appears to model the depletion of carbon well. We have already discussed the possibility that combining studies in M15 may be affecting our interpretation of the data. Although data for M92 has been homogenized it is still the amalgamation of three different studies. Compiling data from various sources may lead to systematic errors. Systematic offsets of 0.3 dex in $[C/Fe]$ are possible and could be the cause of the apparent contradiction. Because we have two clusters at the same metallicity in M92 and M15 displaying similar behavior one has to wonder how likely it is that systematic offsets conspire in such a way to appear to give the same effect.

We note that the clusters showing the largest discrepancy with standard models are also the most massive. Having measured the integrated V magnitudes of the three metal-poor clusters, Gnedin and Ostriker (1997) find that NGC 5466 ($\approx 1.33 \times 10^5 M_{\odot}$) is a lower mass system than M92 ($\approx 3.64 \times 10^5 M_{\odot}$) and M15 ($\approx 9.84 \times 10^5 M_{\odot}$). This raises the question whether there is a correlation between cluster mass and the extent of primordial $[C/Fe]$ spread at low metallicities. The clusters M15 and M92 may have been able to sustain a greater degree of primordial inhomogeneous carbon enrichment than NGC 5466, with a resulting greater dispersion in $[C/Fe]$ at all magnitudes on the main sequence and red giant branch than in NGC 5466. The greater range in $[C/Fe]$ along the RGB of M15 and M92 can contribute to a greater observational uncertainty in identifying the magnitude at which carbon depletions produced by extra mixing set in. By contrast, a smaller primordial carbon spread in NGC 5466 produces a more tightly defined locus of $[C/Fe]$ versus M_V on the RGB of that cluster, making it a preferable test case for mixing studies. When comparing the r-process elements both M92 and M15 show similar star-to-star variations (Roederer, 2011; Roederer and Sneden, 2011) (although this has recently been questioned by Cohen 2011) which may add additional support to the Na and O abundance evidence that both clusters have sustained heterogeneous enrichment across a range of chemical elements. It would be interesting to determine the O, Na, and r-process element patterns in NGC 5466 to see if they are more homogeneous than in M92 and M15, as a mass-dependent primordial enrichment scenario would anticipate.

6.3.3 The Role of Thermohaline Mixing

It is of course possible that thermohaline mixing does not govern the surface composition of low mass giants. It is not the only process by which mixing may occur in the radiative zone. Mechanisms such as those listed throughout this dissertation

may also be involved. The way in which these mechanisms interact is uncertain and as they are inherently three-dimensional our understanding of their behaviour will improve with the study of these processes in hydrodynamical codes (Dearborn et al., 2001; Bazan et al., 2001; Turcotte et al., 2002; Eggleton et al., 2002; Bazán et al., 2003). Still, the current generation of 1D codes are the precursors to more sophisticated modelling and much insight can be gained through them. One-dimensional spherically-symmetric models with multiple extra-mixing mechanisms include those of Cantiello and Langer (2010) and Charbonnel and Lagarde (2010), both of whom demonstrate that the thermohaline mixing diffusion coefficient is larger than the radial component of rotational mixing. The former also show the thermohaline coefficient to be larger than that of magnetic buoyancy. These codes do not explicitly treat the interaction of the mixing mechanisms and how any given instability may react due to the presence of other processes; rather, they simply add the diffusion co-efficients. Charbonnel and Zahn (2007b) have investigated an instance of multi-process interaction through linear analysis and argue that magnetic fields could serve to inhibit the effects of thermohaline mixing.

Charbonnel and Lagarde (2010) and Lagarde et al. (2012) have produced detailed rotational-thermohaline mixing models for stars of various mass and metallicity. They find rotation leads to a deeper penetration of the convective envelope than their non-rotating models. This allows rotational models to begin thermohaline mixing at fainter magnitudes than their static models; this may go some way to reconciling the magnitude at which stars in M92 and M15 begin mixing. It should be noted that low-mass, low-metallicity rotational models have been produced by Palacios et al. (2006) and Denissenkov et al. (2006) and in the former, the depth of first dredge-up depends on the rotational model used. A window of 0.13 magnitudes is possible for the location of the bump depending on the treatment of rotational physics. That is, different implementations of rotation can move the location of the LF bump to higher or lower magnitudes. Different models of rotational mixing are at play here, in much the same way that different codes produce different third dredge-up results based on the treatment of convective stability (Herwig, 2005). However stochastic variations such as rotation, may lead to deeper first dredge-up in the stars of M15 and M92. Peterson (1983) has shown that stars on the horizontal branch of M13 rotate about twice as fast as those on the horizontal branch of M3. Although we find no major discrepancies between the location of the LF bump in these two clusters (0.07 magnitudes Nataf et al. 2013), in the case of M15 and M92 the effect of rotation on the depth of the FDU may be more pronounced. Why the stars in M13 would rotate faster than the stars in M3 would also require an explanation.

Whilst it is generally agreed that the burning of ^3He in a homogenized zone causes an instability, the efficiency of the resultant mixing has been the cause for debate. The exact value of C_t to adopt remains contentious. Recent multi-dimensional models of thermohaline mixing by Denissenkov (2010), Denissenkov and Merryfield (2011) and Traxler et al. (2011a) support the view of Cantiello and Langer (2010) and the suggestion by Kippenhahn et al. (1980) that the “aspect ratio”, α , of the rising element should take a value of $\alpha \approx 1$ ($C_t \approx 12$). Laboratory experiments by Stommel and Faller published in Stern (1960) have lead Ulrich

(1972) and Charbonnel and Zahn (2007a) to prefer a value of α somewhere closer to $\alpha \approx 6$ ($C_t \approx 1000$). Indeed there is great empirical evidence to prefer this value as it appears to match observations of stars across a great range of mass and metallicity. The mechanism is an elegant means of matching C and N abundances in various stars as well as ensuring measurements of ${}^3\text{He}$ in HII regions are consistent with predictions from stellar models and Big Bang nucleosynthesis (Rood et al., 1984; Hogan, 1995; Charbonnel, 1995; Charbonnel and Do Nascimento, 1998; Tosi, 1998; Palla et al., 2000; Romano et al., 2003). Canonical models predict that low-mass, main-sequence stars are net producers of ${}^3\text{He}$ which is returned to the ISM through mass loss. Hata et al. (1995) have shown that about 90% of the ${}^3\text{He}$ produced on the main sequence must be destroyed to reconcile the two fields. Our preferred value of $C_t = 1000$ matches the carbon and nitrogen in clusters and also destroys over 90% of the ${}^3\text{He}$ in the star before the tip of the RGB. The lower value of $C_t = 12$ once again creates a discrepancy between measurements of ${}^3\text{He}$ in HII regions as only $\approx 20\%$ of the initial ${}^3\text{He}$ is destroyed meaning low-mass stars are once again producers of ${}^3\text{He}$.

It is the aim of this work and Angelou et al. (2011) to rely on empirical evidence to determine the best value of C_t to use in the 1D codes. In the models presented here C_t has been fixed at a value of 1000. This is consistent with previous studies where the same factor has reproduced observations of globular cluster stars (Angelou et al., 2011), field stars (Charbonnel and Lagarde, 2010) and where the mixing has been used to explain the dichotomy between extremely metal poor stars and carbon enhanced metal poor stars (Stancliffe et al., 2009) (although the latter point is in disagreement with Denissenkov and Pinsonneault 2008b,a). Angelou et al. (2011) demonstrate that once C_t exceeds 1000, the processing enters into the burning limited regime whereby increasing the diffusion coefficient has little effect on the final surface abundances. They also show values of $C_t < 600$ simply lead to less mixing than is required to match the observations. Although we are modelling the mixing as *diffusive* it is in fact an *advective* process. We have implemented a linear model of thermohaline mixing which operates via a diffusion equation. Recent 3D numerical simulations of thermohaline mixing (Denissenkov and Merryfield, 2011; Traxler et al., 2011a) find blob-like structures, which are identified with the aspect ratio of the idealized “fingers” in the 1D derivation of Ulrich (1972). It is from this identification that the preference for low values of C_t in the numerical simulations is based. Numerical simulations are a very powerful tool, but are subject to numerous caveats - resolution (time and space), viscosity (numerical and molecular), and extrapolation to stellar conditions (e.g., Prandtl numbers that are a factor $\approx 10^5$ too large). In view of these uncertainties we feel it premature to draw definite conclusions from the numerical simulations. Nonetheless, if the low values of C_t coming from the simulations prove to hold then it would result in a conclusion that either the diffusive approximation to thermohaline mixing used here is not applicable or that thermohaline mixing is too weak to produce the observed carbon depletions of globular cluster red giants.

6.4 Conclusions

We have modelled the depletion of carbon via thermohaline mixing on the RGB of the intermediate metallicity clusters M3 and M13 as well as the metal poor clusters NGC 5466, M92 and M15. We conclude:

- Thermohaline mixing in the presence of primordial enrichment can account for the carbon variation seen in M3 and M13. The spread of carbon along the RGB in both clusters can be covered by the same set of models. In order to match the main-sequence spread in M13, we require a model further depleted in $[C/Fe]$. This model however, predicts that some stars on the RGB should have $[C/Fe]$ values lower than seen. The majority of stars in M13 are enriched in nitrogen whilst about half the stars in M3 appear to be CN strong. The results from the hybrid picture here are consistent with the findings of D’Antona and Caloi (2008) and their requirements to match the horizontal branch morphologies of the clusters. In their work the enriched ${}^4\text{He}$ of the second population acts as the second parameter and helps dictate where the star falls along the horizontal branch. The stars in M13 that are most enriched in $[N/Fe]$ suggest they were formed with some primary nitrogen (higher C+N+O than those in M3).
- Thermohaline mixing can explain carbon depletion with magnitude in NGC 5466. A single solar scaled model is sufficient to explain the cluster even though a modest CN spread has been determined (Shetrone et al., 2010). Our models provide a good fit for this cluster if we adopt the LF bump determined by Martell et al. (2008b). However, the data do not exclude the possibility NGC 5466 is depleting carbon before the LF bump as seems to be the case for M15 and M92.
- In M92 and M15 we have combined observations of $[C/Fe]$ from multiple studies. Thermohaline mixing is unable to reproduce the evolution of carbon along the giant branch in these clusters. The models do not deplete carbon rapidly enough along the RGB. In addition depletion appears to begin before first dredge-up in M92, although this may be due to the fact we only have a few observations at low luminosity. A targeted study at low luminosity is required to confirm if the cluster has the same spread in $[C/Fe]$ as M15. Both clusters appear to be mixing before the LF bump and bright stars are not observed near the predicted carbon abundances for initial $[C/Fe] = 0$.
- Both M92 and M15 seem to require deeper FDU in order for the models to fit the current observations but this is not the case for NGC 5466.
- A consideration that inevitably has to serve as a caveat to our discussions is that the comparison between the thermohaline-mixing models and the $[C/Fe]$ as a function of magnitude data may be hindered by the heterogeneity of the latter, particularly in clusters such as M92 and M15 where zero-point offsets of up to 0.3 dex may exist between the various data sources compiled. Although attempts have been made to compensate for these, it

remains nonetheless a source of concern. Determining the behavior of carbon to faint luminosities on the RGB in both M92 and M15 as well as M3, using a single spectrograph and data analysis system could provide a more homogeneous and rigorous test of our models. Such data would need to include C and N values for subgiants also. In addition, observations of lithium abundances over a large luminosity range can be used to better define the character of extra mixing, while measurements of nitrogen, oxygen and/or sodium abundances can define the patterns of primordial enrichment within the clusters.

Chapter 7

The Globular Cluster Na-O Anticorrelation

I do not envy people who think they have a complete explanation of the world, for the simple reason that they are obviously wrong.

- Salman Rushdie

7.1 Introduction

In Chapters 5 and 6, our models of GC stars included a theory of extra mixing to reproduce aspects of the C-N anticorrelation. This abundance pattern, which demonstrates a dependence with luminosity, is comprised of both a primordial component and a contribution from *in situ* processing. Similar p-capture anticorrelations, in O-Na and Mg-Al, are also present in GCs with the former a seemingly ubiquitous feature of these systems. Unlike C-N, they display no such variation with luminosity having been identified in stars at various phases of evolution. This includes unevolved stars yet to undergo significant mixing such as those on, or below, the subgiant branch. Furthermore, the reactions that process O to N, Ne to Na, and Mg to Al are indicative of hydrogen burning at high temperatures. The conditions necessary to produce the anticorrelations *in situ* are not expected in unevolved stars. The implication, therefore, is that these anticorrelations are present in the stars from birth. As we have recounted throughout this dissertation, the existence of the anticorrelations are best explained by the presence of multiple populations. The multiple population scenario suggests that the ejecta from a fraction of first generation of stars (initially C-O-Mg rich, sharing the same chemical composition of field stars at the same metallicity) mixed with the primordial gas, providing a medium from which the second generation stars (C-O-Mg poor and N-Na-Al rich) formed.

The multiple population scenario had been long been suspected by many groups

(Norris et al., 1981; Denissenkov et al., 1998) and in §1.2.1 we discussed the convergent lines of evidence. The high resolution spectroscopic surveys of GCs (Carretta et al., 2010, and the other approximately 50 papers in the series¹) have played a significant role in the paradigm shift by providing the most complete picture of GC chemical evolution to date. Figure 7.1 is taken from Carretta et al. (2010) and is the culmination of over 350 of hours of VLT time. The work has confirmed that whilst the Na-O anticorrelation is a ubiquitous feature of GCs, the Mg-Al chains are only activated in a subset of the systems. Furthermore, the chemical distribution in GCs has revealed that most GC stars are in fact members of the second generation. The residual first generation stars contribute to only (approximately) one third of the cluster population (Gratton et al., 2012a). We have robustly shown a similar result in the GC NGC 6752 (Campbell et al., 2013). Given that dynamical formation models of GCs suggest that up to 90% of the first generation stars are lost (D’Ercole et al., 2008; Decressin et al., 2008; D’Ercole et al., 2011), the current systems are thought to be 10 times less massive now than they were at birth.

In this section we focus on the behaviour of Na-O in the low- and intermediate-metallicity GCs studied in Chapter 6. M13, in particular, displays some curious features not expected from the current paradigm. Sneden et al. (2004) and Johnson and Pilachowski (2012) have found very O-poor stars ($[O/Fe] \approx -1$) near the RGB tip and only near the tip in M13. The large spread in $[O/Fe]$ (≈ 0.7 dex, see Figure 7.3c) may suggest that extra mixing is more efficient in some stars, or the operation of an additional non-standard mixing event near the tip of the giant branch. Although current results indicate that thermohaline mixing only acts upon the the Li, C and N nuclei, we investigate whether it can account for the behaviour of the M13 giants.

D’Antona and Caloi (2008) and Johnson and Pilachowski (2012) have argued that M13 consists of three populations which they identify through their chemical abundances. The stars are labelled as primordial, intermediate and extreme population stars and their chemical definitions are provided below. The above authors suggest that the O-poor stars constitute the extreme population and are necessarily enhanced in ^4He ($Y > 0.38$ which is required to explain the blue horizontal branch). It is only these stars that are able to experience the event that leads to significant oxygen depletion. In the 1D diffusive theory of thermohaline mixing, material is mixed to the minimum in the μ profile. The temperature location at which this occurs is highly dependent on the composition of the star. No results have been published demonstrating its operation in such extreme compositions and thus a systematic study is included here. Given that H and ^4He provide the major contribution to μ by virtue of their large abundance, we investigate whether the enhanced ^4He can shift the location of the μ inversion and hence extend the temperature/depth to which material is mixed. The development of the μ version and its location in low-mass RGB stars is the subject of an upcoming paper (Church et al. submitted).

¹The papers in this series have generated more than 1500 citations.

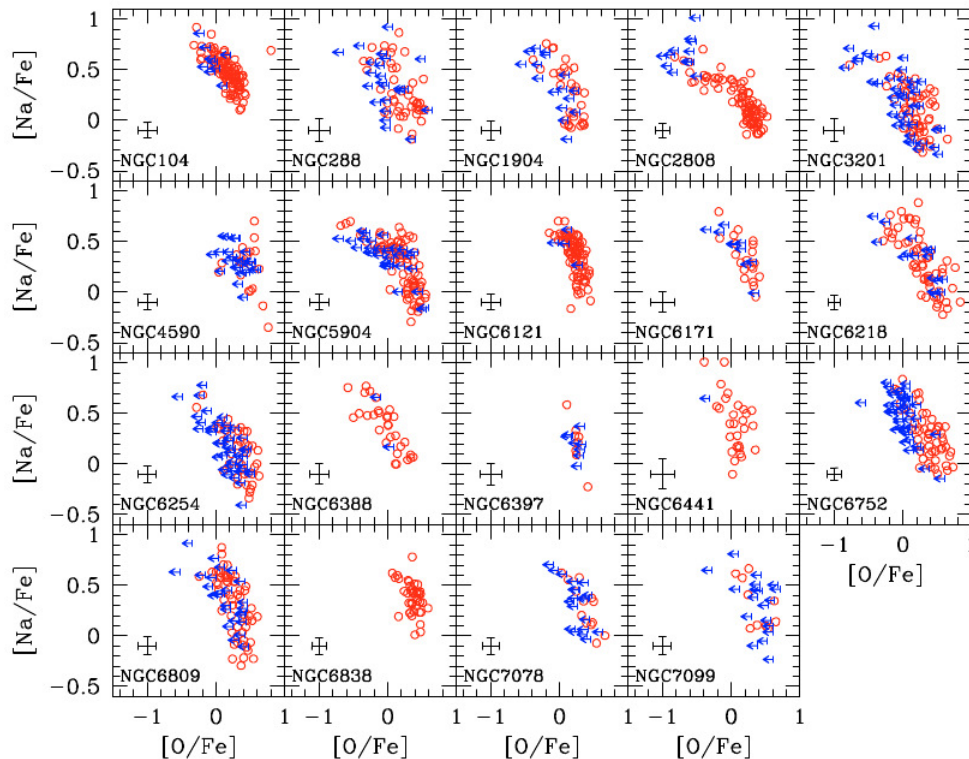


Figure 7.1: The Na-O anticorrelation for various globular clusters. Red points denote VLT Giraffe spectra taken from Carretta et al. (2009b). Blue points denote VLT UVES spectra from Carretta et al. (2009a). The combined data first appeared in Carretta et al. (2010). Reproduced with permission © ESO.

7.2 Oxygen and Sodium in the Low- and Intermediate Metallicity Globular Clusters

7.2.1 M15, M92 and NGC 5466

The massive and bright low-metallicity GCs in M15 and M92 have received much spectroscopic attention whereas their low-mass counterpart, NGC 5466, has been largely ignored. The Na-O anticorrelation was first identified in M15 and M92 by Sneden et al. (1997). Soon afterwards, it was found that the clusters exhibit a similar spread in Na (Sneden et al., 2000). M15 served as one of the target clusters in the Carretta et al. (2010) survey, and we present their findings in Figure 7.1 (M15 is shown as NGC 7078 in this Figure). In addition to the Na-O anticorrelation, stars in M15 display the Mg-Al anticorrelation as well as evidence of efficient CNO burning. Na in M92 stars has been shown to correlate with N and anticorrelate with C (Sneden et al., 2000) suggesting the concurrent operation of CNO cycling and the Ne-Na chains. In addition, Sneden et al. (1991) found that O in M92 can be divided into a high abundance and a low abundance group

which is a further prediction of the enrichment scenario. As Gratton et al. (2004) discuss, it is difficult to identify the Mg-Al anticorrelation in metal poor clusters, and although determined in M15, it is yet to be confirmed in M92 (Shetrone 1996a and Sneden et al. 1997 do provide slight hints).

7.2.2 M3 and M13

Qualitatively the abundance patterns found in the low-metallicity systems are consistent with the current picture of GC chemical evolution. Extra mixing is expected to account for C, N and Li as a function of luminosity (although we were somewhat unsuccessful applying the diffusive formalism of thermohaline mixing) whereas the Na-O and Mg-Al anticorrelations are only possible through hot hydrogen burning in progenitor stars. This scenario is not so clear in M13 where Sneden et al. (2004) and Johnson and Pilachowski (2012) have detected what appears to be a deep mixing event near the RGB tip (Figure 7.3c). The behaviour of oxygen in M13 (see also NGC 2808, Carretta et al. 2006) suggests that the standard primordial-*in situ* picture cannot explain the abundance trends in all GCs.

The O-Na anticorrelation was first detected in M3 and M13 by Kraft et al. (1992, 1993) and Sneden et al. (2004). By analysing the behaviour of the anticorrelation, the authors inferred that the stars in these clusters could be divided into three groups based on their oxygen content. Although similar in many respects, the behaviour of oxygen in these second parameter pairs diverges towards the RGB tip; whereas stars in M3 were consistent with the standard multiple population paradigm, those in M13 display significant depletion. Follow up studies of M13 yielded similar results. Sneden et al. (2004) found six very oxygen poor stars all at a magnitude of $M_V \approx -2.2$ but with a spread in $\Delta[\text{O}/\text{Fe}] = 0.7$ dex. As they justifiably pointed out “It is hard to escape the conclusion that the majority of the brightest M13 giants mix envelope material deep enough into the H-burning shell that significant processing of O to N occurs within the stars themselves.” Their study also demonstrated that brighter giants in M13 tend to be enhanced in Na and Al whilst being depleted in Mg. An expected outcome if the Ne-Na and Mg-Al chains were in operation. We note that M3 demonstrates variations in O, Mg and Al (Sneden et al., 2004; Cohen and Meléndez, 2005; Smith, 2002; Kraft et al., 1992) but these clearly do not correlate with luminosity.

7.3 Resurrecting the Deep Mixing Scenario

The apt title of this section is taken from a line in the paper by Johnson and Pilachowski (2012) who surveyed more than 100 stars in the GC M13. In Figure 7.2 their data are used to reproduce the Na-O anticorrelation in M13. Kraft et al. (1992, 1993) and Sneden et al. (2004) predicted the existence of three groups in the cluster based on the behaviour of oxygen. D’Antona and Caloi (2008), Carretta et al. (2009b) and Johnson and Pilachowski (2012) specify these as the primordial, intermediate and extreme populations. Members of the primordial population (blue circles) are defined as having $[\text{Na}/\text{Fe}] < 0$ and $[\text{O}/\text{Fe}] > 0$ and constitute 15% of the total cluster sample. The intermediate population (lavender circles)

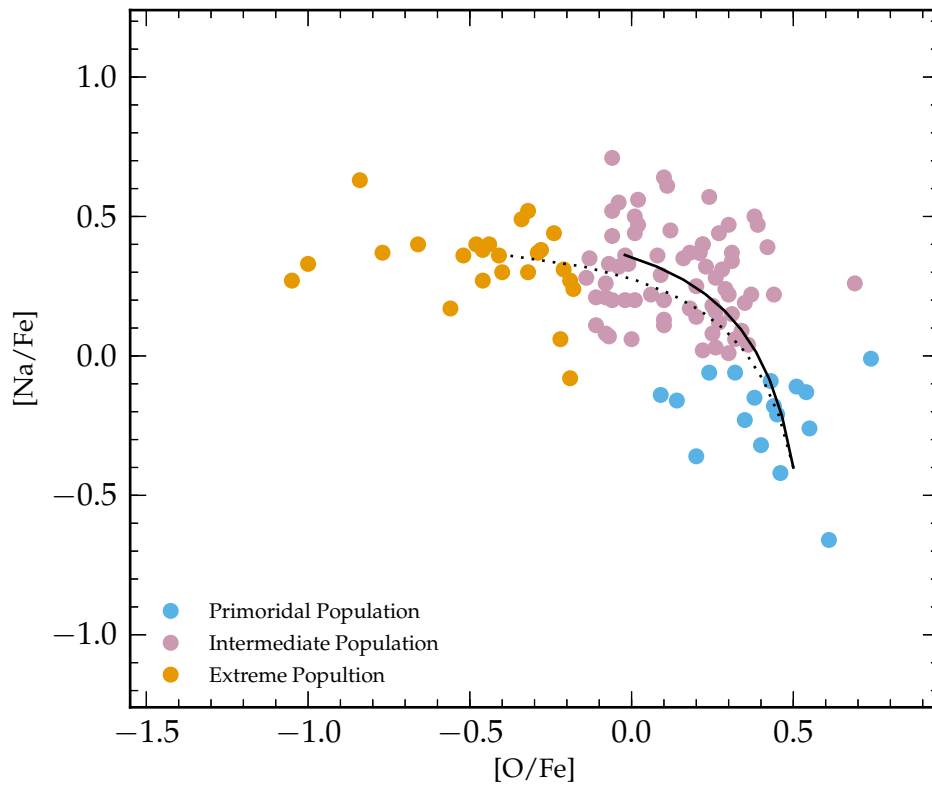


Figure 7.2: $[\text{Na}/\text{Fe}]$ vs $[\text{O}/\text{Fe}]$ in the globular cluster M13. Data are taken from Johnson and Pilachowski (2012) and each star is colour coded according to constituent population (see definition in text). We also include two dilution models for the cluster in an attempt to reproduce the anticorrelation (details of the models are given in text). The black solid line represents the mixture of typical pristine cluster material with the composition of the intermediate population. The dotted line represents the mixture of pristine gas with that from the extreme stars. Both models produce a good fit to the data although the validity of the latter model is undermined if oxygen is depleted *in situ* in the extreme population.

are defined such that $[\text{Na}/\text{Fe}] > 0$ and $[\text{O}/\text{Fe}] > -0.15$ and constitute 63% of the cluster sample. Finally, the extreme population (orange circles) are those stars with $[\text{O}/\text{Fe}] < -0.15$ and make up 22% of the cluster sample. None of the extreme population in Figure 7.2 have been found below the magnitude of the LF bump (see Figure 7.3c, bump denoted by grey line at $M_V \approx 0.55$) and they unexpectedly appear to display a luminosity dependence near the tip of the RGB.

The extreme population were shown to be preferentially the most centrally concentrated of the three groups whilst the primordial are the least centrally concentrated. Such a picture is consistent with GC formation models. The formation scenario for a system with three populations requires the enriched ejecta of the primordial generation to be funnelled into the core of the cluster where the second and extreme populations form. The first generation stars are preferentially stripped from the cluster (up to 90% of the stars from this group) resulting in the observed distribution. Dilution of the ejecta with the pristine gas is also required to reproduce the observed light element abundance trends. In Figure 7.2 we also include two such dilution models for M13 (Prantzos et al., 2007, further details of the model can be found in Chapter 8). Our solid black curve denotes the predicted abundance pattern when pristine material is mixed with the imprinted composition of the intermediate stars. Likewise the dotted curve predicts the abundance pattern if pristine material is mixed with the composition of the extreme population. Both mixing lines (with some spread) provide a satisfactory match to the observed abundances in M13 supporting the need for dilution of material in this cluster. Of course if the oxygen abundance in the extreme population is due to *in situ* processing, then the model represented by the dotted line is not representative of the cluster’s mixing history.

Both Sneden et al. (2004) and Johnson and Pilachowski (2012) have found tentative evidence that the $[\text{O}/\text{Fe}]$ abundance displays a luminosity dependence in the extreme population of M13. Combining data from Figure 6.1 and Johnson and Pilachowski (2012), we reproduce the behaviour in Figure 7.3. In all panels the solid grey line indicates the magnitude of the LF bump as determined by Nataf et al. (2013). This occurs at $M_V \approx 0.55$ in the Figure. Each curve in the panel represents a stellar model which we describe in the next section (thus we ignore panels 7.3e and 7.3f for now). In panel 7.3a we plot $[\text{C}/\text{Fe}]$ data as a function of absolute magnitude from Briley et al. (2004, triangles), Briley et al. (2002, circles), Suntzeff (1981, hexagons), Suntzeff (1981, diamonds) and Smith et al. (1996, squares). In panel 7.3b we plot $[\text{N}/\text{Fe}]$ data as a function of absolute magnitude with the symbols retaining their meaning from panel 7.3a. In panels 7.3c and 7.3d we plot $[\text{O}/\text{Fe}]$ and $[\text{Na}/\text{Fe}]$ as a function of magnitude respectively. Data are taken from Johnson and Pilachowski (2012) and are divided into their populations as per Figure 7.2. Note that we have cross-referenced these stars with the C and N observations. In panels 7.3a and 7.3b the shape and colour (black, green or grey) of each symbol typically identifies the survey from which the data was taken. However, if a target also forms part of the Johnson and Pilachowski (2012) study, then its symbol retains its shape but is coloured according to which of the three populations it belongs. From Figure 7.3c we see that the brightest M13 giants show a relatively large spread in their $[\text{O}/\text{Fe}]$ abundance. The stars

are giving their best impression of having experienced an *in situ* process that depletes oxygen near the RGB tip. The different behaviour identified in M3 and M13 may imply that extra mixing is not a uniform process in every cluster and it is perhaps dependent on (global) stochastic differences between the systems (i.e., chemical composition of the constituent populations, rotation rate of the stars within). Finally we note that none of the AGB stars surveyed by Johnson and Pilachowski (2012) were O-poor. This is consistent with our findings in Campbell et al. (2013) which demonstrated that a majority of second generation stars in GCs fail to make it to the AGB phase of evolution.

7.4 Calculations and Results

A modification to the established picture of GC chemical evolution has been suggested by D’Antona and Ventura (2007) and D’Antona and Caloi (2008) to account for two particularly interesting features of M13:

1. the highly depleted oxygen abundance in stars near the RGB tip,
2. the horizontal branch morphology.

In their scenario, the extreme population are significantly enhanced in helium ($Y = 0.40$) compared to their primordial ($Y = 0.24$) and intermediate ($Y = 0.28$) counterparts. A shallow FDU and smaller μ barrier will allow deeper mixing (proposed with rotational mixing in mind) to process oxygen whilst keeping Na relatively stable due to the paucity of Ne in these second generation stars. The enhanced helium is also necessary to produce the extended blue horizontal branch of the cluster.

We must first ask whether oxygen in the extreme population does in fact display a dependence on luminosity. The surveys of Sneden et al. (2004) and Johnson and Pilachowski (2012) have tentatively supported this conclusion. To date, no (very) O-poor star has been identified below the LF bump. Furthermore, the spread in oxygen does not present itself until the very tip of the RGB as if triggered by a distinct event. We note that in Figure 7.3c there is one point at $M_V \approx -0.5$ and $[O/Fe] = -0.5$ that is an exception. If similar stars are found, it will imply that the spread is (at least) present at all magnitudes beyond the LF bump. The situation remains unclear and we therefore proceed with trepidation in determining whether extra mixing, in particular the thermohaline mechanism, can account for these extreme stars.

7.4.1 Structure and Evolution

Although we already have a set of models to fit $[C/Fe]$ and $[N/Fe]$ abundances in M13, our focus on oxygen have necessitated a new series of calculations for this cluster. If extra mixing is responsible for the significant oxygen depletion, and enhanced helium triggers the extra mixing, then we seek to model a star with oxygen content on the cusp of the extreme and intermediate populations (in Figure

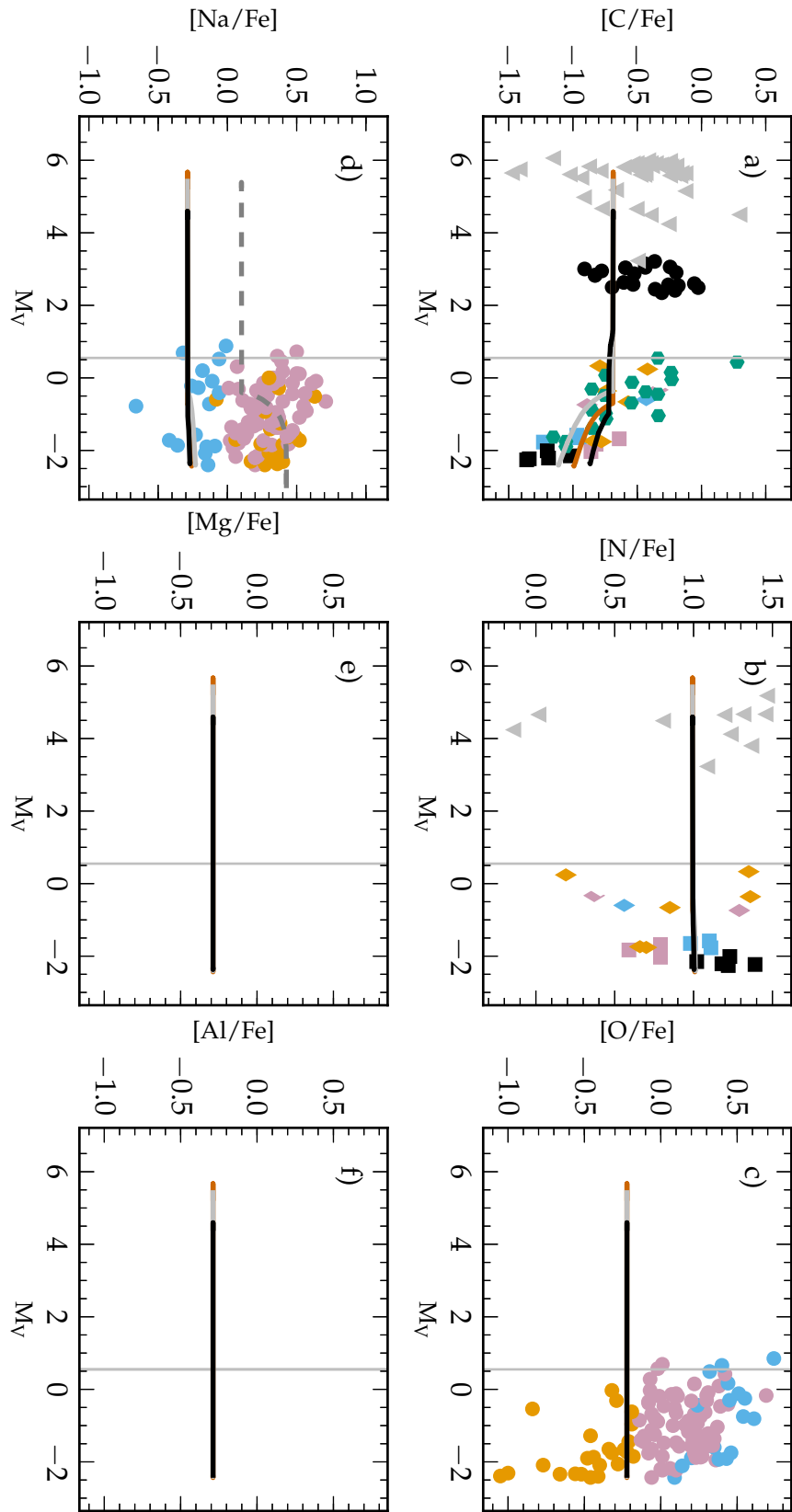


Figure 7.3: From previous page. In all panels the vermilion curve denotes the model of the extreme population star ($M = 0.65 M_{\odot}$, $Y = 0.40$), the grey curve represents the intermediate population star ($M = 0.80 M_{\odot}$, $Y = 0.28$) and the black curve denotes the hybrid model ($M = 0.80 M_{\odot}$, $Y = 0.40$). The vertical grey line indicates the location of the LF bump in M13 as specified by Nataf et al. (2013, $M_V \approx 0.55$). Panel a: $[C/Fe]$ as a function of absolute magnitude with data taken from the sources outlined in Figure 6.1 (see also text for details). Panel b: $[N/Fe]$ as a function of absolute magnitude with data from the same sources as Panel a. Panel c: $[O/Fe]$ as a function of absolute magnitude with data taken from Johnson and Pilachowski (2012). In this panel the colour of the symbols indicate to which population the star belongs as per Figure 7.2. Our models do not predict significant change in the oxygen abundance from thermohaline mixing. Panel d: $[Na/Fe]$ as a function of absolute magnitude. Data for this panel are also taken from Johnson and Pilachowski (2012). We have also included a model (dashed grey curve) that illustrates the spread in Na possible from thermohaline mixing if a large supply of neon is available. Panel e: $[Mg/Fe]$ as a function of absolute magnitude. The temperatures involved with thermohaline mixing are not sufficient to activate this channel. Panel f: $[Al/Fe]$ as a function of absolute magnitude.

7.3, $[Fe/H] \approx 0.20$). A set of calculations with identical CNO, but helium abundance representative of each population will reveal whether thermohaline mixing can form part of the D’Antona and Caloi (2008) paradigm. For our models, we first chose a total C+N+O value from that typically measured by Smith et al. (1996) in M13 stars. From the Johnson and Pilachowski (2012) survey we identified a candidate with $[O/Fe] = -0.22$ which is close enough to the border of both populations for our purposes. This oxygen content was assumed representative of the ZAMS abundance whilst initial C and N abundances were chosen with considerations given to the effects of extra mixing. We set $X(C) = 1.53 \times 10^{-5}$, $X(N) = 2.73 \times 10^{-4}$ and $X(O) = 1.44 \times 10^{-4}$ in all models. Whilst we assume that metallicity $Z = 0.0005$, and thermohaline parameter $C_t = 1000$ is representative of M13, such a large difference in hydrogen abundance between the populations will significantly alter the lifetimes of the stars. If we assume that M13 is ≈ 12 Gyr old, then stars currently evolving on the RGB from the the intermediate population (with $Y = 0.28$) are born with initial mass between $M = 0.75 - 0.80 M_{\odot}$. We have assumed $M = 0.8 M_{\odot}$ to remain somewhat consistent with the models in the previous chapters although $M = 0.75 M_{\odot}$ would be more indicative of these stars. The extreme population, with $Y = 0.40$, must be less massive ($M \approx 0.65 M_{\odot}$). We have considered three combinations of mass and helium content in our calculations which are outlined in Table 7.1.

In Figure 7.4 we present important structural and evolutionary details of the models. In panel 7.4a the evolution across the HR-diagram of the extreme population star (vermilion curve), intermediate population star (grey curve) and star with intermediate population mass but extreme population Y (black curve, included to identify the role of mass and metallicity) are illustrated. Note the slight difference in the core flash luminosity in the enhanced helium models. In panel

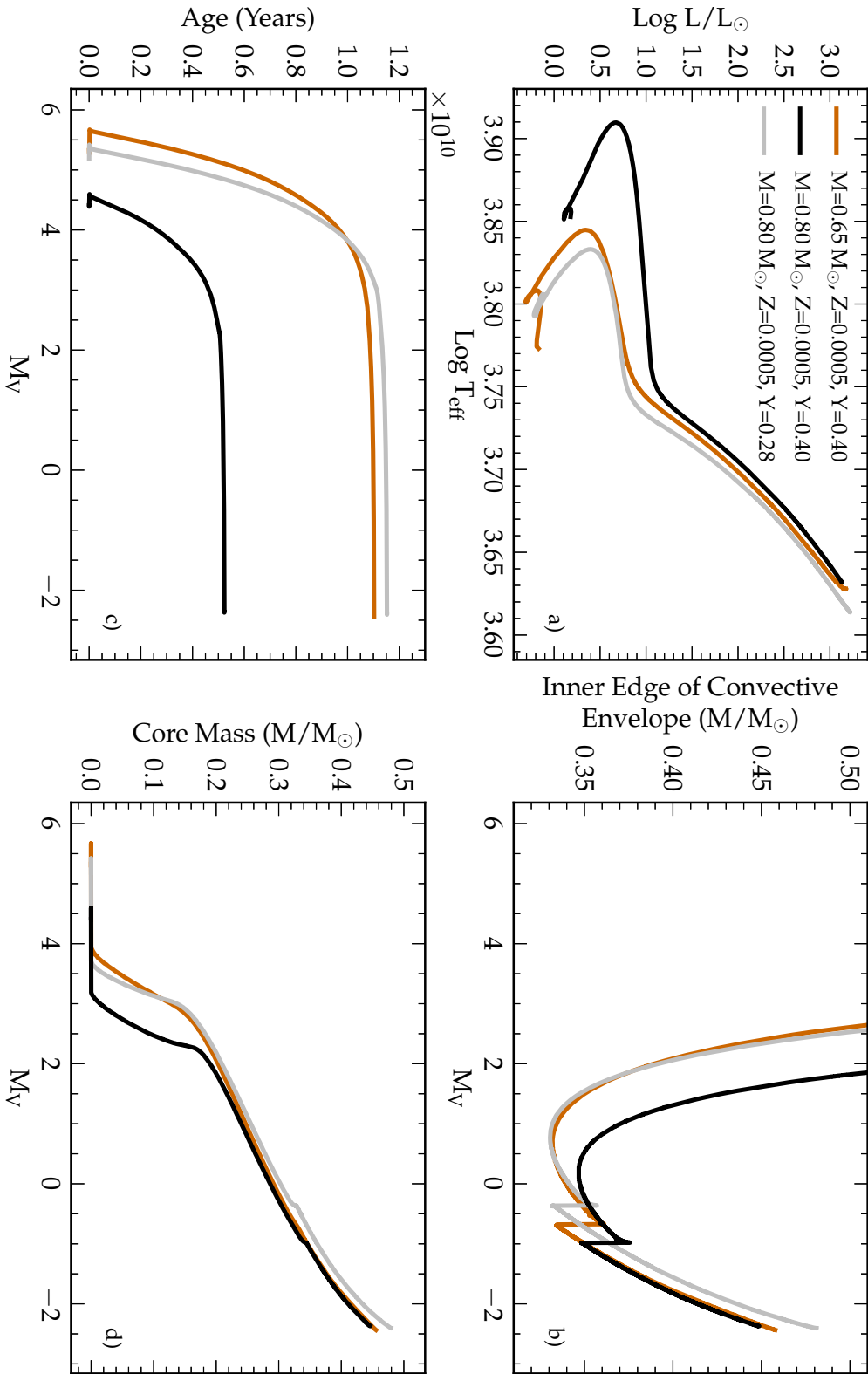


Figure 7.4: From previous page. Key evolutionary details of the intermediate (grey curve) and extreme (vermilion curve) population stars in M13 as well as a star with intermediate population mass but extreme population Y (black curve, included to identify the role of mass and metallicity). Panel a): HR diagram for the calculated models. Panel b): Inner edge of the convective envelope as a function of magnitude. The maximum extent of FDU in each model is illustrated here. Panel c): Age as a function of magnitude for the three stars. Panel d): Core mass and a function of magnitude. The model with $Y=0.28$ has a larger core mass at a given magnitude during the RGB.

Line Style	Mass	X(H)	X(⁴ He)
—	0.65	0.59995	0.40
—	0.80	0.59995	0.40
—	0.80	0.7195	0.28

Table 7.1: Calculations for the models explored in Figures 7.4 and 7.5. In all models $X(C) = 1.53 \times 10^{-5}$, $X(N) = 2.73 \times 10^{-4}$, $X(O) = 1.44 \times 10^{-4}$ $Z=0.0005$ and $C_t = 1000$ are assumed representative of M13.

7.4b the maximum depth of FDU is compared. Recall the previous discussion on the role of the H^- ion on opacity. The higher hydrogen abundance in the intermediate population star results in a deeper penetration of the convective envelope. In panel 7.4c the effect of hydrogen content on stellar lifetime is clearly visible. Whereas our intermediate population star with $M = 0.80 M_\odot$ and $Y = 0.28$ (grey curve) reaches the RGB tip at an age of approximately 11 billion years, the hybrid model with the same mass but $Y = 0.40$ (black curve) does so at an age of approximately five billion years. Although the discrepancy is mostly due to the main-sequence burning lifetime, it does translate to a difference of approximately 450 million years spent on the RGB. The effect of composition is offset by the lower mass star ($M = 0.65 M_\odot$, vermilion curve) which also reaches the RGB tip after approximately 11 billion years (the masses could of course be slightly tweaked if required). Finally, in panel 7.4d the relative core mass at given magnitude is shown for the models. Time spent on the main sequence is obviously the determining factor in the early phase of evolution. However during the RGB, the model with higher hydrogen content is able to maintain a larger core mass for the same luminosity. Naively this does not bode well for our hypothesis as the temperature profile throughout the star is dependent on core mass. However this effect may be offset. Even though the core mass is smaller at a given magnitude, we expect the μ inversion to form closer to the hydrogen burning shell in the extreme population. The enhanced helium in this model creates a larger background μ (i.e., more reactions increasing μ) for the ³He burning to overcome and thus the inversion should develop nearer to the shell.

This is exactly what is found in Figure 7.5 where we plot the mass location

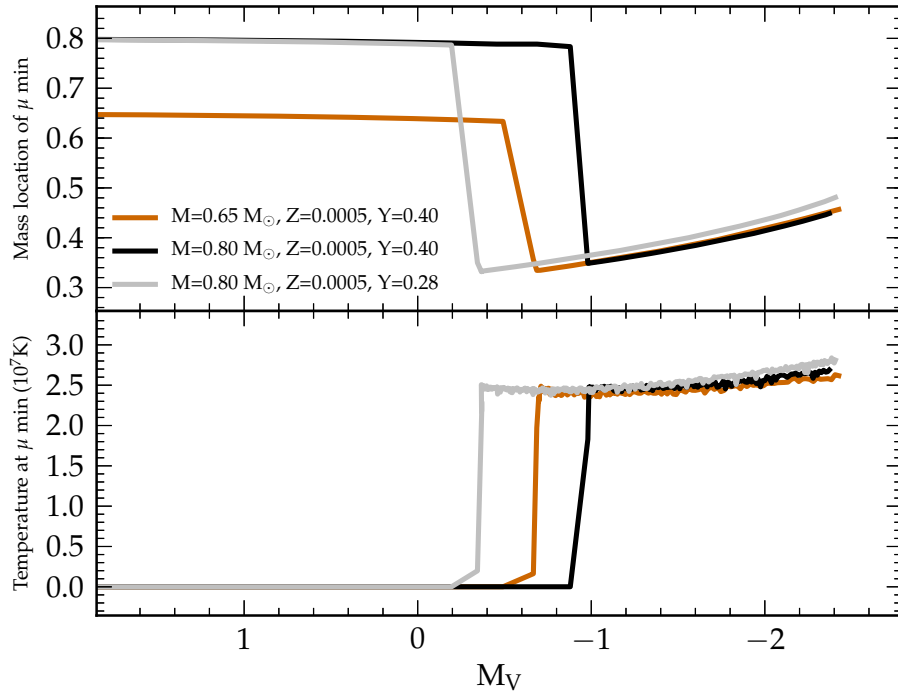


Figure 7.5: Further structural diagnostics of the stellar models. Once again the vermilion curve denotes the evolution of the enhanced helium star ($Y = 0.40$) and the grey curve represents the evolution of the intermediate population star ($Y = 0.28$) and the black curve of a star with intermediate population mass but extreme population Y . Top panel: Mass location of the inversion in the mean molecular weight. In thermohaline mixing the location of the μ inversion sets the mixing depth. Here material is transported closer to the hydrogen burning shell in the stars with $Y = 0.40$. Bottom panel: The corresponding temperature as a function of magnitude. Illustrated is the temperature at the location of the μ inversion. Material in the intermediate population star is exposed to only slightly higher temperatures than in the enhanced helium models.

(top panel) and temperature location (bottom panel) of the μ inversion both as a function of magnitude. The top panel demonstrates that μ inversion develops at a deeper mass location in the enhanced helium models. Material is therefore transported closer to the hydrogen burning shell in these stars. However when we consider the temperature depth, we find material in the two populations are exposed to similar conditions. The difference in core mass (temperature location) and composition (mass location) serve to offset each other in the populations. In fact, we should expect to find more processing in the $Y = 0.28$ case because of the slightly higher temperature exposure. This is not an outcome of the D’Antona and Ventura (2007) paradigm.

7.4.2 Nucleosynthesis

If the behaviour of oxygen at the tip of M13 is really an *in situ* effect then there should be additional nucleosynthetic signatures. As Dearborn (1992) notes, because of the extreme temperature sensitivity of nuclear reactions, relatively sharp boundaries are formed where isotopes are either enhanced or destroyed. In Figure 7.6 we have plotted the reaction rates used in the nucleosynthesis code as a function of temperature for the CNO cycle (top panel), the Ne-Na chains (middle panel) and the Mg-Al chains (bottom panel) as per Iliadis (2007). Whereas Iliadis (2007) normalises these rates to the slowest CNO reaction $^{16}\text{O}(p,\gamma)^{17}\text{F}$, we normalise to the comparatively slow reaction, $^{14}\text{N}(p,\gamma)^{15}\text{O}$, due to our interest in ^{16}O . We indicate with the solid grey line the typical temperature at the μ inversion in the models (25 MK, see Figure 7.5).

From Figure 7.6 we can expect that any cycling of oxygen should be accompanied by production of sodium. The $^{22}\text{Ne}(p,\gamma)^{23}\text{Na}$ reaction is more efficient than $^{16}\text{O}(p,\gamma)^{17}\text{F}$ at the temperatures reached during thermohaline mixing. Whether sodium can be produced on the RGB will depend on the initial neon abundance of the star. Neon enrichment from supernovae will be present in the pristine material from which the primordial population form. However, during the latter stages of burning, the stars will have processed most of the neon into the sodium that gives rise to the anticorrelation.

Due to our interest in the trace elements in this cluster, we have post processed the three stellar models with MONSOON. We employ an 84 species network to follow all hydrogen-burning reactions including the possible activation of Mg-Al chains. Save for the six species calculated in the evolution code (H ^3He , ^4He , ^{12}C , ^{14}N , ^{16}O), all other initial abundances are solar scaled as a first approximation. The high C+N+O content of the star we have based our models upon resulted in further scaling of the trace nuclei to ensure that the metallicity remained at $Z = 0.0005$. The initial abundance for each isotope can be found in Appendix D.

As we have discussed in Part II, the evolution code, MONSTAR, and nucleosynthesis code, MONSOON, have distinct mixing schemes. MONSOON's algorithm requires a mixing length, l , and a mixing velocity, v , which are determined from MONSTAR. In convective regions, MONSTAR calculates v and l through MLT. The values are written out for MONSOON but combined to give a diffusion coefficient ($D = 1/3vl$) for its own diffusive mixing algorithm. In thermohaline regions however, MONSTAR calculates a diffusion coefficient as per Equation 3.21. We approximate the mixing length in these regions by $l = \alpha_{MLT} \times H_P$ to determine an indicative velocity. In order to remain consistent with the predictions of MONSTAR and the diffusive paradigm, a degree of calibration is required. We multiply the v and decrease l by a factor of 1.5 so that both codes calculate the same abundances of Li and ^3He . Note that our conversion from a diffusion coefficient to v and l involves a geometric factor of $1/3$ (coming from our assumptions of spherical symmetry). The mixing length we provide is also only an approximation so the need for this factor is perhaps not unexpected. Whether the diffusion approximation reproduces the correct behaviour of the material is another question all together, and it will hopefully serve as a basis for future work. For this study we

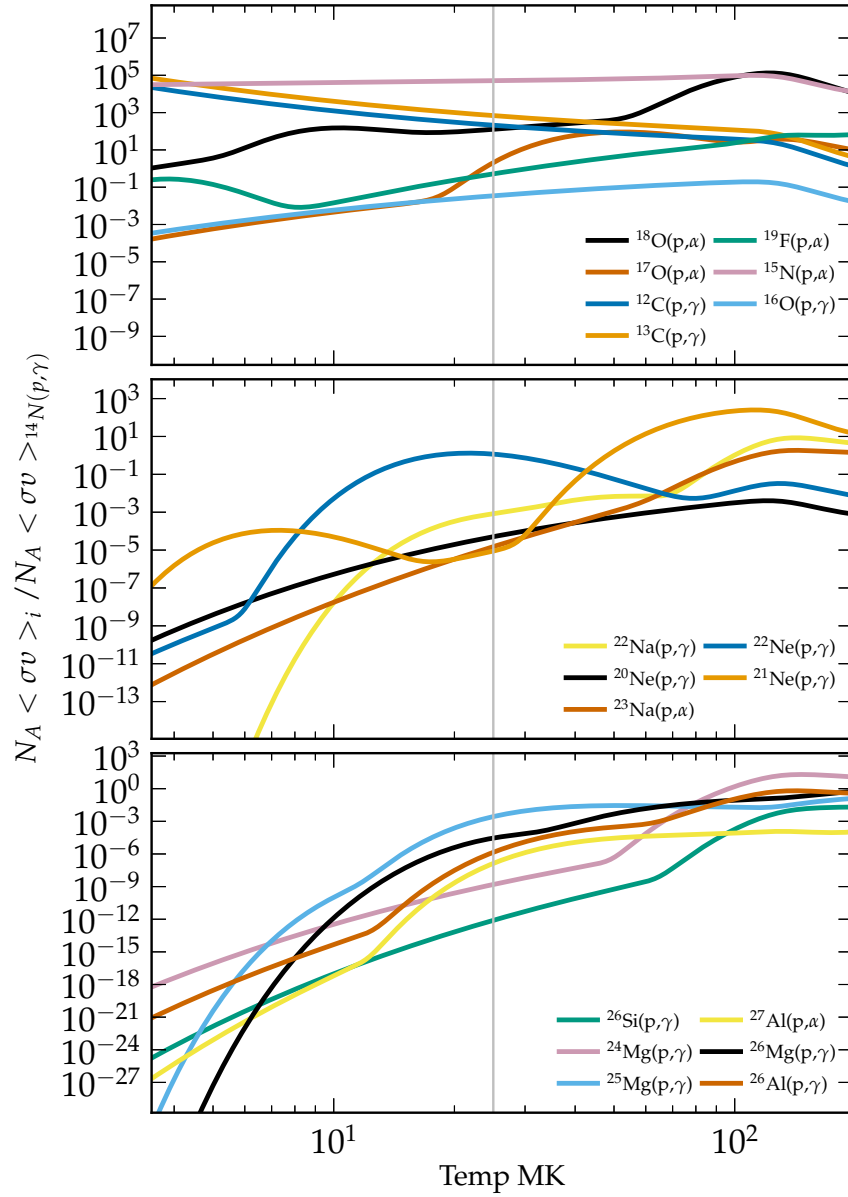


Figure 7.6: Top panel: Reaction rates for the CNO nuclei. Middle panel: Reaction rates for the Ne-Na chains/cycles. Bottom panel: Reaction rates of the Mg-Al chains/cycle. All reactions have been normalised to the $^{14}\text{N}(p,\gamma)$ ^{15}O rate which is one of the slowest CNO channels. The solid grey line in each panel marks 25 MK, the typical temperature to which material is exposed during thermohaline mixing in M13 (see Figure 7.5).

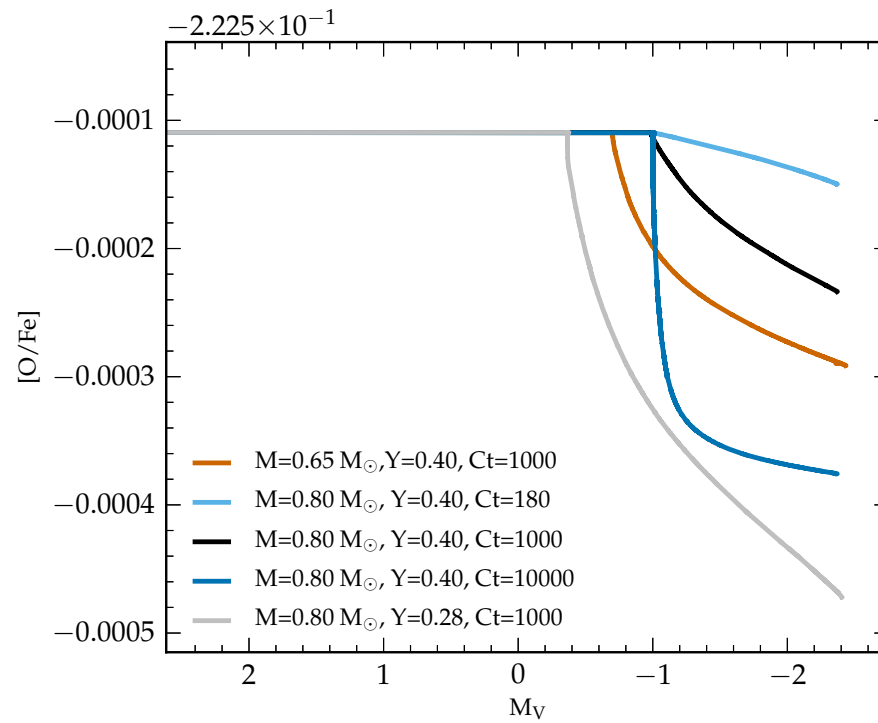


Figure 7.7: $[O/Fe]$ as a function of M_V for models of the GC M13. Note the small scale of the y-axis.

assume that the paradigm is valid.

7.4.3 Discussion

In Figure 7.3 we have included the post-processed stellar models along with the observational data described in §7.3. The models retain their symbols from §7.4.1 where the vermilion curve denotes the enhanced helium star ($M = 0.65 M_{\odot}$, $Y = 0.40$) and the grey curve represents the intermediate population star ($M = 0.80 M_{\odot}$, $Y = 0.28$) and the black curve denotes the hybrid model ($M = 0.80 M_{\odot}$, $Y = 0.40$). From panel 7.3a our assertion that processing will be most efficient in the $Y = 0.28$ model is justified. The intermediate population star, with the higher temperature at the location of the μ inversion, has indeed depleted more carbon and consequently produced more nitrogen than the enhanced helium models. We note that although these models begin to process carbon and nitrogen at a magnitude that is consistent with the spectroscopic data, they in fact disagree with the photometric location of the LF bump in this cluster. The discrepancy is not dissimilar to those issues discovered with the low-metallicity clusters in the previous chapter. We must therefore consider possible systematic uncertainties in our modelling. This issue is addressed in Part IV.

Panel 7.3c reveals that very little oxygen processing has taken place in the models. This is consistent with previous studies of the instability and expected from the preliminary structure details (Figures 7.4 and 7.5). The extent of oxygen depletion is better determined from Figure 7.7 where we focus on the region of interest. Included in this Figure are variations of the C_t parameter for our hybrid model. Although they illustrate that further processing of oxygen is possible, the result is moot given the negligible abundances involved.

Our examination of the reaction rates in Figure 7.6 suggested that sodium production will be more efficient than O destruction in our models and this is indeed the case. Panel 7.3d demonstrates a slight increase in Na due to thermohaline mixing. In this panel we have included a fourth model to illustrate the effect of initial abundance on the possible spread in sodium. Here we have post processed one of our CN strong models from Chapter 6. The evolutionary calculations were carried out with the following initial $X(C) = 7.7 \times 10^{-6}$, $X(N) = 8.8 \times 10^{-5}$ and $X(O) = 2.4 \times 10^{-4}$. We kept these values for the post processing calculations which is denoted by the dashed grey curve. In this nitrogen enhanced model the total $X(C+N+O) = 3.36 \times 10^{-4}$ which comes from scaling the solar abundance. In order to match observations of the CN-strong stars in M3, the total C+N+O abundance was kept constant but the abundance ratio of the three elements altered. For models calculated in the current Chapter, $X(C+N+O) = 4.32 \times 10^{-4}$ which was determined from the observations by Smith et al. (1996). Intuitively, the C+N+O in these calculations is probably too high. The condition that metallicity $Z = 0.0005$ requires all other trace nuclei to be highly sub-solar scaled initially. When a lower C+N+O content is considered, we find that a large spread in sodium is possible from thermohaline mixing (≈ 0.5 dex). The presence of a neon reservoir and exposure to the relevant burning conditions providing a means for sodium production in these models. Whilst such signatures are most certainly possible in

the primordial generation, the intermediate and extreme populations are expected to be neon-poor. The progenitors that produce the cluster enrichment presumably process their residual neon in producing the Na-O anticorrelation. Their ejecta, devoid of neon, will mix with the cluster gas from which the second generation stars form. The intermediate and extreme stars therefore form with a neon content that is diluted compared to the pristine abundance. This is why D’Antona and Ventura (2007) expect the responsible mixing mechanism to substantially deplete oxygen whilst keeping sodium stable. In panels 7.3e and 7.3f we plot $[\text{Mg}/\text{Fe}]$ and $[\text{Al}/\text{Fe}]$ as a function of magnitude respectively. As suggested by the bottom panel in Figure 7.6 any processing of Mg and Al is negligible at this temperature.

The paradigm advocated by D’Antona and Ventura (2007) to explain M13 requires that the stars most depleted in oxygen are necessarily enhanced in helium. The high helium content is responsible for the horizontal branch morphology and the ability of these extreme stars to mix deeper than their intermediate and primordial counterparts. With less hydrogen in their envelope and therefore a reduced source of opacity, they experience a shallow FDU and smaller μ barrier to inhibit extra mixing. Rotation, or a mechanism of the like, is then thought to transport material into regions where oxygen is processed. As the extreme stars are second generation members, the paucity of neon in their envelope prohibits the production of sodium which would normally accompany ON cycling. It is clear that the mechanism responsible for the oxygen depletion in M13 cannot be attributed to thermohaline mixing. Not only do we predict that the intermediate population are more efficient at mixing, but also that the mechanism cannot transport material to the temperatures required for ON cycling.

It may be possible that material overshoots the μ inversion (Denissenkov and Pinsonneault, 2008b), although we have seen from Figure 2.9 that the conditions beyond this are quite stabilising. The stars may be offering us a hint as to the cause of the mixing. Peterson (1983) has shown that stars on the horizontal branch of M13 rotate about twice as fast as those on the horizontal branch of M3. This may argue for a rotational based instability. The removal of the μ barrier is usually sufficient to initiate extra mixing however the large spread in oxygen is not apparent until the very tip of the RGB. One would expect that towards the tip of the RGB, the mass loss rate increases whilst rotation rates conversely decreases. This type of mixing should be more efficient in earlier epochs rather than later. Unfortunately, our investigation has offered little in the way of scientific progress. Our results simply rule out thermohaline mixing as the sole cause (perhaps the interaction of mixing mechanisms is required) of oxygen depletion in M13. This in itself is not surprising and is consistent with previous investigations of the mechanism (Eggleton et al., 2008). It is still unclear whether the process is in fact occurring *in situ* and we are unable to offer any evidence for or against the D’Antona and Ventura (2007) paradigm.

7.5 Conclusions

In our studies of GCs consistency seems to be the exception rather than the rule. Whereas our theory of extra mixing did not reproduce the evolution of $[\text{C}/\text{Fe}]$ or $[\text{N}/\text{Fe}]$ with luminosity in the low-metallicity systems, the behaviour of the high temperature p-capture elements adhered to the predictions of the multiple population scenario. Conversely, in the intermediate-metallicity systems (in particular M13), C and N were well explained by thermohaline mixing but the high temperature p-capture nuclei displayed unexpected variation near the RGB tip which this mechanism cannot account for. In this chapter we tested thermohaline mixing within the paradigm advocated by D’Antona and Ventura (2007). We summarise our findings as follows:

- Thermohaline mixing is unable to account for the O-poor stars near the RGB tip of M13.
- Contrary to the requirements of the paradigm, thermohaline mixing predicts that the intermediate population stars ($Y = 0.28$) process more material than the extreme population ($Y = 0.40$).
- Changes to the oxygen, magnesium and aluminium abundances are negligible.
- The (tiny) processing of oxygen is transport limited at $C_t = 1000$.
- The $^{22}\text{Ne}(p,\gamma)^{23}\text{Na}$ reaction can produce a spread in sodium of ≈ 0.5 dex provided there is sufficient initial neon in the star.
- Possible systematic errors in the stellar models must be a consideration.

In Chapter 7 it appeared that our calculations of M3 and M13 were well modelled by thermohaline mixing. The magnitude at which extra mixing was predicted to begin agreed with spectroscopy. The models provided an envelope to the $[\text{C}/\text{Fe}]$ data but required the large spread in $[\text{N}/\text{Fe}]$ to be predominately primordial in origin rather than an outcome of extra mixing. In Figure 7.3 the inclusion of the LF bump from Nataf et al. (2013, $M_V \approx 0.55$) undermines the previous attributed success of the models. In M13 there is at least some agreement with the spectroscopy whereas in the low-metallicity clusters, the photometry and spectroscopy both are inconsistent with the models. There seems to be some evidence for a systematic modelling issue. Determining whether this is the case and to what extent will serve as one of the foci in Part IV where mid-to-high resolution observations of lithium are used to constrain the stellar models.

Part IV

Lithium in Globular Cluster Stars

Monash University

Declaration for Thesis Chapter 8

Declaration by Candidate

In the case of Chapter 8, a significant part of this work was submitted as:

D’Orazi, V., Angelou, G. C., Gratton, R. G., Lattanzio, J. C, Bragaglia, A., Carretta, E., Lucatello, S., and Momany, Y. (2014). Lithium Abundances in Globular Cluster Giants: NGC 6218 (M12) and NGC 5904 (M5).

The nature and extent of my contribution to the work was the following:

Nature of contribution	Extent of contribution (%)
Secondary research and significant paper writing	30%

The following co-authors contributed to the work, none of whom are students at Monash University.

Name	Nature of contribution
Dr Valentina D’Orazi	Primary research and paper writing
Prof. John Lattanzio	Consultation and revision
Prof. Raffaele Gratton	Consultation and revision
Dr. Angela Bragaglia	Consultation and revision
Dr. Eugenio Carretta	Consultation and revision
Dr. Sara Lucatello	Consultation and revision
Dr. Yazan Momany	Consultation and revision

The undersigned hereby certify that the above declaration correctly reflects the nature and extent of the candidates and co-authors contributions to this work

Candidate’s  **Signature** _____ **Date** 28-Aug-2014

Supervisor’s  **Signature** _____ **Date** 28-Aug-2014

Chapter 8

Lithium abundances in globular cluster giants: NGC 6218 (M12) and NGC 5904 (M5)

There is no royal road to science, and only those who do not dread the fatiguing climb of its steep paths have a chance of gaining its luminous summits.

- Karl Marx

8.1 Introduction

No longer considered simple stellar populations, globular clusters (GCs) are at the crux of several unresolved problems in stellar astrophysics. Accurate photometric surveys have revealed that some clusters display multiple evolutionary sequences, from the main-sequence (MS), to the sub-giant and red-giant branches (SGB and RGB, see e.g., Bedin et al. 2004; Anderson et al. 2009; Piotto et al. 2012; Milone et al. 2012). The simplest interpretation is that there are (at least) two stellar generations present, slightly separated in age and characterised by a different chemical composition (see, however, Bastian et al. 2013 for a different view). Although the presence of multiple populations is now clear through clever use of multi-filter photometry, the seeds for the paradigm shift were planted by high-resolution spectroscopy and detailed abundance determinations across a large sample of GCs (e.g., Gratton et al. 2004; Carretta et al. 2009b, 2009a, 2011, 2013b; Marino et al. 2008, 2011; Johnson and Pilachowski 2010).

In contrast to field stars and open clusters (e.g., Gratton et al. 2000; de Silva et al. 2009; Bragaglia et al. 2012), archetypal GCs exhibit internal variations in elements affected by proton-capture processes (hereafter p-capture elements, such as e.g., C, N, O, F, Na, Mg, Al), but remain homogeneous in iron-peak, heavy α (Ca, Ti), and neutron-capture elements (e.g., James et al. 2004; Smith 2008;

D’Orazi et al. 2010a).¹

The burning patterns give rise to the well known light-element anticorrelations (C-N, O-Na, Mg-Al), with the Na-O anticorrelation suggested as the GC’s defining feature (Carretta et al. 2010). The fact that these chemical peculiarities are detected also in un-evolved or scarcely evolved GC stars (Gratton et al. 2001; Ramírez and Cohen 2002) implies that a fraction of first-generation (FG) stars have activated CNO, NeNa, and (possibly) MgAl cycles in their interiors in order to deplete C, O and Mg and enhance N, Na and Al, respectively. From the ejecta of these progenitors, the second-generation (SG) stars were born and currently account for the majority of the GC population (about 2/3, see Carretta et al. 2010). Unfortunately, the nature of the progenitors responsible for the internal chemical enrichment remains unclear. Intermediate-mass asymptotic giant branch stars (IM-AGB, Cottrell and Da Costa 1981; Ventura et al. 2001) and fast rotating massive stars (FRMS, Decressin et al. 2007) remain the prime candidates, although neither offer a satisfactory explanation (we refer to Gratton et al. 2012a for an updated and comprehensive review on the multiple population framework).

Besides the imprinted abundance patterns in GCs, lighter nuclei such as ${}^7\text{Li}$, C and N display evidence of *in situ* processing; their abundances change as a function of RGB luminosity (beyond the extent of the first-dredge up, FDU). This is not predicted by standard stellar theory and is one example of the need for ‘extra mixing’ in numerical models.

Surveys of C and N in GCs have been used extensively to study the RGB extra-mixing problem (Denissenkov and Vandenberg, 2003; Angelou et al., 2011, 2012) but the recent availability of Li provides a complementary and very powerful diagnostic. By virtue of its fragility, Li is a sensitive probe of mixing in stars. It is produced during H burning when ${}^7\text{Be}$ captures an electron as part of the *pp* II chain. At these temperatures ($T \gtrsim 2$ MK), it is also highly favourable for ${}^7\text{Li}$ to subsequently capture a proton to produce two ${}^4\text{He}$ nuclei. As first pointed out by Cameron and Fowler (1971), efficient mixing in the burning region can transport the material rich in ${}^7\text{Be}$ to cooler temperatures where a further proton capture is avoided. This is the so called “Cameron-Fowler ${}^7\text{Be}$ transport mechanism”. Conversely, ${}^7\text{Li}$ is easily destroyed whenever material is transported from the cool surface to the interior of the star. The surface Li abundance serves as a key indicator for either of these internal processes.

Lithium finds itself at the centre of another long standing discrepancy, that is its abundance, as measured in Population II dwarfs, is factors of 2-3 lower than that predicted by Big Bang nucleosynthesis (e.g., Cyburt et al. 2008). Currently, the favoured explanation for this inconsistency is that the stars themselves are responsible for the depletion via a different kind of process driven by a different mechanism (such as atomic diffusion, i.e., the transport of chemicals due to temperature, pressure and abundance gradients; see e.g., Richard et al. 2005). To date, this cosmological problem has served as the prime motivation for obtaining Li abundances in GC dwarfs (Pasquini et al. 2005; Bonifacio et al. 2007; Lind et al.

¹This picture is further complicated by the presence in the large GC family of some peculiar cases (e.g., ω Centauri, M 22, NGC 1851, M15, Terzan 5, NGC 2419), where variations in metallicity and/or heavy-elements are detected (though at a different level).

2009; Gonzalez et al. 2009; Mucciarelli et al. 2011, and references therein).

D’Orazi & Marino (2010, hereafter DM10) examined the Li abundances in the mildly metal-poor GC NGC 6121 (M4, $[\text{Fe}/\text{H}] = -1.16$, Harris 1996, updated in 2010), but focussed on giant stars (104 RGB stars with 32 targets located below the bump luminosity). The shift in scientific motivation encouraged a shift in target selection: rather than investigate the Spite Plateau (Spite and Spite 1982) and hence un-evolved stars, the purpose of their study was twofold:

- Constrain the nature of the first (polluting) generation of stars in the cluster. At the high temperatures at which the CNO occurs ($T \gtrsim 20$ MK) it is expected that Li is completely destroyed ($T_{\text{burning}} \approx 2.5$ MK). Thus, along with displaying the O-Na, C-N, and possibly Mg-Al anticorrelations, the multiple population scenario predicts that Li and O/C/Mg should be positively correlated, while Li and Na/N/Al anticorrelated (if no Li is produced by the polluters). The FG stars should be Li rich, whereas stars formed from the ejecta processed at extremely high temperatures should be Li poor.
- Under the assumption that there is no Li production within the polluters, shed light on the dilution process within this GC and try to determine the amount of pristine (and of polluted) material present in each star.

For both these goals, any stars not yet experiencing extra mixing are suitable targets. Although Li is depleted by a factor of ≈ 20 during FDU, the abundance change is simply considered a zero-point offset because FG and SG stars are affected in the same way². Thus, DM10 could afford to turn their attention to brighter targets, provided the stars were situated below the bump in the luminosity function (LF bump). Their main finding was the lack of a Li-Na anticorrelation in M4 with the FG (Na poor, $A(\text{Li}) = 1.34 \pm 0.04$) and SG (Na rich, $A(\text{Li}) = 1.38 \pm 0.04$) sharing the same Li abundance. The implications are that Li has been produced between the different stellar generations and, crucially, this abundance pattern is not an outcome of dilution processes with primordial material. This striking result requires the progenitors to produce Li, an outcome which is not currently predicted by massive star evolution (Decressin et al., 2007) or massive binaries (Bastian et al., 2013). DM10 therefore provided, for the first time, strong observational evidence that IM-AGB stars seem to play a significant role in the internal enrichment of GCs (at least in this system).

In this study we expand upon previous results and present Li abundances in the GCs NGC 6218 (M12) and NGC 5904 (M5). Our approach, which focuses on stars brighter than the turn-off, allows us to target more distant systems, whereas previous studies were forced to analyse the near-by GCs (M4, NGC 6397 and 47

²Models in an upcoming paper (Angelou et al. 2014) demonstrate that such an assumption is plausible. Calculations of FG stars ($M = 0.80 M_{\odot}$, $Y = 0.24$) and an extreme population ($M = 0.80 M_{\odot}$ and $Y = 0.40$) exhibit a difference in $A(\text{Li}) \sim 0.1$ dex after FDU, on account of a slightly deeper penetration of the convective envelope. We expect that if a star is still visible on the giant branch and has such an extreme helium abundance it must necessarily be less massive ($M \lesssim 0.65 M_{\odot}$). In such a star the difference in $A(\text{Li})$ is smaller than 0.1 dex after FDU. Even by selecting an unreasonably extreme mass and composition the models predict a difference in Li within the observational uncertainty. See also Chapters 7 and 9

Tuc). M12 and M5 were specifically chosen to improve our understanding of Li across the GC mass and metallicity distributions. Both clusters are similar in metallicity (and they are similar to M4) but they differ significantly in mass. We note that in NGC 6218, Carretta et al. (2007) detected that stars brighter than the LF bump possess statistically higher Na than those below. This is an expected result from the presence of two populations with distinct He abundances and hence different bump luminosities (Salaris et al. 2006).

This work is part of a long-term project aimed at determining homogeneous Li abundances at all RGB luminosities (hundreds of stars) in a large number of GCs. Clusters covering a range in mass, metallicity, HB morphology and shape/extent of the Na-O anticorrelation are required to probe the relationship between the Li abundance and the GC global parameters. Besides the scientific motivation addressed in this study, such a data set will also provide stringent constraints on stellar evolution and mixing processes in stars.

The paper is organised as follows: in Section 8.2 we provide information on sample, data reduction and abundance analysis; our results are presented and discussed in Section 8.3. A summary of our findings concludes the manuscript (Section 8.4).

8.2 Observations, data reduction and analysis

We utilised the multi-object FLAMES@VLT facility (Pasquini et al. 2002) to collect intermediate-resolution spectra of RGB stars, both below and above the bump luminosity, in our target clusters (Program: 087.2-0276(A), PI: VD). Employing the HR15N setup, our wavelength coverage included the Li I doublet at 6707.78\AA with a nominal resolution of $R=17,000$. We observed a total of 72 stars in NGC 6218 and 113 stars in NGC 5904 using this configuration. The sample was selected from the photometric catalogues provided by Momany et al. (private communication). We imposed that targets lack companions within $3''$ or with companions but not closer than $2''$ and fainter than 2 magnitudes. We refer to Momany et al. (2003, 2004) for details about photometric data reduction and analysis. The colour-magnitude diagrams for both GCs is shown in Fig. 8.1, with target stars emboldened. The spectroscopic data reduction was performed by the ESO personnel through the dedicated software that produces extracted, bias subtracted, flat-field corrected and wavelength calibrated spectra. In addition, continuum normalisation, radial velocity computation, shift to rest-frame and combination of multiple exposures were all carried out within IRAF³. The typical S/N ratios (per pixel) of our target stars range from 60 - 150 at 6700\AA .

From the original sample, we discarded 4 stars in NGC 6218 and 6 stars in NGC 5904 as their radial velocities were more than 3σ away from the respective cluster mean. We derived heliocentric radial velocities of $v_{rad} = -43.31 \pm 0.41 \text{ km s}^{-1}$ (r.m.s = 3.35 km s^{-1} , 68 stars for NGC 6218) and $v_{rad} = 53.05 \pm 0.51 \text{ km s}^{-1}$

³IRAF is the Image Reduction and Analysis Facility, a general purpose software system for the reduction and analysis of astronomical data. IRAF is written and supported by National Optical Astronomy Observatories (NOAO) in Tucson, Arizona.

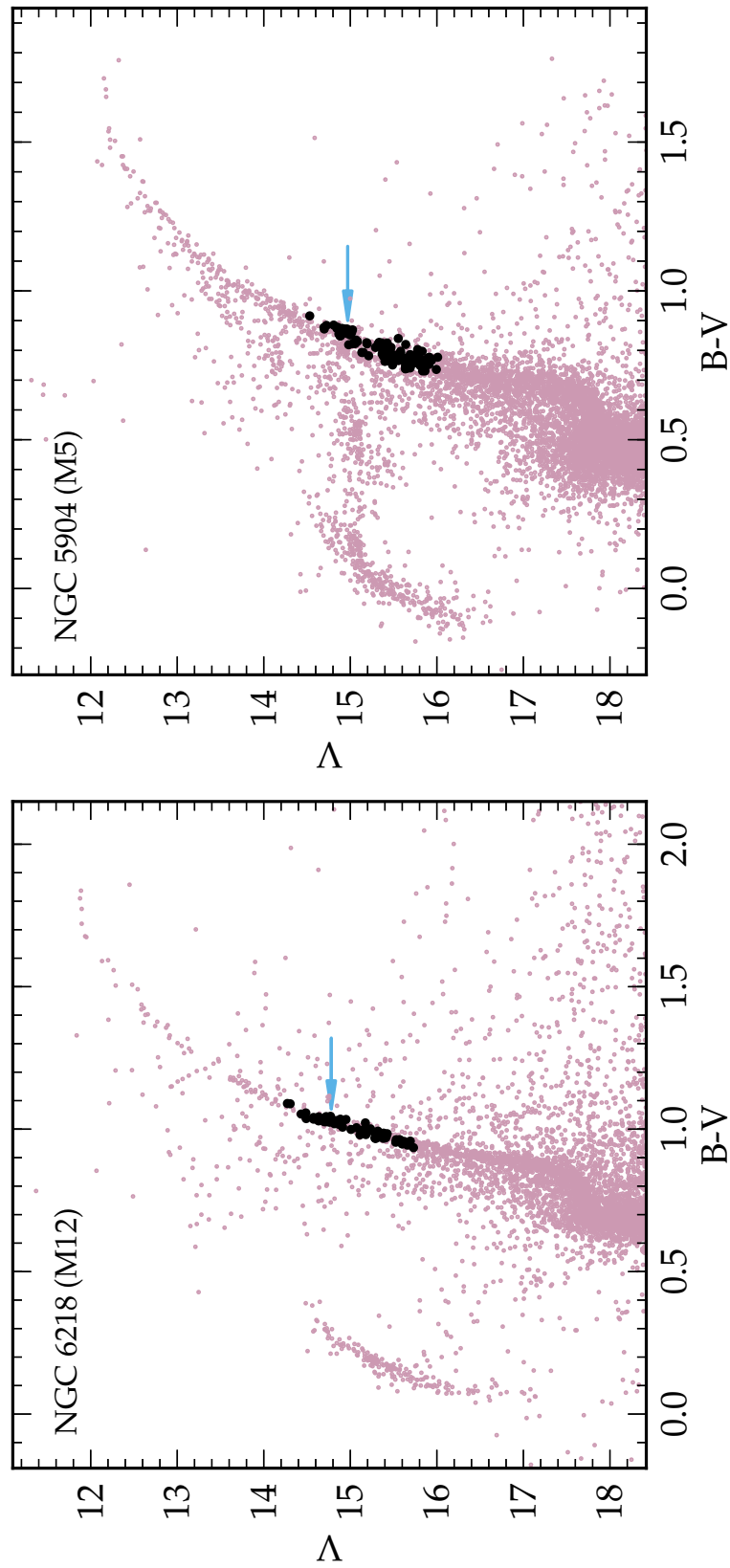


Figure 8.1: The colour-magnitude diagrams for the GCs M12 and M5 (left and right-hand panels, respectively). Stars targeted during this survey are emboldened. The arrows indicate the location of the LF bump from Nataf et al. (2013).

(r.m.s = 5.22 km s⁻¹, 107 stars NGC 5904), which are in reasonable agreement, in view of the zero point uncertainties, with values published by Harris (1996), that is $v_{rad} = -41.4 \pm 0.2$ km s⁻¹ and $v_{rad} = 53.2 \pm 0.4$ km s⁻¹.

The stellar atmospheric parameters for our sample stars were derived in the following way. We first calculated initial T_{eff} values from $(V - K)$ colours (with V from our photometry and 2MASS K magnitudes, Skrutskie et al. 2006) and the calibration by Alonso et al. (1999); metallicity and reddening were retrieved from the Harris’ catalogue, that is $[\text{Fe}/\text{H}] = -1.33$ and $E(B - V) = 0.19$ for NGC 6218, and $[\text{Fe}/\text{H}] = -1.29$ and $E(B - V) = 0.03$ for NGC 5904. The reddening values were converted to $E(V - K)$ via the relationship by Cardelli et al. (1989), i.e., $E(V - K) = 2.75 \times E(B - V)$. Our final adopted temperatures come from a relationship between those T_{eff} values and V magnitudes, following the same approach as in Carretta et al., (2006; 2009b). To derive this relation, we used only “well-behaved” stars in each cluster, that is stars with magnitudes in both visual and infrared filters (keeping only high-quality flagged 2MASS photometry), and lying on the RGB. Comparing the stars in common between the present study and Carretta et al. (2007, 2009b) we obtained a difference (in the sense ours *minus* Carretta) of $\Delta T_{\text{eff}} = -52 \pm 8$ K and $\Delta T_{\text{eff}} = 4.84 \pm 2.22$ for NGC 6218 and NGC 5904. The larger difference for NGC 6218 is likely related to the different photometric catalogue adopted by Carretta et al. (2007). Surface gravities ($\log g$) were then derived by assuming our final T_{eff} values, distance moduli of $(m - M)_V = 14.04$ and $(m - M)_V = 14.46$ (Harris 1996), a bolometric solar magnitude of $M_{\text{bol},\odot} = 4.75$, and masses of $0.85 M_{\odot}$, with the standard formula:

$$\log \frac{g}{g_{\odot}} = \log \frac{M}{M_{\odot}} - \log \frac{L}{L_{\odot}} + 4 \log \frac{T_{\text{eff}}}{T_{\text{eff},\odot}}$$

Finally, microturbulence velocities (ξ) were computed from the relationship by Gratton et al. (1996): $\xi = 2.22 - 0.322 \times \log g$, while the input metallicity was taken from Harris (1996).

The Li abundances were inferred via spectral synthesis with the driver *synth* in MOOG (Snedden 1973, 2013 version) and stellar atmospheres by Castelli and Kurucz (2004), with α -enhancement (+0.4 dex) and no overshooting⁴. We investigated the impact of this choice by deriving Li abundances for all our sample stars using three different sets of atmospheric models, namely the Kurucz (1993) grid with and without overshooting and Castelli & Kurucz (2004) with solar-scaled composition (i.e., no α -enhancement). The differences in the derived Li abundances are always smaller than 0.05 dex and can be safely considered as negligible. Adopting the same line lists as in DM10 (see D’Orazi et al. 2010b and DM10 for details on atomic parameters), we computed a grid of synthetic spectra for each star by varying the Li abundances until the best match between observed and synthetic profiles was attained. The synthetic spectra were calculated covering a wavelength range from 6695Å to 6722Å, exploiting the strong Ca I line at 6717.69Å to evaluate the spectral broadening (which was assumed to be Gaussian). We were able to determine the Li abundances for 63 stars for NGC 6218 and 99 stars for NGC

⁴Available at <http://kurucz.harvard.edu/grids.html>

Table 8.1: Sensitivities of abundances to atmospheric parameters for star #40129.

Species	$T_{\text{eff}}+100$	$\log g+0.2$	$\xi+0.1$
$\Delta A(\text{Li})$	0.10	0.02	0.00
$\Delta[\text{Al}/\text{Fe}]$	0.07	0.06	0.02

5904, because of the occurrence of cosmic rays and/or due to lower S/N ratios that hampered measurements in 5 and 8 stars, respectively for each GC.

The spectral coverage guaranteed by the HR15N grating, although not capturing any suitable features for Na and O abundance determinations, allowed us to investigate the Al content by synthesising the Al I doublet at 6696Å and 6698Å. The adopted atomic parameters for those lines were: $\log gf = -1.35$ and $\log gf = -1.65$, for the 6696Å and 6698Å features, respectively. In NGC 6218 we could obtain Al abundances for a sample of 54 out of 63 stars, whereas in NGC 5904 we analysed 93 stars (out of 99), with 61 detections and 32 upper limits. Examples of spectral synthesis for Li and Al are given in Figures 8.2 and 8.3 for stars in both clusters.

8.2.1 Error budget

Two kind of uncertainties affect our derived abundances, that is internal (star-to-star) and systematic (cluster) errors. The main aim of our paper is to search for (possible) evidence of spreads in Li and Al abundances, thus we focus on the first source of errors.

The internal errors are mainly related to (i) the best-fit determination of synthetic spectra with observed spectra (which is in the range $\Delta A(\text{Li}) = 0.07 - 0.10$ for our target stars and reflect uncertainties in the continuum placement and S/N ratios of the spectra) and (ii) to the atmospheric parameters, i.e., T_{eff} , $\log g$, and microturbulence velocities ξ (the adopted metallicity $[\text{A}/\text{H}]$ in the model atmosphere has a negligible impact). In order to assess the contribution related to the stellar parameters we first need to ascertain the sensitivities of our species to changes in atmospheric quantities (the partial derivatives in Equation 8.1). To do this we proceeded in the standard way, that is by varying one parameter at the time and inspecting the corresponding change in the resulting abundance (see Table 8.1 where sensitivities are reported for one sample star with median T_{eff}). The following step is to evaluate the actual error in atmospheric parameters (i.e., $\sigma_{T_{\text{eff}}}$, $\sigma_{\log g}$, σ_{ξ}). The $\sigma_{T_{\text{eff}}}$ can be estimated from the error on the slope of the relation between initial T_{eff} values (from $(V - K)$ colours) and V magnitudes, which result in 18K for both GCs. Errors in ξ instead come from the scatter around the relationship of ξ vs $\log g$ by Gratton et al. (1996, that is 0.2 km s^{-1}). Finally, the $\sigma_{\log g}$ contains different terms due to the uncertainties in stellar masses (which is, however, less than $\approx 10\%$ of the mass), errors due to luminosity (in turn related to magnitudes, distance moduli and bolometric corrections) and those in temperatures. All these contributions are anyway significantly small and result in internal errors in $\log g$ values less than 0.05 dex.

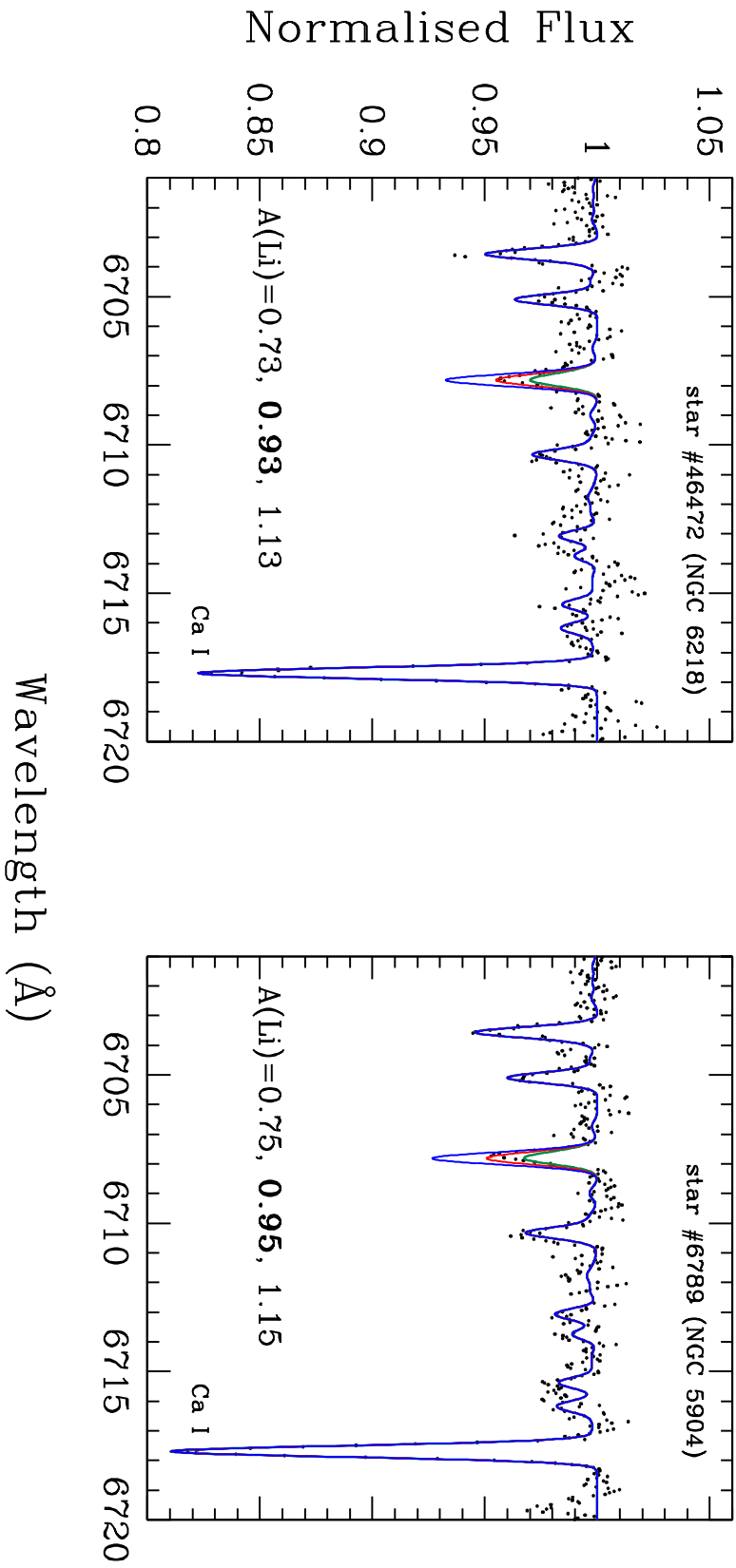


Figure 8.2: Example of the spectral synthesis for the Li I line for stars #46472 (NGC 6218) and #6789 (NGC 5904). The best fit lithium abundance is indicated in bold.

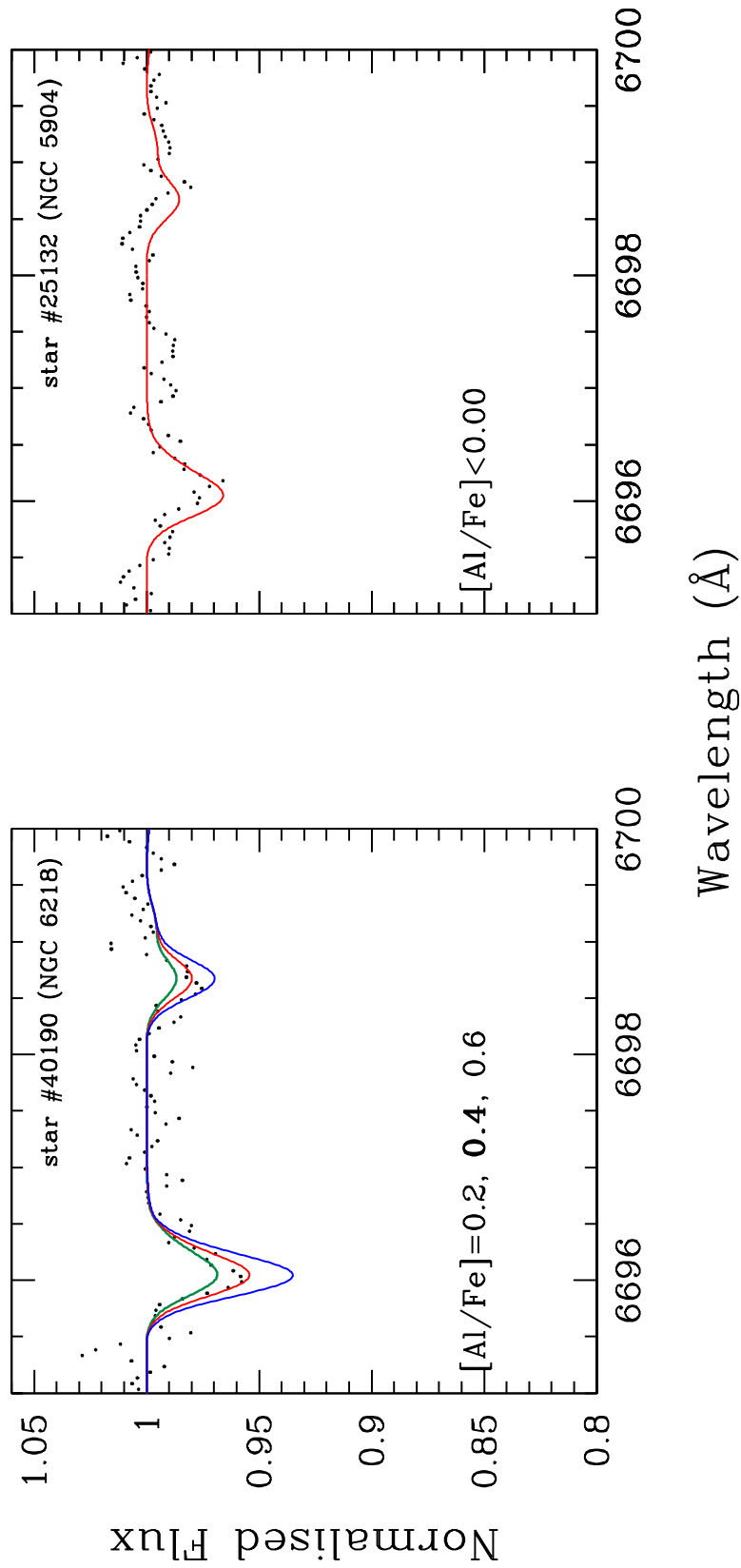


Figure 8.3: Example of the spectral synthesis for the Al I lines for stars #40190 (NGC 6218) and #25132 (NGC 5904; here only an upper limit is given).

Table 8.2: Stellar parameters, Li and Al abundances for targets in NGC 6218 (M12). This table is available in its entirety in a machine-readable form in the online journal. A portion is shown here for guidance regarding its form and content.

Star ID	V	S/N	T_{eff}	$\log g$	ξ	A(Li)	[Al/Fe]
	(mag)		(K)	(cm s^{-2})	(km s^{-1})	dex	dex
10219	15.28	78	4946	2.59	1.39	1.08	—
26629	15.60	60	5016	2.75	1.34	1.06	0.60
26778	14.57	115	4787	2.23	1.50	0.53	0.00
31393	15.17	100	4921	2.53	1.41	0.93	—
31600	14.95	90	4871	2.42	1.44	0.95	0.00

The total internal error on a given species is then calculated by summing in quadrature all the difference contributions, i.e.:

$$\sigma = \sqrt{\sigma_{\text{best}}^2 + \left(\frac{\partial \log(\epsilon)}{\partial T_{\text{eff}}}\right)^2 \sigma_{T_{\text{eff}}}^2 + \left(\frac{\partial \log(\epsilon)}{\partial \log g}\right)^2 \sigma_{\log g}^2 + \left(\frac{\partial \log(\epsilon)}{\partial \xi}\right)^2 \sigma_{\xi}^2} \quad (8.1)$$

Given the small uncertainties in stellar parameters, the total errors on Li and Al abundances are almost entirely related to the best-fit determination; typical values range from 0.10–0.13 for Li and 0.14–0.16 for [Al/Fe].

8.3 Results and Discussion

Elemental abundances (Li and [Al/Fe]) are displayed in Tables 8.2 and 8.3, where we list the identification number for each star and V magnitudes (from the Momeny et al. photometry) the S/N ratios at 6700Å along with stellar atmospheric parameters (the complete Tables are made available online only). Our results are presented separately for each target cluster in the following Sections 8.3.1 and 8.3.2 for NGC 6218 and NGC 5904, respectively. We then provide a general discussion on the Li abundance pattern observed in GCs by summarising and discussing findings from this study along with previous investigations (Section 8.3.3).

8.3.1 NGC 6218 (M12)

In Figure 8.4, A(Li) is plotted as a function of V magnitude for all our sample stars in NGC 6218. Here blue circles denote detections, black triangles upper limits and the solid grey line indicates the magnitude of the LF bump, located at $V=14.78$ according to Nataf et al. (2013). The magnitude of the LF bump is generally believed to denote the beginning of extra mixing in these low-mass stars: there is excellent agreement between photometry and spectroscopy regarding the onset of this event, with stars exhibiting a declining trend of Li abundances as a

Table 8.3: Stellar parameters, Li and Al abundances for targets in NGC 5904 (M5). Entries with asterisks indicate upper limits. This table is available in its entirety in a machine-readable form in the online journal. A portion is shown here for guidance regarding its form and content.

Star ID	V (mag)	S/N	T_{eff} (K)	$\log g$ (cm s^{-2})	ξ (km s^{-1})	A(Li) dex	[Al/Fe] dex
229	15.63	100	5000	2.57	1.39	1.02	0.00*
394	15.13	130	4888	2.32	1.47	0.65*	0.35
1069	15.91	95	5063	2.71	1.35	1.05	0.10*
1476	15.03	140	4865	2.27	1.49	0.97	0.00*
1778	15.56	115	4983	2.53	1.40	1.00	0.10

function of luminosity once the bump is reached. The brightest stars in our sample have had their lithium content significantly depleted and only upper limits can be provided. Moreover, a slightly decreasing trend of Li with magnitudes is present for our targets with V ranging between $V=15.75$ and the bump: the correlation coefficient is found to be $r=0.55$, which is significant at more than 99.9 % level (the probability that this happened by chance is less than 0.1 %). The slope of the correlation is 0.13 ± 0.03 , which is very close to accuracy imposed by our observational uncertainties (~ 0.10 - 0.13 dex). Given that our errors are likely overestimated, we are tempted to conclude that this Li pattern is real. The trend is clearly not related to the multiple population scenario, because it is present in both FG and SG stars (divided according to the Na and O abundances, as in Carretta et al. 2009b). As pointed out by the referee, there could be two possible explanations for this trend: (i) *in situ* depletion as stars evolve along the sub giant branch (contrary to standard theory); or (ii) increased previous Li depletion as a function of mass along the sub giant branch, possibly showing signs of a Li dip in metal-poor stars analogous to the Population I F dwarf dip. By considering only giants fainter than the RGB bump, we find a mean Li abundance of $A(\text{Li}) = 0.98 \pm 0.01$ (r.m.s. 0.06, 44 stars). *This is consistent with no Li variation in this cluster* (the fact that the standard deviation is formally lower than observational uncertainties $-0.10/0.13$ dex- indicates that the measurement errors are probably over-estimated). The constancy of Li abundances is a noteworthy result because NGC 6218 is known to display, along with the large majority of Galactic GCs, large variations in p-capture elements. As previously mentioned in Section 8.2, no information on Na and O abundances can be gathered from our spectra. However, we have stars in common with the survey by Carretta et al. (2007): out of 44 stars (not yet experiencing *in situ* extra mixing), we have Na and O abundances for 21 and 18 stars, respectively. In Figure 8.5 we show our $A(\text{Li})$ against their $[\text{Na}/\text{Fe}]$ and $[\text{O}/\text{Fe}]$ ratios for those stars in common: variations of almost 1 dex

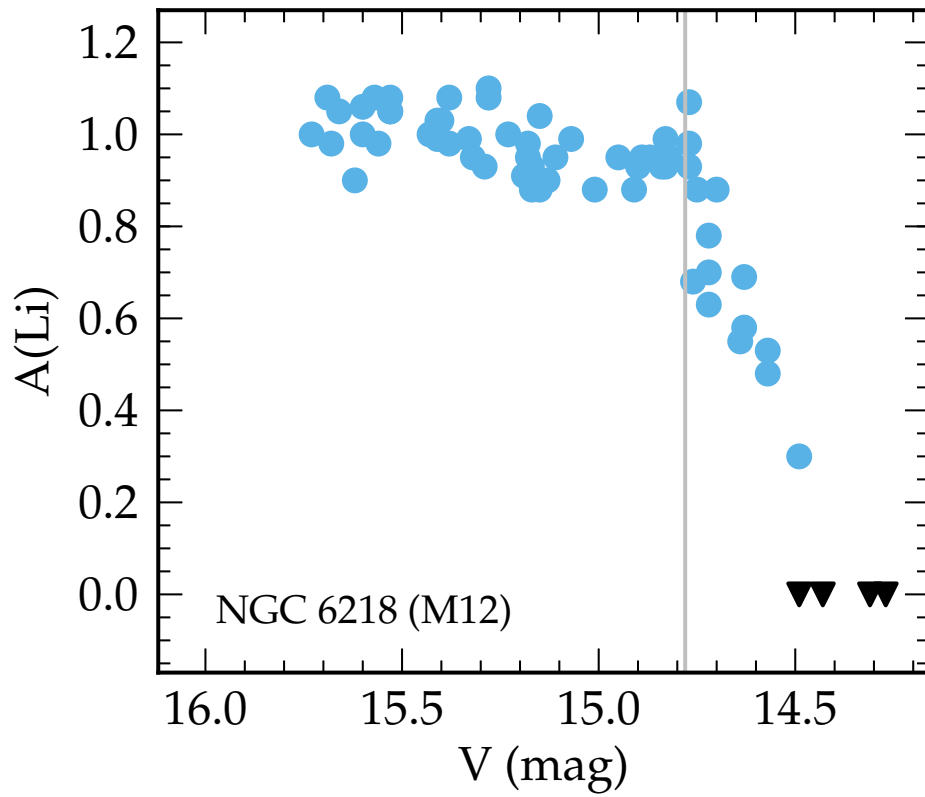


Figure 8.4: $A(\text{Li})$ as a function of visual magnitude in the globular cluster NGC 6218 (M12). Blue circles denote lithium detections whereas black triangles represent upper limits. The solid grey line indicates the magnitude of the LF bump in this cluster, $V = 14.78$, as given by Nataf et al. (2013).

in $[\text{Na}/\text{Fe}]$ and more than 1.2 dex in $[\text{O}/\text{Fe}]$ do not accompany changes in the Li abundance. There seems to be the hint of a weak anticorrelation between Li and Na abundances, however the Pearson's correlation coefficient results in $r = -0.38$ (16 degrees of freedom) and is not statistically meaningful: there is a probability larger than 10% that this correlation could happen by chance. Following the definition introduced by Carretta et al. (2009b), we can group our stars into their respective generation based on their Na content, with FG stars defined as having Na abundance of $[\text{Na}/\text{Fe}] \leq [\text{Na}/\text{Fe}]_{\text{min}} + 0.3$ dex. We find that FG stars have an average Li abundance of $A(\text{Li}) = 1.00 \pm 0.04$ (r.m.s = 0.09), whilst in SG stars $A(\text{Li}) = 0.98 \pm 0.02$ (r.m.s = 0.06). Thus, the different stellar populations identified according to their Na abundances are indistinguishable in terms of their Li content.

In Figure 8.6 we compare the spectra of two stars with very similar parameters ($\Delta T_{\text{eff}} = 37\text{K}$), but differences in Na and O abundances of more than a factor of 2. It is evident that there is no remarkable difference in the Li I line strength, entailing that those stars have to share a very similar Li content (virtually the same within the observational uncertainties).

Our spectral coverage also permitted us to obtain Al abundances for a subsample of 54 stars. We derived a mean Al abundance of $[\text{Al}/\text{Fe}] = +0.21 \pm 0.03$ (r.m.s = 0.19), which is in excellent agreement with values published by Carretta et al. (2009a) ($[\text{Al}/\text{Fe}] = 0.20 \pm 0.05$, r.m.s = 0.18) based on a sample of 11 bright giants observed with the high-resolution UVES spectrograph. Johnson and Pilachowski (2006) analysed intermediate-resolution spectra ($R \approx 15000$) for 21 RGB stars in this GC, deriving stellar parameters, metallicity, p-capture and n-capture element abundances. They obtained an average $[\text{Al}/\text{H}] = -1.00 \pm 0.03$ compared to our value of $[\text{Al}/\text{H}] = -1.16 \pm 0.03$ (we directly compare $[\text{Al}/\text{H}]$ because there is an offset in metallicity of about 0.2 dex between the two studies). Taking into account the measurement uncertainties, and a difference in the $\log gf$ for the Al doublet at 6696–6698 Å of 0.20 and 0.24 (in the sense ours *minus* theirs), the two mean values agree very well. Our results confirm that the Al content does vary in this GC and that Al and Na abundances are positively correlated, as expected from the H-burning at high temperature. This is demonstrated in Figure 8.7, where our $[\text{Al}/\text{Fe}]$ ratios are plotted as a function of $[\text{Na}/\text{Fe}]$ from Carretta et al. for stars in common. Our sample stars span a range of ≈ 0.8 dex in $[\text{Al}/\text{Fe}]$ (peak-to-peak variation), very similar to the value found by Carretta et al. (2009a) from UVES spectra (i.e., $\Delta[\text{Al}/\text{Fe}] \approx 0.7$ dex), whereas this is larger than what has been found by Johnson and Pilachowski (2006), $\Delta[\text{Al}/\text{Fe}] \approx 0.4$ dex. It is not straightforward to determine the cause of such a discrepancy, and statistics may certainly play a role (our sample is a factor of 2 larger). However, we note that according to Johnson and Pilachowski (2006) there are no Al-poor stars (FG) in their sample. The minimum value in this population being $[\text{Al}/\text{Fe}] = 0.35$ dex (while the maximum Al abundance is in good agreement with our value as well as with those by Carretta et al. 2009a, i.e., roughly at ≈ 0.7 dex level).

In Figure 8.8 we plot $A(\text{Li})$ as a function of $[\text{Al}/\text{Fe}]$ abundance, where lavender circles denote detections and the black triangle indicates an upper limit to the $[\text{Al}/\text{Fe}]$ ratio. If we compare the variation in Al from our entire sample (~ 0.8

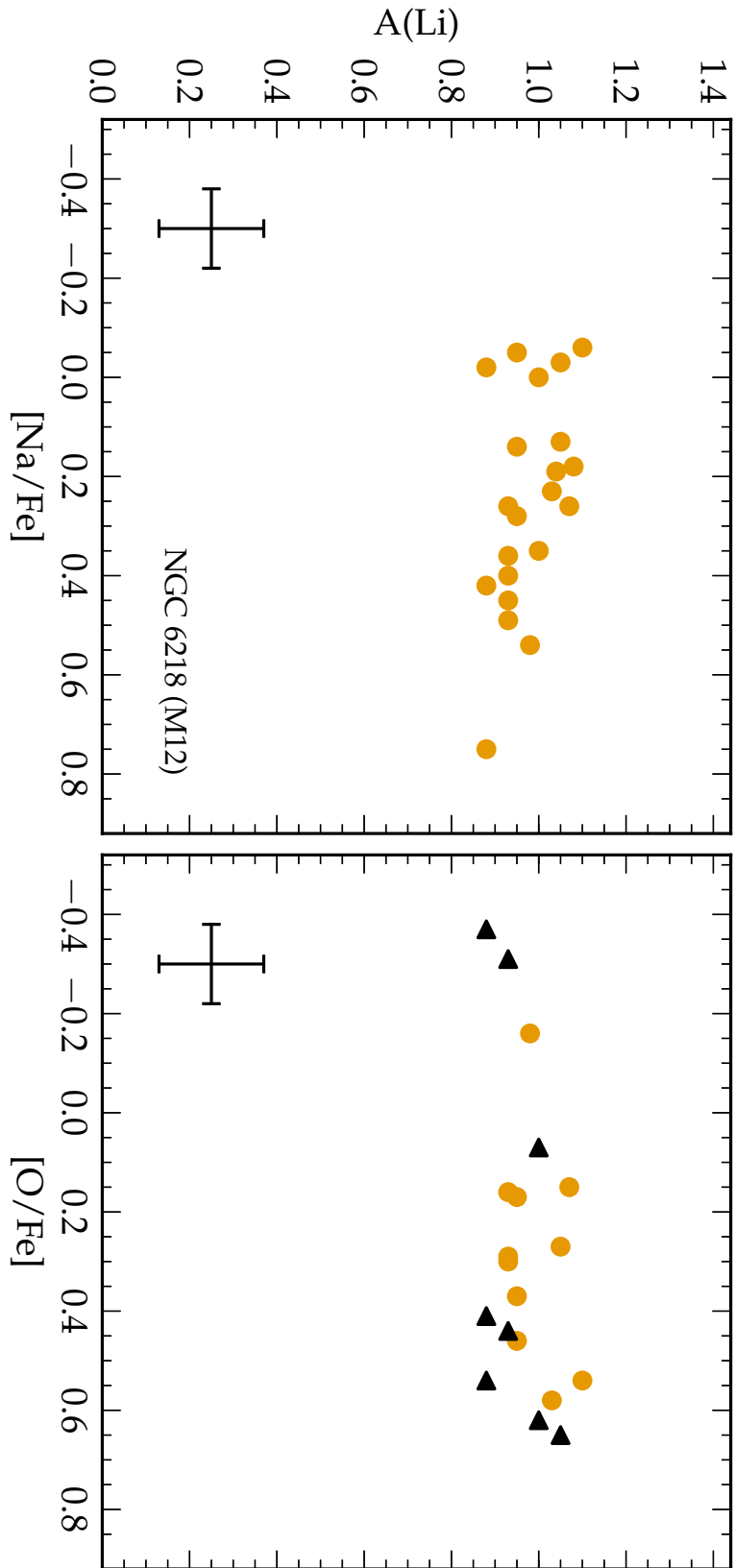


Figure 8.5: Left Panel: $A(\text{Li})$ for stars below the RGB bump as a function of $[\text{Na}/\text{Fe}]$ and $[\text{O}/\text{Fe}]$ as determined by Carretta et al. (2007). Orange circles denote detections and triangles upper limits. Error bars indicate the typical internal error.

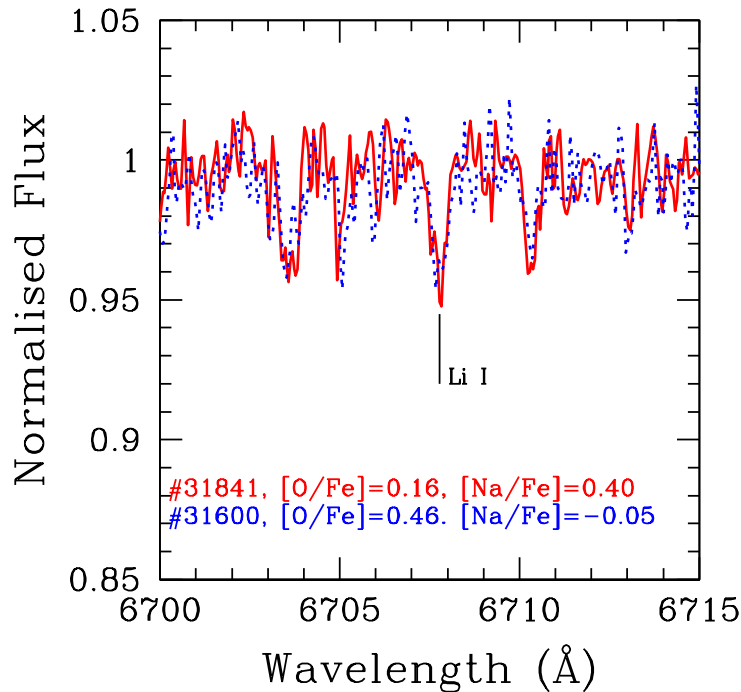


Figure 8.6: Comparison of the spectra for two stars in M12 with very similar stellar parameters and Li abundances, but very different Na and O content (see text for discussion).

dex) to that we determined from common stars with Carretta et al. (2009a, see Figure 8.7, ~ 0.4 dex) there is almost a factor of two difference. This might be a mere statistical effect. However, it could be that, since stars in common between the two works are brighter, the scatter increases as luminosity decreases (because the spectral lines get weaker at higher temperatures). We checked the presence of possible trends between our $[\text{Al}/\text{Fe}]$ ratios and the V magnitudes and we concluded that there is a slight increase in the Al dispersion at lower luminosity but the trend is weak (the effect is anyway well within the observational uncertainties).

Analogously to what is revealed in the Li-O and Li-Na planes, while Al displays a large variation among our sample stars, the Li abundance remains constant. *The large variations in all the p-capture elements under scrutiny here are not accompanied by analogous changes in Li.* The implication is that Li production must have occurred across the different stellar generations, ruling out a major contribution by FRMS to the GC internal enrichment, and favouring the IM-AGB candidate. In this regard, M12 is “ M_4 -like” in its behaviour; we recall that both clusters are of similar (current) mass and metallicity (see Section 8.3.3 for further discussion).

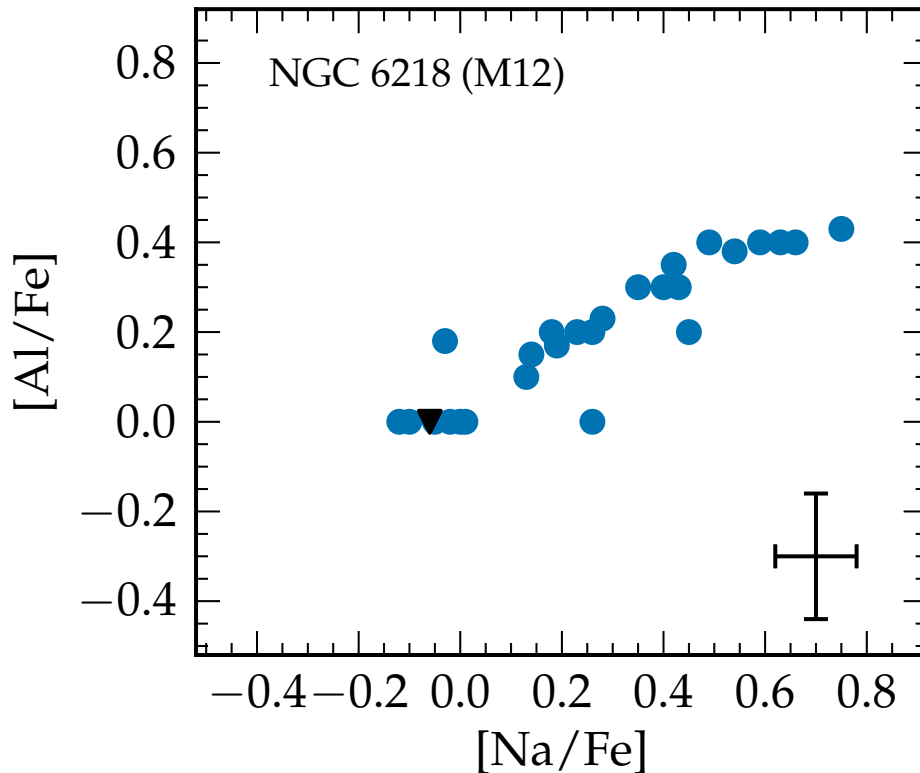


Figure 8.7: $[Al/Fe]$ from the present study as a function of the $[Na/Fe]$ derived by Carretta et al. (2007)

8.3.2 NGC 5904 (M5)

We obtained Li abundances for 99 stars in the massive GC NGC 5904 (M5, $[Fe/H] = -1.29$ dex); once again the magnitude range of our sample included giants beyond the LF bump. Our derived Li abundances are shown as a function of the V magnitudes in Figure 8.9, with symbols retaining their meaning from Figure 8.4 (i.e., blue circles denote detections, black triangles denote upper limits and the solid grey line indicates the magnitude of the LF bump). This GC possesses two features worthy of mention. First, spectroscopically it is ambiguous as to what magnitude extra mixing begins in this cluster. The photometrically derived LF bump, it could be argued, is located at a V magnitude beyond which stars have already begun to deplete their lithium: compared to the trend observed in Figure 8.4, the onset of extra mixing is not as clear as in M12. Despite the fact that our photometric system is different from that of Nataf et al. (2013), we determined very similar values for the location of the LF bump. Nataf et al. (2013) derived $V_{bump} = 14.96 \pm 0.01$ compared to $V_{bump} = 14.97 \pm 0.04$ from the present work. Thus, we can state that no major systematic offsets are present between the two catalogues. On the other hand, a small shift to fainter magnitudes of ≈ 0.1 mag for the bump luminosity would result in an agreement between the photometrically

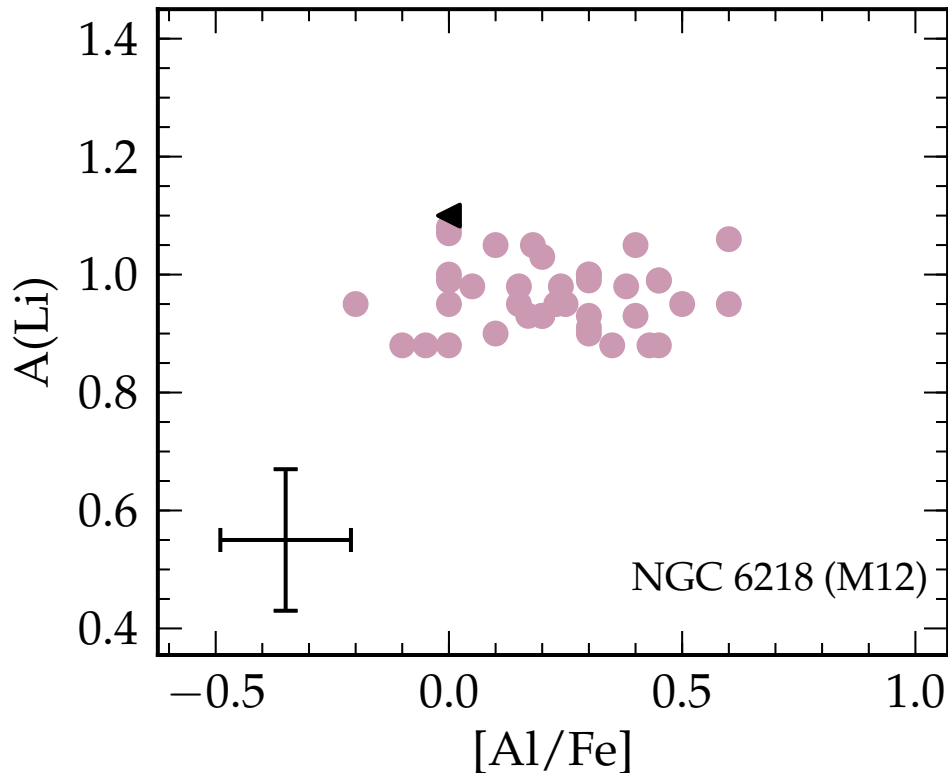


Figure 8.8: $A(\text{Li})$ for stars below the RGB bump as a function of $[\text{Al}/\text{Fe}]$ abundance in the globular cluster NGC 6218 (M12). Lavender circles denote lithium detections whereas the black triangle represents an upper limit to the $[\text{Al}/\text{Fe}]$ abundance. The typical internal error for the abundances are indicated by the error bar.

and spectroscopically determined location at which extra mixing begins. Such a small difference in the required magnitude *could* be attributed to observational errors. Nevertheless, it will be a point of caution in discussions hereinafter. Secondly and most interestingly, two stars in particular (the two upper limits with V magnitude > 15.5 in Figure 8.9) were found to be severely lithium deficient for their evolutionary phase. Both their radial velocity measurements and metallicity suggest that they are indeed members of the cluster but their Li abundances are inconsistent with the post-FDU composition of the other stars. Whether this translates to deeper FDU, some sort of extra mixing, a rare evolutionary event (although it had to happen at least twice) or it is related to variations in p-capture elements remains unclear (see the following discussion).

When considering the 82 stars that are below the magnitude of the LF bump, we find a mean lithium abundance of $A(\text{Li}) = 0.93 \pm 0.01$ (r.m.s 0.11). The standard deviation is roughly of the same order of magnitude of the observational uncertainties, however we need to bear in mind that in the average computation

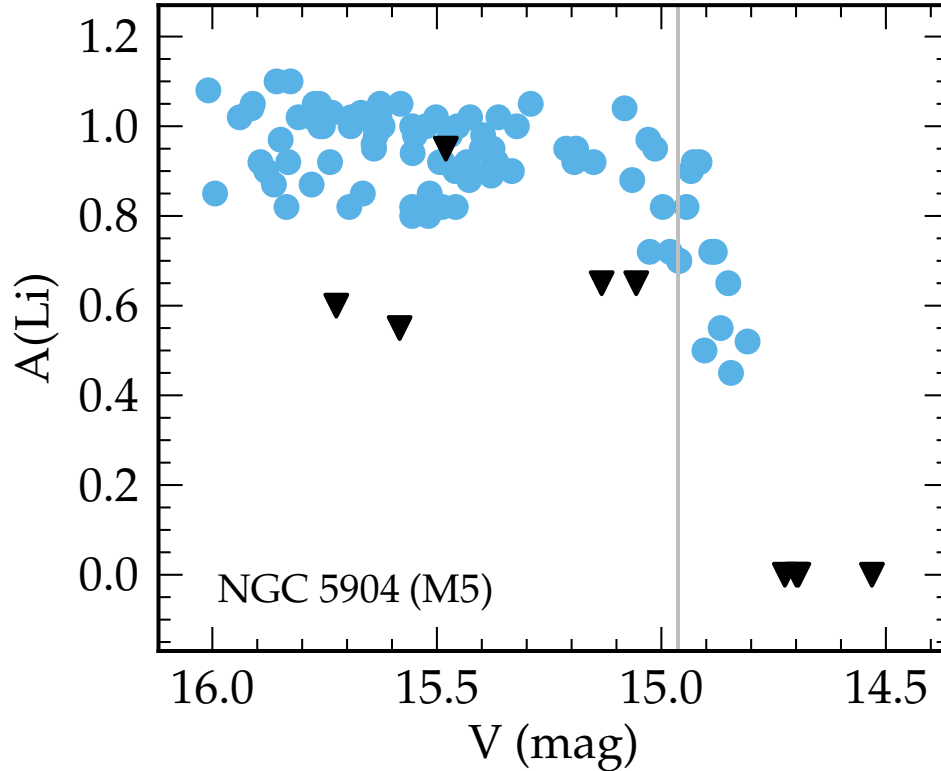


Figure 8.9: $A(\text{Li})$ as a function of visual magnitude in the globular cluster NGC 5904 (M5). Symbols are as for Figure 8.4. The solid grey line indicates the magnitude of the LF bump at $V=14.96$ as given by Nataf et al. (2013).

the upper limits in $A(\text{Li})$ are treated as detections, indicating that this rms is certainly a lower limit to the actual internal dispersion in Li abundances. Furthermore, as already stated in Section 8.3.1, the measurement errors are quite likely overestimated. Unfortunately, we have only 16 and 11 stars for which Carretta et al. (2009b) have gathered Na and O abundances; in Figure 8.10 we show the run of Li with $[\text{Na}/\text{Fe}]$ and $[\text{O}/\text{Fe}]$ ratios for stars in common between the two spectroscopic investigations. There is no evidence for a Li-O positive correlation nor for a Li-Na anticorrelation: Na and O extend for ≈ 0.7 dex, whilst the Li remain almost constant. The only previous determination of Li abundance in this GC is that by Lai et al. (2011) who derived Li abundances for three RGB stars below the RGB bump and found an average of $A(\text{Li}) = 0.81 \pm 0.06$ (r.m.s = 0.11). The authors concluded that, given the small size of their sample, they can not comment on the relationship between Li and p-capture elements (e.g., C, Na, O).

The small number of common stars between this work and Carretta et al. (2009b) may, however, have prevented us from unveiling the presence of Li variations in conjunction with the other species involved in the *hot* H-burning, such as Na and O. Thus, to get deeper insights into the possible relationship between

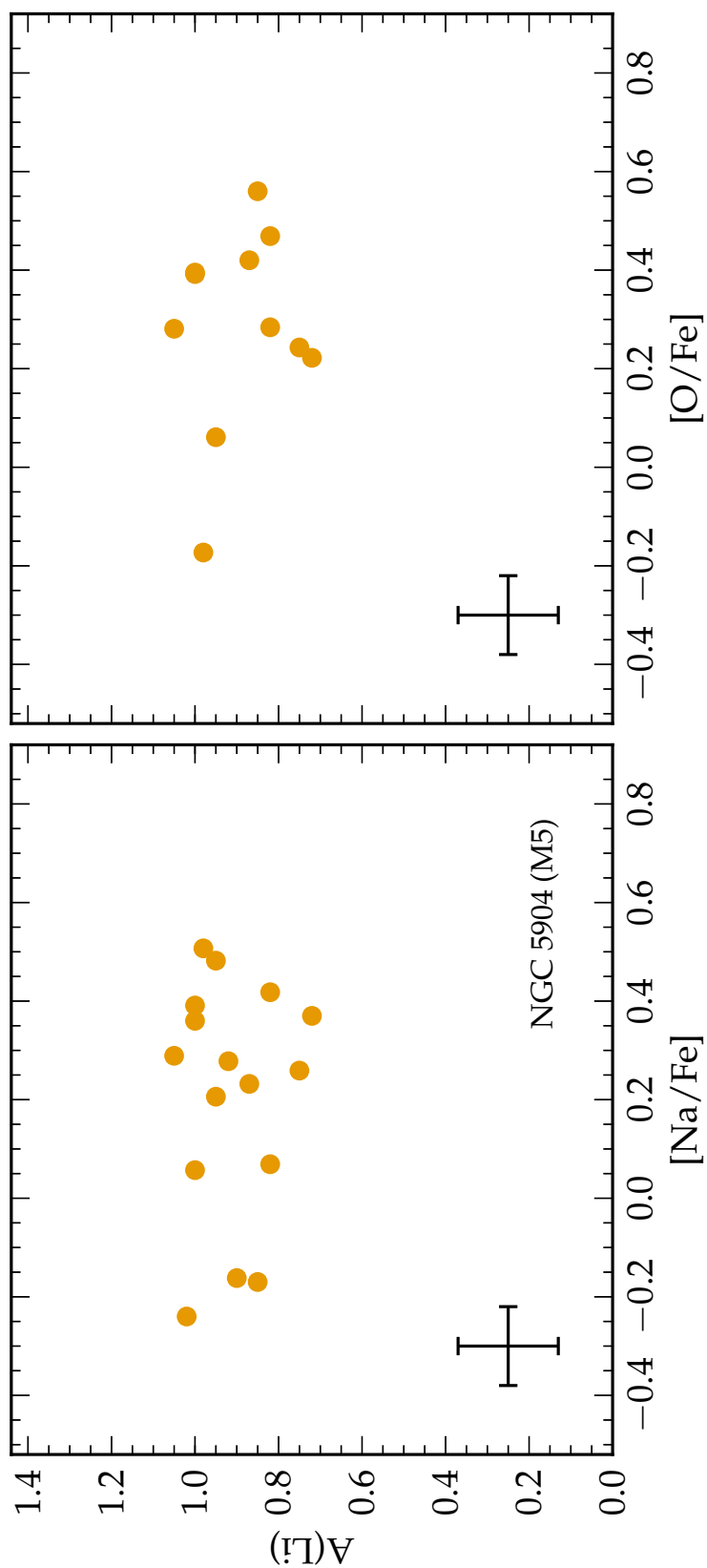


Figure 8.10: Left Panel: $A(\text{Li})$ for stars below the RGB bump as a function of $[\text{Na}/\text{Fe}]$ as determined by Carretta et al. (2009b). Right Panel: $A(\text{Li})$ from this study as a function of $[\text{O}/\text{Fe}]$ as determined by Carretta et al. (2009b). Orange circles denote stars for which the abundances of both species of interest have been measured and error bars indicate the typical internal error in each ratio.

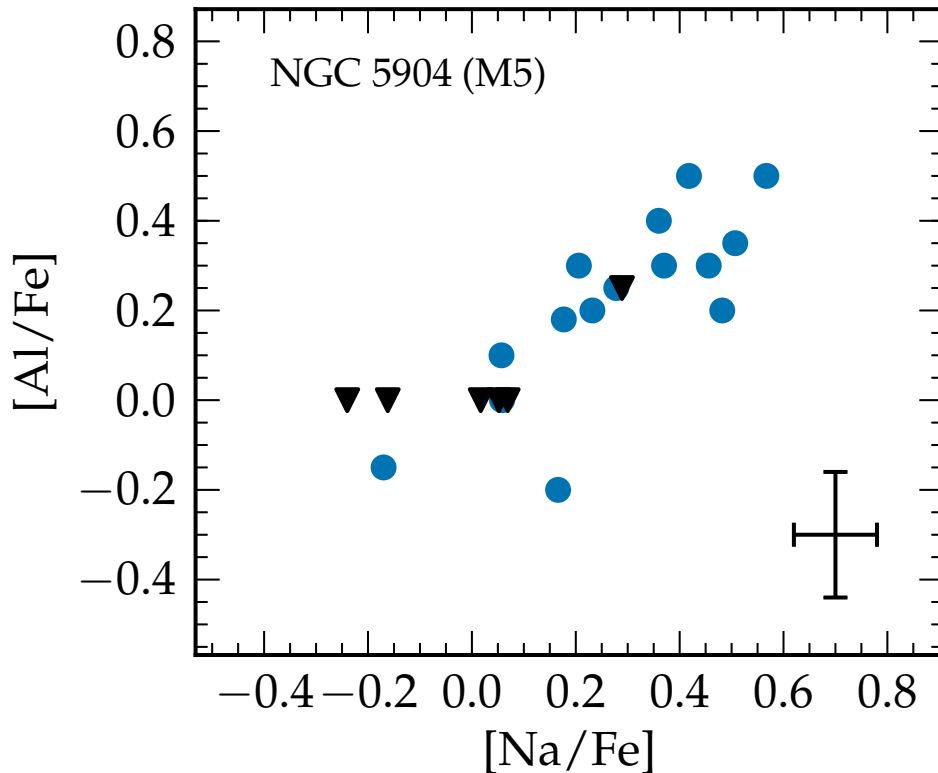


Figure 8.11: $[\text{Al}/\text{Fe}]$ from the present study as a function of the $[\text{Na}/\text{Fe}]$ derived by Carretta et al. (2009b)

Li and p-capture elements, we derived the Al abundances for a total of 93 stars. From our sample we detected a peak-to-peak variation in the $[\text{Al}/\text{Fe}]$ ratio of ≈ 0.7 dex, which is the same value found by Ivans et al. (2001) and is consistent with Shetrone (1996a, ≈ 0.6) and Carretta et al. (2009a, ≈ 0.8 dex). Considering the sub-group of stars in common with Carretta et al. (2009b, 21 stars), we report our derived Al abundances as a function of the Na determined by the Carretta et al study in Figure 8.11. We obtained a very clear Na-Al correlation, with a Pearson's correlation coefficient $r = 0.81$, which is significant at more than 99.99%. In this respect, we confirm results from previous studies (see Carretta et al. 2009a, Ivans et al. 2001, Shetrone 1996a).

As was previously done for NGC 6218, we include a discussion on the $[\text{Al}/\text{Fe}]$ and Li abundances for those stars in the cluster yet to begin *in situ* extra mixing. By adopting a formal V_{bump} of 14.96, as given from photometry (but keeping in mind possible mismatches between photometry and spectroscopy, as mentioned at the beginning of this Section), we plot the derived $A(\text{Li})$ abundances as a function of $[\text{Al}/\text{Fe}]$ in Figure 8.12. Here lavender circles denote stars where both Li and Al have been measured, black triangles represent stars for which an upper limit to the lithium abundance has been determined and blue triangles represent upper limits

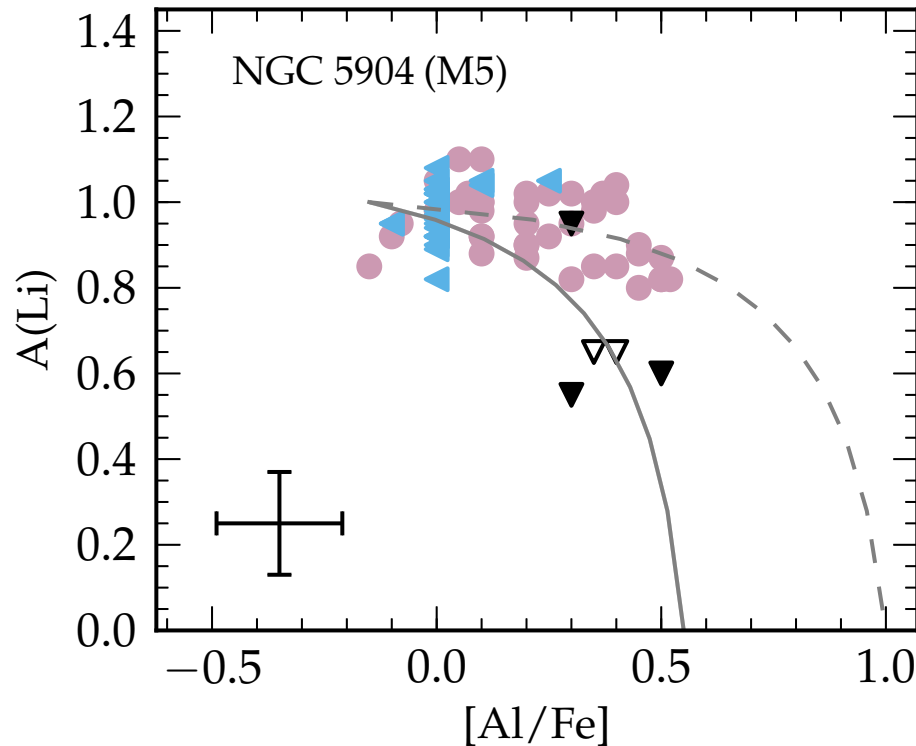


Figure 8.12: $A(\text{Li})$ for stars below the RGB bump as a function of $[\text{Al}/\text{Fe}]$ abundance in the globular cluster NGC 5904 (M5). Lavender circles denote measurements for both species, black triangles denote upper limits to the lithium abundance and blue triangles denote upper limits to the $[\text{Al}/\text{Fe}]$ abundance. The typical internal errors are indicated. The curves represent different dilution models (see text for discussion).

in the derived $[\text{Al}/\text{Fe}]$ abundance. There is evidence for a Li-Al anticorrelation, with a Pearson's coefficient $r = -0.44$ (75 degrees of freedom) which is significant at more than 99.9% (the probability that this event can happen by chance is lower than 0.1%). If we discard those two stars for which the extra mixing might already have begun (i.e., stars very close to the bump and labelled as empty triangles here to emphasise their different behaviour), the anti-correlation is still present ($r = -0.40$). Note that even had we discarded the other two upper limits ($V > 15.5$), there is still evidence for anticorrelation between Li and Al abundances ($r = -0.33$, significance level at 99.9%) However, these other two stars that exhibit Li depletion have magnitudes $V > 15.5$, so they are much fainter than the bump. They demonstrate the expected abundance pattern if we assume that the processed material that forms the SG stars is Li-poor and Al-rich. To convince the reader of this possibility, we show in Figure 8.13 the spectral comparison for one of these stars, namely star #15215, with another GC member with identical atmospheric

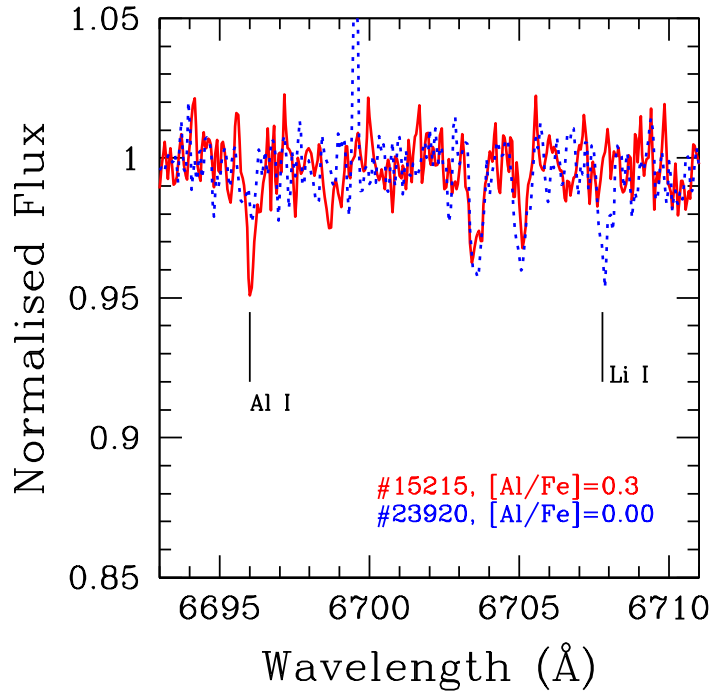


Figure 8.13: Comparison of the spectra for two stars in M5 with different Li and Al abundances (see text for discussion).

parameters (star #23920, $\Delta T_{\text{eff}} = 9\text{K}$). As is clear from the Figure, #15215 is Li-poor and (relatively) Al-rich, whereas #23920 is Li-rich and Al-poor. Thus, we might be tempted to conclude that the two (and perhaps the four?) stars that exhibit significant Li depletion (and corresponding Al enhancement) constitute the extreme (E) SG stars in M5. However, having detected so few of these stars would entail that the fraction of E stars we obtain is about the $3 \pm 1\%$ of the cluster population, which is lower than the value of $7 \pm 2\%$ found by Carretta et al. (2009b) according to their Na and O abundances (see that paper for details on the definition of the PIE groups).

In order to gain a better understanding of the chemical abundance pattern emerging from this study, we determined a dilution model for this GC, as per Prantzos and Charbonnel (2006). In this model $[X]$, the logarithmic abundance of species X, is a mixture (given by a dilution factor, d) of the original abundance, $[X_o]$, and processed material, $[X_p]$. $[X]$ is determined such that:

$$[X] = \text{Log} \left[(1 - d)10^{[X_o]} + d \times 10^{[X_p]} \right]. \quad (8.2)$$

In Figure 8.12 we plot as solid line the dilution model with initial abundances of $\text{Li}=1.00$ and $[\text{Al}/\text{Fe}]=-0.15$ and processed material having $\text{Li}=0.00$ and $[\text{Al}/\text{Fe}]=0.55$, based on the extrema measured in our sample. As can be easily seen from the plot, this dilution curve fails in reproducing the observed trend. More

specifically, we can identify three groups of stars: (1) stars that show primordial Li and Al abundances (FG stars); (2) stars with primordial Li but enhancement in their Al content, at different levels; (3) stars with an extreme composition, characterised by paucity of Li and increased Al abundances (SG stars, with an extreme pattern). The majority of the GC stars, that belong to group 2, cannot be explained by diluting the primordial population with the extreme SG, because they still exhibit a quite large Li abundance (the solid curve is indeed a lower envelope to their distribution). This implies that in order to reproduce their Li abundance, we have to call for a Li production within the stellar polluters.

Alternatively, one possible solution requires the presence of an unobserved population, typified by $[Al/Fe]$ of approximately ≈ 1.0 dex (the dashed curve in Figure 8.12). Both this survey and Carretta et al. (2009a) have failed to identify potential candidates. There might be two reasons why this population is unseen:

- There are no stars formed from the pure ejecta (i.e., with a pollution fraction of 100%). The processed material coming from IM-AGB stars would in this case have Al enhancements of more than $[Al/Fe] \approx 1$ dex (and is naturally Na/N/He rich also). This material is required to mix with primordial material (and hence become diluted) before the formation of the SG started. In a recent paper, D’Antona et al. (2012) examined dynamical models where it is possible, in principle, to accumulate and mix the ejecta for a time t_f before starting star formation (see Table 1 of their paper). However, there is no obvious explanation as to the cause of the delay in the star formation events. Such a scenario requires that the gas from the AGB stars is collected at the GC centre and remains in a quiescent condition for ≈ 40 -50 Myr. Star formation is inhibited until the cleared pristine material (swept out from the SN II explosions) can fall back and mix to produce the subsequent stellar generation.
- These very peculiar stars, characterised by extreme Al over-abundances, should also possess a huge amount of He. At a given age, stars with larger amount of He are less massive than their counterpart with normal He (i.e., $Y \sim 0.24$). Considering the metallicity of M5, stars with $Y > 0.35$ will have $M \lesssim 0.5 M_{\odot}$ (see Gratton et al. 2010a; 2010b) and they might not reach the RGB *tip*. In fact, Castellani and Castellani (1993) have shown that if the mass is smaller than that required to activate the He-core flash, the stars will become *RGB-manqué*. In this circumstance, the He-flash can occur at high effective temperatures after stars have left the RGB (the so-called “hot flashers”) and they eventually move to the *blue hook* of the horizontal branch (HB, see e.g., Moehler et al. 2002). Unfortunately, as widely discussed in Gratton et al. (2013), we can not determine the chemical composition for stars warmer than the *Grundahl u-jump* (Grundahl et al. 1999), because of severe sedimentation and radiative levitation effects.

Nevertheless, if this is the case, then an explanation for the two (or even four) Li-poor stars in Figure 8.12 would still be required, perhaps calling for a rare

event of extra mixing that begins well before the LF bump luminosity is reached.⁵ At the moment there is no compelling evidence to reject them, only because no satisfactory explanation for the cluster’s dilution history has presented itself. *In summary, NGC 5904 displays a degree of complexity that can not be accounted for by a simple dilution model. This cluster demonstrates the presence of three different stellar populations.* This is reminiscent of what Carretta et al. (2012) discovered in the GC NGC 6752, where the intermediate SG stars cannot be explained by simply considering a mixture of primordial composition and (extreme) highly-processed material (i.e., the E stars).

8.3.3 The Li spreads in GCs

Our investigation into the Li abundance and its potential spread within M12 and M5 has revealed that these GCs behave differently. In M12 we recover a chemical pattern very similar to that previously observed in M4 by DM10 (and corroborated by other authors, see e.g., Mucciarelli et al. 2011; Villanova and Geisler 2011). Because FG and SG stars share exactly the same Li abundance, while showing depletion in O of more than 50%, we require that the GC polluters have contributed ashes enriched in Li. As a consequence, FRMS (and massive binaries) cannot be responsible for this trend, because the current theory suggests that they produce Li-free ejecta. On the other hand, in M5 we disclosed the presence of a rather peculiar and complex chemical composition: a simple dilution model fails in reproducing the three populations currently co-existing in the cluster. Furthermore, we also need to invoke Li production within the polluters to explain the abundance pattern in the majority of the GC stars (i.e., the SG stars which are Al-rich but still Li-rich). Crucially, we detected the presence of an extreme population, which is characterised by Al overabundances and Li deficiency (as expected in the case of hot H burning). These stars were not revealed in our M12 sample; however statistics might have played a role in this respect: given that we have 54 stars for which Li and Al have been measured, assuming that the fraction of extreme stars is as in M5 (i.e., about 3%) we would expect to find at least one of those stars. The probability that we missed all of them is 19%, which is not negligible. This should be regarded as a point of caution in the following discussion.

These two GCs share a very similar metallicity, but they significantly differ in current mass. M5 is much more massive than M12 (and M4). In order to determine what role GC mass plays in the Li distribution among the different stellar populations, we plot in Figure 8.14 the internal spread in Li, $\Delta A(\text{Li})$, as a function of the absolute visual magnitude (a proxy for the current cluster mass). To evaluate the extent of the Li spreads in our target GCs, we considered only the stars with magnitudes fainter than the RGB bump luminosity. The peak-to-peak variation in the Li abundances is 0.22 and 0.55 for NGC 6218 and NGC 5904,

⁵It is also possible that these stars are binaries; we might have captured post blue straggler stars in our RGB sample, which could explain the Li depletion (Ryan et al. 2002). As already mentioned, the radial velocity is consistent with the cluster mean, but multi-epoch observations to detect possible variations are currently not in hand. We note, however, that the fact that all of them are Al-rich seems to suggest that the Li deficiency is somehow related to the multiple population scenario.

respectively. We included data for the GC NGC 6397 by selecting a subsample of stars analysed by Lind et al. (2009): in order to be as homogeneous as possible with our target giants, we restricted our attention to those RGB stars within approximately 1 magnitude fainter than the bump. This choice, although limiting the sample size, allows us to minimise the impact of the star-to-star difference in the atmospheric parameters (especially in temperatures, which can increase the internal scatter) and guarantees a reliable comparison with our GC giants. We determined a Li spread of 0.18 dex. We proceeded in the same fashion by including Li abundances for a subsample of giants published by Mucciarelli et al. (2011). We find the Li variation to be 0.25 dex. Unfortunately for the GCs 47 Tuc and NGC 6752, Li abundances in the giant stars have not been determined and we are forced to exploit dwarfs. This should be a point of caution when considering the general trend shown in Figure 8.14. Note, in the same context, that the spectra for NGC6752 by Shen et al. (2010) are characterised by very low S/N ratios, in some cases below 15, possibly suggesting that the spread quoted is over-estimated because of the observational uncertainties.

We detect, for the first time to our knowledge, the existence of an unambiguous correlation between the Li variation and the total cluster luminosity (i.e., mass; the Pearson’s correlation coefficient $r = -0.93$ is significant at more than 99.9%): *the more massive the GC, the larger the Li spread*. This finding seems to suggest that Li production is less efficient in the more massive GCs than in small GCs, because any kind of Li replenishment tends to erase the presence of Li-O and/or Li-Na anticorrelation. We find that in less massive systems the FG and SG stars are very similar as far as the Li content is concerned (even indistinguishable in some cases like M4 and M12). We can speculate that in less massive GCs, the polluter mass range might be biased towards the lower end of the IM-AGB stars ($M \lesssim 6M_{\odot}$) whilst in the most massive GCs we expect the upper envelope of the mass distribution to extend beyond ($M \gtrsim 7M_{\odot}$). This is required to account for the considerable p-capture element variations observed in these massive GCs, such as e.g., NGC 2808, where high levels of O depletion and Na enhancement ($[O/Fe]$ down to ≈ -1.00 and $[Na/Fe]$ up to $\approx +1.00$), as well as significant Mg depletion and Al enrichment have been reported. Regarding Li, any comparison between observed chemical abundances and AGB models must be done bearing in mind all the uncertainties involved. Li production is indeed extremely sensitive to the input physics in the stellar models: in the IM-AGBs there is a very brief phase of Li enrichment at the stellar surface during the first few thermal pulses, with a peak of $A(Li) \sim 4$ dex, but the final Li yield depends on when the star loses most of its mass (Ventura and D’Antona 2010; D’Orazi et al. 2013a). The rate and details of the mass loss are among the most uncertain (and difficult to model) factors in theoretical stellar astrophysics. Interestingly, we have demonstrated that the FG and SG stars display the same Li abundances in GCs like M4 and M12. These results imply that the internal polluters must have produced Li in roughly the same amount as the primordial abundances (that is $A(Li) \sim 2.0-2.3$). Although we recognise that this seems to be an incredible coincidence, it is worth mentioning that AGB models (with their uncertainties) have been shown to provide such abundances. For example, the $5M_{\odot}$ AGB stellar model published in D’Orazi

et al. (2013a) results in $A(\text{Li})=2.00$, by adopting an increased $\alpha_{\text{MLT}}=2.2$ and Bloeker (1995) mass loss law, and $A(\text{Li})=2.35$ with a “standard” $\alpha_{\text{MLT}}=1.75$ and Bloeker mass loss (see Figure 20 of that paper). Similar Li yields have been found previously by D’Orazi et al. (2010b).

The clusters reported in Figure 8.14 are obviously characterised by a range in metallicity. The sample includes the metal-poor GC NGC 6397 ($[\text{Fe}/\text{H}] \approx -2.0$ dex), NGC 6752 ($[\text{Fe}/\text{H}] \approx -1.5$ dex), the intermediate-metallicity GCs M12, M5 and M4 ($[\text{Fe}/\text{H}] \approx -1.3$ dex) and one of the most metal-rich GCs in 47 Tuc ($[\text{Fe}/\text{H}] \approx -0.7$ dex). Given the limited sample size available, we cannot robustly infer the level of contribution provided by metallicity on the spread in Li in GCs. We note that two GCs with almost the same mass (M4 and NGC 6752), but slightly dissimilar $[\text{Fe}/\text{H}]$, do actually exhibit Li variations at a different extent. Irrespective of possible metallicity-related effects, the trend appearing in Figure 8.14 points to the GC mass as the driving parameter of the anticorrelation. This is evident when we compare GCs with similar metallicity but different masses (e.g., M5 *vs* M12 and M4). It is noteworthy, in this context, that these GCs also display different HB morphology, M4 and M5 being an example of the so-called “second-parameter” pair (see e.g., Gratton et al. 2013 and references therein).

The metal-rich GC 47 Tuc (NGC 104, labelled with a different symbol in Figure 8.14) deserves further discussion. In fact, in this GC the large scatter detected in the Li abundance seems to be completely unrelated to variations in p-capture element and, more generally unrelated to the presence of multiple stellar populations. As discussed in D’Orazi et al. (2010b), while SG (O-poor) stars are characterised by a low Li abundance, there is a huge spread within the first stellar generation itself, $A(\text{Li})$ ranging from ~ 1.5 to ~ 2.5 (we ignore for the current purposes the presence of a very Li-rich star with $A(\text{Li})=2.78$). They concluded that this primordial scatter is probably related to the high metallicity of this GC and is likely the Population II analogue of what is observed in Population I stars with similar atmospheric parameters (such as e.g., in the open cluster M67, Randich et al. 2000). In addition, 47 Tuc is known to display peculiar behaviour also in terms of light-element variations and their relationship with the cluster properties, namely its Na-O anticorrelation is relatively short despite the large GC mass. It stands as an outlier in the diagrams of $\text{IQR}^6[\text{Na}/\text{O}]$ *vs* M_V and $\log T_{\text{eff,max}}^{\text{HB}}$ (the maximum temperature on the HB), as derived by Carretta et al. (2010). By discarding this GC, we still can detect the hint for an anticorrelation but the small statistics prevents us from conclusively confirming its existence. The situation will become clear once a larger sample of GCs (encompassing a wide range in current mass) becomes available in the present survey.

They concluded that this primordial scatter is probably related to the high metallicity of this GC and is likely the Population II analogue of what is observed in Population I stars with similar atmospheric parameters, (such as e.g., in the open cluster M67, Randich et al. 2000). By discarding this GC, we still can detect the hint for an anticorrelation but the small statistics prevents us from conclusively confirming its existence. The situation will become clear once a larger sample of

⁶Interquartile range

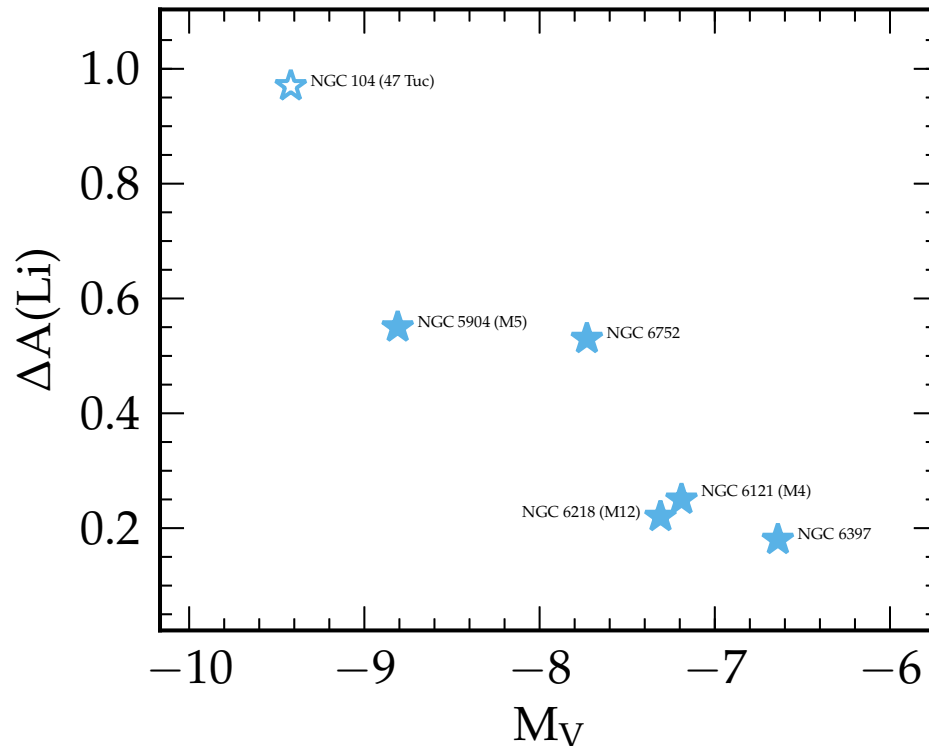


Figure 8.14: $\Delta A(\text{Li})$ as a function of M_V . We denote 47 Tuc with an open star because a spread in lithium in this cluster is found in the first generation and thus is likely due to its metallicity rather than the presence of multiple populations.

GCs (encompassing a wide range in current mass) becomes available.

8.4 Summary and concluding remarks

Lithium provides rare insight into not only the internal processes of stars but also the internal chemical enrichment of GCs. The abundance patterns within these old stellar aggregates are most straightforwardly explained by the presence of multiple populations, whereby a first generation of stars has polluted the medium from which a second generation form. Within this second generation it is still possible for distinct chemical populations to form (see Carretta et al. 2009b and their PIE definitions). Because of its fragility and thus the special conditions required for its production, Li may serve as a unique tracer of the nature of stars that provided the intra-cluster enrichment. Current stellar theory predicts that it is possible for intermediate-mass asymptotic giant branch stars to produce lithium via the Cameron-Fowler mechanism, whereas fast-rotating massive stars and massive binaries will produce Li-free ejecta. How lithium correlates with other p-capture species will reveal whether this element has been produced between the different

stellar generations and thus help to identify the progenitors. Following on from the work of DM10 who focussed on NGC 6121, we have presented lithium and [Al/Fe] abundances in stars on the RGB of the GCs NGC 6218 and NGC 5904. Our findings can be summarised as follows:

In the GC NGC 6218 (M12), any Li variation is less than observational errors and is consistent with no Li variation between the two populations. Thus, whilst the cluster displays clear [Na/Fe] variations (over 1 dex) and [O/Fe] variations (over 1.2 dex), stars across their respective populations remain indistinguishable according to their Li abundance. These variations in Na and O are accompanied by variations in the [Al/Fe] abundance. The (anti)correlations that form between p-capture nuclei are expected when hydrogen burning at high temperatures has been in operation ($T \gtrsim 20$ MK). Because the large variations in p-capture elements are not accompanied by corresponding changes in Li, Li production must have occurred across the different stellar generations. With our current understanding of stellar evolution, such a result favours a major contribution from IM-AGB progenitors, as also found by DM10 in the analogous GC NGC 6121 (M4).

In the GC NGC 5904 (M5), we are unable to statistically confirm Li variation with O or Na; however there is a hint for a Li-Al anticorrelation. We anticipate that the small number of stars with both Li and Na (or O) measured is hindering our ability to detect a relationship between these species. There are possibly four (two confirmed) stars that are very lithium poor for their evolutionary phase. They may be due to non-standard evolution or perhaps members of an extreme (third) population in this cluster, that displays Li deficiency and Al enhancement. Given the presence of a Li-Al anticorrelation in NGC 5904, we have fit a dilution model as per Prantzos and Charbonnel (2006) to explain the chemical history of the cluster. When we mix the composition representative of the primordial population with that of four candidate extreme members, we are unable to account for the abundances of a majority of the cluster stars (which are Li-rich and Al-rich). To do so would require the pristine material to be combined with an unobserved population that has [Al/Fe] of approximately ≈ 1.0 dex. If this is the case, by trying to reproduce a majority of the cluster members we still require an explanation for the (four) extreme population candidates. Thus, NGC 5904 exhibits a level of complexity much higher than its more standard siblings, like M4 and M12. This result is not surprising when we consider the HB morphology of this GC.

There is a clear anticorrelation between the internal Li spread and the current GC mass. Li production appears less efficient in the more massive GCs than in smaller GCs, pointing to a different mass range of the stellar polluters involved in the internal enrichment. Further surveys will help constrain this indication on more robust grounds and reveal what role metallicity plays in the lithium spread found within GCs.

Monash University

Declaration for Thesis Chapter 9

Declaration by Candidate

In the case of Chapter 9, a significant part of this work is to be nominally submitted as:

Angelou, G. C., D’Orazi, V., Constantino, T., Church, R. P., Stancliffe, R. J., and Lattanzio, J. C., (2014). Diagnostics of Mixing in Globular Cluster Red Giant Branch Stars.

The nature and extent of my contribution to the work was the following:

Nature of contribution	Extent of contribution (%)
Primary research and paper writing	80%

The following co-authors contributed to the work, with the contribution from fellow Monash Students indicated.

Name	Nature of contribution	% contr
Dr. Valentina D’Orazi	Consultation and revision	
Prof. John Lattanzio	Consultation and revision	
Mr. Thomas Constantino	Research and consultation	7%
Dr. Richard Stancliffe	Consultation and revision	
Dr. Ross Church	Consultation and revision	

The undersigned hereby certify that the above declaration correctly reflects the nature and extent of the candidates and co-authors contributions to this work

Candidate’s  **Signature** _____ **Date** 28-Aug-2014

Supervisor’s  **Signature** _____ **Date** 28-Aug-2014

Chapter 9

Diagnostics of Mixing in Globular Cluster Red Giant Branch Stars

Dubium sapientiae initium (Doubt is the origin of wisdom)

- Descartes

9.1 Introduction

Mixing in red giant branch (RGB) stars is characterised by two distinct events; the well-understood first dredge-up (FDU) and an additional mixing episode that operates over a longer timescale during a more advanced phase of RGB evolution (“extra mixing” hereinafter). Only mixing during FDU is predicted by standard stellar theory (Iben, 1967). In low-mass stars ($M < 1 M_{\odot}$), deep convective motions develop once the star becomes a giant and can penetrate into regions of the star that have previously experienced partial hydrogen burning. Material enriched in ^4He , ^{14}N and ^{13}C is mixed through the convection zone increasing the prevalence of these nuclei at the stellar surface. Conversely, ^7Li and ^{12}C abundances decrease as they are diluted into the extending envelope. In solar-metallicity stars the $^{12}\text{C}/^{13}\text{C}$ ratio falls from the solar value of ≈ 90 to ≈ 30 after the FDU, whilst ^7Li is depleted by a factor of ≈ 20 . Up to this point the theoretically predicted changes are in good agreement with observations.

It is clear from observations that after FDU the surface compositions are further altered during RGB evolution, (Gilroy and Brown, 1991; Gratton et al., 2000; Smith and Martell, 2003; Shetrone, 2003; Weiss and Charbonnel, 2004; Martell et al., 2008b). This second mixing event sees the cycling of hydrogen burning products into the convective envelope. From a post-FDU value of approximately 30, the $^{12}\text{C}/^{13}\text{C}$ ratio is reduced to ≈ 15 in solar-metallicity stars and to the

equilibrium value of ≈ 4 in metal-poor stars. Lithium is essentially destroyed at all metallicities. These changes are not predicted by standard stellar theory.

The onset of extra mixing seemingly coincides with the bump in the luminosity function (LF bump or bump hereinafter) of globular clusters (GCs). The mixing is therefore associated with when the H shell encounters the composition discontinuity left behind by the deepest extent of FDU. The internal process(es) responsible for the surface changes do not manifest themselves until after the bump because the composition discontinuity, and hence discontinuity in the mean molecular weight (μ) gradient, acts as a barrier to any extra mixing process (Sweigart and Mengel, 1979; Charbonnel et al., 1998).

In this study we are concerned with how well stellar models reproduce the key properties (magnitude of onset, abundance changes) of the mixing events experienced during the RGB phase of evolution. Observations of lithium in GC stars are used to constrain FDU and the extra mixing event associated with the bump in the GC luminosity function. Matching the magnitude of the LF bump has, in the past, been used as a measure of the adequacy of stellar models (King et al., 1985; Fusi Pecci et al., 1990; Alongi et al., 1991; Zoccali et al., 1999; Salaris et al., 2002; Riello et al., 2003; Bjork and Chaboyer, 2006; Meissner and Weiss, 2006; Di Cecco et al., 2010; Cassisi et al., 2011). Here we expand upon these results and focus on two questions in particular:

- Do stellar models match the magnitude of FDU and the onset of extra mixing in the GCs? Recent work by Cassisi et al. (2011) and Angelou et al. (2012) suggest they do not for at least the extra mixing event. Observations of lithium indicate the onset of FDU and compliment the photometric determinations of the LF bump.
- Can the extra mixing associated with the LF bump be explained by a single process? We explore specifically whether the thermohaline mechanism can simultaneously explain the behaviour of $[C/Fe]$ and $A(Li)$ as a function of magnitude along the RGB. Lithium is sensitive to mixing and well determined from high resolution data; reproducing the behaviour of this element is an important test in itself. By matching both $[C/Fe]$ and $A(Li)$ we also ensure that the mixing mechanism is not simply being calibrated to a single species.

The FDU event is predicted by stellar theory because the mixing is an outcome of changes in the radiative temperature gradient. The criteria for convection used by stellar codes are either based on the temperature gradient (Schwarzschild) or both the temperature and μ gradients (Ledoux, 1947). The processes that initiate mixing at the LF bump are unable to develop under the assumptions of canonical theory; a further prescription is required for instability. Although the LF bump and the structural readjustment was a prediction of stellar theory (Thomas, 1967; Iben, 1968a), the associated mixing was not. Spectroscopic surveys and empirical evidence were required to infer its operation.

We note that although we focus on thermohaline mixing, the processes responsible for extra mixing remains uncertain. Several extra mixing mechanisms

have been explored in the literature. They include rotational mixing (Sweigart and Mengel, 1979; Chanamé et al., 2005; Palacios et al., 2006), magnetic fields (Palmerini et al., 2009; Nordhaus et al., 2008; Busso et al., 2007; Hubbard and Dearborn, 1980), internal gravity waves (Denissenkov and Tout, 2000) and more recently thermohaline mixing (Eggleton et al., 2006, 2008; Charbonnel and Zahn, 2007a). In this work we only investigate the thermohaline mixing mechanism.

The thermohaline formalism, as well as the details of the stellar models are discussed in §2. In §3 we highlight the central role lithium plays as a diagnostic of stellar physics whilst emphasising the need for homogeneous data – particularly in complex systems like GCs. In §4 we identify various evolutionary events in GCs using a combination of spectroscopic and photometric indicators. Comparisons with predictions from stellar models across the metallicity range of GCs expose shortfalls in the current state of stellar theory. We examine the contribution from the stellar microphysics, including the choice of equation of state (EOS). As noted by (Salaris et al., 2002), the consequences of the EOS selection on RGB evolution have not been investigated. In addition to the microphysics, we consider the importance of overshoot at convective boundaries. Finally in §5, we determine whether thermohaline mixing can simultaneously account for the depletion of carbon and lithium as a function of luminosity. Such a demand is a stringent test of any extra mixing process.

9.2 Overview of the Stellar Models

The stellar models in this work are calculated with MONSTAR (the Monash version of the Mt. Stromlo evolution code; see Campbell and Lattanzio 2008). Opacities are covered at the high temperature end by the OPAL Rosseland mean opacity tables (Iglesias and Rogers, 1996). High temperature opacities ($T > 10^4\text{K}$) are computed from the OPAL tables. Below 10^4K opacity tables from Lederer and Aringer (2009) with variable C and N content are used (see Campbell 2007 and Campbell and Lattanzio 2008 for further details).

As MONSTAR ordinarily only follows those species that are significant energetically. A seven species network (^1H , ^3He , ^4He , ^{12}C , ^{14}N , ^{16}O as well as a seventh pseudo-element that ensures baryon conservation) is sufficient to include feedback on the structure from the nuclear energy generation. We have extended the network for this study so that the evolution of ^7Be , ^7Li and ^{13}C are now followed; with the necessary changes to temporal and spatial resolution criteria to follow these fragile species (see Lattanzio et al. in prep for the importance of these criteria). The key reactions and source of each adopted rate of reaction can be found in Table 3.2. Note that we employ the $^{14}\text{N}(p, \gamma)^{15}\text{N}$ reaction rate provided by Champagne (private communication) which is consistent with that given by Adelberger et al. (2011) and the LUNA collaboration. Palmerini et al. (2011b) discuss the consequences of the new rate for low-mass stellar evolution, including extra mixing.

Convective energy transport in MONSTAR is treated according to the mixing length theory (MLT, Böhm-Vitense 1958). Mixing of the chemical abundances is

Reaction Rate	Source
${}^1\text{H}(\text{p}, \text{e}^+\nu_e){}^2\text{H}$	Harris et al. (1983)
${}^3\text{He}({}^3\text{He}, 2\text{p}){}^4\text{He}$	Caughlan and Fowler (1988)
${}^3\text{He}({}^4\text{He}, \gamma){}^7\text{Be}$	Caughlan and Fowler (1988)
${}^{12}\text{C}(\text{p}, \gamma){}^{13}\text{N}$	Caughlan and Fowler (1988)
${}^{14}\text{N}(\text{p}, \gamma){}^{15}\text{N}$	Champagne (2004, private comm)
${}^7\text{Be}(\text{e}^-, \nu_e){}^7\text{Li}$	Reaclib electron capture database
${}^7\text{Be}(\text{p}, \gamma){}^8\text{B}$	Angulo et al. (1999)
${}^7\text{Li}(\text{p}, {}^4\text{He}){}^4\text{He}$	Descouvemont et al. (2004)
${}^{13}\text{C}(\text{p}, \gamma){}^{14}\text{N}$	Angulo et al. (1999)

Table 9.1: Key reaction rates used in MONSTAR.

calculated using a diffusion equation (Campbell and Lattanzio, 2008). The MLT parameter $\alpha_{MLT} = 1.75$ best reproduces the solar model at the Sun’s current age (we assume that the Sun has a metallicity $Z = 0.014$ throughout this work, see Asplund et al. 2009). In the models presented here, we employ the Schwarzschild criterion and where specified, allow for non-locality by including a prescription for diffusive overshoot. We follow the procedure of Herwig et al. (1997) who parameterised the numerical simulations of convection by Freytag et al. (1996). The results indicated an exponential decay in velocity of the overshooting material. In analogy to the pressure scale height, H_P , a ‘velocity scale height’, H_v , is defined such that

$$H_v = f_{os} H_P \quad (9.1)$$

where f_{os} is a scaling factor. The resulting equation for the diffusion coefficient is then

$$D_{os} = D_0 e^{\frac{-2z}{H_v}} \quad (9.2)$$

where D_0 is the diffusion coefficient at the last convective point and z is distance from the convective boundary.

Our implementation of the thermohaline mechanism uses the formulation developed by Ulrich (1972) and Kippenhahn et al. (1980), in which thermohaline mixing is modelled as a diffusive process. This prescription has been employed in previous work by Angelou et al. (2012, 2011), Charbonnel and Lagarde (2010), Stancliffe (2010), Stancliffe et al. (2009) and Charbonnel and Zahn (2007a,b). The equation for the diffusion coefficient is:

$$D_t = C_t K \left(\frac{\varphi}{\delta} \right) \frac{-\nabla_\mu}{(\nabla_{\text{ad}} - \nabla)} \quad \text{for } \nabla_\mu < 0, \quad (9.3)$$

where $\varphi = (\partial \ln \rho / \partial \ln \mu)_{P,T}$, $\delta = -(\partial \ln \rho / \partial \ln T)_{P,\mu}$, $\nabla_\mu = (\partial \ln \mu / \partial \ln P)$, $\nabla_{\text{ad}} = (\partial \ln T / \partial \ln P)_{\text{ad}}$, $\nabla = (\partial \ln T / \partial \ln P)$, K is the thermal diffusivity and C_t is a dimensionless free parameter. In this diffusive theory, C_t is related to the aspect ratio, α , of the thermohaline fingers (assumed to be cylindrical) by

$$C_t = \frac{8}{3} \pi^2 \alpha^2. \quad (9.4)$$

The mechanism is elegant in that the depth of mixing is set by the stellar structure resulting in only one free parameter. An empirically derived value of $C_t = 1000$ can reproduce abundance patterns in both globular cluster stars (Angelou et al., 2011, 2012) and field stars (Charbonnel and Lagarde, 2010) as well as the dichotomy between carbon-normal and carbon-enhanced metal-poor stars (Stancliffe et al., 2009). Denissenkov (2010) and Cantiello and Langer (2010) prefer a lower value of $C_t = 12$ on theoretical grounds, which is also supported by 3D hydrodynamical models of the process, suggesting that the mixing is inefficient on the RGB (Denissenkov and Merryfield, 2011; Traxler et al., 2011a). Rightly or wrongly, parametrising extra mixing in this form and comparing to observations can still tell us much about the transport of material in the stars. Similar conclusions could be reached had we elected to include a phenomenological mixing model (Denissenkov and Vandenberg, 2003). Note that in such models the depth of mixing is usually specified by a constant shift in either mass or temperature from the hydrogen-burning shell. An additional free parameter sets the mixing speed; a less physically motivated but similar configuration to that used here.

In order to compare to observations, we convert our stellar models from luminosity space to absolute visual magnitude (M_V) throughout. This requires a V band bolometric correction for each stellar model calculated. Theoretical model atmospheres from Castelli et al. (1997, ATLAS9) provide the necessary tables of bolometric corrections and we determine the most appropriate value by using a cubic spline to interpolate in composition, T_{eff} and surface gravity.

9.3 Observations of Lithium in Globular Clusters

9.3.1 Overview of the Lithium Data

The lithium abundances used to constrain our models come from medium-to-high resolution surveys of GCs. Although far more complex than their classic simple stellar population archetype, GCs are still useful testbeds of stellar theory due to their well populated colour-magnitude diagrams (CMDs). Rather than requiring a single isochrone, through medium-to-high resolution observations, a more robust test of stellar evolution has presented itself. These systems host multiple stellar populations spanning relatively small differences in ages and characterised by internal variations in their light-element (e.g., C, N, Na, O, Al, see Gratton et al. 2012a and references therein for a recent review on multiple populations) and ^4He content (Gratton et al., 2010a, 2011, 2012b).

In addition to these primordial abundance variations, the constituent stars undergo *in situ* composition changes such as those experienced on the RGB. *In*

situ mixing manifests itself as a function of luminosity and is easily discerned. The carbon and nitrogen abundances in particular, have been extensively measured. The $^{12}\text{C}/^{13}\text{C}$ ratio is also a useful tracer of mixing. It scrutinises FDU robustly (Dearborn et al., 1975a; Tomkin et al., 1976; Charbonnel, 1994), but saturates rather rapidly once extra mixing begins. Like lithium, measuring $^{12}\text{C}/^{13}\text{C}$ requires spectra with high resolution and signal-to-noise.

Lithium is perhaps the most versatile probe of mixing during the RGB. It is sensitive enough to identify the onset of each event but not so fragile that it is immediately destroyed. It can therefore provide an indication of the mixing efficiency of both FDU and the extra-mixing event. It also has an advantage in that its abundance determination is reliable: it is derived from the the Li I doublet at 6707.78Å, rather than from molecular bands as is the case with [C/Fe] and [N/Fe].

We have compiled data from four medium-to-high resolution studies that focus on lithium abundances in globular cluster giants. The sample of four clusters spans a range in metallicity that covers most of the globular cluster metallicity distribution. We expect this sample to clearly illustrate how the onset of each mixing event depends on metallicity. A list of our target clusters and their general properties can be found in Table 9.3.1.

The most metal-rich cluster in our sample, M4 ([Fe/H] = -1.10), and the most metal-poor, NGC 6397 ([Fe/H] = -2.10), have subgiant branch abundances consistent with the Spite plateau (Spite and Spite, 1982, Figure 1); a point discussed by the authors of the original surveys. In these two clusters, the first instance of lithium depletion marks the onset of FDU. The difference in metallicity causes stars in M4 to begin FDU approximately $\Delta M_V \approx 0.3$ magnitudes fainter than those in NGC 6397. This is because in metal-rich stars, the additional low-ionisation metals (i.e., Ca, Na, K, and Al) provide an extra source of free electrons and contribute to the higher opacity. In metal-poor stars the only free electrons are those from ionised hydrogen, thus with all other things being equal, the metal-rich stars:

1. begin the inward migration of the convective envelope at a lower luminosity; and
2. develop deeper convective envelopes.

As one might expect from deeper dredge-up, stars in M4 exhibit a post-FDU Li abundance that is generally lower than those in NGC 6397. However it is not certain that we are detecting a metallicity effect because systematic uncertainties may exist between the two studies. The upper range of the abundances in M4 is consistent with the stars in NGC 6397. Furthermore, the significant change in abundance during FDU is due to the transition from shallow surface convection to a deep convective envelope. A slightly deeper convective envelope may not necessarily translate to a detectable difference in the surface abundance. The systematic uncertainties that exist *between* surveys can only truly be eliminated through a homogeneous study of both clusters (i.e., identical instrument, line lists, codes, methodology).

ID	Name	Luminosity (M_V)	[Fe/H]	FDU (M_V)	RGB _{bump} (M_V)	Number of Targets	Source
NGC 5904	M5	-8.81	-1.29	-	0.50	99	VD14
NGC 6218	M12	-7.31	-1.37	-	0.78	63	VD14
NGC 6121	M4	-7.19	-1.10	3.65	0.45	87	Mucciarelli et al. (2011)
NGC 6397	-	-6.64	-2.10	3.3	0.163	454	Lind et al. (2009) and González Hernández et al. (2009)

Table 9.2: General properties of those clusters used to constrain the models in this work.

Cluster	Mass (M_\odot)	Z	X(⁴ He)	X(¹ H)	X(¹² C)	X(¹⁴ N)	X(¹⁶ O)	X(⁷ Li)	α_{MLT}	C_t
NGC 6397	0.80	0.00011	0.24989	0.75	1.99×10^{-5}	5.83×10^{-6}	4.82×10^{-6}	9.39×10^{-10}	1.75	1000
M4	0.80	0.0011	0.2489	0.75	1.99×10^{-4}	5.83×10^{-5}	4.82×10^{-5}	9.39×10^{-10}	1.75	1000

Table 9.3: Model details used to fit the clusters NGC 6397 and M4 in Figure 9.3.

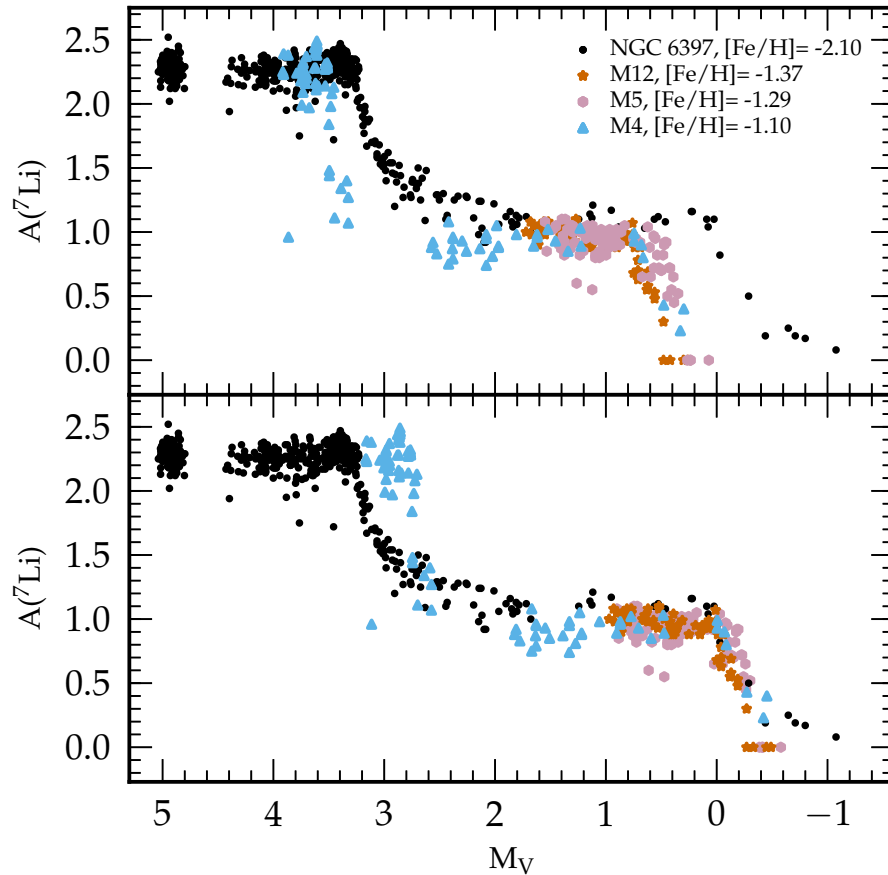


Figure 9.1: Upper panel: $A(^7\text{Li})$ as a function of absolute magnitude (M_V) for NGC 6397 (black circles), M12 (vermilion stars), M4 (blue triangles) and M5 (lavender hexagons). Lower panel: As above but with an offset applied to each cluster so that the magnitude of the LF bump coincides for each cluster.

The clusters present noticeably different gradients of lithium depletion during FDU. Stars in M4 complete FDU over a much smaller luminosity range than those in NGC 6397. Metal-poor stars are more compact and hotter than their metal-rich counterparts which would suggest that they should in fact deplete lithium more efficiently. This abundance trend reflects the rate of advance of FDU which is different because the greater opacity and allows the convective envelope to penetrate faster in the metal-rich regime.

Figure 9.1 also provides insight into the extra mixing process. Our sample covers a luminosity range that also includes the LF bump. Because the depth of FDU is metallicity dependent, so too is this secondary mixing event. Metal-rich stars begin extra mixing at fainter magnitudes because the hydrogen shell is not required to advance as far before it encounters the homogenised region and removes the μ inversion that inhibits the mixing process. We note that such a metallicity

trend is not evident from Figure 9.1 nor from the statistically determined values of the cluster LF bump magnitudes (Nataf et al., 2013) presented in Table 9.3.1. Uncertainty in the metallicity determination¹, determination of the distance modulus, and the role of multiple populations all contribute to the observed behaviour. Such issues with direct comparison of the evolutionary events are a common theme throughout this paper.

In the bottom panel of Figure 9.1 we have applied a luminosity offset to each cluster so that the magnitude at which extra mixing begins is common to all clusters. In all clusters, irrespective of metallicity, extra mixing depletes lithium with equal efficiency. Agreement is further improved when one considers that the abundances of the brightest three stars in NGC 6397 are upper limits. Such strong agreement is perhaps not unexpected given the fragility of lithium but it highlights a clear property (and constraint) of the physics that drives the mixing during this epoch.

9.3.2 Elucidating the Mixing Events in Low-Metallicity Clusters

When trying to match the extra mixing event in M92 ($[\text{Fe}/\text{H}] = -2.2$), Angelou et al. (2012) found that their models overestimated the magnitude of the LF bump by $\Delta M_V \approx 0.7$ mag. They were required to artificially deepen FDU by more than 15%² in their calculations to match the photometrically determined magnitude of the LF bump. An extension of the convective envelope was also required to match the LF bump in M15 (also $[\text{Fe}/\text{H}] = -2.2$). In these clusters, it is unclear if the onset of extra mixing coincides with the photometric bump. One interpretation of the data implies that surface abundance changes began before the LF bump. Possible reasons for the discrepancy were given as uncertainties in the spectroscopy (e.g., combining data sets, determining abundances from molecular bands), difficulties in determining the luminosity of the bump at low metallicity, or that extra mixing had initiated before the LF bump (which would prove to be a serious issue for stellar evolution). The authors noted that homogeneous lithium data would reveal the true behaviour of the cluster.

The three low-metallicity clusters studied by Angelou et al. (2012) are yet to have their lithium abundances systematically measured (M92, M15 and NGC 5466, $[\text{Fe}/\text{H}] = -2.2$). They do, however, have comparable metallicity to the surveyed NGC 6397 ($[\text{Fe}/\text{H}] = -2.1$). In the upper panel of Figure 9.2 we plot $[\text{C}/\text{Fe}]$ from M92 (right axis, lavender triangles) and $A(\text{Li})$ from NGC 6397 (left axis, black circles) as functions of absolute visual magnitude. Data for M92 are taken from Smith and Martell (2003) who applied offsets to the studies by Carbon et al. (1982), Langer et al. (1986) and Bellman et al. (2001) in order to remove systematic differences in abundance scales. Data for NGC 6397 are a combination of the surveys by Lind et al. (2009) and González Hernández et al. (2009). The data taken from González Hernández et al. (2009) were re-analysed by Lind et al. (2009) to enlarge their sample. To reduce the effects of systematic uncertainties

¹Whilst there may be some uncertainty in the metallicity determination of these systems, it is a robust result that NGC 6397 and M4 differ by a approximately a factor of 10.

²The depth of FDU was extended from $0.368 M_\odot$ to $0.320 M_\odot$.

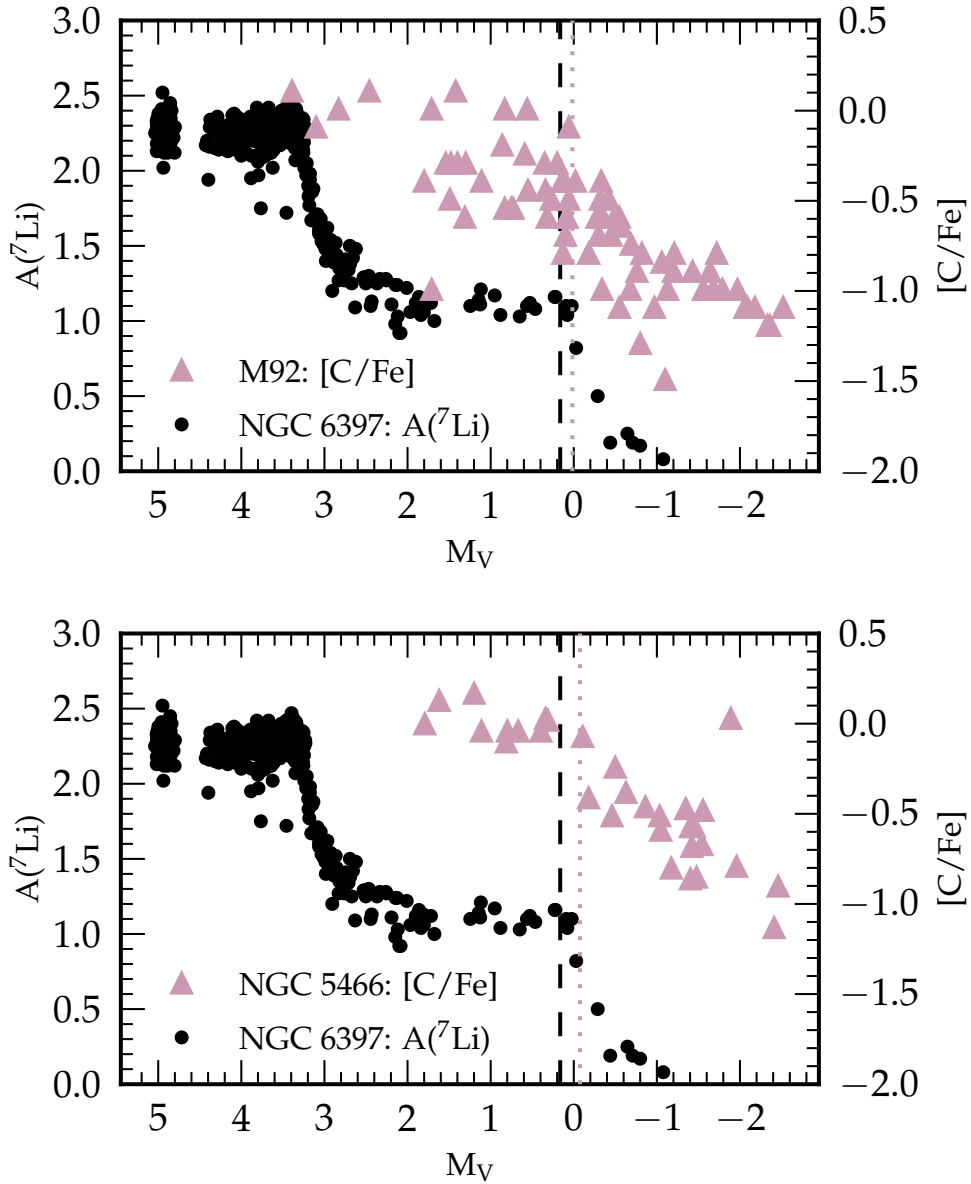


Figure 9.2: Left Axis (both panels): Black circles denote $A(^7\text{Li})$ abundance as a function of magnitude for stars in NGC 6397 ($[\text{Fe}/\text{H}] = -2.1$). The dashed vertical line corresponds to the photometrically determined LF bump of the cluster ($M_V = 0.163$). Right Axis (top panel): Lavender triangles denote $[\text{C}/\text{Fe}]$ abundance as function of magnitude for stars in M92 ($[\text{Fe}/\text{H}] = -2.2$). The dotted vertical line corresponds to the photometrically determined LF bump of the cluster ($M_V = 0.016$). Right Axis (bottom panel): Lavender triangles denote $[\text{C}/\text{Fe}]$ abundance as function of magnitude for stars in NGC 5466 ($[\text{Fe}/\text{H}] = -2.2$). The dotted vertical line corresponds to the photometrically determined LF bump of the cluster ($M_V = -0.075$). The LF bump for each cluster was determined by Nataf et al. (2013).

between the studies, we adopt the abundances presented in the Lind et al. (2009) study. The dotted lavender line indicates the magnitude of the LF bump in M92 ($M_V = 0.016$; Nataf et al. 2013) and the black dashed line the magnitude of the LF bump in NGC 6397 ($M_V = 0.163$; Nataf et al. 2013). Spectroscopically, it is unclear from [C/Fe] what magnitude extra mixing begins in the massive GC M92. The lithium decrease in NGC 6397, on the other hand, has a well defined starting magnitude that corresponds to its photometrically determined bump and the bump of the similarly metal-poor M92. In the lower panel we compare data from the less massive cluster NGC 5466. As per the panel above, [C/Fe] abundances are denoted by lavender triangles with the scale provided on the right axis. Nataf et al. (2013) determined the magnitude of the LF bump in this cluster to be $M_V = -0.075$. In NGC 5466 and NGC 6397 the respective magnitudes of the LF bump and onset of surface abundance changes (due to extra mixing) agree quite well.

Unlike M92, for which the data are a combination of multiple surveys, data from NGC 5466 is homogeneous (it is taken from a single study by Shetrone et al. 2010). It may be that the combination of multiple data sets clouds the true cluster behaviour. If the uncertainty surrounding M92 is purely due to observational error, then results from homogeneous surveys such as APOGEE will shed light on this issue. However, we note that both NGC 6397 and NGC 5466 are much less massive than M92 and Carretta et al. (2010) and VD14 have demonstrated how cluster mass can influence the primordial internal abundance variations (also related to the presence of multiple populations).

Because the Li abundances suggest that the beginning of extra mixing in low-metallicity clusters does indeed coincide with the magnitude of the photometrically derived LF bump, then it is clear that the models are overestimating the luminosity of the onset of this event. This is irrespective of the chosen extra mixing mechanism and dependent on the physics of the stellar codes. Such an inconsistency was identified by King et al. (1985) and Fusi Pecci et al. (1990). We explore the extent of the discrepancy in §4.

9.4 The Onset of the Red Giant Branch Mixing Events

There are three well tried methods by which we can compare theoretical predictions with empirical measurements of the LF bump:

- By comparing the parameter $\Delta V_{\text{HB}}^{\text{bump}} = V_{\text{bump}} - V_{\text{HB}}$; the V magnitude difference between the RGB bump and the horizontal branch at the RR Lyrae instability strip magnitude (Fusi Pecci et al., 1990; Zoccali et al., 1999; Salaris et al., 2002; Riello et al., 2003; Bjork and Chaboyer, 2006; Meissner and Weiss, 2006; Di Cecco et al., 2010).
- By comparing the parameter $\Delta V_{\text{bump}}^{\text{MSTO}} = V_{\text{MSTO}} - V_{\text{bump}}$; the V magnitude difference between the RGB bump and the main sequence turn off (MSTO, Cassisi et al. 2011).

- By converting models and observations to a common magnitude system such as M_V or M_{bol} and comparing theoretical predictions with the empirically determined locations (King et al., 1985; Alongi et al., 1991; Bjork and Chaboyer, 2006; Angelou et al., 2012).

The first two methods have the advantage of being independent of distance and reddening. As discussed by Cassisi et al. (2011), the first method does introduce some uncertainty with respect to the placement of the observed HB level for GCs with blue HB morphologies and in theoretical predictions of the HB luminosity (dependent on the core mass predicted by each code). The third method introduces an extra source of uncertainty because it relies on accurate determination of the distance modulus. In this study we will employ both the second and the third method in our investigation of the RGB mixing events.

The natural method for comparing the key theoretical and photometric indicators of stellar evolution has been through age matching of isochrones. In this study we calculate individual stellar models representative of stars on giant branch after approximately 12 Gyr ($M = 0.8 M_{\odot}$) and compare directly to observations. The individual models are the simplest means by which to investigate the physics that may shift the theoretical onset of mixing events. Once the effects of the microphysics are understood, they can later be incorporated in the grids of models that generate the isochrones. As a consequence of this technique, we expect to find greater disparity between theory and observations compared to studies that employ calibrated isochrone matching, but we perhaps portray a truer state of affairs. In many studies, the isochrones that best fit the magnitude of the LF bump significantly overestimate the age of the cluster compared with that determined by fitting the turn off mass. It is not uncommon to require isochrones with ages greater than the age of the Universe to match luminosity of the LF bump (see Riello et al. 2003 and Cassisi et al. 2011).

Our sample of GCs includes two systems at opposite ends of the GC metallicity distribution. In the metal-poor cluster, NGC 6397 ($[Fe/H] \approx -2.10$), and the metal-rich, NGC 6121 (M4, $[Fe/H] \approx -1.10$), stars have been surveyed across a luminosity range that covers both FDU and the extra mixing event. Li abundance determinations for the stars in NGC 6397 are presented in the top row of Figure 9.3 and in M4 in the bottom row. The data are plotted both as a function of absolute visual magnitude (left panels) and as a function of luminosity (right panels). The two brightness systems are employed as a check on possible systematic errors in our method (see below). We calculate stellar models for each cluster (lavender curves) with the parameters specified in Table 9.2 as a first approximation.

In NGC 6397 the models overestimate the magnitude of both mixing events. The difference in magnitude at FDU (≈ 0.3 mag) is not as pronounced as for the LF bump (≈ 0.7 mag). In the metal-rich cluster, M4, the onset of FDU is consistent with the observations whilst a discrepancy is present at the LF bump (≈ 0.4 mag). It is well documented that theoretical models overestimate the magnitude of the LF bump (Fusi Pecci et al., 1990; Bjork and Chaboyer, 2006; Di Cecco et al., 2010; Cassisi et al., 2011), however this is the first time an issue with FDU has been raised. The recent availability of lithium observations, which

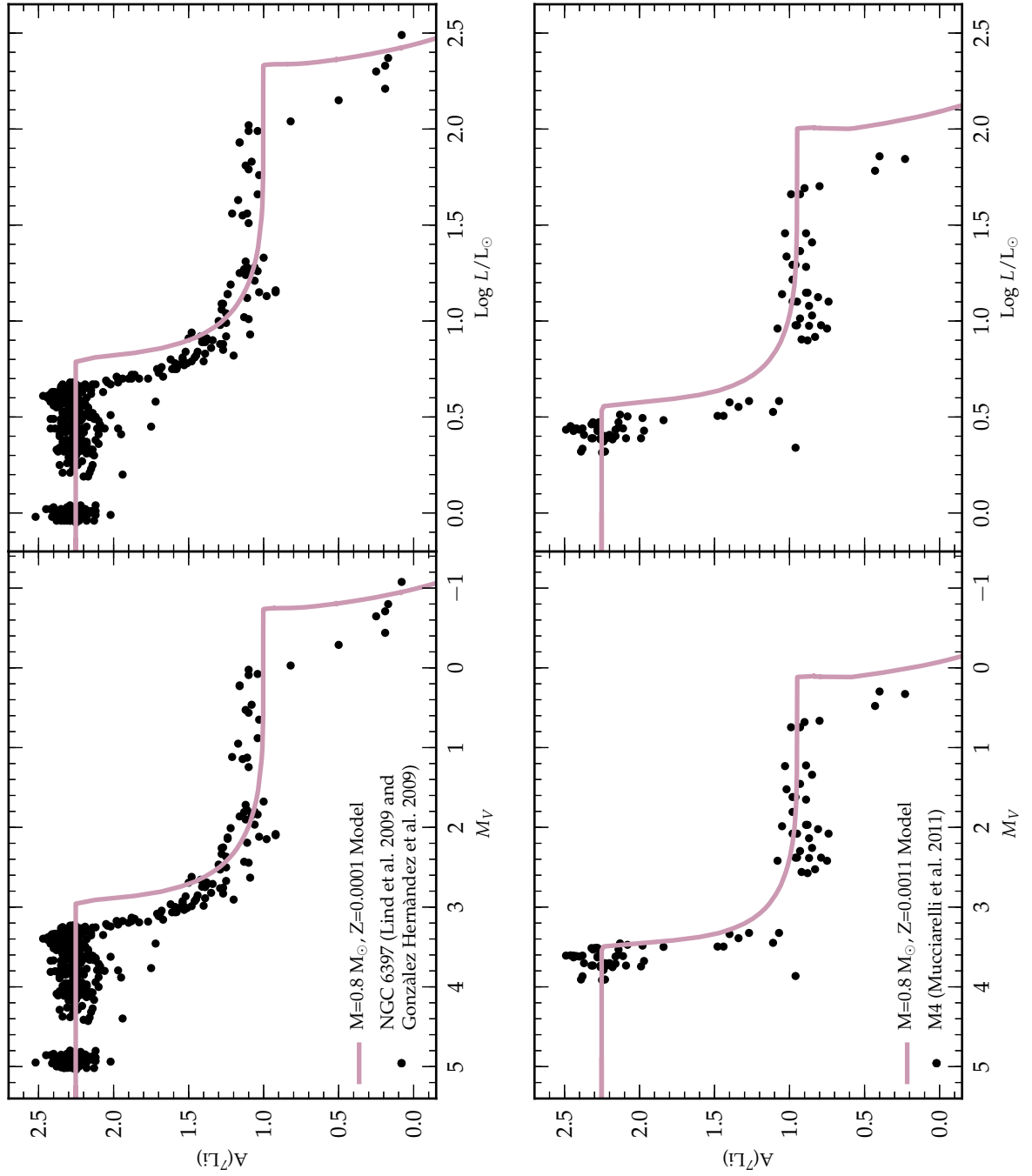


Figure 9.3: Top panels: $A(\text{Li})$ as a function of absolute magnitude (left) and luminosity (right) in the globular cluster NGC 6397. Data are taken from Lind et al. (2009) and González Hernández et al. (2009). Bottom panels: $A(\text{Li})$ as a function of absolute magnitude (left) and luminosity (right) in the globular cluster M4. Data for this cluster are taken from Mucciarelli et al. (2011). In each panel the solid lavender curve denotes a first approximation to the respective cluster (see Table 9.2 for model details).

probe both RGB mixing events, allows for an investigation of FDU across a range of metallicities. Previous investigations of mixing during the RGB have relied on $[\text{C}/\text{Fe}]$ and $[\text{N}/\text{Fe}]$ which are of limited use for the FDU event because these species change very little during FDU at metallicities typical of GCs. Furthermore, their abundance determination (usually from molecular bands) is less robust than is the case for Li. We have seen that in the lowest metallicity clusters there is an intrinsically large spread in $[\text{C}/\text{Fe}]$ and $[\text{N}/\text{Fe}]$ which makes identifying the onset of mixing spectroscopically difficult. Charbonnel (1994, 1995) has used both $^{12}\text{C}/^{13}\text{C}$ and Li to test extra mixing due to rotational instabilities. Model comparisons to M4 and Halo stars at NGC 6397 metallicity were presented with their predicted FDU magnitudes comparable or slightly brighter than ours.

9.4.1 Bolometric Corrections

It is concerning how much the models are over estimating the onset of the mixing events, especially the LF bump at low metallicity. It is prudent to first ascertain whether the magnitude offset between the theoretical and observationally determined LF bump is simply a result of a systematic error introduced through the conversion from luminosity to absolute magnitude. The fact that the magnitude difference at FDU is not as pronounced as for the LF bump does not rule out a conversion problem. The bolometric corrections are functions of metallicity, T_{eff} and surface gravity and thus vary throughout evolution. Salaris et al. (2002) have found that by changing the model atmosphere sets, bolometric corrections can differ by up to 0.1 magnitudes. This is not enough to account for the $\approx 0.3 M_V$ offset between the models and observations at FDU. Even if we were to apply bolometric corrections from an empirically calibrated set of model atmospheres (e.g., Houdashelt et al. 2000), it does not rule out the presence of systematic errors in our conversion. To eliminate this source of error we use independently converted visual magnitudes calculated by Lind et al. (2008) in their study of NGC 6397. Their method, similar to ours described above, converts visual magnitude to luminosity by applying a calibration from Alonso et al. (1999). This calibration, too, is a function of (independently determined) metallicity and T_{eff} . Magnitude was converted to luminosity through a 13.5 Gyr isochrone for the cluster (Richard et al., 2005, which placed their stars in the mass range $0.78 - 0.79 M_{\odot}$; similar to the $0.8 M_{\odot}$ that we have modelled here). The Lind et al. (2008) results are presented in the top right panel of Figure 9.3. Our stellar model is again denoted by the solid lavender curve and in this case, the luminosity is calculated directly from

the equations of stellar structure (without any conversions to the data from us). The left (abundances as a function of M_V) and right (abundance as a function of luminosity) panels look remarkably similar with the expected factor of 2.5 difference in the respective brightness scales. Mucciarelli (private communication) has also provided us with independently determined luminosities for M4 (Figure 9.3). The two brightness scales (M_V and luminosity) yield the same behaviour in each cluster, thus systematic uncertainties in our conversion are unlikely responsible for the magnitude discrepancy between theory and observation.

We also have no reason to believe that there is a systematic issue with bolometric corrections determined from model atmospheres at low metallicity. In fact one would expect the opposite to be true; bolometric corrections at high metallicity should be more uncertain. Synthetic colors perform quite well in the metal poor regime, without significant deviations between metallicities of $[\text{Fe}/\text{H}] = -1.5$ and $[\text{Fe}/\text{H}] = -2.5$ (Casagrande, private communication). As the metallicity increases, however, the choice of atomic line-lists becomes increasingly important. We note that microturbulence in low-metallicity model atmospheres is one possible source for systematic issues. Microturbulence can affect UV/blue wavelengths so if the velocities were to change in the low metallicity regime, then the derived corrections would be systemically offset. As no evidence for such behaviour exists, a closer look at the physics of stellar modelling is required.

9.4.2 Comparison Across the Globular Metallicity Distribution

We have identified the onset of FDU and extra mixing in the GCs NGC 6397 and M4 from the spectroscopic surveys of lithium. Our conversion to a common magnitude system indicates that the stellar models overestimate the magnitude at which extra mixing begins, with the situation seemingly worse at low metallicity. The magnitude of FDU in NGC 6397 is also overestimated but we find no such issue in the higher-metallicity cluster M4. The results from these two clusters raise a series of interesting questions that only a larger sample of GCs will help answer:

1. Do stellar models better reproduce the structure of higher metallicity stars (i.e., the depth of FDU)? Does the level of discrepancy depend on metallicity as suggested by these two clusters?
2. Do uncertainties in the distance modulus make direct comparison too inconsistent to be meaningful?

Such comparisons between theory and observation are common throughout the literature and because GCs are observed to have enhanced α -element abundances compared to scaled-solar values, their metallicities are often expressed in terms of the *total metallicity*, $[\text{M}/\text{H}]$. This is defined by Salaris et al. (1993) as

$$[\text{M}/\text{H}] = [\text{Fe}/\text{H}] + \log(0.638 \times 10^{[\alpha/\text{Fe}]} + 0.362). \quad (9.5)$$

Before proceeding, we summarise the findings of previous comparisons. In comparison of the $\Delta V_{\text{HB}}^{\text{bump}}$ parameter, Riello et al. (2003) find good agreement between

theory and observation at higher metallicities but note significant discrepancies at low metallicity. Investigations of low-metallicity GCs include those by Fusi Pecci et al. (1990) and Di Cecco et al. (2010), who also used the parameter $\Delta V_{\text{HB}}^{\text{bump}}$, to determine that at $[\text{M}/\text{H}] \lesssim -1.7$, models overestimate the magnitude of the LF bump by 0.4 mag or more. Di Cecco et al. (2010) also conducted tests on the effects of various microphysics and determined that models with α -element and CNO-enhancements could not account for the discrepancy nor could the revised solar heavy-element mixture. Cassisi et al. (2011), who employed the $\Delta V_{\text{bump}}^{\text{MSTO}}$ parameter, found that the theoretical bump was too bright by 0.2 magnitudes on average, but uncertainties were consistent with discrepancies in excess of ≈ 0.4 magnitudes in the lowest metallicity clusters. In their test of the stellar microphysics, Bjork and Chaboyer (2006) have determined that the uncertainty in theoretical values for the LF bump magnitude varies with metallicity between +0.13 and -0.12 magnitudes at $[\text{Fe}/\text{H}] = -2.4$ and between +0.23 and -0.21 magnitudes at $[\text{Fe}/\text{H}] = -1.0$. The dominant sources of uncertainty were attributed to α -element abundance, the mixing length parameter, and the high-temperature opacity all of which are increasingly important at higher metallicity. We also note the work by Troisi et al. (2011) who used the empirical brightness difference between the LF bump and the point on the main sequence that is at the same colour as the bump. Their models also overestimated the magnitude of the LF bump unless they employed an initial $Y = 0.2$. We reiterate that the studies above have rightly employed isochrones in their comparisons to GCs. Unfortunately, in order to match the bump parameters, isochrones much older than the cluster age (as determined by fitting the turn-off mass) were often required. Such results hint that the underlying cause of the discrepancy between our calculations and the observations lies with the stellar physics.

Unlike FDU, which requires an additional spectroscopic indicator, the LF bump is readily identified through the CMD and hence has been observed in more clusters. In Figure 9.4, we investigate systematically how the discrepancy between the predicted and empirically determined LF bump magnitudes vary with metallicity. Data are taken from Nataf et al. (2013) who performed statistical analyses on publicly available high-resolution Hubble photometry. From this, the location of the LF bump in 72 GCs was accurately determined. Their data (black circles) are plotted both as functions of $[\text{M}/\text{H}]$ and also $[\text{Fe}/\text{H}]$ in panels 9.4a and 9.4b respectively. Also plotted in each panel are predictions of the LF bump magnitudes from MONSTAR with solar-scaled abundances (triangles), α -element enhancement of $[\alpha/\text{Fe}] = +0.2$ (squares) and α -element enhancement of $[\alpha/\text{Fe}] = +0.4$ (pentagons). In panel 9.4b we also include calculations made with abundances scaled from the solar values of Anders and Grevesse (1989), i.e., with $Z_{\odot} = 0.02$. This highlights the advantage of adopting the total metallicity scale, $[\text{M}/\text{H}]$, in these studies. This panel demonstrates how the choice of initial composition (i.e., the level of α -enhancement) can improve agreement when employing the traditional definition of metallicity (i.e., $[\text{Fe}/\text{H}]$).

The study by Nataf et al. (2013) also included 55 GCs for which the MSTO magnitude was measured. In panel 9.4c we plot the $\Delta V_{\text{bump}}^{\text{MSTO}}$ parameter as a function of $[\text{M}/\text{H}]$ for these systems and compare to the predictions from MONSTAR

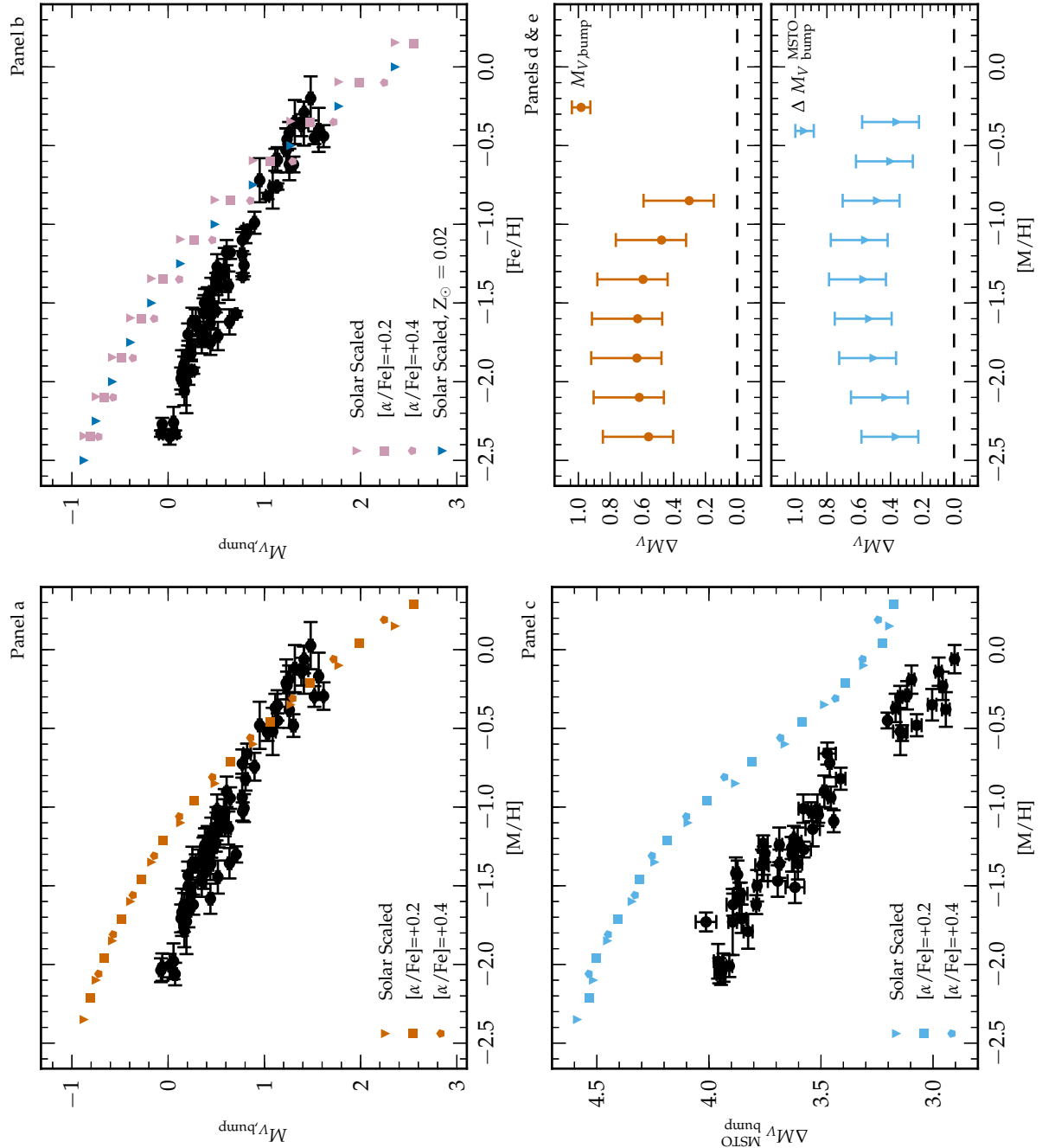


Figure 9.4: Panel a: The empirically determined location of the LF bump in 72 GCs (black circles with associated uncertainties) as a function of total metallicity $[M/H]$ from Nataf et al. (2013). The bump magnitude calculated from our stellar models is also included. Calculations with solar-scaled composition (triangles), enhancement of $[\alpha/Fe]=0.2$ (squares) and $[\alpha/Fe]=0.4$ (pentagons) form part of our grid. Panel b: As per panel A but here data are presented as a function of metallicity $[Fe/H]$. Panel c: Same as Panel a but for the distance independent parameter $\Delta M_V^{\text{MSTO bump}}$. Panel d: The discrepancy between the theoretically and observationally determined magnitude of the LF bump at each metallicity. Panel e: The discrepancy between theoretical and observational determined $\Delta M_V^{\text{MSTO bump}}$ parameter at each metallicity.

with various initial compositions.

At each metallicity, the GCs display a spread in the magnitude at which the LF bump occurs. To quantify the discrepancy between theory and observation, we compare our models to the lines of best fit to the data in panels 9.4a and 9.4c (i.e., equations 1 and 2 in Nataf et al. 2013)

$$M_{V,\text{bump}} = 0.600 + 0.737([M/H] + 1.110) \quad (9.6)$$

$$\Delta M_V^{\text{MSTO bump}} = 3.565 - 0.549([M/H] + 1.152). \quad (9.7)$$

These fits are translated to give upper and lower envelopes to the data in order to provide an indicative uncertainty at each metallicity. The discrepancy between theory and observation for the direct comparison (panel 9.4d, top) and distance independent parameter (panel 9.4e, bottom) are presented in the lower right corner of Figure 9.4.

There is a metallicity band $-1.1 < [M/H] < -0.5$ in which the direct comparison method finds agreement between theory and observation. At metallicity $[M/H] > -1.0$, the models are consistent with the observationally determined values. We in fact omit these last few points from panel 9.4d, as well as our predictions for metallicities $[M/H] > 0$. No GCs exist in this region of the parameter space. The trend of the models suggest agreement once again quickly worsens from the line of best fit beyond $[M/H] > -0.5$, but we refrain from speculatively quantifying this. At low metallicity the data suggest a discrepancy in excess of 0.8 magnitudes.

The distance independent parameter, $\Delta M_V^{\text{MSTO bump}}$, appears to show a constant offset between theory and observation at all metallicities. The results are consistent with a difference of $\Delta M_V \approx 0.4$ which is slightly higher than the value of $\Delta M_V \approx 0.2$ found by Cassisi et al. (2011) using isochrone fitting. A systematic offset of about 0.5 dex in the metallicity scale would explain inconsistency between theory and observation but there is no evidence to support such a hypothesis.

How well the stellar models reproduce the photometrically determined location of the LF bump is dependent on the method of comparison used. It is curious that a method that relies on accurate distance determinations finds agreement in only a limited metallicity range. More pressing is the implication that the stellar models are not correctly reproducing the stellar structure at low metallicity, irrespective

of how the comparison is carried out. If stellar physics is solely to blame, then our model of NGC 6397 overestimates the magnitude at which FDU begins and underestimates the penetration of the convective envelope. If FDU is deeper, then the hydrogen shell will encounter the composition discontinuity at a fainter magnitude. Improvements to stellar models can be attained through either refinement of the microphysics or changes in the treatment of mixing. In Table 9.4 we examine how the magnitude of MSTO, onset of FDU and LF bump are all altered by changes to the microphysics. A stellar model with $Z = 0.0001$ (practically the same composition used for NGC 6397 that approximately matches the metallicity used in studies by other groups) serves as a benchmark for comparison. This is followed by changes to the mixing algorithm to allow for non-local overshoot.

9.4.3 Mass and Helium Enhancement

Figure 9.4 has been constructed without optimising or calibrating the stellar models to each GC. We calculated the evolution of a star with a representative metallicity that reaches the giant branch after 12 Gyr. This does not take into account the mass spread along the RGB which may *slightly* shift the location of the evolutionary indicators. This is why isochrone fitting is generally used in these types of studies, but this comes at the cost of needing to run many models when investigating the parameter space of the microphysics. There is also the issue that GCs contain multiple populations characterised by variations in composition and age. Carretta et al. (2009a), have demonstrated that a majority of stars in GCs in fact belong to the “second generation” (enhanced in Na, depleted in O). There are many pieces of evidence that suggest that these stars are also enhanced in helium. If this is the case, then there will be several evolutionary consequences. We now show that these effects are not responsible for the discrepancies we have identified.

In Figure 9.5 we demonstrate that our choice of initial mass and helium content is not exaggerating the discrepancy with observation. We have included calculations that pertain to models of the GCs NGC 6397 ($M = 0.80 M_{\odot}$, $Z = 0.0001$) and M13 ($M = 0.80 M_{\odot}$, $Z = 0.0005$). Models for M13 are included because its chemical distribution is best explained by a population of stars that are significantly enhanced in helium ($Y = 0.40$) compared to their primordial ($Y = 0.24$) and intermediate ($Y = 0.28$) counterparts (D’Antona and Ventura, 2007; D’Antona and Caloi, 2008). We explore what effect a similar helium enhancement would have in the case of our benchmark cluster.

Such a large difference in helium abundance between the populations will significantly alter the lifetimes of the stars. If we assume that each cluster is ≈ 12 Gyr old, then stars currently evolving on the RGB from the “primordial” population (with $Y = 0.24$) are born with initial mass $M \approx 0.8 M_{\odot}$. The “extreme” population, with $Y = 0.40$, must be less massive ($M \approx 0.65 M_{\odot}$). We have considered three combinations of mass and helium content in our calculations.

In the top two panels of Figure 9.5 we present the important structural and evolutionary details of the models with M13 metallicity ($Z = 0.0005$). The corresponding calculations at NGC 6397 metallicity ($Z = 0.0001$) are plotted in the bottom panels. In panels 9.5a and 9.5c the evolution across the HR-diagram of

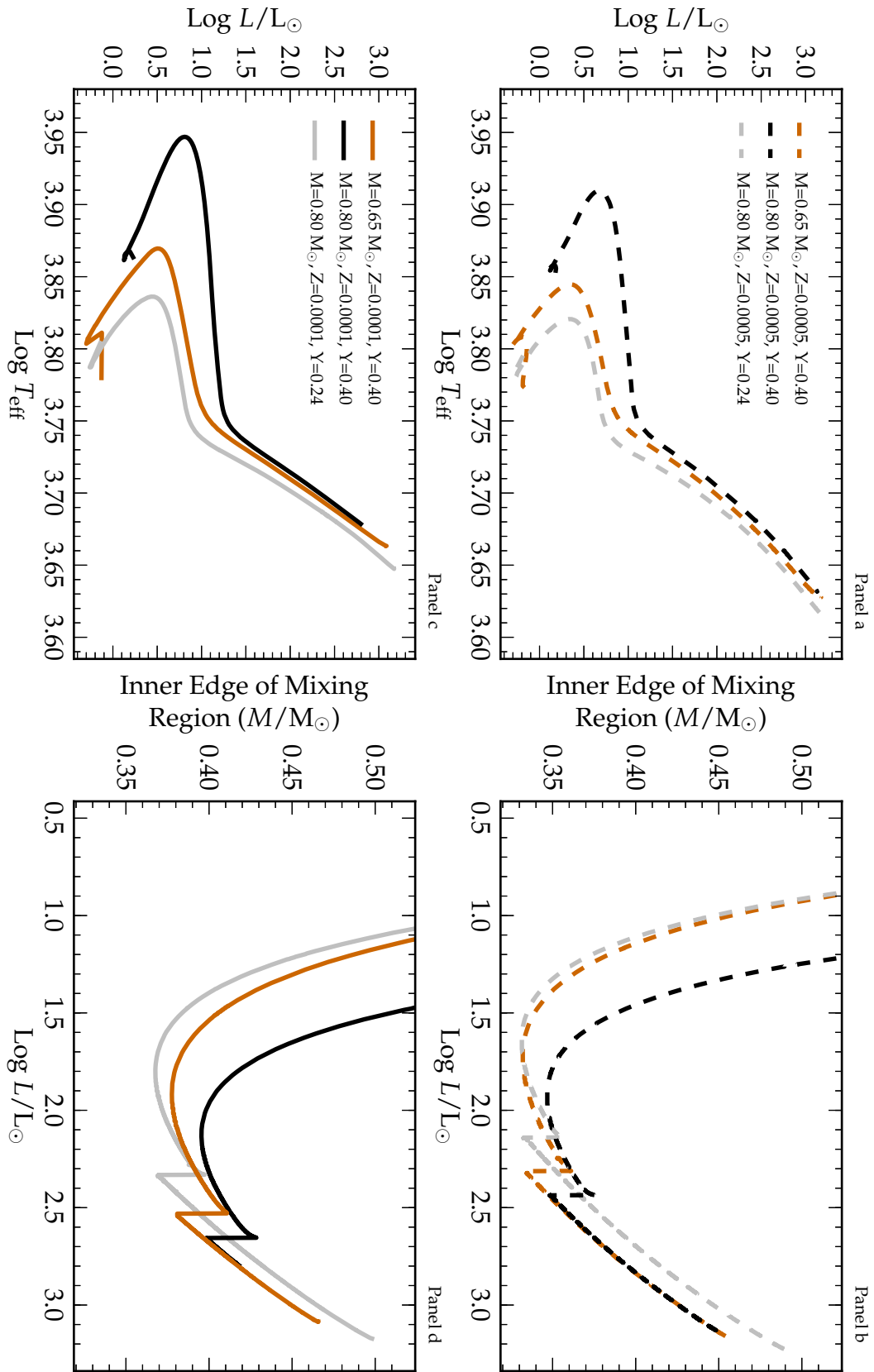


Figure 9.5: Influence of mass and ^4He abundance on the depth of FDU and location of the LF bump. The sudden increase in the size of the convective envelope in each model denotes the onset of extra mixing. Models with metallicity representative of stars in M13 are presented in the top panels. Models representative of stars in NGC 6397 are displayed in the bottom panels. Panel a): HR-diagram for the three variations of M13-metallicity stars specified in the legend. Panel b): The corresponding extent of the mixing region in each M13-metallicity model. Panel c): HR-diagram for the three variations of NGC 6397-metallicity stars specified in the legend. Panel d): The corresponding extent of the mixed envelope in each NGC 6397-metallicity model.

the extreme population star (vermilion curve), primordial population star (grey curve) and star with primordial population mass but extreme population Y (black curve, included to demonstrate the role of mass and metallicity) are illustrated for each cluster.

In panels 9.5b and 9.5d the maximum depth of FDU is compared by plotting the mass of the inner edge of the mixing region. Initially, the inner edge of the mixing region traces the convective envelope. The sudden deepening of this boundary is due to the development and incorporation of the extra-mixing region once the μ discontinuity has been erased. In these plots, we have identified the mixing regions by a minimum mixing velocity rather than stability criteria (i.e., $\nabla_{rad} - \nabla_{ad}$). The latter marks the bottom of the convective envelope determined by the Schwarzschild criterion and not the extent of the extra mixing region. Here the higher hydrogen abundance in the primordial population star results in a deeper penetration of the convective envelope. Including the calculations for two clusters not only demonstrates the role of hydrogen and metal content on the depth of FDU.

The key result taken from Figure 9.5 is that if we were to employ lower mass and necessarily helium-enhanced models to better represent the stellar populations, it would only serve to increase the discrepancy between theory and observation shown in Figure 9.4. The lower mass, higher helium models predict a bump magnitude that is brighter than our benchmark models. We have clearly demonstrated the trend with mass and metallicity and the detailed effects on our benchmark star are highlighted in Table 9.4.

9.4.4 Opacity and MLT Mixing Length Parameter

Opacity is intrinsically linked to convection through its contribution to the radiative temperature gradient. It is an obvious avenue of investigation and has indeed featured in previous studies that have compared theoretical and empirical determinations of the LF bump. As discussed in §9.2, MONSTAR utilises specific sets of tables for low- and high-temperature opacities. Each regime may in fact provide an opportunity to resolve the discrepancy between theory and observation at low metallicity. Figure 9.3 suggest that the models overestimate the magnitude at which FDU begins. The onset of this event is dependent on the the

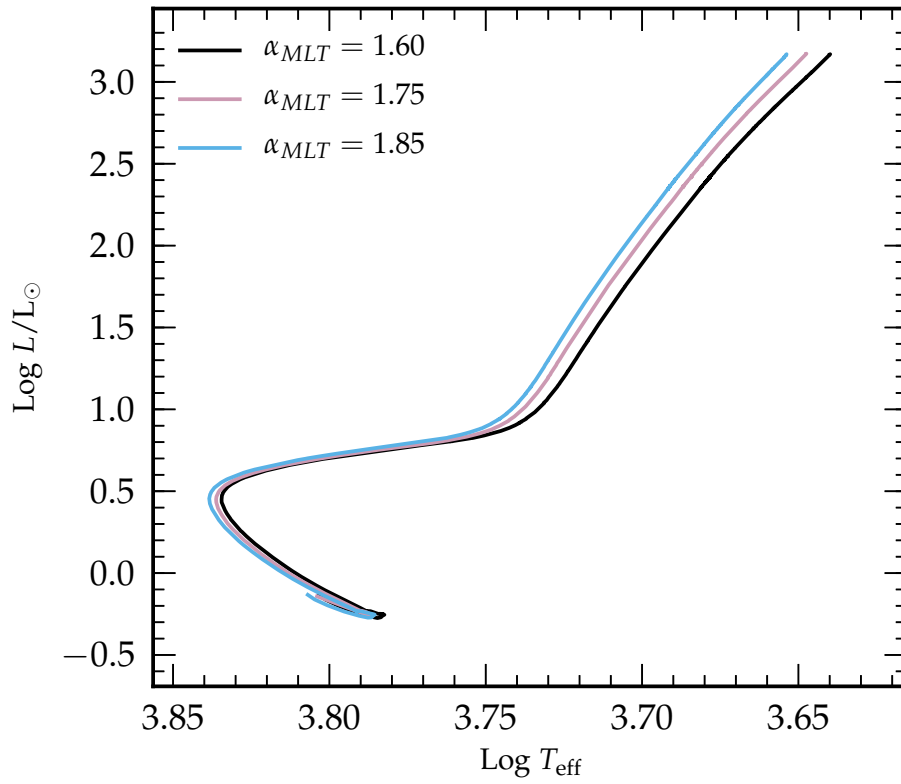


Figure 9.6: HR-diagram for the NGC 6397 stellar model calculated with different values of α_{MLT} .

low-temperature opacities in the outer envelope. The models also overestimate the LF bump magnitude, which can be resolved if theory currently predicts a FDU depth that is too shallow. It is the high-temperature opacities that control the penetration of the convective envelope.

Unfortunately we have no justification for significant changes to our treatment of opacity. Recently, opacity tables to account for changes in C and N have become available (Lederer and Aringer, 2009; Marigo and Aringer, 2009). Whilst the compositional dependent low-temperature opacities are essential during the AGB phase of evolution (Marigo, 2002; Marigo and Aringer, 2009; Ventura and Marigo, 2009; Constantino et al., 2014), their effect during the RGB is negligible. $C/O > 1$ is critical, and this is not achieved by GC stars. Quantifying the uncertainties in the opacity tables has been the subject of analysis by Salaris et al. (2002). They find that the Ferguson et al. (2005) low-temperature opacities predict cooler stellar models ($\Delta T_{\text{eff}} \geq 100\text{K}$) because they include the effect of the H_2O molecule which is significant at RGB temperatures. Since then, we have incorporated the Lederer and Aringer (2009) tables.

The free parameter in the MLT is also a source of uncertainty in the stellar models. α_{MLT} is calibrated to the Sun, a star halfway through its main-sequence lifetime which possesses a shallow convective envelope. It is then applied across the stellar mass and metallicity distribution and through all phases of stellar evolution. The value of α_{MLT} adopted (usually 1.75 in MONSTAR) will significantly shift the model’s position in the Hertzsprung-Russell (HR) diagram. In Figure 9.6 our benchmark star is evolved with various choices of α_{MLT} . Here the assumed efficiency of convection has significant implications for the T_{eff} of the star. From Table 9.4, it is clear that changes in the stellar structure due to α_{MLT} are not large enough to reconcile the discrepancy between theory and observation at neither FDU nor the LF bump. The depth of FDU is not altered by this parameter (see also Alongi et al. 1991) thus we find variability of around 0.01 magnitudes at each of our evolutionary indicators.

9.4.5 Equation of State

The last aspect of the stellar microphysics examined in this work concerns the EOS. To date, there has been no systematic investigation of various EOS choices on RGB evolution. MONSTAR typically employs the fitting formula by Beudet and Tassoul (1971) whilst partially-ionized regions are treated with the Saha equation as described by Bærentzen (1965). In the event of convergence issues, a computationally more expensive analytic solution can be calculated but this method still requires the numerical evaluation of the Fermi-Dirac integrals. To aid in this investigation we have added the OPAL EOS tables from Rogers and Nayfonov (2002). We also include models from Constantino et al. (2014, also calculated with MONSTAR) who incorporate the Timmes EOS (Timmes and Arnett, 1999) and the Helmholtz equation of state (Timmes and Swesty, 2000) which is the tabulated form of the Timmes EOS. The Timmes EOS has allowances for “simple ionization” that includes a simple two-level hydrogen atom like model for ionization. In cases where equations of state are blended, a linear transition occurs over the

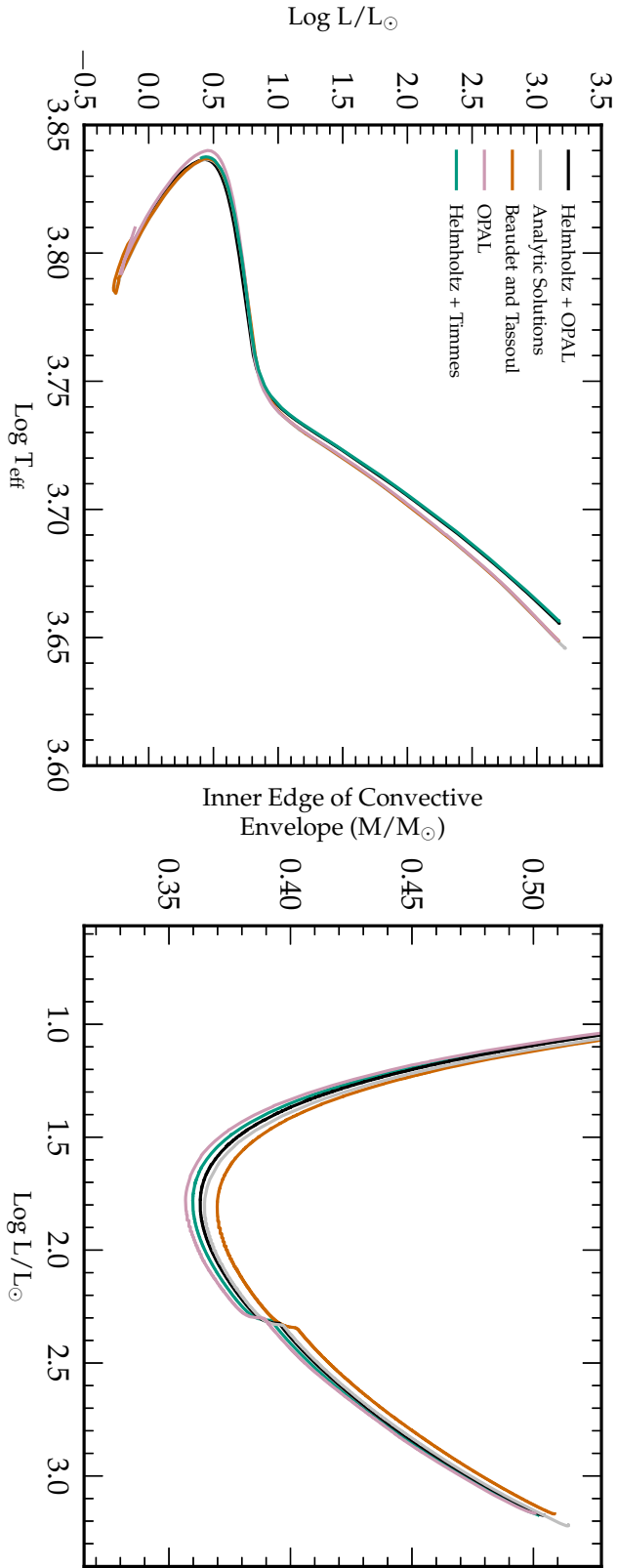


Figure 9.7: Left panel: Evolution through the HR-diagram of the stellar model with metallicity representative of NGC 6397. Each curve corresponds to a different choice for the EOS. Right panel: Penetration of the convective envelope for each EOS choice.

temperature range $T = 2 - 2.5$ MK.

We have calculated the evolution of the benchmark model with five different EOS combinations; the results of which are presented in Figure 9.7 and listed in Table 9.4. In the left panel of Figure 9.7, a legend is provided with the respective HR-diagram for each case. Employing the Helmholtz EOS in the high temperature regime produces a systematically higher T_{eff} at a given luminosity compared with other choices for the EOS. Note that whereas a model with higher α_{MLT} results in an almost constant T_{eff} offset in the HR-diagram, the discrepancy in T_{eff} between the different equations of state increases with RGB luminosity. The depth of FDU for each combination is plotted in the adjacent panel. The Beaudet and Tassoul (1971) fitting formula, which is the default choice in MONSTAR, provides the shallowest penetration of the convective envelope of all the five EOS combinations. As recorded in Table 9.4, this choice of EOS therefore yields the greatest discrepancy with the empirically determined LF bump magnitude. The deepest penetration of the convective envelope is achieved by the OPAL EOS and leads to approximately 0.1 magnitude better agreement with the empirical data. This is still not deep enough to allow the hydrogen shell to encounter the composition discontinuity at the magnitudes that coincide with the LF bump observed in GCs.

The results presented here have offered insight into the role the EOS choice plays in stellar evolution calculations. Timmes and Arnett (1999) tested the thermodynamic accuracy of five equations of state³ under various conditions. In the regimes examined, each EOS provided thermodynamic quantities to within 1% of the exact solutions. This is consistent with our result that the EOS choice leads to only minor differences in the HR-diagram and depth of FDU.

9.4.6 Convective Overshooting

Reasonable variations of the stellar microphysics are unable to reproduce the depth of FDU in low-metallicity stars. Changes to the mixing algorithm are another means to alleviate the discrepancy. Once it had been identified that theory overestimates the LF bump location (King et al., 1985; Fusi Pecci et al., 1990), Alongi et al. (1991) suggested that overshooting by $0.7 - 1.0$ pressure scale heights (H_P) at the base of the convective envelope would provide the required shift in magnitude.

In Figure 9.8 we present a recalculated grid of solar-scaled composition models. They include various degrees of overshoot using the formalism outlined in §2. The impact of the new physics on our benchmark star is also detailed in Table 9.4. In the left panel of Figure 9.8, we once again directly compare the location of the LF bump at each metallicity using a common brightness system. Overshooting has simply shifted the metallicity band in which models and theory agree lower. In the right panel, we compare the distance independent parameter $\Delta M_V^{\text{MSTO bump}}$. Values of $f_{os} = 0.05 - 0.1$ are sufficient to produce the required shift in the theoretical LF bump.

Before comparing to the results of Alongi et al. (1991), it is necessary to describe the details of the overshooting formalism we have employed. The free parameter f_{os} , specifies an e-folding length for the velocity profile. The simulations

³The five EOS choices are not the same five we have compared but do include a subset.

Table 9.4: Variations in the magnitude of the evolutionary events due to changes in the microphysics. We adopt a metallicity of $Z = 0.0001$ in all models.

Variable	M/M_{\odot}	X	Y	$[\alpha/\text{Fe}]$	EOS	α_{MLT}	f_{os}	MSTO			FDU ^a			LF bump		
								$\text{Log } L/L_{\odot}$	M_V	$\text{Log } L/L_{\odot}$	M_V	Depth ^b	$\text{Log } L/L_{\odot}$	M_V	ΔM_V	$M_{\text{bump}}^{\text{MSTO}}$
$[\alpha/\text{Fe}]$	0.80	0.75	0.2499	+0.0	Beaudet and Tassoul	1.75	0.00	0.44	3.77	0.78	2.97	0.368	2.34	-0.75	4.51	
	0.80	0.75	0.2499	+0.2	Beaudet and Tassoul	1.75	0.00	0.42	3.84	0.77	3.01	0.361	2.30	-0.67	4.50	
	0.80	0.75	0.2499	+0.4	Beaudet and Tassoul	1.75	0.00	0.40	3.88	0.74	3.07	0.353	2.27	-0.57	4.45	
m/M_{\odot}	0.65	0.5999	0.4	+0.0	Beaudet and Tassoul	1.75	0.00	0.51	3.57	0.92	2.62	0.378	2.53	-1.22	4.80	
	0.80	0.5999	0.4	+0.0	Beaudet and Tassoul	1.75	0.00	0.81	2.86	1.20	1.91	0.395	2.65	-1.53	4.37	
α_{MLT}	0.80	0.75	0.2499	+0.0	Beaudet and Tassoul	1.60	0.00	0.45	3.74	0.79	2.96	0.368	2.34	-0.73	4.48	
	0.80	0.75	0.2499	+0.0	Beaudet and Tassoul	1.65	0.00	0.45	3.75	0.79	2.96	0.368	2.34	-0.74	4.49	
	0.80	0.75	0.2499	+0.0	Beaudet and Tassoul	1.70	0.00	0.45	3.76	0.77	2.98	0.368	2.34	-0.75	4.51	
	0.80	0.75	0.2499	+0.0	Beaudet and Tassoul	1.80	0.00	0.45	3.76	0.79	2.96	0.368	2.34	-0.77	4.53	
EOS	0.80	0.75	0.2499	+0.0	Beaudet and Tassoul	1.85	0.00	0.45	3.74	0.79	2.95	0.368	2.34	-0.78	4.52	
	0.80	0.75	0.2499	+0.0	Helmholtz + OPAL	1.75	0.00	0.43	3.79	0.77	3.01	0.362	2.32	-0.74	4.53	
	0.80	0.75	0.2499	+0.0	Analytic Solutions	1.75	0.00	0.45	3.75	0.78	2.98	0.365	2.33	-0.73	4.48	
	0.80	0.75	0.2499	+0.0	Helmholtz + Timmes (SI ^c)	1.75	0.00	0.44	3.77	0.78	2.97	0.360	2.31	-0.70	4.47	
f_{os}	0.80	0.75	0.2499	+0.0	OPAL	1.75	0.00	0.46	3.72	0.78	2.98	0.357	2.30	-0.67	4.40	
	0.80	0.75	0.2499	+0.0	Helmholtz + OPAL	1.75	0.02	0.44	3.78	0.77	3.01	0.345	2.26	-0.56	4.34	
	0.80	0.75	0.2499	+0.0	Beaudet and Tassoul	1.75	0.01	0.44	3.77	0.77	2.98	0.357	2.30	-0.65	4.42	
	0.80	0.75	0.2499	+0.0	Beaudet and Tassoul	1.75	0.02	0.45	3.75	0.78	2.98	0.350	2.27	-0.60	4.34	
	0.80	0.75	0.2499	+0.0	Beaudet and Tassoul	1.75	0.03	0.45	3.75	0.78	2.98	0.344	2.25	-0.53	4.28	
	0.80	0.75	0.2499	+0.0	Beaudet and Tassoul	1.75	0.04	0.45	3.75	0.78	2.97	0.339	2.22	-0.47	4.22	
	0.80	0.75	0.2499	+0.0	Beaudet and Tassoul	1.75	0.05	0.45	3.76	0.78	2.97	0.335	2.20	-0.43	4.19	
	0.80	0.75	0.2499	+0.0	Beaudet and Tassoul	1.75	0.075	0.45	3.75	0.77	2.99	0.326	2.15	-0.32	4.06	
	0.80	0.75	0.2499	+0.0	Beaudet and Tassoul	1.75	0.1	0.45	3.75	0.77	3.00	0.319	2.11	-0.22	3.97	

^aDefined in this instance by the luminosity at which surface abundances start to change, rather than by the luminosity at which the convective envelope begins its inward migration. The former definition is useful for comparisons to observation, the latter is the true theoretical definition. In any case there will not be very much difference between the two.

^bIn units of (M/M_{\odot}).

^cSimple Ionisation

by Freytag et al. (1996) demonstrated that velocity field declines exponentially with radius beyond the formal Schwarzschild boundary and is very dependent on the conditions at the edge of the convective zone. Similar conclusions were reached by Singh et al. (1995), Herwig et al. (2006) and Meakin and Arnett (2007b). The resulting (perhaps partially) mixed zone will provide a smooth chemical gradient, and indeed in this study made the identification of the LF bump at low-metallicity difficult.

Freytag et al. (1996) and Herwig et al. (1997), as with similar prescriptions by Chieffi et al. (2001) and Cristallo et al. (2009), calibrate the f_{os} parameter (or the equivalent) to the stellar environment of interest. This method ensures that the velocity field decays smoothly rather than coming to an abrupt end. Such a requirement has been inferred by the analysis of acoustic glitches in observations of the solar convection zone (Christensen-Dalsgaard et al. 2011 and references therein). We note that helioseismology has suggested overshooting at the base of the solar convection zone between $0.05-0.1H_p$ to account for the glitches (Canuto, 2011; Thompson et al., 2003; Basu and Antia, 1994; Basu et al., 1994). In their study of asymptotic giant branch stars in the Large Magellenic Cloud, Kamath et al. (2012) find their models need overshoot up to $3H_P$ is during third dredge-up in order to reproduce the correct oxygen-rich to carbon-rich transition luminosity. These results highlight the need for a calibrated overshoot under different stellar conditions and ultimately suggest that our description of the mechanism is in need of improvement.

The method we employ refrains from specifying an overshooting distance explicitly in terms of the pressure scale height which makes direct comparison to other formalisms less precise. The traditional ballistic approximation of overshoot, in which material pierces a stable layer, can still lead to steep gradients/discontinuities in the velocity and composition. Meakin and Arnett (2007b) describe the process instead as ‘an elastic response by the convective boundary’. Our formalism allows the velocity of the overshooting material to decay without setting the same maximum extent in terms of H_P . The depth of overshoot depends on the conditions at the base of the convection zone and the specified e-folding length.

In Table 9.5 we compare our models to those by Alongi et al. (1991). Note that they have calibrated their models to directly match the LF bump magnitude. We, on the other hand, have calibrated according to the $\Delta M_{\text{bump}}^{\text{MSTO}}$ parameter. Our NGC 6397 model ($Z=0.0001$) still overestimates the location of the LF bump by > 0.1 magnitudes. Both studies find that a similar extension of the convective envelope (in mass) is required to match observations even though we are calibrating to different criteria. The coincidental agreement is due to a combination of our models being systematically ≈ 0.1 dex brighter in luminosity and differences in the bolometric corrections.

9.4.7 The Direct Comparison Method

Overshooting with velocity scale heights between $H_v = 0.05 - 0.1H_p$ results in a sufficient extent of FDU to ensure agreement of the $\Delta M_{\text{bump}}^{\text{MSTO}}$ parameter with ob-

Table 9.5: Comparison between the stellar models calculated in this work and those by Alongi et al. (1991). In all models the initial stellar mass is $M = 0.8 M_{\odot}$

Study	Metallicity (Z)	OS ^a	Depth ^b	L bump ^c	M_V bump ^d
Alongi	0.001	$\Lambda = 0$	0.300	1.95	0.25/0.44/0.34
This Work	0.001	$f_{os} = 0$	0.311	2.00	0.13
Alongi	0.001	$\Lambda = 0.7$	0.282	1.76	0.75/0.85/0.75
This Work	0.001	$f_{os} = 0.05$	0.283	1.84	0.47
Alongi	0.001	$\Lambda = 1.0$	0.275	1.68	0.84/1.05/0.95
This Work	0.001	$f_{os} = 0.075$	0.276	1.80	0.57
Alongi	0.0001	$\Lambda = 0$	0.352	2.25	-0.53/-0.44/-0.44
This Work	0.0001	$f_{os} = 0$	0.368	2.34	-0.75
Alongi	0.0001	$\Lambda = 0.7$	0.331	2.07	-0.08/0.02/-0.05
This Work	0.0001	$f_{os} = 0.05$	0.335	2.20	-0.43
Alongi	0.0001	$\Lambda = 1.0$	0.325	2.02	0.00/0.11/0.04
This Work	0.0001	$f_{os} = 0.075$	0.326	2.15	-0.32

^a The free parameter in the respective overshoot formalisms. Alongi et al. (1991) overshoot a fraction ΛH_P beyond the convective envelope

^b In units of (M/M_{\odot}) .

^c In units of $\text{Log } L/L_{\odot}$.

^d Alongi et al. (1991) applied bolometric corrections from three different sources. See their paper for more details.

servations. However, a difficulty remains with directly comparing the LF bump magnitudes. For this method, overshooting simply shifts the small range that theory and observation agree from the metal-rich end of the GC metallicity distribution to the metal-poor end. Unlike the distance-independent method of comparison, converting the models to a common magnitude system does not reproduce the gradient of the empirical data. Whatever is responsible for this residual offset at the LF bump we assume is also responsible for the discrepancy at FDU. We must therefore take care when using GCs to test theory.

The reason for the discrepancy is hard to pinpoint. Given that the distance-independent method yields agreement with theory, it is possible uncertainties in the distance modulus may contribute to the offset. It is impossible to measure the parallax of individual stars in GCs. Therefore a range of methods are used to determine the distance to these systems. The distance moduli listed in the Harris (1996) catalogue (2010 edition), which we in turn have taken from Nataf et al. (2013), are predominately determined from calibrating the mean V magnitude

of the horizontal branch. Harris (1996) cites an uncertainty in determining this mean magnitude of at least $\pm 0.1 M_V$. There are also unquantified difficulties in the magnitude-metallicity relation used for calibration (Demarque et al., 2000). Some clusters, such as NGC 6397, are too faint for this technique to be useful. Its distance modulus was derived by fitting isochrones to the MSTO (Alcaino et al., 1987). In fact most of these techniques used to determine the distance modulus require some form of calibration from isochrones. This may suggest that the discrepancy in the direct comparison method may reflect systematic modelling differences between MONSTAR and those codes used to generate the isochrones.

The models presented here do not include the effects of rotation which will shift the magnitude of the theoretical LF bump. How rotation impacts upon the stellar models depends on the treatment of angular momentum (Chanamé et al., 2005; Palacios et al., 2006). In their comparison of different transport prescriptions, Palacios et al. (2006) found a negligible difference in the depth of FDU but noted that the predicted LF bump occurred at higher luminosities in their rotating models compared to the non-rotating models. The higher-mass higher-metallicity ($M \geq 1.25 M_\odot$, $Z = Z_\odot$) models by Charbonnel and Lagarde (2010), on the other hand, demonstrate a significantly lower bump luminosity in their rotating models compared to their non-rotating models. The inclusion of extra physics has led to reconciliation with the $\Delta M_V^{\text{MSTO bump}}$ parameter in Figure 9.8. Given that we have exhausted our investigation of the microphysics, it may be necessary that further refinements to the treatment of mixing are required. Additional physics such as rotation or magnetic fields will affect the structure of the star and may be able to offset the current modelling issues.

9.5 Thermohaline Mixing

The final part of our investigation focuses on constraining extra mixing using spectroscopy of the four GCs in our sample. In this section, we compare observations and theoretical predictions of the evolution of two species that are involved in different channels of hydrogen burning: the fragile lithium and the robust carbon. This second test of the models aims to uncover whether the thermohaline mechanism can account for changes in the surface composition of low-mass RGB stars. We have seen that directly comparing stellar models to observations of GCs can be fraught with uncertainty. In order to test the efficiency of the thermohaline process, we have applied artificial offsets in magnitude to the models so that the beginning of extra mixing coincides with the photometrically derived LF bump. Overshoot (with $f_{os} = 0.075$) has been included in the models. This degree of overshoot ensures that the $\Delta M_V^{\text{MSTO bump}}$ parameter is consistent with the value determined from the respective CMDs.

In Figure 9.9 we plot lithium observations from the four GCs in our sample (Table 9.3.1). Data for NGC 6397 (panel 9.9a), M4 (panel 9.9c), M5 (panel 9.9d) and M12 (panel 9.9e) are accompanied by best fit models for each cluster with various choices for the free parameter C_t in the diffusive-thermohaline mixing theory. Although $C_t = 1000$ has been the preferred value in the literature, matching abun-

dances in many stellar environments, values in our models between $C_t = 120 - 300$ account for the Li data in every cluster. The massive GC M5 may be an exception with $C_t = 1000$ acting as a lower bounds⁴ to some of the points.

In panel 9.9b we apply the same calculations used in NGC 6397 (panel 9.9a) to [C/Fe] data for that cluster and for NGC 5466. [C/Fe] data for NGC 6397 were taken from Briley et al. (1990) but determined by assuming that there is no oxygen over-abundance in that system. [C/Fe] in NGC 5466 is taken from Shetrone et al. (2010). We expect that the models are representative of both clusters despite the small difference in metallicity. NGC 5466 was one of the three metal-poor GCs studied by Angelou et al. (2012) in their investigations of thermohaline mixing. Of the three, this was the only system in which thermohaline mixing could reproduce the depletion of [C/Fe] along the RGB. In Figure 9.2 we have seen the uncertainty that the more massive clusters introduce for these types of tests, as well as the complications that arise when combining multiple studies. We note that NGC 6397 seems to display the same issues as its more massive counterparts. It is difficult to identify the onset of extra mixing from the [C/Fe] data and one could argue that it begins well before the expected bump. NGC 5466, with its homogeneous data set and comparable size to NGC 6397, serves as the ideal companion.

We find that a mixing efficiency of $C_t = 1000$ depletes Li much too fast (panel 9.9a) but it is able to account for the depletion of [C/Fe] in both clusters (panel 9.9b). Models with $C_t = 120$ and $C_t = 300$ provide a bounds to the Li data in panel 9.9a but do not process enough carbon to match the trend of [C/Fe] in panel 9.9b. We are unable to simultaneously account for [C/Fe] and A(Li) with the same free parameter. Matching both these abundances will pose challenging requirement for any postulated mixing mechanism. The fragility of Li and robustness of [C/Fe] must be reproduced.

It may indeed be true that thermohaline mixing is not responsible for the surface composition of RGB stars. Objections to the mechanism are based on theoretical grounds and 3D hydrodynamical simulations (Traxler et al., 2011a; Denissenkov and Merryfield, 2011; Brown et al., 2013) which suggest that the mixing is inefficient in the RGB regime. But we have described how the mechanism at work here can be considered a physically based phenomenological model. Rather than mixing to a constant temperature or mass location from the hydrogen burning shell, material is transported to where ${}^3\text{He}$ burning creates an inversion in the μ profile. Church et al. (2014) show how this location depends on the shell-burning conditions that change with RGB luminosity. In this extra mixing formalism we have varied the free parameter that controls the mixing rate. A systematic search of the parameter space, altering both the mixing depth and and diffusion coefficient, is required to determine whether mixing to the location of the μ inversion is sufficient. Perhaps the μ inversion is a red herring and a constant mass or temperature from the H-shell is required. We note that Denissenkov and Pinsonneault (2008a) have advocated that a deeper (than the μ inversion) but slower mixing may be required. It is not clear that this scenario would explain the abundance trends here.

⁴Envelope is the preferred word here but would be misleading given our previous discussions on the convective envelope.

We have modelled thermohaline mixing as a diffusive process. Our evolution code employs a one-dimensional diffusion algorithm to model a process that is inherently three dimensional and advective. Convection is characterised by alternating streams (or plumes) of upward and downward travelling material. The majority of the nuclear processing in the extra mixing region occurs near where material turns over at the radiative boundary. A diffusive treatment of mixing assumes that the composition difference between convective elements at the same mass coordinate is negligible. If the mixing speed in the extra mixing region is much slower than convection (as it generally is believed to be), then the turnover time is closer to the reaction timescale. We therefore expect a difference between the compositions of material approaching and returning from the envelope at the same mass coordinate. It may in fact be necessary to develop a more realistic treatment of convection to better model the extra mixing process. Codes that calculate mixing via advective streams (e.g., see Church et al. 2009) may be enlightening.

9.6 Summary and Conclusion

We have undertaken a systematic investigation of the mixing episodes experienced during the RGB phase of stellar evolution. Medium-to-high resolution spectroscopic surveys of GCs and high-resolution HST photometry from the literature have set a series of constraints for our stellar models to meet. Our spectroscopic sample includes four systems that cover most of the GC metallicity distribution. The surveys of NGC 6397, the most metal-poor cluster in our sample, and M4, the most metal-rich, cover a luminosity range that extends from the subgiant branch to beyond the LF bump. We demonstrate the usefulness of such a large range of homogeneous data and why the sensitivity of Li to temperature makes it preferable to other diagnostics such as [C/Fe] and [N/Fe].

In addition to converting theoretical predictions and observational measurements of the LF bump to a common magnitude system for comparison, we employed the distance-independent parameter $\Delta M_{V_{\text{bump}}}^{\text{MSTO}}$ to gauge the state of the stellar models. The models correctly predict the magnitude of the LF bump at high metallicity but diverge from the observations at lower metallicity. Using the distance independent method, we reproduced the well known result that models overestimate the LF bump at all metallicities by 0.2 – 0.4 magnitudes (on average). Both techniques indicate that stellar models fail to reproduce the true stellar structure, especially in the low-metallicity regime.

Our interpretation suggests that if the stellar structure is responsible, then the discrepancy between theory and observation is due to the models systematically underestimating the depth of FDU. Deeper FDU reduces the distance the hydrogen shell advances before encountering the composition discontinuity left by the convective envelope, and hence reduces the predicted magnitude of the LF Bump. Reasonable variations to the stellar microphysics do not significantly alter the stellar structure. Our investigations covered composition and α -element enhancement, opacity, convective efficiency and the first into the EOS choice on RGB evolution. We also examined the mixing algorithm and we included a pre-

scription for diffusive overshoot in our models. As per Alongi et al. (1991) we were able to reconcile theory with observations by using overshooting at the base of the convective envelope.

Whilst overshooting yielded consistency between the theoretically and empirically determined values for the $\Delta M_V^{\text{MSTO}}_{\text{bump}}$ parameter at all metallicities, the direct comparison method only shifted the small $[M/H]$ rangewhere theory agrees with observation to a slightly lower metallicity. The models produced a gradient in metallicity and magnitude not seen in the observational data. Why direct comparison, which relies on accurate determinations of the distance modulus, would produce such behaviour is currently unclear.

Our final probe of the RGB mixing events focussed on the efficiency of extra mixing. We determined that the thermohaline mechanism could not simultaneously account for the depletion of $[C/Fe]$ and $A(\text{Li})$ as a function of RGB luminosity. In all four GCs, a free parameter between $C_t = 120 - 300$ provided a bounds to the Li data. This is in contrast to a value of $C_t = 1000$ cited throughout the literature to match the carbon and nitrogen abundances of stars in various environments. Whilst this discrepancy is a challenge for thermohaline mixing, the constraints may prove difficult for other mechanisms also, as Li is likely to be destroyed very efficiently under the conditions required to deplete $[C/Fe]$. The diffusive mixing algorithm used in stellar modelling may not be adequate to quantitatively match observations and numerical codes may require a more realistic treatment of mixing.

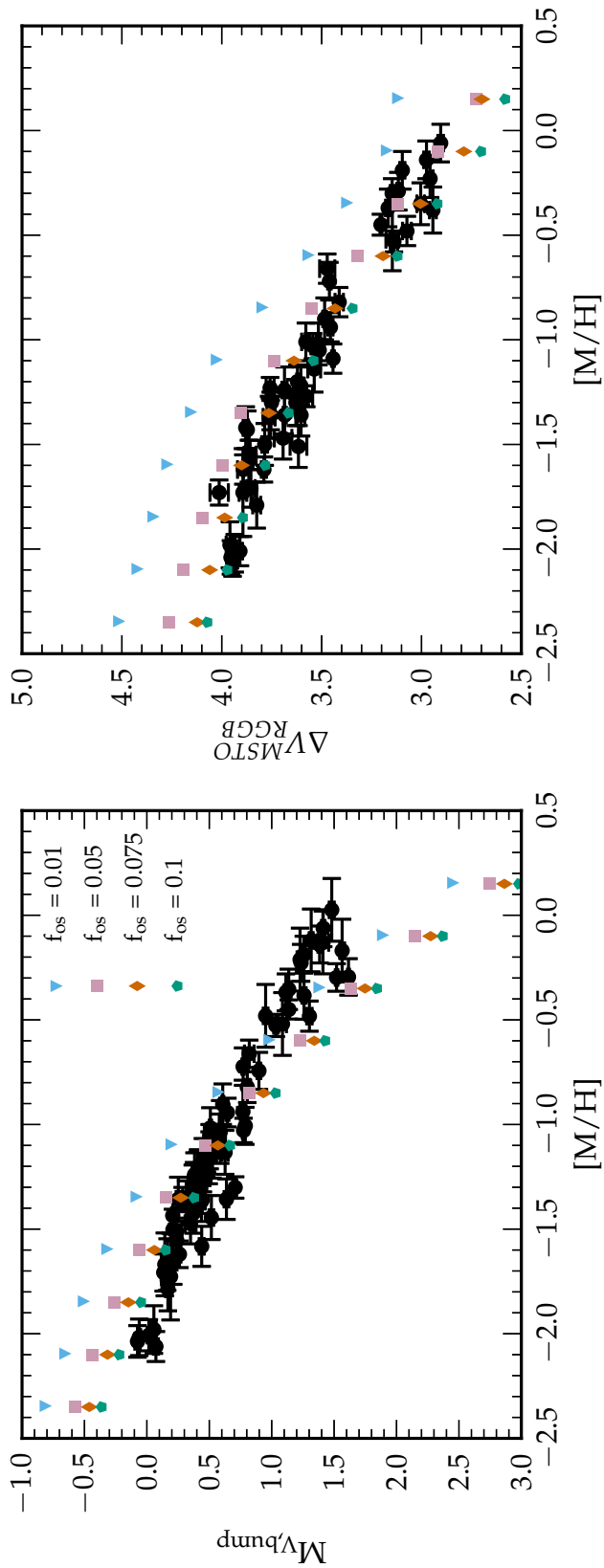


Figure 9.8: Left panel: We compare the predictions from MONSTAR for different overshoot parameters f_{os} to the empirically determined location of the LF bump (Nataf et al., 2013). In each model the abundances are solar scaled and overshoot has been applied at the base of the convective envelope. Our adopted formalism for overshoot is described by Equations 9.1 and 9.2. The four levels of overshoot considered are specified in the legend. Right panel: Comparison of the $\Delta M_V^{\text{MSTO}}_{\text{bump}}$ parameter to theoretical calculations with overshoot as specified in the left panel.

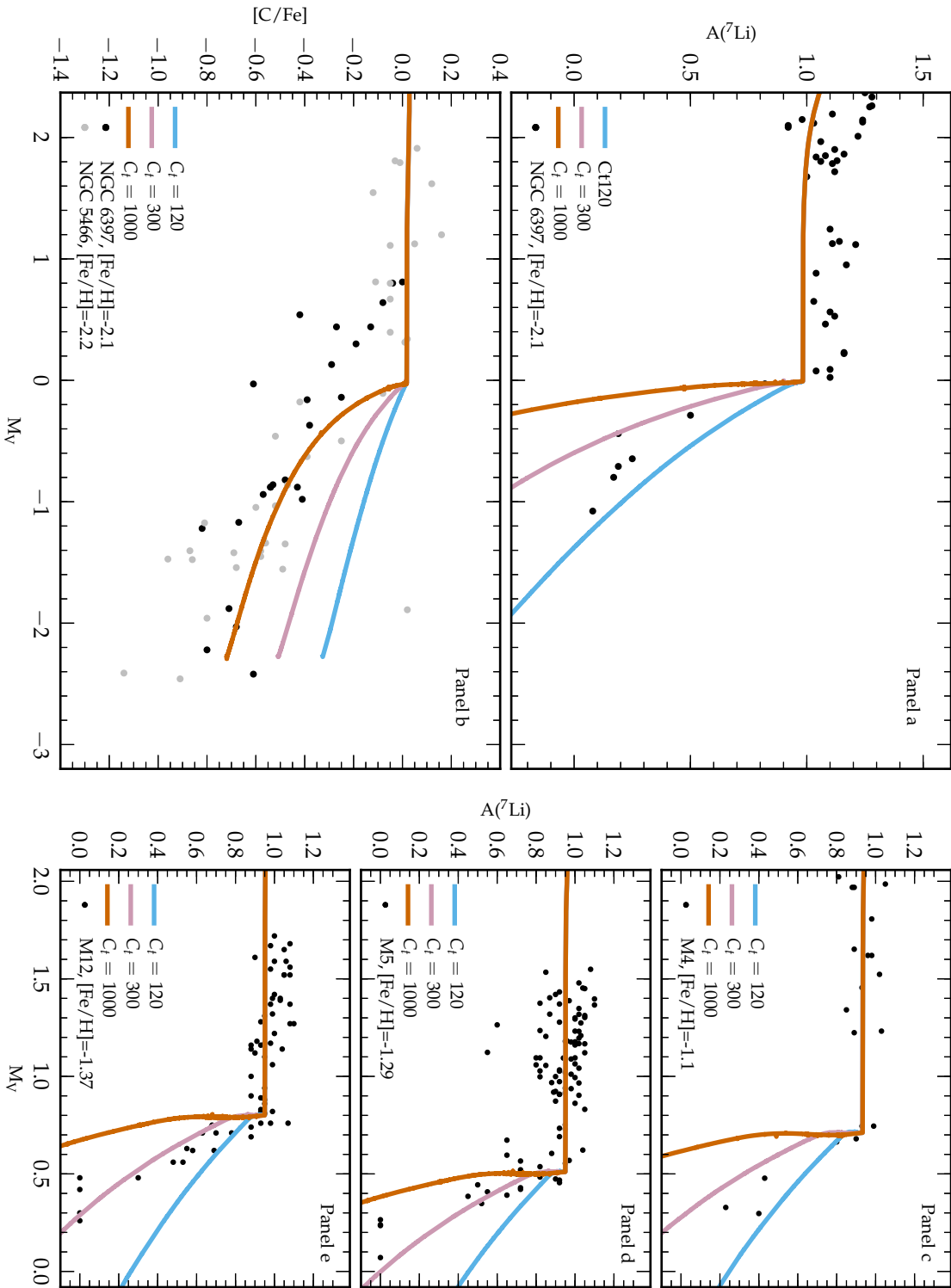


Figure 9.9: Panel A: $A(\text{Li})$ as a function of luminosity for the GC NGC 5466 ($[\text{Fe}/\text{H}] = -2.1$). Panel B: $[\text{C}/\text{Fe}]$ as a function of luminosity in NGC 6397 ($[\text{Fe}/\text{H}] = -2.1$, black circles) and NGC 5466 ($[\text{Fe}/\text{H}] = -2.1$, grey circles). Panel C: $A(\text{Li})$ as a function of luminosity in the GC M4 ($[\text{Fe}/\text{H}] = -1.1$). Panel D: $A(\text{Li})$ as a function of luminosity in the GC M5 ($[\text{Fe}/\text{H}] = -1.29$). Panel E: $A(\text{Li})$ as a function of luminosity in M12 ($[\text{Fe}/\text{H}] = -1.37$). In each panel we calculate stellar models that best represent the metallicity of the respective clusters. We include three variations of the thermohaline mixing parameter C_t . Blue curves denote $C_t = 120$, lavender denote $C_t = 300$ and vermilion curves denote $C_t = 1000$.

Part V

Discussion and Conclusions

Chapter 10

The Evidence Against

*But, Mousie, thou art no thy lane
In proving foresight may be vain:
The best laid schemes o' mice an' men
Gang aft a-gley,
An' lea'e us nought but grief an' pain,
For promised joy.*

- Robert Burns

10.1 Introduction

It was in 2009 that the wheels were set in motion for the research project that would ultimately lead to this dissertation. The momentum following the release of CZ07 and EDL08 generated the impetus to study a formerly explored mixing mechanism in a new context. Three years prior, EDL06 had identified an application of thermohaline mixing that had previously been overlooked. Accretion (Stothers and Simon, 1969), the core flash (Kippenhahn et al., 1980) and ${}^3\text{He}$ burning during the pre-main sequence (Ulrich, 1972) had been suggested as environments in which the process could operate. The latter reliant on a rare property of ${}^3\text{He}({}^3\text{He}, {}^4\text{He})2p$, in that despite being a fusion reaction, actually reduces the local mean molecular weight. In most cases, timescale constraints argued against significant mixing from a secular instability. EDL06 recognised that during the RGB, low-mass stars must necessarily form a μ inversion in the radiative zone above the hydrogen shell. The unique set of circumstances following FDU allowed the ${}^3\text{He}({}^3\text{He}, {}^4\text{He})2p$ reaction to operate in a homogenised zone over a timescale that could impact upon the μ gradient. We discuss how and why this occurs in a forthcoming paper Church et al. (2014, submitted). EDL06 seemed to have identified an environment conducive to the operation of thermohaline mixing and the studies by CZ07 and EDL08 that

followed demonstrated the tantalising potential of the mechanism. It can match several observational criteria without significant tuning:

- The onset of the mixing coincides with the LF bump of globular clusters, i.e., it is linked to the magnitude at which the hydrogen shell encounters the composition discontinuity left by the deepest extent of FDU.
- The depth of mixing, as determined purely by the nuclear reactions, processes those species that display *in situ* variation.
- The mixing efficiency reproduces the correct mass and metallicity dependence.

The mechanism had the potential to solve several problems in stellar physics and as it turned out, did spur much research (one only needs to look at the number of papers on thermohaline mixing after EDL06). With still much unknown about the process, this project was initially broken into two parts:

1. An empirical study based on the linear theory of thermohaline mixing. The diffusive formalism was to be added to the stellar evolution code and its predictions tested against the spectroscopic constraints provided by GCs. These observations would identify the best formula for the diffusion coefficient and an empirically determined mixing efficiency.
2. To expand upon the work of EDL06 and develop 3D hydrodynamical models of the process using Djehuty. This would provide a theoretically based indication of the mixing efficiency.

The results presented throughout this dissertation have been from the empirical study. We determined that the formalisms of Ulrich (1972) and Kippenhahn et al. (1980) with a mixing efficiency of $C_t = 1000$ could account for the $[C/Fe]$ along the giant branch of intermediate-metallicity GCs (Chapter 5 and Angelou et al. 2011). However, in the low-metallicity clusters, the models could only match the $[C/Fe]$ in the system where the data came from a single homogeneous survey. It was coincidentally the least massive of the low-metallicity GCs examined (Chapter 6 and Angelou et al. 2012). To remove any ambiguity in our results we turned to a more sensitive tracer of mixing. We determined lithium abundances along the RGB in two GCs (Chapter 8 and D’Orazi et al. 2014, submitted), and when combined with other surveys in the literature, established a series of tests to refine the stellar models (Chapter 9 and Angelou et al. in prep). The Li data revealed that thermohaline mixing could not simultaneously account for $A(Li)$ and $[C/Fe]$ along the RGB of GCs. During the course of this thesis, the community began to question the role of thermohaline mixing in RGB stars (Denissenkov, 2010; Denissenkov and Merryfield, 2011; Traxler et al., 2011a; Brown et al., 2013), and in particular whether the linear theory captured the true behaviour of the instability. The results from Chapter 9, which demonstrated that the Ulrich (1972) and Kippenhahn et al. (1980) formalism is unable to reproduce the behaviour of two nuclides simultaneously, only adding further doubt.

Unfortunately, the models that would contribute to the second of the project aims did not materialise. There were several reasons for this including the hydrodynamical inexperience of the author. Stored on a tape somewhere at Lawrence Livermore Laboratories are several 3D hydrodynamical simulations of the thermohaline instability that are unlikely to see the light of day again. The simulations involved mapping the interior of a low-mass RGB star calculated from a 1D stellar evolution code to the 3D domain of Djehuty. A parcel of material, cubic in shape, was artificially altered (chemically and thermodynamically) to mimic the effects of significant ${}^3\text{He}$ burning (having been reduced by 10% by mass fraction). Without going into too much detail, our simulations lead to diapiric (mushroom like tendrils) mixing. This perhaps is not unexpected given the initial set up of the system. Previous numerical simulations, admittedly that modelled oceanic conditions, have shown similar behaviour when the density ratio R_ρ is low (≈ 1) or, as in our case, when there is a high-gradient interface (rather than say a perturbed background gradient (see Shen 1989; Shen and Veronis 1997)). The reasons for this are discussed in Kunze (2003) e.g., the destabilizing compositional step across the interface, the density ratio, the thickness of the interface). According to the published literature, what is not expected from the cube simulations are the elongated structures formed by the rising material. Howard and Veronis (1992) have found that the dominant instability in the fluid can change because of the turbulence introduced from the shear of long fingers. Radko (2010) also concluded that in conditions relevant to stellar interiors ($Pr \ll 1$), the shear instability impedes the growth of the tendrils. We had also carried out tests on the domain size, resolution, composition contrast of the parcel and geometry of the parcel. These simulations are mentioned only in brief highlighting the unpredictable nature of research. The availability of other hydro codes make it possible that this aspect of the research plan may one day be revisited.

Even though the Djehuty simulations do not form part of this dissertation, there have been studies of thermohaline mixing in multiple dimensions by several accomplished groups. It has been hinted throughout, that there exists a discrepancy between the empirical value derived from various studies (ours included) and the flux laws determined from 3D simulations. It would be remiss not to discuss these simply because they do not support our initial conclusions. We review the findings of these studies and discuss the implications for this work. Much of the discussion here follows on from the linear analysis performed in Chapter 2.

10.2 3D Simulations of Thermohaline Mixing

10.2.1 The EDL06 Djehuty Simulation

In their seminal paper, EDL06 set out to model the onset of the helium flash in a low-mass RGB star. They reported that their simulation unexpectedly developed minor motions in the radiative zone above the hydrogen burning shell. It was recognised that a μ inversion, brought about by ${}^3\text{He}$ burning, had created a configuration that was hydrodynamically unstable. The timescale upon which the motions developed ($\mathcal{O}800\text{s}$) suggested that they were observing a dynamical

process which they attributed to a Rayleigh-Taylor instability.

The results of the Djehuty simulation were questioned by Denissenkov and Pinsonneault (2008a). These authors argued that the instability described by EDL06 was a thermohaline instability and that due to timescale and resolution arguments, that the effects of thermohaline mixing, a secular instability, should not be detectable in the Djehuty simulation. Charbonnel and Zahn (2007a) also concluded that the configuration discussed by EDL was best described by a thermohaline instability

We note that Djehuty found motions only ‘modestly slower’ than convection. This is likely due to the initial conditions. Because Djehuty had mapped a 1D model without any extra mixing and with the inversion already present, the configuration was highly unstable. Mixing throughout the RGB would serve to somewhat smear the μ gradient. As EDL06 point out, the mixing helped dilute the μ inversion but was unable to erase it. As a result, one would expect a less vigorous mixing in true stellar interiors.

EDL06 and EDL08 had identified a means by which instability due to a molecular weight inversion may lead to efficient mixing during the RGB. Their major concern, was that by placing this mechanism squarely in the thermohaline (and even Rayleigh-Taylor) box, it would lead to all sorts of presumptions about the process that were not yet understood. They argued that the process should be called $\delta\mu$ mixing because it may not be as straightforward as ‘doubly-diffusion’ as seen in the oceans or explained by the linear theory (especially as diffusion is not always a good approximation to the fluid behaviour). In this section we will see the wisdom in their forewarning.

10.2.2 Denissenkov

Denissenkov (2010) and Denissenkov and Merryfield (2011) carried out 2D and 3D simulations of thermohaline mixing with the specific aim of modelling the process under the conditions found in the stellar environment. Denissenkov’s initial analysis of the linear theory determined that the fastest growing modes could reach diameters of 1.5×10^4 cm in the homogenised region above hydrogen burning shell. Also from his dispersion relationship (equivalent to our Equation 2.56), he calculated the growth rate of the fingers to be 0.86 times their aspect ratio. The aspect ratio (α), like in theory of Ulrich (1972) and Kippenhahn et al. (1980) is a free parameter. Denissenkov (2010) noted that its value can only be determined from solving the equations that govern the system (Equations 2.48 - 2.50). Initially, he applied his formalism to a 1D stellar evolution code to empirically calibrate α , and like the results presented in this dissertation, found fingers with length several times their diameter are required to match observational constraints at both high and low metallicity. From the empirical calibration, Denissenkov’s preferred value was $\alpha = 7$ ($C_t \approx 1200$ in Ulrich’s formalism).

Denissenkov (2010) also employed a 2D doubly-periodic hydrodynamics code to solve Equations 2.48 - 2.50 and numerically determine α . Recall that our system can be described by a series of dimensionless numbers (Table 2.1 provides the necessary summary). Of these, the Prandtl number (Pr), the inverse Lewis num-

ber (τ) and the density ratio (R_p) are required to analyse the multi-dimensional simulations. In the stellar fluid they take the values $Pr \approx 10^{-6}$, $\tau \approx 10^{-6}$ and $R_p \approx 1700$. To mimic stellar conditions, Denissenkov artificially increased the numerical viscosity of his simulations to increase the μ -flux. Although the density ratio was indeed around 1700 it was not explicitly clear in what regime of Pr and τ the calculations were conducted ($Pr = \nu/K_T$ therefore increasing ν will increase Pr). Nevertheless, the results indicated that the mixing developed with an effective aspect ratio of $\alpha = 0.5$ (recall from Equation 2.128 this is close to the value advocated by Kippenhahn et al. 1980) suggesting that process cannot account for the surface composition of RGB stars.

In fact, the behaviour of the fluid displayed many interesting facets as the simulations approached the stellar regime. When he increased the viscosity by 10^2 , the fingers hinted that secondary mean-field effects disrupted their growth. Radko (2010) and Stern (1969) had detailed the conditions in which secondary instabilities could be significant, and the inhibition of the finger growth appeared related to vertical shear as explained by Radko (2010) and predicted by Kippenhahn et al. (1980). Increasing the viscosity by 10^4 seemed to inhibit these secondary effects, however, the numerical viscosity in the simulations was beyond what is expected from microscopic viscosity in the radiative zone of RGB stars. Denissenkov argued that additional processes (e.g. rotation) would serve to increase the viscosity in this region, which may allow the fingers to form but they would also induce turbulence that would necessarily mix the composition and smooth out the molecular weight gradient.

The follow up 3D simulations of Denissenkov and Merryfield (2011) yielded similar behaviour, although the focus of this work was on the formation of the mean-field instabilities that follow the initial elevator modes (modes that lead to the development of the fingers). Like Traxler et al. (2011b), they concluded that the γ -instability, which leads to the formation of thermohaline staircases and increases the efficiency of mixing in the ocean by an order of magnitude, is unable to develop under stellar conditions. We explore this secondary instability further in discussions of the simulations by the Santa Cruz group.

10.2.3 Santa Cruz

The Santa Cruz group, lead by Pascale Garuad, published a series of papers on doubly-diffusive mixing. Their analysis covered oceanic and stellar environments including both semi-convection and thermohaline mixing (Traxler et al., 2011b,a; Stellmach et al., 2011; Rosenblum et al., 2011; Brown et al., 2013). Here we focus on the work of Traxler et al. (2011a) and Brown et al. (2013) in particular.

In these studies, the total flux of the competing quantities, and hence the appropriate diffusion coefficient to use in the stellar codes, are related through the Nusselt numbers Nu_T and Nu_μ (i.e., the ratio of the flux of the quantity of interest to the total flux). Their simulations were conducted at Pr , $\tau = 10^{-2}$ for different values of the density ratio. The parameter space that they investigated suggested that a universal scaling law, determined from the respective Nu fluxes, could be extrapolated across four orders of magnitude into the true stellar regimes. They

concluded that

$$Nu_\mu - 1 = \frac{C_P}{\tau R_0^*} \quad (10.1)$$

where $C_P = 12$ according to Kippenhahn et al. (1980) and $C_P = 8/3\pi^2\alpha^2$ from Ulrich (1972). Both of which overestimated the flux determined from their simulations with large R_ρ .

Having also analysed the thermohaline mixing in the oceanic environment, they were interested in layer formation and the formation of thermo-compositional staircases. The layering increases the efficiency of mixing in the oceans by up to an order of magnitude and the onset of this secondary instability had not been analysed in the stellar environment. The theory behind the spontaneous formation of staircases has been derived in Radko (2003) and later numerically modelled by Traxler et al. (2011b) using a mean field approximation. Layering will develop if

$$\frac{\partial\gamma}{\partial R_0} < 0 \quad \text{with} \quad \gamma = \frac{R_0 Nu_T}{\tau Nu_\mu}, \quad (10.2)$$

where γ takes on distinct meanings depending on regime of interest. In the astrophysical environment γ is the sum of turbulent and diffusive fluxes where it is just the turbulent flux in the ocean. The condition states that the ratio of temperature to μ flux is required to decrease as function of the density ratio. However the conditions in the stellar fluid where low Pr and τ numbers ensure that this always increases. This result was consistent with the findings of Denissenkov and Merryfield (2011, although they used only the turbulent flux in their calculation of γ) in that this secondary instability is unable to develop in the stellar environment.

Brown et al. (2013) refined these simulations to lower Pr and τ with several interesting results. They observed that the growth rate of the fastest growing modes were twice that predicted from the linear theory indicating the presence of a secondary instability. Although their calculations still demonstrated that γ increased with R_ρ , fully convective layers developed in the simulations. They determined the behaviour was due to a collective instability from the mean field effects. This had first been predicted by Stern (1969) and is obviously distinct from the γ instability that gives rise to the staircases. The collective instability is due to the fingers exciting large scale gravity waves. Waves can be excited and grow exponentially which then advect momentum, heat and heavy elements until they ‘break’ and mix with the background. Although this secondary instability increased the efficiency of mixing, it still did not result in a D_μ large enough to match the value required by observation. Like in the simulations by Denissenkov (2010) a secondary instability, the vertical shearing on the elevator modes, inhibited their growth. Radko and Smith (2012) in fact discuss possible sources of secondary instabilities in different regimes for Pr and τ .

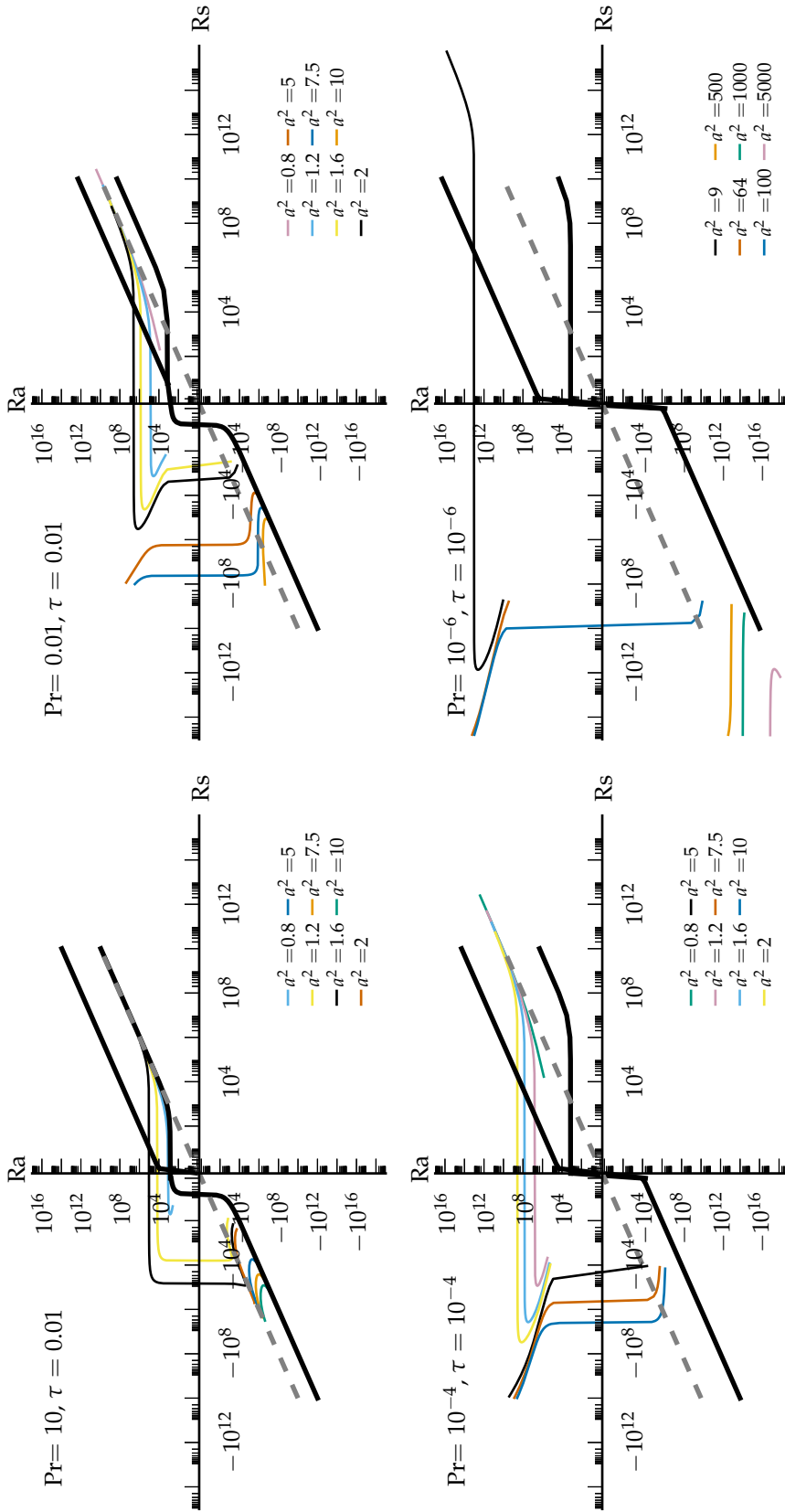


Figure 10.1: Curves showing the nature of the most unstable mode for combinations of Ra and Rs in conditions approaching the stellar regime. It is assumed that the vertical wavenumber $n=1$, whilst our curves follow constant horizontal wavenumber a . We mark the different convective regimes with the solid black lines as per Figure 2.6. The grey dashed line marks the location of neutral buoyancy $Ra = Rs$. The top left panel marks the oceanic regime ($Pr = 10, \tau = 0.01$) and reproduces Figure 2.7. The bottom right panel is calculated with $Pr = 10^{-6}, \tau = 10^{-6}$ and representative of the conditions found in the stellar environment. Current numerical models fall between these regimes with most representative by the top right panel.

10.2.4 Aside - The Behaviour of the Fluid Approaching Stellar Conditions

Results from 3D modelling reviewed here have indicated that thermohaline mixing is characterised by secondary instabilities, which are expected to operate in the stellar regime. It has become more and more apparent that the linear theory only forms part of the thermohaline story. Unfortunately, it is difficult to conduct hydrodynamically simulations with Pr , τ and Re (as we have seen for convection) numbers approaching those found in stellar interiors. Once the Santa Cruz group were able to refine their numerical techniques to model systems closer to the stellar regime, they found a different class of behaviour than at higher Pr and τ numbers. Extrapolation across many orders of magnitude can be somewhat uncertain. Based on our method of linear stability analysis in Chapter 2 we are able to illustrate how quickly the behaviour of the fluid changes in the linear regime. Our analysis is an extension of that carried out by Baines and Gill (1969). We do not consider secondary instabilities or the limiting wavenumber of maximum growth (Equation 2.64) but this is not necessary to highlight our point. The analysis still gives an indication of how quickly the fluid behaviour changes for different values of Pr and τ .

From our third order dispersion relationship (Equation 2.56)

$$p^3 + (Pr + 1 + \tau)k^2p^2 + [(Pr + \tau Pr + \tau)k^4 - (Ra - Rs)Pr \pi^2 a^2 / k^2]p + \tau Pr k^6 + (Rs - \tau Ra)Pr \pi^2 a^2 = 0, \quad (10.3)$$

we make a series of substitutions such that

$$r = \frac{Ra}{n^4 \pi^4}, \quad r_s = \frac{R_s}{n^4 \pi^4}, \quad P = \frac{p}{n^2 \pi^2}, \quad y = \frac{a^2}{n^2} \quad (10.4)$$

and we can determine the most unstable mode for all R_a and R_s

$$r = \frac{(P+1+y)^2}{Pr(1+\tau)y^2P} [P^2 + (Pr+\tau)(1-y^2)P + Pr\tau(1+y)^2(1-2y)]$$

$$r_s = \frac{(P+\tau(1+y))^2}{Pr(1-\tau)y^2P} [P^2 + (\tau+1)(1-y^2)P + Pr(1+y)^2(1-2y)]. \quad (10.5)$$

In Figure 10.1 we have plotted four combinations of Pr and τ that range from oceanic to stellar conditions. In each panel we include a series of modes with the horizontal wavenumber, a (recall this is distinct from α , the aspect ratio), as specified in the respective legends (recall that the most unstable modes correspond to $n=1$). We have essentially combined Figures 2.6 and 2.7. In each panel the solid black lines mark the boundaries between stable, direct (convection), oscillating (semi-convection) and thermohaline modes. The dashed grey line indicates the location of neutral stability such that $R_a = R_s$. Recall from our analysis in Chapter 2 that thermohaline mixing operates when the most unstable modes develop in the bottom left quadrant in the region between stability and neutral stability. Although we do not perform further analysis to determine the aspect ratio of the fingers, it is clear that higher wavenumbers indicate taller and thinner fluid elements (Baines and Gill, 1969).

The top left panel of Figure 10.1 corresponds to oceanic conditions and reproduces our Figure 2.7. The bottom right panel corresponds to the expected stellar conditions whilst the two intermediate plots demonstrate the regimes in which the numerical simulations strive to operate. Under stellar conditions, the most unstable thermohaline modes have horizontal wavenumbers much higher than found in the oceanic conditions or predicted by current modelling. Recall that Ulrich (1972) argued that these are not likely to survive inside the star and thus the mixing must be due to thermally limited modes. Our simple linear calculations, whilst not quantitatively useful here, do demonstrate a clear fact. There is a significant and rapid change in behaviour of the modes approaching stellar conditions. The complex set of behaviours arising from the numerical simulations have been identified by extending the modelling from the conditions in the top left panel to those in the top right. By simply considering the fastest growing modes, our linear analysis suggests the change in fluid behaviour is far more significant going from $Pr, \tau = 10^{-4}$ to 10^{-6} . As we have seen already, extrapolating our analysis into the stellar regime may be wrought with danger.

10.2.5 Mocák et al. (2011)

It is worthwhile discussing related work by Mocák et al. (2011). In 3D hydrodynamical simulations of the shell flash, the authors noted unstable motions in the region below the shell. The conditions were indeed unstable to thermohaline mixing, but the instability developed on a dynamical timescale, and their simulations were without full radiative transfer making it very unlikely that they were witnessing thermohaline mixing. Closer inspection determined that the regions that underwent mixing were forced by waves in the region adjacent to the the turbulent convective zone. A wave induced turbulent mixing process operating in stably stratified layer was the origin of the instability.

We summarise these results for two reasons. Like the Djehuty simulation, they witnessed what appeared to be secular instability on a dynamical timescale. Secondly it reiterated a common theme from the 3D hydrodynamic simulations; interactions with gravity waves play a significant role in the fluid transport.

10.3 Doubts Arising from the Linear Theory

Doubts surrounding the role of thermohaline mixing in RGB stars started to arise before the results of the 3D simulations. In addition to questioning the instability discovered in Djehuty, Denissenkov and Pinsonneault (2008a) were concerned that horizontal shearing (say from rotation) would render thermohaline mixing inefficient. This secondary shearing is distinct from the vertical shearing of the elevator modes found by Radko (2010) and Brown et al. (2013). As Denissenkov (2010) showed, whilst rotation may increase the viscosity and allow finger formation, it should also be accompanied by turbulence that will serve to stabilise the molecular weight gradient.

Charbonnel and Zahn (2007b) argued that magnetic fields always serve to overcome the destabilizing effect of the inverse μ gradient. This is reminiscent of

the buoyancy force and its stabilising effects in the GSF instability. If so inclined, one may also argue that magnetic fields could serve to inhibit shearing in the thermohaline region thus it is not clear from linear analysis what role interactions from other mechanisms play.

We can now add Angelou et al. (in prep) to this list. Their results, presented in Chapter 9, demonstrate that $[C/Fe]$ and $A(Li)$ cannot be reproduced with the same value of C_t . Whether the abundances can be matched through a diffusive model of mixing or whether the blame lies with the shortcomings of the linear theory of thermohaline mixing will drive our future work.

Chapter 11

Summary and Concluding Thoughts

The essence of the independent mind lies not in what it thinks, but in how it thinks.

- Christopher Hitchens

That which can be asserted without evidence, can be dismissed without evidence.

- Christopher Hitchens

11.1 Summary

Stars in all stellar environments display evidence of significant mixing as they approach the tip of the red giant branch. This is contrary to the predictions of standard stellar theory which indicate that FDU is the only means by which the stars alter their surface composition. The stellar evolution codes that calculate the numerical models fail to consider the vital physics that drives extra mixing beyond the FDU event. In Chapter 1 we described the empirically determined constraints of the mixing with the key requirement being that the process responsible does not connect the burning region to the convective envelope until the hydrogen shell has removed the composition discontinuity left behind by FDU (Gilroy and Brown, 1991; Gratton et al., 2000; Martell et al., 2008b). The onset of mixing must therefore coincide with the bump in the luminosity function of GCs.

GCs provide an environment in which the onset of extra mixing can be determined from both spectroscopic and photometric means. High-resolution photometry offers a precise method to identify the magnitude at which the mixing process is initiated. The detection of a luminosity function and, by virtue, a well populated

CMD is one reason why GCs remain useful testbeds for stellar theory. Decades of spectroscopic surveys, designed to unravel the origin of their abundance patterns, have provided us with a large data set to mine. Their abundance patterns are best explained by a contribution of primordial pollution and *in situ* processing. In Chapter 1 we outlined the convergent lines of evidence that suggest that GCs are more complex than the classical simple stellar population hypothesis. The detection of a primordial component in the GC abundance patterns and the splitting of their evolutionary sequences are straightforwardly explained by the presence of multiple populations. Distinguishing between primordial and *in situ* contributions was essential in our examination of the extra mixing.

The first study to investigate a specific mechanism for extra mixing in RGB stars, and that also significantly impacted upon the literature, was that by Sweigart and Mengel (1979). In their investigation of meridional circulation, they compared their models to observations of the giant branch in the metal-poor GC M92 (as we have done in Chapter 6). The cause of the mixing remains unresolved and the topic still contentious 35 years later. Solutions in the form of rotational mixing (Sweigart and Mengel, 1979; Chanamé et al., 2005; Palacios et al., 2006), magnetic fields (Palmerini et al., 2009; Nordhaus et al., 2008; Busso et al., 2007; Hubbard and Dearborn, 1980), internal gravity waves (Denissenkov and Tout, 2000) and more recently thermohaline mixing (Eggleton et al., 2006; Charbonnel and Zahn, 2007a; Eggleton et al., 2008) have all been suggested but no one mechanism has managed to generate a consensus in the literature.

This dissertation has focussed exclusively on the thermohaline mechanism. The physics of this process was first identified through comparisons of thermal and salt diffusion in sea water. Configurations that are initially stably stratified according to density, can become unstable when two diffusing quantities in the fluid are in competition (doubly-diffusive). In the oceans, thermal diffusion is much more rapid than molecular diffusion which can create instability and drive motions that can efficiently transport both salt and heat. Stern (1960) was the first to mathematically describe the stability of such a system and laboratory experiments from Stommel and Fowler reported in that work demonstrated that fluid transport occurs via means of ‘salt fingers’. Although finger like mixing is synonymous with Rayleigh-Taylor instabilities, the instability described here is secular and initially stably stratified in density. We carried out a more general form of Stern’s linear stability analysis in Chapter 2. Although performed with oceanic conditions in mind, the dimensionless parameters allowed for a straightforward extension into the stellar regimes in later sections. The purpose of the analysis was to determine some of the interesting properties of doubly-diffusive fluids and highlight the complex set of behaviours that can arise out of these systems.

In the stellar environment, the destabilising quantity in competition with the thermal diffusion is not salt but rather the mean molecular weight gradient ($\nabla\mu$). The name ‘thermohaline’ has simply been borrowed from the doubly-diffusive analogue in the ocean. The configuration that drives the finger like mixing described by Stern has an equivalent in stellar interiors. Regions that are stable according to the Ledoux criterion but where the mean molecular weight increases outward are thermohaline unstable. Stothers and Simon (1969) were the first to identify an

astrophysical situation in which this configuration may arise. They suggested that the process may be responsible for the pulsations of β -Cepheids. The diffusive formalisms of Ulrich (1972) and Kippenhahn et al. (1980) that followed allowed the process to be straightforwardly incorporated into stellar evolution codes and for other astrophysical applications to be investigated. The derivation by Ulrich (1972) was based on the linear stability analysis but with assumptions that would impact upon the resulting mixing efficiency. In oceanic conditions it is assumed that the fastest growing modes dominate the mixing. In stellar conditions Ulrich argued that mixing was determined by the growth rate of the thermally limited modes. The analysis by Kippenhahn et al. (1980) considered the stability of a blob moving through the stellar medium. The phenomenological ‘blob theory’ arguments followed from earlier analysis of the Goldreich-Schubert-Fricke instability; a doubly-diffusive configuration that arises from stellar rotation. In each derivation of the formula for the diffusion coefficient the mixing length for the travelling material, was parameterised in terms of α , the aspect ratio of the rising fingers (assumed cylindrical). How far material could travel before being disrupted by its environment was the key point of difference in the analyses. One of the more interesting applications of thermohaline mixing was suggested by Ulrich. During pre-main sequence evolution the reaction ${}^3\text{He}({}^3\text{He}, {}^4\text{He})2\text{p}$ is able to dominate and help halt contraction. Although a fusion reaction, it has a rare property in that it reduces the value of μ despite being a fusion reaction. Given the right conditions ${}^3\text{He}$ burning could create an inversion in the homogenised μ profile and drive instability. From timescale arguments, it was determined that the effect was not significant during the pre-main sequence.

Thermohaline mixing, and its prevalence in the literature, experienced somewhat of a renaissance following the publication of EDL06. The authors had initially set out to model the core flash using the 3D hydrodynamics code, Djehuty. Having mapped the structure of a red giant branch star into Djehuty, their simulation developed motions in radiative zone above the hydrogen shell. The mixing was unexpected and the cause was attributed to the presence of a molecular weight inversion on account of ${}^3\text{He}$ burning. Furthermore, they realised that this inversion must form in all low-mass stars. EDL06 and their follow up, EDL08, gave the following explanation for the mechanism. During the main sequence, low-mass stars build up a reservoir of ${}^3\text{He}$ in their outer envelope. Following FDU, the envelope is homogenised and the reservoir is mixed through the outer part of the star leading to a ${}^3\text{He}$ content far above the equilibrium value. As the convective envelope recedes and the hydrogen shell advances, the fragile ${}^3\text{He}({}^3\text{He}, {}^4\text{He})2\text{p}$ reaction is one of the first to occur. The reaction will occur whenever the pp chains are in operation, but ordinarily its ability to lower μ is swamped by the background μ gradient and the impact of other reactions that raise μ . However, once the hydrogen shell approaches the deepest extent of FDU, ${}^3\text{He}({}^3\text{He}, {}^4\text{He})2\text{p}$ can dominate in a homogenised region and create a μ inversion. In this way mixing is initiated at essentially the same point as the bump in the luminosity function, since both are caused by the H-shell reaching the abundance discontinuity left behind from FDU.

Due to the timescale on which motions developed in their simulation, EDL06 described the instability as a dynamical Rayleigh-Taylor process. However several

authors argued that the configuration described should give rise to the secular thermohaline mixing. Having being made aware of the compulsory μ inversion, CZ07 implemented the formula for the diffusion coefficient derived by Ulrich (1972) and Kippenhahn et al. (1980) in their 1D stellar evolution code and adopted a α similar to that advocated by Ulrich. EDL08 designed their own phenomenological prescription for the mixing for their evolution code. In Chapter 2 we analysed four derivations of the formula for the diffusion coefficient. The assumptions made by each of Ulrich (1972), Kippenhahn et al. (1980) CZ07 and EDL08 to arrive at their value of the free parameter were explored.

The thermohaline mechanism removes a free parameter in the extra mixing theory. The location of the μ inversion dictates the depth of mixing and is set by the stellar structure. Both EDL08 and CZ07 noted that this mixing depth qualitatively reproduced the abundance patterns across a range of mass and metallicities. This served as the impetus for our systematic investigation of the process. Our analysis had three main components: a) identify the most appropriate formula for the diffusion coefficient and understand why it was preferable, b) determine the required mixing efficiency within that formalism to match observation, c) investigate the ubiquity of the mechanism across the GC metallicity distribution. Once the empirical analysis was completed, we compared the requirements of the diffusive theory to 3D hydrodynamical simulations of the process. The work of Denissenkov (2010); Denissenkov and Merryfield (2011); Traxler et al. (2011a); Brown et al. (2013) providing the means to do so.

Our empirical investigation of extra mixing, in which our models were compared to spectroscopic studies of GCs, required that a prescription for the process be included in our 1D stellar physics codes. In order to determine what effects thermohaline mixing had over a nuclear timescale, we implemented the necessary changes to our stellar evolution code and post-processing nucleosynthesis code. The details of each, including their mixing algorithms are described in Chapters 3 and 4 respectively. For consistency most of the work carried out in this dissertation has been in the diffusive mixing paradigm.

Reproducing the [C/Fe] abundance with luminosity in the archetypal GC M3 served as the first test of the models in this work. The cluster is of intermediate metallicity demonstrating the expected abundance patterns from extra mixing. In Chapter 5 it was determined that the formalism adopted by CZ07 (UKRT) with $\alpha \approx 6$ ($C_t = 1000$) best reproduced the abundance trend. The EDL08 formalism destroyed the all important ${}^3\text{He}$ much too quickly. In Chapter 6 the formalism and free parameter were applied to GCs across a range in mass and metallicity. We investigated carbon abundances along the red giant branches of M3, M13, M92, M15 and NGC 5466 as a means to test a theory of thermohaline mixing. The second parameter pair M3 and M13 are of intermediate metallicity and our models were able to account for the evolution of [C/Fe] along the RGB in both clusters. In the metal-poor regime only carbon abundances in NGC 5466 were tentatively explained by thermohaline mixing. We found that thermohaline mixing is unable to model the depletion of [C/Fe] with magnitude in M92 and M15. In addition the models seemed to significantly overestimate the magnitude of the onset of mixing in these clusters. We were provided with the first hints that FDU

is not deep enough in our stellar models. In Chapter 8 we turned our attention to the large spread in oxygen found in stars near the tip of the RGB in M13. The chemical distribution of stars in this cluster is best explained by the presence of three populations. We determined whether the extreme population, with their enhanced ^4He , would shift the location of the μ inversion to temperatures where oxygen could be impacted. Even under these extreme circumstances thermohaline mixing was unable to significantly effect the $[\text{O}/\text{Fe}]$. We note that in an upcoming paper (Church et al. 2014) we describe how and why the μ inversion settles at the location that it does.

The issues surrounding extra mixing in low-metallicity clusters necessitated further investigation. The models appeared to overestimate the magnitude of the onset of mixing which would serve as an issue for standard stellar physics; the onset of extra mixing is dictated by the depth of FDU and is not related to the choice of mechanism. We were also unable to reproduce $[\text{C}/\text{Fe}]$ as a function of luminosity in those low-metallicity systems where the data was combined. It was unclear whether systematic offsets in the data were to blame, whether the observed abundances were a vestige of a complex mixing history or whether the stellar models were in need of refinement. In Chapter 8 we sought a secondary test of the models by obtaining Li in two GCs. Lithium is a sensitive tracer of mixing and would reveal much about the stellar modelling as well as thermohaline mixing and its applicability as an RGB mixing mechanism.

The Li data collected in Chapter 8 had uses beyond serving as a probe of extra mixing. The multiple populations within GCs have left distinct abundance patterns not observed in the field. These systems possess large internal variations in elements involved in proton-capture reactions (e.g., C, N, O, Na, Al). The simplest explanation for such behaviour is that GCs experience at least two episodes of star formation whereby a fraction of relatively massive first-generation stars contribute nuclear-processed ejecta to form the later generation(s). However the nature of the polluting progenitors is not clear. To shed light on the nature of these polluters we require distinguishing chemical signatures. Theoretical models predict that Li can be synthesised in asymptotic giant branch stars, whereas no net Li production is expected from massive stars. In Li, we therefore possess a means to identify the polluting progenitors. We derived Li and Al abundances for a large sample of red-giant branch stars (below and above the bump luminosity) in the globular clusters NGC 6218 (M12) and NGC 5904 (M5). In both globular clusters we require Li production across the different stellar generations favouring the AGB scenario, but production seems to have occurred to different extents. We suggested that such a difference might be related to the cluster mass with the Li production being more efficient in less-massive clusters. This was the first time a statistically significant correlation between the spread in Li within a GC and its luminosity had been demonstrated.

Unlike $[\text{C}/\text{Fe}]$, lithium is also a robust tracer of FDU at GC metallicity. In Chapter 9 we utilised medium-to-high resolution spectroscopic surveys of lithium in globular clusters, as well as complimentary photometric analysis, to determine the predictive power of stellar theory during the red giant branch phase. The two mixing episodes served as the key evolutionary tests. We reproduced the known

result that stellar models overestimate the magnitude of the bump. A direct comparison of theoretical and observed bump magnitudes found some agreement at high metallicities. We also compared the magnitude difference between the main-sequence turn off and the bump, $\Delta M_{V_{\text{bump}}}^{\text{MSTO}}$, which is independent of distance. This method suggested that there is a systematic offset at all metallicities. Both techniques cast doubt on the accuracy of stellar modelling, particularly with first dredge-up at low metallicity. We investigated the role of the stellar microphysics, including the first systematic tests of the equation of state, and concluded that any reasonable variations are unable to reconcile the discrepancy. The inclusion of overshoot at the base of the convective envelope, however, enabled models to reproduce the empirically determined $\Delta M_{V_{\text{bump}}}^{\text{MSTO}}$ parameter but did not resolve the issues with direct comparison.

Having refined our models satisfactorily, we conducted our final test of thermohaline mixing. We determined whether the thermohaline mechanism is able to simultaneously account for the depletion of [C/Fe] and A(Li) in our globular cluster sample. A free parameter of $C_t = 120 - 300$ was sufficient explain the lithium data. This is less efficient than the value of $C_t = 1000$ required to match [C/Fe]. There is still much work to be done in determining whether any combination of mixing depth and mixing speed can simultaneously reproduce [C/Fe] and A(Li) or whether a diffusion approximation to the mixing is inappropriate.

Empirically, the value of the free parameter in the linear theory of thermohaline mixing is dependent on which nuclide one is trying to match. The depletion of [C/Fe] as a function of luminosity in GCs is best reproduced by $C_t = 1000$ ($\alpha = 6$) whereas $C_t < 300$ ($\alpha < 3$) is sufficient to explain the depletion of A(Li). Both these values implying a mixing that is more efficient than suggested by 3D hydrodynamical modelling of the process. From the previous chapter it was clear that as the simulations approached stellar conditions, thermohaline mixing is characterised by secondary instabilities. These additional instabilities inhibit the formation of fingers predicted by the linear theory. The conditions being modelled are yet to reach those representative of stellar interiors and they seem to suggest that interactions with gravity waves play a significant role in determining the mixing efficiency. How the fluid behaves in the true stellar environment and in the potential presence of magnetic fields and horizontal shearing remains to be seen.

11.2 Personal Reflection

Attempting to contribute to such a dynamic area of research has been challenging. Extra mixing in red giant branch stars has featured prominently in the literature for well over 35 years. That is a lot of time for senior research scientists to build up an impressive anthology of knowledge. In comparison I have been thinking about the problem for five years during which time I have been trying to bridge the gaps in my knowledge as well as contribute. Papers on thermohaline mixing were published in mathematical, fluid, oceanic and stellar journals. The problem could be investigated from many different perspectives using different analytic tools. It was initially daunting knowing how much there was still to understand

every time I made some progress. The breadth in background material required to address the process in the context of extra mixing during the RGB is reflected in the size of this dissertation. One must come to terms with stellar evolution and modelling, GCs, numerical methods, observational techniques, stability analysis and the language of 3D hydrodynamics. As with any graduate student, there are also the misconceptions as well as deficiencies in programming and communication that needed addressing. Although some of the results presented already feel dated, the skills that I have developed do not.

When I began looking at thermohaline mixing in 2009, it seemed like a very promising thesis topic. The theory predicted that mixing began at the exact location determined by observation. The process has been directly observed to operate in the oceans and the conditions for instability in stars arose naturally from the nuclear burning. Through linear stability analysis (i.e., a sound mathematical base), a formulation had been derived that seemingly displayed the correct dependence on stellar mass and metallicity with a single free parameter. The key to the mixing was of course the development of an inversion in the mean molecular weight gradient. The results we have presented in this work now force us to question what, if any, is the significance of the the development of a μ inversion in the radiative zone of RGB stars. I preface my next statement with a warning: it is only a philosophical point and perhaps the outcome of some irrational loyalty having chosen the mechanism as the topic of my dissertation. But, it seems like nature has gone to a lot of effort to create the conditions for a μ inversion to develop, at exactly the right magnitude extra mixing begins on the RGB. But as many have argued previously it is perhaps the molecular weight barrier and not the inversion that is significant. The predictions of thermohaline mixing produce another intriguing coincidence. The temperature location of the μ inversion develops in such a way that processing is more efficient in low-metallicity stars. The fact that the $^{12}\text{C}/^{13}\text{C}$ value is reduced to its equilibrium value in the lowest-metallicity stars I interpret as a hint that the location to which material is mixed is highly dependent on the nuclear burning.

The crux of this thesis has been to look at one mixing mechanism in isolation. It is not necessary to capture every aspect of the process if the physical basis is understood and the prescription can reproduce the observational results. This is a definition of a ‘model’ (e.g., MLT). Unfortunately our survey of lithium has recently shown that thermohaline mixing, in its current formalism, cannot simultaneously account for $A(\text{Li})$ and $[\text{C}/\text{Fe}]$ with the same free parameter. In fact, with the data sets currently available, just trying to fit $[\text{C}/\text{Fe}]$ raises questions about the mechanism. The story is of course much more complex than the 1D-linear-diffusive formalism we have applied. There are many coupled force interactions in the stellar fluid. Stars rotate, they have magnetic fields, convective boundaries constantly readjust whilst pressure waves and gravity waves traverse through the star. What we can be certain of is that linear theory applied here does not capture essential secondary instabilities that the 3D simulations have demonstrated. These secondary instabilities impact upon the μ -flux of this mechanism and must be considered. The caveat being that the mechanism is in operation in isolation and the conditions modelled by these simulations can be extrapolated to the stellar

interior.

EDL06 advocated calling the process $\delta\mu$ mixing because applying an established name to the mechanism could be confused with understanding how it works. They believed there were many aspects to the mixing we did not yet understand and their warning proved to be right. If the process we are modelling in stellar interiors is thermohaline mixing, then we are slowly improving our understanding of its operation in these extreme conditions. However there has to be some doubt as to whether the process that is causing the mixing is in fact secular. The motions detected by the Djehuty simulation, although initially well out of equilibrium, were dynamical. And although our own analysis in Figure 2.9 has shown the conditions meet the definition of a thermohaline instability, so too did the simulations by Mocák et al. (2011). Gravity waves from the convection zone were able to drive mixing on timescales much faster than that predicted by a thermohaline instability. How and if this impacts on the extra mixing process is unknown.

During every stage of this thesis we have tried to understand the theoretical basis of the mechanism and any assumptions that have gone into the models, whether they be from the 1D linear theory or the 3D simulations. Although not as cite-able as providing yields, the constant questioning of the models led me down a path to other interesting problems. It extended the reach of this thesis, with some attention paid to issues other than extra mixing. Even though I have spent five years thinking about the problem I still feel I do not know enough to answer whether the process does govern the surface composition of RGB giants. We have seen a significant paradigm shift as the 3D models approach stellar conditions with the linear theory seemingly superseded. But the same may be true again as the simulations do attain stellar conditions. The behaviour of the fluid may be very different to that which is currently modelled by the hydrodynamical codes. The presence of other instabilities, yet unknown, may impact upon the μ -flux. It is an interesting problem and I just don't know. The current state of the literature may be the first steps towards a more complex and complete formalism.

Part VI
Appendicies

Appendix A

Convection in Stellar Evolution

There exists no analytical treatment that can accurately predict the radiation flux carried by convection. In fact, the calculation of energy transport in stellar models is based on a formalism described by its author as “only a rough approximation”. This use of the so-called mixing length theory (MLT) has been a major criticism of stellar evolution theory despite the relatively good agreement that exists between models and observations. It was outlined in the previous sections that convective stability is usually determined from the Schwarzschild criterion (and sometimes the Ledoux criterion). How the convection proceeds, according to Richard Feynman, “is the most important unsolved problem of classical physics.”

Laboratory experiments are unable to reproduce the turbulent conditions found in the convective envelope. They must contend with issues such as boundaries, incompressibility (hence no scale height) and viscosity (hence unobtainable Rayleigh numbers, $Ra \sim 10^{20}$, see Spiegel 1971). Studies including those of Heslot et al. (1987), Castaing et al. (1989) and Wu and Libchaber (1992) have managed to reach $Ra \approx 10^{14}$, however these experiments are short lived, lack many of the features of the stellar environment and are yet to reach comparable Rayleigh numbers (still $>$ six orders of magnitude away from stellar conditions).

Numerical simulations of convection provide a secondary avenue of investigation. They are constantly improving but require techniques that overcome the computational cost of solving the Navier-Stokes equations. Turbulent motion transports an enormous flux of energy, in a very compressible gas, which operates on length scales that vary by many orders of magnitude (Kolmogorov, 1941). The stellar conditions are also steeply stratified in density, pressure, temperature, and gravity all of which also need to be resolved. Apart from direct numerical simulations (Kuhlen et al., 2003; Hotta et al., 2012) there are several approaches which have yielded promising results. These include: large eddy simulations such as the piecewise parabolic method (Porter and Woodward, 1994, 2000), the Reynolds-averaged Navier-Stokes method (Monin and I’Aglom, 1971; Davidson, 2004), and the $k - \epsilon$ model (Meakin and Arnett, 2007b; Gastine and Dintrans, 2010). It is not feasible for stellar evolution codes to follow the dynamical timescale required to model the energy cascade of turbulence, rather they are concerned with changes to the structure on a nuclear timescale (although sometimes on a thermal timescale).

The aim of these 3D simulations is to gain enough insight to develop a ‘321D’ theory which can be applied to the 1D codes. Stancliffe et al. (2011) have taken this approach with their Djehuty simulations of proton ingestion episodes. The stability criteria in 1D codes suggest the process drives two distinct convection zones whereas this is not *yet* seen in the 3D hydrodynamical models. Many groups are working towards improving the current 1D formalism (see Arnett et al. 2010).

In lieu of an appropriate theory, approximations in the form of mixing length theory (Prandtl, 1925; Biermann, 1951; Böhm-Vitense, 1958) and full spectrum of turbulence (FST, Canuto and Mazzitelli, 1991, 1992) have been developed. FST tries to take into account the theory of Richardson and Kolmogorov in that a range of blob sizes are responsible for mixing and turbulence occurs on all length scales. MLT on the other hand is a single-eddy approach which averages the effect of turbulence into a single blob size. The blob moves some characteristic distance, ℓ , comparable to the pressure scale height, H_P , before mixing with the surroundings. The theory is intentionally analogous to molecular heat transfer. These theories assume that work is done on the moving blob by buoyancy forces and in this regard, they are similar to the linear thermohaline theory in §2.3.3 which is based on the Boussinesq approximation. MLT and FST are considered to be ‘local’ theories as the convective heat flux at any point in the convective region is given uniquely by the local temperature gradient, plus the local thermodynamic variables. Such theories lead to one of the greatest sources of contention between stellar codes: the treatment of material at convective boundaries. The conditions at the Schwarzschild boundary will demand that mixing stop even though a moving parcel will have attained significant momentum during its displacement. It is expected that some form of overshooting should occur and this is discussed in §3.2.4.2. In fact 3D modelling from Meakin and Arnett (2007b) suggests that:

Convective mixing regions are better predicted using a dynamic boundary condition based on the bulk Richardson number than by purely local, static criteria like Schwarzschild or Ledoux. MLT gives a good description of the velocity scale and temperature gradient for shell convection; however, there are other important effects that it does not capture, mostly related to the dynamical motion of the boundaries between convective and nonconvective regions.

Similar conclusions are reached in studies by Ludwig et al. (1999) and Abbett et al. (1997). The kind of behaviour Meakin and Arnett (2007b) were referring to, which can lead to the diffusion of protons from the envelope into the radiative burning regions, is thought to be responsible for the formation of the ^{13}C pocket and the s-process in AGB stars. Currently, a proton profile is artificially added into the AGB stellar models to produce s-process yields as the local theories can not lead to the formation of a ^{13}C pocket naturally. MLT and FST have been extended to include some form of ‘non-locality’ (see for example Shaviv and Salpeter 1973; Maeder 1976; Eggleton 1983; Xiong 1985; Baker and Kuhfuss 1987; Roxburgh 1989; Zahn 1991).

Grossman (1996) and Mazzitelli et al. (1999) have compared the differences between various local and non-local theories. Depending on the mixing formalism,

the strength of the thermal pulse and temperature at the base of the convective envelope can differ significantly. This difference in structure can alter the nucleosynthesis and in particular the lithium abundance. We ourselves have found similar issues with the choice of mixing formalism (see Chapter 4). The most appropriate formalism to use remains a matter of preference. FST with its apparent stronger physical basis carries a larger convective flux but both have a free parameter that can be used to match observations.

Appendix B

Solving the Diffusion Equation

Diffusive mixing was implemented into MONSTAR by Campbell (2007) and Campbell and Lattanzio (2008). After testing various schemes, Campbell elected to solve the diffusion equation using an implicit finite differences method based on that of Meynet et al. (2004). The abundance, X at time t , and mesh point j , is given by:

$$X_j^t = \left(1 + \frac{[j, j-1]}{\Delta m_j} + \frac{[j+1, j]}{\Delta m_j}\right) X_j^{t+1} - \left(\frac{[j, j-1]}{\Delta m_j}\right) X_{j-1}^{t+1} - \left(\frac{[j+1, j]}{\Delta m_j}\right) X_{j+1}^{t+1} \quad (\text{B.1})$$

where the following notation is used:

$$[j, j-1] = \Delta t \frac{4\pi r_{j-1/2}^2 D_{j-1/2}}{r_j - r_{j-1}}. \quad (\text{B.2})$$

where r and m are the radius and mass location respectively. Here Meynet et al. (2004) have used the radius coordinate in the differencing equation to approximate the second order diffusion equation as a first order equation. Looping throughout the star one arrives at a matrix in the form

$$\begin{bmatrix} b_1 & c_1 & 0 & \dots & & & & \\ a_2 & b_2 & c_2 & \dots & & & & \\ & & & \dots & a_{j-1} & b_{j-1} & c_{j-1} & \\ & & & \dots & 0 & a_j & b_j & \end{bmatrix} \begin{bmatrix} X_1^{t+1} \\ X_2^{t+1} \\ \dots \\ X_{j-1}^{t+1} \\ X_j^{t+1} \end{bmatrix} = \begin{bmatrix} X_1^t \\ X_2^t \\ \dots \\ X_{j-1}^t \\ X_j^t \end{bmatrix} \quad (\text{B.3})$$

where the a coefficients in the matrix are from the second bracketed term in Equation B.1, the coefficient b from the first bracketed term and the coefficients c are from the third bracketed term. From Equation B.3 it can be seen that back substitution is required as the current terms are known and diffused terms are desired. Once the $t+1$ terms are known the abundances are updated accordingly. In general the method for solving such a matrix is through Gaussian elimination

or more specifically *LU Decomposition*. Turing (1948) showed that for systems in the form

$$\mathbf{A} \cdot \mathbf{x} = \mathbf{b} \quad (\text{B.4})$$

such as we have above, decomposing the matrix \mathbf{A} into the product of two matrices of upper triangular form \mathbf{U} and lower triangular form \mathbf{L}

$$\mathbf{L} \cdot \mathbf{U} = \mathbf{A} \quad (\text{B.5})$$

can reduce the number of steps from $O(n^3)$ to $O(n^2)$ where n is the number of unknowns in the system (i.e, the number of mesh points). Furthermore the diffusion equation permits a special case of LU decomposition in that the matrix is tridiagonal.

Tridiagonal systems can be treated efficiently using the Thomas algorithm from Numerical Recipes (Press et al., 1992). For simplicity let us express Equation B.1 in the form

$$a_i x_{i-1} + b_i x_i + c_i x_{i+1} = d_i \quad (\text{B.6})$$

where $a_1 = 0$ and $c_n = 0$. Similar to B.3 we have a system of equations in the form

$$\begin{bmatrix} b_1 & c_1 & & & 0 \\ a_2 & b_2 & c_2 & & \\ & a_3 & b_3 & \ddots & \\ & & \ddots & \ddots & c_{n-1} \\ 0 & & & a_n & b_n \end{bmatrix} \begin{bmatrix} x_1 \\ x_2 \\ x_3 \\ \vdots \\ x_n \end{bmatrix} = \begin{bmatrix} d_1 \\ d_2 \\ d_3 \\ \vdots \\ d_n \end{bmatrix}. \quad (\text{B.7})$$

To solve the system we first modify the coefficients as follows, where the modified coefficients will be denoted with primes:

$$c'_i = \begin{cases} \frac{c_i}{b_i} & i = 1 \\ \frac{c_i}{b_i - c'_{i-1} a_i} & i = 2, 3, \dots, n-1 \end{cases} \quad (\text{B.8})$$

and

$$d'_i = \begin{cases} \frac{d_i}{b_i} & i = 1 \\ \frac{d_i - d'_{i-1} a_i}{b_i - c'_{i-1} a_i} & ; i = 2, 3, \dots, n. \end{cases} \quad (\text{B.9})$$

The solution is then obtained by back substitution:

$$\begin{aligned} x_n &= d'_n \\ x_i &= d'_i - c'_i x_{i+1} \quad i = n-1, n-2, \dots, 1. \end{aligned} \quad (\text{B.10})$$

As is the case for any LU decomposition, it is essential that diagonals are non-zero. We can see here that the Thomas Algorithm uses two loops over n (the number

of steps),

1. decomposition and forward substitution (A first sweep eliminates the a_i 's)
2. backward substitution

thus for such systems, the solution can be obtained in $O(n)$ operations instead of $O(n^2)$ for general LU decomposition and $O(n^3)$ required by Gaussian elimination. The method also provides a saving in memory as the three vectors containing the diagonal elements (\mathbf{a} , \mathbf{b} , \mathbf{c}) are used instead of the large predominantly empty matrix, \mathbf{A} .

Appendix C

MONSTAR_GRID

C.1 The Grid Hierarchy

As shown in Figure 3.5, the Grid directory contains five subfolders:

- *files* which itself contains:
 - the compiled *MONSTAR* Fortran executable;
 - *infiles.list*, a now redundant parameter file describing naming convention for output files;
 - *grid.param*, the default set of input parameters for *MONSTAR*;
 - the *Opal* directory which house the opacity and EOS tables;
 - *Raw_Fort* (Python libraries for reading Fortran binary files) which we describe below;
- *initial_models* which holds every starting model produced by the code;
- *source* which contains the *MONSTAR* source code;
- *run* where the grid of models are created, organised and executed;
- *utils* which contains an assortment of diagnostic utilities;
- the two files, *grid.py* and *grid.list*, are the keys to the grid code and described below.

C.2 Raw_Fort

Raw_Fort is a set of Python libraries that allow Fortran binary files to be read in by the interpreter. These files are best copied into the user's Python path but are stored under this directory structure for portability. The binary to Python libraries were created by Prof. Alex Heger and are the most powerful this author has seen, eclipsing anything available in the Python repositories. They have been applied to many different codes and for many different purposes, particularly post processing and visualisation of model data. The libraries are available on request from their developer.

C.3 grid.list

A nomenclature has been introduced for all starting models which specifies the mass, hydrogen fraction, metallicity, helium fraction and an optional further descriptor of the model. In the example starting model,

```
m1.00_z0.02_y0.27_CNOsolar.dat,
```

the descriptor CNOsolar is not required but provides extra information about the composition in this case. All starting model file names are required to be in this format. As the name suggests, grid.list is the list of every star the user wishes to create for the current grid. Grid.list takes input in two different formats. The simplest is to provide the starting model name and a distinguishing appendix for the folder name in which the calculations will be run. The input

```
m1.00_z0.02_y0.27_CNOsolar.dat, wratio4.5,
```

for example, will force the code to search the *initial_models* folder for the file

```
m1.00_z0.02_y0.27_CNOsolar.dat.
```

The Grid code will then create a directory,

```
run/m1.00_z0.02_y0.27_CNOsolar.dat_wratio4.5,
```

where all input files will be copied, the executable run and output files generated. The appendix in the directory name (wratio4.5 here) is designed for resolution tests or the like, where the same mass and composition are run but a single input parameter is changed (e.g., recall from Table 3.2.5 that the meshing criterion, wratio, is typically set to 7.5). Although not strictly necessary, the executable is always copied to the run directory so that results can be reproduced at any stage. The source executable in directory *files* is likely to be updated or recompiled often.

The second method of input in grid.list is to specifically outline the mass and composition of the star for which an input model may not already exist. The code will then find the closest starting model, enforce very small time steps (on the Kelvin-Helmholtz timescale) and gradually adjust the mass and composition as required. The code is run with an initial increment in mass and composition for a handful of consecutive models to ensure convergence, then the composition homogenised throughout to ensure that the star will arrive on the zero-age main sequence with the correct composition and structure. There are criteria in place for mass and composition increments so the process is repeated until the specified values are reached. Note that there are contingencies in place for failed convergence (e.g., temporarily changing the mixing length or convergence criteria). An example input is as follows:

```
1.25, 0.7383, 0.2495, 0.0122, 2.17e-3, 6.2e-4, 5.39e-3, 0.0, 0, 8000models,
```

The first seven numbers specify mass, X(H), X(⁴He), Z, X(¹²C), X(¹⁴N) and X(¹⁶O) respectively. If a solar scaled model is preferred, providing a negative

carbon abundance will ensure CNO is scaled accordingly. This saves the user having to calculate the mass fractions by hand for different Z . The eighth number dictates the level of alpha enhancement in the starting model. The code will change the $X(^{16}\text{O})$ and Z as required. The ninth number is a flag to generate a starting model for this mass and composition. As before the last term is an appendix to the directory name. Here the user intends to only run for 8000 models and uses an appropriate descriptor. From this input, the code will generate the directory

run/m1.25_z0.0122_y0.7383_8000models.

Any number or combinations of these inputs can be provided in `grid.list` and the code will queue and distribute the jobs as threads become available. We provide an example of a `grid.list` file for reference:

```
#M,X,Y,Z,C,N,O,AE,SM,APPEND !DESCRIPTION

# Standard Library
# 1.0, 0.71, 0.27, 0.02, 3.02e-3, 9.28e-4, 8.42e-3, 0.0, 0, 0, !Old Solar
# 1.0, 0.7327, 0.2539, 0.0134, -2.37e-3, 6.94e-4, 5.74e-3, 0.0, 0,
# 0.80, 0.75, 0.2495, 5.00e-4, 5.45e-5, 1.50e-5, 2.86e-4, 0.0, 0, M3, !M3FG
# 0.80, 0.7195, 0.28, 5.00e-4, 1.90e-5, 5.50e-5, 2.60e-4, 0.4, 1, A0.4,
  0.80, 0.7499, 0.25, 1.00e-4, 1.60e-5, 5.03e-6, 4.57e-5, 0.0, 0, 0,

# Or List model names
  m1.00_z0.02_y0.27_dp.dat,0
# m1.00_z0.02_y0.27_dp.dat,Li
# m1.25_z0.0001_y0.2486_dp.dat,0
```

where `#` and `!` are comments to be ignored. Therefore, only two models will be run in this example. The appendix 0 simply indicates no extra descriptor is to be used in the directory name.

C.4 grid.py

`Grid.py` is the actual python script that organises and controls the execution of MONSTAR. We describe some of its key operations sequentially:

1. The initial models and opacity directories are located.
2. All initial model names are read in and an inventory created.
3. The grid of models to be calculated are read in from `grid.list`.
4. A directory in `run` is created for each model listed. If the directory name already exists, a time and date descriptor are appended to the folder name.
5. A log file is created with diagnostic information about each star calculated during the session.

6. The default parameter file is copied to the output directory and opened in a text editor for the user to tweak parameters. This is done for every star in the grid list.
7. A job queue is created and the number of free threads determined. Each processor is dedicated to a single star and will not receive a new job until its assigned calculation is finished. The jobs are sent to free processors according to the order in they are listed in grid.list.
8. For each job the closest starting model is located. An algorithm is in place to search the inventory list created in step 2.
9. A series of diagnostic checks are performed on each input model. In order to save disk space, the starting files and output files of MONSTAR are all in binary. The Raw_Fort libraries are used here to ensure that the mass and composition specified in the file name agree with that in the actual input model. It also checks the size of the nuclear network and whether the starting model includes the secondary ${}^7\text{Li}$ nuclear network. Including lithium in the calculations is optional as its convergence conditions can slow the evolution down. All of this information is recorded in the log file.
10. Once the starting model, input files, and executable are copied to the respective directories, MONSTAR is started for each star.
11. If a the desired starting model does not match any of those found in the directory initial_models, MONSTAR automatically creates the requested model.
12. Once a calculation is finished and a processor becomes available, any jobs remaining in the queue are sent to that processor.

These set of operations need to be slightly modified when running the code on a cluster. Shared memory across nodes becomes an issue when storing the opacity and EOS tables in a parent directory. The way the script distributes jobs in this environment must also be considered. On a local machine is easy enough to distribute the jobs across available processors but on a cluster there usually a queuing system. If I had a grid of 20 stars I want run, it is more efficient to ask for a single processor 20 times, rather than wait for 20 processors and then distribute jobs. Therefore, when running the grid code on a cluster, grid.py will generate the directory structure and a submission script for each star.

Although initially setting up the evolution code is not as easy as it once was, it is now far easier to set a grid of models running. Python wrappers and special libraries are required to run the code in an automated fashion, but designed in such a way that the code can be executed manually like it once was. All of this comes at the cost of requiring extra care when merging updated routines from other contributors and their forked versions of the code.

Appendix D

MONSOON 86 Species Network

Table D.1: Initial abundances of the 86 species considered in calculations for Chapter 7.

Isotope	Molar Fraction	Isotope	Molar Fraction
g	7.44E-006	si27	0.00E+000
n	0.00+000	si28	5.83E-007
p	evoln (0.60)	si29	2.95E-008
d	0.00E+000	si30	1.96E-008
he3	evoln (1.67E-005)	si31	0.00E+000
he4	evoln (1.00E-001)	p29	0.00E+000
li7	3.34E-011	p30	0.00E+000
be7	0.00E+000	p31	6.58E-009
b8	0.00E+000	p32	0.00E+000
c12	evoln (1.28E-006)	s32	3.09E-007
c13	7.02E-008	s33	2.44E-009
c14	0.00E+000	s34	1.37E-008
n13	0.00E+000	s35	0.00E+000
n14	evoln (1.95E-005)	s36	6.51E-011
n15	7.27E-009	s37	0.00E+000
o14	0.00E+000	cl33	0.00E+000
o15	0.00E+000	cl34	0.00E+000
o16	evoln (9.00E-006)	cl35	1.81E-009
o17	5.72E-009	cl36	0.00E+000
o18	3.01E-008	cl37	5.77E-010
o19	0.00E+000	cl38	0.00E+000
f17	0.00E+000	ar36	5.37E-008
f18	0.00E+000	ar37	0.00E+000
f19	5.33E-010	ar38	1.01E-008
f20	0.00E+000	ar39	0.00E+000
ne20	2.02E-006	ar40	1.58E-011

Table D.1 – continued from previous page

Isotope	Molar Fraction	Isotope	Molar Fraction
ne21	4.91E-009	ar41	0.00E+000
ne22	1.48E-007	k37	0.00E+000
ne23	0.00E+000	k38	0.00E+000
na21	0.00E+000	k39	2.22E-009
na22	0.00E+000	k40	3.47E-012
na23	3.62E-008	k41	1.60E-010
na24	0.00E+000	k42	0.00E+000
mg23	0.00E+000	ca40	3.74E-008
mg24	5.36E-007	ca41	0.00E+000
mg25	6.76E-008	ca42	2.50E-010
mg26	7.46E-008	ca43	5.22E-011
mg27	0.00E+000	ca44	6.20E-007
al25	0.00E+000	ca45	0.00E+000
al-6	0.00E+000	sc41	0.00E+000
al*6	0.00E+000	sc42	0.00E+000
al27	5.37E-008	sc43	0.00E+000
al28	0.00E+000	sc44	0.00E+000

Bibliography

- Abbett, W. P., Beaver, M., Davids, B., Georgobiani, D., Rathbun, P., and Stein, R. F. (1997). Solar Convection: Comparison of Numerical Simulations and Mixing Length Theory. *ApJ*, 480:395.
- Abraham, Z. and Iben, Jr., I. (1970). The Abundances of ^3He and ^4He in the Initial Sun Implied by the Kocharov and Starbunov Assumption. *ApJ*, 162:L125.
- Acheson, D. J. (1978). On the instability of toroidal magnetic fields and differential rotation in stars. *Royal Society of London Philosophical Transactions Series A*, 289:459–500.
- Adelberger, E. G., García, A., Robertson, R. G. H., Snover, K. A., Balantekin, A. B., Heeger, K., Ramsey-Musolf, M. J., Bemmerer, D., Junghans, A., Bertulani, C. A., Chen, J.-W., Costantini, H., Prati, P., Couder, M., Uberseder, E., Wiescher, M., Cyburt, R., Davids, B., Freedman, S. J., Gai, M., Gazit, D., Gialanella, L., Imbriani, G., Greife, U., Hass, M., Haxton, W. C., Itahashi, T., Kubodera, K., Langanke, K., Leitner, D., Leitner, M., Vetter, P., Winslow, L., Marcucci, L. E., Motobayashi, T., Mukhamedzhanov, A., Tribble, R. E., Nollett, K. M., Nunes, F. M., Park, T.-S., Parker, P. D., Schiavilla, R., Simpson, E. C., Spitaleri, C., Strieder, F., Trautvetter, H.-P., Suemmerer, K., and Typel, S. (2011). Solar fusion cross sections. II. The pp chain and CNO cycles. *Reviews of Modern Physics*, 83:195–246.
- Alcaino, G., Buonanno, R., Caloi, V., Castellani, V., Corsi, C. E., Iannicola, G., and Liller, W. (1987). The CM diagram of the nearby globular cluster NGC 6397. *AJ*, 94:917–947.
- Alexander, D. R. (1975). Low-Temperature Rosseland Opacity Tables. *ApJS*, 29:363.
- Alexander, D. R., Rypma, R. L., and Johnson, H. R. (1983). Effect of molecules and grains on Rosseland mean opacities. *ApJ*, 272:773–780.
- Alongi, M., Bertelli, G., Bressan, A., and Chiosi, C. (1991). Effects of envelope overshoot on stellar models. *A&A*, 244:95–106.
- Alonso, A., Arribas, S., and Martínez-Roger, C. (1999). The effective temperature scale of giant stars (F0-K5). II. Empirical calibration of T_{eff} versus colours and $[\text{Fe}/\text{H}]$. *A&AS*, 140:261–277.

- Alves, D. R., Cook, K. H., and Wishnow, E. (2004). Mass Loss from Red Giants in 2nd-Parameter Globular Clusters: The Ages of M3 and M13. In *Bulletin of the American Astronomical Society*, volume 36 of *Bulletin of the American Astronomical Society*, pages 1425–+.
- Anders, E. and Grevesse, N. (1989). Abundances of the elements - Meteoritic and solar. *Geochim. Cosmochim. Acta*, 53:197–214.
- Andersen, J., Clausen, J. V., and Nordstrom, B. (1990). New strong evidence for the importance of convective overshooting in intermediate-mass stars. *ApJ*, 363:L33–L36.
- Anderson, J., Piotto, G., King, I. R., Bedin, L. R., and Guhathakurta, P. (2009). Mixed Populations in Globular Clusters: Et Tu, 47 Tuc? *ApJ*, 697:L58–L62.
- Angelou, G. and Lattanzio, J. (2008). A Small Step on the Long Road to Understanding the R Stars: CNO Cycling in Candidate R Star Progenitors. *Publications of the Astronomical Society of Australia*, 25:155–160.
- Angelou, G. C., Church, R. P., Stancliffe, R. J., Lattanzio, J. C., and Smith, G. H. (2011). Thermohaline Mixing and its Role in the Evolution of Carbon and Nitrogen Abundances in Globular Cluster Red Giants: The Test Case of Messier 3. *ApJ*, 728:79–+.
- Angelou, G. C., Lattanzio, J. C., Church, R. P., and Stancliffe, R. J. (2010). Observational constraints for delta mu mixing. *Mem. Soc. Astron. Italiana*, 81:1057–+.
- Angelou, G. C., Stancliffe, R. J., Church, R. P., Lattanzio, J. C., and Smith, G. H. (2012). The Role of Thermohaline Mixing in Intermediate- and Low-metallicity Globular Clusters. *ApJ*, 749:128.
- Angulo, C., Arnould, M., Rayet, M., Descouvemont, P., Baye, D., Leclercq-Willain, C., Coc, A., Barhoumi, S., Aguer, P., Rolfs, C., Kunz, R., Hammer, J. W., Mayer, A., Paradellis, T., Kossionides, S., Chronidou, C., Spyrou, K., degl’Innocenti, S., Fiorentini, G., Ricci, B., Zavatarelli, S., Providencia, C., Wolters, H., Soares, J., Grama, C., Rahighi, J., Shotton, A., and Laméhi Rachti, M. (1999). A compilation of charged-particle induced thermonuclear reaction rates. *Nuclear Physics A*, 656:3–183.
- Arnett, D., Meakin, C., and Young, P. A. (2010). Convection Theory and Sub-Photospheric Stratification. *ApJ*, 710:1619–1626.
- Arp, H. C. (1955). Color-magnitude diagrams for seven globular clusters. *AJ*, 60:317–+.
- Arp, H. C., Baum, W. A., and Sandage, A. R. (1952). The HR diagrams for the globular clusters M 92 and M 3. *AJ*, 57:4–5.
- Asplund, M., Grevesse, N., Sauval, A. J., and Scott, P. (2009). The Chemical Composition of the Sun. *ARA&A*, 47:481–522.

- Ávila, J. N., Lugaro, M., Ireland, T. R., Gyngard, F., Zinner, E., Cristallo, S., Holden, P., Buntain, J., Amari, S., and Karakas, A. (2012). Tungsten Isotopic Compositions in Stardust SiC Grains from the Murchison Meteorite: Constraints on the s-process in the Hf-Ta-W-Re-Os Region. *ApJ*, 744:49.
- Bærentzen, J. (1965). The Adiabatic Temperature-gradient and the Specific Heat c_p in Outer Hydrogen-Helium Convection Zones. *ZAp*, 62:221.
- Bahcall, J. N. (1964). Solar neutrinos. i. theoretical. *Phys. Rev. Lett.*, 12:300–302.
- Bahcall, J. N., Pinsonneault, M. H., and Wasserburg, G. J. (1995). Solar models with helium and heavy-element diffusion. *Reviews of Modern Physics*, 67:781–808.
- Baines, P. G. and Gill, A. E. (1969). On thermohaline convection with linear gradients journal of fluid mechanics, 37 , pp doi:10.1017/s0022112069000553. *J. Fluid Mech*, 37:289–306.
- Baker, N. and Kippenhahn, R. (1959). Untersuchungen über rotierende Sterne. III. Meridionale Zirkulation bei nichtstarrer Rotation. *ZAp*, 48:140.
- Baker, N. H. and Kuhfuss, R. (1987). Roxburgh’s criterion for convective overshooting. *A&A*, 185:117–120.
- Balsler, D. S., Bania, T. M., Rood, R. T., and Wilson, T. L. (1997). The ^3He Abundance in Planetary Nebulae. *ApJ*, 483:320–+.
- Balsler, D. S., Goss, W. M., Bania, T. M., and Rood, R. T. (2006). The Detection of $^3\text{He}^+$ in a Planetary Nebula Using the VLA. *ApJ*, 640:360–368.
- Balsler, D. S., Rood, R. T., and Bania, T. M. (1999). The ^3He Abundance in the Planetary Nebula NGC 3242. *ApJ*, 522:L73–L76.
- Bastian, N., Lamers, H. J. G. L. M., de Mink, S. E., Longmore, S. N., Goodwin, S. P., and Gieles, M. (2013). Early disc accretion as the origin of abundance anomalies in globular clusters. *MNRAS*, 436:2398–2411.
- Basu, S. and Antia, H. M. (1994). Effects of Diffusion on the Extent of Overshoot Below the Solar Convection Zone. *MNRAS*, 269:1137.
- Basu, S., Antia, H. M., and Narasimha, D. (1994). Helioseismic measurement of the extent of overshoot below the solar convection zone. *MNRAS*, 267:209.
- Bazan, G., Castor, J., Dearborn, D. S. P., Dossa, D., Eastman, R., and Taylor, A. (2001). Djehuty - A full physics, 3D hydrodynamic stellar structure and evolution code. *APS Meeting Abstracts*, pages 1047–+.
- Bazán, G., Dearborn, D. S. P., Dossa, D. D., Eggleton, P. P., Taylor, A., Castor, J. I., Murray, S., Cook, K. H., Eltgroth, P. G., Cavallo, R. M., Turcotte, S., Keller, S. C., and Pudliner, B. S. (2003). Djehuty, a code for modeling stars in three dimensions. In S. Turcotte, S. C. Keller, & R. M. Cavallo, editor, *3D*

- Stellar Evolution*, volume 293 of *Astronomical Society of the Pacific Conference Series*, pages 1–58381.
- Carretta, E., Bragaglia, A., Gratton, R., and Lucatello, S. (2009a). Na-O anticorrelation and HB. VIII. Proton-capture elements and metallicities in 17 globular clusters from UVES spectra. *A&A*, 505:139–155.
- Carretta, E., Bragaglia, A., Gratton, R. G., Lucatello, S., Catanzaro, G., Leone, F., Bellazzini, M., Claudi, R., D’Orazi, V., Momany, Y., Ortolani, S., Pancino, E., Piotto, G., Recio-Blanco, A., and Sabbi, E. (2009b). Na-O anticorrelation and HB. VII. The chemical composition of first and second-generation stars in 15 globular clusters from GIRAFFE spectra. *A&A*, 505:117–138.
- Beaudet, G., Petrosian, V., and Salpeter, E. E. (1967). Energy Losses due to Neutrino Processes. *ApJ*, 150:979.
- Beaudet, G. and Tassoul, M. (1971). Fitting Formulae for a Relativistic and/or Degenerate Electron Gas. *A&A*, 13:209.
- Bedin, L. R., Piotto, G., Anderson, J., Cassisi, S., King, I. R., Momany, Y., and Carraro, G. (2004). ω Centauri: The Population Puzzle Goes Deeper. *ApJ*, 605:L125–L128.
- Bellman, S., Briley, M. M., Smith, G. H., and Claver, C. F. (2001). Carbon Abundances of M92 Red Giant Branch Stars. *PASP*, 113:326–334.
- Bessell, M. S., Brett, J. M., Wood, P. R., and Scholz, M. (1989). The effects of photospheric extension upon the spectra of M-type Mira variables. *A&A*, 213:209–225.
- Biehle, G. T. (1991). High-mass stars with degenerate neutron cores. *ApJ*, 380:167–184.
- Biermann, L. (1951). Bemerkungen über das Rotationsgesetz in irdischen und stellaren Instabilitätszonen. Mit 1 Textabbildung. *ZAp*, 28:304.
- Bjork, S. R. and Chaboyer, B. (2006). Theoretical Uncertainties in Red Giant Branch Evolution: The Red Giant Branch Bump. *ApJ*, 641:1102–1112.
- Bloecker, T. (1995). Stellar evolution of low and intermediate-mass stars. I. Mass loss on the AGB and its consequences for stellar evolution. *A&A*, 297:727.
- Böhm-Vitense, E. (1958). Über die Wasserstoffkonvektionszone in Sternen verschiedener Effektivtemperaturen und Leuchtkräfte. Mit 5 Textabbildungen. *ZAp*, 46:108.
- Bonanno, A., Schlattl, H., and Paternò, L. (2002). The age of the Sun and the relativistic corrections in the EOS. *A&A*, 390:1115–1118.

- Bonifacio, P., Pasquini, L., Molaro, P., Carretta, E., François, P., Gratton, R. G., James, G., Sbordone, L., Spite, F., and Zoccali, M. (2007). Variations in the lithium abundances of turn off stars in the globular cluster 47 Tucanae. *A&A*, 470:153–159.
- Bragaglia, A., Gratton, R. G., Carretta, E., D’Orazi, V., Sneden, C., and Lucatello, S. (2012). Searching for multiple stellar populations in the massive, old open cluster Berkeley 39. *A&A*, 548:A122.
- Briley, M. M., Bell, R. A., Hoban, S., and Dickens, R. J. (1990). An analysis of G-band strengths in NGC 6397 and M55 red giants. *ApJ*, 359:307–318.
- Briley, M. M. and Cohen, J. G. (2001). Calibration of the CH and CN Variations Among Main-Sequence Stars in M71 and in M13. *AJ*, 122:242–247.
- Briley, M. M., Cohen, J. G., and Stetson, P. B. (2002). Carbon Abundances of Faint Stars in M13: Evidence of Two Abundance-altering Mechanisms. *ApJ*, 579:L17–L20.
- Briley, M. M., Cohen, J. G., and Stetson, P. B. (2004). The Chemical Inhomogeneity of Faint M13 Stars: Carbon and Nitrogen Abundances. *AJ*, 127:1579–1587.
- Briley, M. M., Grundahl, F., and Andersen, M. I. (1999). Nitrogen Variations Among Faint Globular Cluster Stars via *ubvy* Photometry. In *American Astronomical Society Meeting Abstracts*, volume 31 of *Bulletin of the American Astronomical Society*, page 1369.
- Briley, M. M., Hesser, J. E., and Bell, R. A. (1991). C and N abundances among 47 Tucanae main-sequence stars. *ApJ*, 373:482–496.
- Brown, J. A. (1987). Carbon-to-nitrogen ratios along the evolutionary sequence of M67. *ApJ*, 317:701–709.
- Brown, J. A. and Wallerstein, G. (1993). High resolution CCD spectra of stars in globular clusters. VIII - The self-enrichment history of Omega Centauri. *AJ*, 106:133–141.
- Brown, J. M., Garaud, P., and Stellmach, S. (2013). Chemical Transport and Spontaneous Layer Formation in Fingering Convection in Astrophysics. *ApJ*, 768:34.
- Buckley, D. R. V. and Longmore, A. J. (1992). The distance to M13 via a subdwarf fit in the optical-infrared colour-magnitude plane. *MNRAS*, 257:731–736.
- Buonanno, R., Corsi, C. E., Buzzoni, A., Cacciari, C., Ferraro, F. R., and Fusi Pecci, F. (1994). The stellar population of the globular cluster M 3. I. Photographic photometry of 10 000 stars. *A&A*, 290:69–103.
- Buonanno, R., Corsi, C. E., and Fusi Pecci, F. (1985). The giant, asymptotic, and horizontal branches of globular clusters. II - Photographic photometry of the metal-poor clusters M15, M92, and NGC 5466. *A&A*, 145:97–117.

- Burbidge, E. M., Burbidge, G. R., Fowler, W. A., and Hoyle, F. (1957). Synthesis of the Elements in Stars. *Reviews of Modern Physics*, 29:547–650.
- Busso, M., Gallino, R., and Wasserburg, G. J. (1999). Nucleosynthesis in Asymptotic Giant Branch Stars: Relevance for Galactic Enrichment and Solar System Formation. *ARA&A*, 37:239–309.
- Busso, M., Picchio, G., Gallino, R., and Chieffi, A. (1988). Are s-elements really produced during thermal pulses in intermediate-mass stars? *ApJ*, 326:196–207.
- Busso, M., Wasserburg, G. J., Nollett, K. M., and Calandra, A. (2007). Can Extra Mixing in RGB and AGB Stars Be Attributed to Magnetic Mechanisms? *ApJ*, 671:802–810.
- Cameron, A. G. W. (1957). Stellar Evolution, Nuclear Astrophysics and Nucleogenesis (Chalk River Rep. AECL; Chalk River, Ont.: Atomic Energy of Canada, Ltd.). *CRL-41*.
- Cameron, A. G. W. and Fowler, W. A. (1971). Lithium and the s-PROCESS in Red-Giant Stars. *ApJ*, 164:111.
- Campbell, S. (2007). *Structural and Nucleosynthetic Evolution of Metal-Poor / \mathcal{E} Metal-free Low and Intermediate Mass Stars*. PhD thesis, Monash University.
- Campbell, S. W., D’Orazi, V., Yong, D., Constantino, T. N., Lattanzio, J. C., Stancliffe, R. J., Angelou, G. C., Wylie-de Boer, E. C., and Grundahl, F. (2013). Sodium content as a predictor of the advanced evolution of globular cluster stars. *Nature*, 498:198–200.
- Campbell, S. W. and Lattanzio, J. C. (2008). Evolution and nucleosynthesis of extremely metal-poor and metal-free low- and intermediate-mass stars. I. Stellar yield tables and the CEMPs. *A&A*, 490:769–776.
- Campbell, S. W., Yong, D., Wylie-de Boer, E. C., Stancliffe, R. J., Lattanzio, J. C., Angelou, G. C., D’Orazi, V., Martell, S. L., Grundahl, F., and Sneden, C. (2012). Cyanogen in NGC 1851 Red Giant Branch and Asymptotic Giant Branch Stars: Quadrimodal Distributions. *ApJ*, 761:L2.
- Campbell, S. W., Yong, D., Wylie-de Boer, E. C., Stancliffe, R. J., Lattanzio, J. C., Angelou, G. C., Grundahl, F., and Sneden, C. (2010). The case of the disappearing CN-strong AGB stars in Galactic Globular Clusters - preliminary results. *Mem. Soc. Astron. Italiana*, 81:1004.
- Campbell, S. W., Yong, D., Wylie-de Boer, E. C., Stancliffe, R. J., Lattanzio, J. C., Angelou, G. C., Grundahl, F., and Sneden, C. (2011). AGB Stars in Galactic Globular Clusters: Are They Really Chemically Distinct from Their Fellow RGB and HB Stars? In F. Kerschbaum, T. Lebzelter, & R. F. Wing, editor, *Why Galaxies Care about AGB Stars II: Shining Examples and Common Inhabitants*, volume 445 of *Astronomical Society of the Pacific Conference Series*, page 63.

- Cannon, R. C. (1993). Massive Thorne-Żytkow Objects - Structure and Nucleosynthesis. *MNRAS*, 263:817.
- Cannon, R. C., Eggleton, P. P., Zytzkow, A. N., and Podsiadlowski, P. (1992). The structure and evolution of Thorne-Zytkow objects. *ApJ*, 386:206–214.
- Cannon, R. D., Croke, B. F. W., Bell, R. A., Hesser, J. E., and Stathakis, R. A. (1998). Carbon and nitrogen abundance variations on the main sequence of 47 Tucanae. *MNRAS*, 298:601–624.
- Cantiello, M. and Langer, N. (2010). Thermohaline mixing in evolved low-mass stars. *A&A*, 521:A9+.
- Canuto, V. M. (1999). Turbulence in Stars. III. Unified Treatment of Diffusion, Convection, Semiconvection, Salt Fingers, and Differential Rotation. *ApJ*, 524:311–340.
- Canuto, V. M. (2009). Turbulence in Astrophysical and Geophysical Flows. In W. Hillebrandt & F. Kupka, editor, *Interdisciplinary Aspects of Turbulence*, volume 756 of *Lecture Notes in Physics*, Berlin Springer Verlag, page 107.
- Canuto, V. M. (2011). Stellar mixing. V. Overshooting. *A&A*, 528:A80.
- Canuto, V. M. and Mazzitelli, I. (1991). Stellar turbulent convection - A new model and applications. *ApJ*, 370:295–311.
- Canuto, V. M. and Mazzitelli, I. (1992). Further improvements of a new model for turbulent convection in stars. *ApJ*, 389:724–730.
- Carbon, D. F., Romanishin, W., Langer, G. E., Butler, D., Kemper, E., Trefzger, C. F., Kraft, R. P., and Suntzeff, N. B. (1982). Carbon and nitrogen abundances in giant stars of the metal-poor globular cluster M92. *ApJS*, 49:207–258.
- Cardelli, J. A., Clayton, G. C., and Mathis, J. S. (1989). The relationship between infrared, optical, and ultraviolet extinction. *ApJ*, 345:245–256.
- Carretta, E., Bragaglia, A., Gratton, R. G., Catanzaro, G., Leone, F., Sabbi, E., Cassisi, S., Claudi, R., D’Antona, F., François, P., James, G., and Piotto, G. (2007). Na-O anticorrelation and horizontal branches. IV. Detection of He-rich and He-poor stellar populations in the globular cluster NGC 6218. *A&A*, 464:939–951.
- Carretta, E., Bragaglia, A., Gratton, R. G., Leone, F., Recio-Blanco, A., and Lucatello, S. (2006). Na-O anticorrelation and HB. I. The Na-O anticorrelation in NGC 2808. *A&A*, 450:523–533.
- Carretta, E., Bragaglia, A., Gratton, R. G., Lucatello, S., and D’Orazi, V. (2012). Chemical Tagging of Three Distinct Populations of Red Giants in the Globular Cluster NGC 6752. *ApJ*, 750:L14.

- Carretta, E., Bragaglia, A., Gratton, R. G., Lucatello, S., D’Orazi, V., Bellazzini, M., Catanzaro, G., Leone, F., Momany, Y., and Sollima, A. (2013a). NGC 362: another globular cluster with a split red giant branch. *A&A*, 557:A138.
- Carretta, E., Bragaglia, A., Gratton, R. G., Recio-Blanco, A., Lucatello, S., D’Orazi, V., and Cassisi, S. (2010). Properties of stellar generations in globular clusters and relations with global parameters. *A&A*, 516:A55.
- Carretta, E., Gratton, R. G., Bragaglia, A., D’Orazi, V., and Lucatello, S. (2013b). An aluminium tool for multiple stellar generations in the globular clusters 47 Tucanae and M 4. *A&A*, 550:A34.
- Carretta, E., Gratton, R. G., Lucatello, S., Bragaglia, A., and Bonifacio, P. (2005). Abundances of C, N, O in slightly evolved stars in the globular clusters NGC 6397, NGC 6752 and 47 Tuc. *A&A*, 433:597–611.
- Carretta, E., Lucatello, S., Gratton, R. G., Bragaglia, A., and D’Orazi, V. (2011). Multiple stellar populations in the globular cluster NGC 1851. *A&A*, 533:A69.
- Cassisi, S., Marín-Franch, A., Salaris, M., Aparicio, A., Monelli, M., and Pietrinferni, A. (2011). The magnitude difference between the main sequence turn off and the red giant branch bump in Galactic globular clusters. *A&A*, 527:A59.
- Cassisi, S., Salaris, M., Pietrinferni, A., Piotto, G., Milone, A. P., Bedin, L. R., and Anderson, J. (2008). The Double Subgiant Branch of NGC 1851: The Role of the CNO Abundance. *ApJ*, 672:L115–L118.
- Castaing, B., Gunaratne, G., Kadanoff, L., Libchaber, A., and Heslot, F. (1989). Scaling of hard thermal turbulence in Rayleigh-Benard convection. *Journal of Fluid Mechanics*, 204:1–30.
- Castellani, M. and Castellani, V. (1993). Mass loss in globular cluster red giants - an evolutionary investigation. *ApJ*, 407:649–656.
- Castellani, V., Giannone, P., and Renzini, A. (1971). Induced Semi-Convection in Helium-Burning Horizontal-Branch Stars II. *Ap&SS*, 10:355–362.
- Castelli, F., Gratton, R. G., and Kurucz, R. L. (1997). Notes on the convection in the atlas9 model atmospheres. *A&A*, 318:841–869.
- Castelli, F. and Kurucz, R. L. (2004). New Grids of ATLAS9 Model Atmospheres. *ArXiv Astrophysics e-prints*.
- Catelan, M., Borissova, J., Ferraro, F. R., Corwin, T. M., Smith, H. A., and Kurtev, R. (2002). M75, A Globular Cluster with a Trimodal Horizontal Branch. I. Color-Magnitude Diagram. *AJ*, 124:364–378.
- Caughlan, G. R. and Fowler, W. A. (1988). Thermonuclear Reaction Rates V. *Atomic Data and Nuclear Data Tables*, 40:283.

- Cavallo, R. M. and Nagar, N. M. (2000). Aluminum Abundances, Deep Mixing, and the Blue-Tail Second-Parameter Effect in the Globular Clusters M3 and M13. *AJ*, 120:1364–1383.
- Chaboyer, B., Sarajedini, A., and Demarque, P. (1992). Ages of globular clusters and helium diffusion. *ApJ*, 394:515–522.
- Chaboyer, B. and Zahn, J.-P. (1992). Effect of horizontal turbulent diffusion on transport by meridional circulation. *A&A*, 253:173–177.
- Chanamé, J., Pinsonneault, M., and Terndrup, D. M. (2005). Abundance Anomalies and Rotational Evolution of Low-Mass Red Giants: A Maximal Mixing Approach. *ApJ*, 631:540–571.
- Charbonnel, C. (1994). Clues for non-standard mixing on the red giant branch from C-12/C-13 and C-12/N-14 ratios in evolved stars. *A&A*, 282:811–820.
- Charbonnel, C. (1995). A Consistent Explanation for $^{12}\text{C}/^{13}\text{C}$, ^7Li and ^3He Anomalies in Red Giant Stars. *ApJ*, 453:L41+.
- Charbonnel, C. (1996). Destruction of ^3He in Low Mass Stars and Implications for Chemical Evolution. In C. Leitherer, U. Fritze-von-Alvensleben, & J. Huchra, editor, *From Stars to Galaxies: the Impact of Stellar Physics on Galaxy Evolution*, volume 98 of *Astronomical Society of the Pacific Conference Series*, page 213.
- Charbonnel, C. (2010). Globular cluster abundances: the imprint of first-generation massive stars. 266:131–142.
- Charbonnel, C. and Balachandran, S. C. (2000). The Nature of the lithium rich giants. Mixing episodes on the RGB and early-AGB. *A&A*, 359:563–572.
- Charbonnel, C., Brown, J. A., and Wallerstein, G. (1998). Mixing processes during the evolution of red giants with moderate metal deficiencies: the role of molecular-weight barriers. *A&A*, 332:204–214.
- Charbonnel, C. and Do Nascimento, Jr., J. D. (1998). How many low-mass stars do destroy $(3) \text{He}$? *A&A*, 336:915–919.
- Charbonnel, C. and Lagarde, N. (2010). Thermohaline instability and rotation-induced mixing. I. Low- and intermediate-mass solar metallicity stars up to the end of the AGB. *A&A*, 522:A10+.
- Charbonnel, C. and Zahn, J. (2007a). Thermohaline mixing: a physical mechanism governing the photospheric composition of low-mass giants. *A&A*, 467:L15–L18.
- Charbonnel, C. and Zahn, J. (2007b). Inhibition of thermohaline mixing by a magnetic field in Ap star descendants: implications for the Galactic evolution of ^3He . *A&A*, 476:L29–L32.

- Chen, X. and Han, Z. (2004). Effects of chemical composition and thermohaline mixing on the accreting components for low-mass close binaries: application to blue stragglers. *MNRAS*, 355:1182–1195.
- Chieffi, A., Domínguez, I., Limongi, M., and Straniero, O. (2001). Evolution and Nucleosynthesis of Zero-Metal Intermediate-Mass Stars. *ApJ*, 554:1159–1174.
- Chiosi, C., Wood, P. R., and Capitanio, N. (1993). Theoretical models of Cepheid variables and their BVI(c) colors and magnitudes. *ApJS*, 86:541–598.
- Christensen-Dalsgaard, J., Monteiro, M. J. P. F. G., Rempel, M., and Thompson, M. J. (2011). A more realistic representation of overshoot at the base of the solar convective envelope as seen by helioseismology. *MNRAS*, 414:1158–1174.
- Church, R. P., Cristallo, S., Lattanzio, J. C., Stancliffe, R. J., Straniero, O., and Cannon, R. C. (2009). montage: AGB Nucleosynthesis with Full s-Process Calculations. *PASA*, 26:217–224.
- Church, R. P., Lattanzio, J., Angelou, G., Tout, C. A., and Stancliffe, R. J. (2014). Which physics determines the location of the mean molecular weight minimum in red giants? *Monthly Notices of the Royal Astronomical Society*, 443(2):977–984.
- Claret, A. (2007). Does convective core overshooting depend on stellar mass?. Tests using double-lined eclipsing binaries. *A&A*, 475:1019–1025.
- Clayton, D. D. (1983). *Principles of stellar evolution and nucleosynthesis*.
- Cohen, J. G. (1978). Abundances in globular cluster red giants. I - M3 and M13. *ApJ*, 223:487–508.
- Cohen, J. G. (1999). The Spectra of Main-Sequence Stars in Galactic Globular Clusters. I. CH and CN Bands in M13. *AJ*, 117:2428–2433.
- Cohen, J. G. (2011). No Heavy-element Dispersion in the Globular Cluster M92. *ApJ*, 740:L38.
- Cohen, J. G., Briley, M. M., and Stetson, P. B. (2005). C and N Abundances in Stars at the Base of the Red Giant Branch in M15. *AJ*, 130:1177–1193.
- Cohen, J. G. and Meléndez, J. (2005). Abundances in a Large Sample of Stars in M3 and M13. *AJ*, 129:303–329.
- Colucci, J. E. and Bernstein, R. A. (2012). Comparison of Convective Overshooting Models and Their Impact on Abundances from Integrated Light Spectroscopy of Young (less than 3 Gyr) Star Clusters. *ApJ*, 749:124.
- Constantino, T., Campbell, S., Gil-Pons, P., and Lattanzio, J. (2014). On the Necessity of Composition-dependent Low-temperature Opacity in Models of Metal-poor Asymptotic Giant Branch Stars. *ApJ*, 784:56.

- Cook, C. W., Fowler, W. A., Lauritsen, C. C., and Lauritsen, T. (1957). b^{12} , c^{12} , and the red giants. *Phys. Rev.*, 107:508–515.
- Cottrell, P. L. and Da Costa, G. S. (1981). Correlated cyanogen and sodium anomalies in the globular clusters 47 Tuc and NGC 6752. *ApJ*, 245:L79–L82.
- Cristallo, S., Straniero, O., Gallino, R., Piersanti, L., Domínguez, I., and Lederer, M. T. (2009). Evolution, Nucleosynthesis, and Yields of Low-Mass Asymptotic Giant Branch Stars at Different Metallicities. *ApJ*, 696:797–820.
- Cyburt, R. H., Amthor, A. M., Ferguson, R., Meisel, Z., Smith, K., Warren, S., Heger, A., Hoffman, R. D., Rauscher, T., Sakharuk, A., Schatz, H., Thielemann, F. K., and Wiescher, M. (2010). The jina reaclib database: Its recent updates and impact on type-i x-ray bursts. *The Astrophysical Journal Supplement Series*, 189(1):240.
- Cyburt, R. H., Fields, B. D., and Olive, K. A. (2008). An update on the big bang nucleosynthesis prediction for ${}^7\text{Li}$: the problem worsens. *J. Cosmology Astropart. Phys.*, 11:12.
- D’Antona, F., Bellazzini, M., Caloi, V., Pecci, F. F., Galleti, S., and Rood, R. T. (2005). A Helium Spread among the Main-Sequence Stars in NGC 2808. *ApJ*, 631:868–878.
- D’Antona, F. and Caloi, V. (2008). The fraction of second generation stars in globular clusters from the analysis of the horizontal branch. *MNRAS*, 390:693–705.
- D’Antona, F., Caloi, V., Montalbán, J., Ventura, P., and Gratton, R. (2002). Helium variation due to self-pollution among Globular Cluster stars. Consequences on the horizontal branch morphology. *A&A*, 395:69–75.
- D’Antona, F., D’Ercole, A., Carini, R., Vesperini, E., and Ventura, P. (2012). Models for the lithium abundances of multiple populations in globular clusters and the possible role of the big bang lithium. *MNRAS*, 426:1710–1719.
- D’Antona, F. and Ventura, P. (2007). A model for globular cluster extreme anomalies. *MNRAS*, 379:1431–1441.
- Davidson, P. A. (2004). *Turbulence : an introduction for scientists and engineers*.
- Davis, R. (1964). Solar neutrinos. ii. experimental. *Phys. Rev. Lett.*, 12:303–305.
- de Mink, S. E., Pols, O. R., Langer, N., and Izzard, R. G. (2009). Massive binaries as the source of abundance anomalies in globular clusters. *A&A*, 507:L1–L4.
- de Silva, G. M., Gibson, B. K., Lattanzio, J., and Asplund, M. (2009). O and Na abundance patterns in open clusters of the Galactic disk. *A&A*, 500:L25–L28.
- Dearborn, D. S., Bolton, A. J. C., and Eggleton, P. P. (1975a). The effect on the ${}^{12}\text{C}/{}^{13}\text{C}$ ratio of repeated deep mixing to the hydrogen burning shell in a red giant. *MNRAS*, 170:7P–10P.

- Dearborn, D. S. P. (1992). Diagnostics of stellar evolution: The oxygen isotopes. *Phys. Rep.*, 210:367–382.
- Dearborn, D. S. P., Bazan, G., Castor, J., Cavallo, R., Cohl, H., Cook, K., Dossa, D., Eastman, R., Eggleton, P. P., Eltgroth, P., Keller, S., Murray, S., Taylor, A., Turcotte, S., and Djehuty Team (2001). Djehuty: A 3D Hydrodynamic Stellar Evolution Code. In *Bulletin of the American Astronomical Society*, volume 33 of *Bulletin of the American Astronomical Society*, pages 886–+.
- Dearborn, D. S. P., Lambert, D. L., and Tomkin, J. (1975b). The C-12/C-13 ratio in stellar atmospheres. V - Twelve K giants and subgiants. *ApJ*, 200:675–681.
- Dearborn, D. S. P., Lattanzio, J. C., and Eggleton, P. P. (2006). Three-dimensional Numerical Experimentation on the Core Helium Flash of Low-Mass Red Giants. *ApJ*, 639:405–415.
- Dearborn, D. S. P., Schramm, D. N., and Steigman, G. (1986). Destruction of He-3 in stars. *ApJ*, 302:35–38.
- Dearborn, D. S. P., Steigman, G., and Tosi, M. (1996). Galactic Evolution of D and ^3He Including Stellar Production of ^3He . *ApJ*, 465:887–+.
- Decressin, T., Baumgardt, H., and Kroupa, P. (2008). The evolution of two stellar populations in globular clusters. I. The dynamical mixing timescale. *A&A*, 492:101–109.
- Decressin, T., Meynet, G., Charbonnel, C., Prantzos, N., and Ekström, S. (2007). Fast rotating massive stars and the origin of the abundance patterns in galactic globular clusters. *A&A*, 464:1029–1044.
- Demarque, P., Sarajedini, A., and Guo, X.-J. (1994). The gap in the color-magnitude diagram of NGC 2420: A test of convective overshoot and cluster age. *ApJ*, 426:165–169.
- Demarque, P., Zinn, R., Lee, Y.-W., and Yi, S. (2000). The Metallicity Dependence of RR Lyrae Absolute Magnitudes from Synthetic Horizontal-Branch Models. *AJ*, 119:1398–1404.
- Denissenkov, P. A. (2010). Numerical Simulations of Thermohaline Convection: Implications for Extra-mixing in Low-mass RGB Stars. *ApJ*, 723:563–579.
- Denissenkov, P. A., Chaboyer, B., and Li, K. (2006). From Canonical to Enhanced Extra Mixing in Low-Mass Red Giants: Tidally Locked Binaries. *ApJ*, 641:1087–1101.
- Denissenkov, P. A., Da Costa, G. S., Norris, J. E., and Weiss, A. (1998). The puzzling MgAl anticorrelation in globular-cluster red giants: primordial plus deep mixing scenario? *A&A*, 333:926–941.

- Denissenkov, P. A. and Merryfield, W. J. (2011). Thermohaline Mixing: Does it Really Govern the Atmospheric Chemical Composition of Low-mass Red Giants? *ApJ*, 727:L8+.
- Denissenkov, P. A. and Pinsonneault, M. (2008a). ^3He -driven Mixing in Low-Mass Red Giants: Convective Instability in Radiative and Adiabatic Limits. *ApJ*, 684:626–634.
- Denissenkov, P. A. and Pinsonneault, M. (2008b). The Impact of Carbon Enhancement on Extra Mixing in Metal-poor Stars. *ApJ*, 679:1541–1548.
- Denissenkov, P. A. and Tout, C. A. (2000). On a physical mechanism for extra mixing in globular cluster red giants. *MNRAS*, 316:395–406.
- Denissenkov, P. A. and Vandenberg, D. A. (2003). Canonical Extra Mixing in Low-Mass Red Giants. *ApJ*, 593:509–523.
- D’Ercole, A., D’Antona, F., and Vesperini, E. (2011). Formation of multiple populations in globular clusters: constraints on the dilution by pristine gas. *MNRAS*, 415:1304–1309.
- D’Ercole, A., Vesperini, E., D’Antona, F., McMillan, S. L. W., and Recchi, S. (2008). Formation and dynamical evolution of multiple stellar generations in globular clusters. *MNRAS*, 391:825–843.
- Descouvemont, P., Adahchour, A., Angulo, C., Coc, A., and Vangioni-Flam, E. (2004). Compilation and R-matrix analysis of Big Bang nuclear reaction rates. *Atomic Data and Nuclear Data Tables*, 88:203–236.
- di Cecco, A., Becucci, R., Bono, G., Monelli, M., Stetson, P. B., Degl’Innocenti, S., Prada Moroni, P. G., Nonino, M., Weiss, A., Buonanno, R., Calamida, A., Caputo, F., Corsi, C. E., Ferraro, I., Iannicola, G., Pulone, L., Romaniello, M., and Walker, A. R. (2010). On the Absolute Age of the Globular Cluster M92. *PASP*, 122:991–999.
- Di Cecco, A., Bono, G., Stetson, P. B., Pietrinferni, A., Becucci, R., Cassisi, S., Degl’Innocenti, S., Iannicola, G., Prada Moroni, P. G., Buonanno, R., Calamida, A., Caputo, F., Castellani, M., Corsi, C. E., Ferraro, I., Dall’Ora, M., Monelli, M., Nonino, M., Piersimoni, A. M., Pulone, L., Romaniello, M., Salaris, M., Walker, A. R., and Zoccali, M. (2010). On the ΔV^{bump}_{HB} Parameter in Globular Clusters. *ApJ*, 712:527–535.
- Dicus, D. A., Kolb, E. W., Schramm, D. N., and Tubbs, D. L. (1976). Neutrino pair bremsstrahlung including neutral current effects. *ApJ*, 210:481–488.
- Doherty, C. L., Gil-Pons, P., Lau, H. H. B., Lattanzio, J. C., and Siess, L. (2014). Super and massive AGB stars - II. Nucleosynthesis and yields - $Z = 0.02, 0.008$ and 0.004 . *MNRAS*, 437:195–214.
- Doherty, C. L., Siess, L., Lattanzio, J. C., and Gil-Pons, P. (2010). Super asymptotic giant branch stars. I - Evolution code comparison. *MNRAS*, 401:1453–1464.

- Dolan, M., Dearborn, D., Mathews, G., and Wilson, J. (2007). Relativistically Induced Supernovae. In *APS Meeting Abstracts*, page 15006.
- D’Orazi, V., Campbell, S. W., Lugaro, M., Lattanzio, J. C., Pignatari, M., and Carretta, E. (2013a). On the internal pollution mechanisms in the globular cluster NGC 6121 (M4): heavy-element abundances and AGB models. *MNRAS*, 433:366–381.
- D’Orazi, V., Gratton, R., Lucatello, S., Carretta, E., Bragaglia, A., and Marino, A. F. (2010a). Ba Stars and Other Binaries in First and Second Generation Stars in Globular Clusters. *ApJ*, 719:L213–L217.
- D’Orazi, V., Lucatello, S., Gratton, R., Bragaglia, A., Carretta, E., Shen, Z., and Zaggia, S. (2010b). Lithium and Proton-capture Elements in Globular Cluster Dwarfs: The Case of 47 Tuc. *ApJ*, 713:L1–L5.
- D’Orazi, V., Lucatello, S., Lugaro, M., Gratton, R. G., Angelou, G., Bragaglia, A., Carretta, E., Alves-Brito, A., Ivans, I. I., Masseron, T., and Mucciarelli, A. (2013b). Fluorine Variations in the Globular Cluster NGC 6656 (M22): Implications for Internal Enrichment Timescales. *ApJ*, 763:22.
- D’Orazi, V. and Marino, A. F. (2010). Lithium Abundances in Red Giants of M4: Evidence for Asymptotic Giant Branch Star Pollution in Globular Clusters? *ApJ*, 716:L166–L169.
- Drazin, P. and Reid, W. (2004). *Hydrodynamic Stability*. Cambridge University Press.
- Eddington, A. S. (1925). Circulating currents in rotating stars. *The Observatory*, 48:73–75.
- Eggleton, P. P. (1971). The evolution of low mass stars. *MNRAS*, 151:351–+.
- Eggleton, P. P. (1972). Composition changes during stellar evolution. *MNRAS*, 156:361.
- Eggleton, P. P. (1983). Towards consistency in simple prescriptions for stellar convection. *MNRAS*, 204:449–461.
- Eggleton, P. P., Bazan, G., Cavallo, R. M., Dearborn, D. S. P., Dossa, D. D., Keller, S., Taylor, A. G., and Turcotte, S. (2002). DJEHUTY: a code for 3-D modeling of whole stars. In *Bulletin of the American Astronomical Society*, volume 35 of *Bulletin of the American Astronomical Society*, pages 570–+.
- Eggleton, P. P., Dearborn, D. S. P., and Lattanzio, J. C. (2006). Deep Mixing of ^3He : Reconciling Big Bang and Stellar Nucleosynthesis. *Science*, 314:1580–.
- Eggleton, P. P., Dearborn, D. S. P., and Lattanzio, J. C. (2008). Compulsory Deep Mixing of ^3He and CNO Isotopes in the Envelopes of Low-Mass Red Giants. *ApJ*, 677:581–592.

- Eich, C., Zimmermann, M. E., Thorne, K. S., and Zytkow, A. N. (1989). Giant and supergiant stars with degenerate neutron cores. *ApJ*, 346:277–283.
- Epelbaum, E., Krebs, H., Lee, D., and Meißner, U.-G. (2011). Ab Initio Calculation of the Hoyle State. *Physical Review Letters*, 106(19):19–2501.
- Faulkner, D. J. (1968). The evolution of helium shell-burning stars. *MNRAS*, 140:223.
- Fekadu, N., Sandquist, E. L., and Bolte, M. (2007). Photometry of the Globular Cluster NGC 5466: Red Giants and Blue Stragglers. *ApJ*, 663:277–295.
- Fenner, Y., Campbell, S., Karakas, A. I., Lattanzio, J. C., and Gibson, B. K. (2004). Modelling self-pollution of globular clusters from asymptotic giant branch stars. *MNRAS*, 353:789–795.
- Ferguson, J. W., Alexander, D. R., Allard, F., Barman, T., Bodnarik, J. G., Hauschildt, P. H., Heffner-Wong, A., and Tamanai, A. (2005). Low-Temperature Opacities. *ApJ*, 623:585–596.
- Festa, G. G. and Ruderman, M. A. (1969). Neutrino-Pair Bremsstrahlung from a Degenerate Electron Gas. *Physical Review*, 180:1227–1231.
- Fowler, W. A., Caughlan, G. R., and Zimmerman, B. A. (1975). Thermonuclear Reaction Rates, II. *ARA&A*, 13:69–+.
- Freytag, B., Ludwig, H.-G., and Steffen, M. (1996). Hydrodynamical models of stellar convection. The role of overshoot in DA white dwarfs, A-type stars, and the Sun. *A&A*, 313:497–516.
- Fricke, K. (1968). Instabilität stationärer Rotation in Sternen. *ZAp*, 68:317.
- Frost, C. (1997). *Effects of Third Dredge-Up on the Structure of Asymptotic Giant Branch Stars*. PhD thesis, Monash University.
- Fusi Pecci, F., Ferraro, F. R., Crocker, D. A., Rood, R. T., and Buonanno, R. (1990). The variation of the red giant luminosity function 'Bump' with metallicity and the age of the globular clusters. *A&A*, 238:95–110.
- Gallino, R., Busso, M., and Lugaro, M. (1997). Neutron capture nucleosynthesis in AGB stars. In Bernatowicz, T. J. and Zinner, E., editors, *American Institute of Physics Conference Series*, volume 402 of *American Institute of Physics Conference Series*, pages 115–153.
- Gastine, T. and Dintrans, B. (2010). Numerical simulations of the κ -mechanism with convection. *Ap&SS*, 328:245–251.
- Gilroy, K. K. (1989). Carbon isotope ratios and lithium abundances in open cluster giants. *ApJ*, 347:835–848.
- Gilroy, K. K. and Brown, J. A. (1991). Carbon isotope ratios along the giant branch of M67. *ApJ*, 371:578–583.

- Gnedin, O. Y. and Ostriker, J. P. (1997). Destruction of the Galactic Globular Cluster System. *ApJ*, 474:223–+.
- Goldreich, P. and Schubert, G. (1967). Differential Rotation in Stars. *ApJ*, 150:571.
- Gonzalez, O. A., Zoccali, M., Monaco, L., Hill, V., Cassisi, S., Minniti, D., Renzini, A., Barbuy, B., Ortolani, S., and Gomez, A. (2009). Li-rich red giant branch stars in the Galactic bulge. *A&A*, 508:289–295.
- González Hernández, J. I., Bonifacio, P., Caffau, E., Steffen, M., Ludwig, H.-G., Behara, N. T., Sbordone, L., Cayrel, R., and Zaggia, S. (2009). Lithium in the globular cluster NGC 6397. Evidence for dependence on evolutionary status. *A&A*, 505:L13–L16.
- Gratton, R., Sneden, C., and Carretta, E. (2004). Abundance Variations Within Globular Clusters. *ARA&A*, 42:385–440.
- Gratton, R. G., Bonifacio, P., Bragaglia, A., Carretta, E., Castellani, V., Centurion, M., Chieffi, A., Claudi, R., Clementini, G., D’Antona, F., Desidera, S., François, P., Grundahl, F., Lucatello, S., Molaro, P., Pasquini, L., Sneden, C., Spite, F., and Straniero, O. (2001). The O-Na and Mg-Al anticorrelations in turn-off and early subgiants in globular clusters. *A&A*, 369:87–98.
- Gratton, R. G., Carretta, E., and Bragaglia, A. (2012a). Multiple populations in globular clusters. Lessons learned from the Milky Way globular clusters. *A&A Rev.*, 20:50.
- Gratton, R. G., Carretta, E., Bragaglia, A., Lucatello, S., and D’Orazi, V. (2010a). The second and third parameters of the horizontal branch in globular clusters. *A&A*, 517:A81.
- Gratton, R. G., Carretta, E., and Castelli, F. (1996). Abundances of light elements in metal-poor stars. I. Atmospheric parameters and a new T_{eff} scale. *A&A*, 314:191–203.
- Gratton, R. G., D’Orazi, V., Bragaglia, A., Carretta, E., and Lucatello, S. (2010b). The connection between missing AGB stars and extended horizontal branches. *A&A*, 522:A77.
- Gratton, R. G., Fusi Pecci, F., Carretta, E., Clementini, G., Corsi, C. E., and Lattanzi, M. (1997). Ages of Globular Clusters from HIPPARCOS Parallaxes of Local Subdwarfs. *ApJ*, 491:749–+.
- Gratton, R. G., Lucatello, S., Carretta, E., Bragaglia, A., D’Orazi, V., Al Momany, Y., Sollima, A., Salaris, M., and Cassisi, S. (2012b). The Na-O anticorrelation in horizontal branch stars. II. NGC 1851. *A&A*, 539:A19.
- Gratton, R. G., Lucatello, S., Carretta, E., Bragaglia, A., D’Orazi, V., and Momany, Y. A. (2011). The Na-O anticorrelation in horizontal branch stars. I. NGC 2808. *A&A*, 534:A123.

- Gratton, R. G., Lucatello, S., Sollima, A., Carretta, E., Bragaglia, A., Momany, Y., D’Orazi, V., Cassisi, S., Pietrinferni, A., and Salaris, M. (2013). The Na-O anticorrelation in horizontal branch stars. III. 47 Tucanae and M 5. *A&A*, 549:A41.
- Gratton, R. G., Sneden, C., Carretta, E., and Bragaglia, A. (2000). Mixing along the red giant branch in metal-poor field stars. *A&A*, 354:169–187.
- Grossman, S. A. (1996). A theory of non-local mixing-length convection - III. Comparing theory and numerical experiment. *MNRAS*, 279:305–336.
- Grossman, S. A. and Taam, R. E. (1996). Double-Diffusive Mixing-Length Theory, Semiconvection and Massive Star Evolution. *MNRAS*, 283:1165–1178.
- Grundahl, F., Catelan, M., Landsman, W. B., Stetson, P. B., and Andersen, M. I. (1999). Hot Horizontal-Branch Stars: The Ubiquitous Nature of the “Jump” in Strömgren u , Low Gravities, and the Role of Radiative Levitation of Metals. *ApJ*, 524:242–261.
- Grundahl, F., VandenBerg, D. A., Bell, R. A., Andersen, M. I., and Stetson, P. B. (2000). A Distance-Independent Age for the Globular Cluster M92. *AJ*, 120:1884–1891.
- Hansen, C. J. and Kawaler, S. D. (1994). *Stellar Interiors. Physical Principles, Structure, and Evolution*.
- Harris, M. J., Fowler, W. A., Caughlan, G. R., and Zimmerman, B. A. (1983). Thermonuclear reaction rates. III. *ARA&A*, 21:165–176.
- Harris, W. E. (1996). A Catalog of Parameters for Globular Clusters in the Milky Way. *AJ*, 112:1487–+.
- Hata, N., Scherrer, R. J., Steigman, G., Thomas, D., Walker, T. P., Bludman, S., and Langacker, P. (1995). Big Bang nucleosynthesis in crisis? *Physical Review Letters*, 75:3977–3980.
- Heney, L. G., Forbes, J. E., and Gould, N. L. (1964). A New Method of Automatic Computation of Stellar Evolution. *ApJ*, 139:306.
- Herwig, F. (2001). The Evolutionary Timescale of Sakurai’s Object: A Test of Convection Theory? *ApJ*, 554:L71–L74.
- Herwig, F. (2005). Evolution of Asymptotic Giant Branch Stars. *ARA&A*, 43:435–479.
- Herwig, F., Bloeker, T., Schoenberner, D., and El Eid, M. (1997). Stellar evolution of low and intermediate-mass stars. IV. Hydrodynamically-based overshoot and nucleosynthesis in AGB stars. *A&A*, 324:L81–L84.
- Herwig, F., Freytag, B., Hueckstaedt, R. M., and Timmes, F. X. (2006). Hydrodynamic Simulations of He Shell Flash Convection. *ApJ*, 642:1057–1074.

- Heslot, F., Castaing, B., and Libchaber, A. (1987). Transitions to turbulence in helium gas. *Phys. Rev. A*, 36:5870–5873.
- Hesser, J. E. and Bell, R. A. (1980). CN variations among main-sequence 47 Tucanae stars. *ApJ*, 238:L149–L153.
- Hogan, C. J. (1995). Giant branch mixing and the ultimate fate of primordial deuterium in the Galaxy. *ApJ*, 441:L17–L20.
- Hoppe, P., Amari, S., Zinner, E., Ireland, T., and Lewis, R. S. (1994). Carbon, nitrogen, magnesium, silicon, and titanium isotopic compositions of single interstellar silicon carbide grains from the Murchison carbonaceous chondrite. *ApJ*, 430:870–890.
- Hotta, H., Iida, Y., and Yokoyama, T. (2012). Estimation of Turbulent Diffusivity with Direct Numerical Simulation of Stellar Convection. *ApJ*, 751:L9.
- Houdashelt, M. L., Bell, R. A., and Sweigart, A. V. (2000). Improved Color-Temperature Relations and Bolometric Corrections for Cool Stars. *AJ*, 119:1448–1469.
- Howard, L. N. and Veronis, G. (1992). Stability of salt fingers with negligible diffusivity. *Journal of Fluid Mechanics*, 239:511–522.
- Hoyle, F. (1954). On Nuclear Reactions Occuring in Very Hot STARS.I. the Synthesis of Elements from Carbon to Nickel. *ApJS*, 1:121.
- Hubbard, E. N. and Dearborn, D. S. P. (1980). Magnetic mixing and the Arcturus problem. *ApJ*, 239:248–252.
- Hubbard, W. B. and Lampe, M. (1969). Thermal Conduction by Electrons in Stellar Matter. *ApJS*, 18:297.
- Iben, I. (1968a). Age and Initial Helium Abundance of Stars in the Globular Cluster M15. *Nature*, 220:143–146.
- Iben, Jr., I. (1967). Stellar Evolution.VI. Evolution from the Main Sequence to the Red-Giant Branch for Stars of Mass $1 M_{\odot}$, $1.25 M_{\odot}$, and $1.5 M_{\odot}$. *ApJ*, 147:624–+.
- Iben, Jr., I. (1968b). Low-Mass Red Giants. *ApJ*, 154:581.
- Iben, Jr., I. (1975). Thermal pulses; p-capture, alpha-capture, s-process nucleosynthesis; and convective mixing in a star of intermediate mass. *ApJ*, 196:525–547.
- Iben, Jr., I. and Ehrman, J. R. (1962). The Internal Structure of Middle Main-Sequence Stars. *ApJ*, 135:770–+.
- Iben, Jr., I. and Faulkner, J. (1968). On the Age and Initial Helium Abundance of Extreme Population II Stars. *ApJ*, 153:101–+.

- Iben, Jr., I. and Renzini, A. (1983). Asymptotic giant branch evolution and beyond. *ARA&A*, 21:271–342.
- Iglesias, C. A. and Rogers, F. J. (1996). Updated Opal Opacities. *ApJ*, 464:943.
- Iliadis, C. (2007). *Nuclear Physics of Stars*. Wiley-VCH Verlag.
- Itoh, N., Mitake, S., Iyetomi, H., and Ichimaru, S. (1983). Electrical and thermal conductivities of dense matter in the liquid metal phase. I - High-temperature results. *ApJ*, 273:774–782.
- Ivans, I. I., Kraft, R. P., Sneden, C., Smith, G. H., Rich, R. M., and Shetrone, M. (2001). New Analyses of Star-to-Star Abundance Variations among Bright Giants in the Mildly Metal-poor Globular Cluster M5. *AJ*, 122:1438–1463.
- James, G., François, P., Bonifacio, P., Carretta, E., Gratton, R. G., and Spite, F. (2004). Heavy elements and chemical enrichment in globular clusters. *A&A*, 427:825–838.
- Jimenez, R., Thejll, P., Jorgensen, U. G., MacDonald, J., and Pagel, B. (1996). Ages of globular clusters: a new approach. *MNRAS*, 282:926–942.
- Johnson, C. I., Kraft, R. P., Pilachowski, C. A., Sneden, C., Ivans, I. I., and Benman, G. (2005). A 235 Star Sample Sodium, Magnesium, and Aluminum Abundance Study in the Globular Clusters M3 (NGC 5272) and M13 (NGC 6205). *PASP*, 117:1308–1324.
- Johnson, C. I. and Pilachowski, C. A. (2006). A Moderate Sample Size, Multielement Analysis of the Globular Cluster M12 (NGC 6218). *AJ*, 132:2346–2359.
- Johnson, C. I. and Pilachowski, C. A. (2010). Chemical Abundances for 855 Giants in the Globular Cluster Omega Centauri (NGC 5139). *ApJ*, 722:1373–1410.
- Johnson, C. I. and Pilachowski, C. A. (2012). Oxygen and Sodium Abundances in M13 (NGC 6205) Giants: Linking Globular Cluster Formation Scenarios, Deep Mixing, and Post-RGB Evolution. *ApJ*, 754:L38.
- Johnson, H. L. and Sandage, A. R. (1955). The galactic cluster M67 and its significance for stellar evolution. *ApJ*, 121:616–+.
- Kamath, D., Karakas, A. I., and Wood, P. R. (2012). Evolution and Nucleosynthesis of Asymptotic Giant Branch Stars in Three Magellanic Cloud Clusters. *ApJ*, 746:20.
- Karakas, A. I. (2003). *Asymptotic Giant Branch Stars: their influence on binary systems and the interstellar medium*. PhD thesis, Monash University.
- Karakas, A. I. (2010). Updated stellar yields from asymptotic giant branch models. *MNRAS*, 403:1413–1425.
- Keller, L. D., Pilachowski, C. A., and Sneden, C. (2001). $^{12}\text{C}/^{13}\text{C}$ in Metal-poor Field Halo Giants. *AJ*, 122:2554–2560.

- Kelley, D. (1984). Effective Diffusivities Within Oceanic Thermohaline Staircases. *Geophys Res.*, 89:10484–10488.
- King, C. R., Da Costa, G. S., and Demarque, P. (1985). The luminosity function on the subgiant branch of 47 Tucanae A comparison of observation and theory. *ApJ*, 299:674–682.
- Kippenhahn, R. (1969). Secularly Unstable Differential Rotation in Stars. *A&A*, 2:309.
- Kippenhahn, R., Ruschenplatt, G., and Thomas, H. (1980). The time scale of thermohaline mixing in stars. *A&A*, 91:175–180.
- Kippenhahn, R. and Thomas, H.-C. (1978). Accretion belts on white dwarfs. *A&A*, 63:265–272.
- Kippenhahn, R. and Weigert, A. (1990). *Stellar Structure and Evolution*.
- Knobloch, E. and Spruit, H. C. (1982). Stability of differential rotation in stars. *A&A*, 113:261–268.
- Knobloch, E. and Spruit, H. C. (1983). The molecular weight barrier and angular momentum transport in radiative stellar interiors. *A&A*, 125:59–68.
- Kolmogorov, A. (1941). The Local Structure of Turbulence in Incompressible Viscous Fluid for Very Large Reynolds' Numbers. *Akademiia Nauk SSSR Doklady*, 30:301–305.
- Kozitskii, S. (2000). Amplitude equations for a system with thermohaline convection. *Journal of Applied Mechanics and Technical Physics*, 41:429–438. 10.1007/BF02465292.
- Kraft, R. P. (1994). Abundance differences among globular-cluster giants: Primordial versus evolutionary scenarios. *PASP*, 106:553–565.
- Kraft, R. P., Sneden, C., Langer, G. E., and Prosser, C. F. (1992). Oxygen abundances in halo giants. II - Giants in the globular clusters M13 and M3 and the intermediately metal-poor halo field. *AJ*, 104:645–668.
- Kraft, R. P., Sneden, C., Langer, G. E., and Shetrone, M. D. (1993). Oxygen abundances in Halo giants. IV - The oxygen-sodium anticorrelation in a sample of 22 bright giants in M13. *AJ*, 106:1490–1507.
- Krishnamurti, R. (2003). Double-diffusive transport in laboratory thermohaline staircases. *Journal of Fluid Mechanics*, 483:287–314.
- Kuhlen, M., Woosley, W. E., and Glatzmaier, G. A. (2003). 3D Anelastic Simulations of Convection in Massive Stars. In Turcotte, S., Keller, S. C., and Cavallo, R. M., editors, *3D Stellar Evolution*, volume 293 of *Astronomical Society of the Pacific Conference Series*, page 147.

- Kunze, E. (2003). A review of oceanic salt-fingering theory. *Progress In Oceanography*, 56(34):399 – 417. [jce:title;Double-Diffusion in Oceanography;/ce:title;](#)
- Kurucz, R. (1993). ATLAS9 Stellar Atmosphere Programs and 2 km/s grid. *ATLAS9 Stellar Atmosphere Programs and 2 km/s grid. Kurucz CD-ROM No. 13. Cambridge, Mass.: Smithsonian Astrophysical Observatory, 1993.*, 13.
- Lagadec, E., Sloan, G. C., Zijlstra, A. A., Maun, N., and Houck, J. R. (2012). Dust and gas in carbon stars towards the Galactic halo. *MNRAS*, 427:2588–2596.
- Lagarde, N., Decressin, T., Charbonnel, C., Eggenberger, P., Ekström, S., and Palacios, A. (2012). Thermohaline instability and rotation-induced mixing. III. Grid of stellar models and asymptotic asteroseismic quantities from the pre-main sequence up to the AGB for low- and intermediate-mass stars of various metallicities. *A&A*, 543:A108.
- Lai, D. K., Smith, G. H., Bolte, M., Johnson, J. A., Lucatello, S., Kraft, R. P., and Sneden, C. (2011). Chemical Abundances for Evolved Stars in M5: Lithium through Thorium. *AJ*, 141:62.
- Laird, J. B. (1985). Abundances in field dwarf stars. II - Carbon and nitrogen abundances. *ApJ*, 289:556–569.
- Lambert, D. L. and Ries, L. M. (1977). Carbon, nitrogen, and oxygen abundances in 11 G and K giants. *ApJ*, 217:508–520.
- Lambert, D. L. and Ries, L. M. (1981). Carbon, nitrogen, and oxygen abundances in G and K giants. *ApJ*, 248:228–248.
- Langer, G. E., Kraft, R. P., Carbon, D. F., Friel, E., and Oke, J. B. (1986). On the carbon abundance of subgiant stars in the globular cluster M 92. *PASP*, 98:473–485.
- Langer, N., El Eid, M. F., and Fricke, K. J. (1985). Evolution of massive stars with semiconvective diffusion. *A&A*, 145:179–191.
- Larson, R. B. (1996). Globular Clusters as Fossils of Galaxy Formation. In Morrison, H. L. and Sarajedini, A., editors, *Formation of the Galactic Halo...Inside and Out*, volume 92 of *Astronomical Society of the Pacific Conference Series*, page 241.
- Lattanzio, J. (1984). *The Evolution of Initially Inhomogeneous Stars and Low Mass AGB Stars*. PhD thesis, Monash University.
- Lattanzio, J. C. (1986). The asymptotic giant branch evolution of 1.0-3.0 solar mass stars as a function of mass and composition. *ApJ*, 311:708–730.
- Lattanzio, J. C., Vallenari, A., Bertelli, G., and Chiosi, C. (1991). NGC 1866 revisited - Semiconvection versus overshoot. *A&A*, 250:340–350.

- Lebzelter, T. and Hron, J. (2003). Technetium and the third dredge up in AGB stars. I. Field stars. *A&A*, 411:533–542.
- Lederer, M. T. and Aringer, B. (2009). Low temperature Rosseland opacities with varied abundances of carbon and nitrogen. *A&A*, 494:403–416.
- Ledoux, W. P. (1947). Stellar Models with Convection and with Discontinuity of the Mean Molecular. *ApJ*, 105:305.
- Lee, S. (1999). CN and CH Band Strengths of Bright Giants in M3. *AJ*, 118:920–925.
- Lee, S. and Cannon, R. D. (1980). The C-M Diagram of the Globular Cluster, NGC 6752. *Journal of Korean Astronomical Society*, 13:15–26.
- Lee, Y., Joo, S., Han, S., Chung, C., Ree, C. H., Sohn, Y., Kim, Y., Yoon, S., Yi, S. K., and Demarque, P. (2005). Super-Helium-rich Populations and the Origin of Extreme Horizontal-Branch Stars in Globular Clusters. *ApJ*, 621:L57–L60.
- Lind, K., Korn, A. J., Barklem, P. S., and Grundahl, F. (2008). Atomic diffusion and mixing in old stars. II. Observations of stars in the globular cluster NGC 6397 with VLT/FLAMES-GIRAFFE. *A&A*, 490:777–786.
- Lind, K., Primas, F., Charbonnel, C., Grundahl, F., and Asplund, M. (2009). Signatures of intrinsic Li depletion and Li-Na anti-correlation in the metal-poor globular cluster NGC 6397. *A&A*, 503:545–557.
- Ludwig, H.-G., Freytag, B., and Steffen, M. (1999). A calibration of the mixing-length for solar-type stars based on hydrodynamical simulations. I. Methodical aspects and results for solar metallicity. *A&A*, 346:111–124.
- Lugaro, M. (2001). *Nucleosynthesis in AGB Stars*. PhD thesis, Monash University.
- Lugaro, M. (2005). *Stardust from meteorites*.
- Lugaro, M., Karakas, A. I., Stancliffe, R. J., and Rijs, C. (2012). The s-process in Asymptotic Giant Branch Stars of Low Metallicity and the Composition of Carbon-enhanced Metal-poor Stars. *ApJ*, 747:2.
- Maccarone, T. J. and Zurek, D. R. (2012). Novae from isolated white dwarfs as a source of helium for second-generation stars in globular clusters. *MNRAS*, 423:2–6.
- Maeder, A. (1976). Stellar evolution. V - Evolutionary models of population I stars with or without overshooting from convective cores. *A&A*, 47:389–400.
- Maeder, A. (1997). Stellar evolution with rotation. II. A new approach for shear mixing. *A&A*, 321:134–144.
- Maeder, A. (2009). *Physics, Formation and Evolution of Rotating Stars*.

- Marigo, P. (2002). Asymptotic Giant Branch evolution at varying surface C/O ratio: effects of changes in molecular opacities. *A&A*, 387:507–519.
- Marigo, P. and Aringer, B. (2009). Low-temperature gas opacity. *ÆSOPUS*: a versatile and quick computational tool. *A&A*, 508:1539–1569.
- Marino, A. F., Milone, A. P., Piotto, G., Villanova, S., Gratton, R., D’Antona, F., Anderson, J., Bedin, L. R., Bellini, A., Cassisi, S., Geisler, D., Renzini, A., and Zoccali, M. (2011). Sodium-Oxygen Anticorrelation and Neutron-capture Elements in Omega Centauri Stellar Populations. *ApJ*, 731:64.
- Marino, A. F., Villanova, S., Piotto, G., Milone, A. P., Momany, Y., Bedin, L. R., and Medling, A. M. (2008). Spectroscopic and photometric evidence of two stellar populations in the Galactic globular cluster NGC 6121 (M 4). *A&A*, 490:625–640.
- Martell, S. L., Smith, G. H., and Briley, M. M. (2008a). CN Bimodality at Low Metallicity: The Globular Cluster M53. *PASP*, 120:7–15.
- Martell, S. L., Smith, G. H., and Briley, M. M. (2008b). Deep Mixing and Metallicity: Carbon Depletion in Globular Cluster Giants. *AJ*, 136:2522–2532.
- Mathis, S., Palacios, A., and Zahn, J.-P. (2004). On shear-induced turbulence in rotating stars. *A&A*, 425:243–247.
- Mazzitelli, I., D’Antona, F., and Ventura, P. (1999). Full spectrum of turbulence convective mixing. II. Lithium production in AGB stars. *A&A*, 348:846–860.
- Meakin, C. A. and Arnett, D. (2006). Active Carbon and Oxygen Shell Burning Hydrodynamics. *ApJ*, 637:L53–L56.
- Meakin, C. A. and Arnett, D. (2007a). Anelastic and Compressible Simulations of Stellar Oxygen Burning. *ApJ*, 665:690–697.
- Meakin, C. A. and Arnett, D. (2007b). Turbulent Convection in Stellar Interiors. I. Hydrodynamic Simulation. *ApJ*, 667:448–475.
- Meissner, F. and Weiss, A. (2006). Global fitting of globular cluster age indicators. *A&A*, 456:1085–1096.
- Mestel, L. (1953). Rotation and stellar evolution. *MNRAS*, 113:716.
- Meynet, G., Maeder, A., and Mowlavi, N. (2004). Diffusion in stellar interiors: Critical tests of three numerical methods. *A&A*, 416:1023–1036.
- Mikolaitis, Š., Tautvaišienė, G., Gratton, R., Bragaglia, A., and Carretta, E. (2010). Chemical composition of clump stars in the open cluster NGC 6134. *MNRAS*, 407:1866–1874.
- Milone, A. P., Marino, A. F., Piotto, G., Bedin, L. R., Anderson, J., Aparicio, A., Cassisi, S., and Rich, R. M. (2012). A Double Main Sequence in the Globular Cluster NGC 6397. *ApJ*, 745:27.

- Mitake, S., Ichimaru, S., and Itoh, N. (1984). Electrical and thermal conductivities of dense matter in the liquid metal phase. II - Low-temperature quantum corrections. *ApJ*, 277:375–378.
- Mocák, M., Meakin, C. A., Müller, E., and Siess, L. (2011). A New Stellar Mixing Process Operating below Shell Convection Zones Following Off-center Ignition. *ApJ*, 743:55.
- Moehler, S., Sweigart, A. V., Landsman, W. B., and Dreizler, S. (2002). Spectroscopic analyses of the “blue hook” stars in omega Centauri: A test of the late hot flasher scenario. *A&A*, 395:37–43.
- Momany, Y., Bedin, L. R., Cassisi, S., Piotto, G., Ortolani, S., Recio-Blanco, A., De Angeli, F., and Castelli, F. (2004). The ubiquitous nature of the horizontal branch second U-jump. A link with the Blue Hook scenario? *A&A*, 420:605–617.
- Momany, Y., Cassisi, S., Piotto, G., Bedin, L. R., Ortolani, S., Castelli, F., and Recio-Blanco, A. (2003). Why hot horizontal branch stars can appear redder than red giants. *A&A*, 407:303–309.
- Monin, A. S. and I’Aglom, A. M. (1971). *Statistical fluid mechanics; mechanics of turbulence*.
- Mucciarelli, A., Salaris, M., Lovisi, L., Ferraro, F. R., Lanzoni, B., Lucatello, S., and Gratton, R. G. (2011). Lithium abundance in the globular cluster M4: from the turn-off to the red giant branch bump. *MNRAS*, 412:81–94.
- Nataf, D. M., Gould, A. P., Pinsonneault, M. H., and Udalski, A. (2013). Red Giant Branch Bump Brightness and Number Counts in 72 Galactic Globular Clusters Observed with the Hubble Space Telescope. *ApJ*, 766:77.
- Newell, E. B. (1970). The Blue Horizontal-Branch Stars of M15, M92, M13, and M3. *ApJ*, 159:443–+.
- Nield, D. A. (1967). The thermohaline rayleigh-jeffreys problem. *Journal of Fluid Mechanics*, 29(03):545–558.
- Noels, A., Montalbán, J., Miglio, A., Godart, M., and Ventura, P. (2010). Overshooting and semiconvection: structural changes and asteroseismic signatures. *Ap&SS*, 328:227–236.
- Nordhaus, J., Busso, M., Wasserburg, G. J., Blackman, E. G., and Palmerini, S. (2008). Magnetic Mixing in Red Giant and Asymptotic Giant Branch Stars. *ApJ*, 684:L29–L32.
- Norris, J., Cottrell, P. L., Freeman, K. C., and Da Costa, G. S. (1981). The abundance spread in the giants of NGC 6752. *ApJ*, 244:205–220.
- Norris, J. and Pilachowski, C. A. (1985). The sodium-nitrogen correlation within globular clusters. *ApJ*, 299:295–302.

- Norris, J. and Smith, G. H. (1984). A search for cyanogen variations on the lower giant branch of M3. *ApJ*, 287:255–260.
- Oke, J. B. and Schwarzschild, M. (1952). Inhomogeneous Stellar Models. I. Models with a Convective Core and a Discontinuity in the Chemical Composition. *ApJ*, 116:317–+.
- Osborn, W. (1971). Two new CN-strong globular cluster stars. *The Observatory*, 91:223–224.
- Palacios, A., Charbonnel, C., Talon, S., and Siess, L. (2006). Rotational mixing in low-mass stars. II. Self-consistent models of Pop II RGB stars. *A&A*, 453:261–278.
- Palla, F., Bachiller, R., Stanghellini, L., Tosi, M., and Galli, D. (2000). Measurements of $^{12}\text{C}/^{13}\text{C}$ in planetary nebulae: Implications on stellar and Galactic chemical evolution. *A&A*, 355:69–78.
- Palmerini, S., Busso, M., Maiorca, E., and Guandalini, R. (2009). Nucleosynthesis of Light-Element Isotopes in Evolved Stars Experiencing Extended Mixing. *Publications of the Astronomical Society of Australia*, 26:161–167.
- Palmerini, S., Cristallo, S., Busso, M., Abia, C., Uttenthaler, S., Gialanella, L., and Maiorca, E. (2011a). Deep Mixing in Evolved Stars. II. Interpreting Li Abundances in Red Giant Branch and Asymptotic Giant Branch Stars. *ApJ*, 741:26–+.
- Palmerini, S., La Cognata, M., Cristallo, S., and Busso, M. (2011b). Deep Mixing in Evolved Stars. I. The Effect of Reaction Rate Revisions from C to Al. *ApJ*, 729:3–+.
- Pancino, E., Rejkuba, M., Zoccali, M., and Carrera, R. (2010). Low-resolution spectroscopy of main sequence stars belonging to 12 Galactic globular clusters. I. CH and CN band strength variations. *A&A*, 524:A44+.
- Pasquini, L., Avila, G., Blecha, A., Cacciari, C., Cayatte, V., Colless, M., Damiani, F., de Propris, R., Dekker, H., di Marcantonio, P., Farrell, T., Gillingham, P., Guinouard, I., Hammer, F., Kaufer, A., Hill, V., Marteaud, M., Modigliani, A., Mulas, G., North, P., Popovic, D., Rossetti, E., Royer, F., Santin, P., Schmutzer, R., Simond, G., Vola, P., Waller, L., and Zoccali, M. (2002). Installation and commissioning of FLAMES, the VLT Multifibre Facility. *The Messenger*, 110:1–9.
- Pasquini, L., Bonifacio, P., Molaro, P., Francois, P., Spite, F., Gratton, R. G., Carretta, E., and Wolff, B. (2005). Li in NGC 6752 and the formation of globular clusters. *A&A*, 441:549–553.
- Paust, N. E. Q., Chaboyer, B., and Sarajedini, A. (2007). BVI Photometry and the Luminosity Functions of the Globular Cluster M92. *AJ*, 133:2787–2798.

- Pavlenko, Y. V., Jones, H. R. A., and Longmore, A. J. (2003). Carbon abundances and $^{12}\text{C}/^{13}\text{C}$ from globular cluster giants. *MNRAS*, 345:311–324.
- Peterson, R. C. (1980). Evidence from sodium-abundance variations among red giants of M13 for inhomogeneities in the protocluster gas. *ApJ*, 237:L87–L91.
- Peterson, R. C. (1983). The rotation of horizontal-branch stars. II - Members of the globular clusters M3, M5, and M13. *ApJ*, 275:737–751.
- Pignatari, M., Herwig, F., Bennet, M. E., Diehl, S., Fryer, C. L., Hirschi, R., Hungerford, A., Magkotsios, G., Rockefeller, G., Timmes, F. X., and Young, P. (2008). Complete nucleosynthesis calculations for low-mass stars from NuGrid. In *Nuclei in the Cosmos (NIC X)*.
- Pilachowski, C., Sneden, C., Freeland, E., and Casperson, J. (2003). Carbon Isotope Ratios for Giants in Globular Cluster M3: The Unique Lithium-Rich Giant IV-101. *AJ*, 125:794–800.
- Piotto, G. (2009). Observations of multiple populations in star clusters. 258:233–244.
- Piotto, G., Bedin, L. R., Anderson, J., King, I. R., Cassisi, S., Milone, A. P., Villanova, S., Pietrinferni, A., and Renzini, A. (2007). A Triple Main Sequence in the Globular Cluster NGC 2808. *ApJ*, 661:L53–L56.
- Piotto, G., Milone, A. P., Anderson, J., Bedin, L. R., Bellini, A., Cassisi, S., Marino, A. F., Aparicio, A., and Nascimbeni, V. (2012). Hubble Space Telescope Reveals Multiple Sub-giant Branch in Eight Globular Clusters. *ApJ*, 760:39.
- Piotto, G., Villanova, S., Bedin, L. R., Gratton, R., Cassisi, S., Momany, Y., Recio-Blanco, A., Lucatello, S., Anderson, J., King, I. R., Pietrinferni, A., and Carraro, G. (2005). Metallicities on the Double Main Sequence of ω Centauri Imply Large Helium Enhancement. *ApJ*, 621:777–784.
- Pols, O. R. and Tout, C. A. (2001). Thermal pulses and dredge-up in AGB stars with a consistent solution for stellar structure and composition: dependence on convection prescriptions. *Mem. Soc. Astron. Italiana*, 72:299–308.
- Popper, D. M. (1947). Spectral Types of Stars in the Globular Clusters Messier 3 and Messier 13. *ApJ*, 105:204–+.
- Porter, D. H. and Woodward, P. R. (1994). High-resolution simulations of compressible convection using the piecewise-parabolic method. *ApJS*, 93:309–349.
- Porter, D. H. and Woodward, P. R. (2000). Three-dimensional Simulations of Turbulent Compressible Convection. *ApJS*, 127:159–187.
- Prandtl, L. (1925). *Zs. Angew. Math. Mech.*, 5:136.
- Prantzos, N. and Charbonnel, C. (2006). On the self-enrichment scenario of galactic globular clusters: constraints on the IMF. *A&A*, 458:135–149.

- Prantzos, N., Charbonnel, C., and Iliadis, C. (2007). Light nuclei in galactic globular clusters: constraints on the self-enrichment scenario from nucleosynthesis. *A&A*, 470:179–190.
- Press, W. H., Teukolsky, S. A., Vetterling, W. T., and Flannery, B. P. (1992). *Numerical recipes in FORTRAN. The art of scientific computing*.
- Pumo, M. L., Contino, G., Bonanno, A., and Zappalà, R. A. (2010). Convective overshooting and production of s-nuclei in massive stars during their core He-burning phase. *A&A*, 524:A45.
- Radko, T. (2003). A mechanism for layer formation in a double-diffusive fluid. *Journal of Fluid Mechanics*, 497:365–380.
- Radko, T. (2010). Equilibration of weakly nonlinear salt fingers. *Journal of Fluid Mechanics*, 645:121–143.
- Radko, T. and Smith, D. P. (2012). Equilibrium transport in double-diffusive convection. *Journal of Fluid Mechanics*, 692:5–27.
- Raikh, M. E. and Iakovlev, D. G. (1982). Thermal and electrical conductivities of crystals in neutron stars and degenerate dwarfs. *Ap&SS*, 87:193–203.
- Ramadurai, S. (1976). Neutral current and the onset of the helium flash. *MNRAS*, 176:9–13.
- Ramírez, S. V. and Cohen, J. G. (2002). Abundances in Stars from the Red Giant Branch Tip to Near the Main-Sequence Turnoff in M71. III. Abundance Ratios. *AJ*, 123:3277–3297.
- Randich, S., Pasquini, L., and Pallavicini, R. (2000). Evolution of lithium in solar-type stars: clues from intermediate age clusters. *A&A*, 356:L25–L29.
- Rauscher, T. and Thielemann, F.-K. (2000). Astrophysical Reaction Rates From Statistical Model Calculations. *Atomic Data and Nuclear Data Tables*, 75:1–351.
- Recio-Blanco, A. and de Laverny, P. (2007). The extra-mixing efficiency in very low metallicity RGB stars. *A&A*, 461:L13–L16.
- Reid, I. N. (1997). Younger and Brighter - New Distances to Globular Clusters Based on HIPPARCOS Parallax Measurements of Local Subdwarfs. *AJ*, 114:161–+.
- Reimers, D. (1975). Circumstellar absorption lines and mass loss from red giants. *Memoires of the Societe Royale des Sciences de Liege*, 8:369–382.
- Renzini, A. and Voli, M. (1981). Advanced evolutionary stages of intermediate-mass stars. I - Evolution of surface compositions. *A&A*, 94:175–193.
- Riahi, D. (2000). *Flow Instability*. WIT Press.

- Ribas, I., Jordi, C., and Giménez, Á. (2000). The mass dependence of the overshooting parameter determined from eclipsing binary data. *MNRAS*, 318:L55–L59.
- Richard, O., Michaud, G., and Richer, J. (2005). Implications of WMAP Observations on Li Abundance and Stellar Evolution Models. *ApJ*, 619:538–548.
- Riello, M., Cassisi, S., Piotto, G., Recio-Blanco, A., De Angeli, F., Salaris, M., Pietrinferni, A., Bono, G., and Zoccali, M. (2003). The Red Giant Branch luminosity function bump. *A&A*, 410:553–563.
- Robertson, J. W. and Faulkner, D. J. (1972). Semiconvection in the Core-Helium Phase of Stellar Evolution. *ApJ*, 171:309.
- Roederer, I. U. (2011). Primordial r-process Dispersion in Metal-poor Globular Clusters. *ApJ*, 732:L17+.
- Roederer, I. U. and Sneden, C. (2011). Heavy-element Dispersion in the Metal-poor Globular Cluster M92. *AJ*, 142:22+.
- Rogers, F. J. and Nayfonov, A. (2002). Updated and Expanded OPAL Equation-of-State Tables: Implications for Helioseismology. *ApJ*, 576:1064–1074.
- Romano, D., Tosi, M., Matteucci, F., and Chiappini, C. (2003). Light element evolution resulting from WMAP data. *MNRAS*, 346:295–303.
- Rood, R. T., Bania, T. M., and Wilson, T. L. (1984). The 8.7 GHz hyperfine line of He-3(+) in galactic H II regions. *ApJ*, 280:629–647.
- Rosenblum, E., Garaud, P., Traxler, A., and Stellmach, S. (2011). Turbulent Mixing and Layer Formation in Double-diffusive Convection: Three-dimensional Numerical Simulations and Theory. *ApJ*, 731:66.
- Roxburgh, I. W. (1989). Integral constraints on convective overshooting. *A&A*, 211:361–364.
- Russell, S. C. and Dopita, M. A. (1992). Abundances of the heavy elements in the Magellanic Clouds. III - Interpretation of results. *ApJ*, 384:508–522.
- Ryan, S. G., Gregory, S. G., Kolb, U., Beers, T. C., and Kajino, T. (2002). Rapid Rotation of Ultra-Li-depleted Halo Stars and Their Association with Blue Stragglers. *ApJ*, 571:501–511.
- Sabbah, C., Pasquetti, R., Peyret, R., Levitsky, V., and Chashechkin, Y. (2001). Numerical and laboratory experiments of sidewall heating thermohaline convection. *International Journal of Heat and Mass Transfer*, 44(14):2681 – 2697.
- Sackmann, I. and Boothroyd, A. I. (1999). Creation of ^7Li and Destruction of ^3He , ^9Be , ^{10}B , and ^{11}B in Low-Mass Red Giants, Due to Deep Circulation. *ApJ*, 510:217–231.

- Sackmann, I.-J. (1977). What quenches the helium shell flashes. *ApJ*, 212:159–170.
- Salaris, M., Cassisi, S., and Weiss, A. (2002). Red Giant Branch Stars: The Theoretical Framework. *PASP*, 114:375–402.
- Salaris, M., Chieffi, A., and Straniero, O. (1993). The alpha-enhanced isochrones and their impact on the FITS to the Galactic globular cluster system. *ApJ*, 414:580–600.
- Salaris, M. and Weiss, A. (2002). Homogeneous age dating of 55 Galactic globular clusters. Clues to the Galaxy formation mechanisms. *A&A*, 388:492–503.
- Salaris, M., Weiss, A., Ferguson, J. W., and Fusilier, D. J. (2006). On the Primordial Scenario for Abundance Variations within Globular Clusters: The Isochrone Test. *ApJ*, 645:1131–1137.
- Sandage, A. (1970). Main-sequence photometry, color-magnitude diagrams, and ages for the globular clusters M3, M13, M15, and M92. *ApJ*, 162:841–+.
- Sandage, A. and Wildey, R. (1967). The Anomalous Color-Magnitude Diagram of the Remote Globular Cluster NGC 7006. *ApJ*, 150:469–+.
- Sandage, A. R. (1953). The color-magnitude diagram for the globular cluster M 3. *AJ*, 58:61–75.
- Sandage, A. R. (1954). A Survey of Present Knowledge of Globular Clusters and its Significance for Stellar Evolution. *Memoires of the Societe Royale des Sciences de Liege*, 1:254–+.
- Schmitt, R. W., Ledwell, J. R., Montgomery, E. T., Polzin, K. L., and Toole, J. M. (2005). Enhanced diapycnal mixing by salt fingers in the thermocline of the tropical atlantic. *Science*, 308(5722):685–688.
- Schwarzschild, M. and Härm, R. (1958). Evolution of Very Massive Stars. *ApJ*, 128:348.
- Schwarzschild, M. and Härm, R. (1965). Thermal Instability in Non-Degenerate Stars. *ApJ*, 142:855.
- Shaviv, G. and Salpeter, E. E. (1973). Convective Overshooting in Stellar Interior Models. *ApJ*, 184:191–200.
- Shen, C. Y. (1989). The evolution of the double-diffusive instability: Salt fingers. *Physics of Fluids A: Fluid Dynamics*, 1(5):829–844.
- Shen, C. Y. and Veronis, G. (1997). Numerical simulation of two-dimensional salt fingers. *Journal of Geophysical Research: Oceans*, 102(C10):23131–23143.
- Shen, Z.-X., Bonifacio, P., Pasquini, L., and Zaggia, S. (2010). Li - O anticorrelation in NGC 6752: evidence for Li-enriched polluting gas. *A&A*, 524:L2.

- Shetrone, M., Martell, S. L., Wilkerson, R., Adams, J., Siegel, M. H., Smith, G. H., and Bond, H. E. (2010). Light-element Abundance Variations at Low Metallicity: The Globular Cluster NGC 5466. *AJ*, 140:1119–1127.
- Shetrone, M. D. (1996a). Al, Mg and Eu Abundances in Globular Cluster Giants. I. Tests of Deep Mixing. *AJ*, 112:1517–+.
- Shetrone, M. D. (1996b). Magnesium and Carbon isotopes in Globular Cluster Giants. Test of Deep Mixing.II. *AJ*, 112:2639.
- Shetrone, M. D. (2003). Carbon Isotopes in Globular Clusters Down to the Bump in the Luminosity Function. *ApJ*, 585:L45–L48.
- Siess, L. (2006). Evolution of massive AGB stars. I. Carbon burning phase. *A&A*, 448:717–729.
- Siess, L. (2009). Thermohaline mixing in super-AGB stars. *A&A*, 497:463–468.
- Siess, L., Dufour, E., and Forestini, M. (2000). An internet server for pre-main sequence tracks of low- and intermediate-mass stars. *A&A*, 358:593–599.
- Singh, H. P., Roxburgh, I. W., and Chan, K. L. (1995). Three-dimensional simulation of penetrative convection: penetration below a convection zone. *A&A*, 295:703.
- Skrutskie, M. F., Cutri, R. M., Stiening, R., Weinberg, M. D., Schneider, S., Carpenter, J. M., Beichman, C., Capps, R., Chester, T., Elias, J., Huchra, J., Liebert, J., Lonsdale, C., Monet, D. G., Price, S., Seitzer, P., Jarrett, T., Kirkpatrick, J. D., Gizis, J. E., Howard, E., Evans, T., Fowler, J., Fullmer, L., Hurt, R., Light, R., Kopan, E. L., Marsh, K. A., McCallon, H. L., Tam, R., Van Dyk, S., and Wheelock, S. (2006). The Two Micron All Sky Survey (2MASS). *AJ*, 131:1163–1183.
- Smiljanic, R., Gauderon, R., North, P., Barbuy, B., Charbonnel, C., and Mowlavi, N. (2009). CNONa and $^{12}\text{C}/^{13}\text{C}$ in giant stars of 10 open clusters. *A&A*, 502:267–282.
- Smith, G. H. (2002). CN Abundance Inhomogeneities in the Globular Cluster M3: Results Based on Merged Data Sets from the Literature. *PASP*, 114:1097–1107.
- Smith, G. H. (2006). Wolf-Rayet and OB Star Self-Enrichment of Globular Clusters? *PASP*, 118:1225–1237.
- Smith, G. H. (2008). Are Inhomogeneities of the Lighter Elements C through Al in Globular Clusters Accompanied by Variations in Heavy Neutron-Addition Elements? *PASP*, 120:952–971.
- Smith, G. H., Briley, M. M., and Harbeck, D. (2005). A Comparison between Carbon and Nitrogen Abundances of Bright Giants in the Globular Clusters M13, M10, and NGC 7006. *AJ*, 129:1589–1595.

- Smith, G. H. and Kraft, R. P. (1996). On the Possibility of Nova Enrichment of Globular Clusters. *PASP*, 108:344–+.
- Smith, G. H. and Martell, S. L. (2003). Comparing Deep Mixing in Globular Cluster and Halo Field Giants: Carbon Abundance Data from the Literature. *PASP*, 115:1211–1219.
- Smith, G. H., Shetrone, M. D., Bell, R. A., Churchill, C. W., and Briley, M. M. (1996). CNO Abundances of Bright Giants in the Globular Clusters M3 and M13. *AJ*, 112:1511–+.
- Smith, G. H., Shetrone, M. D., and Strader, J. (2007). Carbon Isotope Ratios on the Upper Red Giant Branch of Messier 71. *PASP*, 119:722–732.
- Smolinski, J. P., Martell, S. L., Beers, T. C., and Lee, Y. S. (2011). A Survey of CN and CH Variations in Galactic Globular Clusters from Sloan Digital Sky Survey Spectroscopy. *AJ*, 142:126.
- Snedden, C., Kraft, R. P., Guhathakurta, P., Peterson, R. C., and Fulbright, J. P. (2004). The Chemical Composition Contrast between M3 and M13 Revisited: New Abundances for 28 Giant Stars in M3. *AJ*, 127:2162–2184.
- Snedden, C., Kraft, R. P., Prosser, C. F., and Langer, G. E. (1991). Oxygen abundances in halo giants. I - Giants in the very metal-poor globular clusters M92 and M15 and the metal-poor halo field. *AJ*, 102:2001–2021.
- Snedden, C., Kraft, R. P., Prosser, C. F., and Langer, G. E. (1992). Oxygen abundances in halo giants. III - Giants in the mildly metal-poor globular cluster M5. *AJ*, 104:2121–2140.
- Snedden, C., Kraft, R. P., Shetrone, M. D., Smith, G. H., Langer, G. E., and Prosser, C. F. (1997). Star-To-Star Abundance Variations Among Bright Giants in the Metal-Poor Globular Cluster M15. *AJ*, 114:1964–+.
- Snedden, C., Pilachowski, C. A., and Kraft, R. P. (2000). Barium and Sodium Abundances in the Globular Clusters M15 and M92. *AJ*, 120:1351–1363.
- Snedden, C., Pilachowski, C. A., and Vandenberg, D. A. (1986). Carbon isotope ratios in field Population II giant stars. *ApJ*, 311:826–842.
- Snedden, C. A. (1973). *Carbon and Nitrogen Abundances in Metal-Poor Stars*. PhD thesis, THE UNIVERSITY OF TEXAS AT AUSTIN.
- Sollima, A., Ferraro, F. R., Bellazzini, M., Origlia, L., Straniero, O., and Pancino, E. (2007). Deep FORS1 Observations of the Double Main Sequence of ω Centauri. *ApJ*, 654:915–922.
- Spiegel, E. A. (1971). Convection in Stars: I. Basic Boussinesq Convection. *ARA&A*, 9:323.

- Spite, F. and Spite, M. (1982). Abundance of lithium in unevolved halo stars and old disk stars - Interpretation and consequences. *A&A*, 115:357–366.
- Spite, M., Cayrel, R., Hill, V., Spite, F., François, P., Plez, B., Bonifacio, P., Molaro, P., Depagne, E., Andersen, J., Barbuy, B., Beers, T. C., Nordström, B., and Primas, F. (2006). First stars IX - Mixing in extremely metal-poor giants. Variation of the $^{12}\text{C}/^{13}\text{C}$, $[\text{Na}/\text{Mg}]$ and $[\text{Al}/\text{Mg}]$ ratios. *A&A*, 455:291–301.
- Spite, M., Cayrel, R., Plez, B., Hill, V., Spite, F., Depagne, E., François, P., Bonifacio, P., Barbuy, B., Beers, T., Andersen, J., Molaro, P., Nordström, B., and Primas, F. (2005). First stars VI - Abundances of C, N, O, Li, and mixing in extremely metal-poor giants. Galactic evolution of the light elements. *A&A*, 430:655–668.
- Spruit, H. C. (1992). The rate of mixing in semiconvective zones. *A&A*, 253:131–138.
- Stancliffe, R. J. (2005). *The Evolution and Nucleosynthesis of Thermally Pulsing Asymptotic Giant Branch Stars*. PhD thesis, Cambridge University.
- Stancliffe, R. J. (2006). Does simultaneous solution matter for stellar evolution codes? *MNRAS*, 370:1817–1822.
- Stancliffe, R. J. (2010). The effects of thermohaline mixing on low-metallicity asymptotic giant branch stars. *MNRAS*, 403:505–515.
- Stancliffe, R. J., Church, R. P., Angelou, G. C., and Lattanzio, J. C. (2009). The depletion of carbon by extra mixing in metal-poor giants. *MNRAS*, 396:2313–2318.
- Stancliffe, R. J., Dearborn, D. S. P., Lattanzio, J. C., Heap, S. A., and Campbell, S. W. (2011). Three-dimensional Hydrodynamical Simulations of a Proton Ingestion Episode in a Low-metallicity Asymptotic Giant Branch Star. *ApJ*, 742:121.
- Stancliffe, R. J. and Glebbeek, E. (2008). Thermohaline mixing and gravitational settling in carbon-enhanced metal-poor stars. *MNRAS*, 389:1828–1838.
- Stellmach, S., Traxler, A., Garaud, P., Brummell, N., and Radko, T. (2011). Dynamics of fingering convection. Part 2 The formation of thermohaline staircases. *Journal of Fluid Mechanics*, 677:554–571.
- Stern, M. (1960). The salt-fountain and thermohaline convection. *Tellus*, 12.
- Stern, M. E. (1969). Collective instability of salt fingers. *Journal of Fluid Mechanics*, null:209–218.
- Stommel, H., Arons, A. B., and Blanchard, D. (1956). An oceanographical curiosity: the perpetual salt fountain. *Deep Sea Research (1953)*, 3(2):152 – 153.

- Stothers, R. (1970). Internal structure of upper main-sequence stars. *MNRAS*, 151:65.
- Stothers, R. and Simon, N. R. (1969). An Explanation for the Blue Sequence of Variable Stars. *ApJ*, 157:673–+.
- Straniero, O., Gallino, R., and Cristallo, S. (2006). s process in low-mass asymptotic giant branch stars. *Nuclear Physics A*, 777:311–339.
- Straniero, O., Limongi, M., Chieffi, A., Dominguez, I., Busso, M., and Gallino, R. (2000). Thermally pulsing AGB models of intermediate mass stars. *Mem. Soc. Astron. Italiana*, 71:719.
- Suntzeff, N. B. (1981). Carbon and nitrogen abundances in the giant stars of the globular clusters M3 and M13. *ApJS*, 47:1–32.
- Suntzeff, N. B. (1989). CNO abundances in the metal-poor globular clusters. In G. Cayrel de Strobel, editor, *The Abundance Spread within Globular Clusters: Spectroscopy of Individual Stars*, pages 71–81.
- Suntzeff, N. B. and Smith, V. V. (1991). Carbon isotopic abundances in giant stars in the CN-bimodal globular clusters NGC 6752 and M4. *ApJ*, 381:160–172.
- Sweigart, A. V. (1978). Survey of some recent stellar-evolution calculations. In A. G. D. Philip & D. S. Hayes, editor, *The HR Diagram - The 100th Anniversary of Henry Norris Russell*, volume 80 of *IAU Symposium*, pages 333–343.
- Sweigart, A. V. and Mengel, J. G. (1979). Meridional circulation and CNO anomalies in red giant stars. *ApJ*, 229:624–641.
- Tait, R. I. and Howe, M. R. (1971). Thermohaline Staircases nature, 178 , pp doi:10.1038/231178a0. *Nature*, 231:178–179.
- Thomas, H.-C. (1967). Sternentwicklung VIII. Der Helium-Flash bei einem Stern von 1. 3 Sonnenmassen. *ZAp*, 67:420.
- Thompson, M. J., Christensen-Dalsgaard, J., Miesch, M. S., and Toomre, J. (2003). The Internal Rotation of the Sun. *ARA&A*, 41:599–643.
- Thorne, K. S. and Żytkow, A. N. (1975). Red giants and supergiants with degenerate neutron cores. *ApJ*, 199:L19–L24.
- Thorne, K. S. and Żytkow, A. N. (1977). Stars with degenerate neutron cores. I - Structure of equilibrium models. *ApJ*, 212:832–858.
- Thorpe, S. A., Hutt, P. K., and Soulsby, R. (1969). The effect of horizontal gradients on thermohaline convection. *Journal of Fluid Mechanics*, 38(02):375–400.
- Timmes, F. X. and Arnett, D. (1999). The Accuracy, Consistency, and Speed of Five Equations of State for Stellar Hydrodynamics. *ApJS*, 125:277–294.

- Timmes, F. X. and Swesty, F. D. (2000). The Accuracy, Consistency, and Speed of an Electron-Positron Equation of State Based on Table Interpolation of the Helmholtz Free Energy. *ApJS*, 126:501–516.
- Tomkin, J., Luck, R. E., and Lambert, D. L. (1976). The $^{12}\text{C}/^{13}\text{C}$ ratio in stellar atmospheres. VII. 38 giants and supergiants. *ApJ*, 210:694–701.
- Tosi, M. (1998). Galactic Evolution of D and 3He . *Space Sci. Rev.*, 84:207–218.
- Traxler, A., Garaud, P., and Stellmach, S. (2011a). Numerically Determined Transport Laws for Fingering (“Thermohaline”) Convection in Astrophysics. *ApJ*, 728:L29+.
- Traxler, A., Stellmach, S., Garaud, P., Radko, T., and Brummell, N. (2011b). Dynamics of fingering convection. Part 1 Small-scale fluxes and large-scale instabilities. *Journal of Fluid Mechanics*, 677:530–553.
- Trefzger, D. V., Langer, G. E., Carbon, D. F., Suntzeff, N. B., and Kraft, R. P. (1983). Carbon and nitrogen abundances in giant stars of the metal-poor globular cluster M15. *ApJ*, 266:144–159.
- Troisi, F., Bono, G., Stetson, P. B., Pietrinferni, A., Weiss, A., Fabrizio, M., Ferraro, I., Cecco, A. D., Iannicola, G., Buonanno, R., Calamida, A., Caputo, F., Corsi, C. E., Dall’Ora, M., Kunder, A., Monelli, M., Nonino, M., Piersimoni, A. M., Pulone, L., Romaniello, M., Walker, A. R., and Zoccali, M. (2011). On a New Parameter to Estimate the Helium Content in Old Stellar Systems. *PASP*, 123:879–891.
- Turcotte, S., Bazan, G., Castor, J., Cavallo, R., Cohl, H., Cook, K., Dearborn, D. S. P., Dossa, D., Eastman, R., Eggleton, P. P., Eltgroth, P., Keller, S., Murray, S., and Taylor, A. (2002). Djehuty: a Code for Modeling Whole Stars in Three Dimensions. In C. Aerts, T. R. Bedding, & J. Christensen-Dalsgaard, editor, *IAU Colloq. 185: Radial and Nonradial Pulsations as Probes of Stellar Physics*, volume 259 of *Astronomical Society of the Pacific Conference Series*, pages 72+.
- Turing, A. M. (1948). Rounding-off errors in matrix processes. *The Quarterly Journal of Mechanics and Applied Mathematics*, 1(1):287–308.
- Turner, J. (1973). *Buoyancy Effects in Fluids*. Cambridge at the University Press.
- Ulrich, R. K. (1971). Evolution of Stars Containing ^3He . *ApJ*, 168:57+.
- Ulrich, R. K. (1972). Thermohaline Convection in Stellar Interiors. *ApJ*, 172:165+.
- VandenBerg, D. A. (2000). Models for Old, Metal-Poor Stars with Enhanced α -Element Abundances. II. Their Implications for the Ages of the Galaxy’s Globular Clusters and Field Halo Stars. *ApJS*, 129:315–352.

- Vassiliadis, E. and Wood, P. R. (1993). Evolution of low- and intermediate-mass stars to the end of the asymptotic giant branch with mass loss. *ApJ*, 413:641–657.
- Ventura, P. and D’Antona, F. (2010). The role of lithium production in massive AGB and super-AGB stars for the understanding of multiple populations in globular clusters. *MNRAS*, 402:L72–L76.
- Ventura, P. and D’Antona, F. (2011). Hot bottom burning in the envelope of super asymptotic giant branch stars. *MNRAS*, 410:2760–2766.
- Ventura, P., D’Antona, F., Mazzitelli, I., and Gratton, R. (2001). Predictions for Self-Pollution in Globular Cluster Stars. *ApJ*, 550:L65–L69.
- Ventura, P. and Marigo, P. (2009). Evolution and chemical yields of AGB stars: effects of low-temperature opacities. *MNRAS*, 399:L54–L58.
- Veronis, G. (1965). On Finite Amplitude Instability in Thermohaline Convection. *J. mar. Res.*, 23:1 – 17.
- Villanova, S. and Geisler, D. (2011). Bimodality of light and s-elements in M4 (NGC 6121). A hint for the massive main-sequence star pollution scenario. *A&A*, 535:A31.
- Vogt, H. (1925). Zum Strahlungsgleichgewicht der Sterne. *Astronomische Nachrichten*, 223:229–+.
- von Zeipel, H. (1924a). The radiative equilibrium of a rotating system of gaseous masses. *MNRAS*, 84:665–683.
- von Zeipel, H. (1924b). The radiative equilibrium of a slightly oblate rotating star. *MNRAS*, 84:684–701.
- Wasserburg, G. J., Boothroyd, A. I., and Sackmann, I. (1995). Deep Circulation in Red Giant Stars: A Solution to the Carbon and Oxygen Isotope Puzzles? *ApJ*, 447:L37+.
- Weigert, A. (1966). Sternentwicklung VI: Entwicklung mit Neutrinoverlust und thermische Pulse der Helium-Schalenquelle bei einem Stern von 5 Sonnenmassen. *ZAp*, 64:395.
- Weiss, A. and Charbonnel, C. (2004). Mixing along the Red Giant Branch. *Memorie della Societa Astronomica Italiana*, 75:347–+.
- Weiss, A., Hillebrandt, W., Thomas, H.-C., and Ritter, H. (2004). *Cox and Giuli’s Principles of Stellar Structure*.
- Winters, J. M., Le Bertre, T., Jeong, K. S., Helling, C., and Sedlmayr, E. (2000). A systematic investigation of the mass loss mechanism in dust forming long-period variable stars. *A&A*, 361:641–659.

- Wood, P. R. (1981). On the entropy of mixing, with particular reference to its effect on dredge-up during helium shell flashes. *ApJ*, 248:311–314.
- Wood, P. R. (2007). Mass Loss from Low- and Intermediate-mass Stars. In Stancliffe, R. J., Houdek, G., Martin, R. G., and Tout, C. A., editors, *Unsolved Problems in Stellar Physics: A Conference in Honor of Douglas Gough*, volume 948 of *American Institute of Physics Conference Series*, pages 335–343.
- Wu, X.-Z. and Libchaber, A. (1992). Scaling relations in thermal turbulence: The aspect-ratio dependence. *Phys. Rev. A*, 45:842–845.
- Xiong, D. R. (1985). Convective overshooting in stellar internal models. *A&A*, 150:133–138.
- Yong, D., Aoki, W., and Lambert, D. L. (2006). Mg Isotope Ratios in Giant Stars of the Globular Clusters M13 and M71. *ApJ*, 638:1018–1027.
- Yong, D., Grundahl, F., Lambert, D. L., Nissen, P. E., and Shetrone, M. D. (2003). Mg isotopic ratios in giant stars of the globular cluster NGC 6752. *A&A*, 402:985–1001.
- Zahn, J.-P. (1991). Convective penetration in stellar interiors. *A&A*, 252:179–188.
- Zhang, Q. S. (2012a). Testing the Core Overshoot Mixing Described by a Turbulent Convection Model on the Eclipsing Binary Star HY VIR. *ApJ*, 761:153.
- Zhang, Q. S. (2012b). The diffusive overshooting approach to Li abundance in clusters. *MNRAS*, 427:1441–1448.
- Zinner, E. (2008). Stardust in the Laboratory. *PASA*, 25:7–17.
- Zoccali, M., Cassisi, S., Piotto, G., Bono, G., and Salaris, M. (1999). Comparison between Predicted and Empirical $\Delta V^{\text{bump}}_{\text{HB}}$ in Galactic Globular Clusters. *ApJ*, 518:L49–L52.